SEVEN-COORDINATE COMPLEXES FOR WATER OXIDATION CATALYSIS: FROM MOLECULAR CHARACTERIZATION TO SOLID STATE PHOTOCATALYSIS

Roc Matheu Montserrat

Acreditation

FAIG CONSTAR que aquest treball, titulat “Seven-Coordinate Complexes for Water Oxidation Catalysis: From Molecular Characterization To Solid State Photocatalysis”, que presenta Roc Matheu Montserrat per a l’obtenció del títol de Doctor, ha estat realitzat sota la meva direcció al grup d’Antoni Llobet a l’ Institut Català d’Investigació Química.

I STATE that the present study, entitled “Seven-Coordinate Complexes for Water Oxidation Catalysis: From Molecular Characterization To Solid State Photocatalysis”, presented by Roc Matheu Montserrat for the award of the degree of Doctor, has been carried out under my supervision at the group of Antoni Llobet in the Institut Català d’Investigació Química

Tarragona, 27 de Juny, 2017

Els directors de la tesi doctoral

Dr. Antoni Llobet i Dalmases

Group leader

Insitut Català d’Investigació Química

Dr. Xavier Sala Román

Associate Professor

Universitat Autònoma de Barcelona

Agraïments/ *Acknowledgements*

Durant la tesis he relacionat fer la tesis amb el senderisme: has de saber on vas , has d'estar ben organitzat i has de mantenir un bon ritme per arribar a bon port abans que el sol es pongui.

El primer que necessites en el viatge és tenir guies i referencies. M'agradaria agrair de manera molt sincera als meus directors de tesis, l'Antoni Llobet I el Xavier Sala, per ser referents i guies durant aquests anys: tant els moments pífies inicials com en els darrers moments d'incertesa existencial. Per suposat, no cal mencionar que m'agradaria agrair-los la oportunitat de endinsar-me en el viatge. La segona norma de qualsevol viatge és no es pot anar sol. Un equip per compartir experiències i fer-se suport. Aquí m'encantaria agrair el meu equip: des de les primeres etapes que vaig fer amb el Craig, el Maji i el Joan i d'altres, a la segona etapa amb els dos labs i el Sam, la Serena, el Lorenzo, la Laia; i la darrera amb el Sergi, el Jordi, el CJ, l'Abi, el Asmaul, la Laura la Natalii, Primavera, Marcos i Dooshaye. Però especialement m'agradaria agrair al Pablo, la Mª José i la Carolina per carregar-me la meva motxilla moltes vegades i animar-me moltes altres. Han estat molts anys compartint! Finalment, estar ben equipat és fonamental per fer els passos més perillosos de les etapes. Aquí és indubtable que equip tècnic que tenim a l'ICIQ és excepcional. Infinits agraïments a ChromTae, RMN, Chem Reactions, Fernando, X-ray, compres, logística, manteniment, el vidrier o el taller mecànic. Sense vosaltres, seria una imprudència fer cap viatge a l'ICIQ.

Els viatges a peu han estat sempre molt relacionat a alguna cosa més profunda, a allò que no es pot descriure. Alguns feien travesses per veure màrtirs, altres fan pelegrinatge per contemplar cubs i d'altres per amor sincer . En el meu cas el meu amor està partit entre tres parts equilàters: la meva família, les meves amistats i la Ariane. A les dues primeres dedico el meu viatge. Amb la tercera encara hi estic viatjant.

During the development of my PhD I have related the thesis with trekking: you must know where you go, you must be organized and you have to be constant to arrive to the destination before the sunset.

The first thing you need for your trip are guides and references. I would like to acknowledge to my directors, Antoni Llobet and Xavier Sala, to be my referents during these years: both in initial moments with lots of mistakes and in the last moments of existential doubts. Also, I am extremely grateful with them for the opportunity to start this trip. Secondly, a fundamental rule in any trip is that you must not go alone. You need a team to share experiences and to provide mutual support. Here, I would like to acknowledge my team: from the first period with Craig, Maji and Joan; to the second period with Sam, Serena, Lorenzo and Laia; or the last one with Sergi, Jordi, CJ, Abi, Asmaul, Laura, Natalii, Primavera, Marcos and Dooshaye. But I would like to specially thank Pablo, Mª Jose and Carolina to carry my backpack many times and hurry me up many others. Finally, having the proper equipment to tackle the most difficult steps is fundamental. Here it is indubitable that the technical support we have at ICIQ is exceptional. I sincerely thank to the ChromTae, RMN, Chem Reactions, Fernando, X-ray, compres, logística, manteniment, el vidier or el taller mecànic units. Without your support, any trip at ICIQ would be a very dangereous thing.

Trekking has always been related to something deep, something indescribable. Many walk to see martyrs, others make a pilgrimage to contemplate cubes or others it is for honest love. To me, the love is shared in three identical parts: my family, my friends and Ariane. I dedicate my trip to the first two. With the third one I am still travelling.

The work performed in the present doctoral thesis has been possible thanks to the funding of:

Institut Català d'Investigació Química, Ministerio de Economía y Competitividad and FEDER (PRI-PIBN-2011-1278, CTQ 2013 - 49075 – R, CTQ 2015 – 64261 - R and CTQ 2016 - 80058 – R), AGAUR (2014 SGR-915) and la Caixa Fundation (PhD scholarship).

Abstract

Chapter 1. *General Introduction*

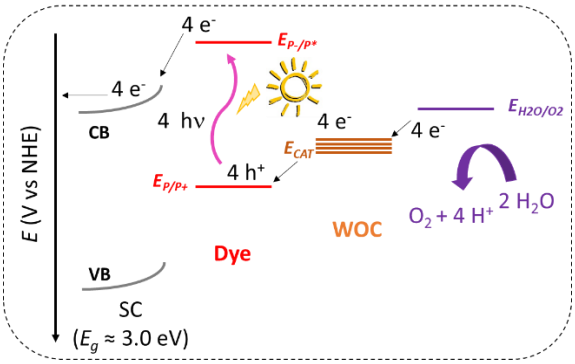

This chapter briefly introduces the motivation and background for the field of research of this thesis, molecular water oxidation. The most relevant molecular water oxidation catalysts in the homogeneous phase are presented together with the relevant features that determine the enhancement in their performance. The challenge of transferring the activity in solution to solid-state molecular anodes and photoanodes is also introduced. The progress in the design and performance of the latters is also described and their major breakthroughs highlighted.

Chapter 2. *Objectives*

Chapter 3. H-bonding rockets water oxidation catalysis in new Ru complexes

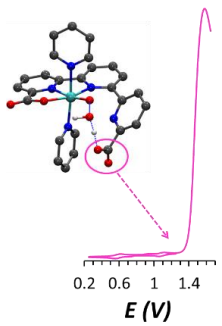

The synthesis, characterization, redox properties and catalytic activity of two new families of complexes based on the tda^{2-} or the $t5a^{3-}$ ligand and pyridine as axial ligands are reported. The related Ru=O species of the presented Ru-tda and Ru-t5a complexes are among the fastest molecular water oxidation catalysts in the literature due to H intramolecular bonding provided by a pendant carboxylate.

Chapter 4. Tuning the catalytic performance of seven-coordinate Ru complexes in water oxidation: quantification of the pi-pi stacking effect and intramolecular H bonding

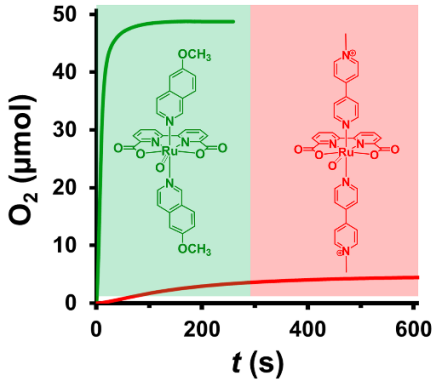

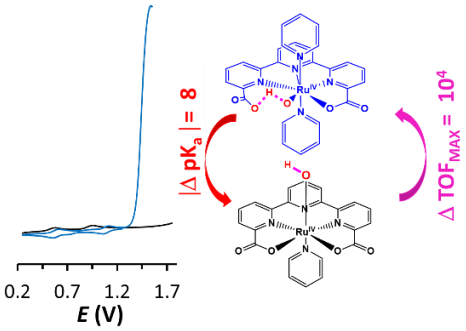

New Ru-bda and Ru-tda complexes are developed to quantify the factors that determine their activity in water oxidation catalysis. In the first work, new Ru-bda complexes bearing axial ligands that favor and disfavor intermolecular pi-pi stacking interactions are synthetized and tested as water oxidation catalysts. In the second and third works, Ru-tda complexes with one or two Ru-OH_2 groups that do not promote intramolecular H bonding are prepared. The comparison of the electrochemical and catalytic data obtained allows quantifying the role of the intramolecular H bonding in the water oxidation catalysis by Ru-tda complexes

Chapter 5. Foot of the Wave Analysis for Mechanistic Elucidation and Benchmarking Applications in Molecular Water Oxidation Catalysis

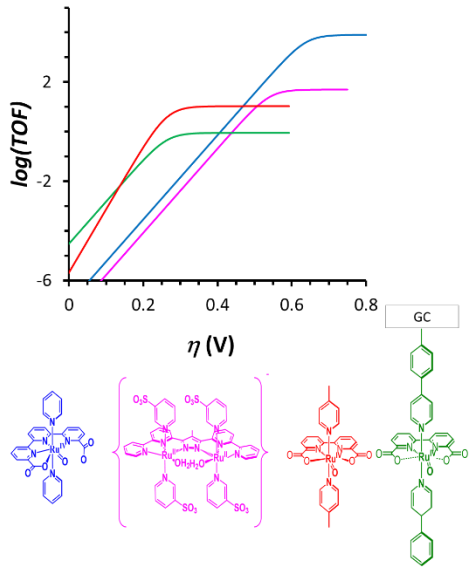

The mathematical description for the foot of the wave analysis (FOWA) applied to the electrocatalytic oxidation of water to dioxyen is reported either for water oxidation catalysts (WOCs) working through the water nucleophilic attack or the interaction of two M-O units. Further, the application of the FOWA at different catalyst concentrations allows elucidating the reaction mechanism that operates in each case. This has been used in one hand to corroborate previously reported WOC mechanisms and to elucidate the reaction mechanism of seven-coordinate Ru catalysts.

Chapter 6. Nature and Behaviour of molecular anodes based on Ru-bda and Ru-tda and carbon surfaces.

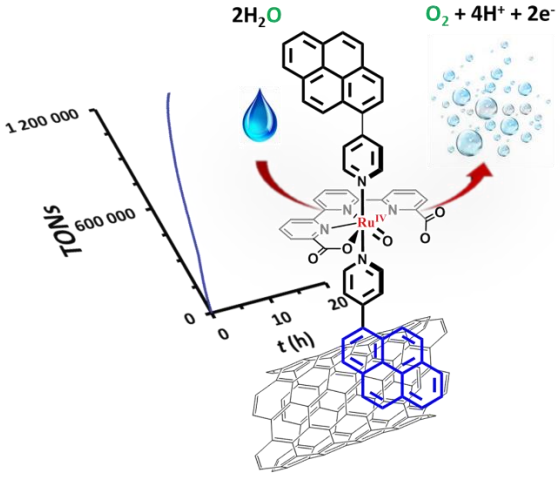

Molecular anodes based on the seven-coordinate Ru-bda and Ru-tda complexes and glassy carbon electrodes are prepared. The axial ligands of the Ru-bda complex are modified to introduce diazonium moieties able to generate a C-C bond with the carbon surface through electroreduction while pyrene-modified pyridine ligands are used to immobilize a Ru-tda complex on multi-walled carbon nanotubes. The performance of the two molecular anodes is assessed and X-ray Absorption Spectroscopy and Electrochemistry are used to monitor the nature of the molecular catalyst.

Chapter 7. Photoelectrochemical Behavior of Ru-Based Water-Oxidation Catalysts Bound to TiO_2-Protected Si Photoanodes.

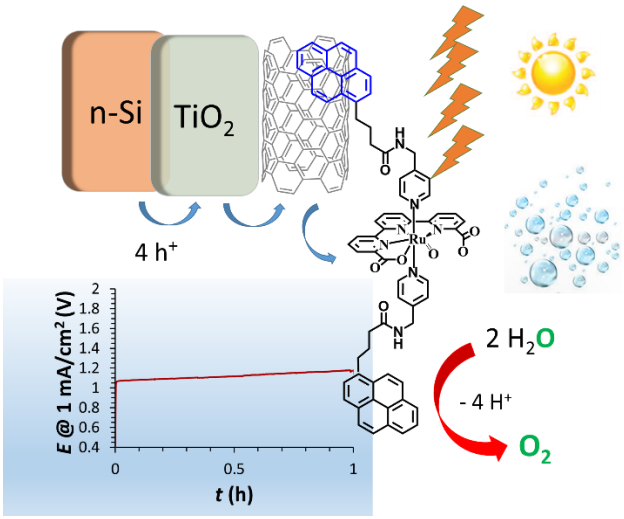

A molecular photoanode based on the Ru-tda catalyst and the TiO_2-Si semiconductor is tested for catalytic photoelectrochemical water oxidation to O_2. The Ru based hybrid photoanode is remarkably stable for over 60 minutes at current densities of 1 mA cm^{-2}, maintaining intact the nature of the Ru-tda scaffold. The novel photoanode configuration permits an exquisite and unprecedented monitoring of the nature and fate of the molecular species before and during catalysis.

Chapter 8*: General Conclusions*

Chapter 9*: Annexes*

UNIVERSITAT ROVIRA i VIRGILI

Table of Contents

Chapter 1

General Introduction

This chapter briefly introduces the motivation and background for the field of research of this thesis, the molecular water oxidation. The most relevant molecular water oxidation catalysts in the homogeneous phase are presented together with the relevant features that determine the enhancement in their performance. The challenge of transferring the activity in solution to solid-state anodes and photoanodes is also introduced. Finally, the progress in the design and performance of the latters is described and their major breakthroughs highlighted.

General Introduction

1.1 The Energy Problem, Solar Energy and Solar Fuels

In November 2016, 195 countries around the world signed the Paris agreement to mitigate climate change and to maintain temperature increase bellow 2^0C above pre-industrial levels.[1] The world's first climate agreement envisioned a deep change in the energy sector that is dominated by fossil fuels; see Figure 1 for the breakdown of the global energy consumption.[2] Some of the measures that derivate from the agreement are schematized in Figure 1B: increase of the share of renewables by 60 %, multiplying the number of electric vehicles by a factor of 115, and the replacement of coal by natural gas. Besides the high social and economic cost of these measures and many others, their implantation will not reduce the concentration of CO_2 in the atmosphere to meet the 2^0C scenario by 2100 as shown in Figure 1C.[3] To ensure a sustainable future for next generations, our societies should either implement more measures to meet the 2^0C scenario or develop new C-neutral sources of energy.[4]

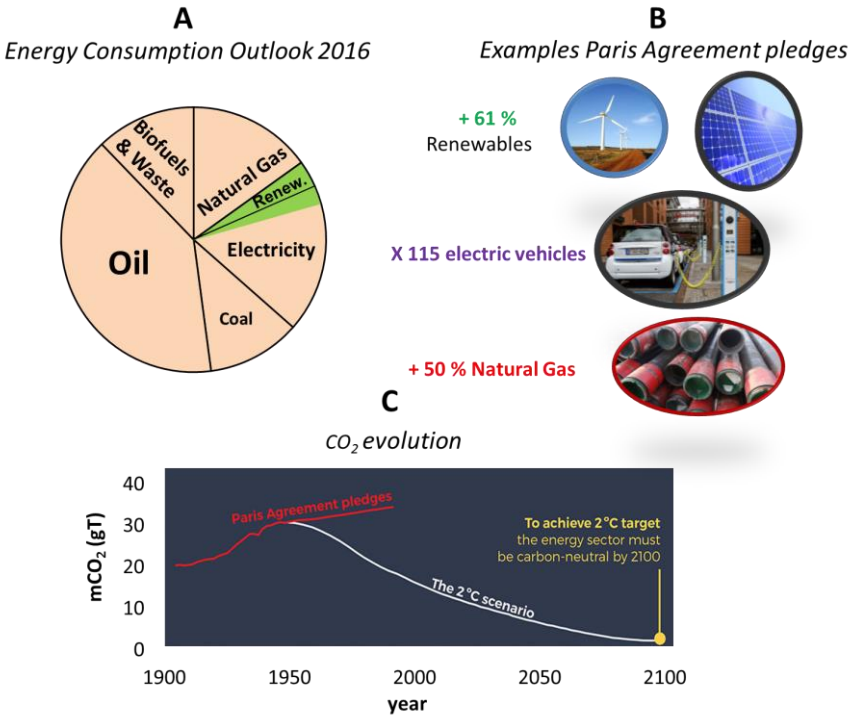

Figure 1. A, World energy consumption: oil, 39.9 %; biofuels & waste, 12.2%; Natural gas, 15.1%; Renewable, 3.3%; Coal; 11.3 % and Electriciy, 18.1 % (4.1% of the electricity is also from renewable sources, in green).[2] **B**, Example of Paris pledges in COP21.[1] **C,** Estimation of the atmospheric CO_2 in the 2^0C scenario (white line) and with the Paris Agreement Pledges (red line).[3]

The energy provided by the sun is the largest neutral carbon source of energy in the globe: everyday it exceeds by a factor of 1000 our global energetic consumption. Photovoltaic cells (PV) started to harvest the energy from the sun and transform it to electricity in the "Vanguarde" Satellite in 1958. The subsequent price reduction in the solar panels triggered the terrestrial installation in the 1990 decade. Nowadays, the amount of energy harvested by this technology represents around 5% of the total energy consumption and the percentage is expected to double by 2040.[1,2,3] Despite its growth, PV technology is limited to the electricity production that is only the 18.1% of the total energy consumption. The other 66 % of the energy consumption is nowadays provided by fossil fuels that cannot be replaced by the current solar technology.

In order to harvest more energy from the sunlight, an attractive option is to mimic how nature stores this kind of energy, see Figure 2.[5,6,7,8] For millions of years, plants and algae have collected the energy of the sun in the chloroplast and have used it to transform CO_2 into sugars and starches. The two reactions of the process are the water oxidation reactions (eq. 1) and reducetion of CO_2 to sugars and starches (eq. 2).

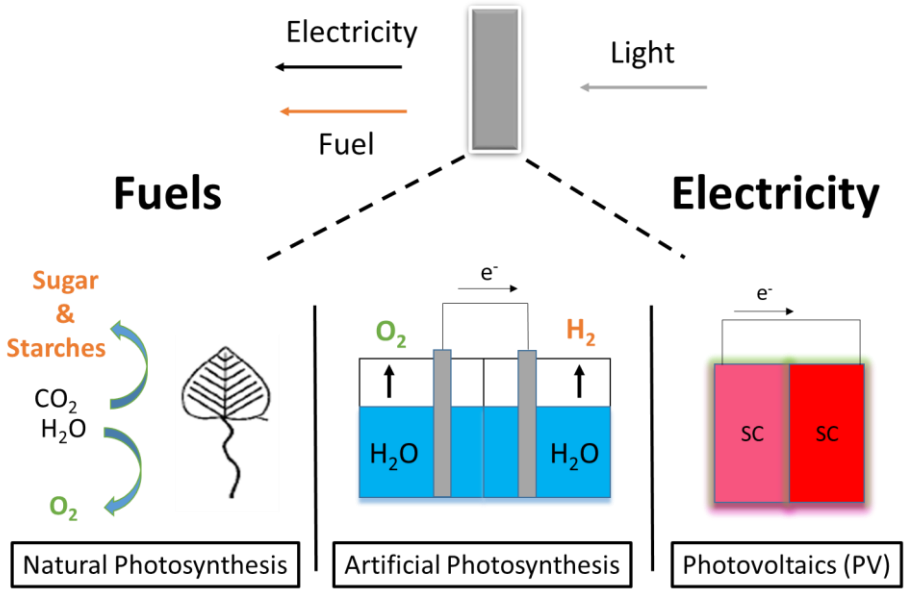

Figure 2. Methods of solar energy conversion. SC is Semiconductor.

$$2H_2O \rightarrow O_2 + 4e^- + 4H^+ \quad \text{eq. 1}$$

$$4e^- + 4H^+ + CO_2 \rightarrow [CH_2O] + H_2 \quad \text{eq. 2}$$

$$4e^- + 4H^+ \rightarrow 2H_2 \quad \text{eq. 3}$$

$$4e^- + 4H^+ + \frac{2}{3}N_2 \rightarrow \frac{4}{3}NH_3 \quad \text{eq. 4}$$

By analogy, the artificial photosynthetic devices harvest energy from the sun and store it in chemical bonds. The energy in this case may be used to split water and generate O_2 (eq. 1) and H_2 as products (eq. 3). Other designs also involve the reduction of CO_2 or N_2 to generate hydrocarbons or NH_3 (eq. 2 and 4). All the resulting chemicals are named "solar fuels" and are C-neutral. Artificial photosynthetic devices at least contain a light absorber, an electrolyte solution, catalysts for the redox reactions and means to separate the products. Many designs are nowadays being explored[9] and they can be rationalized in three large groups that are summarized in Figure 3.[10,11]

The first model consists of connecting PV cells with anodes and cathodes that are immersed in the electrolyze solutions. A commercial PV is used as light absorber and heterogeneous catalysts are located in the anode and the cathode. The advantage of the PV/electrolyzer model is the availability of both the PV cells and few heterogeneous catalysts. The main drawback of this model is the high cost of the PV cells: only systems with Solar-to-Hydrogen (STH) efficiencies close to the theoretical limit (> 25 %) are economically competitive.[12,13,14]

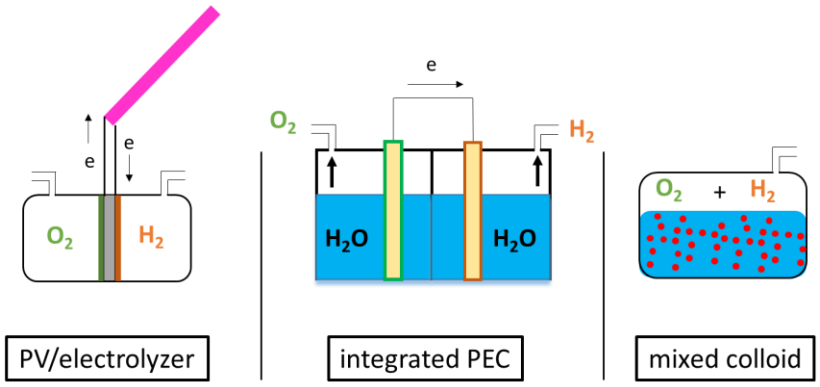

Figure 3. Designs of artificial photosynthetic devices. **Left,** photovoltaic(PV)/electrolyzer contains a photovoltaic cell (pink rectangle), water oxidation catalyst anode (green) and water reduction cathode (orange). **Middle,** The integrated photoelectrochemical cell contains a photoanode and a

photocathode (yellow rectangles) covered with water splitting catalysts (water oxidation; green, water reduction; orange). **Right,** the mixed colloid contains the water splitting catalysts and the light absorber in individual particles (red dots).

The opposite model of the PV-electrolyzer model is the mixed colloid system. This system integrates light absorbers and water splitting catalysts in single particles. A smaller STH is required for this approach to be economically competitive (STH between 5% - 10%) due to the solution-suspension design. However, these systems are still in a proof-of-concept stage with reported STH between 1% - 3%. [10,15]

Integrated photoelectrochemical cells (PEC) represent a compromise between the feasibility of PV-electrolyzer models and the simplicity of the mixed colloids. The integrated photoelectrochemcial cells rely on the development of individual photoanodes and photocathodes. The individual efficiency of the two electrodes must be around 10-15 %, which is approximately third of the theoretical limit. In addition, the availably of many absorbers and some oxidation and reduction catalysts simplifies this approach.

All the photosynthetic designs in Figure 3 are adaptable for the generation of different type of solar fuels such as Hydrocarbons, NH_3 or H_2.[16,17] In the cell, the oxidative counter reaction of any of these reduction reactions occurs simultaneously in the anode. The most common counter reaction is the oxidation of water to dioxygen.

1. 2 General View of the Water Oxidation Catalysis

The water oxidation reaction is a thermodynamically demanding reaction (1.23 V vs NHE at *pH* = 0) that requires the removal of four protons and four electrons from two water molecules. This kinetic complexity is translated into additional potential (overpotential, η) to perform the reaction.[18] The discovery of fast water oxidation catalysts that evolve O_2 at low overpotentials is a key challenge for the development of photosynthetic devices.[10,19,20,21]

One source of inspiration for the water oxidation catalysis has been the natural oxygen evolving center (OEC) that is located in plant and algal cells. The OEC is composed by a Mn_4O_5 cluster as an active center that catalyzes the water oxidation reaction.[22] X-ray Diffraction (XRD), X-ray Absorption Spectroscopy (XAS) and Differential Functional Theory (DFT) have determined the structure of the natural catalyst. [23,24,25,26] Figure 4 illustrates the structure and metric parameters of the Mn_4O_5 cluster (1.95 Å resolution),[24] where oxo groups assemble the four Mn centers. The most remarkable feature of the cluster is its efficient performance as water oxidation catalyst:

it oxidizes water at a mild overpotential (0.43 V) and at a high turnover frequency (100-400 s^{-1}), which have inspired many biomimetic water oxidation catalysts. [27,28,29,30]

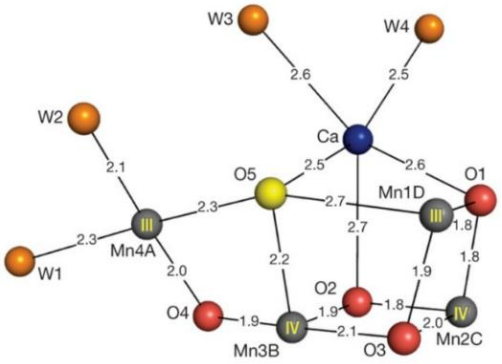

Figure 4. Metric parameters for the active center of the Oxygen Evolving Center in the PSII at 1.95 Å resolution.

However, the first artificial water oxidation catalyst was reported many years before the discovery of the Mn_4O_5 cluster. In 1902, Glazer and Coehn reported the ability of nickel oxide to generate O_2.[31] In the last decades, the need of water oxidation catalysts for eventual photosynthetic devices have accelerated the search and the benchmarking of new oxides. The ability of first row metal oxides (Mn, Ni, Fe, Co , Cu) and noble metal oxides (Ru and Ir) to oxidize water has been discovered[32] and recently benchmarked by electrochemical techniques.[33,34,35]Jaramillo *et al* compared the ability of a dozen of oxides to perform water oxidation catalysis under strong acid and basic conditions. At high pH, most metal-oxide based anodes require a similar overpotential (0.35 V <*E* < 0.5 V) to oxidize water at current densities of 10 mA/cm^2, see Figure 5. By sharp contrast, only highly loaded IrO_2 and RuO_2 based anodes show similar behavior at *pH* = 1.

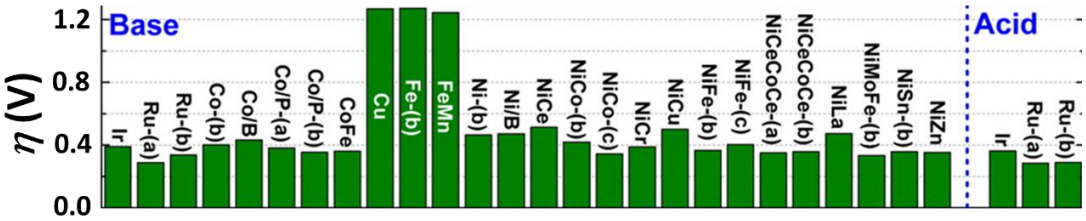

Figure 5. Required overpotential for different metal oxide films to reach 10 mA/cm^2 after two hours of operation. The measurements in base conditions were performed at *pH* = 14 and the acid conditions at *pH* = 0. Refer to the original Figure in reference 34 for further details.

The high performance of the metal oxides at high *pH* have triggered the development of few powerful photoanodes. The most successful strategy has been to couple semiconductors such as Si, GaAs or GaP with nickel oxide to perform unassisted water splitting for several months. [36,37] Nevertheless, the performance of the electrodes is restricted at high *pH* due to the lack of highly active water oxidation catalysts for more acidic conditions. The development of photosynthetic devices relies on generating photoanodes at lower *pH* where partner reduction reactions are favored. Hence, there is a need to explore alternative strategies for the development of water oxidation catalysts. [10]

1.3 Molecular Water Oxidation

The molecular water oxidation catalysis started later than the other water oxidation fields because it needed the development of the coordination chemistry. In 1982, the first molecular water oxidation catalyst was discovered; the so-called blue dimer, see complex *cis,cis*-$[(bpy)_2(H_2O)Ru^{III}(\mu\text{-}O)Ru(H_2O)(bpy)_2]^{4+}$ (**1**) in Chart 1 (bpy is bipyridine).[38] The activity of the blue dimer to oxidize water was analyzed in the catalytic cycle by an arsenal of spectroscopic, electrochemical and analytical techniques together with the energetic calculation through Differential Functional Theory (DFT).[18,39,40,41,42,43,44]

The discovery of the first molecular catalyst triggered the design of more powerful water oxidation catalyst based on transition metal complexes containing Cu,[45,46,47,48] Fe,[49] Ir,[50] Mn,[51] Co, [52,53,54] or Ru [55,56,57,58] as metal centers. However, most of the detailed kinetic, electrochemical and mechanistic studies involved Ru complexes. Hereafter, we will only refer to the most relevant Ru metal complexes for the water oxidation catalysis. The most representative Ru catalysts for water oxidation are provided in Chart 1, 2 and 3 and their catalytic data are depicted in Table 1. In water oxidation catalysis, the "chemical efficiency" is used to assess the stability of the complex under water oxidation conditions and Turnover Frequency (TOF, s^{-1}) to assess the specific rate of the catalyst, see Table 1 for more details.

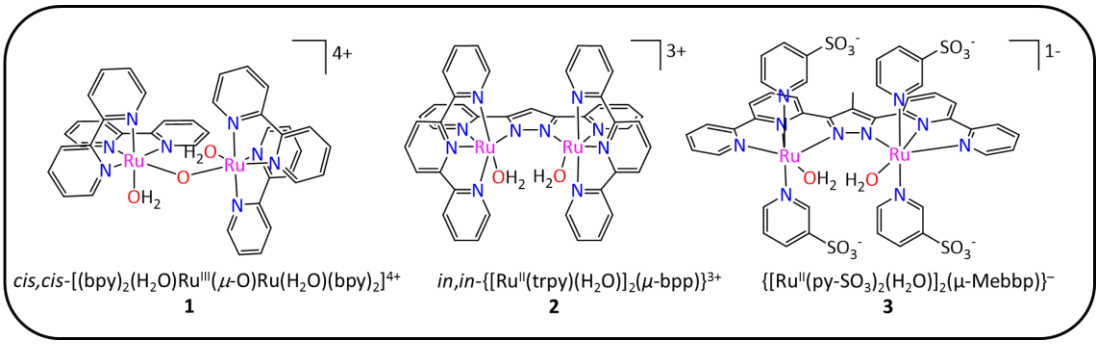

Chart 1. Structure for dinuclear Ru complexes **1**, **2** and **3**. bpy is 2,2'-bipyridine, trpy is 2,2':6',2''-terpyridine, Hbbp is 2,2'-(1H-pyrazole-3,5-diyl)dipyridine, py-SO_3H is pyridine-4-sulfonic acid and HMebbpis 6,6''-(1H-pyrazole-3,5-diyl)di-2,2'-bipyridine.

In 1982, the just born molecular water oxidation community hypothesized that only dinuclear complexes could catalyze the water oxidation reaction. The hypothesis was based on the ability of the dinuclear complexes to accumulate the four oxidative equivalents. Consequently, successive redesigns of the initial blue dimer complex were performed to enhance its catalytic performance. In 2004, the Ru-O-Ru bridge of the blue dimer was replaced by the more rugged bpp^- scaffold, see complex *in*,*in*-$\{[Ru^{II}(trpy)(H_2O)]_2(\mu\text{-}bpp)\}^{3+}$, **2** in Chart 1 (Hbbp is 2,2'-(1H-pyrazole-3,5-diyl)dipyridine).[59] The bridge offered better communication between the two Ru centers due to the rigid structure and, as a result, complex **2** oxidized water to O_2 with higher efficiencies (70%) and higher TOF (0.01 s^{-1}) than the parent complex **1** (see Table 1). However, complex **2** did not reach 100 % efficiency under water oxidation conditions due to oxidation of the CH group in the pyrazole. [60] In a further redesign step, the dinuclear complex $\{[Ru^{II}(py\text{-}SO_3)_2(H_2O)]_2(\mu\text{-Mebbp})\}^-$ (**3**) included the $Mebbp^-$ ligand that stabilized the complex under water oxidation conditions (90 % efficiency) through methylation of the easily oxidative pyrazole (HMebbp is 6,6''-(1H-pyrazole-3,5-diyl)di-2,2'-bipyridine).[61]

Table 1. Catalytic data for dinuclear complexes **1**-**3**, six-coordinate mononuclear complexes, **5** and seven-coordinate mononuclear complexes **9** and **11.**

Complex	*Efficiency*[a]	*TOF* (s^{-1})[b]	*O-O mechan.*	*Ref.*
cis,cis-$[(bpy)_2(H_2O)Ru^{III}(\mu\text{-}O)Ru(H_2O)(bpy)_2]^{4+}$ **1**	---[c]	0.004	WNA	38
in,in-$\{[Ru^{II}(trpy)(H_2O)]_2(\mu\text{-}bpp)\}^{3+}$ **2**	73 %	0.01	I2M	59
$\{[Ru^{II}(py\text{-}SO_3)_2(H_2O)]_2(\mu\text{-}Mebbp)\}^{-}$ **3**	90 %	0.07	WNA	61
$[Ru(trpy)(bpy)(OH_2)]^{2+}$ **5**	70 %	0.01	WNA	62
[Ru(bda)(Me-py)(OH)] **9**	100 %	30	I2M	65
[Ru(bda)(isoq-Br)(OH)] **11**	100 %	1000	I2M[d]	66

[a] Efficiency defined $n_{O2}/(4 \cdot n_{SA})$, where n_{O2} are the measured moles of O_2 and n_{SA} are the moles of Sacrificial Acceptor (SA). The concentration of the complexes was 1 mM for complexes **2**, **3** and **5** and 62.5 μM for complexes **9** and **11**. The concentration of the SA(Ce^{4+}) = 100 mM. [b] Initial turnover frequency. [c]Only under stoichiometric conditions (turnover number < 10). [d]Mechanism elucidated for the related complex **10**.

In 2004, Thummel *et al* reported the first family of mononuclear complexes that catalyzed the water oxidation reaction, see the example of complex $[Ru(tnp)(Me\text{-}py)_2(OH_2)]^{2+}$ (**4**) in Chart 2 (tnp is 2,2'-(4-(tert-butyl)pyridine-2,6-diyl)bis(1,8-naphthyridine)).[63] The report generated a large convulsion in the water oxidation community because the work did not provide detailed kinetic data and, more importantly, the report stated against the idea that only dinuclear complexes could catalytically oxidize water. The controversy ended when Meyer *et al* probed spectroscopically that the mononuclear complexes $[Ru(trpy)(bpm)(OH_2)]^{2+}$, **6**, and$[Ru(trpy)(bpz)(OH_2)]^{2+}$, **7**, behaved as single site catalysts (bpm is 2,2'-bipyrimidine, bpz is 2,2'-bipyrazine).[56] In terms of efficiency and rate, the new mononuclear water oxidation catalysts (such as complex $[Ru(trpy)(bpy)(OH_2)]^{2+}$, **5** in Table 1) did not exceed the performance of the previous dinuclear complexes. However, the straightforward synthesis of mononuclear

complexes compared to the former dinuclear complexes permitted a rapid expansion of the field. An example of the straightforward synthesis is the mononuclear complex $[Ru(trpy)(bpp)(OH_2)]^+$(**8**) that is the monomeric form of complex **2**.[64] While Llobet's group invested years in the synthesis and isolation of complex **2**, it invested few weeks to develop the mononuclear complex **8**.

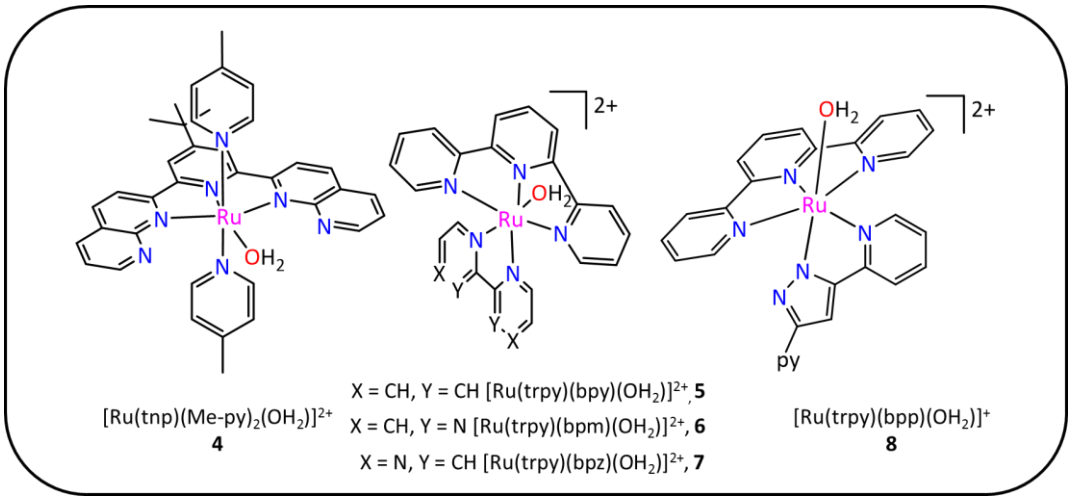

Chart 2. Structure for mononuclear six-coordinate Ru complexes **4**-**8**. tnp is 2,2'-(4-(tert-butyl)pyridine-2,6-diyl)bis(1,8-naphthyridine), bpm is 2,2'-bipyrimidine, bpz is 2,2'-bipyrazine and Hbpp is 2,2'-(1H-pyrazole-3,5-diyl)dipyridine.

However, the real increase in activity and efficiency came with the development of the Ru complexes based on the bda^{2-} ligand (H_2bda is [2,2'-bipyridine]-6,6'-dicarboxylic acid).[57,65] The pentadentate bda^{2-} ligand coordinates Ru in the equatorial plane and two pyridine or isoquinoline type of ligands (isoq, isoq-Br) coordinate in the axial plane (see complexes $[Ru(bda)(Me\text{-}py)_2(OH)]$, **9**; $[Ru(bda)(isoq)_2(OH)]$, **10**; and $[Ru(bda)(isoq\text{-}Br)_2(OH)]$, **11** in Chart 3). The bda^{2-} ligand stabilizes the high oxidation states of the Ru center through the two anionic charges and the access to a seven-coordinate Ru center. Complexes **9**, **10** and **11** exhibit 100% efficiency and high catalytic rates as a result of this stabilization.[57,66,65] Furthermore, a final tuning of the axial ligand to favor the binuclear nature of the mechanism permitted rocketing the rates to 1000 s^{-1}. [66]

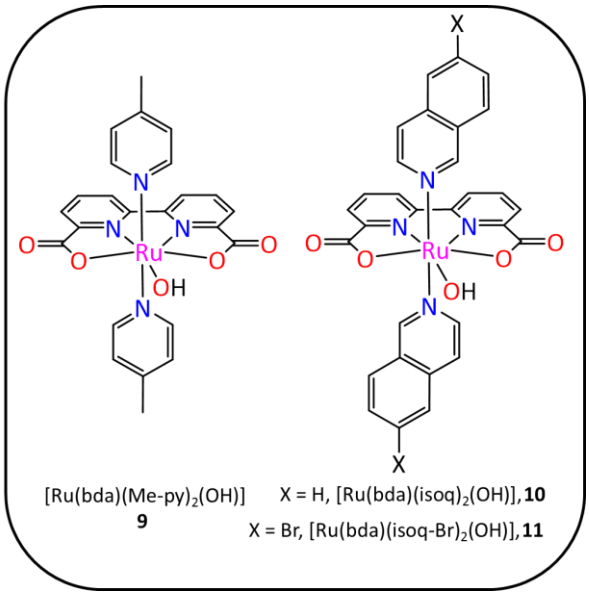

Chart 3. Structure for mononuclear seven-coordinate Ru^{III} complexes. H_2bda is [2,2'-bipyridine]-6,6'-dicarboxylic acid, Me-py is 4-methylpyridine, isoq is isoquinoline and isoq-Br is 6-bromoisoquinoline.

Up to this point, we have focused on the evolution of the performance of the water oxidation catalysts based on Ru complexes over the last 35 years. Through the chronological analysis, we have discussed the molecules that have participated in the 5 orders of magnitude increase of turnover frequency since 1982. However, it is also interesting to analyze which are the fundamental features of the catalysts that have permitted this exponential increase. Figure 6 highlights the three most relevant features for molecular water oxidation catalysts: the ability to perform Proton Couple Electron Transfer (PCET); the nature of the O-O bond formation mechanism; and a ligand environment that provides a seven-coordination.[58] The following section analyses their influence in the performance of the water oxidation catalysis.

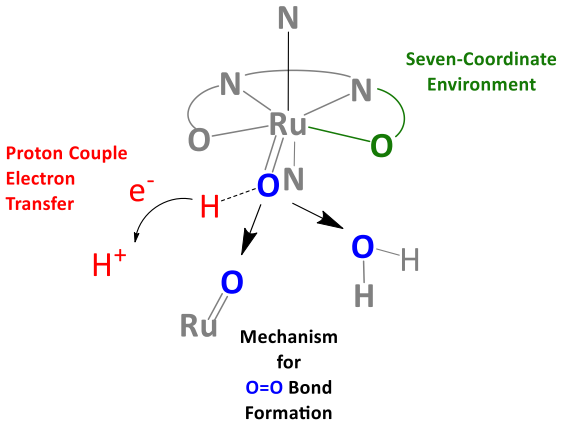

Figure 6. Important features for the design of a powerful water oxidation catalyst.

1.3.1 Proton-coupled Electron Transfer (PCET)

Proton-coupled Electron Transfer (PCET) is a reaction mechanism where a proton and an electron move in a concerted manner. This phenomenon was first discovered in the late 1970 decade by Prof. Thomas J. Meyer,[67,68] whose group also discovered the blue dimer few years after.[38] PCET allows leveling up the oxidation state without building up the charge of the center, which renders the process indispensable for many natural enzymes, catalytic and electrochemical systems.[69,70,71,72]

The effect of PCET in Ru complexes can be observed by comparing the Pourbaix diagrams of the monomeric parent of the blue dimer, complex $[Ru(bpy)_2(py)(OH_2)]^{2+}$; **12**, and its chloro relative complex $[Ru(bpy)_2(Cl)_2]$, **13**, see Figure 7**.** In the II oxidation state, complex **13** is neutral while complex **12** is double positive charged at *pH* = 7. As a consequence, the potential for the III/II redox couple for complex **13** is lower than that exhibited by complex **12.** The interesting part of the Pourbaix diagram is related to the access to the IV oxidation state. Complex **13** requires 700 mV more than complex **12** to reach the IV oxidation state at *pH* = 7**.** This is clearly due to the PCET mechanism that has prevented the built up in charge for complex **12** while the charge has increased +2 units for complex **13**.

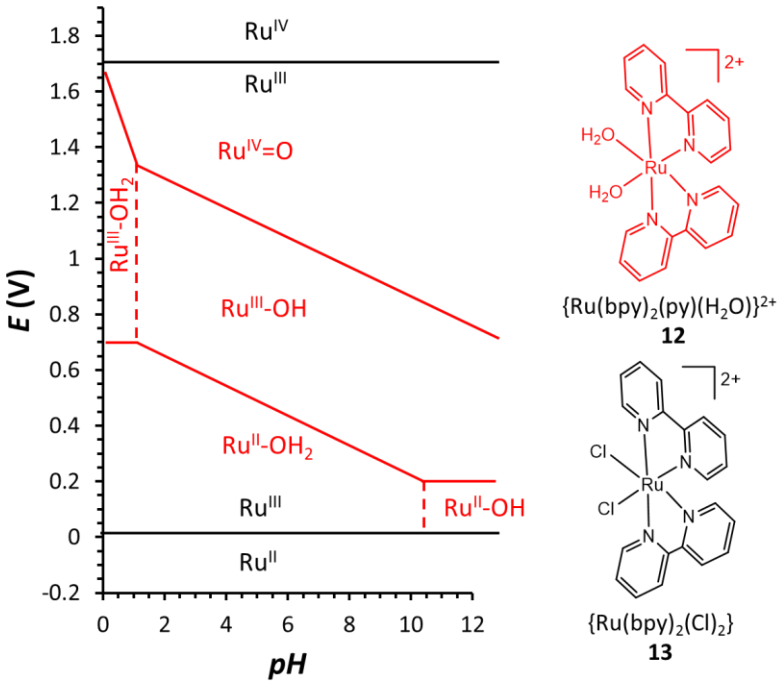

Figure 7. Pourbaix diagram for complexes **12** and **13**.

The ultimate cause of the PCET mechanism is the increase of acidity of the Ru-OH_2 group upon oxidation of the metal center. Note how the *pKa* of complex **12** decreases from the II oxidation

state (10.6), to the III oxidation state (0.85) and IV oxidation state (< 0.0). The increase of acidity upon oxidation ultimately results in deprotonation that reduces the potential for accessing to the Ru=O moieties. In the case of water oxidation catalysis, the reactive Ru=O moieties are crucial because they are the gate to O-O bond formation.

1.3.2 Water oxidation mechanism

The catalytic cycle of the water oxidation reaction has been studied both for the natural occurring Mn cluster in the PSII and artificial oxidation catalysts **1**, **2**, **3**, **6**, **9** and **10.**[39,43,44,56,57, 26] Among all systems, Figure 8 summarizes the two general mechanisms for O-O bond formation. The left part of the diagram illustrates the Water Nucleophilic Attack (WNA) mechanism that involves a water molecule attacking a highly oxidized metal oxide (M=O) unit. The other (Figure 8, right) is the Inter/Intramolecular coupling (I2M) that consists in the merging of two highly oxidized M=O moieties.[48,73,74]

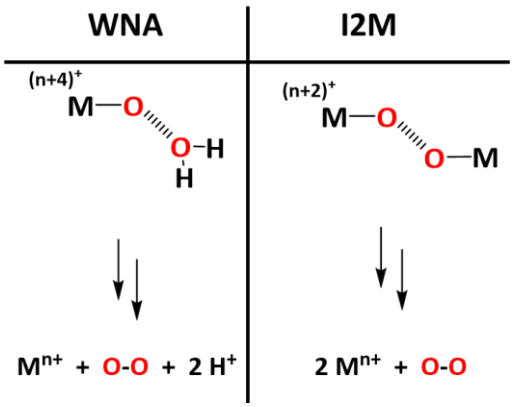

Figure 8. General Mechanisms for the formation of an O-O bond.

The mechanism for complexes **1**, **2**, **3**, **5**, **9** and **11** is depicted in Table 1 together with their catalytic data. For the dinuclear complexes **1**-**3,** the relative position of the two Ru-OH_2 groups determines the nature of the O-O bond formation mechanism. For example, complex **1** generates the O-O bond through a WNA mechanism due to the free rotation of the Ru-O-Ru bond.[75] By sharp contrast, the rigid scaffold of the bpp^- ligand in complex **2** forces the two Ru=O groups to generate oxygen through an I2M mechanism.[73] Finally, the subtitle opening of the scaffold in the $Mebbp^-$ ligand of complex **3** favors the WNA mechanism.[61]

The mononuclear complex **6** oxidizes water through a WNA mechanism while complexes **9-11** undergo through a I2M mechanism. The steps for the two mechanisms are detailed in Figure 9.[56,57] The common point of the two mechanisms is that both regenerate the initial Ru-OH_2 after

the liberation of O_2. The main difference is that the O-O formation needs two Ru=O units in the I2M mechanism while the WNA mechanism only requires a single Ru=O unit. This is critical because the O-O formation is often the rate determining step (rds) of the catalytic cycle. Consequently, the water oxidation mechanism determines the order of the reaction for mononuclear Ru complexes.

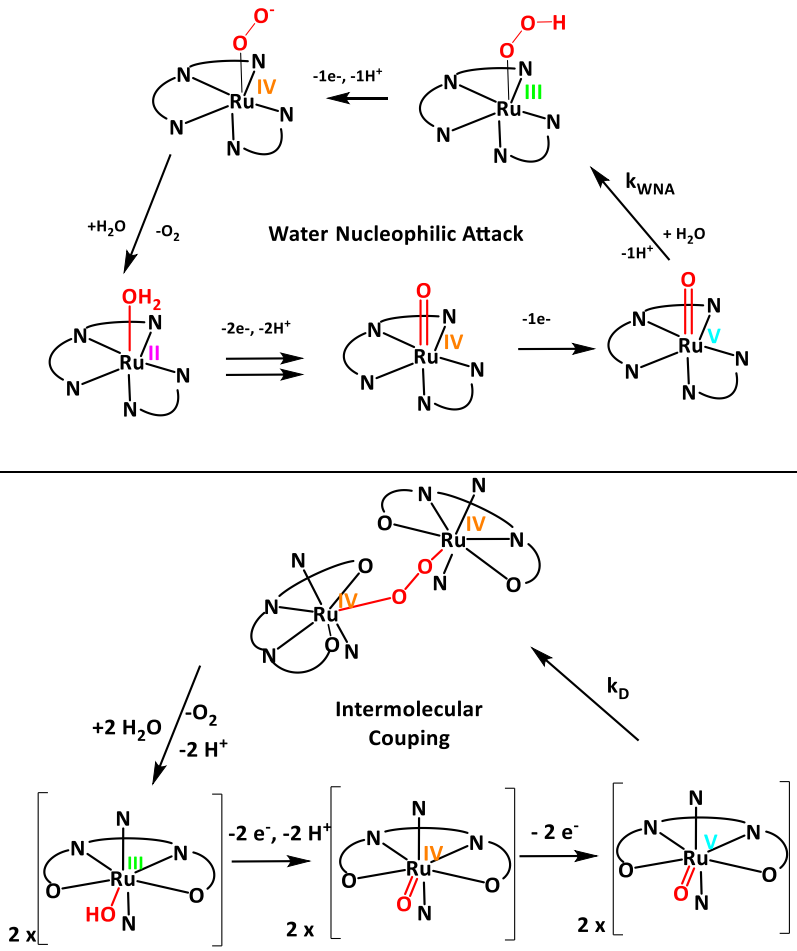

Figure 9. Water oxidation catalytic cycles for complex **6** (top) and **9** (bottom)

The different nuclearity of the two mechanisms (unimolecular for complex **6** and bimolecular for complex **9**) may be a useful tool to control the catalytic performance. For example, the bimolecular nature of complex **9** has been exploited to increase the activity of this family of Ru catalysts.[57,76,77] The initial axial Me-py ligands were replaced by isoquinoline-type of pyridines that can favor pi-pi stacking interactions during the catalytic cycles, *e.g* complexes **10** and **11** in Chart 3.[57,66] Due to the bimolecular nature of the catalysis, the pi-pi interaction can stabilize the Ru-O-O-Ru intermediates and decrease the activation barrier of the O-O bond formation. This approach has enabled to increase the TOF from 30 s^{-1} for complex **9** to 1000 s^{-1} for complex

11.[57,66] In the following section, we will discuss the heterogenization of the Ru catalysts on surfaces to generate anodes and photoanodes. For this particular application, the nature of the O-O bond forming step of the catalysts is again crucial for the design of powerful systems.

1.3.3 Seven-coordinate complexes

Another interesting asset from complexes **9-11** is the seven coordination positions that the bda^{2-} ligand provides to the Ru center in the equatorial plane. Single-crystal XRD evidenced the seven coordination of the Ru center at the IV oxidation state, see Figure 10 left for the ORTEP view published in 2009.[65] The seven coordination stabilizes the Ru center because provides electron density to a deficient Ru^{IV} ion. In addition, the extra coordination lowers the energy of the d_{xz} and d_{yz} orbitals compared to the six-coordinate Ru complex, see Figure 10 right.[78] Finally, the bda^{2-} ligand also provides two negative charges to the Ru center that altogether reduce the catalytic potential for water oxidation (E_{CAT}). At *pH* = 1, its E_{CAT} is the lowest potential in the literature and it is close to the thermodynamic potential ($\eta \approx 150$ mV). [57]

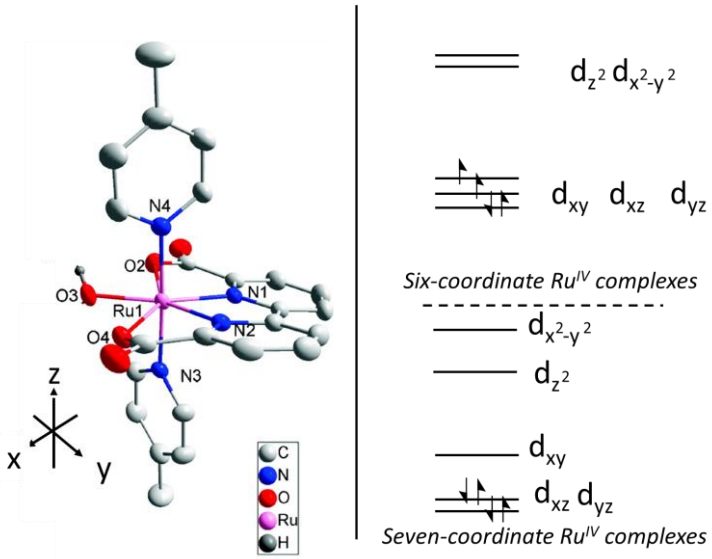

Figure 10. Left, ORTEP plot for complex **9** in the IV oxidation state**. Right**, relative energy of the d_{xy}, d_{xz} and d_{yz} orbitals for six- and seven- coordinate Ru^{IV} complexes.

Among all complexes discussed, the seven-coordinate complexes are the fastest water oxidation catalysts reaching TOF of 1000 s^{-1}. However, TOF is measured by using Ce^{4+} as chemical oxidant, which determines the potential (*E*) of the solution. TOF is extremely sensitive to the difference between the potential of the solution (*E*) and the catalytic potential (E_{CAT}) as shown in the generic eq. 5.[79] Therefore, it is not possible to distinguish if the high Turnover Frequency (TOF) exhibited by the seven-coordinate complexes is due to an intrinsically high kinetics (high *k*) or due to the

seven coordination stabilization (low E_{CAT}). Electrochemical methods can distinguish between the Turnover Frequency (TOF) at a certain potential (E) and the intrinsic kinetics (k).[80] These electrochemical methods have been recently employed to benchmark the activity of H^+ and CO_2 reduction catalysts[81] but not that of water oxidation catalysts.

$$\mathrm{TOF} = \frac{k}{1 + \exp\left(\frac{F(E - E_{CAT})}{RT}\right)} \qquad \text{eq. 5}$$

1.4 Molecular Anodes

The next rational step towards the construction of an artificial photosynthetic cell is nowadays to anchor the best molecular catalysts on (semi)conductive materials to generate powerful anodes and photoanodes. In the following subsections, we discuss the design and the performance of the best-performing molecular anodes (subsections 1.41-1.42) and photoanodes (subsections 1.51-1.52).

The main challenge in these systems is that the catalyst immobilized on the anodes retained the high activity exhibited in solution.[10,34] Consequently, the following sections aim to highlight the factors that benefit the high performance of the immobilized catalysts.

1.4.1 Design of Molecular Anodes

Molecular anodes consist of a molecular catalyst and a conductive material. The link between the material and the catalyst is provided by a functional group that is included in the ligand scaffold of the complex. The link that assembles the complex and the material provides a strong and conductive interaction that can be covalent or not covalent.[82,83]

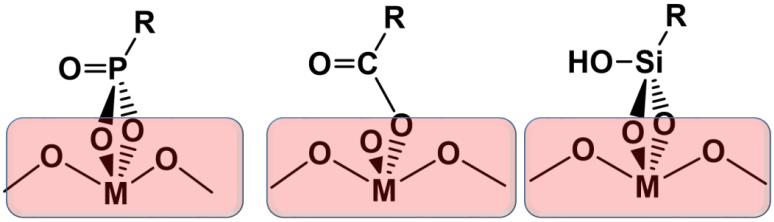

Figure 11. Representative linkage between a metal surface and a phosphonate, carboxylate and silicate respectively (from left to right).

Most examples of molecular anodes are based on the immobilization of Ru catalysts on oxide surfaces such as fluorine doped SnO_2 (FTO), Sn(IV) doped In_2O_3(ITO) or TiO_2 nanoparticles. The

linkers for these surfaces are based on phosphonate, carboxylate or silicate functional groups that generate a covalent bond with the surface, see Figure 11.

Other molecular anodes are based on carbon materials that range from flat glassy carbon electrodes to nanostructured carbon materials. The phosphonate, carboxylate and silicate linkers are not used for the immobilization on carbon materials due to the few COOH groups available on the surface. Alternatively, the three most relevant strategies for the immobilization on carbon surfaces are based on pi-pi stacking with carbon nanostructures, the electroreduction of diazonium salts and the anodic deposition of N-substituted pyrroles or C-substituted tiophenes, see Figure 12. While two of the strategies are not based on covalent interactions, the electrografting of the diazonium salts generates a C-C bond with the surface.

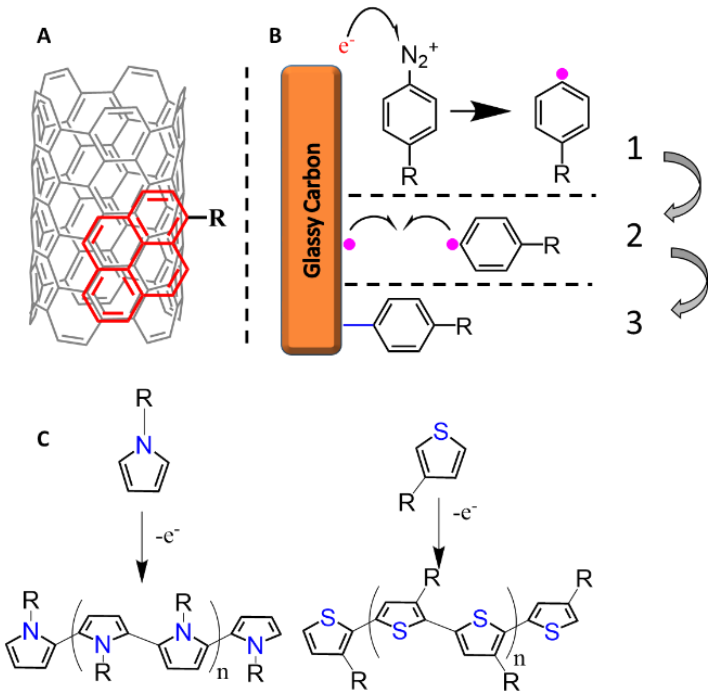

Figure 12. Schematic representation of the strategies for the immobilization of molecular catalyst on carbon Surfaces. **A**, Strong pi-pi interaction between a pyrene moiety and a carbon nanostructured material. **B**, 1->2->3 sequence of the electroreduciton of diazonium salts that leads to a C-C bond. **C**, Anodic electropolymerization of N-substituted pyrroles or C-substituted thiophenes.

Llobet and Meyer laboratories provided several examples of immobilized molecular system on oxide surfaces during the last decade. Their laboratories initially substituted the initial trpy and bpy ligands of complexes **2** and **5** by the phosphonate-derived PO_3H_2-trpy and diPO_3H_2-bpy ligands.[84] The resulting complexes *in*,*in*-{[Ru^{II}(trpy-PO_3)(H_2O)]$_2$(μbpp)}, **14**, and [Ru(Mebimpy)(di-PO_3-bpy)(OH_2)], **16**, contained a phosphonate group that attached to oxides surfaces. Complex

14 was deposited on TiO_2 nanoparticles to generate the **14**@TiO_2 anode and **16** was immobilized on ITO electrodes to generate the **16**@ITO anode. To simplify the reading, the full nomenclature of the abbreviated ligands (*e.g* trpy-PO_3 or di-PO_3-bpy) will be only detailed in the corresponding chart and not in the text from this point.[85]

Llobet *et al* followed a related strategy to immobilize complex **3** through a carboxylate group. In this work, a phenyl-carboxylic group replaced the Methyl of the Mebbp ligand to prepare complex {[$Ru^{II}(py)_2(H_2O)]_2$(μ-COO-Ph-bbp)}, **15**, see Chart 4.[85] The complex decorated mesoporous ITO electrodes (*meso*ITO) to generate **15**@*meso*ITO electrodes. In addition to the anchoring function, the extra phenyl carboxylate group also protected the easily oxidative position of the pyrrole.

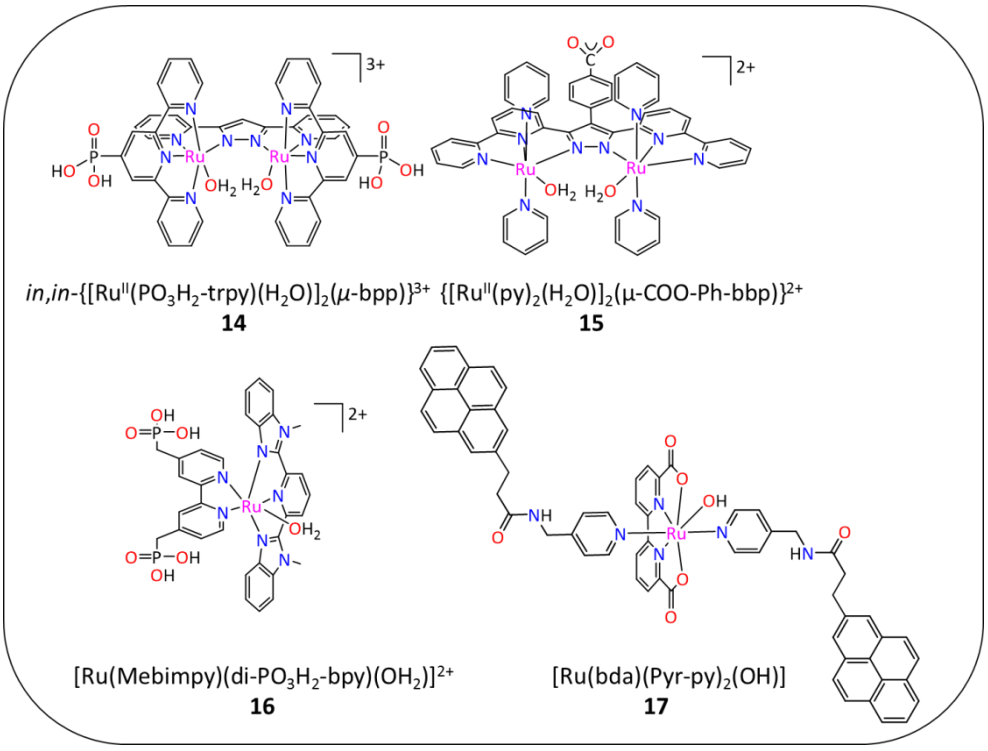

Chart 4. Structures of dinuclear (**14**-**15**) and mononuclear (**16**-**17**) Ru complexes modified to be immobilized on electrodes. PO_3H_2-trpy is [2,2':6',2''-terpyridin]-4'-ylphosphonic acid, COOH-Ph-Hbbp is 4-(3,5-di([2,2'-bipyridin]-6-yl)-1H-pyrazol-4-yl)benzoic acid, Mebimpy is 2,6-bis(1-methylbenzimidazol-2-yl)pyridil, diPO_3H_2-bpy is ([2,2'-bipyridine]-4,4'-diylbis(methylene)) bis(phosphonic acid) and Pyr-py is 3-(pyren-2-yl)-N-(pyridin-4-ylmethyl)propanamide.

Simultaneously, Sun *et al* replaced the axial Me-py of complex **9** by Pyr-py ligands to generate an anode based on Multiwalled Carbon Nanotubes (MWCNT). The resulting complex [Ru(bda)$(Pyr\text{-}py)_2$(OH)] (**17**)[86] was attached to MWCNT through pi-pi stacking and generated the

17@MWCNT/ITO electrode when combined with a flat ITO electrode. [86] The same group also explored other strategies to anchor complexes related to complex **9** on carbon surfaces. For example, glassy carbon electrode was modified through the electroreduction of diazonium salts and click chemistry of a **9**-related complex.[87] In addition, the axial ligands of complex **9** were modified to incorporate pyrroles and C-substituted thiophene groups to anchor complex **9** onto glassy carbon surfaces through anodic polymerization.[88] Some of these immobilization strategies were employed both for the preparation of anodes and photoanodes and are discussed in the photoanode section.

1.4.2 Performance of Molecular Anodes

Table 2 illustrates the electrochemical data for the **14**@TiO_2, **15**@*meso*ITO, **16**@FTO and **17**@MWCNT@ITO anodes together with the catalytic data for the related homogeneous complexes **2, 3, 5** and **9** respectively. The four examples allow the reader to compare relevant electrochemical features of the best-performing molecular anodes: the superficial concentration, the turnover frequencies and the current density.

Table 2. Electrochemical data for **14**@TiO_2, **15**@*meso*ITO, **16**@FTO and **17**@MWCNT/ITO anodes together with catalytic activity of the analogous homogeneous complexes **2**, **3**, **5** and **9.**

	Γ (nmol/cm^2)	*TOF het.* *(TOF hom.)* s^{-1}	*j* /time (μA/cm^2)/ (min)	Ref. het. (Ref. hom.)
in,in-{[Ru^{II}(trpy-PO_3)(H_2O)]$_2$(*μ*bpp)}@FTO **14**@TiO_2	10	0 (0.01)[a]	0[a]/--	83 (59)
{[Ru^{II}(py)$_2$(H_2O)]$_2$(μ-COO-Ph-bbp)}@ITO **15**@*meso*ITO	0.5	0.3[b] (0.07)[c]	15[b]/--	85 (61)
[Ru(Mebimpy)(di-PO_3-bpy)(OH_2)]@FTO **16**@FTO	0.1	0.36[d] (0.15)[e]	5[d]/480[d]	84 (62)
[Ru(bda)(Pyr-py)$_2$(OH)]@MWCNT/ITO **17**@MWCNT/ITO	1.8	0.3[f] (30)[g]	220[f]/416[f]	86 (57)

Experimental details: **a**, Ce^{IV} (100 mM) and **2** (1 mM) at *pH* = 1; **b**, Chronoamperometry using a Rotating Disk electrode at *E* = 1.69 V at *pH* = 1; **c**, Ce^{IV} (100 mM) and **3** (1 mM) at *pH* = 1; **d**, Chronoamperometry at *E* = 1.85 V at pH= 1; **e**, Ce^{IV}(100 mM) and complex **5** (1 mM) at *pH* = 1;[89,39] **f**, Chronoamperometry at *E* = 1.45 V at *pH* = 7; **g**, Ce^{IV} (365 mM) at *pH* = 1 and complex **9** (62.5 μM).

The superficial concentration of the catalyst (Γ, nmol/cm^2) is an extremely important parameter that directly influences the current density and stability of the hybrid anodes. The best way to boost the superficial concentration of a catalyst is to use electrodes that possess a high surface area. For example, the hybrid electrode **14**@TiO_2 that is based on TiO_2 nanoparticles show Γ that are two orders of magnitude higher than hybrid electrodes based on flat FTO electrodes, such as **16**@FTO. In a similar way, the use of nanostructured carbon, such as MWCNT, also increased the loading: the **17**@MWCNT/ITO hybrid electrode shows one order of higher loading that the flat glassy carbon electrode. [87]

The other crucial parameter of the hybrid anodes is related to the specific activity of the catalyst. The Turnover Frequency (TOF) of the catalyst on the hybrid electrode is informative about the activity of the catalyst in the hybrid system. In addition, it is interesting to compare the activity of the molecular catalyst on the surface to that of the related complex in the homogenous phase. Accordingly, Table 2 shows the Turnover Frequency of the hybrid systems (TOF_{het}) together with that of the analogue systems in solution (TOF_{hom}). In the case of molecular catalyst immobilized on the surface, the nature of the water oxidation mechanism is fundamental. For example, the hybrid materials based on first-order water oxidation catalysts, such as **15**@*meso*ITO and **16**@FTO hybrid electrodes, showed increased TOF as hybrid electrodes compared to the homogeneous counterparts. In sharp contrast, the Ru-bda complex ancored on MWCNT, **17**@MWCNT/ITO, showed decreased perfomance when ancored on the surface. The loss of activity of Ru-bda complexes on hybrid anodes is clearly a major drawback because the family of Ru-bda complexes are the fastest water oxidation catalyst in the literature. The bimolecular nature of the Ru-bda complexes explains the low activity of the immobilized Ru-bda complexes: the molecular catalyst cannot oxydize water throught the preferred bimolecular mechanism and their activity shrinks.

Finally, complex **14**@TiO_2 illustrates a potential problem that hybrid materials can suffer when molecular catalysts are anchored on oxide surfaces: the Ru-OH_2 of complex **14** interacts with the M-O functionalities of the oxides and blocks the catalytic activity of the catalyst. The relative position of the Ru-OH_2 in respect to the oxide surface have been underlined as critical by a recent work.[83]

The current density (j, mA/cm^2) is the most important parameter for oxygen evolving anodes. An ideal anode in a commercial cell must maintain 10 mA/cm^2 for months at the lowest potential. In the hybrid anodes, the current density is proportional to the product of Γ and the

turnover frequency of the catalyst. Consequently, the **17**@MWCNT/ITO hybrid anode exhibits the highest current density (220 μA/cm^2) in the literature. However, the current density relies on the higher loading of **17** on the MWCNT electrodes rather than on the high activity of the molecular catalyst. The current density of the **17**@MWCNT/ITO electrode could reach the commercially relevant values of 10 mA/cm^2 if the complex retained the specific activity in solution. Hence, the development of fast first order molecular catalysts as fast as complex **9** in solution is of high interest.

1.5 Molecular Photoanodes

1.5.1 Design of Molecular Photoanodes

Molecular photoanodes consist of a water oxidation catalyst, a light absorber and an electrical field that ensures charge separation. The way that photoanodes absorb light divides them into two groups as shown in Figure 13. The first group is named "dye-sensitized" photoanodes because a dye absorbs the light. The second group is named "Semiconductor-catalyst" because a small band gap semiconductor absorbs the light.

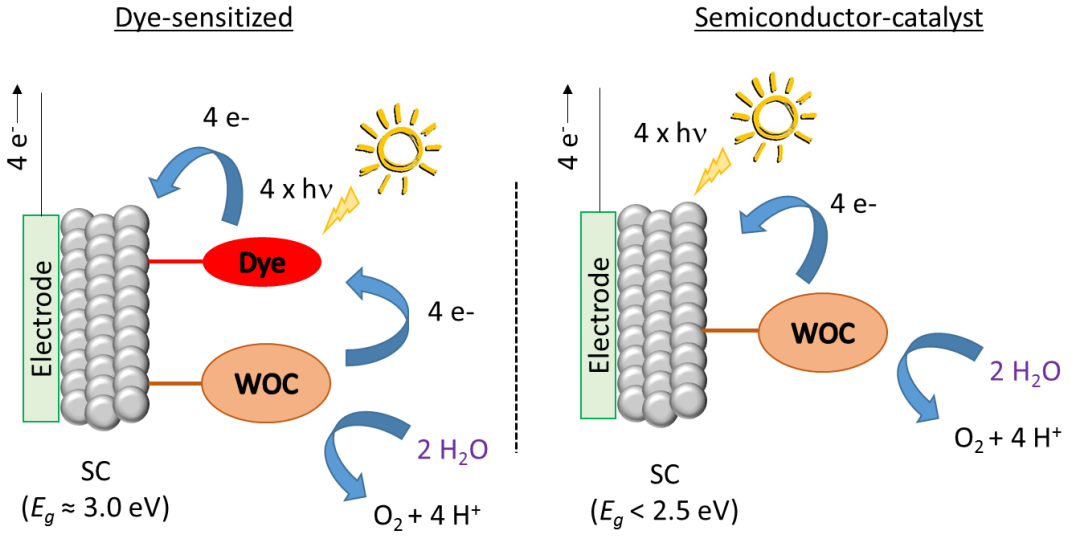

Figure 13. General designs for molecular photoanodes. WOC is Water Oxidation Catalyst, SC is Semiconductor, E_g is band gap and the dye is often a $[Ru(bpy)_3]^{2+}$ derivative.

The band diagram for the dye-sensitized photoanodes is depicted in Scheme 1. As the dye is involved in the light absorption and charge separation, most of the requirements in the Scheme are related to the dye. The first requirement is that the HOMO-LUMO difference of the dye is in visible light energies to absorb most of the solar spectrum. The other requirement is that the potential of the oxidized dye ($E_{P/P+}$) is greater that the water oxidation catalyst onset potential

(E_{CAT}) to catalyze the water oxidation reaction. Derivatives of $[Ru(bpy)_3]^{2+}$ have been extensively used in this Scheme due to the ideal thermodynamic match. Finally, the Conduction Band (CB) of the semiconductor must be able to accept the electrons from the Photoexcited species (P*). Large band gap oxides such as TiO_2 possess CB that are suitable for the electron injection of $[Ru(bpy)_3]^{2+}$ dyes. In addition, the large band gap of TiO_2 (E_g = 3 eV) do not absorb a large portion of visible light. [90,91]

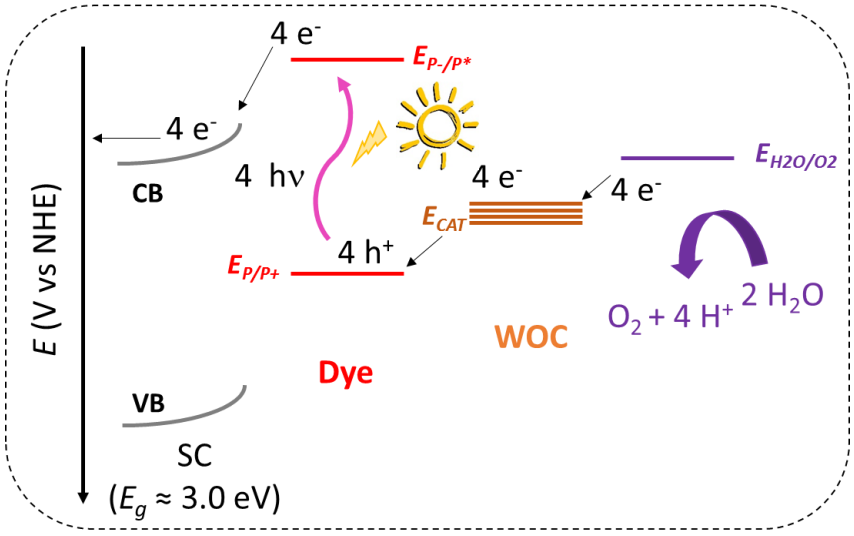

Scheme 1. Band diagram for a Dye-sensitized photoanode. CB and VB are the conduction and valence band of the semiconductor (SC) respectively. E_g is the bandgap of the SC. The P, P^+, P^- and P* are the dye and their oxidized, reduced and photoexcited forms, respectively. The $E_{P/P+}$ and the $E_{P-/P*}$ are their redox potential. E_{cat} is the turn on potential of the water oxidation catalyst (WOC), $E_{H2O/O2}$ is the thermodynamic potential.

In dye-sensitized photoanodes, the molecular dyes and catalysts are anchored on the surface of the semiconductor by the linkers described in section 1.4.1. For example, Meyer *et al* used the Phosphonate derivate complex **16** in Chart 4 to generate a molecular dye-sensitized photoanode. [92] In order to co-deposit the dye, one of the bpy of the $[Ru(bpy)_3]^{2+}$ dye was replaced by a diPO_3H_2-bpy ligand yielding the complex $Ru(bpy)_2$(di-PO_3H_2-bpy)$]^{2+}$, **18**. An electrode coated with a core-shell of TiO_2/ITO was modified by anchoring the two molecules to yield the hybrid photoanode (**18**+**16**)@TiO_2/ITO.[92] Similarly, Sun and Meyer groups generated photoanodes from complex **9** by replacing the initial axial pyridines by PO_3H_2-py and $Si(OH)_3$-Py ligands respectively: see complex $[Ru(bda)_2(PO_3H_2\text{-}py)_2(OH)]$ (**19**) and complex $[Ru(bda)_2$(Me-Py)(SiO_3H_3-Py)(OH)] (**20)** in Chart 5.[93,94] Both groups prepared dye sensitized photoanodes by codepositing the water oxidation catalysts and the dye on TiO_2/ITO core shell nanoparticles and TiO_2 nanoparticles.[93,94]

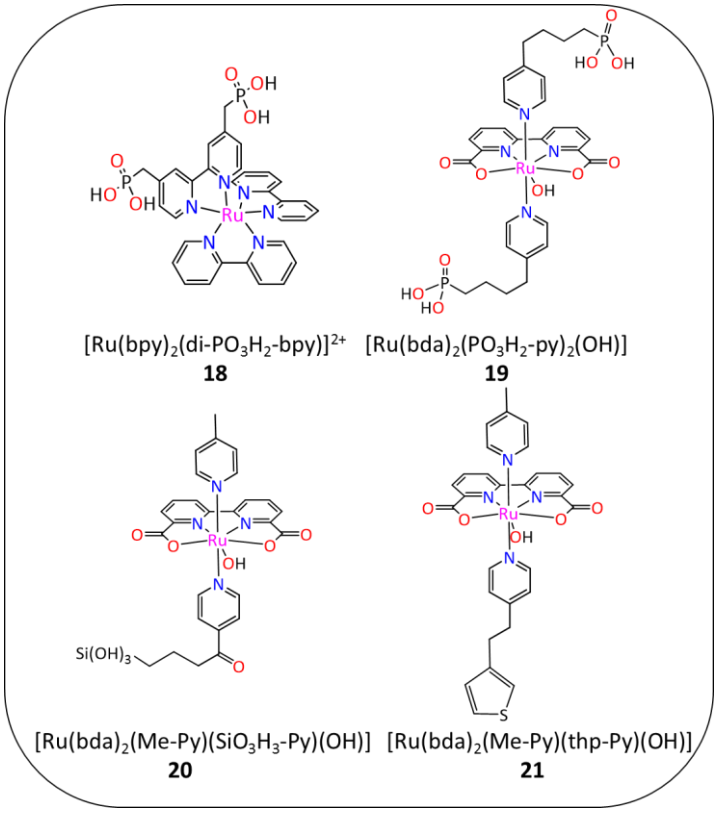

Chart 5. Dye (**18**) and complexes (**19**, **20** and **21**) used for the construction of molecular photoanodes. diPO_3H_2-bpy is ([2,2'-bipyridine]-4,4'-diylbis(methylene)) bis(phosphonic acid), PO_3H_2-py is(4-(pyridin-4-yl)butyl)phosphonic acid. thp-Py is 4-(2-(thiophen-3-yl)ethyl)pyridine.

Part of the knowledge required for the dye-sensitized photoanodes has been acquired by studying an equivalent system in solution. In the homogeneous systems, the $[Ru(bpy)_3]^{3+}$ dye is dissolved together with a water oxidation catalyst. An electron acceptor is also dissolved that removes electrons from the photoexcited dye under light illumination. The quantum efficiency for the three-compound mixture under 1 sun illumination is *circa* 10%.[95,96] Furthermore, the use of Transient Absorption Spectroscopy (TAS) enables quantifying the kinetics of the processes involved in the photocatalytic system together with other undesired processes, such as back electron transfer. [97]

Scheme 2 illustrates the band diagram for the semiconductor-catalyst design. In these photoanodes, the semiconductor absorbs the light in the visible region of the spectrum. In order to absorb significant part of the spectrum, the band gap of the seminconductor (E_g) must be below 2.5 eV. Once the semiconductor has absorbed the photons from the light, the electrical field generated in the semiconductor-solution junction directs the charges to the water

oxidation reaction (holes, h^+) and to the rear of the electrode (electrons, e^-). This phenomenon is analogous to the charge separation in a p-n junction of the PV cells.[8] A requirement is that the VB of the Semiconductor must fall above the onset of the water oxidation catalyst (E_{cat}).[98]

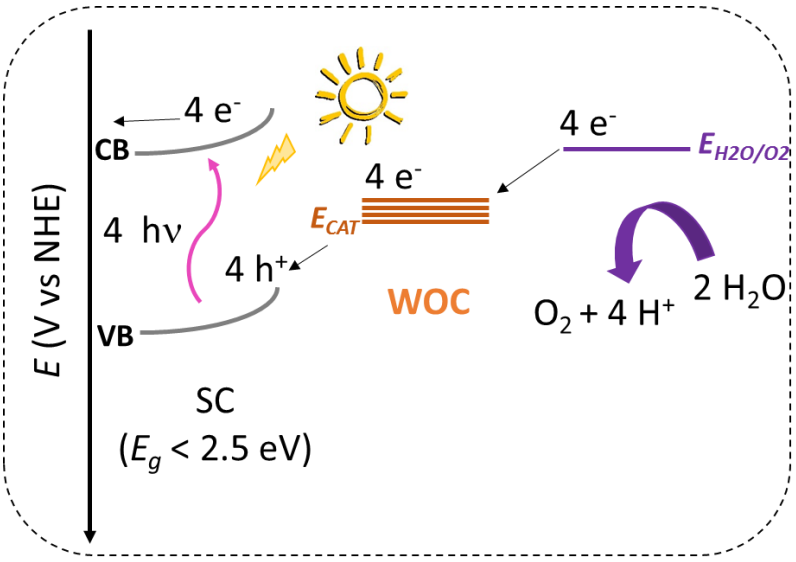

Scheme 2. Band diagram for a Semiconductor + Catalysts photoanode. E_g is the bandgap of the SC. E_{cat} is the turn on potential of the water oxidation catalyst (WOC), $E_{H2O/O2}$ is the thermodynamic potential.

Sun *et al* reported the only example in the literature of a semiconductor directly coupled to a molecular water oxidation catalyst.[99] The semiconductor-catalyst photoanode consisted of the anodic polymerization of complex [Ru(bda)$_2$(Me-Py)(thp-Py)(OH)] (**21**) containing a thiophene axial ligand (thp-Py), see Chart 5. The polymerization was performed on the surface of the α-Fe_2O_3 semiconductor (E_g = 2.3 eV) to generate the **21**@α-Fe_2O_3 photoanode.

1.5.2 Performance of Molecular Photoanodes

Table 3 summarizes the photochemical features of the two best-performing dye sensitized photoanodes, (**18**+**19**)@TiO_2/ITO and (**18**+**20**)@TiO_2, and the only example of semiconductor-catalyst molecular photoanode **21**@α-Fe_2O_3.[90,91]

Table 3. Photoeletrochemical data for (**18**+**19**)@TiO_2/ITO, (**18**+**20**)@TiO_2 and **21**@α-Fe_2O_3 photoanodes.

Photoanode	*Semiconductor*	*Dye*	*WOC*[c]	*j (mA/cm²) / time (min)*[d]	*Ref.*
(18+19)@TiO_2/ITO	TiO_2/ITO[a]	**18**	**19**	1.5 / 20	93
(18+20)@TiO_2	TiO_2[b]	**18**	**20**	1/ 2	94
21@α-Fe_2O_3	α-Fe_2O_3	---	**21**	0.3 / 5	99

[a]nanoITO/TiO_2 core/shell structure. [b] TiO_2 nanoparticles on FTO electrode, [c] Water Oxidation Catalyst, [d] time of sustained current

The first remarkable feature of the performance of the three photoanodes is the relative high current density. Photoanodes (**18**+**19**)@TiO_2/ITO and (**18**+**20**)@TiO_2) exhibit current densities around 1 mA /cm^2 under illumination, which exceed the 0.2 mA/ cm^2 exhibited by the related **17**@MWCNT/ITO anode.[77] The relative high current density of the anodes clearly comes from the nanoparticulate nature of the TiO_2 and TiO_2/ITO semiconductors that allows high catalyst loadings.

Despite the relative high current density, the performance is limited to less than 20 minutes for all the molecular photoanodes. This clearly limits their eventual incorporation in any commercial device in the future. Several hypothesis are nowadays available to explain the low stability.One possible hypothesis is the low stability of the phosphonate, carboxylate and silicate bonds under light illumination. Meyer *et al.* reported that phosphonate-metal oxide bonds broke under light illumination conditions.[100] This partially explains the low stability of the dye-sensitized photoanodes in the literature, such as (**18**+**19**)@TiO_2/ITO and (**18**+**20**)@TiO_2), that are based on phosphonate and silicate groups as linkers for the dyes and catalysts.

An alternative to the Phosphonate/carboxylate and silicate linkers may arise from the development of semiconductor-catalyst photoanodes. Future photoanode designs might include assemblies between water oxidation catalyst and small bandgap semiconductors such as carbon nitides[101] or Si.[36] The different nature of the surface of the semiconductors might permit using stronger linkers than ester bonds with metal oxides.

However, the main hypothesis for the low stability involves the nature of the water oxidation catalyst. Most of the photoanodes in the literature are based on second order water oxidation catalysts: such as complex **9** or its derived forms (**17, 19, 20** or **21**). When these catalyst are anchored to surfaces, they cannot follow their lowest energetic path and they must oxidize

water through high energetic paths. The high energetic paths might induce undesired reactions, namely degradation, that will reduce the stability of the catalyst. In the case of water oxidation, the inefficient catalytic reaction might also result in back electron transfer complications, which can further reduce the stability of the electrodes. Hence, the future attainment of stable molecular photoanodes depends on the discovery of fast first-order water oxidation catalysts.

1.6 References

1 *Adoption of the Paris Agreement. Proposal by the President*, Paris Climate Change Conference – November 2015, COP 21, Paris, France, 2015.
2 *Key world energy statistics 2016*, International Energy Agency, 2016.
3 *World Energy Outlook 2016*, International Energy Agency, 2016.
4 Llobet, A; Meyer, F. *Angew. Chem. Int. Ed.* **2011**, *50*, A30-33.
5 Fujishima, A.; Honda, K. *Nature* **1972**, *238*, 37-38.
6 Lewis, N. S.; Nocera, D. G. *Proc. Natl. Acad. Sci. U.S.A.***2006**, *103*, 15729-15735.
7 Gray, H. B. *Nat. Chem.* **2009**, *1*, 7-7.
8 Lewis, N. S. *Science* **2016**, *351*, 19201-19209.
9 Nielander, A. C.; Shaner, M. R.; Papadantonakis, K. M.; Francis, S. A.; Lewis, N. S. *Energy Environ. Sci.* **2015**, *8*, 16-25.
10 McKone, J. R.; Lewis, N. S.; Gray, H. B. *Chem. of Mat.* **2014**, *26*, 407-414.
11 Montoya, J. H.; Seitz, L. C.; Chakthranont, P.; Vojvodic, A.; Jaramillo, T. F.; Norskov, J. K. *Nat. Mater.* **2017**, *16*, 70-81.
12 Khaselev, O.; Turner, J. A. *Science* **1998**, *280*, 425-427.
13 Bonke, S. A.; Wiechen, M.; MacFarlane, D. R.; Spiccia, L. *Energy Environ. Sci.* **2015**, *8*, 2791-2796.
14 Jia, J.; Seitz, L. C.; Benck, J. D.; Huo, Y.; Chen, Y.; Ng, J. W. D.; Bilir, T.; Harris, J. S.; Jaramillo, T. F. *Nat. Commun.* **2016**, *7*, 13237-13237.
15 Fabian, D. M.; Hu, S.; Singh, N.; Houle, F. A.; Hisatomi, T.; Domen, K.; Osterloh, F. E.; Ardo, S. *Energy Environ. Sci.* **2015**, *8*, 2825-2850.
16 Appel, A. M.; Bercaw, J. E.; Bocarsly, A. B.; Dobbek, H.; DuBois, D. L.; Dupuis, M.; Ferry, J. G.; Fujita, E.; Hille, R.; Kenis, P. J. A.; Kerfeld, C. A.; Morris, R. H.; Peden, C. H. F.; Portis, A. R.; Ragsdale, S. W.; Rauchfuss, T. B.; Reek, J. N. H.; Seefeldt, L. C.; Thauer, R. K.; Waldrop, G. L. *Chem. Rev.* **2013**, *113*, 6621-6658.
17 Schrock, R. R. *Proc. Natl. Acad. Sci. U.S.A.* **2006**, *103*, 17087-17087.
18 Liu, F.; Concepcion, J. J.; Jurss, J. W.; Cardolaccia, T.; Templeton, J. L.; Meyer, T. J. *Inorg. Chem.* **2008**, *47*, 1727-1752.
19 Grätzel, M. *Acc. Chem. Res.* **1981**, 14, 376– 384.
20 Walter, M. G.; Warren, E. L.; McKone, J. R.; Boettcher, S. W.; Mi, Q.; Santori, E. A.; Lewis, N. S. *Chem. Rev.* **2010**, 110, 6446– 6473.
21 Vesborg, P. C. K.; Jaramillo, T. F. *RSC Adv.* **2012**, 2, 7933-7940.
22 Rappaport, F.; Guergova-Kuras, M.; Nixon, P. J.; Diner, B. A.; Lavergne, J. *Biochemistry* **2002**, *41*, 8518-8527.
23 Umena, Y.; Kawakami, K.; Shen, J.-R.; Kamiya, N. *Nature* **2011**, *473*, 55-60.
24 Suga, M.; Akita, F.; Hirata, K.; Ueno, G.; Murakami, H.; Nakajima, Y.; Shimizu, T.; Yamashita, K.; Yamamoto, M.; Ago, H.; Shen, J.-R. *Nature* **2015**, *517*, 99-103.
25 Glöckner, C.; Kern, J.; Broser, M.; Zouni, A.; Yachandra, V.; Yano, J. *J. Biol. Chem.* **2013**, *288*, 22607-22620.
26 Blomberg, M. R. A.; Borowski, T.; Himo, F.; Liao, R.-Z.; Siegbahn, P. E. M. *Chem. Rev.* **2014**, *114*, 3601-3658.
27 Cox, N.; Pantazis, D. A.; Neese, F.; Lubitz, W. *Acc. Chem. Res.* **2013**, *46*, 1588-1596.
28 Berardi, S.; Drouet, S.; Francas, L.; Gimbert-Surinach, C.; Guttentag, M.; Richmond, C.; Stoll, T.; Llobet, A. *J. Chem. Soc. Rev.* **2014**, *43*, 7501-7519.
29 Nocera, D. G. *Acc. Chem. Res.* **2012**, *45*, 767–776.
30 Dismukes, G. C.; Brimblecombe, R.; Felton, G. A. N.; Pryadun, R. S.; Sheats, J. E.; Spiccia, L.; Swiegers, G. F. *Acc. Chem. Res.* **2009**, *42*, 1935-1943.
31 Coehn, A.; Gläser, M. *Zeits. Anorg. Chem*. **1902***, 33,* 9-24.
32 Matsumoto, Y.; Sato, E. *Mater. Chem. Phys.* **1986**, *14*, 397-426.

33 McCrory, C. C. L.; Jung, S.; Peters, J. C.; Jaramillo, T. F. *J. Am. Chem. Soc.* **2013**, *135*, 16977-16987.
34 McCrory, C. C. L.; Jung, S.; Ferrer, I. M.; Chatman, S. M.; Peters, J. C.; Jaramillo, T. F. *J. Am. Chem. Soc.* **2015**, *137*, 4347-4357.
35 Jung, S.; McCrory, C. C. L.; Ferrer, I. M.; Peters, J. C.; Jaramillo, T. F. *J. Mater. Chem. A* **2016**, *4*, 3068-3076.
36 Hu, S.; Shaner, M. R.; Beardslee, J. A.; Lichterman, M.; Brunschwig, B. S.; Lewis, N. S. *Science* **2014**, *344*, 1005-1009.
37 Zhou, X.; Liu, R.; Sun, K.; Papadantonakis, K. M.; Brunschwig, B. S.; Lewis, N. S. *Energy Environ. Sci.* **2016**, *9*, 892-897.
38 Gersten, S. W.; Samuels, G. J.; Meyer, T. J. *J. Am. Chem. Soc.* **1982**, 104, 4029– 4030.
39 Concepcion, J. J.; Jurss, J. W.; Brennaman, M. K.; Hoertz, P. G.; Patrocinio, A. O. T.; Murakami Iha, N. Y.; Templeton, J. L.; Meyer, T. J. *Acc. Chem. Res.* **2009**, *42*, 1954-1965.
40 Alperovich, I.; Smolentsev, G.; Moonshiram, D.; Jurss, J. W.; Concepcion, J. J.; Meyer, T. J.; Soldatov, A.; Pushkar, Y. *J. Am. Chem. Soc.* **2011**, *133*, 15786-15794.
41Jurss, J. W.; Concepcion, J. J.; Butler, J. M.; Omberg, K. M.; Baraldo, L. M.; Thompson, D. G.; Lebeau, E. L.; Hornstein, B.; Schoonover, J. R.; Jude, H.; Thompson, J. D.; Dattelbaum, D. M.; Rocha, R. C.; Templeton, J. L.; Meyer, T. J. *Inorg. Chem.* **2012**, *51*, 1345-1358.
42 Moonshiram, D.; Jurss, J. W.; Concepcion, J. J.; Zakharova, T.; Alperovich, I.; Meyer, T. J.; Pushkar, Y. *J. Am. Chem. Soc.* **2012**, *134*, 4625-4636.
43 Hurst, J. K.; Cape, J. L.; Clark, A. E.; Das, S.; Qin, C. *Inorg. Chem.* **2008**, *47*, 1753-1764.
44 Hurst, J. K.; Roemeling, M. D.; Lymar, S. V. *J. Phys. Chem. B* **2015**, *119*, 7749-7760.
45 Barnett, S. M.; Goldberg, K. I.; Mayer, J. M. *Nat. Chem.* **2012**, *4*, 498-502.
46 Zhang, M.-T.; Chen, Z.; Kang, P.; Meyer, T. J. *J. Am. Chem. Soc.* **2013**, *135*, 2048-2051.
47 Zhang, T.; Wang, C.; Liu, S.; Wang, J.-L.; Lin, W. *J. Am. Chem. Soc.* **2014**, *136*, 273-281.
48 Garrido-Barros, P.; Funes-Ardoiz, I.; Drouet, S.; Benet-Buchholz, J.; Maseras, F.; Llobet, A. *J. Am. Chem. Soc.* **2015**, *137*, 6758-6761.
49 Ellis, W. C.; McDaniel, N. D.; Bernhard, S.; Collins, T. J. *J. Am. Chem. Soc.* **2010**, *132*, 10990-10991.
50 Hull, J. F.; Balcells, D.; Blakemore, J. D.; Incarvito, C. D.; Eisenstein, O.; Brudvig, G. W.; Crabtree, R. H. *J. Am. Chem. Soc.* **2009**, *131*, 8730-8731.
51 Cady, C. W.; Crabtree, R. H.; Brudvig, G. W. *Coordination chemistry reviews* **2008**, *252*, 444.
52 Leung, C.-F.; Ng, S.-M.; Ko, C.-C.; Man, W.-L.; Wu, J.; Chen, L.; Lau, T.-C. *Energy Environ. Sci.* **2012**, *5*, 7903-7907.
53 Rigsby, M. L.; Mandal, S.; Nam, W.; Spencer, L. C.; Llobet, A.; Stahl, S. S. *Chem. Sci.* **2012**, *3*, 3058-3062.
54 Gimbert-Suriñach, C.; Moonshiram, D.; Francàs, L.; Planas, N.; Bernales, V.; Bozoglian, F.; Guda, A.; Mognon, L.; López, I.; Hoque, M. A.; Gagliardi, L.; Cramer, C. J.; Llobet, A. *J. Am. Chem. Soc.* **2016**, *138*, 15291-15294.
55 Bozoglian, F.; Romain, S.; Ertem, M. Z.; Todorova, T. K.; Sens, C.; Mola, J.; Rodriguez, M.; Romero, I.; Benet-Buchholz, J.; Fontrodona, X.; Cramer, C. J.; Gagliardi, L.; Llobet, A. *J. Am. Chem. Soc.* **2009**, *131*, 15176-15187.
56 Concepcion, J. J.; Jurss, J. W.; Templeton, J. L.; Meyer, T. J. *J. Am. Chem. Soc.* **2008**, *130*, 16462-16463.
57 Duan, L.; Bozoglian, F.; Mandal, S.; Stewart, B.; Privalov, T.; Llobet, A.; Sun, L. *Nat. Chem.* **2012**, *4*, 418-423.
58 Sala, X.; Maji, S.; Bofill, R.; Garcia-Anton, J.; Escriche, L.; Llobet, A. *Acc. Chem. Res.* **2014**, *47*, 504-516.
59 Sens, C.; Romero, I.; Rodriguez, M.; Llobet, A.; Parella, T.; Benet-Buchholz, J. *J. Am. Chem. Soc.* **2004**, *126*, 7798-7799.
60 Unpublished Results

61 Neudeck, S.; Maji, S.; López, I.; Meyer, S.; Meyer, F.; Llobet, A. *J. Am. Chem. Soc.* **2014**, *136*, 24-27.
62 Wasylenko, D. J.; Ganesamoorthy, C.; Henderson, M. A.; Koivisto, B. D.; Osthoff, H. D.; Berlinguette, C. P. *J. Am. Chem. Soc.* **2010**, *132*, 16094–16106.
63 Zong, R.; Thummel, R. P. *J. Am. Chem. Soc.* **2005**, *127*, 12802-12803.
64 Mognon, L.; Benet-Buchholz, J.; Llobet, A. *Inorg. Chem.* **2015**, *54*, 11948-11957.
65 Duan, L.; Fischer, A.; Xu, Y.; Sun, L. *J. Am. Chem. Soc.* **2009**, *131*, 10397-10399.
66 Wang, L.; Duan, L.; Wang, Y.; Ahlquist, M. S. G.; Sun, L. *Chem. Commun.* **2014**, *50*, 12947-12950.
67 Moyer, B. A.; Meyer, T. J. *J. Am. Chem. Soc.* **1978**, *100*, 3601-3603.
68 Nagle, J. K.; Bernstein, J. S.; Young, R. C.; Meyer, T. J. *Inorg. Chem.* **1981**, *20*, 1760-1764.
69 Saveant, J.-M. *Energy Environ. Sci.* **2012**, *5*, 7718-7731.
70 Weinberg, D. R.; Gagliardi, C. J.; Hull, J. F.; Murphy, C. F.; Kent, C. A.; Westlake, B. C.; Paul, A.; Ess, D. H.; McCafferty, D. G.; Meyer, T. J. *Chem. Rev.* **2012**, *112*, 4016-4093.
71 Gagliardi, C. J.; Vannucci, A. K.; Concepcion, J. J.; Chen, Z.; Meyer, T. J. *Energy Environ. Sci.* **2012**, *5*, 7704-7717.
72 Huynh, M. T.; Mora, S. J.; Villalba, M.; Tejeda-Ferrari, M. E.; Liddell, P. A.; Cherry, B. R.; Teillout, A.-L.; Machan, C. W.; Kubiak, C. P.; Gust, D.; Moore, T. A.; Hammes-Schiffer, S.; Moore, A. L. *ACS Centr. Sci.* **2017**, *in press*
73 Romain, S.; Bozoglian, F.; Sala, X.; Llobet, A. *J. Am. Chem. Soc.* **2009**, *131*, 2768-2769.
74 Funes-Ardoiz, I.; Garrido-Barros, P.; Llobet, A.; Maseras, F. *ACS Catal.* **2017**, *7*, 1712-1719.
75 Moonshiram, D.; Alperovich, I.; Concepcion, J. J.; Meyer, T. J.; Pushkar, Y. *Proc. Natl. Acad. Sci. U. S. A.* **2013**, *110*, 3765.
76 Duan, L.; Araujo, C. M.; Ahlquist, M. S. G.; Sun, L. *Proc. Natl. Acad. Sci. U. S. A.* **2012**, *109*, 15584-15588.
77 Jiang, Y.; Li, F.; Zhang, B.; Li, X.; Wang, X.; Huang, F.; Sun, L. *Angew. Chem. Int. Ed.* **2013**, *52*, 3398-3401.
78 Ohzu, S.; Ishizuka, T.; Hirai, Y.; Jiang, H.; Sakaguchi, M.; Ogura, T.; Fukuzumi, S.; Kojima, T. *Chem. Sci.* **2012**, *3*, 3421-3431.
79 Costentin, C.; Drouet, S.; Robert, M.; Savéant, J.-M. *J. Am. Chem. Soc.* **2012**, *134*, 11235-11242.
80 Costentin, C.; Savéant, J.-M. *ChemElectroChem* **2014**, *1*, 1226-1236.
81 Artero, V.; Saveant, J.-M. *Energy Environ. Sci.* **2014**, *7*, 3808-3814.
82 Concepcion, J. J.; House, R. L.; Papanikolas, J. M.; Meyer, T. J *Proc. Natl. Acad. Sci. U. S. A.* **2012**, *109*, 15560-15564.
83 Francas, L.; Richmond, C.; Garrido-Barros, P.; Planas, N.; Roeser, S.; Benet-Buchholz, J.; Escriche, L.; Sala, X.; Llobet, A. *Chem. Eur. J.* **2016**, *22*, 5261-5268.
84 Chen, Z.; Concepcion, J. J.; Jurss, J. W.; Meyer, T. J. *J. Am. Chem. Soc.* **2009**, *131*, 15580-15581.
85 Odrobina, J.; Scholz, J.; Pannwitz, A.; Francàs, L.; Dechert, S.; Llobet, A.; Jooss, C.; Meyer, F. *ACS Catal.* **2017**, *7*, 2116-2125.
86 Li, F.; Zhang, B.; Li, X.; Jiang, Y.; Chen, L.; Li, Y.; Sun, L. *Angew. Chem. Int. Ed.* **2011**, *50*, 12276-12279.
87 Tong, L.; Gothelid, M.; Sun, L. *Chem. Commun.* **2012**, *48*, 10025-10027.
88 Mola, J.; Mas-Marza, E.; Sala, X.; Romero, I.; Rodríguez, M.; Viñas, C.; Parella, T.; Llobet, A. *Angew. Chem. Int. Ed.* **2008**, *47*, 5830-5832.
89 Maji, S.; López, I.; Bozoglian, F.; Benet-Buchholz, J.; Llobet, A. *Inorg. Chem.* **2013**, *52*, 3591-3593.
90 Alibabaei, L.; Brennaman, M. K.; Norris, M. R.; Kalanyan, B.; Song, W.; Losego, M. D.; Concepcion, J. J.; Binstead, R. A.; Parsons, G. N.; Meyer, T. J. *Proc. Natl. Acad. Sci. U.S.A.* **2013**, *110*, 20008-20013.
91 Brennaman, M. K.; Dillon, R. J.; Alibabaei, L.; Gish, M. K.; Dares, C. J.; Ashford, D. L.; House, R. L.; Meyer, G. J.; Papanikolas, J. M.; Meyer, T. J. *J. Am. Chem. Soc.* **2016**, *138*, 13085-13102.

92 Song, W.; Vannucci, A. K.; Farnum, B. H.; Lapides, A. M.; Brennaman, M. K.; Kalanyan, B.; Alibabaei, L.; Concepcion, J. J.; Losego, M. D.; Parsons, G. N.; Meyer, T. J. *J. Am. Chem. Soc.* **2014**, *136*, 9773-9779.
93 Sheridan, M. V.; Sherman, B. D.; Coppo, R. L.; Wang, D.; Marquard, S. L.; Wee, K.-R.; Murakami Iha, N. Y.; Meyer, T. J. *ACS Energy Lett.* **2016**, *1*, 231-236.
94 Gao, Y.; Ding, X.; Liu, J.; Wang, L.; Lu, Z.; Li, L.; Sun, L. *J. Am. Chem. Soc.* **2013**, *135*, 4219-4222.
95 Lewandowska-Andralojc, A.; Polyansky, D. E.; Zong, R.; Thummel, R. P.; Fujita, E. *Phys. Chem. Chem. Phys.* **2013**, *15*, 14058-14068.
96 Berardi, S.; Francàs, L.; Neudeck, S.; Maji, S.; Benet-Buchholz, J.; Meyer, F.; Llobet, A. *ChemSusChem* **2015**, *8*, 3688-3696.
97 Gimbert-Suriñach, C.; Albero, J.; Stoll, T.; Fortage, J.; Collomb, M.-N.; Deronzier, A.; Palomares, E.; Llobet, A. *J. Am. Chem. Soc.* **2014**, *136*, 7655- 7661.
98 Tan, M. X.; Laibinis, P. E.; Nguyen, S. T.; Kesselman, J. M.; Stanton, C. E.; Lewis, N. S. In *Progress in Inorganic Chemistry*; John Wiley & Sons, Inc.: 2007, 21-144.
99 Wang, L.; Fan, K.; Chen, H.; Daniel, Q.; Philippe, B.; Rensmo, H.; Sun, L. *Catal. Today*, **2017***, in press*
100 Hyde, J. T.; Hanson, K.; Vannucci, A. K.; Lapides, A. M.; Alibabaei, L.; Norris, M. R.; Meyer, T. J.; Harrison, D. P. *ACS Appl. Mater. Interfaces* **2015**, *7*, 9554-9562.
101 Shalom, M.; Inal, S.; Fettkenhauer, C.; Neher, D.; Antonietti, M. *J. Am. Chem. Soc.* **2013**, *135*, 7118-7121.

Chapter 2

Objectives

Some of the knowledge gaps highlighted in Chapter 1 have been transformed into objectives during the development of the present thesis. The objectives travel from the design and performance of molecular catalysts in solution to the development of powerful anodes and photoanodes.

II

The main challenge in molecular Ru-based water oxidation catalysis is to develop powerful molecular anodes and photoanodes. The field of molecular water oxidation has boomed with the appearance of new mononuclear seven-coordinate water oxidation catalysts with activities exceededing that of the natural Mn_4O_5 cluster. At the start of this thesis, we envisioned potentially seven-coordinate Ru complexes based on the [2,2'-bipyridine]-6,6'-dicarboxylate (bda^{2-}), [2,2':6',2''-terpyridine]-6,6''-dicarboxylate (tda^{2-}) and 2,5-bis(6-carboxylatopyridin-2-yl)pyrrol-1-ide ($t5a^{3-}$) scaffolds as equatorial ligands.

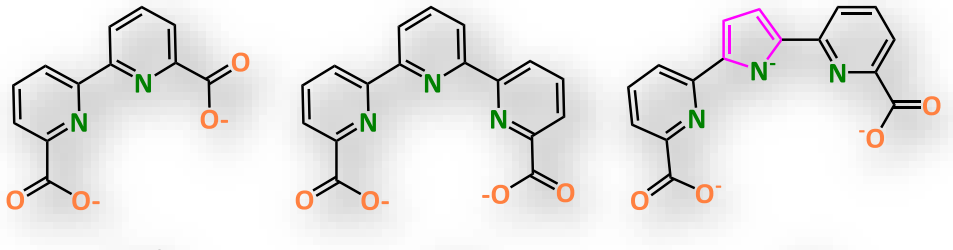

bda^{2-} tda^{2-} $t5a^{3-}$

Therefore, the main objective of this thesis is the generation of powerful anodes and photoanodes based on Ru-bda, Ru-tda and Ru-t5a complexes and the understanding of the factors that rule their water oxidation catalysis. From this general objective, specific objectives have been pursued during the development of the thesis.

Objective A: "To Synthesize new Ru seven-coordinate complexes based on the 2,2':6',2''-terpyridine]-6,6''-dicarboxylate (tda^{2-}) and 2,5-bis(6-carboxylatopyridin-2-yl)pyrrol-1-ide ($t5a^{3-}$) ligand and pyridine as axial ligands, to test their capability to catalyze the water oxidation reaction".

Objective B - "To determine and to quantify the ruling factors of seven coordination water oxidation catalysis in solution: the effect of the pi-pi stacking, the H bonding and the O-O bond mechanism implications on the activity".

Objective C: "To develop electrochemical methods to elucidate and to benchmark the new seven-coordinate Ru catalysts.

Objective D: "To prepare anodes based on the most powerful seven-coordination complexes, to quantify their performance and to analyze their active species".

Objective E: "To prepare photoanodes based on the most powerful seven-coordination complexes.

Chapter 3

H-Bonding Rockets Water Oxidation Catalysis In New Ru Complexes

III

The synthesis, characterization, redox properties and catalytic activity of two new families of seven-coordinate Ru complexes based on the (2,2':6',2''-terpyridine]-6,6''-dicarboxylate) (tda^{2}) or the 2,5-bis(6-carboxylatopyridin-2-yl)pyrrol-1-ide ($t5a^{3-}$) ligand and pyridine as axial ligands are reported. The corresponding Ru=O complexes are among the fastest molecular water oxidation catalysts in the literature due to H intramolecular bonding provided by a pendant carboxylate.

The chapter consist of the following indendependent papers:

PAPER A Matheu, R.; Ertem, M. Z.; Benet-Buchholz, J.; Coronado, E.; Batista, V. S.; Sala, X.; Llobet, A. *J. Am. Chem. Soc,* **2015**, *137*, 10786-10795

PAPER B Matheu, R.; Ertem, M. Z.; Pipelier, M.; Lebreton, J.; Dubreuil, D.; Benet-Buchholz, J.; Sala, X.; Tessier, A.; Llobet, A.; **2017***, submitted*

III

PAPER A Intramolecular Proton Transfer Boosts Water Oxidation Catalyzed By A Ru Complex

Matheu, R.; Ertem, M. Z.; Benet-Buchholz, J.; Coronado, E.; Batista, V. S.; Sala, X.; Llobet, A. *J. Am. Chem. Soc.* **2015**, *137*, 10786-10795.

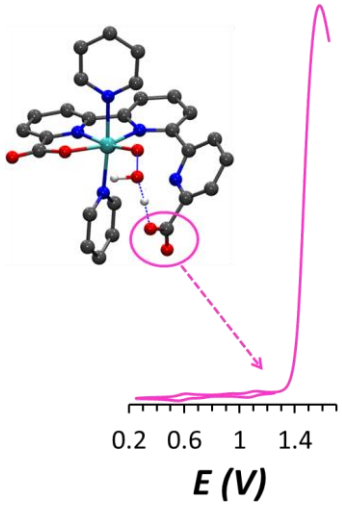

Abstract

We introduce a new family of complexes of general formula $[Ru^{n}(tda)(py)_2]^{m+}$ (n=2, m=0, **1;** n=3, m=1, $\mathbf{2}^{+}$**;** n=4, m=2, $\mathbf{3}^{2+}$), with tda^{2-}=[2,2':6',2''-terpyridine]-6,6''-dicarboxylate, including complex $[Ru^{IV}(OH)(tda\text{-}\kappa\text{-}N^{3}O)(py)_2]^{+}$ $\mathbf{4H}^{+}$ which we find to be an impressive water oxidation catalyst, formed by hydroxo coordination to $\mathbf{3}^{2+}$ under basic conditions. The complexes are synthesized, isolated and thoroughly characterized by analytical, spectroscopic (UV-Vis, NMR, EPR), computational and electrochemical techniques (CV, DPV, Coulometry), including solid state monocrystal X-ray diffraction analysis. In the oxidation state IV, the Ru center is seven coordinated and diamagnetic, whereas in oxidation state II the complex has an unbonded dangling carboxylate, so is six coordinated while still diamagnetic. With oxidation state III, the coordination number is halfway between the coordination of oxidation state II and IV. Species generated in situ have also been characterized by spectroscopic, computational and electrochemical techniques, together with the related species derived from a different degree of protonation and oxidation states. $\mathbf{4H}^{+}$ can be generated potentiometrically, or voltammetrically, from $\mathbf{3}^{2+}$ and both coexist in solution. While complex $\mathbf{3}^{2+}$ is not catalytically active, the catalytic performance of complex $\mathbf{4H}^{+}$ is characterized by the foot of the wave analysis (FOWA), giving an impressive TOF record of 8,000 s^{-1} at pH = 7.0 and 50,000 s^{-1} at pH = 10.0. DFT calculations provide a complete description of the water oxidation catalytic cycle of $\mathbf{4H}^{+}$ manifesting the key functional role of the dangling carboxylate in lowering the activation free energies leading to O-O bond formation.

Contributions

Roc Matheu synthetized and characterized the new compounds, performed the electrochemical and spectroscopic analysis and prepared the manuscript.

A 1 Introduction

Fundamental understanding of the electronic and structural factors that determine the ultimate performance of water oxidation catalysts (WOCs) is critical for the development of catalytic systems for energy conversion.[1-6] Efficient functionality for fast and oxidatively rugged[7,8] performance at neutral pH can provide durability for sufficiently long times as necessary for practical applications.[9,10] Here, we introduce and characterize a new family of Ru complexes, including compound $[Ru^{IV}(OH)(tda\text{-}\kappa\text{-}N^3O)(py)_2]^+$ with tda^{2-}=[2,2':6',2''-terpyridine]-6,6''-dicarboxylate, found to be an impressive water oxidation catalyst both under neutral and alkaline conditions.

III

Transition metal complexes provide an excellent platform for mechanistic studies based on ligand design.[11-13] In particular, Ru-aqua complexes with polypyridylic ligands[14-17] are robust catalysts that allow for the analysis of mechanisms much more accessible than those of first row transition metals with labile ligands.[18-22] When combined with the theoretical analysis, via density functional theory (DFT) calculations, spectroscopic and electrochemical measurements provide detailed information on the nature of reaction intermediates and activation free energies along the catalytic cycle of water oxidation.[23-30] Strong sigma donation groups like carboxylate ligands in 2,2'-bipyridine-6,6'-dicarboxylic acid (H_2bda; see Chart 1 for a drawing), together with seven coordination have allowed easy access to reactive species in high oxidation states such as $[Ru^V(O)(bda)(pic)_2]^+$ (pic is 4-picoline) where the metal center is at formal oxidation state of V.[31] Additional tuning of the activation energy barriers can result from supramolecular interactions, based on π- π stacking of ligands with π -extended conjugation such as isoquinoline and its derivatives favoring formation of dinuclear peroxo intermediates.[32,33] Furthermore, hydrogen bonding interactions can play a significant role in the kinetics as demonstrated with strategically substituted fluro-2,2'-bpy ligands.[34-36] Finally, the presence of an external base can also strongly influence the kinetics of water oxidation reaction by facilitating proton coupled electron transfer (PCET) and deprotonation of the incoming water molecule at the O-O bond formation step as has been recently proposed using phosphate, borate or carboxylate as a base. Also, a direct interaction of OH^- with the Ru high valent reactive species at high pH has also been shown to enhance kinetics.[37,38]

Chart 1. Ligands used and discussed in this work with labeling for NMR assignment.

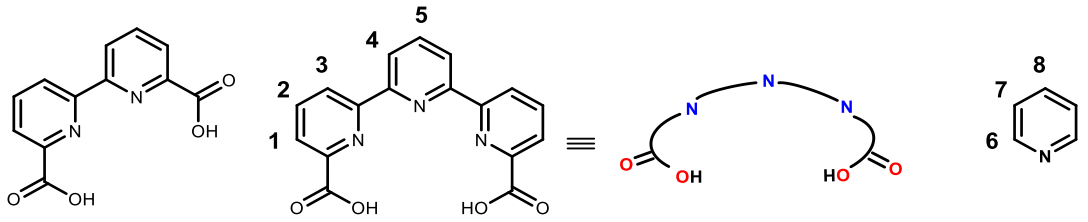

III

Using the knowledge accumulated over recent years, we have designed new Ru complexes that could potentially benefit from most of the considerations mentioned above. In particular, the new catalyst $[Ru^{IV}(OH)(tda\text{-}\kappa\text{-}N^3O)(py)_2]^+$ combines the various types of interactions responsible for redox leveling effects and exhibits an impressive catalytic performance of water oxidation with turnover frequencies (TOF) of 8,000-50,000 s^{-1} depending on pH. To the best of our knowledge, these TOFs are the highest ever reported under analogous conditions. We describe the synthesis, spectroscopic, electrochemical and theoretical characterization of the series of Ru complexes with the pentadentate ligand [2,2':6',2''-terpyridine]-6,6''-dicarboxylic acid (H_2tda; see Chart 1). This ligand can *potentially* coordinate to a metal center, in a $\kappa\text{-}N^3O^2$ fashion in the equatorial zone. The auxiliary axial positons are coordinated by pyridine ligands that are generally not directly involved in the electron transfer and/or proton transfer, or in the O-O bond formation.

A 2 Results and Discussion

A 2.1 Synthesis and solid state structure

The synthesis of the Ru complexes described in this work is summarized in Scheme 1. Reaction of $[Ru^{II}Cl_2(dmso)_4]$ with H_2tda, in the presence of NEt_3 as a base at reflux with MeOH, followed by addition of pyridine and further reflux in a mixture of water and pyridine produces complex $[Ru^{II}(tda\text{-}\kappa\text{-}N^3O)(py)_2]$, **1**, in 50% isolated yield. Treatment of the latter with one equivalent of Ce(IV) as an oxidant generates the $[Ru^{III}(tda\text{-}\kappa\text{-}N^3O^2)(py)_2](PF_6)$, **2**$(PF_6)$, complex. Subsequent addition of one more equivalent of Ce(IV) to $\mathbf{2}^+$ generates $[Ru^{IV}(tda\text{-}k\text{-}N^3O^2)(py)_2](PF_6)_2$, **3**$(PF_6)_2$, in 39% and 32% isolated yield, respectively. All of these new complexes are characterized analytically and spectroscopically by UV-vis, EPR and 1D and 2D NMR in solution as presented and discussed in the following section. In addition, monocrystal X-ray diffraction analysis has been carried out to characterize the complexes in the solid state. Ortep drawings of **1** and those of the cationic moieties of $\mathbf{2}^+$ and $\mathbf{3}^{2+}$ are presented in Figure 1.

Scheme 1. Synthetic strategy for the preparation of the complexes described in this work and nomenclature used. Broken lines indicate bonds that are simultaneously formed and broken.

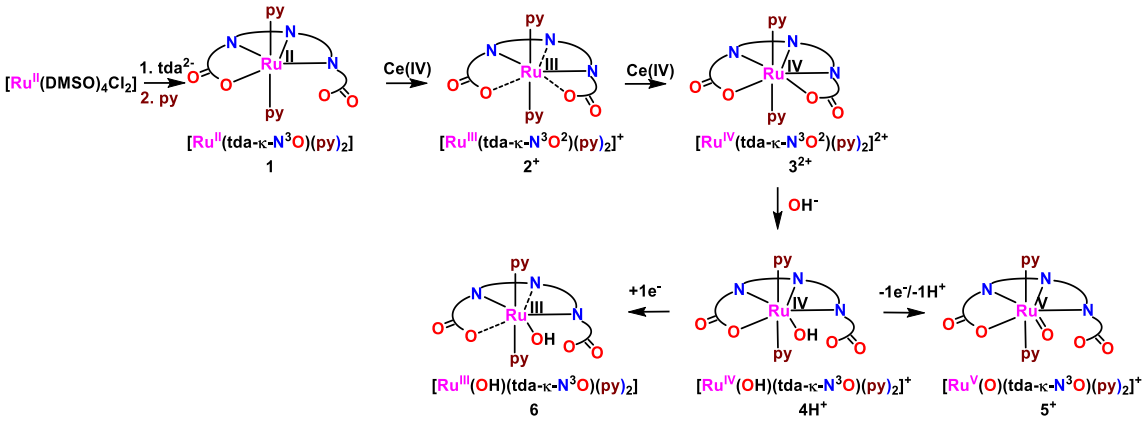

Complex **1** displays the typical distorted octahedral geometry around the Ru center as expected for low spin d^6 Ru(II).[29,32,39,40] The pyridine monodentate ligands occupy the axial positions whereas tda^{2-} binds as an equatorial ligand. With Ru in oxidation state II, tda^{2-} binds in a tetradentate κ-N^3O fashion with a non-bonding dangling carboxylate as shown in Figure 1. In oxidation state III, two different structural units are found in the unit cell of complex $[Ru^{III}(tda\text{-}\kappa\text{-}N^3O^2)(py)_2]^+$, $\mathbf{2}^+$. One of these structures has the tda^{2-} ligand bound in a κ-N^2O^2 mode with the central pyridyl of this ligand formally non-bonded although at "contact" distance (Ru-N distance = 2.38 Å). The other Ru(III) structure also has tda^{2-} as a tetradentate ligand although bound in a κ-N^3O mode, with the two carboxylates weakly bonded with long Ru-O distances of 2.33 Å and 2.23 Å, respectively (typical Ru(III)-$O_{carboxylate}$ bonds are in the 1.9–2.1 Å range).[31,41] Given the fact that the five N^3O^2 atoms are all partially involved in bonding at 100 K, we label the complex "tda-κ-N^3O^2" although the 18-electron rule is satisfied when only four of the atoms are effectively bound to Ru(III).[42]As the axial pyridines are always fully bound to Ru, we expect that the Ru-N and Ru-O bonds are simultaneously made and broken very quickly at room temperature, as represented by the dashed lines in Scheme 1. Density functional theory (DFT) calculations based on the M06-L[43] and M11-L[44] functionals (see Computational Methods in SI for details) provide optimized structures for the Ru-tda complexes at different oxidation states (Figure S25 in the SI). The comparison of the calculated and X-ray bond lengths indicate good agreement (Table S2 in the SI). For Ru^{II} oxidation state, we carried out optimizations for both $[Ru^{II}(tda\text{-}\kappa\text{-}N^3O)(py)_2]$, **1**, and $[Ru^{II}(tda\text{-}\kappa\text{-}N^2O^2)(py)_2]$ conformers and found **1** to be more stable by 5.6 kcal/mol in line with the experimental observations. For oxidation states III and IV, the DFT calculations favored one conformer, namely $[Ru^{III}(tda\text{-}\kappa\text{-}N^2O^2)(py)_2]^+$ and $[Ru^{IV}(tda\text{-}\kappa\text{-}N^3O^2)(py)_2]^{2+}$, $\mathbf{3}^{2+}$, which will be discussed in the following sections.

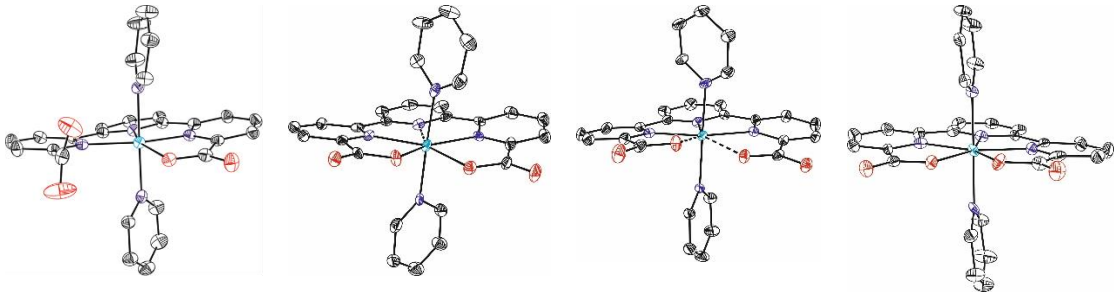

Figure 1: X-Ray ORTEP plots of: $[Ru^{II}(tda\text{-}k\text{-}N^3O)Py_2]$, $[Ru^{III}(tda\text{-}k\text{-}N^2O^2)Py_2]^+$, $[Ru^{III}(tda\text{-}k\text{-}N^3O)Py_2]^+$ and $[Ru^{IV}(tda\text{-}k\text{-}N^3O^2)Py_2\}^{2+}$ Ellipsoids are plotted at 50 % probability. Broken lines indicate contacts. Color codes: Ru, cyan; N, blue; O, red; C, black. H-atoms are not shown.

III

A 2.2 Spectroscopic Characterization based on NMR, EPR and UV-vis.

Figure 2 shows the ^{1}H NMR spectra of complexes **1**, **2**$^+$ and **3**$^{2+}$ in pD = 7.0 solutions of phosphate buffer. As expected, the high-field octahedral d^6 Ru(II) complex **1** is diamagnetic and all resonances could be easily assigned based on integrations, multiplicity and the combination of 1D and 2D NMR (see SI for a complete set of spectra). For **1**, the resonances due to the tda^{2-} ligand are symmetric indicating a fast dynamic behavior at room temperature. Further, the room temperature 2D ^{15}N-^{1}H HMBC (see figure S6) of **1** shows that all of the N atoms of tda^{2-} are bonded to the metal center. Therefore, the dynamical ligand exchange behavior is limited to the carboxylate sites, as indicated by equation 1.

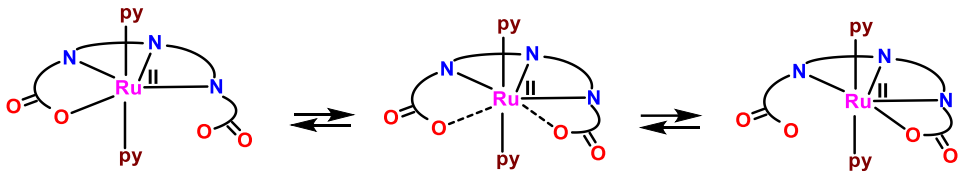

(1)

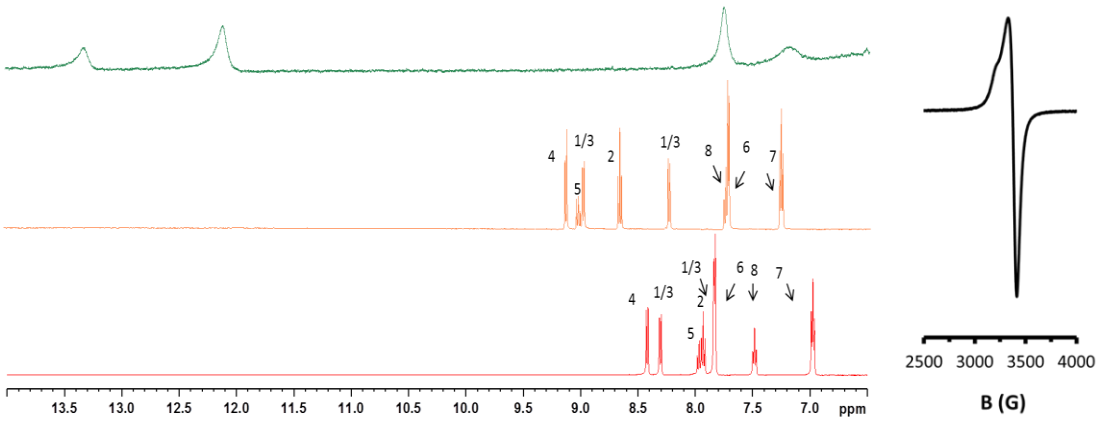

Figure 2: Left, ^{1}H NMR spectra in a phosphate buffer pD = 7.0 solution for [Ru^{II}(tda-k-N^{3}O)Py$_2$], **1** (red), [Ru^{III}(tda-k-N^{3}O^{2})Py$_2$]$^{+}$, **2**$^{+}$ (green) and [Ru^{IV}(tda-k-N^{3}O^{2})Py$_2$}$^{2+}$, **3**$^{2+}$ (orange). Right, EPR of **2**$^{+}$ at pH = 7.0. The assignment is keyed in Chart 1.

Complex **3**$^{2+}$ is also diamagnetic, as expected for a low spin d^{4} Ru(IV) ion with a (dxz, dyz)^{4} electronic configuration and pentagonal bipyramidal geometry. When compared to the ^{1}H NMR spectra of the Ru(II) complexes, the resonances of the Ru(IV) complex are shifted to a lower field in accordance with the higher oxidation state of the Ru center. In contrast, complex **2**$^{+}$ is paramagnetic as expected for an octahedral low spin d^{5} ion with an unpaired electron. As can be observed in Figure 2, all resonances are broadened and highly shifted with regard to those of the Ru(II) analogue, partly due to the paramagnetic effect of the unpaired electron over the nuclear spin. On the other hand, complex **2**$^{+}$ shows an axial EPR spectrum with $g_{//}$ = 2.10 and $g_{\perp}$ = 2.0, which is in agreement with the presence of two py ligands occupying the axial positions of the octahedron (Figure 2). Both Ru(II) and Ru(IV) are EPR silent as expected for complexes with no unpaired electrons. The EPR experiments were carried out at 4 K on frozen solutions by using a X-band spectrometer.

The UV-vis spectra of complexes **1**, **2**$^{+}$ and **3**$^{2+}$, dissolved in 0.1 M triflic acid aqueous solutions (pH = 1.0), are shown in Figure 3. Analogous spectra could be obtained by spectrophotometric redox titration of **1** with Ce(IV) exhibiting isosbestic points as displayed in the SI. Typical Ru-bpy MLCT bands are observed in the 420–620 nm range for **1**, whereas a single transition at 420 nm is observed in that range of the spectrum for Ru(III), which is essentially featureless for Ru(IV).

It is important to mention that complex **3**$^{2+}$ is very stable at pH = 1.0, as evidenced by the UV-vis spectrum which remains unchanged for several days. However, at pH = 7.0 the spectrum decays slowly (in about 3 h) back and cleanly to oxidation state (III) to form **2**$^{+}$ through isosbestic points as shown in Figure 3 (right). The spectral decay is associated with slow oxidation

of water by $\mathbf{3}^{2+}$, since at neutral pH the redox couple IV/III is above the thermodynamic potential for water oxidation, consistent with previous observations for related Ru complexes.[45,46]

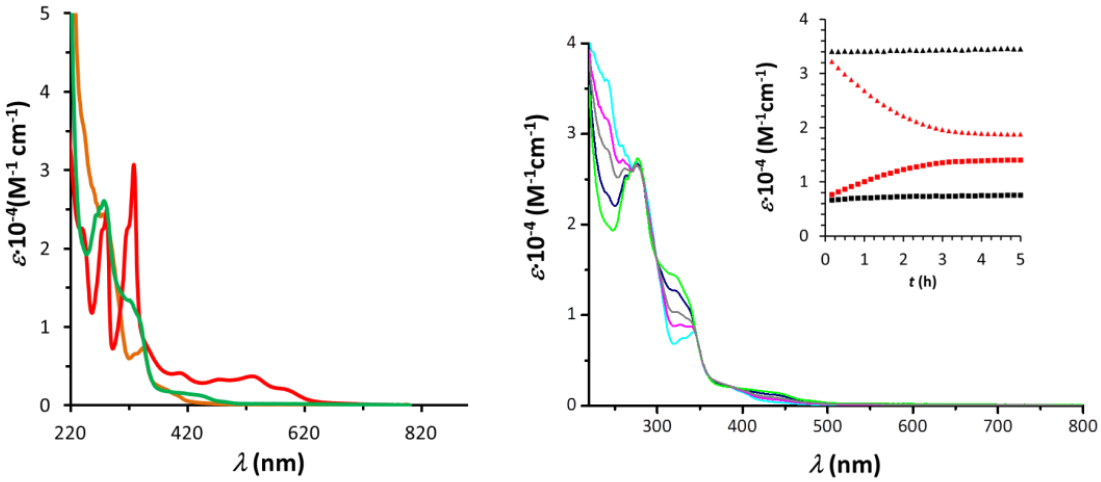

Figure 3: Left, UV-vis spectra of $[Ru^{II}(tda\text{-}k\text{-}N_3O)Py_2]$ (**1**) (red), $[Ru^{III}(tda\text{-}k\text{-}N_3O)Py_2]^{+}$ (**2**$^{+}$) (green), and $[Ru^{IV}(tda\text{-}k\text{-}N_3O_2)Py_2]^{2+}$ (**3**$^{2+}$) (yellow), in a 0.1 M triflic acid aqueous solution. Right, stability of high oxidation states monitored by UV-vis spectroscopy at pH = 1.0 and at pH = 7.0. Right, UV-vis spectra of pH = 7.0 phosphate buffer solution of 50 μM $[Ru^{IV}(tda\text{-}k\text{-}N^3O^2)Py_2]^{2+}$, **3**$^{2+}$, after one minute of its preparation (cyan) and subsequent spectra after, 0.5 (pink), 1 (grey), 2 (blue) and 4h (green). Inset, plot of molar absorbance (ε) *vs*. time for λ = 243 nm and λ = 315 nm (squares and triangles respectively) at pH = 1.0 (black) and pH = 7.0 (red)

A 2.3 Stability of high oxidation states and formation of Ru-aqua species.

We have analyzed the redox properties of the complex $[Ru^{II}(tda\text{-}N^3O)(py)_2]$, **1,** in aqueous solutions at different pH by the electrochemical measurements based on cyclic voltammetry (CV), differential pulse voltammetry (DPV) and coulometry. The CV and DPV experiments were carried out using glassy carbon disk working electrodes and a platinum wire as auxiliary, and mercury sulfate as reference electrode (MSE) and reported *vs*. NHE.

Two chemically reversible and electrochemically quasireversible waves are observed at $E_{1/2}$ = 0.52 V (ΔE = 60 mV) and 1.10 V (60 mV) as detected by CV at pH = 7.0 and shown in Figure 4 left. Both waves are pH-independent in the pH = 2–10 range and are assigned to two consecutive metal based one-electron oxidation processes, namely Ru(II) -> Ru(III) -> Ru(IV). It is interesting to analyze the scan rate dependence (ν = 20, 10 and 7.5 mV/s) in the 1.35-1.45 V zone. As can be noticed in Figure 4, the current intensity at 1.4 V increases as the scan rate decreases, relative to the current intensity of the second anodic wave at 1.10 V suggesting the presence of a new electroactive process that is favored at longer time scales. A similar

phenomenon can be detected by DPV under analogous conditions while changing the pH (Figure 4, right). As the pH increases from 6.5 all the way to 10.0, the intensity of the current increases dramatically in the 1.35–1.45 V range. This phenomenon is *attributed* to the coordination of the hydroxide anion to the metal center, followed by a one electron oxidation as indicated in equations 2 and 3. This assumption is further supported by electrochemical and spectroscopic evidence as will be described here on.

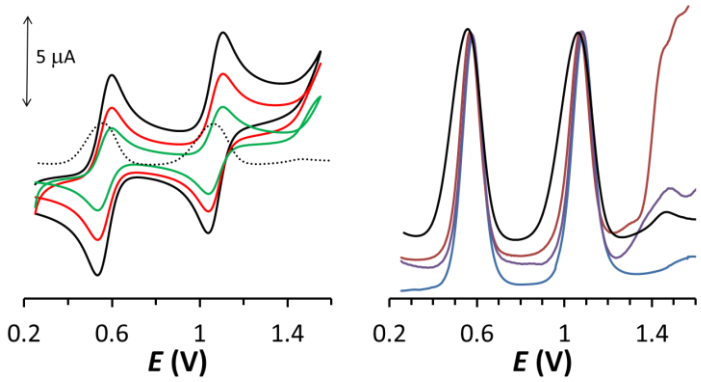

Figure 4. Left, cyclic voltammetry of approx. 1.7 mM $[Ru^{II}(tda\text{-}k\text{-}N_3O)Py_2]$ (**1**), in a pH = 7.0 in aqueous phosphate buffer at a scan rate of 20 (black), 10 (red) and 7.5 (green) mV/s and differential pulse voltammetry (dashed black) using a glassy carbon was used as working electrode. Right, normalized differential pulse voltammetry for 1.7 mM **1**, at pH = 6.5 (blue), 7.5 (black), 8.0 (purple) and 10.0 (brown).

$$[Ru^{IV}(tda\text{-}\kappa\text{-}N^3O^2)(py)_2]^{2+} + OH^- \rightarrow [Ru^{IV}(OH)(tda\text{-}\kappa\text{-}N^3O)(py)_2]^+ \quad (2)$$

$$\mathbf{3}^{2+} \qquad\qquad \mathbf{4H}^+$$

$$[Ru^{IV}(OH)(tda\text{-}\kappa\text{-}N^3O)(py)_2]^+ - e^- - H^+ \rightarrow [Ru^{V}(O)(tda\text{-}\kappa\text{-}N^3O)(py)_2]^+ \quad (3)$$

$$\mathbf{4H}^+ \qquad\qquad \mathbf{5}^+$$

Complex $\mathbf{4H}^+$ has a pK_a = 5.5, as shown in the Pourbaix diagram discussed below. Therefore, at pH > 5.5, $\mathbf{4H}^+$ is deprotonated to form $[Ru^{IV}(O)(tda\text{-}\kappa\text{-}N^3O)(py)_2]$, **4**. Further oxidation of $\mathbf{4H}^+$ or **4** (depending on the pH) forms the Ru(V) species that is a highly reactive water oxidation catalyst that can be detected in very small concentrations. These electrochemical experiments clearly show that two set of species coexist at high pH, including species with hydroxo or oxo terminal ligands ($\mathbf{4H}^+$, $\mathbf{5}^+$, **6**), named from now on "Ru-aqua", and others not containing these ligands (**1**, $\mathbf{2}^+$, $\mathbf{3}^{2+}$), called from now "Ru non-aqua" species, as shown in Scheme 1. The redox properties of the "Ru-aqua" species are summarized in Scheme 2 and their spectroscopic and catalytic properties are discussed below.

Scheme 2. Redox process of "Ru-aqua" complexes including a square cycle at oxidation states II and III. The red colored structures are used to denote species that undergo fast linkage isomerization.

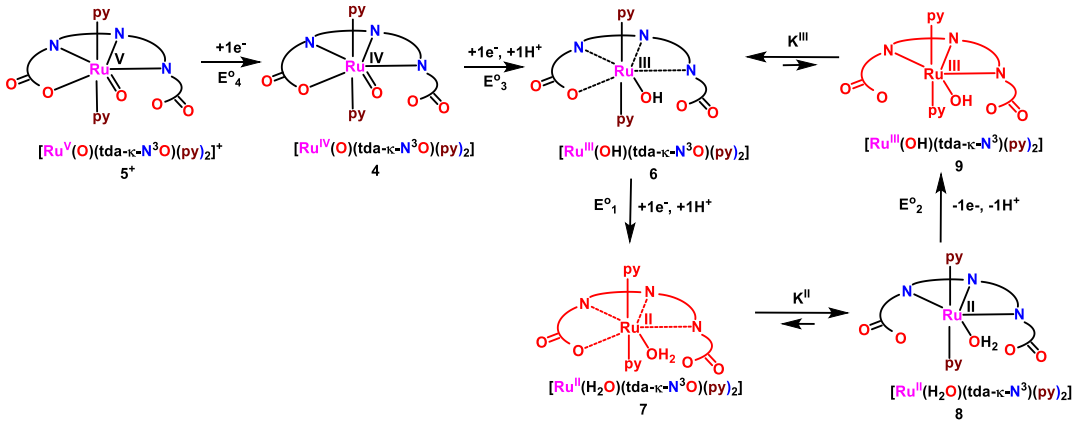

III

Complex **4** can also be generated potentiostatically and monitored voltammetrically in a pH = 7.0 phosphate buffer solution using a bipotentiostat in a two compartment cell as shown in Figure 5 (see SI for further details). For this experiment a glassy carbon disk is used as a working electrode for the CV experiments whereas a Pt grid is used as working electrode to potentiostatically generate **4** at an applied potential of 1.25 V for 10 hours. As can be seen in Figure 5, only **1**, $\mathbf{2}^{+}$ and $\mathbf{3}^{2+}$ are initially present in solution as shown by the red dashed line. As time elapses (333 scans at a scan rate of 20 mV/s), the waves due to first and second oxidation of **1** decrease in intensity and new waves are formed at around 0.7 and 0.9 V. In addition, a large electrocatalytic wave develops at 1.30 V. Judging by the relative integrated charge, obtained under the cathodic wave for the IV/III couple ($\mathbf{3}^{2+}$ + $1e^{-}$ -> $\mathbf{2}^{+}$) versus the new cathodic wave at 0.7 V, the ratio of "Ru non-aqua" versus the "Ru-aqua" complexes is about 2:1. The generation of the "Ru-aqua" species was found to be much faster when the initial non-aqua complex **1** was dissolved at higher pH in agreement with the DPV shown in Figure 4 (right).

The redox properties of "Ru-aqua" species were analyzed based on CV experiments and are shown in Figure 5 (right) at pH = 8.2. A summary of the redox processes of "Ru-aqua" complexes is given in Scheme 2 and can be easily rationalized following the reduction process starting form the most oxidized seven coordinated species $[Ru^{V}(O)(tda\text{-}\kappa\text{-}N^{3}O)(py)_2]^{+}$, $\mathbf{5}^{+}$, and keeping in mind that the geometry of the ligand tda^{2-} together with the different electronic nature of Ru(II) and Ru(III) foster linkage isomerization processes.[47-49] Complex $\mathbf{5}^{+}$ is responsible for the catalytic water oxidation reaction that will be described in the next section, and its formal V/IV redox couple at this pH is obtained by DPV ($E_{1/2}$[4] = 1.43 V; Figure S20). The one electron reduction of $\mathbf{5}^{+}$ (Scheme 2), generates $[Ru^{IV}(O)(tda\text{-}\kappa\text{-}N^{3}O)(py)_2]$, **4**, that in turn can be further

reduced by a one electron process ($E_{1/2}^3$ = 0.87 V) to generate [Ru^{III}(OH)(tda-κ-N^3O)$(py)_2$], **6.** The latter has Ru-O and Ru-N bonds that form and break very quickly since Ru(III) is now six coordinated. Subsequent reduction to Ru(II) ($E_{1/2}^1$= 0.70 V) generates a Ru(II)-aqua complex, [$Ru^{II}(H_2O)$(tda-κ-N^3O)$(py)_2$], **7,** that is highly unstable and isomerizes to form [$Ru^{II}(H_2O)$(tda-κ-N^3)$(py)_2$], **8**, a process denoted by K^{II} in Scheme 2. Oxidation of the latter to Ru(III), ($E_{1/2}^2$= 0.77 V), forms a very unstable species, [Ru^{III}(OH)(tda-κ-N^3)$(py)_2$], **9**, that quickly isomerizes to form **6** (K^{III} in Scheme 2) closing the thermodynamic square cycle. This square mechanism is further corroborated by DPV in the oxidative and reductive scans, shown in Figure 5 (top right).

III

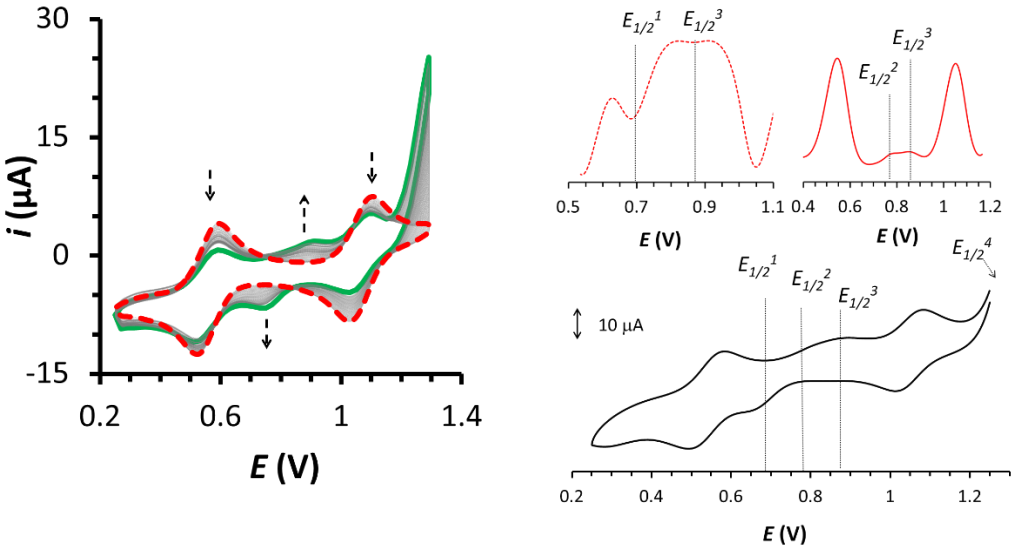

Figure 5: Left, repetitive cyclic voltammetry experiment (v = 20 mV/s) showing the generation of the "Ru-aqua" species from a pH = 7.0 phosphate buffers solution of 1.7 mM of complex **1**, using a glassy carbon disk as a working electrode. The red dashed line represents the first scan whereas the green solid line represents the last scan with 333 cycles in between. Right bottom, CV of $\mathbf{3}^{2+}$:**4** (2:1) mixture at pH = 8.2 generated potentiostatically (see SI for details). The potential scan is swept cathodically starting at E_i = 1.25 V reversed at E_r = 0.25 V and back to the initial potential. The dashed vertical lines indicate the assignment of the redox couples of the newly generated "Ru-aqua" species. Right top, cathodic (E_i = 1.10 V; dashed red line) and anodic (E_i = 0.40 V; solid red line) and DPV sweep of the same solution.

We studied the redox behavior of the "Ru-aqua" species derived from complex **1**, as a function of pH, to generate the Pourbaix diagram that defines the zones of equilibrium between species with different oxidation and protonation states (Figure 6). For comparison, the pH-independent redox potentials of the "Ru non-aqua" species are included (solid blue line) together with the thermodynamic potential of the $4e^-$ water oxidation to dioxygen (green broken line). Several interesting features of the Pourbaix diagram are worth mentioning: i) the

change in slope for the Ru(V)/Ru(IV) redox couple ($E_{1/2}^4$) gives a pK_a of 5.5 for Ru(IV)-OH to Ru(IV)-O species; ii) above pH = 4.0 the redox potential for the couple "$\mathbf{3}^{2+}$ + 1e$^-$ -> $\mathbf{2}^{+}$" (Ru(IV) + 1e -> Ru(III), in blue in the diagram), is higher than the potential of the four electron oxidation of water to dioxygen. Thus, it is in agreement with the stability of complex $\mathbf{3}^{2+}$ at pH = 1.0 and the decay to lower oxidation states at higher pH due to water oxidation;[43] iii) for the "Ru-aqua" complex system, a plot of the III/II couple associated with $E_{1/2}^1$ is presented. The $E_{1/2}^2$ potential is roughly over 100 mV from that of $E_{1/2}^1$ and is not shown; iv) the label Ru-OH_3 refers to the complex $[Ru^{II}(H_2O)(Htda\text{-}\kappa\text{-}N^3O)(py)_2]$, **7**, with one of the dangling carboxylate ligands protonated, $\mathbf{7H}^+$. Again here as in oxidation state III, the tda^{2-} ligand only provides and overall of 3 coordination positions.

III

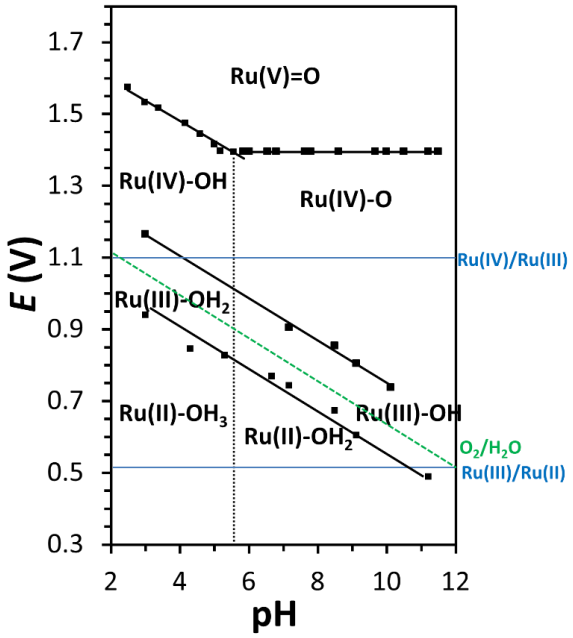

Figure 6. Pourbaix diagram for the "Ru-aqua" species derived from **1**. The black solid lines indicate the redox potentials for the different redox couples whereas the dashed vertical lines indicate the pKa. The zone of stability of the different species is indicated only with the Ru symbol, its oxidation state and its degree of protonation of the aqua ligand. For instance "Ru(V)=O" is used to indicate the zone of stability of $[Ru^V(O)(tda\text{-}k\text{-}N^3O)(py)_2]^+$. The III/II redox couple represents that of $E_{1/2}^1$ (see text for details). The redox potentials for the pH-independent IV/III and III/II redox couples of the "Ru non-aqua" species **1**, $\mathbf{2}^+$ and $\mathbf{3}^{2+}$ are shown in blue. Finally the dashed green line represents the thermodynamic potential for the 4e$^-$ oxidation of water to dioxygen.

Finally, addition of a chemical reducing agent like ascorbic acid to the solution containing a 2:1 ratio of "Ru non-aqua":"Ru-aqua" species generates a solution with **1** as the only present species as demonstrated by ^{1}H NMR spectroscopy (see SI for details). These results suggest a slow equilibrium between **1** and **8** thermodynamically favored towards the former.

$$[Ru^{II}(H_2O)(tda\text{-}\kappa\text{-}N^3)(py)_2] \rightleftharpoons [Ru^{II}(tda\text{-}\kappa\text{-}N^3O)(py)_2] + H_2O \quad K > 1 \qquad (4)$$

8 **1**

In addition, the full recovery of **1**, with no other species in solution, highlights the ruggedness of the system with no deactivation pathways detected. (see Figure S21 in the ESI)

A 2.4 Spectroscopic characterization of "Ru-aqua" species based on NMR and EPR spectroscopy.

The "Ru-aqua" species were characterized by NMR and EPR spectroscopy, as shown in Figure 7. A solution with 5 mM : 1 mM "Ru non-aqua":"Ru-aqua" species was generated potentiostatically by applying 1.25 V for 1.5 h to a 7.0 mM solution of **1** in a D_2O phosphate buffer at pH = 10.5. After the bulk electrolysis, the final pH is reduced to 7. The solution was then exposed to additional bulk electrolysis at several applied potentials to generate species with different degree of oxidation and protonation. The NMR spectra were recorded after 7 minutes of sample collection. For EPR analysis, the samples were frozen after 30 s and measured as frozen solutions at 4 K. Figure 7 (center) includes a CV of the solution where the applied potential is indicated with vertical arrows as a guiding reference. For comparison, Figure 7 also includes the NMR and EPR spectra of $[Ru^{III}(tda\text{-}\kappa\text{-}N^3O^2)(py)_2]^+$, $\mathbf{2}^+$, (black line).

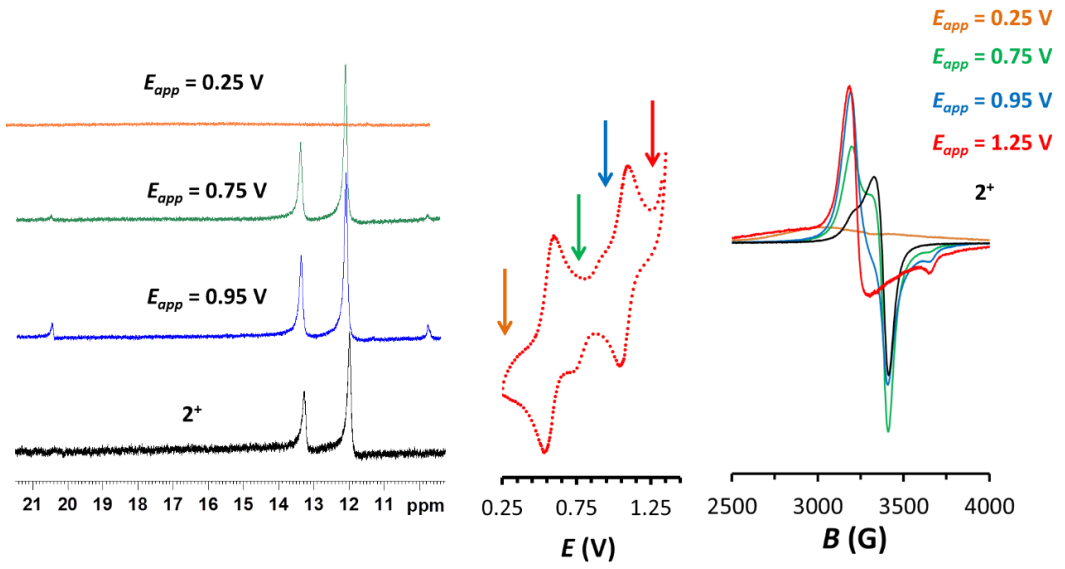

Figure 7: ^{1}H-NMR (left) and EPR (right) of the species generated by bulk electrolysis at the indicated applied potential for a solution containing $\mathbf{3}^{2+}$ (5.0 mM) and **4** (1.0 mM) at pD = 7.0 phosphate buffer solution in D_2O. Center, CV of the initial solution where the applied potentials are indicated with an arrow. The spectra of $\mathbf{2}^+$ obtained independently, as indicated in Figure 2, is shown in black for

comparative purposes. The NMR spectra were recorded after 7 minutes of extraction of the aliquot whereas EPR samples were measured in frozen solutions after 30 s.

The red spectra is obtained at applied potential E_{app} = 1.25 V until the current flow was below 5% of the initial current (approximately 15 minutes). At this potential, two diamagnetic species were generated, the $[Ru^{IV}(tda\text{-}\kappa\text{-}N^3O^2)(py)_2]^{2+}$, $\mathbf{3}^{2+}$ and $[Ru^{IV}(O)(tda\text{-}\kappa\text{-}N^3O)(py)_2]$, **4.** The latter decays to $[Ru^{III}(OH)(tda\text{-}\kappa\text{-}N^3O)(py)_2]$, **6**, whose EPR spectrum is shown in red. This spectrum shows a rhombic signal with g_1 = 2.12, g_2 = 2.08 and g_3 = 1.85. The larger spin anisotropy found in **6** compared with that found in **2** is in agreement with the larger distortion of the octahedral Ru^{III} site upon OH^- coordination**.** The instability of Ru(IV)=O species, $[Ru^{IV}(O)(tda\text{-}\kappa\text{-}N^3O)(py)_2]$, **4,** decaying to Ru(III) is unlikely due to direct water oxidation by this species since the oxidation potential of Ru(IV) is not sufficiently high to drive that reaction. However, upon disproportionation, it can generate Ru(V) and Ru(III). The Ru(V) species in $[Ru^{V}(O)(tda\text{-}\kappa\text{-}N^3O)(py)_2]^+$, $\mathbf{5}^+$, is a very powerful oxidant that can oxidize H_2O to O_2 very quickly, as will be shown in the next section, and thus is the driving force for the disproportionation. A similar mechanism was proposed recently for related mononuclear complexes.[43,50] Furthermore, such a mechanism based on disproportionation of **4** is consistent with the lack of a returning wave for the IV/III redox couple as shown in the CV in Figure 5 (right).

The blue spectra is obtained with E_{app} = 0.95 V until reaching 5% of the initial current flow. The reduction generates $[Ru^{III}(tda\text{-}\kappa\text{-}N^3O^2)(py)_2]^+$, $\mathbf{2}^+$ and the diamagnetic complex $[Ru^{IV}(O)(tda\text{-}\kappa\text{-}N^3O)(py)_2]$, **4**, that decays to $[Ru^{III}(HO)(tda\text{-}\kappa\text{-}N^3O)(py)_2]$, **6**. In the NMR, the Ru(III) species $\mathbf{2}^+$ is identified by intense resonances at 12.0 and 13.2 ppm. New resonances at 9.5 and 20.2 ppm are assigned to **6**. The EPR also shows a mixture of the spectra of $\mathbf{2}^+$ and **6**. The green spectra is obtained with E_{app} = 0.75 V and shows that the predominant species is $\mathbf{2}^+$ with a small amount of **6**. Finally, at E_{app} = 0.25 V, all species are diamagnetic and no EPR resonances are obtained or NMR in the 11-21 ppm range, indicating formation of **1.** This is again fully consistent with the chemical reduction carried out with ascorbic acid where the only species present was **1** as described in the previous section.

A 2.5 Catalytic performance of the Ru-OH_2 complex and proposed mechanism based on DFT calculations

Figure 8 shows the CV of a solution of 0.30 mM $[Ru^{IV}(tda\text{-}\kappa\text{-}N^3O^2)(py)_2]^{2+}$, $\mathbf{3}^{2+}$ and 0.15 mM $[Ru^{IV}(O)(tda\text{-}\kappa\text{-}N^3O)(py)_2]$, **4** at pH = 7.0. It is impressive to see the large electrocatalytic wave of roughly 10 mA/cm^2, in the 1.3-1.4 V range considering the small amount of the precursor species **4** present in solution that have a reductive III/II wave with a peak intensity of approximately 25

μA/cm^2. This electrocatalytic wave is due to one electron oxidation of **4** and formation of the highly active species [Ru^V(O)(tda-κ-N^{3}O)(py)$_2$]$^+$, **5**$^+$ ($E_{1/2}$[4] = 1.43 V). To quantitatively characterize the kinetics of the water oxidation catalysis, a foot of the wave analysis (FOWA) was carried out following the procedures proposed by Saveant et al.[51-53] A plot of i/ip *vs*. 1/(1+e(F(E^0-E)/RT)) (see Figure 8) gives an impressive scan rate-independent TOF$_{max}$ of 8,000 cycles per second, which is the highest ever reported at neutral pH. It is actually one order of magnitude higher than the best one reported so far at pH 1.0, based on Ru-bda type of complexes (see Chart 1).[32-33]Further, at pH 7.0, the complex [Ru(bda)(pic)$_2$] under exactly the same conditions as **3**$^+$ is about 3-4 orders of magnitude slower (see SI), assuming a first order behavior of the catalyst at pH = 7.0 as has been recently proposed.[36] In addition, the performance of **4** was evaluated at pH = 8.0 and 10.0, giving impressive TOFs of 25,000 s^{-1} and 50,000 s^{-1} respectively, indicating a significant rate enhancement as the pH increases. Finally, bulk electrolysis experiments using glassy carbon rods (S = 8.2 cm^2) as working electrodes further confirm O_2 evolution with Faradaic efficiency around 92%. (See Figure S22).

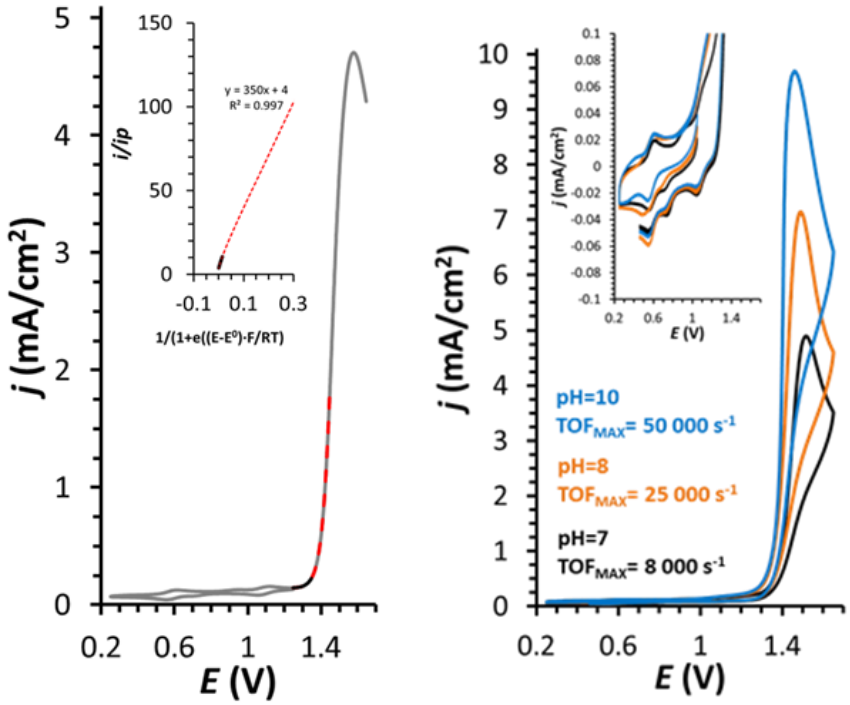

Figure 8: Left, CV of a mixture of 0.3 mM [Ru^{IV}(tda-k-N^{3}O^2)(py)$_2$]$^{2+}$, **3**$^{2+}$, and 0.15 mM [Ru^{IV}(O)(tda-k-N^{3}O)(py)$_2$], **4**, at pH = 7.0 phosphate buffer. Inset, FOWA plot of the catalytic current. The red dashed line in both cases represent the experimental data used for the FOWA analysis and the black solid line are the experimental data used for the extraction of TOF$_{MAX}$. Right, CV obtained at pH = 7.0, pH = 8.0 and pH = 10.0 under identical conditions. Inset, enlargement of the 0.2-1.2 V zone in the CV showing both the full

recovery of catalyst and cathodic shift of the Ru-aqua wave, due to the pH change after the proton generation during the electrocatalytic process.

The catalytic cycle was also studied via DFT calculations. We started with the Ru-aqua complex $[Ru^{II}(H_2O)(tda\text{-}\kappa\text{-}N^3)(py)_2]$, **7**, (Scheme 3). From **7**, a PCET results in the formation of **6**, followed by another PCET step to generate **4**. Further oxidation forms the seven coordinate complex $\mathbf{5}^+$ (Figure 9,) with a calculated potential of 1.32 V in very good agreement with the onset of the electrocatalytic wave in the 1.3 – 1.4 V range. It is worth noting that for complex $\mathbf{5}^+$ we found the $\kappa\text{-}N^3O$ conformer to be more stable than the $\kappa\text{-}N^3$ conformer by 13.6 kcal/mol showing the enhanced stability of the seven coordination mode due to the tda^{2-} ligand framework. Next, we considered the O-O bond formation step and located a transition state (TS) structure which features a water nucleophilic attack (WNA) to the oxyl radical $Ru^{IV}\text{–}O^{\cdot}$ (formally a Ru^{V}=O unit), with concomitant proton transfer to the dangling carboxylate group of the tda^{2-} ligand (Figure 9). The calculated free energy of activation ($\Delta G^{\ddagger}$) is 19.5 kcal/mol and 16.8 kcal/mol respectively at M11-L and M06-L level of theories. The calculated activation free energies are significantly lower than those calculated for other mononuclear ruthenium catalysts at same level of theory[27,54,55]due to the intramolecular proton transfer to the dangling carboxylate, next to the oxyl radical. While previous examples have shown this effect, intermolecularly increasing rates by a 2 or 3 fold,[35,36] we find that the intramolecular proton transfer has a much more dramatic effect leading to an extraordinary increase of the overall kinetics. The resulting product of the WNA step is $[Ru^{III}(OOH)(Htda\text{-}\kappa\text{-}N^2O^1)(py)_2]^+$ (ΔG = 3.5 kcal/mol) which could undergo a PCET step (E = 0.66 V) to generate $[Ru^{IV}(OO)(Htda\text{-}\kappa\text{-}N^2O^1)(py)_2]^+$ (See Figure 9 and structures in blue in Scheme 3). In the final step of the mechanism, O_2 evolution with concomitant loss of proton and addition of H_2O (ΔG = -3.5 kcal/mol) regenerates the initial $[Ru^{II}(tda\text{-}\kappa\text{-}N^3)(py)_2(OH_2)]$ species and completes the catalytic cycle.

Scheme 3. Proposed suit of reactions involved in the water oxidation catalysis mechanism at pH = 7.0 based on DFT calculations. Broken lines indicate bonds that are rapidly formed and broken at room temperature. In blue are depicted species that have not been experimentally isolated but that are characterized by DFT.

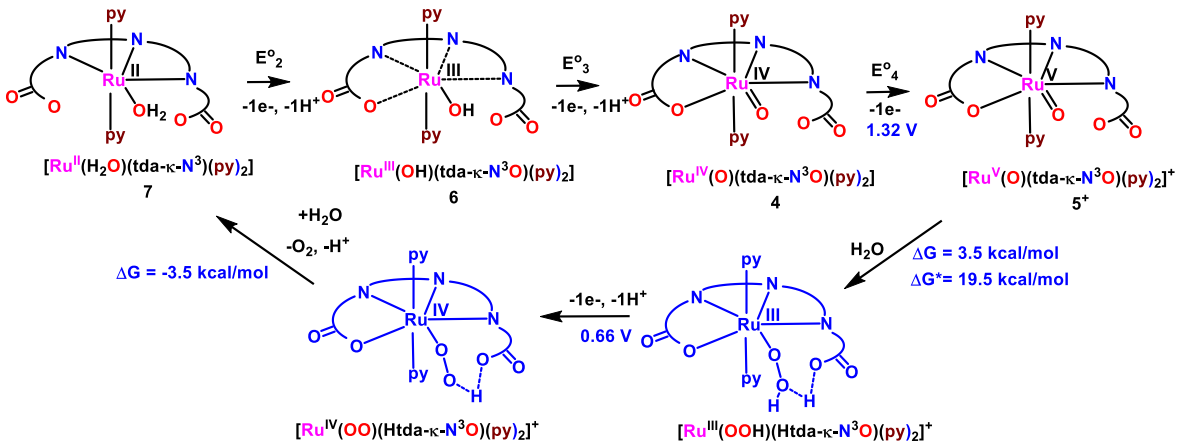

III

It is interesting to compare the catalytic rates of water oxidation catalyzed by the related complex [Ru(bda)(pic)$_2$], analogous to **4** but without the dangling carboxylate. At pH = 7.0, a k_{obs} = 6 s^{-1} has been reported[38] and at pH = 12.2 the k_{obs} increases up to 14000 s^{-1}. It is impressive to see that for complex **4** with the capacity to undergo proton transfer intramolecularly boosts the rate up to 8,000 s^{-1} at pH = 7.0 and 50,000 s^{-1} at pH = 10. Thus, an increase of more than three orders of magnitude in rate is achieved at pH = 7.0 with regard to the current benchmark catalyst. The increase of catalytic rate based on intramolecular proton transfer is reminiscent of other catalytic systems that also exploit acid-base functional groups in the second coordination sphere of the metal center, including Ni complexes introduced by Dubois et al,[56] where the ligands have pendant amines that function as proton relays.

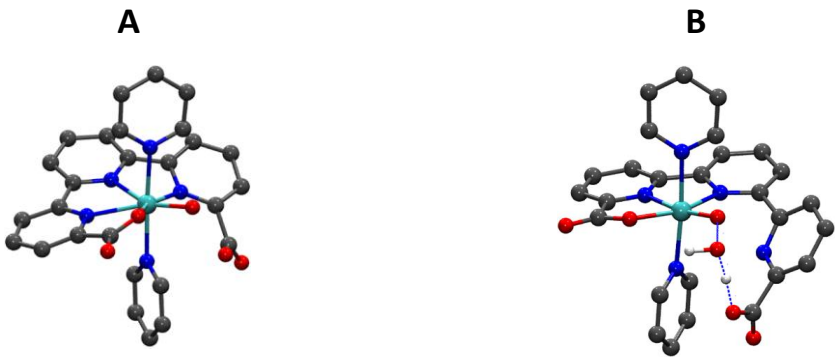

Figure 9. Optimized structures of (A) [Ru^{V}(tda-κ-N^3O^1)$(py)_2(O)]^+$, **5**$^+$, and (B) associated water nucleophilic attack transition state at M11-L level of theory for the reaction, "**5**$^+$ + H_2O -> [Ru^{III}(OOH)(Htda-κ-N^3O^1)$(py)_2(O)]^{+}$". Color code: Ru, turquoise; C, gray; N, blue; O, red; H, white. Hydrogen atoms on the ligands are omitted for clarity.

A 3 Conclusions

We have introduced a new family of complexes where the pentadentate tda^{2-} coordinates to Ru metal center as an equatorial ligand while monodenate pyridine ligands coordinate to the axial positions. The strong sigma donation of the carboxylate moieties of tda^{2-}, stabilizes a seven coordinate Ru(IV) complex, $[Ru^{IV}(tda\text{-}\kappa\text{-}N^3O^2)(py)_2]^{2+}$, $\mathbf{3}^{2+}$, both in organic solvents as well as in water, or in acidic aqueous solutions. In basic solutions, hydroxide displaces one of the carboxylate groups, forming $[Ru^{IV}(OH)(tda\text{-}\kappa\text{-}N^3O)(py)_2]^{+}$, $\mathbf{4H}^{+}$, with pKa = 4.5 where the displaced carboxylate is dangling although functionally important since it is *cis* to the Ru-OH group.

III

Species **4** turns out to be a very robust catalyst with an impressive TOF = 8,000 s^{-1} at pH = 7.0 that is the best ever reported at this pH and about 3-4 orders of magnitude better than $[Ru(bda)(pic)_2]$ at the same pH, the best reported so far. The key for fast reactivity is mainly due to two factors: a) the easy access to high oxidation states, provided by the tda^{2-} ligand through the anionic nature of the carboxylate moieties and the capability of stabilizing a seven coordination to Ru in high oxidation states; and b) the functionality of the dangling carboxylate as a proton acceptor in an intramolecular fashion, while the incoming substrate water molecule undergoes a nucleophilic attack to the oxyl radical during the critical O-O bond formation step, as shown by our DFT calculations.

A 4 Acknowledgments

R.M. thanks “La Caixa” foundation for a PhD grant. A.L. thanks MINECO (CTQ-2013-49075-R, SEV-2013-0319; CTQ-2014-52974-REDC) and “La Caixa” foundation for financial support. COST actions, CM1202 and CM1205 from the EU are also gratefully acknowledged. V.S.B. acknowledges supercomputer time from NERSC and financial support as part of the Argonne-Northwestern Solar Energy 524 Research (ANSER) Center, an Energy Frontier Research Center funded by the U.S. Department of Energy, Office of 526 Science, Office of Basic Energy Sciences under Award Number 527 DE-SC0001059. The work at BNL (M.Z.E.) was carried out under contract DE-SC00112704 with the U.S. Department of Energy, Office of Science, Office of Basic Energy Sciences. We thank J. M. Martínez-Agudo from the Universidad de Valencia for his assistance with the EPR measurements.

A 5 References

1 Berardi, S.; Drouet, S.; Francàs, L.; Gimbert-Suriñach, C.; Guttentag, M.; Richmond, C.; Stoll, T.; Llobet, A. *Chem. Soc. Rev*. **2014**, *43*, 7501-7519.
2 Zeng, Q.; Lewis, F. W.; Harwood, L. M.; Hartl, F. *Coord. Chem. Rev*., **2015**, , *304*, 88-101.

3 McCrory, C. C. L.; Jung, S.; Peters, J. C.; Jaramillo, T. F. *J. Am. Chem. Soc.* **2013**, *135*, 16977-16987.
4 McCrory, C. C. L.; Jung, S.; Ferrer, I. M.; Chatman, S. M.; Peters, J. C.; Jaramillo, T. F. *J. Am. Chem. Soc.* **2015**, *137*, 4347-4357.
5 Trotochaud, L.; Ranney, J. K.; Williams, K. N.; Boettcher, S. W. *J. Am. Chem. Soc.* **2012**, *134*, 17253-17261.
6 Smith, R. D. L.; Prévot, M. S.; Fagan, R. D.; Zhang, Z.; Sedach, P. A.; Siu, M. K. J.; Trudel, S.; Berlinguette, C. P. *Science* **2013**, *340*, 60-63.
7 Matheu, R.; Francàs, L.; Chernev, P.; Ertem, M. Z.; Batista, V. S.; Haumann, M.; Sala, X.; Llobet, A. *ACS Catal.* **2015**, *5,* 3422-3429.
8 Radaram, B.; Ivie, J. A.; Singh, W. M.; Grudzien, R. M.; Reibenspies, J. H.; Webster, C.E.; Zhao, X. *Inorg. Chem*. **2011**, *50*, 10564-10571.
9 Reece, S. Y.; Hamel, J. A.; Sung, K.; Jarvi, T. D.; Esswein, A. J.; Pijpers, J. J. H.; Nocera, D. G. *Science* **2011**, *334*, 645-648.
10 Mei, A.; Li, X.; Liu, L.; Ku, Z.; Liu, T.; Rong, Y.; Xu, M.; Hu, M.; Chen, J.; Yang, Y.; Grätzel, M.; Han, H. *Science* **2014**, *345*, 295-298.
11 Sala, X.; Romero, I.; Rodríguez, M.; Escriche, L.; Llobet, A. *Angew. Chem. Int. Ed*. **2009**, *48*, 2842-2852.
12 Romain, S.; Vigara, L.; Llobet, A. *Acc. Chem. Res*. **2009**, *42*, 1944-1953.
13 Molecular Water Oxidation Catalysis: A Key Topic for New Sustainable Energy Conversion Schemes. Edited by A. Llobet. **2014** John Wiley and Sons Ltd. ISBN: 9781118413371
14 Gersten, S. W.; Samuels, G. J.; Meyer, T. J. *J. Am. Chem. Soc.* **1982**, *104*, 4029–4030.
15 Sens, C.; Romero, I.; Rodriguez, M.; Llobet, A.; Parella, T.; Benet-Buchholz, J. *J. Am. Chem. Soc.* **2004**, *126*, 7798-7799.
16 Polyansky, D. E.; Muckerman, J. T.; Rochford, J.; Zong, R.; Thummel, R. P.; Fujita, E. *J. Am. Chem. Soc.* **2011**, *133*, 14649-14665.
17 Concepcion, J. J.; Jurss, J. W.; Templeton, J. L.; Meyer, T. J. *J. Am. Chem. Soc* **2008**, *130*, 16462-16463.
18 Hong, D.; Mandal, S.; Yamada, Y.; Lee, Y.-L.; Nam, W.; Llobet, A.; Fukuzumi, S. *Inorg. Chem.* **2013**, *52*, 9522–9531.
19 Wang D., Ghirlanda G., Allen J. P. *J. Am. Chem. Soc.*, **2014**, *136*, 10198-10201.
20 Chen, G.; Chen, L.; Ng, S.-M.; Lau, T.-C. *ChemSusChem* **2014,** *7*, 127-134.
21 Zhang, M.-T.; Chen, Z.; Kang, P.; Meyer, T. J., *J. Am. Chem. Soc.* **2013,** *135*, 2048-2051.
22 Garrido-Barros, P.; Funes-Ardoiz, I.; Drouet, S.; Benet-Buchholz, J.; Maseras, F.; Llobet, A. *J. Am. Chem. Soc.* **2015**, *137*, 6758-6761.
23 Sala, X.; Ertem, M. Z.; Vigara, L.; Todorova, T. K.; Chen, W.; Rocha, R. C.; Cramer, C. J.; Gagliardi, L.; Llobet, A. *Angew. Chem. Int. Ed.* **2010**, *49*, 7745-7747.
24 Lianpeng Tong, L.; Duan, L.; Xu, Y.; Privalov, T.; Sun , L. *Angew. Chem. Int. Ed*. **2011**, *50*, 445-449.
25 López, I.; Ertem, M. Z.; Maji, S.; Benet-Buchholz, J.; Keidel, A.; Kuhlmann, U.; Hildebrandt, P.; Cramer, C. J.; Batista, V. S.; Llobet, A. *Angew. Chem. Int. Ed.* **2014,** *53*, 205-209.
26 Sala, X.; Maji, S.; Bofill, R.; Garcia-Anton, J.; Escriche, L.; Llobet, A., *Acc. Chem. Res.* **2014,** *47*, 504-516.
27 Vigara, L.; Ertem, M. Z.; Planas, N.; Bozoglian, F.; Leidel, N.; Dau, H.; Haumann, M.; Gagliardi, .; Cramer, C. J.; Llobet, A. *Chem. Sci.* **2012,** *3*, 2576-2586.
28 Bozoglian, F.; Romain, S.; Ertem, M. Z.; Todorova, T. K.; Sens, C.; Mola, J.; Rodríguez, M.; Romero, I.; Benet-Buchholz, J.; Fontrodona, X.; Cramer, C. J.; Gagliardi, L.; Llobet, A. *J. Am. Chem. Soc.* **2009,** *131*, 15176-15187.
29 Duan, L.; Bozoglian, F.; Mandal, S.; Stewart, B.; Privalov, T.; Llobet, A.; Sun, L. *Nat. Chem.* **2012,** *4,* 418-423.

30 Concepcion, J. J.; Tsai, M. K.; Muckerman, J. T.; Meyer, T. J. *J. Am. Chem. Soc.* **2010,** *132*, 1545-1557.
31 Duan, L.; Fischer, A.; Xu, Y.; Sun, L. *J. Am. Chem. Soc.* **2009**, *131*, 10397-10399.
32 Richmond, C. J.; Matheu, R.; Poater, A.; Falivene, L.; Benet-Buchholz, J.; Sala, X.; Cavallo, L.; Llobet, A. *Chem. Eur. J.* **2014**, *20*, 17282–17286.
33 Wang, L.; Duan, L.; Wang, Y.; Ahlquist, M. S. G.; Sun, L. *Chem. Commun.* **2014**, *50*, 12947-12950.
34 Maji, S.; López, I.; Bozoglian, F.; Benet-Buchholz, J.; Llobet, A. *Inorg. Chem.* **2013,** *52*, 3591-3593.
35 Privalov, T.; Åkermark, B.; Sun, L., *Chem. Eur. J.* **2011**, *17*, 8313-8317.
36 Marelius, D. C.; Bhagan, S.; Charboneau, D. J.; Schroeder, K. M.; Kamdar, J. M.; McGettigan, A. R.; Freeman, B. J.; Moore, C. E.; Rheingold, A. L.; Cooksy, A. L.; Smith, D. K.; Paul, J. J.; Papish, E. T.; Grotjahn, D. B. *Eur. J. Inorg. Chem*., **2014**, *4*, 676–689.
37 Chen, Z.; Concepcion, J. J.; Hu, X.; Yang, W.; Hoertz, P. G.; Meyer, T. J. *Proc. Natl. Acad. Sci. U.S.A.* **2010,** *107*, 7225-7229.
38 Song, N.; Concepcion, J. J.; Binstead, R. A.; Rudd, J. A.; Vannucci, A. K.; Dares, C. J.; Coggins, M. K.; Meyer, T. J. *Proc. Natl. Acad. Sci. U.S.A.* **2015,** *112*, 4935-4940.
39 Planas, N.; Christian, G. J.; Roeser, S.; Mas-Marzá, E.; Kollipara, M. R.; Benet-Buchholz, J.; Maseras, F.; Llobet, A. *Inorg. Chem.* **2012**, *5*, 1889-1901.
40 Planas, N.; Christian, G. J.; Mas-Marza, E.; Sala, X.; Fontrodona, X.; Maseras, F.; Llobet, A. *Chem. Eur. J.* **2010***, 16*, 7965–7968.
41 Sander, A. C.; Maji, S.; Francas, L.; Böhnisch, T.; Dechert, S.; Llobet, A.; Meyer, F. *ChemSusChem* **2015**, *8*, 1697-1702.
42 Pyykkö, P., *J. Organomet. Chem.* **2006,** *691*, 4336-4340.
43 Zhao, Y.; Truhlar, D. G. *J. Chem. Phys.* **2006**, *125*, 194101-194101.
44 Peverati, R.; Truhlar, D. G. *J. Phys. Chem. Lett.* **2012**, 3, 117-117.
45 Roeser, S.; Farràs, P.; Bozoglian, F.; Martínez-Belmonte, M.; Benet-Buchholz, J.; Llobet, A. *ChemSusChem* **2011,** *4*, 153-153.
46 Farras, P.; Maji, S.; Benet-Buchholz, J.; Llobet, A. *Chem. Eur. J.* **2013,** *19*, 7162-7172.
47 Pearson, R. G. *J. Am. Chem. Soc.* **1963**, *85*, 3533-3539.
48 Sens, C.; Rodriguez, M.; Romero, I.; Llobet, A.; Parella, T.; Sullivan, B. P.; Benet-Buchholz, J. *Inorg. Chem.* **2003**, *42*, 2040-2048.
49 Francas, L.; Gonzalez-Gil, R. M.; Moyano, D.; Benet-Buchholz, J.; García-Antón, J.; Escriche, L.; Llobet, A.; Sala, X. *Inorg. Chem.* **2014**, *53*, 10394-10402.
50 Wasylenko, D. W.; Ganesamoorthy, C.; Henderson, M.; Koivisto, B. D.; Osthoff, H.; Berlinguette, C. P. *J. Am. Chem. Soc*. **2010**, *132*, 16094-16106.
51 Costentin, C.; Drouet, S.; Robert, M.; Savéant, J.-M. *J. Am. Chem. Soc.* **2012**, *134*, 11235-11242.
52 Costentin, C.; Savéant, J.-M. *ChemElectroChem* **2014**, *1*, 1226-1236.
53 Rountree, E. S.; McCarthy, B. D.; Eisenhart, T. T.; Dempsey, J. L. *Inorg. Chem.* **2014**, *53*, 9983.
54 Hirahara, M.; Ertem, M. Z.; Komi, M.; Yamazaki, H.; Cramer, C. J.; Yagi, M. *Inorg. Chem.*, **2013**, *52*, 6354–6364.
55 Angeles-Boza, A. M.; Ertem, M. Z.; Sarma, R.; Ibanez, C. H.; Maji, S.; Llobet, A.; Cramer, C. J.; Roth, J. P. *Chem. Sci.*, **2014**, *5,* 1141-1152.
56 Helm, L. M.; Stewart, M. P.; Bullock, R. M.; DuBois, M. R.; DuBois, D. L. *Science*, **2011**, *333*, 863-866

III

A 6 Supporting Information

Paper A: Intramolecular proton transfer boosts water oxidation catalyzed by a Ru complex

Outline

III

Materials

All materials were provided by Sigma-Aldrich unless indicated. [2,2':6',2''-terpyridine]-6,6''-dicarboxylic acid (H_2tda) [S1] [2,2'-bipyridine]-6,6'-dicarboxylic acid (H_2bda)[S2] and RubdaPic_2[S2] (where Pic is Picoline) and $RuCl_2DMSO_4$[S3] were synthesized and purified according to the literature. High-purity deionized water was obtained by passing distilled water through a nanopure Milli-Q water purification system.

Synthesis of [Ru^{II}(tda-κ-N^3O)Py_2], **1***:* $RuCl_2$dmso$_4$ (150 mg, 0.31 mmol), 2',2'':6',2''-terpyridine-6',6''-dicarboxylic acid (H_2tda) (99 mg, 0.31 mmol) and Et_3N (0.3 mL) were degassed in dry MeOH (6 mL), refluxed for 6 hours and cooled down to RT. A brown solid appeared in the reaction mixture and was filtered, washed with MeOH and Ether. The solid was suspended in water (5mL) and pyridine (15 mL) and refluxed overnight. The resulting red-wine solution was cooled to RT and washed with DCM (3x100mL). The watery solution was evaporated and the red solid was dissolved with MeOH and precipitated with Ether. (95 mg, 0.16 mmol, 51 % yield). ^{1}H-NMR (500Hz, [d4] Methanol) δ: 7.09 (4H, t, J=7.5 Hz), 7.58 (2H, tt, J=1.4 and 7.5 Hz), 8.03 (3H, t, J=7.9 Hz), 8.05 (2H, t, J=8.1 Hz), 8.12 (4H, dd, J=1.4 and 7.5), 8.15 (2H, d, 7.9 Hz), 8.49 (2H, d, 7.9 Hz), 8.61 (2H, d, J=8.1 Hz). ^{13}C-NMR (500Hz, [d4] Methanol) δ: 125.2, 125.4, 126.1, 128.1, 133.8, 138.0, 138.1, 153.6, 158.4, 159.6, 163.8, 172.4. UV-vis [λ_{max}, nm (ε, M^{-1} cm^{-1})]: 236 (21700), 282 (24800), 327 (30700) and 530 (3700). ESI^+-HRMS m/z: calc. for RutdaPy_2-Na^+ ($C_{27}H_{19}N_5NaO_4Ru^+$): 602.03727, found m/z: 602.03678 (0.7 ppm). *Anal.* Calc. *for* ***1****·3.5* H_2O: C, 50.54%; H, 4.08 %; N, 10.92 %. Found: C, 50.46 %; H, 3.78 %; N, 10.87%.

*Synthesis of [Ru^{III}(tda-κ-N^3O)Py_2] [PF_6], (****2****)(PF_6):* A solution of Ceric Ammonium Nitrate (CAN) (1.82 mM, 1.05 eq, 2mL) was added drop wise to a solution of **1** in triflic acid (1.72 mM, 25 mL) and the mixture was stirred for 15 minutes. A green powder was obtained when a saturated solution of KPF_6 was added. The suspension was centrifuged for 10 minutes, the solid filtrated and washed with water, methanol and ether (12 mg, 39%). UV-vis [λ_{max}, nm (ε, M^{-1} cm^{-1})]: 279 (25800, 322 (13200) and 441 (1300). *Anal. Calc. for* (***2***)(PF_6)*·0.5* H_2O : C, 44.27%; H, 2.75 %; N, 9.56 %. Found: C, 44.23 %; H, 2.50 %; N, 9.39%.

*Synthesis of [Ru^{IV}(tda-κ-N^3O^2)Py_2] [PF_6], (****3****)(PF_6)$_2$.* A solution of CAN (3.64 mM, 2.1 eq, 2mL) was added drop wise to a solution of **1** in triflic acid (1.72 mM, 25 mL) and the mixture was stirred for 15 minutes. A brown powder was obtained when a saturated solution of KPF_6 was added. The suspension was centrifuged for 10 minutes, the solid filtrated and washed with cold water and ether (12 mg, 32%). ^{1}H-NMR (500 Hz, D_2O) δ: 7.24 (4H, t, J=7.0 Hz), 7.70 (6H, m), 8.20 (2H, d, J=7.8 Hz), 8.62 (2H, t, J=7.8 Hz), 8.93 (2H, d, J=7.8 Hz), 8.98 (1H, d, J=7.9 Hz), 9.08 (2H, d, J=7.9

Hz). ^{13}C-NMR (500Hz, D_2O) δ: 127.3, 123.0, 131.0, 132.2, 141.5, 147.3, 147.6, 150.3, 152.5, 157.8, 157.9, 168.0. UV-vis [λ_{max}, nm (ε, M^{-1} cm^{-1})]: 280 (23600) and 347 (6800).

Preparation of 0.1 M ionic strenght phospahte solutions.

a) pH = 2.0 buffered solution: Powders of H_3PO_4 (10.5 g, 0.1073 M) and NaH_2PO4 (11.83 g, 0.0986 M) were dissolved with deionised water up to 1 L solution.

b) pH = 7.0 buffered solution: Powders of NaH_2PO4 (2.31 g, 0.0193 M) and Na_2HPO_4 (3.77g, 0.0266 M) were with deionised water up to 1 L solution.

c) pH = 12.0 buffered solution: Powders of Na_2HPO_4 (10.293g, 0.0073 M) and Na_3PO_4 (2.06g, 0.0126 M) were dissolved with deionised water up to 1 L solution.

Solutions at pHs between 2.0 and 12.0 were prepared by mixing the above solutions. The pH of all solutions were measured by a pHmeter. All solutions contained a ionic strengh equal to 0.1 M.

*Preparation of the **3**$^{2+}$/**4** mixtures.*

Bulk electrolysis at E_{app} = 1.25 V (see electrochemical methods for more details) was applied to a phosphate buffer solution of **1** at pH = 7.0 or 10.5 for a given period of time. The final pH was adjusted by further addition of a phosphate buffer solution till the desired pH, monitored by a pH meter. This ensures that all solutions end up with a 0.1 M ionic strength.

The ratio of the **3**$^{2+}$/**4** species depends on the initial pH and concentration of **1**, as well as on the duration of the bulk electrolysis, see table S1 for details.

In the case of deuterated solvents for ^{1}H NMR experiments, the same procedure was followed.

Methods

General instrumentation

Electrospray ionization (ESI) and matrix-assisted laser desorption ionization (MALDI) mass spectrometry (MS) experiments were performed on a Waters Micromass LCT Premier equipment and a Bruker Daltonics Autoflex equipped with a nitrogen laser (337 nm), respectively. UV–Vis spectroscopy was performed on a Cary 50 Bio (Varian) UV–Vis spectrophotometer with 1 cm quartz cells unless indicated. A 400 MHz Bruker Avance II spectrometer and a Bruker Avance 500 MHz were used to carry out NMR spectroscopy. FT-IR measurements were carried out on a Bruker Optics FTIR Alpha spectrometer equipped with a DTGS detector, and a KBr beamsplitter at 4 cm^{-1} resolution. The EPR experiments were carried out at 4 K on frozen solutions by using a X-band spectrometer (Bruker ELEXYS E580). The pH of the solutions was determined by a pHmeter (CRISON, Basic 20^{+}) calibrated before measurements through a standard solutions at pH= 4.01, 7.00 and 9.21. Oxygen evolution was analysed with a gas phase Clark type oxygen electrode (Unisense Ox-N needle microsensor) and calibrate by the addition of small quantities of oxygen (99%).

Electrochemical methods

General considerations

All electrochemical experiments were performed in an IJ-Cambria HI-730 bipotentiostat, using a three-electrode cell. $E_{1/2}$ values reported in this work were estimated from CV experiments as the average of the oxidative and reductive peak potentials ($\frac{Ep,a + Ep,c}{2}$) or from DPV. The Reference Electrode (RE) was Hg/Hg_2SO_4 (K_2SO_4 saturated) unless indicated and potentials were converted to NHE by adding 0.65 V.

Cells: A 20 mL vial was used as an electrochemical cell for CV measurements. A Teflon-made with holes for the three electrodes was used as a lid to ensure a reproducible distance between the electrodes. A two compartments cell (25 mL per compartment) with a separation grid was used for Bulk Electrolysis Experiments.

Cyclic voltammetry (CV) and Differential Pulse Voltammetry

Glassy carbon disk (ϕ = 0.3 cm, S = 0.07 cm^2), Pt disk and Hg/Hg_2SO_4 (K_2SO_4 saturated) were used as Working Electrode (WE), Counter Electrode (CE) and Reference Electrode (RE) respectively, unless explicitly mentioned. Glassy carbon electrodes were polished successively with 1.0, 0.3,

and 0.05 µm alumina (Al_2O_3), sonicated with MeCN for 15 minutes and washed with acetone. CVs and DPVs were iR compensated by the potentiostat in all the measurements unless indicated. Cyclic Voltammograms (CV) were recorded at 100 $mV \cdot s^{-1}$ scan rate, unless explicitly expressed. The DPV parameters were ΔE = 4 mV, Amplitude = 0mV, Pulse width = 5 s, Sampling width = 0.0167 s, Pulse period = 5 s unless explicated.

Bulk electrolysis

A Pt grid was used as a WE, another Pt grid as a CE and a Hg/Hg_2SO_4 (K_2SO_4 saturated) as a RE. iR compensation by the potentiostat was not applied in this technique. For the bulk electrolysis experiment described in Figure S22, a glassy carbon rod (S = 8.2 cm^2) was used as a working electrode and Ag/AgCl (sat. KCl) as a RE.

CV-monitored Bulk electrolysis in a bipotentiostat

A glassy carbon and a Pt grid were used as working electrodes, another Pt grid as a counter electrode and Hg/Hg_2SO_4 as a Reference electrode. The glassy carbon electrode was used to perform the consecutive CVs and the Pt grid was used to apply a continuous potential through a coulometry technique. The counter electrode was placed in one compartment provided with a magnetic stirrer and the other 3 electrodes were placed in the other compartment also provided with a magnetic stirrer. To be able to simultaneously stir the solution and to perform the CV, the magnetic stirrer power was set at low frequency (100-200 rpm). In addition, the reference electrode was placed between the glassy carbon working electrode and the magnetic stirrer.

Foot of the wave analysis

The analysis was performed by following the procedure of Savéant *et al* in the literature. [S4] The expression (equation S1) was deduced for a general scheme where a single chemical step, which is the rate determining step, and a single electron transfer, which is fast, are responsible for the rate of the reaction. Where R is the gas constant, T is the temperature, k_{obs} is a pseudoconstant (s^{-1}), E^0 and are the potentials of the chemical step prior to the electron transfer.

$$\frac{i}{i_p} = \frac{8.97\sqrt{\left(\frac{R \cdot T}{F \cdot v}\right) \cdot k_{obs}}}{1+\exp\left(\frac{F(E^0-E)}{RT}\right)} \qquad \text{(S1)}$$

$$TON = \frac{k_{obs}t}{1 + \exp\left[\frac{F}{R \cdot T}(\mathrm{E}^0 - \mathrm{E})\right]} \quad \text{(S2)}$$

The value of the intensity anodic wave of the Ru^{III}-OH_2/Ru^{II}-OH redox couple was used as ip as an approximation. E^0 was extracted from DPV of the same solution.

III

The value of k_{obs} is equivalent to TOF_{MAX} (s^{-1}) in the used electrocatalytic scheme. TOF_{MAX} is the maximum Turn Over Frequency (s^{-1}) that a molecule can catalyze the water oxidation reaction when *Eapp* tends to infinite potential.[S4]

The Turn Over Number (TON) of **4** in the bulk electrolysis experiments were calculated according to formula S2.[S4]

Single Crystal XRD Methods

X-ray Crystal Structure Determination

Crystals of **1** were obtained by slow diffusion of ether to a methanol solution (0.2 mM). Crystals of (**2**)(PF_6) (1 mM) were obtained from a pH=7 phosphate buffer solution saturated with KPF_6**.** Crystals of (**3**)(PF_6)$_2$ were obtained from a pH=1 solution (1mM, 0.1 M triflic acid) saturated with KPF_6. The measured crystals were prepared under inert conditions immersed in perfluoropolyether as protecting oil for manipulation.

Data collection

Crystal structure determinations for **1,** (**2**)(PF_6) and (**3**)(PF_6)$_2$ were carried out using a Bruker-Nonius diffractometer equipped with an APPEX 2 4K CCD area detector, a FR591 rotating anode with MoK_α radiation, Montel mirrors as monochromator and an Oxford Cryosystems low temperature device Cryostream 700 plus (T = -173 ˚C). Full-sphere data collection was used with ω and φ scans. *Programs used:* Data collection APEX-2 [S5]data reduction Bruker Saint[S6] V/.60A and absorption correction SADABS. [S7]

Structure Solution and Refinement

Crystal structure solution was achieved using direct methods as implemented in SHELXTL[S8] and visualized using the program XP. Missing atoms were subsequently located from difference Fourier synthesis and added to the atom list. Least-squares refinement on F^2 using all measured

intensities was carried out using the program SHELXTL. All non hydrogen atoms were refined including anisotropic displacement parameters.

Comments to the structures

1: The asymmetric unit contains two independent molecules of the metal complex, two methanol molecules and one molecule of water. The independent molecules of the metal complex are distributed in three positions with the ratio 1:0.5:0.5. The two half molecules of the metal complex are located on a twofold rotation axes and have *C*2 symmetry. The carboxylate rests of the two half molecules are disordered in two positions (ratio 50:50). The water molecule is disordered in two positions with a ratio of 58:38. One of the methanol molecules is disordered in two positions with a ratio of 52:48. (**2**)(PF_6): The asymmetric unit contains two independent molecules of the metal complex and two PF_6 anions. In one of molecules of the metal complex one of the pyridine rings is disordered in two positions (ratio 60:40). The asymmetric unit contains four half PF_6 anions which have *C*i symmetry and are located on center of inversions. The half PF_6 anions are shared with neighboring molecules. (**3**)(PF_6)$_2$: The asymmetric unit contains two independent molecules of the metal complex and four PF_6 anions. One of the PF_6 anions is disordered in two orientations (ratio 77:23).

Computational Methods

Density functional theory

Geometry optimizations were performed at M06-L[S9] and M11-L[S10] levels of density functional theory using the Stuttgart [8s7p6d2f | 6s5p3d2f] ECP28MWB contracted pseudopotential basis set[S11] on Ru and the 6-31G(d) basis set[S12] on all other atoms. Non-analytical integral evaluations made use of a pruned grid having 99 radial shells and 590 angular points per shell and an automatically generated density-fitting basis set was used within the resolution-of-the-identity approximation to speed the evaluation of Coulomb integrals as implemented in Gaussian 09 software package.[S13] The nature of all stationary points was verified by analytic computation of vibrational frequencies, which were also used for the computation of zero-point vibrational energies, molecular partition functions (with all frequencies below 50 cm^{-1} replaced by 50 cm^{-1} when computing free energies), and for determining the reactants and products associated with each transition-state structure (by following the normal modes associated with imaginary frequencies). Partition functions were used in the computation of 298 K thermal contributions to free energy employing the usual ideal-gas, rigid-rotator, harmonic oscillator approximation.[S14] Free energy contributions were added to single-point M06-L and M11-L electronic energies

computed with the SDD basis set on ruthenium and the 6-311+G(2df,p) basis set on all other atoms to arrive at final, composite free energies.

Solvation and standard reduction potentials

Solvation effects associated with water as solvent were accounted for using the SMD continuum solvation model.[S15] A 1 M standard state was used for all species in aqueous solution except for water itself, for which a 55.6 M standard state was employed. Thus, for all molecules but water, the free energy in aqueous solution is computed as the 1 atm gas-phase free energy, plus an adjustment for the 1 atm to 1 M standard-state concentration change of *RT* ln (24.5), or 1.9 kcal/mol, plus the 1 M to 1 M transfer (solvation) free energy computed from the SMD model. In the case of water, the 1 atm gas-phase free energy is adjusted by the sum of a 1 atm to 55.6 M standard-state concentration change, or 4.3 kcal/mol, and the experimental 1 M to 1 M solvation free energy, –6.3 kcal/mol. The 1 M to 1 M solvation free energy of the proton was taken from experiment as –265.9 kcal/mol.[S16-S19]

Standard reduction potentials were calculated for various possible redox couples to assess the energetic accessibility of different intermediates at various oxidation states. For a redox reaction of the form

$$O_{(aq)} + n\,e^-_{(g)} \rightarrow R_{(aq)} \qquad \text{(S3)}$$

where *O* and *R* denote the oxidized and reduced states of the redox couple, respectively, and *n* is the number of electrons involved in redox reaction, the reduction potential $E^{o}_{O|R}$ relative to NHE was computed as

$$E^{o}_{O|R} = -\frac{\Delta G^{o}_{O|R} - \Delta G^{o}_{\mathrm{NHE}}}{nF} \qquad \text{(S4)}$$

where $\Delta G^{o}_{O|R}$ is the free energy change associated with eq. 1 (using Boltzmann statistics for the electron), $\Delta G^{0}_{\mathrm{NHE}}$ is the free energy change associated with

$$\mathrm{H}^{+}_{(aq)} + e^-_{(g)} \rightarrow \frac{1}{2}\mathrm{H}_{2(g)} \qquad \text{(S5)}$$

which is –4.28 eV with Boltzmann statistics for the electron,[S18,S20,S21] and *F* is the Faraday constant.

*Non-single-determinantal state energies***.** Several possible intermediates in the water oxidation mechanism have electronic structures that are not well described by a single determinant. In such instances, standard Kohn-Sham DFT is not directly applicable, [S14,S22-S24] and we adopt the Yamaguchi broken-spin-symmetry (BS) procedure [S25,S26]to compute the energy of the spin-purified low-spin (LS) state as

$$ {}^{LS}E = \frac{{}^{BS}E\left({}^{HS}\left\langle S^2 \right\rangle - {}^{LS}\left\langle S^2 \right\rangle \right) - {}^{HS}E\left({}^{BS}\left\langle S^2 \right\rangle - {}^{LS}\left\langle S^2 \right\rangle \right)}{{}^{HS}\left\langle S^2 \right\rangle - {}^{BS}\left\langle S^2 \right\rangle} \qquad \text{(S6)} $$

where HS refers to the single-determinantal high-spin coupled state that is related to the low-spin state by spin flip(s) and $< S^2 >$ is the expectation value of the total spin operator applied to the appropriate determinant. This broken-symmetry DFT approach has routinely proven effective for the prediction of state-energy splittings in metal coordination compounds. [S23,S27-S30]

III

Characterization of complexes 1, 2^{+} and 3^{2+}

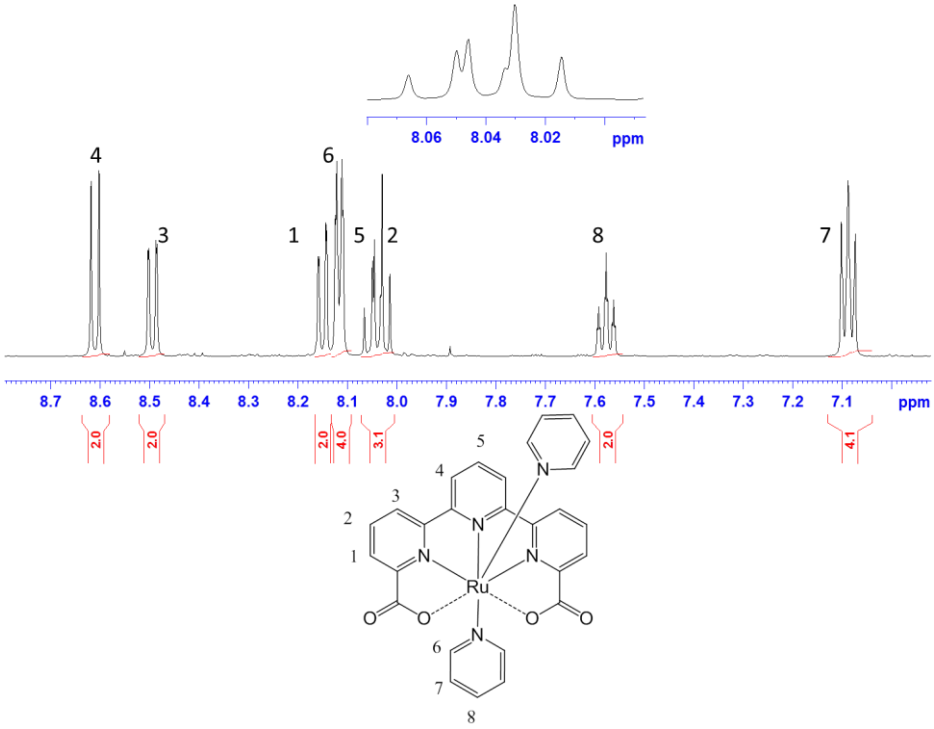

Figure S1: ^{1}H NMR of **1** in [d4]-methanol. T=298K.

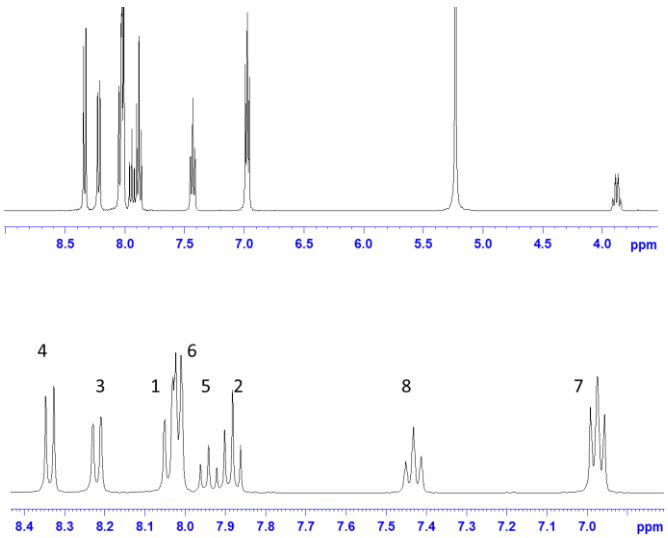

Figure S2: ^{1}H NMR of **1** [d3]-trifluoroehtanol. T=298K.

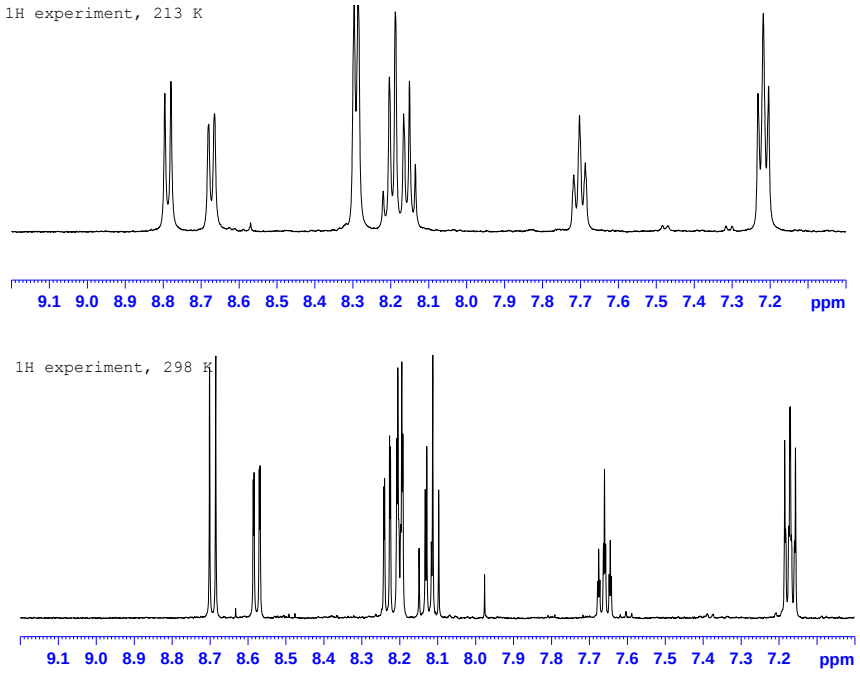

Figure S3: ^{1}H NMR of **1** in [d4]-methanol at 213K and 298K.

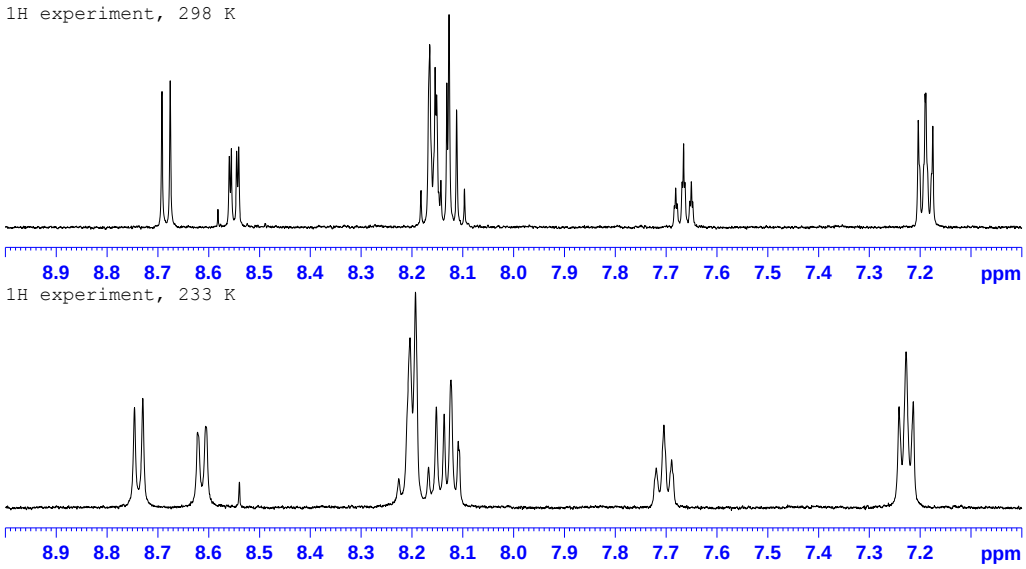

Figure S4: ^{1}H NMR of **1** in [d4]-methanol/ D_2O mixture (4:1) at 298K and 233K.

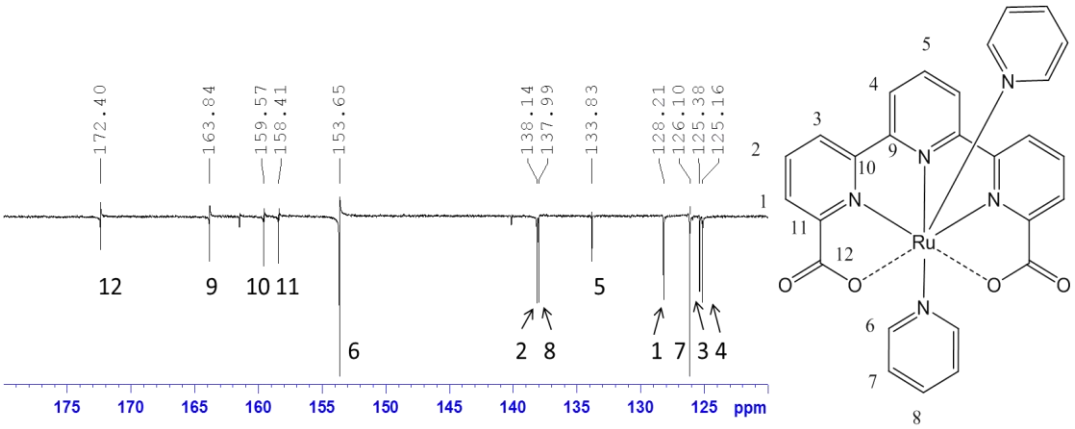

III

Figure S5: ^{13}C-{H}-NMR (DEPT45) of **1** in [d4]-methanol, T=298K.

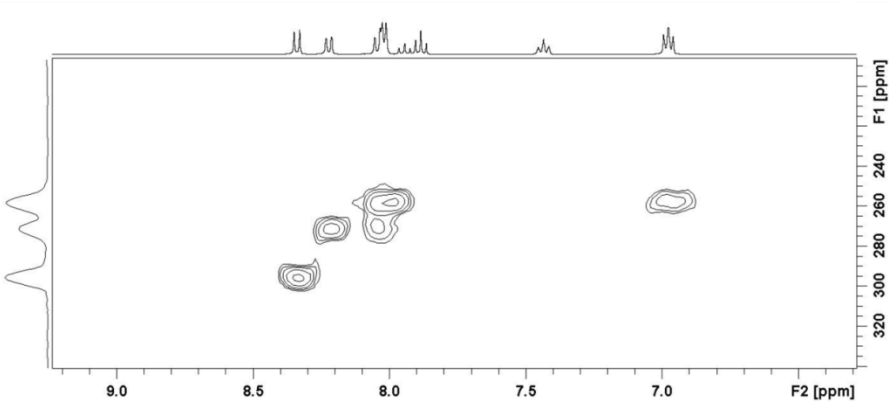

Figure S6: ^{1}H-^{15}N-HMBC of **1** in [d4]-trifluoroethanol, T=298K.

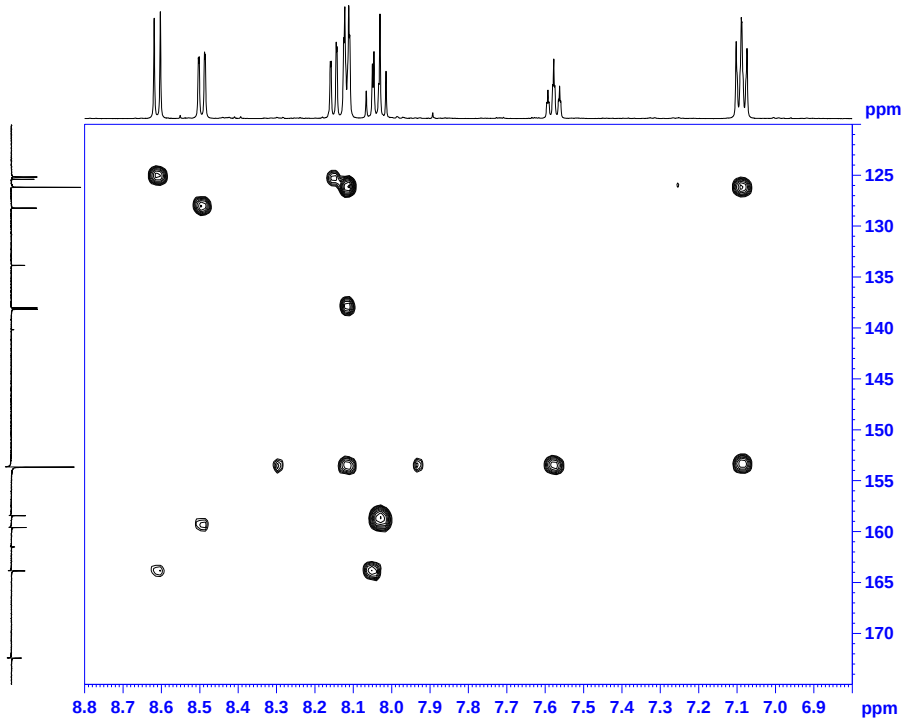

Figure S7: ^{1}H-^{13}C-HMBC NMR of **1** in [d4]-methanol, T=298K.

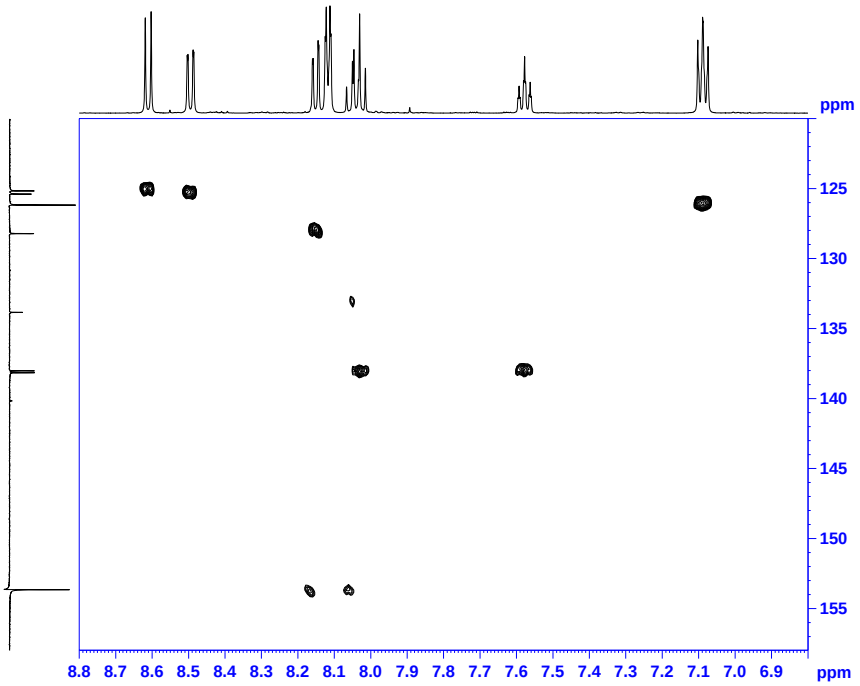

Figure S8: ^{1}H-^{13}C-HQSC NMR of **1** in [d4]-methanol, T=298K.

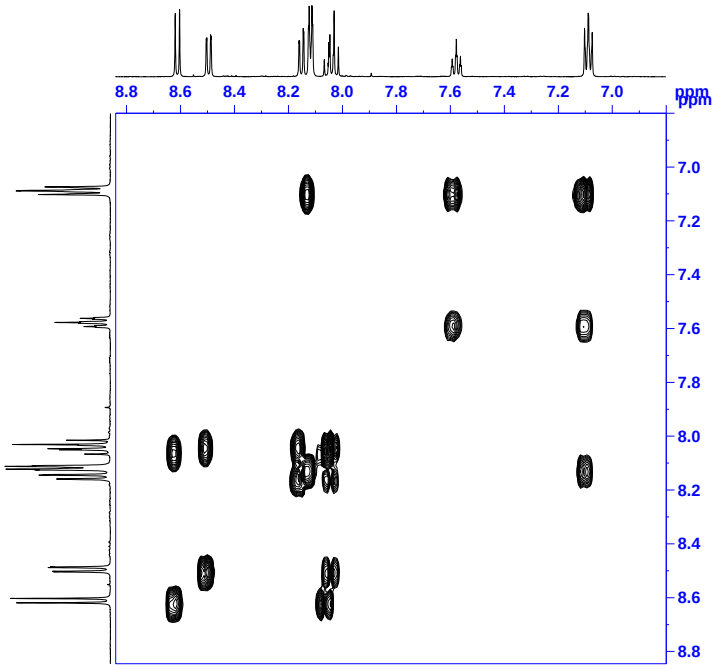

Figure S9: ^{1}H-^{1}H-COSY NMR of **1** in [d4]-methanol, T=298K.

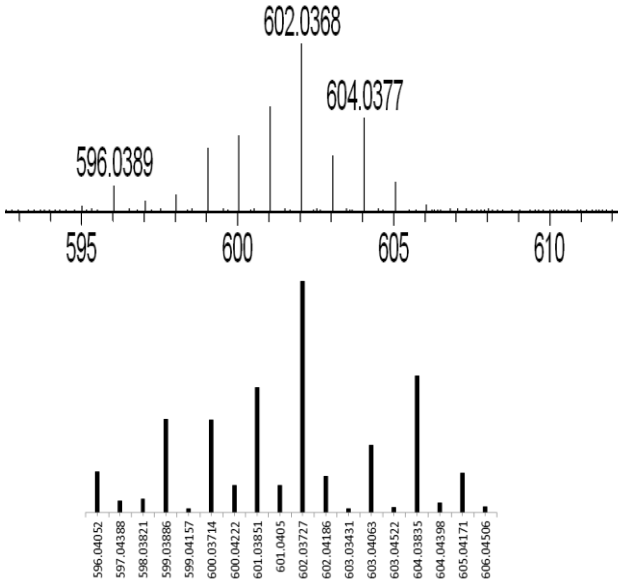

Figure S10: HR-MS for **1**-Na^{+} ($C_{27}H_{19}N_5NaO_4Ru^{+}$) (0.7 ppm error) (left) and simulated (right).

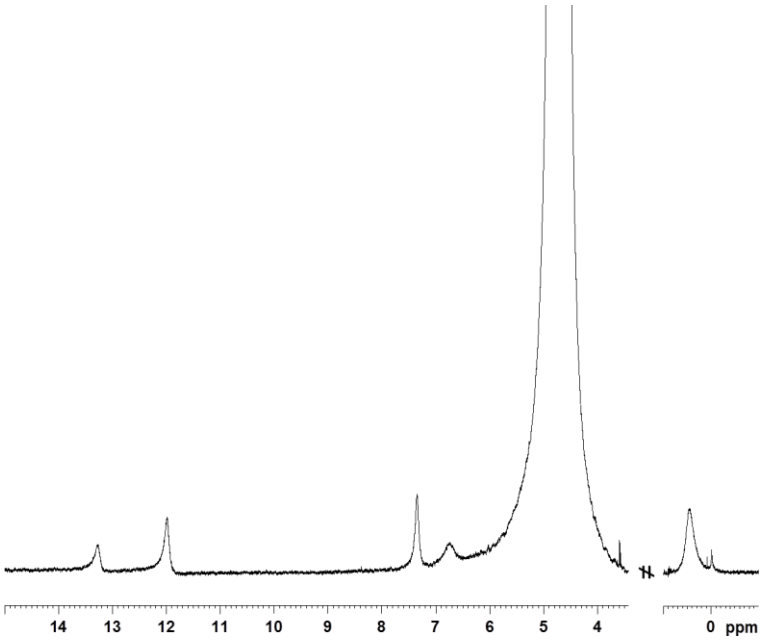

Figure S11: ^{1}H NMR of **2**$^{+}$ in pD = 7 phosphate buffered solution.

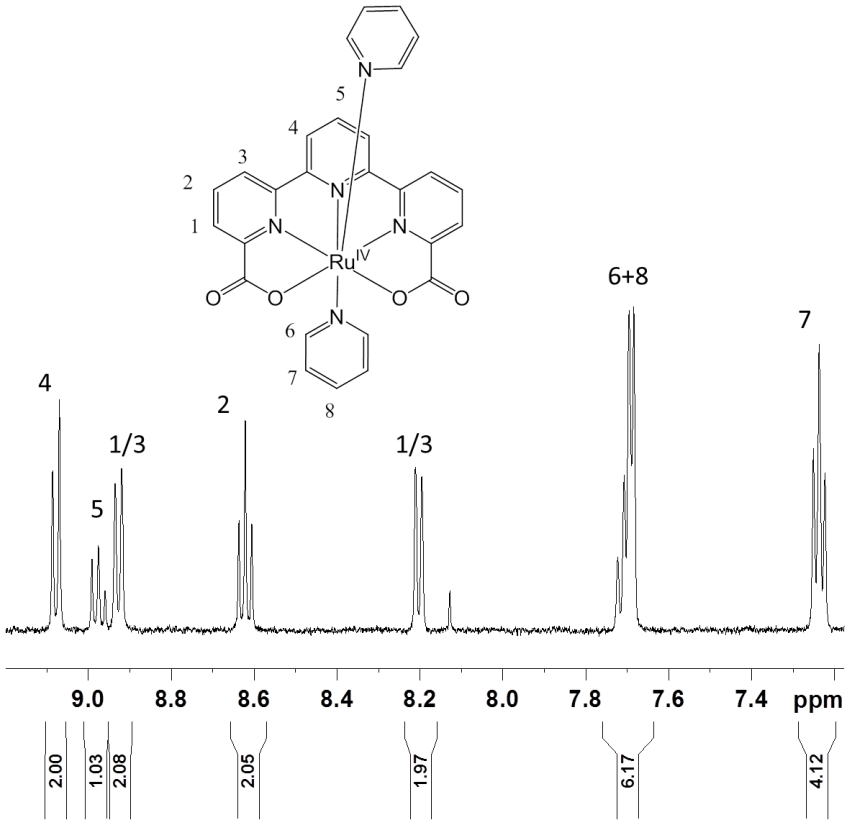

Figure S12: ^{1}H NMR of **3**$^{2+}$ in D_2O (0.1M [d1]-triflic acid).

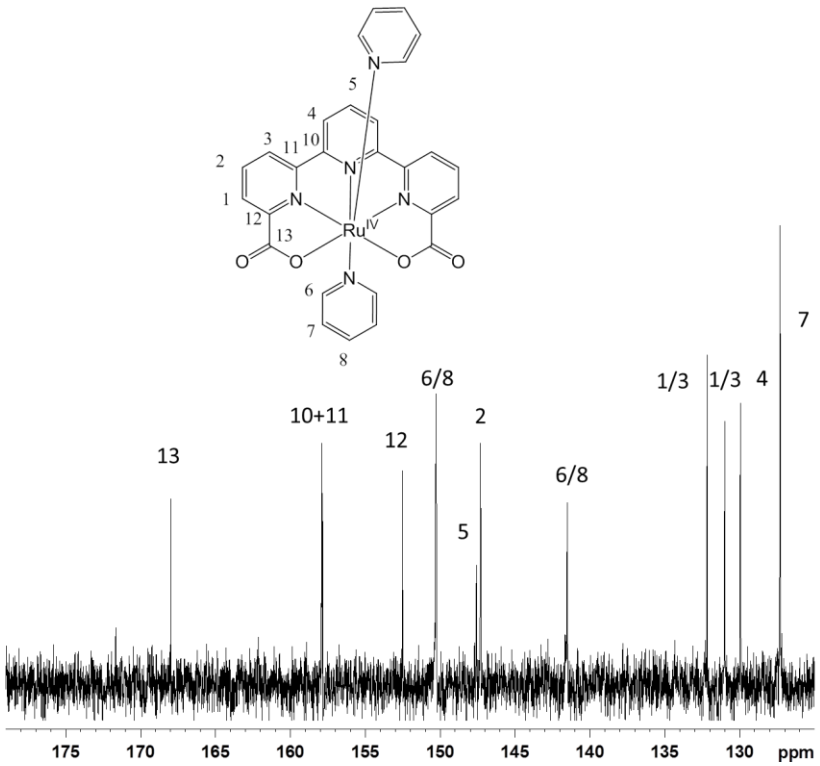

Figure S13: ^{13}C NMR of $\mathbf{3}^{2+}$ in D_2O (0.1M [d1]-triflic acid).

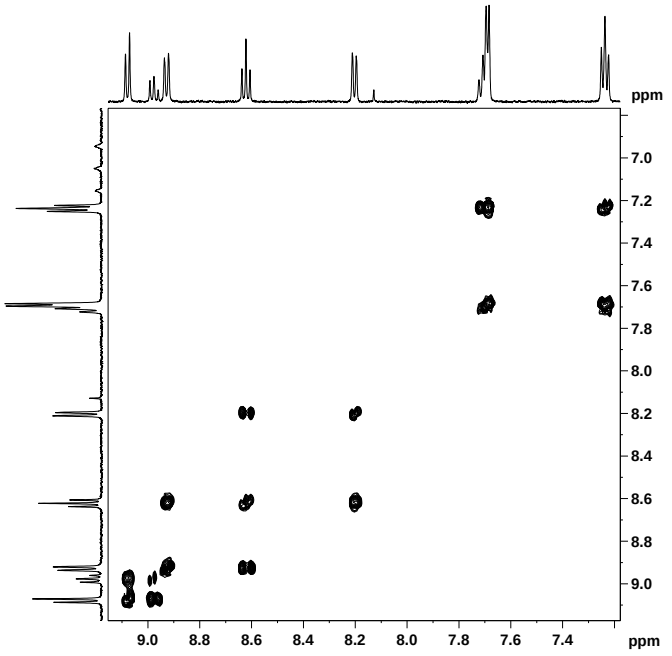

Figure S14: ^{1}H-^{1}H-COSY NMR of $\mathbf{3}^{2+}$ in D_2O (0.1M [d1]-triflic acid).

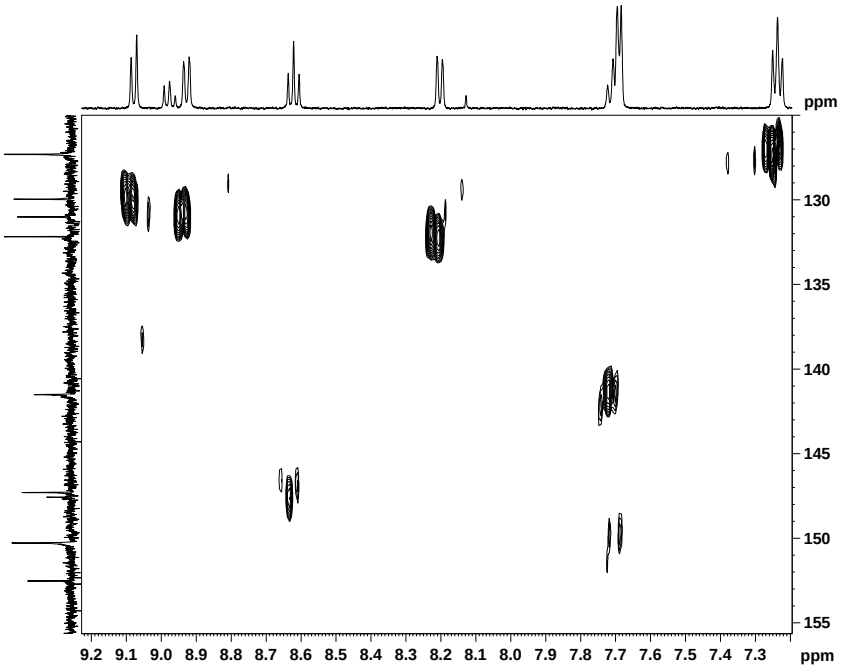

Figure S15: ^{1}H-^{13}H-HSQC NMR of $\mathbf{3}^{2+}$ in D_2O (0.1M [d1]-triflic acid).

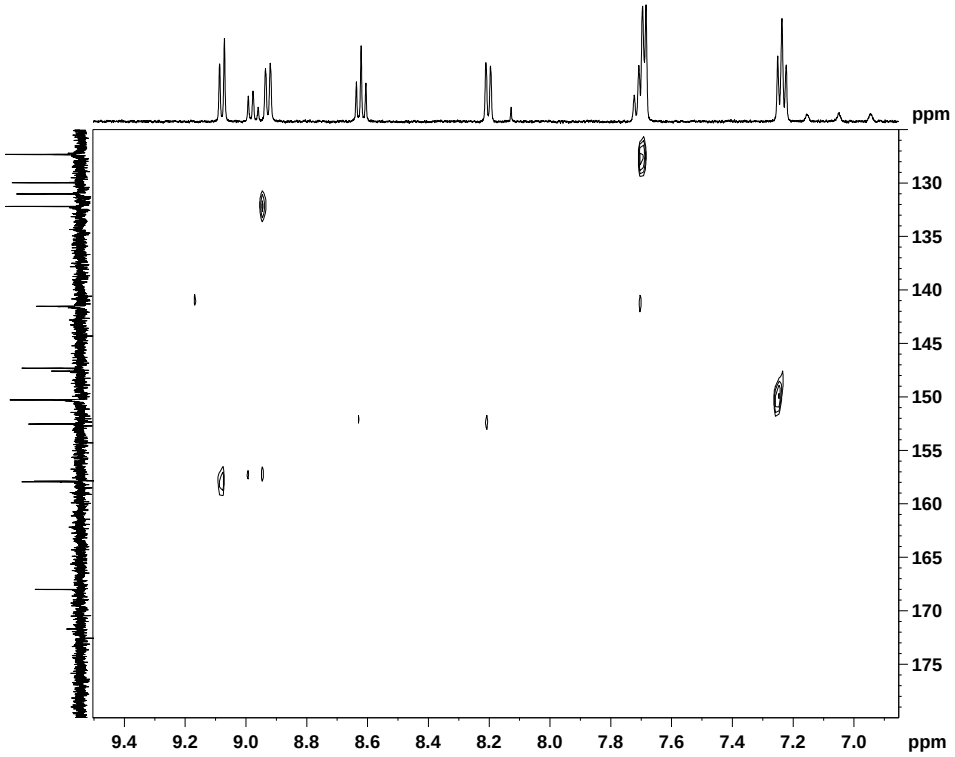

Figure S16: ^{1}H-^{13}H-HMBC NMR of $\mathbf{3}^{2+}$ in D_2O (0.1M [d1]-triflic acid).

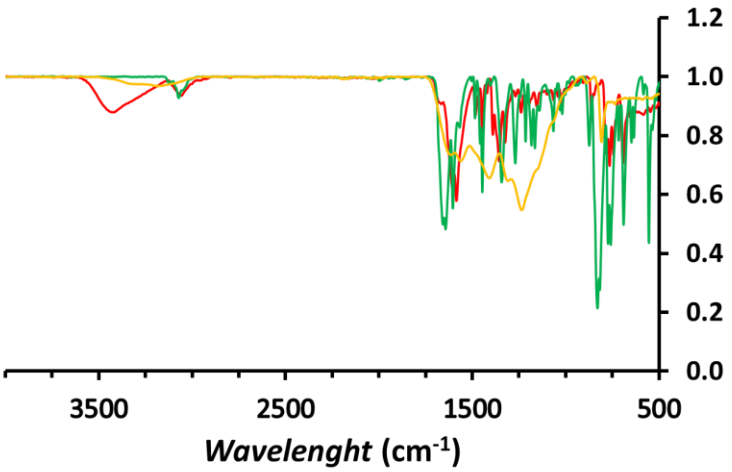

Figure S17: IR of **1** (red line), **2**$^{+}$(green line) and **3**$^{2+}$ (orange line).

Table S1: Experimental conditions to generate different rations of **3**$^{2+}$/**4** after applying a bulk electrolysis at E_{app} = 1.25 V to a solution of **1**.

[1] (mM)	Initial pH[a]	I (M)	Time (h)	Ratio 3^{2+} / 4[a]
1.7	7	0.1	12	2:1
1.7	10.5	0.1	1.5	2:1
7	10.5	0.1	1.5	5:1

a) The ratio was estimated from the charge (Q) under the III/II cathodic waves of the "Ru-non aqua" and "Ru-aqua" species, the estimation has a 10% error.

Redox properties of Ru-non aqua and Ru-aqua complexes

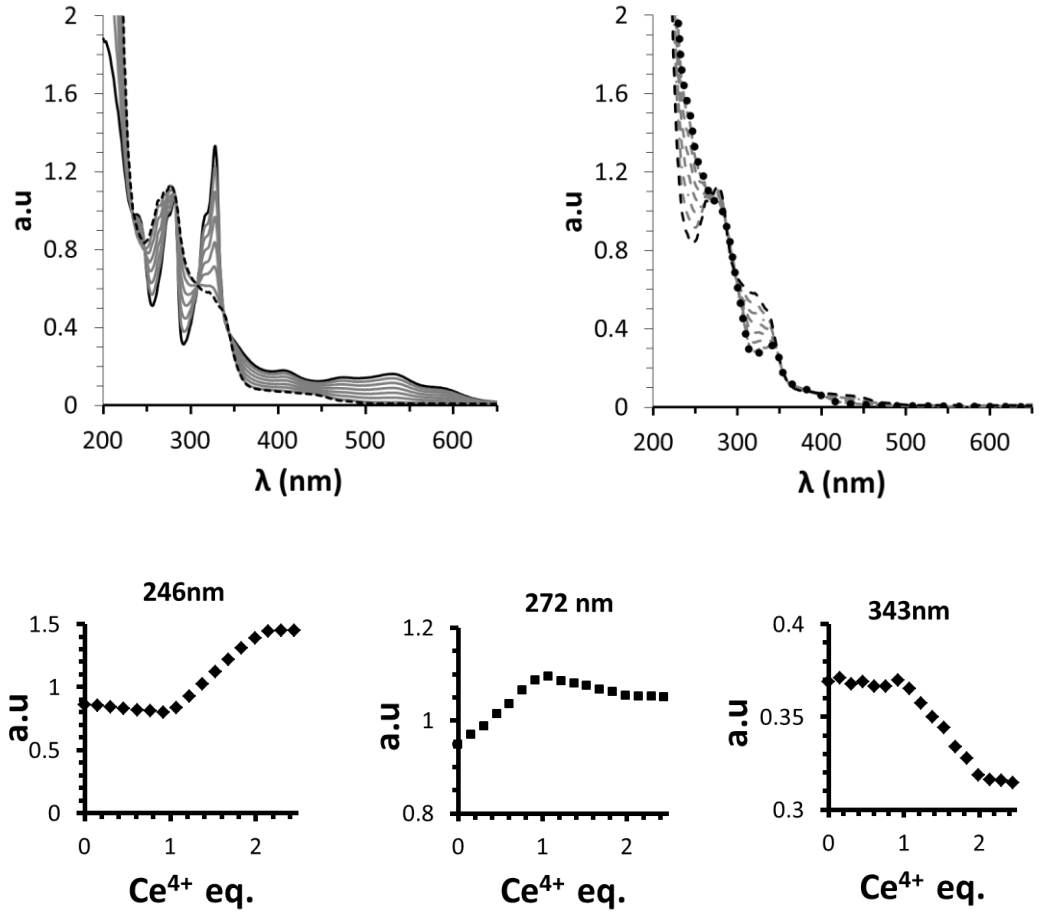

Figure S18: Spectrophotometric redox titration of **1** at pH = 1.0 by CAN (10 μL, 1.66 mM).Top left: UV-vis spectra of **1** (solid black line) and successive additions of 0.152 eq of Ce^{4+} (grey solid lines) up to aprox. 1 equivalent of Cerium (dashed black line). Top Right: UV-vis spectra of one-electron oxidized **1** (dashed black line), and successive additions of 0.152 eq. of Ce^{4+} (dashed grey lines) up to 2 equivalents of Ce^{4+} (pointed black line). Bottom: plot of absorbance against equivalents of CAN at selected wavelengths (246 nm, 272 nm and 343 nm).

pH dependency of Ru-aqua species

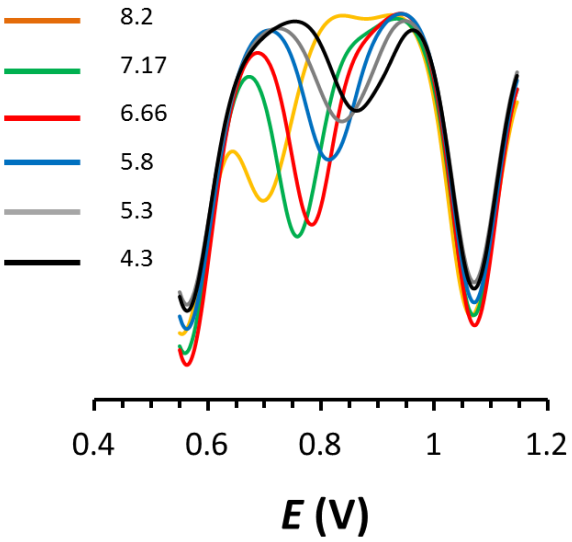

Figure S19: DPV of $\mathbf{3}^{2+}$/**4** mixture at the pHs indicated in the legend. The conditions for the generation of the $\mathbf{3}^{2+}$/**4** mixture were E_{app} = 1.25 V, initial pH=10.5, initial [**1**] = 1.7 mM. Buffered solutions at pH=2 and pH=12 were used to ajust the pH

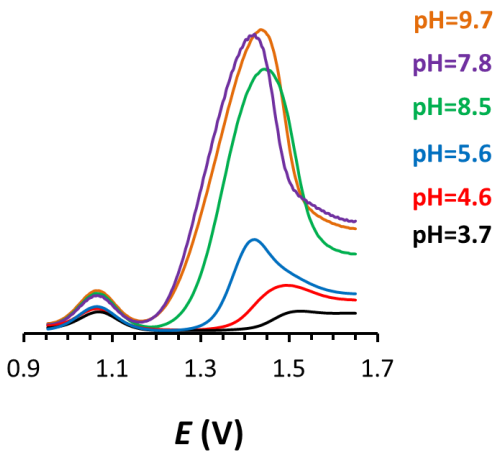

Figure S20: DPV of $\mathbf{3}^{2+}$/**4** mixture at the pHs indicated in the legend. The conditions for the generation of the $\mathbf{3}^{2+}$/**4** mixture were E_{app} = 1.25 V, initial pH=10.5, initial [**1**] = 1.7 mM. Buffered solutions at pH=2 and pH=12 were used to ajust the pH.

Recovery of 1 upon reduction

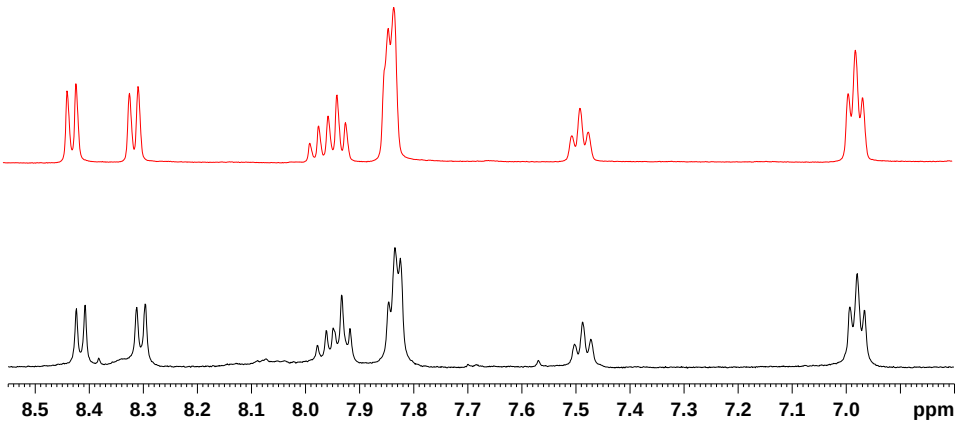

Figure S21. ^{1}H-NMR spectrum of **1** at pD = 7.0 phosphate buffer, obtained from chemical reduction with ascorbic acid of: top, $\mathbf{3}^{2+}$; bottom, from a mixture of $\mathbf{3}^{2+}$/**4** (2/1)**.**

Faradaic efficiency of the electrocatalysis by 4.

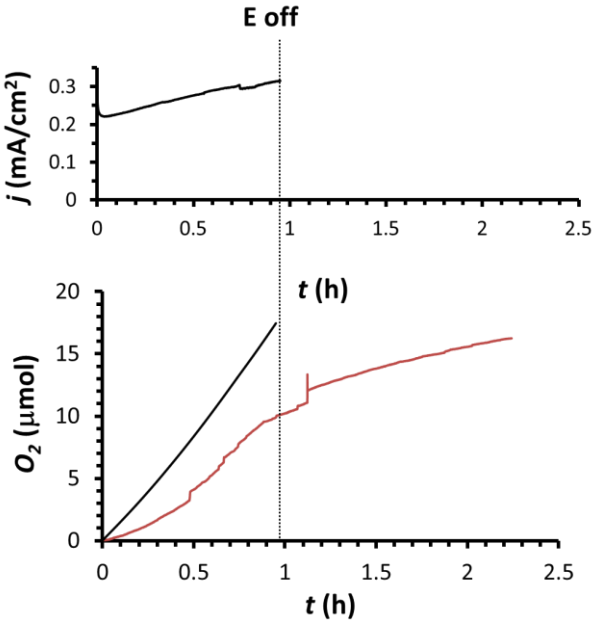

Figure S22: Bulk electrolysis for a mixture of $\mathbf{3}^{2+}$ (0.3 mM) and **4** (0.1 mM) at pH = 7.0 (3 mL) at E_{app} = 1.5 V (vs. NHE). A glassy carbon rod (S = 8.2 cm^2) was used as working, a Pt grid as counter electrode and Ag/AgCl (sat KCl) as a reference electrode. Top, current density over time. Bottom, oxygen evolution *vs.* time monitored with a Clark electrode (red line) and the theoretical amount of oxygen obtained assuming 100 % Faradaic efficiency from the measured current density on the top (black solid line). The E_{app} was stopped at 1 h, but oxygen evolution continued till approx. 2.2 h, due to a large number of bubbles trapped in the working electrode. The Faradaic efficiency turned out to be 92%. A blank experiment with a bare glassy carbon rod showed no O_2 formation

under the same conditions. It is interesting to observe that the current density in the top figures increases with time due to the increasing [**4**] during the experiment.

Electrocatalytic behavior of [Ru(bda)(pic)$_2$] and 4 at pH = 7.0.

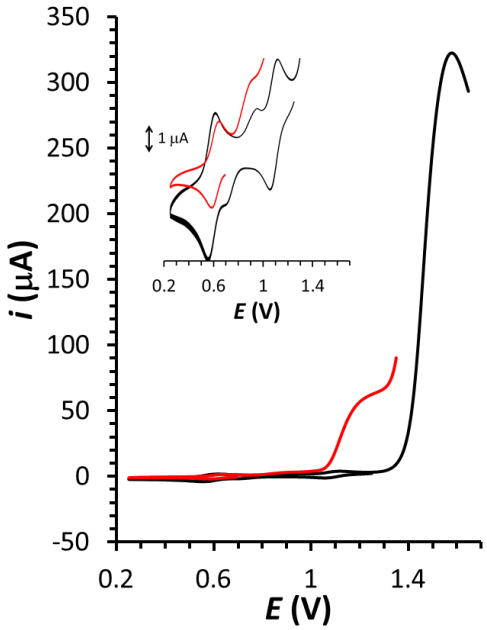

Figure S23: Comparison of the electrocatalytic response of [Ru(bda)(pic)$_2$] and **4** catalyst at pH=7 by cyclic voltammetry. CV of [Ru(bda)(pic)$_2$] (red solid line, 0.28 mM) and mixture of $\mathbf{3}^{2+}$ /**4** (black line, 0.3 mM and 0.15 mM respectively) at pH = 7 buffered phosphate solution (I = 0.1M). The inset shows an enlargement of the CV in the 0.2-1.4 V region.

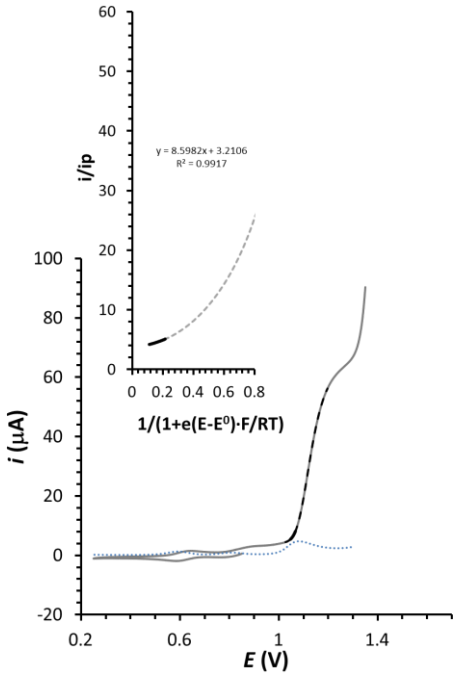

Figure S24: CV and DPV (grey solid line and blue dotted line respectively) of [Ru(bda)(pic)$_2$] (0.28 mM at pH = 7.0) and FOWA plot (inset). The points from the catalytic wave used for FOWA are plotted as a dashed black line and the fitting points at the foot of the wave are represented as a black solid line. A TOF_{MAX} of 5 s^{-1} assuming a first order kinetics.

Computational results

The "Ru non-aqua" species and optimized structures for **1**, $\mathbf{2}^{+}$ and $\mathbf{3}^{2+}$ (Figure S25). Complexes **1** and $\mathbf{3}^{2+}$ have closed-shell singlets in their ground electronic states while the ground state of $\mathbf{2}^{+}$ is a doublet, in agreement with EPR data. The calculated oxidation potentials for III/II and IV/III couples are 0.15 V and 0.84 V, respectively, at M11-L level of theory and 0.01 V and 0.47 V at the M06-L level. The corresponding experimental measurements are 0.52 V and 1.10 V, which indicate that the potential for III/II couple is significantly underestimated by the calculations. Following this observation and noting that **1** has a dangling carboxylate group that coordinates at oxidation state III, we performed calculations including explicit H_2O molecules with hydrogen bonding interactions to the carboxylate groups. This led to calculated potentials of 0.41 V and 0.85 V for III/II and IV/III couples, respectively at the M11-L level of theory, in fair agreement with experimental observations. This finding, one more time shows the importance of explicitly including H_2O molecules in modeling of reactions, especially for the cases where hydrogen bonding could impact the relative energetics of the species involved.

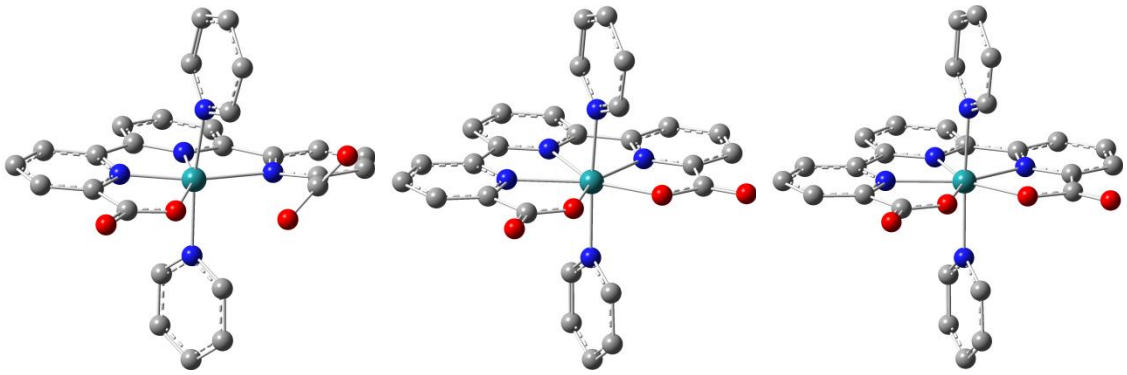

$[Ru^{II}(tda\text{-}\kappa\text{-}N^3O)Py_2]$ $[Ru^{III}(tda\text{-}\kappa\text{-}N^2O^2)Py_2]^+$ $[Ru^{IV}(tda\text{-}\kappa\text{-}N^3O^2)Py_2]^{2+}$

III

Figure S25. The optimized structures of $[Ru^{II}(tda\text{-}\kappa\text{-}N^3O)Py_2]$, $[Ru^{III}(tda\text{-}\kappa\text{-}N^2O^2)Py_2]^+$ and $[Ru^{IV}(tda\text{-}\kappa\text{-}N^3O^2)Py_2]^{2+}$ at M11-L level of theory. Color code: Ruthenium teal, carbon gray, oxygen red, nitrogen blue, hydrogen atoms were omitted for clarity.

Table S2. Selected geometrical features for $[Ru^{II}(tda\text{-}\kappa\text{-}N^3O)Py_2]$, $[Ru^{III}(tda\text{-}\kappa\text{-}N^2O^2)Py_2]^+$ and $[Ru^{IV}(tda\text{-}\kappa\text{-}N^3O^2)Py_2]^{2+}$ for calculated structures at M11-L and M06-L (in parenthesis) level of theories. The X-ray data are also presented for comparison.

	$[Ru^{II}(tda\text{-}\kappa\text{-}N^3O)Py_2]$		$[Ru^{III}(tda\text{-}\kappa\text{-}N^2O^2)Py_2]^+$		$[Ru^{IV}(tda\text{-}\kappa\text{-}N^3O^2)Py_2]^{2+}$	
r (Å)	**M11-L (M06-L)**	**X-ray**	**M11-L (M06-L)**	**X-ray**	**M11-L (M06-L)**	**X-ray**
$Ru–N_1$ (tda)	1.92 (1.95)	1.96	2.19 (2.24)	2.16	2.09 (2.13)	2.10 / 2.11
$Ru–N_2$ (tda)	1.93 (1.94)	1.92	2.46 (2.50)	2.38	2.09 (2.13)	2.12 / 2.11
$Ru–N_3$ (tda)	2.19 (2.21)	2.14	2.19 (2.24)	2.22	2.09 (2.13)	2.13 / 2.11
$Ru–N_4$ (py)	2.05 (2.10)	-	2.06 (2.11)	-	2.08 (2.13)	-
$Ru–N_5$ (py)	2.04 (2.09)	-	2.06 (2.11)	-	2.08 (2.13)	-
$Ru–O_1$ (tda)	2.09 (2.18)	2.20	1.95 (2.01)	2.04	1.96 (2.03)	2.02 / 2.03
$Ru–O_2$ (tda)	2.99 (3.22)	-	1.95 (2.01)	2.04	1.96 (2.03)	2.02 / 2.02

The presence of possible different binding modes at oxidation states II-IV for the “Ru-aqua” coupled with different hydrogen bonding capabilities of each of the isomers have brought a complex picture in terms of calculated redox potentials (Scheme S1-S2.) The possible competition between thermodynamically and kinetically favored species towards the PCET

reactions further complicates the comparison between the calculated redox potentials and those obtained from Pourbaix diagrams as recently shown for a Co-based hydrogen evolution catalyst.[31] Noting these points, we tentatively assigned the first PCET step to oxidation of $[Ru^{II}(H_2O)(tda\text{-}\kappa\text{-}N^3)(py)_2]$ to $[Ru^{III}(OH)(tda\text{-}\kappa\text{-}N^3)(py)_2]$ ($E_{1/2}{}^2$ = 0.70 V calc obs 0.70), which could isomerize to $[Ru^{III}(OH)(tda\text{-}\kappa\text{-}N^2O)(py)_2]$. The second PCET step results in generation of $[Ru^{IV}(O)(tda\text{-}\kappa\text{-}N^2O)(py)_2]$ from $[Ru^{III}(OH)(tda\text{-}\kappa\text{-}N^3)(py)_2]$ ($E_{1/2}{}^3$ = 1.18 V calc obs 0.87 V), which will be in equilibrium with $[Ru^{IV}(O)(tda\text{-}\kappa\text{-}N^3O)(py)_2]$. The dynamic nature of the catalyst requires further work to gain more insight on the equilibrium of different binding modes and interaction with solvent molecules.

III

Table S3. Absolute and relative free energies at pH 0.0 and 7.0 for computed species at M06-L level of theory. The structures are grouped in an order following the water oxidation pathway and in each group a relative zero free energy species is chosen.

Complex	**Absolute Free Energy (G) (a.u.)**	**Relative Free Energy (ΔG) (kcal/mol)**	
		pH 0.0	**pH 7.0**
$[Ru^{II}(Htda\text{-}\kappa\text{-}N^3O)Py_2]^+$ (closed-shell singlet)	**-1710.5191**	**0.0**	**0.0**
$[Ru^{II}(tda\text{-}\kappa\text{-}N^2O^2)Py_2]$ (closed-shell singlet)	-1710.0557	20.5	11.0
$[Ru^{II}(tda\text{-}\kappa\text{-}N^3O)Py_2]$ (closed-shell singlet)	-1710.0774	6.9	-2.6
$[Ru^{II}(Htda\text{-}\kappa\text{-}N^3)Py_2(OH_2)]^+$ (closed-shell singlet)	-1786.9496	7.0	7.0
$[Ru^{II}(tda\text{-}\kappa\text{-}N^3)Py_2(OH_2)]$ (closed-shell singlet)	-1786.5106	12.2	2.7
$[Ru^{II}(tda\text{-}\kappa\text{-}N^3)Py_2(OH)]$ (closed-shell singlet)	-1786.0363	39.6	20.6

$[Ru^{III}(tda\text{-}\kappa\text{-}N^2O^2)Py_2]^+$ (doublet)	**-1709.9200**	**0.0**	**0.0**
$[Ru^{III}(Htda\text{-}\kappa\text{-}N^3)Py_2(OH_2)]^{2+}$ (doublet)	-1786.7664	16.3	25.9
$[Ru^{III}(Htda\text{-}\kappa\text{-}N^3)Py_2(OH)]^+$ (doublet)	-1786.3274	21.5	21.5
$[Ru^{III}(Htda\text{-}\kappa\text{-}N^2O)Py_2(OH)]^+$ (doublet)	-1786.3412	12.9	12.9
$[Ru^{III}(tda\text{-}\kappa\text{-}N^3)Py_2(OH_2)]^+$ (doublet)	-1786.3320	18.6	18.6
$[Ru^{III}(tda\text{-}\kappa\text{-}N^3)Py_2(OH)]$ (doublet)	-1785.8836	29.7	20.2
$[Ru^{III}(tda\text{-}\kappa\text{-}N^2O)Py_2(OH)]$ (doublet)	-1785.8783	33.1	23.5
$[Ru^{III}(tda\text{-}\kappa\text{-}N^3)Py_2(O)]^-$ (doublet)	-1785.4154	53.2	34.2
$[Ru^{III}(tda\text{-}\kappa\text{-}N^3)Py_2(O)]^-$ (quartet)	-1785.3893	69.6	50.6
$[Ru^{IV}(tda\text{-}\kappa\text{-}N^3O^2)Py_2]^{2+}$ (closed-shell singlet)	**-1709.7460**	**0.0**	**0.0**
$[Ru^{IV}(Htda\text{-}\kappa\text{-}N^3O)Py_2(OH)]^{2+}$ (closed-shell singlet)	-1786.1512	22.9	22.9

$[Ru^{IV}(Htda\text{-}\kappa\text{-}N^2O)Py_2(OH)]^{2+}$ (closed-shell singlet)	-1786.1408	29.4	22.9
$[Ru^{IV}(Htda\text{-}\kappa\text{-}N^2O)Py_2(O)]^{+}$ (triplet)	-1785.7169	25.2	15.7
$[Ru^{IV}(Htda\text{-}\kappa\text{-}N^3)Py_2(O)]^{+}$ (broken-symmetry singlet)	-1785.6854	44.9	35.4
$[Ru^{IV}(Htda\text{-}\kappa\text{-}N^3)Py_2(O)]^{+}$ (triplet)	-1785.7062	31.9	22.4
$[Ru^{IV}(tda\text{-}\kappa\text{-}N^3O)Py_2(OH)]^{+}$ (closed-shell singlet)	-1785.7179	24.6	15.0
$[Ru^{IV}(tda\text{-}\kappa\text{-}N^2O)Py_2(O)]$ (triplet)	-1785.2720	34.1	15.1
$[Ru^{IV}(tda\text{-}\kappa\text{-}N^3)Py_2(O)]$ (broken-symmetry singlet)	-1785.2633	39.6	20.5
$[Ru^{IV}(tda\text{-}\kappa\text{-}N^3)Py_2(O)]$ (triplet)	-1785.2761	31.5	12.5
$[Ru^{V}(tda\text{-}\kappa\text{-}N^3O^2)Py_2]^{3+}$ (doublet)	**-1709.4987**	**0.0**	**0.0**
$[Ru^{V}(tda\text{-}\kappa\text{-}N^3)Py_2(O)]^{+}$ (doublet)	-1785.0764	1.7	-17.4
$[Ru^{V}(tda\text{-}\kappa\text{-}N^2O)Py_2(O)]^{+}$ (doublet)	-1785.0780	0.6	-18.4
$[Ru^{V}(tda\text{-}\kappa\text{-}N^3O)Py_2(O)]^{+}$	-1785.0839	-3.1	-22.1

(doublet)			
$[Ru^{V}(tda\text{-}\kappa\text{-}N^{2}O)Py_{2}(O)]^{+}$ WNA TS (doublet)	-1861.4989	13.7	-5.3
$[Ru^{III}(Htda\text{-}\kappa\text{-}N^{2}O)Py_{2}(OOH)]^{+}$ Conformer 1 (doublet)	**-1861.4997**	**0.0**	**0.0**
$[Ru^{III}(Htda\text{-}\kappa\text{-}N^{2}O)Py_{2}(OOH)]^{+}$ Conformer 1 (quartet)	-1861.4631	23.0	23.0
$[Ru^{III}(Htda\text{-}\kappa\text{-}N^{2}O)Py_{2}(OOH)]^{+}$ Conformer 2 (doublet)	-1861.4915	5.1	5.1
$[Ru^{III}(Htda\text{-}\kappa\text{-}N^{2}O)Py_{2}(OOH)]^{+}$ Conformer 2 (quartet)	-1861.4528	29.4	29.4
$[Ru^{III}(Htda\text{-}\kappa\text{-}N^{2}O)Py_{2}(OO)]$ (doublet)	-1861.0422	16.8	7.3
$[Ru^{III}(Htda\text{-}\kappa\text{-}N^{2}O)Py_{2}(OO)]$ (quartet)	-1861.0008	42.8	33.3
$[Ru^{III}(tda\text{-}\kappa\text{-}N^{2}O)Py_{2}(OOH)]$ (doublet)	-1861.0515	11.0	1.4
$[Ru^{IV}(Htda\text{-}\kappa\text{-}N^{2}O)Py_{2}(OOH)]^{2+}$ (closed-shell singlet)	**-1861.3061**	**0.0**	**0.0**
$[Ru^{IV}(Htda\text{-}\kappa\text{-}N^{2}O)Py_{2}(OOH)]^{2+}$ (triplet)	-1861.2993	4.3	4.3
$[Ru^{IV}(Htda\text{-}\kappa\text{-}N^{2}O)Py_{2}(OO)]^{+}$	-1860.8904	-9.4	-19.0

(broken-symmetry singlet)			
$[Ru^{IV}(Htda\text{-}\kappa\text{-}N^2O)Py_2(OO)]^+$ (triplet)	-1860.8846	-5.8	-15.3
$[Ru^{IV}(tda\text{-}\kappa\text{-}N^2O)Py_2(OOH)]^+$ (triplet)	-1860.8629	7.8	-1.7
$[Ru^{IV}(tda\text{-}\kappa\text{-}N^3O)Py_2(OO)]$ (triplet)	-1860.4184	16.5	-2.6
$[Ru^{V}(tda\text{-}\kappa\text{-}N^2O)Py_2(OO)]^+$ (doublet)	**-1860.2320**	**0.0**	**0.0**
$[Ru^{V}(tda\text{-}\kappa\text{-}N^2O)Py_2(OO)]^+$ (quartet)	-1860.2340	-1.2	-1.2

Table S4. Absolute and relative free energies at pH 0.0 and 7.0 for computed species at M11-L level of theory. The structures are grouped in an order following the water oxidation pathway and in each group a relative zero free energy species is chosen.

Complex	**Absolute Free Energy (G) (a.u.)**	**Relative Free Energy (ΔG) (kcal/mol)**	
		pH 0.0	**pH 7.0**
$[Ru^{II}(Htda\text{-}\kappa\text{-}N^3O)Py_2]^+$ (closed-shell singlet)	**-1710.4742**	**0.0**	**0.0**
$[Ru^{II}(Htda\text{-}\kappa\text{-}N^3O)Py_2]^+ \bullet H_2O$ (closed-shell singlet)	-1786.9080	-0.9	-0.9
$[Ru^{II}(tda\text{-}\kappa\text{-}N^3O)Py_2]$ (closed-shell singlet)	-1710.0281	9.7	0.1

III

$[Ru^{II}(tda\text{-}\kappa\text{-}N^3O)Py_2]\bullet H_2O$ (closed-shell singlet)	-1786.4595	10.3	0.8
$[Ru^{II}(tda\text{-}\kappa\text{-}N^3O)Py_2]\bullet(H_2O)_2$ (closed-shell singlet)	-1862.8921	10.2	0.7
$[Ru^{II}(tda\text{-}\kappa\text{-}N^2O^2)Py_2]$ (closed-shell singlet)	-1710.0191	15.3	5.8
$[Ru^{II}(tda\text{-}\kappa\text{-}N^2O^2)Py_2]\bullet H_2O$ (closed-shell singlet)	-1786.4507	15.8	6.3
$[Ru^{II}(tda\text{-}\kappa\text{-}N^2O^2)Py_2]\bullet(H_2O)_2$ (closed-shell singlet)	-1786.4482	17.4	7.8
$[Ru^{II}(Htda\text{-}\kappa\text{-}N^3)Py_2(OH_2)]^+$ (closed-shell singlet)	-1786.8916	9.4	9.4
$[Ru^{II}(tda\text{-}\kappa\text{-}N^3)Py_2(OH_2)]$ (closed-shell singlet)	-1786.4536	14.0	4.5
$[Ru^{II}(tda\text{-}\kappa\text{-}N^3)Py_2(OH_2)]\bullet H_2O$ Conformer 1 (closed-shell singlet)	-1862.8794	18.2	8.6
$[Ru^{II}(tda\text{-}\kappa\text{-}N^3)Py_2(OH_2)]\bullet H_2O$ Conformer 2 (closed-shell singlet)	-1862.8852	14.5	5.0
$[Ru^{II}(tda\text{-}\kappa\text{-}N^2O)Py_2(OH_2)]$ (closed-shell singlet)	-1786.4457	18.9	9.4
$[Ru^{II}(tda\text{-}\kappa\text{-}N^2O)Py_2(OH_2)]\bullet H_2O$ (closed-shell singlet)	-1862.8747	21.1	11.6
$[Ru^{II}(tda\text{-}\kappa\text{-}N^3)Py_2(OH)]^-$ (closed-shell singlet)	-1785.9755	43.7	24.7

$[Ru^{III}(Htda\text{-}\kappa\text{-}N^3O)Py_2]^{2+}$ (doublet)	**-1710.2897**	**0.0**	**0.0**
$[Ru^{III}(tda\text{-}\kappa\text{-}N^2O^2)Py_2]^{+}$ (doublet)	-1709.8658	-4.3	-13.8
$[Ru^{III}(tda\text{-}\kappa\text{-}N^2O^2)Py_2]^{+}\bullet H_2O$ (doublet)	-1786.2931	-1.1	-10.6
$[Ru^{III}(tda\text{-}\kappa\text{-}N^2O^2)Py_2]^{+}\bullet (H_2O)_2$ (doublet)	-1862.7203	2.2	-7.3
$[Ru^{III}(Htda\text{-}\kappa\text{-}N^3)Py_2(OH_2)]^{2+}$ (doublet)	-1786.6881	21.3	21.3
$[Ru^{III}(Htda\text{-}\kappa\text{-}N^3)Py_2(OH)]^{+}$ (doublet)	-1786.2515	25.0	15.5
$[Ru^{III}(tda\text{-}\kappa\text{-}N^3)Py_2(OH_2)]^{+}$ (doublet)	-1786.2521	24.7	15.2
$[Ru^{III}(tda\text{-}\kappa\text{-}N^3)Py_2(OH)]$ (doublet)	-1785.8098	31.9	12.9
$[Ru^{III}(tda\text{-}\kappa\text{-}N^3)Py_2(OH)]\bullet (H_2O)$ (doublet)	-1862.2567	22.8	3.8
$[Ru^{III}(tda\text{-}\kappa\text{-}N^2O)Py_2(OH)]$ (doublet)	-1785.8122	30.4	11.3
$[Ru^{III}(tda\text{-}\kappa\text{-}N^2O)Py_2(OH)]\bullet (H_2O)$ (doublet)	-1862.2404	33.0	14.0
$[Ru^{III}(tda\text{-}\kappa\text{-}N^3)Py_2(O)]^{-}$	-1785.3380	57.7	29.1

(doublet)			
$[Ru^{III}(tda\text{-}\kappa\text{-}N^3)Py_2(O)]^-$ (quartet)	-1785.3071	77.1	48.5
$[Ru^{IV}(tda\text{-}\kappa\text{-}N^3O^2)Py_2]^{2+}$ (closed-shell singlet)	**-1709.6782**	**0.0**	**0.0**
$[Ru^{IV}(tda\text{-}\kappa\text{-}N^3O^2)Py_2]^{2+}\bullet H_2O$ (closed-shell singlet)	-1786.1045	3.8	3.8
$[Ru^{IV}(tda\text{-}\kappa\text{-}N^3O^2)Py_2]^{2+}\bullet (H_2O)_2$ (closed-shell singlet)	-1862.5320	6.9	6.9
$[Ru^{IV}(Htda\text{-}\kappa\text{-}N^3O)Py_2(OH)]^{2+}$ Conformer 1 (closed-shell singlet)	-1786.0733	23.4	23.4
$[Ru^{IV}(Htda\text{-}\kappa\text{-}N^2O)Py_2(OH)]^{2+}$ Conformer 1 (triplet)	-1786.0566	33.9	33.9
$[Ru^{IV}(Htda\text{-}\kappa\text{-}N^3O)Py_2(OH)]^{2+}$ Conformer 2 (closed-shell singlet)	-1786.0640	29.2	29.2
$[Ru^{IV}(Htda\text{-}\kappa\text{-}N^2O)Py_2(OH)]^{2+}$ Conformer 2 (triplet)	-1786.0564	34.0	34.0
$[Ru^{IV}(Htda\text{-}\kappa\text{-}N^2O)Py_2(O)]^{+}$ (triplet)	-1785.6350	28.2	18.6
$[Ru^{IV}(tda\text{-}\kappa\text{-}N^3O)Py_2(OH)]^{+}$ (closed-shell singlet)	-1785.6397	25.2	15.7
$[Ru^{IV}(tda\text{-}\kappa\text{-}N^3O)Py_2(OH)]^{+}\bullet H_2O$ (closed-shell singlet)	-1862.0664	28.8	19.3
$[Ru^{IV}(tda\text{-}\kappa\text{-}N^2O)Py_2(O)]$	-1785.1761	45.9	26.8

III

(broken-symmetry singlet)			
$[Ru^{IV}(tda\text{-}\kappa\text{-}N^2O)Py_2(O)]$ (triplet)	-1785.1900	37.1	18.1
$[Ru^{IV}(tda\text{-}\kappa\text{-}N^2O)Py_2(O)]\bullet H_2O$ (triplet)	-1861.6107	44.5	25.5
$[Ru^{IV}(tda\text{-}\kappa\text{-}N^3O)Py_2(O)]$ (triplet)	-1785.1805	43.1	24.1
$[Ru^{IV}(tda\text{-}\kappa\text{-}N^3)Py_2(O)]$ (triplet)	-1785.1829	41.6	22.5
$[Ru^{IV}(tda\text{-}\kappa\text{-}N^3)Py_2(O)]\bullet H_2O$ (triplet)	-1861.6208	38.1	19.1
$[Ru^{IV}(tda\text{-}\kappa\text{-}N^3O)Py_2(OO)]$ (triplet)	-1860.3144	15.9	-3.1
$[Ru^{V}(tda\text{-}\kappa\text{-}N^3O^2)Py_2]^{3+}$ (doublet)	**-1709.4171**	**0.0**	**0.0**
$[Ru^{V}(tda\text{-}\kappa\text{-}N^3O)Py_2(OH)]^{2+}$ (doublet)	-1785.3974	13.4	3.9
$[Ru^{V}(tda\text{-}\kappa\text{-}N^3O)Py_2(O)]^{+}$ (doublet)	-1784.9846	2.2	-16.9
$[Ru^{V}(tda\text{-}\kappa\text{-}N^3)Py_2(O)]^{+}$ (doublet)	-1784.9629	15.8	-3.2
$[Ru^{V}(tda\text{-}\kappa\text{-}N^2O)Py_2(O)]^{+}$ WNA TS (doublet)	-1861.3859	21.7	2.6

$[Ru^{III}(Htda\text{-}\kappa\text{-}N^2O)Py_2(OOH)]^+$ Conformer 1 (doublet)	**-1861.4114**	**0.0**	**0.0**
$[Ru^{III}(Htda\text{-}\kappa\text{-}N^2O)Py_2(OOH)]^+$ Conformer 1 (quartet)	-1861.3624	30.8	30.8
$[Ru^{III}(Htda\text{-}\kappa\text{-}N^2O)Py_2(OOH)]^+$ Conformer 2 (doublet)	-1861.4032	5.2	5.2
$[Ru^{III}(Htda\text{-}\kappa\text{-}N^2O)Py_2(OOH)]^+$ Conformer 2 (quartet)	-1861.3541	35.9	35.9
$[Ru^{III}(Htda\text{-}\kappa\text{-}N^2O)Py_2(OO)]$ (doublet)	-1860.9532	17.2	7.7
$[Ru^{III}(Htda\text{-}\kappa\text{-}N^2O)Py_2(OO)]$ (quartet)	-1860.9089	45.0	35.5
$[Ru^{III}(tda\text{-}\kappa\text{-}N^2O)Py_2(OOH)]$ (doublet)	-1860.9618	11.8	2.3
$[Ru^{III}(tda\text{-}\kappa\text{-}N^2O)Py_2(OOH)]$ (quartet)	-1860.8902	56.7	47.2
$[Ru^{IV}(Htda\text{-}\kappa\text{-}N^2O)Py_2(OOH)]^{2+}$ (closed-shell singlet)	**-1861.2013**	**0.0**	**0.0**
$[Ru^{IV}(Htda\text{-}\kappa\text{-}N^2O)Py_2(OOH)]^{2+}$ (triplet)	-1861.1947	4.1	4.1
$[Ru^{IV}(Htda\text{-}\kappa\text{-}N^2O)Py_2(OO)]^+$ (triplet)	-1860.7845	-8.7	-18.3

$[Ru^{IV}(tda\text{-}\kappa\text{-}N^2O)Py_2(OOH)]^+$ (triplet)	-1860.7540	10.4	0.9
$[Ru^{IV}(tda\text{-}\kappa\text{-}N^3O)Py_2(OO)]$ (triplet)	-1860.3144	15.9	-3.1
$[Ru^{V}(tda\text{-}\kappa\text{-}N^2O)Py_2(OO)]^+$ (doublet)	**-1860.1154**	**0.0**	**0.0**
$[Ru^{V}(tda\text{-}\kappa\text{-}N^2O)Py_2(OO)]^+$ (quartet)	-1860.1163	-0.5	-0.5
$[Ru^{V}(tda\text{-}\kappa\text{-}N^3O)Py_2(OO)]^+$ (doublet)	-1860.1212	-3.6	-3.6

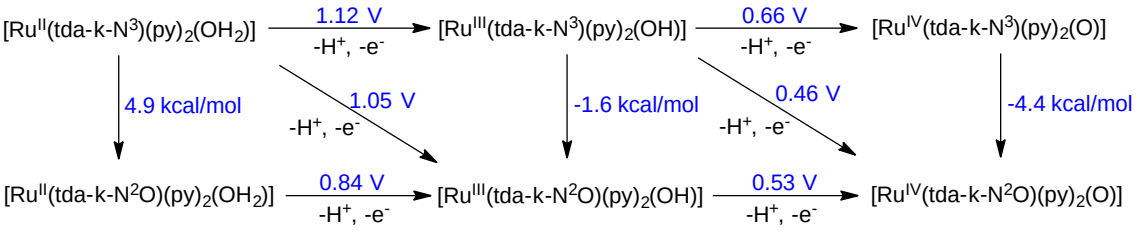

Scheme S1. Calculated free energy changes (in units of kcal/mol) and redox potentials (in units of volts) for relevant species at oxidation states of II, III and IV for Ru center.

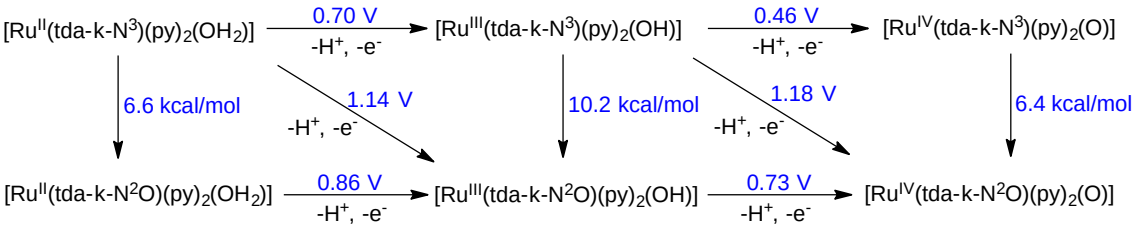

Scheme S2. Calculated free energy changes (in units of kcal/mol) and redox potentials (in units of volts) for relevant species including one explicit H_2O molecule hydrogen bonded to complex at oxidation states of II, III and IV for Ru center.

REFERENCES

S1 Galaup, C.; Couchet, J.-M.; Bedel, S.; Tisnès, P.; Picard, C. *J. Org. Chem.* **2005**, *70*, 2274-2284.

S2 Duan, L.; Bozoglian, F.; Mandal, S.; Stewart, B.; Privalov, T.; Llobet, A.; Sun, L. *Nat. Chem.* **2012**, *4*, 418-423.

S3 Evans, I. P.; Spencer A.; Wilkinson, G.; *J. Chem. Soc., Dalton Trans.* **1973**, 204-209.

S4 Costentin, C.; Drouet, S.; Robert, M.; Savéant, J.-M. *J. Am. Chem. Soc.* **2012**, *134*, 11235-11242.

S5 Data collection with APEX II versions v2009.1-02 and v2013.4-1. Bruker (2007). Bruker AXS Inc., Madison, Wisconsin, USA.

S6 Data reduction with Bruker SAINT versions V7.60A and V8.30c. Bruker (2007). Bruker AXS Inc., Madison, Wisconsin, USA.

S7 SADABS: V2008/1 and V2012/1 Bruker (2001). Bruker AXS Inc., Madison, Wisconsin, USA. Blessing, Acta Cryst. (1995) A51 33-38.

S8 Sheldrick, G.M. *Acta Cryst*. **2008** A64, 112-122. SHELXTL version V6.14.

S9 Zhao, Y.; Truhlar, D. G. *J. Chem. Phys.* **2006**, *125*, 194101.

S10 Peverati, R.; Truhlar, D. G. J. Phys. Chem. Lett. **2012**, 3, 117.

S11 D. Andrae, U. Haussermann, M. Dolg, H. Stoll, H. Preuss, *Theor. Chim. Acta* **1990**, *77*, 123.

S12 W. J. Hehre, L. Radom, P. v. R. Schleyer, J. Pople, A. *Ab Initio Molecular Orbital Theory*; Wiley: New York, 1986.

S13 M. J. Frisch, G. W. Trucks, H. B. Schlegel, G. E. Scuseria, M. A. Robb, J. R. Cheeseman, G. Scalmani, V. Barone, B. Mennucci, G. A. Petersson, H. Nakatsuji, M. Caricato, X. Li, H. P. Hratchian, A. F. Izmaylov, J. Bloino, G. Zheng, J. L. Sonnenberg, M. Hada, M. Ehara, K. Toyota, R. Fukuda, J. Hasegawa, M. Ishida, T. Nakajima, Y. Honda, O. Kitao, H. Nakai, T. Vreven, J. A. Montgomery, J. E. Peralta, F. Ogliaro, M. Bearpark, J. J. Heyd, E. Brothers, K. N. Kudin, V. N. Staroverov, R. Kobayashi, J. Normand, K. Raghavachari, A. Rendell, J. C. Burant, S. S. Iyengar, J. Tomasi, M. Cossi, N. Rega, J. M. Millam, M. Klene, J. E. Knox, J. B. Cross, V. Bakken, C. Adamo, J. Jaramillo, R. Gomperts, R. E. Stratmann, O. Yazyev, A. J. Austin, R. Cammi, C. Pomelli, J. W. Ochterski, R. L. Martin, K. Morokuma, V. G. Zakrzewski, G. A. Voth, P. Salvador, J. J. Dannenberg, S. Dapprich, A. D. Daniels, Ö. Farkas, J. B. Foresman, J. V. Ortiz, J. Cioslowski, D. J. Fox, D. J. *Gaussian 09, Revision C.01*; Gaussian, Inc.: Wallingford, CT, 2010.

S14 C. J. Cramer, *Essentials of Computational Chemistry: Theories and Models*; 2nd ed.; John Wiley & Sons: Chichester, 2004.

S15 A. V. Marenich, C. J. Cramer, D. G. Truhlar, *J. Phys. Chem. B* **2009**, *113*, 6378.

S16 M. D. Tissandier, K. A. Cowen, W. Y. Feng, E. Gundlach, M. H. Cohen, A. D. Earhart, J. V. Coe, T. R. Tuttle, *J. Phys. Chem. A* **1998**, *102*, 7787.

S17 D. M. Camaioni, C. A. Schwerdtfeger, *J. Phys. Chem. A* **2005**, *109*, 10795.

S18 C. P. Kelly, C. J. Cramer, D. G. Truhlar, *J. Phys. Chem. B* **2006**, *110*, 16066.

S19 V. S. Bryantsev, M. S. Diallo, W. A. Goddard, *J. Phys. Chem. B* **2008**, *112*, 9709.

S20 A. Lewis, J. A. Bumpus, D. G. Truhlar, C. J. Cramer, *J. Chem. Educ.* **2004**, *81*, 596.

III

S21 P. Winget, C. J. Cramer, D. G. Truhlar, *Theor. Chem. Acc.* **2004**, *112*, 217.

S22 T. Ziegler, A. Rauk, E. J. Baerends, *Theor. Chim. Acta* **1977**, *43*, 261.

S23 L. Noodleman, *J. Chem. Phys.* **1981**, *74*, 5737.

S24 C. J. Cramer, D. G. Truhlar, *Phys. Chem. Chem. Phys.* **2009**, *11*, 10757.

S25 K. Yamaguchi, F. Jensen, A. Dorigo, K. N. Houk, *Chem. Phys. Lett.* **1988**, *149*, 537.

S26 T. Soda, Y. Kitagawa, T. Onishi, Y. Takano, Y. Shigeta, H. Nagao, Y. Yoshioka, K. Yamaguchi, *Chem. Phys. Lett.* **2000**, *319*, 223.

S27 L. Noodleman, C. Y. Peng, D. A. Case, J.-M. Mouesca, *Coord. Chem. Rev.* **1995**, *144*, 199.

S28 I. Ciofini, C. A. Daul, *Coord. Chem. Rev.* **2003**, *238*, 187.

S29 J. N. Harvey, *Struct. Bond.* **2004**, *112*, 151.

S30 F. Neese, *Coord. Chem. Rev.* **2009**, *253*, 526.

S31 Lewandowska-Andralojc, A.; Baine, T.; Zhao, X.; Muckerman, J. T.; Fujita, E.; Polyansky, D. E. *Inorg. Chem.* **2015**, *54*, 4310-4321.

III

PAPER B Is Seven Coordination Required for Fast Molecular Water Oxidation Catalysis by Ru Complexes?

Matheu, R.; Ertem, M. Z.; Pipelier, M.; Lebreton, J.; Dubreuil, D.; Benet-Buchholz, J.; Sala, X.; Tessier, A.; Llobet, A. **2017**, *submitted*

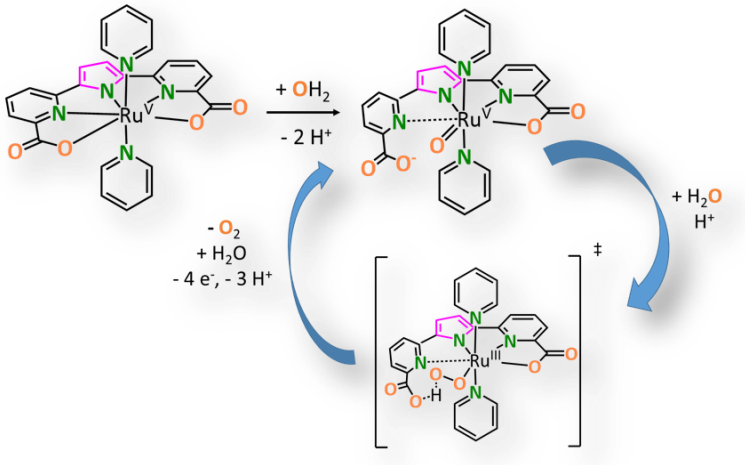

Abstract: We have prepared and characterized a new family of Ru complexes based on the $t5a^{3-}$ ligand ((2,5-bis(6-carboxylatopyridin-2-yl)pyrrol-1-ide) and pyridine (py) that include, $\{Ru^{II}(Ht5a\text{-}\kappa\text{-}N^2O)(py)_3\}$, $\mathbf{1H^{II}}(\kappa\text{-}N^2O)$, $\{Ru^{III}(t5a\text{-}\kappa\text{-}N^3O^{1.5})(py)_2\}$, $\mathbf{2^{III}}(\kappa\text{-}N^3O^{1.5})$ and $\{Ru^{IV}(t5a\text{-}\kappa\text{-}N^3O^2)(py)_2\}$, $\mathbf{2^{IV}}(\kappa\text{-}N^3O^2)$. Complexes $\mathbf{1H^{II}}(\kappa\text{-}N^2O)$, $\mathbf{2^{III}}(\kappa\text{-}N^3O^{1.5})$ and $\mathbf{2^{IV}}(\kappa\text{-}N^3O^2)$ have been investigated in solution by spectroscopic methods (NMR, UV-vis) and in the solid state by single-crystal X-ray diffraction analysis and complemented by density functional theory (DFT). The redox properties of complex $\mathbf{2^{III}}(\kappa\text{-}N^3O^{1.5})$ have been uncovered by electrochemical methods (CV and DPV), showing its easy access to high oxidation states, thanks to the trianionic nature of the $t5a^{3-}$ ligand. In neutral to basic conditions complex $\mathbf{2^{IV}}(\kappa\text{-}N^3O^2)$ undergoes aquation generating $\{Ru^{IV}(OH)(t5a\text{-}\kappa\text{-}N^2O)(py)_2\}$, $\mathbf{2^{IV}}(OH)(\kappa\text{-}N^2O)$. Further oxidation of the complex forms $\{Ru^{V}(O)(t5a\text{-}\kappa\text{-}N^2O)(py)_2\}$, $\mathbf{2^{V}}(O)(\kappa\text{-}N^2O)$ that is a very efficient water oxidation catalysts, reaching TOF_{MAX} of 9400 s^{-1}, as measured via foot of the wave analysis. The key to fast kinetics for the catalytic oxidation of water to dioxygen by $\mathbf{2^{V}}(O)(\text{?}\text{-}N^2O)$ is due to not only the easy access to high oxidation states but also to the intramolecular hydrogen bonding provided by the non-coordinated dangling carboxylate at the transition state, as put forward by DFT calculations.

Contributions: Roc Matheu synthetized and characterized the new compounds, performed the electrochemical and spectroscopic analysis and prepared the manuscript.

B 1 Introduction

The future energetic scenario relies on our capacity to generate technologies that can store solar energy into chemical bonds.[1-3]This so called artificial photosynthesis requires catalysts that efficiently reduce abundant substrates such as H_2O, CO_2 or N_2 to hydrogen, hydrocarbons or NH_3 respectively that obtained in this way are named solar fuels.[4-7] An ideal partner for these reductions is the challenging $4e^-/4H^+$ oxidation of H_2O to O_2 that again requires efficient catalysts.[8-10] Recent advances on molecular water oxidation catalysis (WOC) based on Ru complexes, has generated an impressively detailed understanding of their mode of action and as a result robust WOCs with spectacular efficiencies have been achieved.[11-13] This understanding has been accomplished thanks to electrochemical, kinetic and spectroscopic characterization of reaction intermediates complemented with density functional theory (DFT) calculations.[6-7,14-17]

Ru complexes containing the equatorial bda^{2-} ([2,2'-bipyridine]-6,6'-dicarboxylate) and tda^{2-} ([2,2':6',2''-terpyridine]-6,6''-dicarboxylate) ligands are the fastest molecular water oxidation catalysts described so far in the literature (see Chart 1 for the ligand drawings).[12,18-20] The most paradigmatic Ru-bda complex is $\{Ru^V(O)(bda)(Me\text{-}py)_2\}^+$, $\{\mathbf{5}^V(O)\}^+$, where two 4-picoline (Me-py) ligands coordinate as axial ligands. Similarly, complex $\{Ru^V(O)(tda\text{-}\kappa\text{-}N^3O)(py)_2\}^+$, $\{\mathbf{3}^V(O)\}^+$, that bears two pyridines (py) in the axial positions is the most representative Ru-tda complex, see Table 1 for a drawing of these complexes. The two families of complexes can oxidize water at maximum turn over frequencies (TOF_{MAX}) between 10^3 s^{-1} and 10^4 s^{-1}, which exceeds by 1-2 orders of magnitude the oxygen evolving catalyst in the natural photosystem II.[11,16,21] Two crucial features render Ru-bda and Ru-tda type of complexes as the best performing water oxidation catalysts in the literature. In the first place the capacity of the carboxylato moieties in bda^{2-} and tda^{2-} ligands to form intramolecular hydrogen bonds with the active Ru-OH group at different oxidation states. This is beneficial for catalysis in terms of both thermodynamics and kinetics.[7,14,22] Secondly, the other key issue in tda^{2-} and bda^{2-} ligands is their capacity to stabilize Ru high oxidation states via the anionic character of the carboxylato groups (see Chart 1 for the H_2bda and H_2tda structures) and also via the formation of seven coordination (CN7) beyond oxidation state IV. This stabilization reduces the overpotential (η) for the catalytic reaction up to 740 mV compared to other mononuclear Ru complexes bearing neutral polypyridine type of ligands with classical octahedral coordination.[7,23] Given these remarkable benefits a question that unavoidably arises is whether or not CN7 is indispensable for fast catalysis.

Here on we present the synthesis, spectroscopic, electrochemical and catalytic properties of {Ru^{V}(O)(t5a-κ-N^2O)$(py)_2$}, **2**^{V}(O)(κ-N^2O), where $t5a^{3-}$ is 2,5-bis(6-carboxylatopyridin-2-yl)pyrrol-1-ide (see Chart 1). $t5a^{3-}$ is a pentadentate ligand that can occupy the equatorial positions of a transition metal center with a pentagonal bipyramid type of geometry. Further it contains three anionic charges, one from the pyrrolato group and two from the carboxylatos, where the latters can also provide potential intramolecular hydrogen bonding.

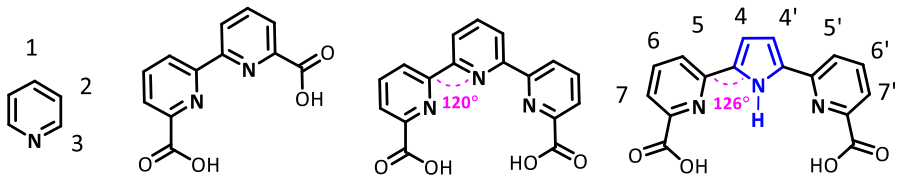

py **H_2bda** **H_2tda** **H_3t5a**

Chart 1: Ligands used and discussed in this work together with labeling.

B 2 Results

B 2.1 Synthesis and Structure

The synthesis of the H_3t5a ligand was originally described using a synthetic strategy based on pyridazine ring contraction via electrochemical reduction.[24] The strategy consisted of a nine-step process with a 4% overall yield and the last electrochemical reduction step limited the synthesis to milligram scale. In this work, we prepare H_3t5a at a 1 g scale in 26% overall yield in a novel procedure (Scheme 1A). The 2-step synthesis involves a Stetter reaction [25,26] and a 1,4-diketone Paal Knorr condensation followed by ester hydrolysis.

The H_3t5a ligand reacts with the Ru precursor, {$Ru^{II}Cl_2$(p-cymene)}$_2$, in the presence of an excess of Et_3N to ensure deprotonation of the ligand (Scheme 1B). Subsequent addition of pyridine (py) generates a red octahedral complex {Ru^{II}(Ht5a-κ-N^2O)$(py)_3$}, **1**H^{II}(κ-N^2O), where the $Ht5a^{2-}$ ligand acts as tridentate meridional ligand with one of the pyridyl-carboxylate arms decoordinated. The monodentate pyridyl ligands occupy the other three positions as shown in the ORTEP plot depicted in Figure 1. Further, the ^{1}H NMR spectrum of **1**H^{II}(κ-N^2O) in methanol-d_4 confirms that the solid-state structure is maintained in solution (Figure 2). Bonding distances and angles are unexceptional and similar to related Ru(II) complexes reported in the literature.[27]

Aerial oxidation of complex **1**H^{II}(κ-N^2O) dissolved in water generates the green paramagnetic Ru^{III} complex {Ru^{III}(t5a-κ-$N^3O^{1.5}$)$(py)_2$}, **2**^{III}(κ-$N^3O^{1.5}$), where the pyridyl-carboxylate arm substitutes the initial equatorial pyridyl ligand as shown in the ORTEP plot in Figure 1. The

coordination around the Ru metal center can be considered as 6.5 because one of the carboxylate Ru-O bonds is slightly elongated (d_{Ru-O} = 2.31 Å). The structure parallels that of Ru-tda in the III oxidation state reported earlier.[7] The elongated bond distance or contact displayed in the X-ray structure is referred as half a bond in this paper and thus we used the notation **2**^{III}(κ-N^{3}O$^{1.5}$). Finally, the ^{1}H NMR spectrum of **2**^{III}(κ-N^{3}O$^{1.5}$) in methanol-d_4 (Figure 2), shows two broad resonances in the 0-10 ppm window that reflects its paramagnetic electronic structure.

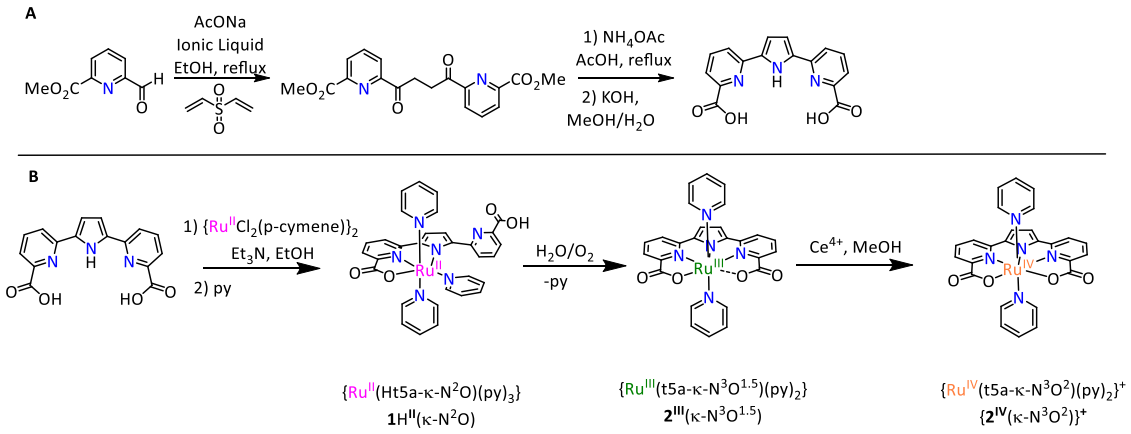

Scheme 1: Synthetic route for the preparation of H$_3$t5a ligand (**A**) and **1**H^{II}(κ-N^{2}O), **2**^{III}(κ-N^{3}O$^{1.5}$) and {**2**^{IV}(κ-N^{3}O^2)}$^+$ complexes (**B**).

Addition of Ce^{IV} to a methanol solution of **2**^{III}(κ-N^{3}O$^{1.5}$) generates the orange diamagnetic Ru^{IV} complex {Ru^{IV}(t5a-κ-N^{3}O^2)(py)$_2$}$^+$, {**2**^{IV}(κ-N^{3}O^2)}$^+$, with a 7-coordinate Ru metal center. The t5a^{3-} acts as a pentadentate ligand and generates a distorted pentagonal bipyramid geometry as can be observed in the ORTEP plot in Figure 1. It is worth mentioning the "outer equatorial angle" defined as the ORuO angle where the more external atoms of the t5a^{3-} ligand are coordinating of approximately 72º in line with the pentagonal bipyramid geometry. Under this geometry, the d^4 Ru^{IV} ion is low spin and diamagnetic with fully occupied d_{xz} and d_{yz} orbitals.[28] The symmetry increase and high oxidation state of the complex results in a ^{1}H NMR spectrum where fewer resonances appear at lower fields with respect to the Ru^{II} parent complex. Finally, half a molecule of {Ce^{III}(CH$_3$OH)(NO$_3$)$_5$}$^{2-}$ compensates the positive charge of {**2**^{IV}(κ-N^{3}O^2)}$^+$ as shown in the crystal structure (Figure S29).

DFT calculations at M06-L level of theory [29] provide optimized structure for complex **2**^{III}(κ-N^{3}O$^{1.5}$) and {**2**^{IV}(κ-N^{3}O^2)}$^+$ (see computational methods in the Supporting Information). The structure of {**2**^{IV}(κ-N^{3}O^2)}$^+$ shows a 7-coordinate complex that nicely agrees with the metric parameters of the XRD structure as shown in Table S1. However, the DFT optimized structure of **2**^{III} also has a 6.5 coordination but with an elongated Ru-N pyridyl from the t5a^{3-} ligand at 2.50 Å (κ-N$^{2.5}$O^2) instead of the carboxylate found in the crystal structure. Nevertheless, the relative energies of

the two isomers, where t5a^{3-} coordinates the Ru center in the κ-N$^{2.5}$O^{2} and κ-N^{3}O$^{1.5}$ fashions, are likely to be very similar and thus both isomers might rapidly interconvert in solution. For simplicity purposes, from now on we will use the label **2**$^{\mathbf{III}}$(κ-N^{3}O$^{1.5}$) to refer to both of them. A similar phenomenon was experimentally observed for Ru-tda complex {**3**$^{\mathbf{III}}$}$^{+}$, where the unit cell of its X-ray structure contained one molecule of the κ-N$^{2.5}$O^{2} isomer and another one of the κ-N^{3}O$^{1.5}$ isomer.[7]

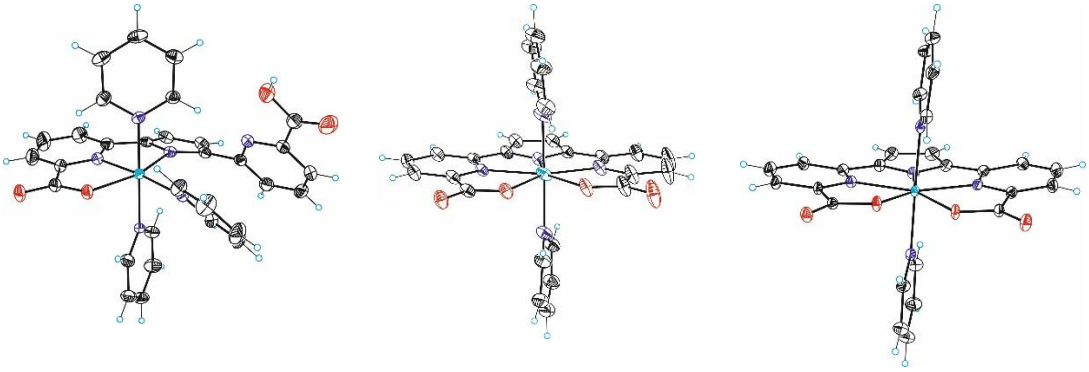

Figure 1: ORTEP plot (ellipsoids 50% of probability) of complexes **1**H$^{\mathbf{II}}$(κ-N^{2}O) (left), **2**$^{\mathbf{III}}$(κ-N^{3}O$^{1.5}$) (middle) and {**2**$^{\mathbf{IV}}$(κ-N^{3}O^{2})}$^{+}$ (right). Color codes: Ru, cyan; N, blue; O, red; C, black and H; white. See Table S1 for the distances.

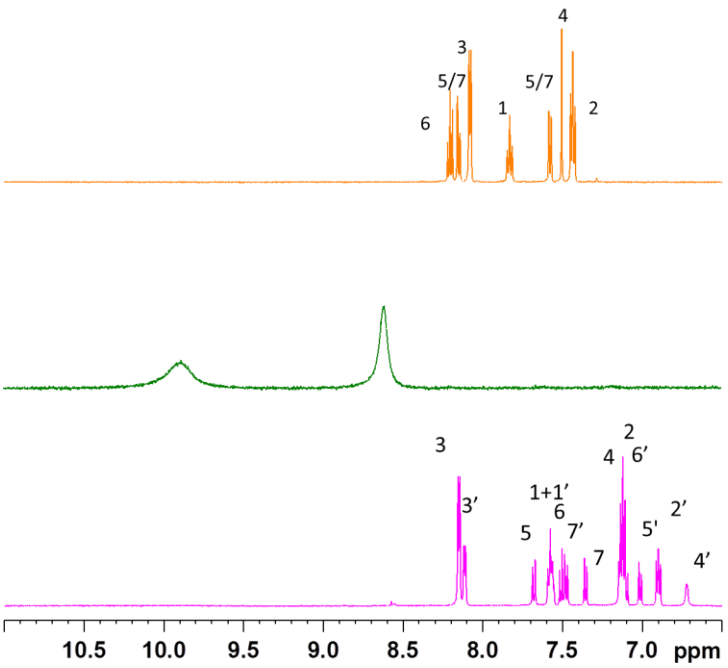

Figure 2: ^{1}H NMR of complexes **1**H$^{\mathbf{II}}$(κ-N^{2}O) (pink), **2**$^{\mathbf{III}}$(κ-N^{3}O$^{1.5}$) (green) and {**2**$^{\mathbf{IV}}$(κ-N^{3}O^{2})}$^{+}$ (orange) in methanol-d$_4$.

B 2.2 Redox Properties

We assess the electrochemical properties of complexes described in this work by Cyclic Voltammetry (CV) and Differential Pulse Voltammetry (DPV). The electrochemical experiments are carried out in a typical three-electrode configuration using glassy carbon as working electrode, Pt as the counter electrode and Hg/Hg_2SO_4 (MSE) as reference electrode. All potentials in this work are reported versus NHE ($E_{NHE} = E_{MSE} + 0.65$ V).

Figure 3A shows the electrochemical behavior for $\mathbf{2}^{\mathbf{III}}(\kappa\text{-}N^3O^{1.5})$ analyzed by CV and DPV at *pH* = 7.0. The open circuit potential of $\mathbf{2}^{\mathbf{III}}(\kappa\text{-}N^3O^{1.5})$ appears at 0.35 V and is used as the starting potential of the CV. The potential is then scanned anodically to 1.15 V and back to -0.15 V where the scan direction is again changed to 0.70 V. A chemically reversible and electrochemically quasireversible wave appears at $E^o_1 = 0.50$ V ($\Delta E = 80$ mV), which is associated with the reversible Ru^{IV}/Ru^{III} redox process. A second cathodic event occurs at lower potentials ($E_{c,p} = -0.05$ V) and is associated to the reduction from the Ru^{III} to the Ru^{II} state. The returning anodic wave appears at $E_{a,p} = 0.35$ V with a large peak to peak separation ($\Delta E = 0.40$ V) associated with the linkage isomerization outlined in the upper right part of Scheme 2. The square cycle is generated because 6.5 coordination is favored in the III oxidation state and disfavored at oxidation state II. In the latter, the pyridyl carboxylate arm decoordinates and the complex in the II oxidation states prefers 5.5-coordination. Further evidence for the presence of this square mechanism is obtained repeating the CV at faster scan rates both in MeOH and at *pH* = 7.0 where the cathodic wave of the $E^o_{2'}$ process can be observed (Figure S30-S31). This allows to calculate the III/II redox couple at *pH* = 7.0 for $\mathbf{2}^{\mathbf{III}}(\kappa\text{-}N^{2.5}O)$ that appears at $E_{2'}{}^o = 0.24$ V ($\Delta E = 0.13$ V). This value is consistent with the lower coordination number of the latter.

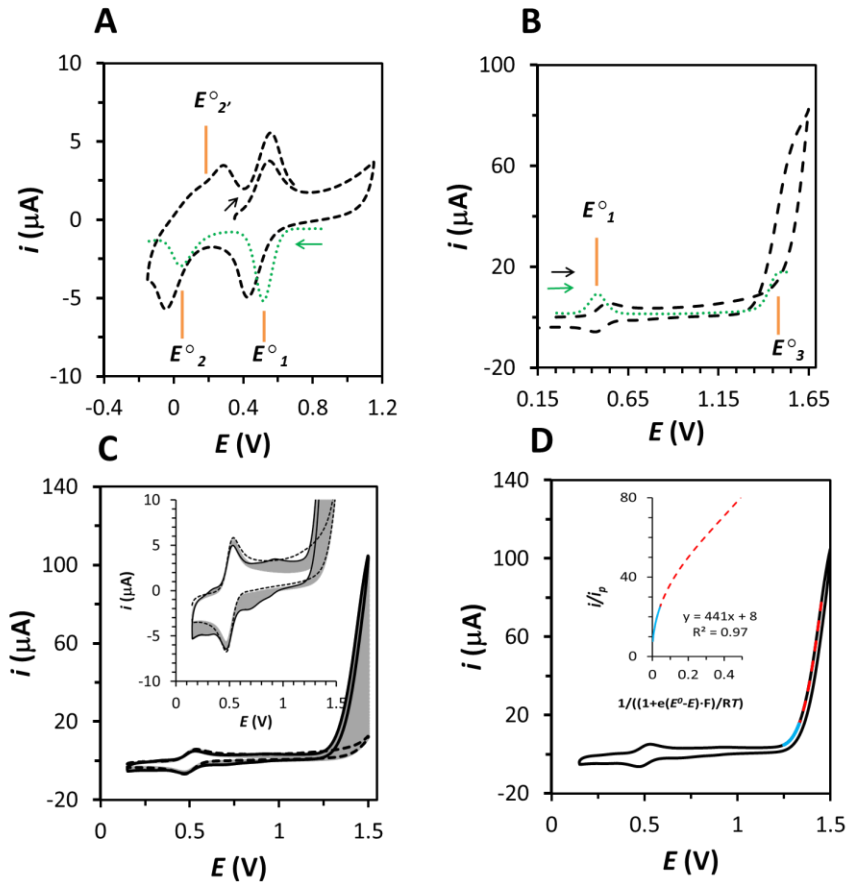

Figure 3: **A** and **B,** CV experiments (black dashed line) and DPVs experiments (green pointed line) of 0.5 mM $\mathbf{2}^{\mathbf{III}}(\kappa\text{-}N^3O^{1.5})$ at *pH* = 7.0. Arrows indicate initial potential and scan direction for CV (black line) and DPV (green line). The orange lines indicate the E^o associated with the different redox couples outlined in Scheme 2. Measurements were done under N_2 and the scan rate was 0.1 V/s. **C**, 50-repetivitve CV experiment of $\mathbf{2}^{\mathbf{III}}(\kappa\text{-}N^3O^{1.5})$ (0.5 mM) at *pH* = 7.0 (dashed black line is the first cycle, solid black line is the 50th cycle and grey lines are the cycles in between). The inset shows an enlargement between -10 μA and 10 μA. The scan rate was 0.1 V/s. **D**, 50th CV cycle containing a mixture of complex $\{\mathbf{2}^{\mathbf{IV}}(\kappa\text{-}N^3O^2)\}^+$ and complex $\mathbf{2}^{\mathbf{V}}(O)(\kappa\text{-}N^2O)$ (black solid line) together with the Foot of the Wave Analysis (FOWA) of complex $\mathbf{2}^{\mathbf{V}}(O)(\kappa\text{-}N^2O)$. The points used for FOWA are in the red dashed line and the points used for the lineal fit are cyan. $\mathbf{TOF_{MAX}}$ = 9400 s^{-1}.

We attempted to compute the free energy of the 6.5-coordinate and 5.5-coordinate structures for the III and II oxidation states including explicit water molecules to account for hydrogen bonding interactions. The comparison of relative energies at M06 level of theory[30,31] indicates that 5.5-coordinate Ru-t5a complex is favored by 6.9 kcal/mol at oxidation state II. On the other hand, we could not obtain a fully optimized structure for 5.5-coordinate complex at III oxidation state as interconverts to the 6.5-coordinate isomer during geometry optimizations but we estimated the 5.5-coodinated complex to be ≈ 5 kcal/mol unstable compared to the 6.5-

coordinate isomer (see Table S2 for the relative free energies and details). Overall, the computed energies support the proposed squared mechanism.

To further spectroscopically characterize the species involved in this square system we carried out a spectroelectrochemical experiment using an OTTLE cell for **2**^{III}(κ-N^{3}O$^{1.5}$).[32] Figure S32 shows the UV-vis spectral changes recorded every 19.5 mV for a CV experiment analogous to that of Figure 3A but at a scan rate of 2 mV/s. The UV-vis spectra exhibit isosbestic points in the Ru^{IV}/Ru^{III} and Ru^{III}/Ru^{II} reductive conversions while upon reaching the initial potential the spectrum obtained at this point is identical to the initial one, manifesting the reversibility of this system. This allows to obtain the UV-vis spectra for the dominating species at each oxidation state namely, **2**^{IV}(κ-N^{3}O^2), **2**^{III}(κ-N^{3}O$^{1.5}$) and **2**^{II}(κ-N$^{2.5}$O).

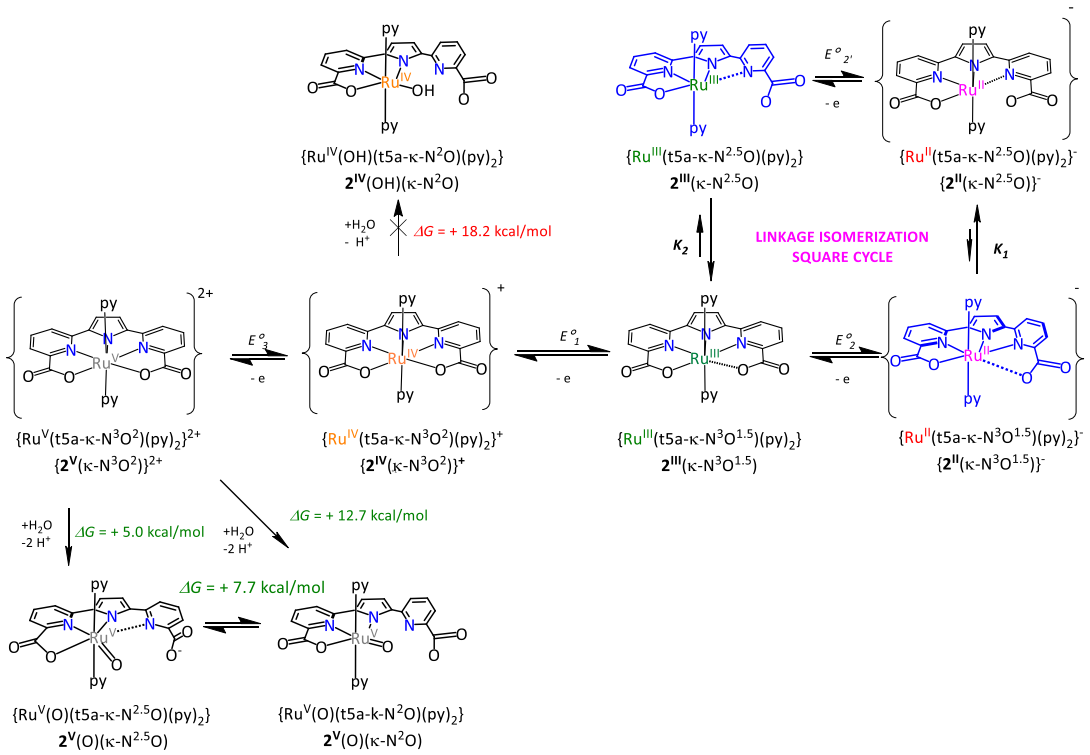

Scheme 2: Redox processes related to complex **2**^{III}(κ-N^{3}O$^{1.5}$) together with the generation of catalyst **2**^{V}(O)(κ-N^{2}O)**.** Blue colored species undergo fast isomerization in the square cycle. The free energy changes (ΔG) are at M06 level of theory at *pH* = 7.0. Dashed lines indicate elongated bonds or contacts (2.3-2.8 Å).

The redox properties of complex **2**^{III}(κ-N^{3}O$^{1.5}$) were further analyzed at different *pHs* by CV and DPV. Figure 4 shows the derived Pourbaix diagram together with that of {Ru^{II}(tda-κ-N^{3}O)(py)$_2$}, **3**^{II}, for comparative purposes. The IV/III redox couple for both complexes is *pH* independent and is approximately 550 mV lower for the Ru-t5a complex. The extra negative charge of the t5a^{3-}

ligand clearly lowers the potential of the Ru^{IV}/Ru^{III} couple at the whole *pH* range as well as that of the Ru^{III}/Ru^{II} couple at *pH* > 5. Finally, the protonation of the dangling carboxylate of the $t5a^{3-}$ ligand results in the *pH* dependent process between *pH* = 1.0 and *pH* = 5.0 for the Ru^{III}/Ru^{II} couple, showing a slope of 60 mV/*pH*, with a pK_a = 5.0.

The ability of $\mathbf{2}^{III}(\kappa\text{-}N^3O^{1.5})$ to act as precursor of a water oxidation catalyst was explored by scanning the potential up to 1.65 V at *pH* = 7.0. Figure 3B shows the presence of a large electrocatalytic current starting at 1.40 V associated with the generation of $\{\mathbf{2}^{V}(\kappa\text{-}N^3O^2)\}^{2+}$. The latter suffers fast water coordination and H^+ loss generating $\mathbf{2}^{V}(O)(\kappa\text{-}N^2O)$, that is responsible for water oxidation catalysis (see left hand side of Scheme 2 and DFT below for the characterization of the active species at oxidation state V). The crossing at *E* = 1.35 V in the returning scan is attributed to the increase of the active catalyst species $\mathbf{2}^{V}(O)(\kappa\text{-}N^2O)$ generated over the positive scanning process, while catalysis is occurring in parallel, together with the potential adsorption of the catalyst at the surface of the electrode.

Density functional theory (DFT) calculations at M06 level of theory were performed to assess the coordination of water to Ru-t5a and relative stabilities of different protonation states and isomers at different oxidation states (Figure S40-45, Table S3-12, Scheme S2-S7). At *pH* = 7.0, the coordination of a water molecule to the Ru^{IV}-t5a is uphill by 18.2 kcal/mol (see upper part of Scheme 2 and Table S10). In the V oxidation state, the free energy cost decreases to 5.0 or 12.7 kcal/mol respectively for $\mathbf{2}^{V}(O)(\kappa\text{-}N^{2.5}O)$ and $\mathbf{2}^{V}(O)(\kappa\text{-}N^2O)$ isomers (see lower part of Scheme 2). The decrease in free energy cost is consistent with the electrochemical results that show that water mainly coordinates at oxidation state V.

The optimized structures for both complexes, $\mathbf{2}^{V}(O)(\kappa\text{-}N^2O)$ and $\mathbf{2}^{V}(O)(\kappa\text{-}N^{2.5}O)$, are shown in Figure 5 and illustrate the different coordination subtleties of the pyridyl-carboxylate arm. For $\mathbf{2}^{V}(O)(\kappa\text{-}N^{2.5}O)$ the complex can be considered 6.5-coordinate with a Ru-N bond distance of 2.4 Å, whereas for $\mathbf{2}^{V}(O)(\kappa\text{-}N^2O)$ the same distance is 3.2 Å, and thus the complex is clearly 6-coordinate. The free energies for the 6.5-coordinate $\mathbf{2}^{V}(O)(\kappa\text{-}N^{2.5}O)$ and the 6-coordinate $\mathbf{2}^{V}(O)(\kappa\text{-}N^2O)$ only differ by 7.7 kcal/mol as indicated in Scheme 2 and thus at RT they probably interconvert very fast. For simplicity, in the description of the catalytic cycle we will only consider the 6-coordinate complex $\mathbf{2}^{V}(O)(\kappa\text{-}N^2O)$.

B 2.3 Water oxidation catalysis

The active catalyst $\mathbf{2}^{V}(O)(\kappa\text{-}N^2O)$ can be generated in solution in equilibrium with its precursor complex $\mathbf{2}^{V}(\kappa\text{-}N^3O^2)$, by carrying out 50 repetitive CV scans as show in Figure 3C. For this

experiment, the potential was scanned up to 1.50 V to avoid the crossing point described in the previous section. In the CV, a progressive increase of current density is observed in the 1.25 V – 1.50 V region as the repetitive cycling proceeds consistent with increase concentration of active species. In addition, new waves appear in the potential range 0.60 V - 0.95 V associated with the formation of reduced active species derived from **2**$^{\mathbf{V}}$(O)(κ-N^{2}O) generating their corresponding Ru-aqua/hydroxo species whose potential structures were calculated based on DFT and are drawn in Scheme 3 and in the SI.

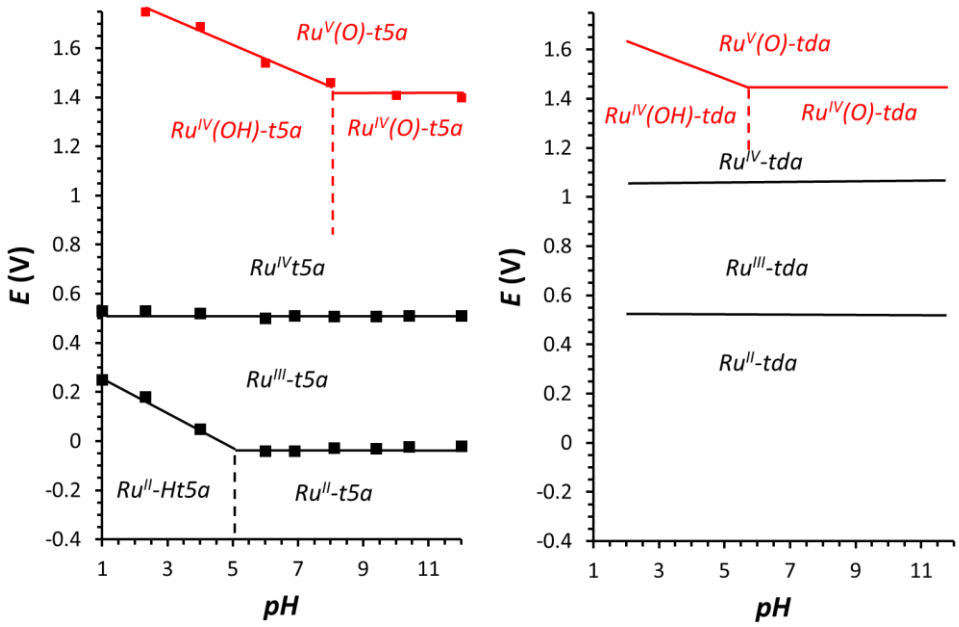

Figure 4: Left, Pourbaix diagram for **2**$^{\mathbf{III}}$(κ-N^{3}O$^{1.5}$) (black dots and black solid lines) and for the Ru^{V}/Ru^{IV} redox couple of complex **2**$^{\mathbf{IV}}$(OH)(κ-N^{3}O^2) (red dots and red solid lines). Both slopes for the *pH* dependent processes are circa 59 mV/*pH*. Right, Pourbaix diagram for {Ru^{IV}(tda-κ-N^{3}O^2)(py)$_2$}$^{2+}$, {**3**$^{\mathbf{IV}}$}$^{2+}$ (black solid line) and for the Ru^{V}/Ru^{IV} redox couple of {Ru^{V}(O)(tda-κ-N^{3}O)(py)$_2$}$^{+}$, {**3**$^{\mathbf{V}}$(O)}$^{+}$, taken from the literature,[13] (red solid line).

The *pH* dependency of the Ru^{V}/Ru^{IV} redox couple of complex **2**$^{\mathbf{V}}$(O)(κ-N^{2}O) is reported in the SI (Figure S35) and a plot of its E^o vs. *pH* in shown in Figure 4. As it can be seen in the Pourbaix diagram the pK_a of the Ru^{IV} couple (Ru^{IV}-OH -> Ru^{IV}-O + H$^+$) is 8.0 (pK_a^{calc} = 7.5). Thus, above *pH* = 8.0 the potential of the Ru^{V}/Ru^{IV} couple is *pH* independent whereas below *pH* 8.0 increases by approximately 60 mV per *pH* unit. The Ru^{V}-O analog {Ru^{V}(O)(tda-κ-N^{3}O)(py)$_2$}$^{+}$, {**3**$^{\mathbf{V}}$(O)}$^{+}$, is also plotted in Figure 4B for comparison purposes. It is striking to see that for the V/IV aqua containing species their redox potential differs by less than 20 mV at the same *pH* given the sharp differences among the redox couples of their precursors, due to the different number of anionic donors of their equatorial ligands, t5a^{3-} and tda^{2-}. A kinetic analysis was also carried out

for $\mathbf{2}^{\mathbf{V}}$(O)(κ-N^2O) at *pH* = 7.0 based on Foot of the Wave Analysis (FOWA) giving a calculated TOF_{MAX} of 9400 s^{-1} (Figure 3D). This value is in the same range of that exhibited by $\mathbf{3}^{\mathbf{V}}$(O). An additional phenomenon that occurs during the electrocatalytic process at *pH* = 7.0 is the absorption of reduced species of {$\mathbf{2}^{\mathbf{V}}$(κ-N^3O^2)}$^{2+}$ and $\mathbf{2}^{\mathbf{V}}$(O)(κ-N^2O) at the electrode surface. This is observed when placing the electrode used after catalysis in a clean electrolyte solution at the same *pH* and running again a CV as reported in Figure S36 in the SI. The absorbed species account for roughly 25 % of the catalytic activity. In sharp contrast, at *pH* = 1.0 the absorbed species are responsible for practically all the catalytic activity as can be observed in Figures S37-S38.

III

B 2.4 The water oxidation catalytic cycle

DFT calculations at M06 level of theory were carried out to investigate the catalytic cycle starting from $\mathbf{2}H^{II}(OH_2)$(κ-N^2O) (Scheme 3). As shown in Scheme 3, one possible activation pathway is three consecutive proton-coupled electron transfer steps, which results in generation of the $\mathbf{2}^{\mathbf{V}}$(O) complex. Details on other possible activation pathways are available in the supporting information. We studied both the energetics of the 6-coordinate and 6.5-coordinate complexes in the V oxidation state to be involved in O-O bond formation *via* a Water Nucleophilic Attack (WNA) mechanism. Additionally, we studied the catalytic cycle starting from the complex in the VI oxidation state, complex {$\mathbf{2}^{\mathbf{VI}}$(O)(κ-$N^{2.5}$O)}$^+$, where the Ru^{VI} is used to display the formal oxidation state since the last oxidation occurs in the pyrrolato ligand due to its high electron density.

Scheme 3 shows the catalytic cycle starting from the 6-coordinate $\mathbf{2}^{\mathbf{V}}$(O)(κ-N^2O) complex computed at *pH* = 0.0 and the analogous catalytic cycle starting from the 6.5-coordinate $\mathbf{2}^{\mathbf{V}}$(O)(κ-$N^{2.5}$O) and $\mathbf{2}^{\mathbf{VI}}$(O)(κ-$N^{2.5}$O) can be found in Scheme S3. The optimized transition state structures in the three cases consist of a water molecule interacting with the Ru=O moiety while the dangling carboxylate assists the proton transfer (Figure 5C and Figure S45). Among the three cases, the lowest activation free energy ($\Delta G^{\ddagger}$) is of 14.2 kcal/mol and it is displayed by the 6-coordinate complex $\mathbf{2}^{\mathbf{V}}$(O)(κ-N^2O) to yield to the 6-coordinate TS structure. Preserving 6.5-coordination in the O-O bond formation transition state requires an additional water molecule and is energetically unfavorable by ≈10 kcal/mol (Figure S45). In all cases, the products of the WNA steps are the hydroperoxo complexes that are further oxidized to the superoxo complexes. The liberation of O_2 and coordination of a water molecule yields the initial complex in the II oxidation state, complex $\mathbf{2}H^{II}(OH_2)$(κ-N^2O) (Scheme 3 and Scheme S3). The $\mathbf{2}^{\mathbf{V}}$(O)(κ-$N^{2.5}$O) complex is 7.7 kcal/mol more stable than $\mathbf{2}^{\mathbf{V}}$(O)(κ-N^2O) so that there will be competition between WNA pathway of $\mathbf{2}^{\mathbf{V}}$(O)(κ-N^2O) and isomerization to $\mathbf{2}^{\mathbf{V}}$(O)(κ-$N^{2.5}$O). It is worth noting

that the computed potential for oxidation of $\mathbf{2}^{V}(O)(\kappa\text{-}N^{2.5}O)$ to $\mathbf{2}^{VI}(O)(\kappa\text{-}N^{2.5}O)$ is only 1.26 V vs NHE. Furthermore, the WNA attack to this species has a $\Delta G^{\ddagger}$ = 18.1 kcal/mol and thus can be competing with the previous species at oxidation state V.

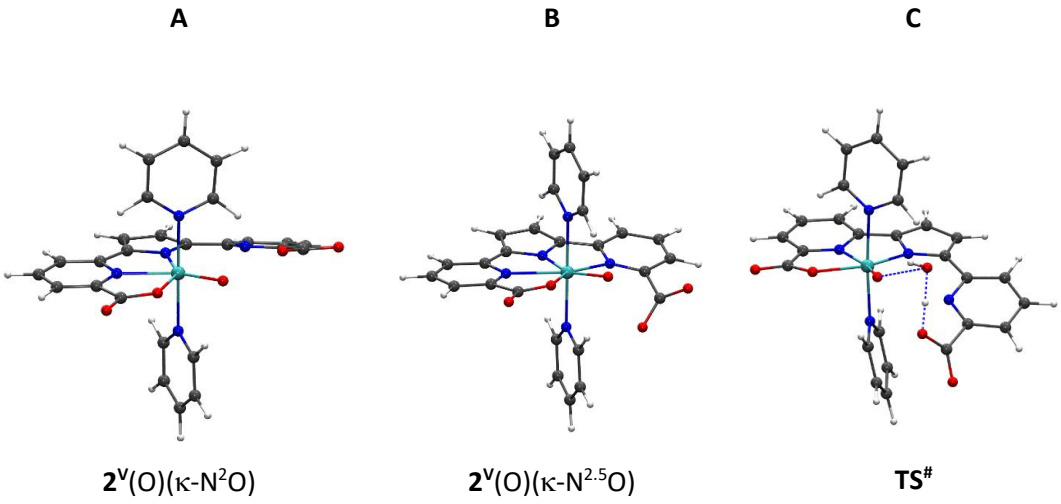

Figure 5: Optimized structures for $\{Ru^{V}(O)(t5a\text{-}\kappa\text{-}N^{2}O)(py)_2\}$, (**A**), $\{Ru^{V}(O)(t5a\text{-}\kappa\text{-}N^{2.5}O)(py)_2\}$, (**B**), and structure associated with the transition state $\{Ru^{V}(O)(t5a\text{-}\kappa\text{-}N^{2}O)(py)_2\}$ + H_2O, (**C**) at M06-L level of theory. Dashed lines indicate breaking and forming bonds in the TS. Color code: Ru, turquoise; C, gray; N, blue; O, red; H, white.

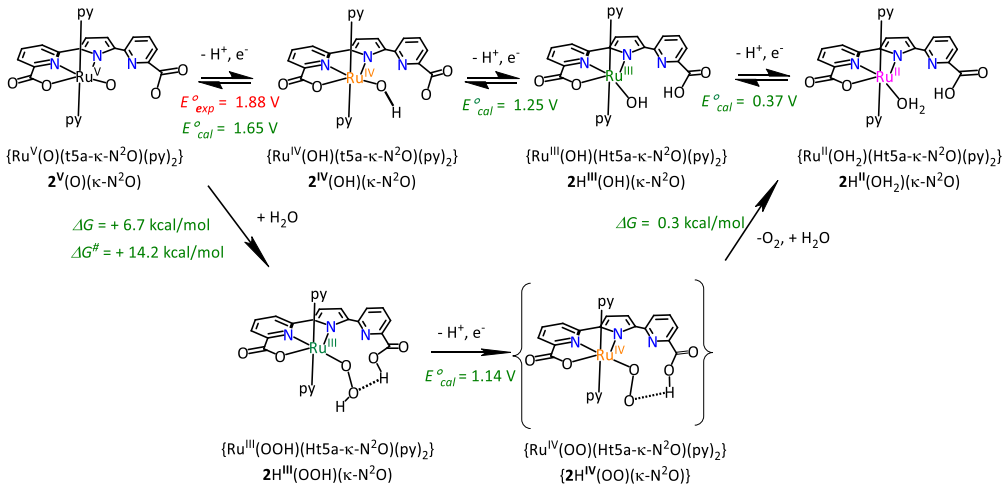

Scheme 3: Schematic representation of Ru-aqua species together with key intermediates and reactions in the catalytic water oxidation mechanism exhibited by complex $\mathbf{2}^{V}(O)(\kappa\text{-}N^{2}O)$ at *pH* = 0.0.

We also computed redox potentials for the processes in the catalytic cycle which are summarized in Scheme 3. Among them, that associated with the Ru^{V}=O/Ru^{IV}-OH redox couple is the highest of the catalytic cycle. The computed potential is E_{calc} = 1.65 V at *pH* = 0.0, which is in

agreement with the value extrapolated from the experimental Pourbaix diagram in Figure 4 (E_{exp} = 1.88 V).

Table 1: Selected redox potentials and pK_a values for complex **2**^{V}(O)(κ-N^{2}O) and related complexes previously described in the literature.

	7-coordinate Ru^{V}-O			**6-coordinate Ru^{V}-O**		
	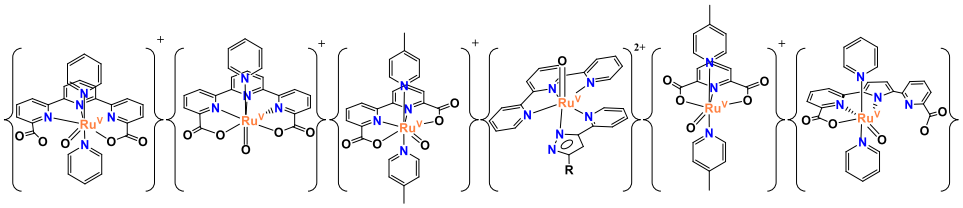					
Complex	{Ru^{V}(O)(tda-κ-N^{3}O)(py)$_2$}$^+$ {**3**^{V}(O)}$^+$	{Ru^{V}(O)(tda-κ-N^{3}O^2)(py)}$^+$ {**4**^{V}(O)}$^+$	{Ru^{V}(O)(bda)(Me-py)$_2$}$^+$ {**5**^{V}(O}$^+$	[b]{Ru^{V}(O)(trpy)(ppc)}$^{2+}$ {**6**^{V}(O)}$^{2+}$	[c]{Ru^{V}(O)(pdc)(Me-py)$_2$}$^+$ {**7**^{V}(O)}$^+$	{Ru^{V}(O)(t5a-κ-N^{2}O)(py)$_2$} {**2**^{V}(O)(κ-N^{2}O)}
[a]*n*$^-$	1	2	2	1	2	2
E^o (V)						
Ru^{V}=O/Ru^{I} ^{V}=O[b]	1.43	1.12	1.12	1.59	1.35	1.41
Ref.	7	14	11	33	34	this work

a. negative charges given by the first coordination sphere excluding oxo/hydroxo groups.
b. Hppc = ethyl 3-(pyridin-2-yl)-1H-pyrazole-5-carboxylate
c. H_2pdc = pyridine-2,6-dicarboxylic acid

B 3 Discussion

Seven-coordinate Ru complexes such as {Ru^{V}(O)(bda)(Me-py)$_2$}$^+$, {**5**^{V}(O)}$^+$, and {Ru^{V}(O)(tda-κ-N^{3}O)(py)$_2$}$^+$, {**3**^{V}(O)}$^+$, are receiving a great deal of attention because they are among the fastest and more rugged water oxidation catalysts described today. The latter at *pH* = 10.0 reaches TOF_{max} of 50.000 s^{-1} that is the fastest WOC ever reported and is actually two orders of magnitude faster than the OEC-PSII that turns at the millisecond time scale.[35,36] A question that arises here is if seven coordination is essential for Ru complexes in order to obtain fast water oxidation catalysis. For [Ru^{II}(bda)(Me-py)$_2$], **5**^{II}, and {Ru^{II}(tda-κ-N^{3}O)(py)$_2$}, **3**^{II}, seven coordination was achieved thanks to the presence of tetra- and pentadentate ligands respectively that coordinate at the equatorial positions of the Ru metal center. The constrained geometry of these ligands produce large "outer equatorial angles" O-Ru-X (X = O or N) of 123° and 122° respectively, that gives room for a seven coordination upon reaching oxidation states IV and above, see Chart 1.

In the present work we report the rich chemistry of a family of related Ru complexes containing the pentadentate adaptative ligand H_3t5a that can potentially loose up to three protons. The

t5a^{3-} ligand is similar to the tda^{2-} but replacing the central pyridyl ring by a pyrrolyl group (see Chart 1 for a drawing). This produces two major changes in coordination properties of this ligand. First, it is a much powerful electron donating ligand since it can act as trianionic ligand as opposed to the maximum dianonic capacity of tda^{2-} and secondly the five member pyrrolyl ring generates $CCN_{pyrrolyl}$ angles 6 degrees larger than $CCN_{pyridyl}$ (See Chart 1). This will further increase the equatorial constrain of the ligand by further opening up the "outer equatorial angles". This can be nicely observed by comparing this angle in the X-ray structure of [Ru(tda)(py)(dmso)] that is of 123º with that of the DFT calculated structure {Ru^{II}(t5a-κ-N$^{2.5}$O)(py)$_2$}, that increase up to 135º.

These electronic and geometrical particularities influence the coordination structure and reactivity both a low oxidation states (II and III) and at high oxidation states (IV and V).

B 3.1 Low oxidation states chemistry and linkage isomerism

At oxidation state III, DFT calculations at M06-L level of theory [37] suggest the presence of two isomers for the non-aqua type of species, **2**^{III}(κ-N^{3}O$^{1.5}$) and **2**^{III}(κ-N$^{2.5}$O^2), with relatively similar energies. These isomers have the same coordination number and closely related structures where the Ru metal center can easily glide in the equatorial plane within the coordination framework established by the coordinating atoms of the t5a^{3-} ligand, accessing two limiting geometrical positions at κ-N^{3}O$^{1.5}$ and κ-N$^{2.5}$O^2, as a consequence of the ligand flexibility.

At oxidation state II, DFT proposes a 5.5 coordination complex, **2**^{II}(κ-N$^{2.5}$O), as the most stable isomer that is quite remarkable for a d^6 low spin Ru(II) center, that is generally six coordinated with an octahedral type of geometry. The 5.5 coordination, not found in the related Ru-tda complexes, is a consequence of the equatorial nature of the coordinating atoms of the t5a^{3-} ligand together with the additional geometrical constrains due to the 6 degrees larger $CCN_{pyrrolyl}$ angles imposed by the pyrrolyl groups as compared to the pyridyl one.

This peculiar ligand geometry and flexibility is also responsible for the linkage isomerism found within oxidation sates II and III displayed in the right upper part of Scheme 2, that is not observed for related Ru-tda complexes. On the other hand the trianionic character of the ligand is manifested in a large cathodic shift of approximately 600 mV for the III/II couple of **2**^{III}(κ-N^{3}O$^{1.5}$) as compared to that of {Ru^{III}(tda-κ-N^{3}O$^{1.5}$)(py)$_2$}$^+$, **3**^{III}(κ-N^{3}O$^{1.5}$) where the tda^{2-} ligand is dianionic.

B 3.2 High oxidation states chemistry and implications for water oxidation catalysis.

At oxidation state IV both the x-ray structure and DFT calculations for {**2**^{IV}(κ-N^{3}O^2)}$^+$, show a seven coordinated Ru center with at pentagonal bipyramid geometry, expected for a d^4 ion with

the t5a^{3-} favoring this geometry at the equatorial plane. The electronic influence of an additional charge is manifested again by a 500 mV cathodic shift upon comparing the IV/III redox couple of {**2**^{IV}(κ-N^{3}O^2)}$^+$ with regard to that of {**3**^{IV}(κ-N^{3}O^2)}$^{2+}$ (See Pourbaix diagram in Figure 4).

In sharp contrast, for the aquated species at oxidation state V DFT proposes a coordination environment of 6.5 and 6 for species **2**^{V}(O)(κ-N$^{2.5}$O) and **2**^{V}(O)(κ-N^{2}O), respectively. The energy of these species only differs in 7.7 kcal/mol and thus in solution they are interconverting very fast, thus manifesting again the adaptative capacity of the t5a^{3-} ligand. This 6-6.5 coordination number is also consistent with the potential of the V/IV redox couple shown in the Pourbaix diagram (Figure 4, red line). In this regard we have recently uncovered a correlation between the E^o (Ru^{V}=O/Ru^{IV}=O) and the number of negative charges in the first coordination sphere together with the coordination number at oxidation state V, for a series of water oxidation catalysts. Table 1 gathers selected electrochemical and electronic properties of complex **2**^{V}(O)(κ-N^{2}O) together with those of related water oxidation catalysts already described in the literature for comparison purposes. The $E^o_{(RuV=O/RuIV=O)}$ for **2**^{V}(O)(κ-N^{2}O) is 1.41 V, aligning very well with the other 6-coordinate complexes containing two anionic charges such as {Ru^{V}(O)(pdc)(Me-py)$_2$}$^+$, {**7**^{V}(O)}$^+$ that has a $E^o_{(RuV=O/RuIV=O)}$ = 1.35 V (See Table 1; pdc^{2-} is 2,6-dicarboxylatopyrine).

The lower coordination number for **2**^{V}(O)(κ-N$^{2.5}$O) with regard to that of {**3**^{V}(O)(κ-N^{3}O)}$^+$, is a consequence of mainly two factors. First a steric effect related to the 2x6 = 12° CCN$_{pyrrolyl}$ angles that largely increases the "outer coordination angle" at the equatorial zone described above and secondly the large electron density transmitted to the Ru center via the pyrrolato and carboxlato groups. The latters already transmit a large degree of electron density to the metal center and thus an additional coordination is not crucial to stabilize the putative oxidation state V for this complex.

From a mechanistic perspective the O-O bond formation occurs at oxidation state V as proposed by DFT (see Scheme 3) and evidenced by the electrocatalytic phenomena observed in Figure 3. At this stage the transition state structure shown in Figure 5C, shows the key role of the dangling carboxylate as an intramolecular proton acceptor. This decreases the energies of activation of the rds to 14.2 kcal/mol and ensures fast catalysis. Indeed we calculate a TOF_{max} of 9400 s^{-1}, which is among the highest reported in the literature.[7,38,39]

B 4 Conclusions

In conclusion we report the detailed characterization of the spectroscopic, electrochemical and catalytic properties of a family of Ru complexes containing the adaptative t5a^{3-} ligand, nicely

complemented with DFT calculations. This work manifests how subtle changes on ligand geometry, the 12º effect, can exert dramatic effects on complex geometry and reactivity. In particular, it highlights the interplay between CN6 and CN7 at different oxidation states, the degree of anionic character of the ligand, and the crucial role of the terminal carboxylate strategically situated close to the Ru-OH moiety can act as both H-bonding site and proton acceptor.

The present work reveals that for the design of fast water oxidation catalysts that contain ligands that are highly anionic and that sufficiently reduce the redox potential of the V/IV couple, the seven coordination is actually not needed provided the ligand design is such that it offers the means of an intramolecular proton transfer at the O-O bond formation step. On the other hand, for ligands that have less electron donating capacity the seven coordination will be crucial to be able to achieve oxidation state V at a relatively low potential.

B 5 Acknowledgments

R.M., AL and XS acknowledge MINECO and FEDER (CTQ2016-80058-R, CTQ2015-64261-R, SEV 2013-0319, ENE2016-82025-REDT, CTQ2016-81923-REDC), AGAUR (2014-SGR-915) and "La Caixa" foundation.

B 6 References

1 Lewis, N. S. *Science* **2016**, *351*, aad19201-aad19209.
2 McKone, J. R.; Lewis, N. S.; Gray, H. B. *Chem. of Mat.* **2014**, *26*, 407-414.
3 Montoya, J. H.; Seitz, L. C.; Chakthranont, P.; Vojvodic, A.; Jaramillo, T. F.; Norskov, J. K. *Nat. Mater.* **2017**, *16*, 70-81.
4 Helm, M. L.; Stewart, M. P.; Bullock, R. M.; DuBois, M. R.; DuBois, D. L. *Science* **2011**, *333*, 863.
5 Costentin, C.; Drouet, S.; Robert, M.; Savéant, J.-M. *Science* **2012**, *338*, 90-94.
6 Anderson, J. S.; Rittle, J.; Peters, J. C. *Nature* **2013**, *501*, 84-87.
7 McCrory, C. C. L.; Jung, S.; Ferrer, I. M.; Chatman, S. M.; Peters, J. C.; Jaramillo, T. F. *J. Am. Chem. Soc*. **2015**, *137*, 4347-4357.
8 Blakemore, J. D.; Crabtree, R. H.; Brudvig, G. W. *Chem. Rev.* **2015**, *115*, 12974-13005.
9 Singh, A.; Spiccia, L. *Coord. Chem. Rev.* **2013**, *257*, 2607-2622.
10 Garrido-Barros, P.; Gimbert-Suriñach, C.; Matheu, R.; Sala, X.; Llobet, A. *Chem. Soc. Rev.* **2017**, *DOI:* 10.1039/C7CS00248C
11 Concepcion, J. J.; Tsai, M. K.; Muckerman, J. T.; Meyer, T. J. *J. Am. Chem. Soc.* **2010,** *132*, 1545-1557.
12 Matheu, R.; Ertem, M. Z.; Benet-Buchholz, J.; Coronado, E.; Batista, V. S.; Sala, X.; Llobet, A. *J. Am. Chem. Soc.* **2015**, *137,* 10786-10795.
13 Schulze, M. Kunz; V. Frischmann, P. D.; Würthner, F. *Nat. Chem.* **2016***, 8,* 576-583.
14 Gersten, S. W.; Samuels, G. J.; Meyer, T. J. *J. Am. Chem. Soc.* **1982**, *104*, 4029–4030
15 Wasylenko, D. W.; Ganesamoorthy, C.; Henderson, M.; Koivisto, B. D.; Osthoff, H.; Berlinguette, C. P. *J. Am. Chem. Soc*. **2010**, *132*, 16094-16106.

16 D. E. Polyansky, J. T. Muckerman, J. Rochford, R. Zong, R. P. Thummel and E. Fujita, *J. Am. Chem. Soc.* **2011**, *133*, 14649-14665.
17 Duan, L.; Bozoglian, F.; Mandal, S.; Stewart, B.; Privalov, T.; Llobet, A.; Sun, L. *Nat. Chem.* **2012,** *4,* 418-423.
18 Francàs, L.; Matheu, R.; Pastor, E.; Reynal, A.; Berardi, S.; Sala, X.; Llobet, A.; Durrant, J. R. *ACS Catal.* **2017**, 7, 5142-5150.
19 Duan, L.; Fischer, A.; Xu, Y.; Sun, L. *J. Am. Chem. Soc.* **2009**, *131*, 10397-10399
20 Richmond, C. J.; Matheu, R.; Poater, A.; Falivene, L.; Benet-Buchholz, J.; Sala, X.; Cavallo, L.; Llobet, A. *Chem. Eur. J.* **2014**, *20*, 17282-17286.
21 Suga, M.; Akita, F.; Hirata, K.; Ueno, G.; Murakami, H.; Nakajima, Y.; Shimizu, T.; Yamashita, K.; Yamamoto, M.; Ago, H.; Shen, J.-R. *Nature* **2015**, *517*, 99-103.
22 Xie, Y.; Shaffer, D. W.; Lewandowska-Andralojc, A.; Szalda, D. J.; Concepcion, J. J. *Angew. Chem. Int. Ed.* **2016**, *55*, 8067-8071.
23 Matheu, R.; Ertem, M.; Gimbert-Suriñach, C.; Benet-Buchholz, J.; Sala, X.; Llobet *submitted*
24 Lautrette G., Aube C., Ferrand Y., Pipelier M., Blot V., Kauffmann B., Dubreuil D. Huc I. *Chem. Eur. J.* **2014**, *20*, 1547-1553.
25 Stetter, H. *Angew. Chem. Int. Ed. Engl.* **1976**, *15*, 639–647.
26 Imler, G. H.; Lu, Z.; Kistler, K. A.; Carroll, P. J.; Wayland, B. B.; Zdilla, M. J. *Inorg. Chem.* **2012**, *51*, 10122–10128.
27 Richmond, C. J.; Matheu, R.; Poater, A.; Falivene, L.; Benet-Buchholz, J.; Sala, X.; Cavallo, L.; Llobet, A. *Chem. Eur. J.* **2014**, *20*, 17282-17286.
28 Ohzu, S.; Ishizuka, T.; Hirai, Y.; Jiang, H.; Sakaguchi, M.; Ogura, T.; Fukuzumi, S.; Kojima, T. *Chem. Sci.* **2012**, *3*, 3421-3431
29 Zhao, Y.; Truhlar, D. G. *J. Chem. Phys.* **2006**, *125,* 1941011-19410118.
30 Zhao, Y.; Truhlar, D. G. *Theor. Chem. Acc.***2008**, *120*, 215-241
31 Zhao, Y.; Truhlar, D. G. *Acc. Chem. Res* **2008**, *41*, 157-167
32 Domingos, S. R.; Luyten, H.; Anrooij, F. v.; Sanders, H. J.; Bakker, B. H.; Buma, W. J.; Hartl, F.; Woutersen, S. *Rev. Sci. Instrum.* **2013**, *84*, 033103
33 Mognon, L.; Benet-Buchholz, J.; Llobet, A. *Inorg. Chem* .**2015**, *54*, 11948-11957.
34 Li, F.; Li, L.; Tong L.; Daniel, Q.; Gothelid, M.; Sun, L. *Chem. Commun.* **2014**, *50*, 13948-13951
35 Dismukes, G. C.; Brimblecombe, R.; Felton, G. A. N.; Pryadun, R. S.; Sheats, J. E.; Spiccia, L.; Swiegers, G. F. *Acc. Chem. Res.* **2009**, *42*, 1935-1943.
36 Nocera, D. G. *Acc. Chem. Res.* **2012**, *45*, 767–776.
37 Zhao, Y.; Truhlar, D. G. *J. Chem. Phys.* **2006**, *125,* 194101/1-194101/18.
38 Vigara, L.; Ertem, M. Z.; Planas, N.; Bozoglian, F.; Leidel, N.; Dau, H.; Haumann, M.; Gagliardi, L.; Cramer, C. J.; Llobet, A. *Chem. Sci.* **2012**, *3*, 2576-2586.
39 Hirahara, M.; Ertem, M. Z.; Komi, M.; Yamazaki, H.; Cramer, C. J.; Yagi, M. *Inorg. Chem.* **2013**, *52*, 6354-6364.

III

B 7 Supporting information

Paper B Is Seven Coordination Required for Fast Molecular Water Oxidation Catalysis by Ru Complexes?

Outline

III

III

MATERIALS

General considerations for the synthesis of the ligand H_3t5a:

Solvents were purified and dried by standard methods prior to use; alternatively, the MB SPS-800-dry solvent system was used to dry dichloromethane. Commercially available reagents were purchased from Sigma Aldrich and were used without purification. Dry dichloromethane was obtained by refluxing solvent on calcium hydride for an hour and distilled under argon. Glassware used for reaction was either flame dried under vacuum or under argon stream for several minutes. Reactions were carried out under rigorous anhydrous conditions and argon stream/positive pressure of argon. ^{1}H and ^{13}C NMR spectra were recorded on a *Bruker Avance 300* spectrometer fitted with a 5 mm i.d. BBO probe carefully tuned to the recording frequency of 300.13 MHz (for ^{1}H) and 75.47 MHz (for ^{13}C), the temperature of the probe was set at room temperature (around 293-294 K), on a *Bruker Avance 400* spectrometer fitted with a 5 mm i.d. BBFO+ probe carefully tuned to the recording frequency of 400.13 MHz (for ^{1}H) and 100.61 MHz (for ^{13}C). The spectra are referenced to the solvent in which they were run (7.26 ppm for ^{1}H $CDCl_3$ and 77.16 ppm for ^{13}C $CDCl_3$, 2.5 ppm for ^{1}H DMSO and 39.52 ppm for ^{13}C DMSO). Chemical shifts (δ) are given in ppm, and coupling constants (J) are given in Hz with the following splitting abbreviations: s = singlet, d = doublet, t = triplet, q = quartet, qt = quintet, sx = sextuplet, sp = septuplet, m = massif and br = broad. All assignments were confirmed with the aid of two-dimensional ^{1}H, ^{1}H (COSY), or ^{1}H, ^{13}C (HSQC, HMBC) experiments using standard pulse programs. All reactions were monitored by TLC on commercially available precoated plates (Kieselgel 60 F254), and the compounds were visualized with $KMnO_4$ solution [$KMnO_4$ (3 g), K_2CO_3 (20 g), NaOH (5% aq.; 5 mL), H_2O (300 mL)] and heating or by UV (254 nm) when possible. Flash column chromatography was carried out using high purity grade (Merck grade 9385) pore size 60Å, 230-400 mesh particle size silica gel (Sigma Aldrich). Solvents used for chromatography were prior distilled on a Buchi rotavapor R-220-SE. Low resolution mass spectrometry (MS) were recorded on a ThermoFinnigan DSQII quadripolar spectrometer (coupled with a TracUltra GC apparatus) for Chemical Ionization (CI), on a ThermoFinnigan LCQ Advantage spectrometer for ElectroSpray Ionisation (ESI). High resolution mass spectrometry (HRMS) were recorded on a ThermoFinnigan MAT95XL spectrometer (for CI) and on a ThermoFisher Scientific LTQ-Orbitrap spectrometer (for ESI).

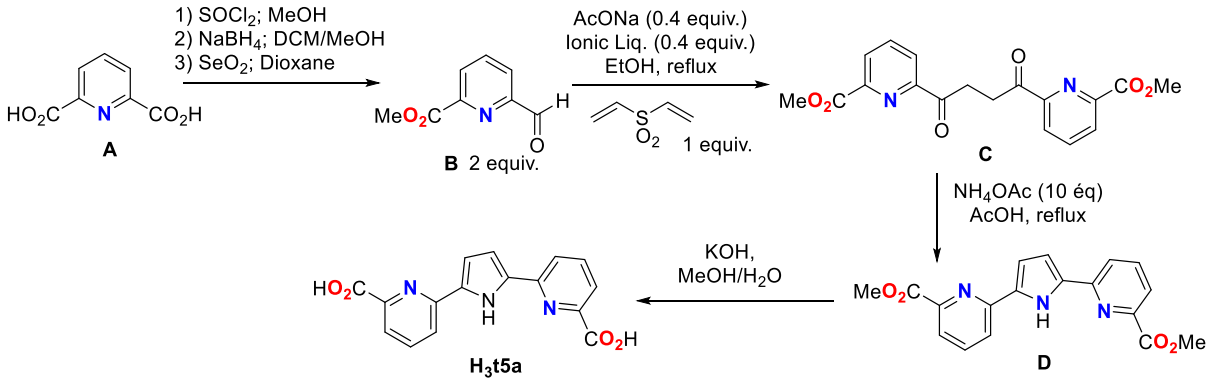

Scheme S1: Synthesis of *the ligand* ***H₃t5a*** (6,6'-(1H-pyrrole-2,5-diyl)dipicolinic acid)

III

Synthesis of the Methyl 6-formylpicolinate ***B:***

1) Dimethyl 2,6-pyridinedicarboxylate: To an ice-cooled solution of 2,6-pyridinedicarboxylic acid (**A**) (5g, 30 mmol; 1 equiv) in 40 mL of dry methanol, was added thionyl chloride (8.68 mL; 4 equiv.). After heating at reflux overnight, the reaction mixture was concentrated under *vacuo*. The resulting crude mixture was diluted with 50 mL of dichloromethane and was subsequently washed with 30 mL of saturated solutions of $NaHCO_3$ and NaCl. After drying over $MgSO_4$, the organic layer was concentrated under *vacuo* affording the expected dimethyl 2,6-pyridinedicarboxylate (5.04 g, 86% yield). ^{1}H NMR (400 MHz, $CDCl_3$) δ 8.30 (d, *J*=7.8 Hz, 2H); 8.01 (t, *J*=7.8 Hz, 1H); 4.02 (s, 6H). ^{13}C NMR (100.6 MHz, $CDCl_3$) δ 165.2; 148.4; 138.5; 128.2; 53.3. HRMS m/z: calc for $[M + Na]^+$: 218.0429. found m/z: 218.0429

2) Methyl 6-(hydroxymethyl)picolinate : To an ice-cooled solution of dimethyl 2,6-pyridinedicarboxylate (2.5 g ; 12.81 mmol, 1 equiv.) in DCM (18 mL) and methanol (21 mL) was added $NaBH_4$ (0.31 g; 8.3 mmol; 0.65 equiv.). After 2 h at 0°C, the TLC monitoring (PE/Ethyl Acetate: 1/2) showed partial conversion. After adding an extra amount of $NaBH_4$ (0.35 equiv.), the complete conversion was achieved in 2 additionnal hours of reaction. The reaction mixture was quenched by 21 mL of HCl (1M). After removal of the volatiles, a saturated solution of $NaHCO_3$ (80 mL) was added. The aqueous layer was extracted with $CHCl_3$ (3*50 ml) and was then subsequently dried over $MgSO_4$. After concentration under *vacuo*, the resulting crude was purified over silicagel by column chromatography (DCM/MeOH : 98/ 2) affording the Methyl 6-hydroxymethyl)picolinate (1.5 g; 70% yield). ^{1}H NMR (400 MHz, $CDCl_3$) δ 8.02 (d, *J*=7.13 Hz, 1H); 7.84 (t, *J*=7.81 Hz, 1H) ; 7.53 (d, *J*=7.87 Hz, 1H); 4,86 (d, *J*=5.5 Hz, 2H); 3,99 (s, 3H) ; 3,54 (t, *J*=5.5 Hz, 1H). ^{13}C NMR (100.6 MHz, $CDCl_3$) δ 165.7; 160.3; 147.2; 137.8; 124.1; 123.9; 64.8; 53.0. HRMS m/z: calc for $[M + Na]^+$: 190.0480 , found m/z: 190.0480.

3) Methyl 6-formylpicolinate (B): To a solution of methyl 6-hydroxymethyl)picolinate (1.23 g, 7.36 mmol, 1equiv.) in dioxane (25mL) was added SeO_2 (0.41 g, 0.5 equiv.). The reaction was monitored by TLC (DCM/MeOH : 98/2) and showed complete conversion after 2h30 of heating at reflux. The hot reaction mixture was filtered over a pad of celite. After washing with $CHCl_3$ (30 mL), the filtrate was evaporated under *vacuo*. The crude mixture was purified on silicagel by column chromatography and afforded the methyl 6-formylpicolinate **B** (1.15 g, 95% yield). ^{1}H NMR (400 MHz, $CDCl_3$) δ 10.18 (d, *J*=0.85 Hz, 1H); 8.33 (dd, *J* = 1.27 Hz, *J* = 7.72 Hz, 1H), 8.14 (dd, *J* = 1.27 Hz, *J* = 7.78 Hz, 1H) ; 8.04 (dt, *J*=0.84 Hz, *J* = 7.74 Hz, 1H) ; 4.06 (s, 3H). ^{13}C NMR (100.6 MHz, $CDCl_3$) δ 192.8 ; 165.0 ; 153.0 ; 148.8 ; 138.5 ; 129.2 ; 124.5 ; 53.4. HRMS m/z: Calc for $[M + Na]^+$: 188.0324, found m/z: 188.0328.

III

*Synthesis of the Dimethyl-6,6'-succinyldipicolinate (**C**):*

Sodium acetate (332 mg, 4.05 mmol, 0.4 equiv.) and 3-benzyl-5-(2-hydroxyethyl)-4-methylthiazolium chloride (1.09 g, 4.05 mmol, 0.4 equiv.) were diluted in absolute ethanol (6 mL). After degassing over 15 minutes, the suspension was heated at reflux under stirring. In the meantime, a mixture of pyridine-2-carboxaldehyde (3.34 g, 20.22 mmol, 2 equiv.) and divinylsulfone (1.02 mL, 10.12 mmol, 1 equiv.) was diluted in absolute ethanol (11 mL). This latter solution was added to the ionic liquid solution. The precipitation of the reaction mixture occured rapidly and an additional amount of absolute ethanol (11 mL) was added. After heating at reflux during 12 hours (TLC monitoring by DCM/ Ethyl Acetate: 9/1), the reaction mixture was concentrated off. The crude mixture was purified over silicagel by column chromatography (DCM 100%, then DCM/ Ethyl Acetate: 95/5). The pure expected dimethyl-6,6'-succinyldipicolinate (**C**) (1.61 g, 45% yield) was obtained. Another fraction was isolated as pure compound corresponding to dimethyl-6,6'-(1,2-dihydroxyethene-1,2-diyl)-dipicolinate (1.28 g, 38% yield) (arising from benzoin as side product).

Dimethyl-6,6'-succinyldipicolinate (**C**): ^{1}H NMR (400 MHz, DMSO) δ 8.28 (dd, *J*= 1.15, *J* = 7.74 Hz, 2H) ; 8.19 (dd, *J*=1.14 Hz, *J* = 7.83 Hz, 2H) ; 7.98 (t, *J*=7.78 Hz, 2H) ; 4.03 (s, 6H) ; 3.80 (s, 4H). ^{13}C NMR (100.6 MHz, DMSO) δ 200.0; 165.4; 153.4; 147.7; 138.1; 128.4; 124.8; 53.1; 32.2. HRMS m/z: calc for $[M+Na]^+$: 379.0901, found m/z: 379.0898.

Dimethyl-6,6'-(1,2-dihydroxyethene-1,2-diyl)-dipicolinate (benzoin side product): ^{1}H NMR (400 MHz, $CDCl_3$) δ 13.07 (bs, 2H) ; 8.07-8.14 (m, 2H); 7.97-8.02 (m, 4H); 4.04 (s, 6H). ^{13}C NMR (100.6 MHz, $CDCl_3$) δ 165.1; 156.9; 144.6; 139.1; 136.7; 123.5; 123.0; 53.6. HRMS m/z: Calc for $[M-H]^-$: 329.0768, found m/z: 329.0758.

*-Synthesis of the dimethyl 6,6'-(1H-pyrrole-2,5-diyl)dipicolinate (**D**):*

To a solution of dimethyl-6,6'-succinyldipicolinate (1.37 g, 3.85 mmol) in acetic acid (20 mL) was added under argon atmosphere ammonium acetate (2.89 g, 37.5 mmol, 10 eq). After heating at reflux over 3 hours (TLC monitoring DCM / Ethyl acetate: 8/2), the reaction mixture was diluted with 70 mL of water. The resulting aqueous layer was extracted with DCM (5*70 mL). The combined organic phases were dried over Na_2SO_4 and were concentrated under *vacuo*. The crude mixture was purified over silicagel by column chromatography (DCM/ Ethyl Acetate: 99/1) to afford the expected dimethyl 6,6'-(1*H*-pyrrole-2,5-diyl)dipicolinate (**D**) (0.9 g, 71% yield). ^{1}H NMR (300 MHz, $CDCl_3$) δ 11.31 (bs, 1H); 7.89 (dd, *J* = 1.5 Hz , *J* = 7.1 Hz, 2H); 7.81-7.72 (m, 4H); 6.82 (d, *J* = 2.6 Hz, 2H); 4.04 (s, 3H). ^{13}C NMR (75 MHz, $CDCl_3$) δ 166.1; 150.7; 147.6; 137.4; 133.4; 122.3; 122.1; 110.3; 52.9. HRMS m/z: calc for $[M+Na]^+$: 360.0955, found m/z: 360.0953.

*- Synthesis of the ligand **H_3t5a** (6,6'-(1H-pyrrole-2,5-diyl)dipicolinic acid):*

To a solution of dimethyl 6,6'-(1*H*-pyrrole-2,5-diyl)dipicolinate (0.95 g, 2.83 mmol) in MeOH (39 mL) and water (2 mL) was added a solution of KOH (476 mg, 8.48 mmol, 3 equiv.) in water (1.2 mL). After heating at reflux over 4h30 (TLC monitoring with PE/ Ethyl Acetate: 8/2), the reaction mixture was concentrated under *vacuo*. The resulting crude mixture was dissolved in water (4 mL) and was acidified with HCl (1M) until pH=2. After filtration on sintered funnel, the yellow solid **H_3t5a** (819 mg; 93% yield) (m.p.= 269.2°C) was washed with water and then with cold diethyl ether. ^{1}H NMR (400 MHz, DMSO) δ 13.03 (bs, 2H) ; 11.88 (s, 1H); 8.07 (dd, *J* = 7.99 Hz, *J* = 1.05 Hz, 2H); 8.01 (t, *J*=7.51 Hz, 2H); 7.87 (dd, *J* = 7.42, *J* = 1.00 Hz, 2H); 7,07 (d, *J* = 2.47 Hz, 2H) ^{13}C NMR (100.6 MHz, DMSO) δ 165.1, 149.6, 147.1, 138.5, 133.2, 122.3, 121.4, 111.3. ESI$^-$HRMS m/z: calc. for $[M-H]^-$: 308.0671, found m/z: 308.0662. *Anal.* Calc. for $C_{16}H_{11}N_3O_4$: %N : 13.59; %C : 62.14; %H : 3.59, found : %N : 13.48; %C : 62.37; %H : 3.61.

General considerations for the synthesis of ruthenium complexes

All materials were provided by Sigma-Aldrich unless indicated. High-purity deionized water was obtained by passing distilled water through a nanopure Milli-Q water purification system.

Synthesis of {Ru^{II}(Ht5a-κ-N^{2}O)(py)$_3$}, **1**H^{II}(κ-N^{2}O)*:* Powders of diclhoro(p-cymene)ruthenium (II) dimer (150 mg, 0.24 mmol) and 6,6'-(1H-pyrrole-2,5-diyl)dipicolinic acid (150 mg, 0.48 nmol) were degassed in ethanol (9 mL) and trimethylamine (0.1 mL). The suspension was refluxed for 3 hours and Pyridine (9 mL) was added to the warm mixture and refluxed overnight. The red solution was cooled down to Room Temperature and the solvent evaporated. The product was purified though Silica Chromatography (elution with

methanol:dichloromethane:trimethylamine 5:100:1 proportion) (150 mg, 50 % yield). ^{1}H NMR (500 MHz, methanol-d4) δ: 6.72 (1 H, s), 6.90 (2 H, q, J=4.8 Hz), 7.01 (1 H, d, J=7.4 Hz), 7.10 (2 H, d, J=7.4 Hz), 7.12 (4 H, t, J=5.2 Hz), 7.14 (1 H, d, J=6.0 Hz), 7.50 (2 H, m), 7.57 (3 H, m), 7.68 (1 H, dd, J=0.70, 6.0 Hz), 8.11 (2 H, d, J=4.8 Hz), 8.15 (4 H, d, J=5.2 Hz). ^{13}C NMR (500 MHz, methanol-d4), δ: 112.7, 114.1, 116.9, 118.0, 120.0, 123.9, 124.0, 124.2, 132.5, 134.7, 134.8, 135.0, 141.6, 147.4, 152.5, 154.5, 154.7, 155.1, 155.5, 159.7, 172.1, 175.9. ESI^{+}-HRMS m/z: calc. for [**1**H^{II}(κ-N^{2}O)$^{+}$] ($C_{31}H_{24}N_6O_4Ru$): 646.0897, found m/z: 646.0889 (1.2 ppm error). *Anal.* Calc. for [**1**H^{II}(κ-N^{2}O)·1.75 CH_2Cl_2] ($C_{32.75}H_{27.5}Cl_{3.5}N_6O_4Ru$): C, 49.53 %; H, 3.49 %; N, 10.58 Found: C, 49.31%; H, 3.62%; N, 10.72.

*Synthesis of {Ru^{III}(t5a-κ-N^{3}O$^{1.5}$)(py)$_2$}, **2^{III}**(κ-N^{3}O$^{1.5}$):*

Complex **1**H^{II}(κ-N^{2}O) (80 mg, 0.12 mmol) was dissolved in water (20 mL) in a round flask. A needle in the septum ensured that interior of the flask communicate with open air. The solution was stirred for 4 days and a green solid appeared in the reaction mixture. The solid was filtrated, washed with water and air-dried (45 mg, 64 % yield). ^{1}H NMR (500 MHz, methanol-d4) δ: 0.65, 8.63, 9.89. ESI^{+}-HRMS m/z: calc. for [**2**^{III}(κ-N^{3}O$^{1.5}$)-H^{+}] ($C_{26}H_{19}N_5O_4Ru^{+}$): 567.0475, found m/z: 567.0490. *Anal.* Calc. for [**2**^{III}(κ-N^{2}O)·4 H_2O] ($C_{26}H_{26}N_5O_8Ru$): C, 48.98 %; H, 4.11 %; N, 10.98 %. Found: C, 48.74 %; H, 3.54 %; N, 10.97 %.

*Synthesis of {Ru^{IV}(t5a-κ-N^{3}O^2)(py)$_2$}(NO$_3$)}{Ce^{III}(MeOH)(NO$_3$)$_5$}$_{0.5}$, {**2**^{IV}(κ-N^{3}O^2)}{Ce^{III}(MeOH)(NO$_3$)$_5$}$_{0.5}$*

A solution of cerium ammonium nitrate (1 mL, 20 mg, 2.1 eq) was added dropwise to a stirred solution of complex **2**^{III}(κ-N^{3}O$^{1.5}$) in methanol (1 mL, 10 mg, 0.017 mmol). A solid was filtrated from the solution and dried with ether (6 mg, 42 % yield). ^{1}H NMR (500 MHz, methanol-d4) δ: 7.44 (4 H, t, J=7.3 Hz), 7.51 (2 H, s), 7.58 (2 H, d, J=7.6 Hz), 7.83 (2 H, t, J=7.3 Hz), 8.08 (4 H, d, J=7.3 Hz), 8.15 (2 H, d, J=7.6 Hz), 8.21 (2 H, t, J=7.6 Hz).^{13}C-NMR (500 MHz, methanol-d4) δ: 117.2, 123.3, 124.0, 126.6, 140.5, 143.9, 144.9, 151.0, 151.3, 156.4, 168.3.

METHODS

General Instrumentation

Electrospray ionization (ESI)) mass spectrometry (MS) experiments were performed on a Waters Micromass LCT Premier equipment. UV–Vis spectroscopy was performed on a Cary 50 Bio (Varian) UV–Vis spectrophotometer with 1 cm quartz cells unless indicated. A Bruker Avance 500 MHz were used to carry out NMR spectroscopy. The *pH* of the solutions was determined by a *pH*meter (CRISON, Basic 20^{+}) calibrated before measurements through standard solutions at *pH*= 4.01, 7.00 and 9.21.

III

Single Crystal X-Ray Methods

Crystal preparation

Crystals of **1**$H^{II}(\kappa\text{-}N^2O)$, **2**$^{III}(\kappa\text{-}N^3O^{1.5})$ and $\{\mathbf{2}^{IV}(\kappa\text{-}N^3O^2)\}^{+}$ were obtained by slow diffusion of ether to a methanol solution.

Data collection

Crystal structure determinations for samples **1**$H^{II}(\kappa\text{-}N^2O)$, **2**$^{III}(\kappa\text{-}N^3O^{1.5})$ were carried out using a Apex DUO Kappa 4-axis goniometer equipped with an APPEX 2 4K CCD area detector, a Microfocus Source E025 IuS using MoK_α radiation, Quazar MX multilayer Optics as monochromator and an Oxford Cryosystems low temperature device Cryostream 700 plus (T = -173 ˚C).

Crystal structure determination for sample $\{\mathbf{2}^{IV}(\kappa\text{-}N^3O^2)\}\{Ce^{III}(MeOH)(NO_3)_5\}_{0.5}$ was carried out using a Rigaku diffractometer equipped with a Pilatus 200K area detector, a Rigaku MicroMax-007HF microfocus rotating anode with MoK_α radiation, Confocal Max Flux optics and an Oxford Cryosystems low temperature device Cryostream 700 plus (T = -173 ˚C). Full-sphere data collection was used with ω and φ scans.

Programs used: Bruker Device: Data collection APEX-2[S1], data reduction Bruker Saint [S2]V/.60A and absorption correction SADABS [S3]. Rigaku device: Data collection CrystalClear, [S4] data reduction with CrysAlisPro [S5] V/.60A and absorption correction with Scale3 Abspack scaling algorithm.[S6]

Structure Solution and Refinement

Crystal structure solution was achieved using the computer program SHELXT.[S7] Visualization was performed with the program SHELXle.[S8] Missing atoms were subsequently located from difference Fourier synthesis and added to the atom list. Least-squares refinement on F^2 using all measured intensities was carried out using the program SHELXL 2015.[S9] All non-hydrogen atoms were refined including anisotropic displacement parameters.

Comments to the structures

The asymmetric unit in the structure of compound $\mathbf{2}^{\mathbf{III}}(\kappa\text{-}N^3O^{1.5})$ contains one molecule of the metal complex and 2.5 highly disordered methanol molecules. The methanol molecules are located disordered in 11 different positions. The measured sample was formed by two crystals with a ratio of 56:44. The collected data for both crystals were processed with TWINABS taking in account overlapping reflections. [S10]

The asymmetric unit in the structure of $\{\mathbf{2}^{\mathbf{IV}}(\kappa\text{-}N^3O^2)\}\{Ce^{III}(MeOH)(NO_3)_5\}_{0.5}$ contains two independent molecules of the metal complex, two non-coordinated molecules of methanol and one Cerium cation coordinated to five NO_3 anions and one methanol molecule. One of the NO_3 anions at the Cerium cation are disordered in two orientations. Evaluation of the data set collected was showing pseudo-symmetry (89 % fit) between the space groups $Pca2_1$ and Pbcn. [Platon] Refinement in the space group Pbcn did not lead to a suitable structure model. Finally, the structure was refined in the polar space group $Pca2_1$ leading to a Flack-parameter of -0.028(8) and a suitable structure model.

Electrochemical methods

All electrochemical experiments were performed in an IJ-Cambria HI-730 bipotentiostat, using a three-electrode cell. $E_{1/2}$ values reported in this work were estimated from DPV experiments. The Reference Electrode (RE) was Hg/Hg_2SO_4 (K_2SO_4 saturated) and potentials were converted to NHE by adding 0.65 V.

Cells

A 20 mL vial was used as an electrochemical cell for CV and DPV measurements. A Teflon-made with holes for the three electrodes was used as a lid to ensure a reproducible distance between the electrodes.

Solutions

All solutions contained 0.1 M ionic strength. For aqueous solutions, $HClO_4$ acid (0.1 M) and phosphate buffer (43 mM) were used as electrolytes for *pH* = 1.0 and *pH* = 7.0 solutions. For organic solutions, Tetrabutylammonium hexafluorophosphate was added to the solution.

Cyclic voltammetry (CV) and Differential Pulse Voltammetry

Glassy carbon disk (ϕ = 0.3 cm, S = 0.07 cm^2), Pt disk and Hg/Hg_2SO_4 (K_2SO_4 saturated) were used as Working Electrode (WE), Counter Electrode (CE) and Reference Electrode (RE) respectively, unless explicitly mentioned. Glassy carbon electrodes were polished 0.05 µm alumina (Al_2O_3) washed with water and acetone and air-dried. CVs and DPVs were iR compensated by the potentiostat in all the measurements unless indicated. Cyclic Voltammograms (CV) were recorded at 0.1 V/s scan rate, unless explicitly expressed. The DPV parameters were ΔE = 4 mV, Amplitude = 0 mV, Pulse width = 5 s, Sampling width = 0.0167 s, Pulse period = 5 s unless explicated.

Foot of the Wave Analysis

The global kinetic constant of the catalytic oxidation of water (k_{WNA}, s^{-1}) was extracted from the linear fit at the foot of the wave of the i/i_p *vs*. $[1+e((E^{0,ap}-E)\cdot(F/RT))]$ plot assuming a WNA mechanism. k_{WNA} is equal to TOF_{MAX}, which is a particular case of the Turn Over Frequency (TOF) where TOF is calculated for potentials much higher than the corresponding E^o.i_p was estimated from the peak cathodic current intensity of the wave at E = 0.7 V and E^0 was extracted from DPV.[11]

Spectroelectrochemistry

Spectroelectrochemical study was carried out in an optically transparent thin-layer electrochemical (OTTLE) cell (OMNI-CELL SPECAC, by Prof. Frantisek Hartl's group, University of Reading).[S12] Two Pt grid electrodes and a silver wire act as working, counter and pseudo reference electrode respectively. The cell is filled 0.2-0.3 ml of solution and the optical path length is approximately 0.2 mm. The cyclic voltammetry is performed at 2 mV/s and UV-vis spectra were recorded continuously to monitor the changes in the UV-Vis spectra.

Computational Methods

Density functional theory. Geometry optimizations were performed at M06-L[S13] level of density functional theory using the Stuttgart [8s7p6d2f | 6s5p3d2f] ECP28MWB contracted pseudopotential basis set[S14] on Ru and the 6-31G(d) basis set[S15]on all other atoms. Non-analytical integral evaluations made use of a pruned grid having 99 radial shells and 590 angular points per shell and an automatically generated density-fitting basis set was used within the resolution-of-the-identity approximation to speed the evaluation of Coulomb integrals as implemented in Gaussian 09 software package.[S16] The nature of all stationary points was verified by analytic computation of vibrational frequencies, which were also used for the computation of zero-point vibrational energies, molecular partition functions (with all frequencies below 50 cm^{-1} replaced by 50 cm^{-1} when computing free energies), and for determining the reactants and products associated with each transition-state structure (by following the normal modes associated with imaginary frequencies). Partition functions were used in the computation of 298 K thermal contributions to free energy employing the usual ideal-gas, rigid-rotator, harmonic oscillator approximation.[S1717] Free energy contributions were added to single-point M06-L, M06[S18,S19] and B3LYP[S20] (with the D3 version of Grimme's dispersion with Becke-Johnson damping[S21]) electronic energies computed with SMD aqueous continuum solvation model[S22] and the SDD basis set on ruthenium and the 6-311+G(2df,p) basis set on all other atoms to arrive at final composite free energies.

Solvation and standard reduction potentials. As stated above**,** solvation effects associated with water as solvent were accounted for using the SMD continuum solvation model. A 1 M standard state was used for all species in aqueous solution except for water itself, for which a 55.6 M standard state was employed. Thus, for all molecules but water, the free energy in aqueous solution is computed as the 1 atm gas-phase free

energy, plus an adjustment for the 1 atm to 1 M standard-state concentration change of *RT* ln (24.5), or 1.9 kcal/mol, plus the 1 M to 1 M transfer (solvation) free energy computed from the SMD model. In the case of water, the 1 atm gas-phase free energy is adjusted by the sum of a 1 atm to 55.6 M standard-state concentration change, or 4.3 kcal/mol, and the experimental 1 M to 1 M solvation free energy, –6.3 kcal/mol. The 1 M to 1 M solvation free energy of the proton was taken from experiment as –265.9 kcal/mol.[S23-S26]

III

Standard reduction potentials were calculated for various possible redox couples. For a redox reaction of the form

$$O_{(aq)} + n\,e^-_{(g)} \rightarrow R_{(aq)} \qquad \text{(S1)}$$

where *O* and *R* denote the oxidized and reduced states of the redox couple, respectively, and *n* is the number of electrons involved in redox reaction, the reduction potential $E^0_{O|R}$ relative to NHE was computed as

$$E^0_{O|R} = -\frac{\Delta G^0_{O|R} - \Delta G^0_{\mathrm{NHE}}}{nF} \qquad \text{(S2)}$$

where $\Delta G^0_{O|R}$ is the free energy change associated with eq. 1 (using Boltzmann statistics for the electron), $\Delta G^0_{\mathrm{NHE}}$ is the free energy change associated with

$$\mathrm{H}^+_{(aq)} + e^-_{(g)} \rightarrow \frac{1}{2}\mathrm{H}_{2(g)} \qquad \text{(S3)}$$

which is –4.28 eV with Boltzmann statistics for the electron,[S25,S27,S28] and *F* is the Faraday constant.

Non-single-determinantal state energies. Several possible intermediates in the water oxidation mechanism have electronic structures that are not well described by a single determinant. In such instances, standard Kohn-Sham DFT is not directly applicable,[S17,S29-S31] and we adopt the Yamaguchi broken-spin-symmetry (BS) procedure[S32,S33] to compute the energy of the spin-purified low-spin (LS) state as

$$ {}^{LS}E = \frac{{}^{BS}E\left(\left\langle S^2\right\rangle_{HS} - \left\langle S^2\right\rangle_{LS}\right) - {}^{HS}E\left(\left\langle S^2\right\rangle_{BS} - \left\langle S^2\right\rangle_{LS}\right)}{\left\langle S^2\right\rangle_{HS} - \left\langle S^2\right\rangle_{BS}} \qquad \text{(S4)} $$

where HS refers to the single-determinantal high-spin coupled state that is related to the low-spin state by spin flip(s) and $< S^2 >$ is the expectation value of the total spin operator applied to the appropriate determinant.

Characterizations of the synthetic intermediates and the ligand H_3t5a

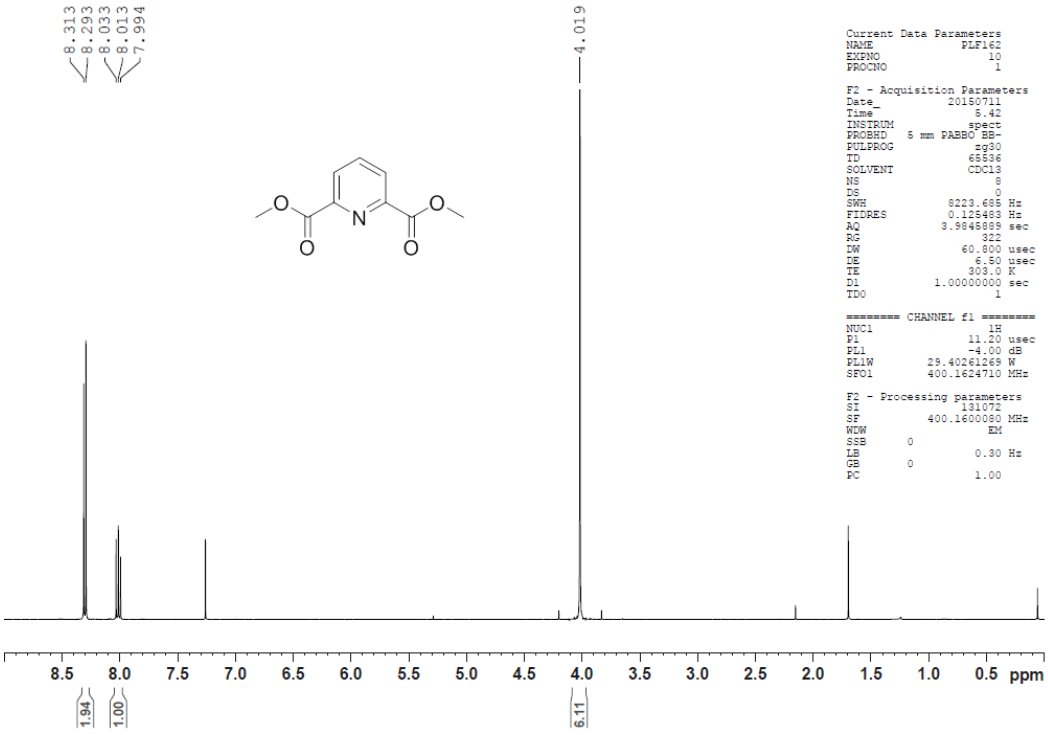

Figure S1: ^{1}H NMR of Dimethyl 2,6-pyridinedicarboxylate in $CDCl_3$

III

III

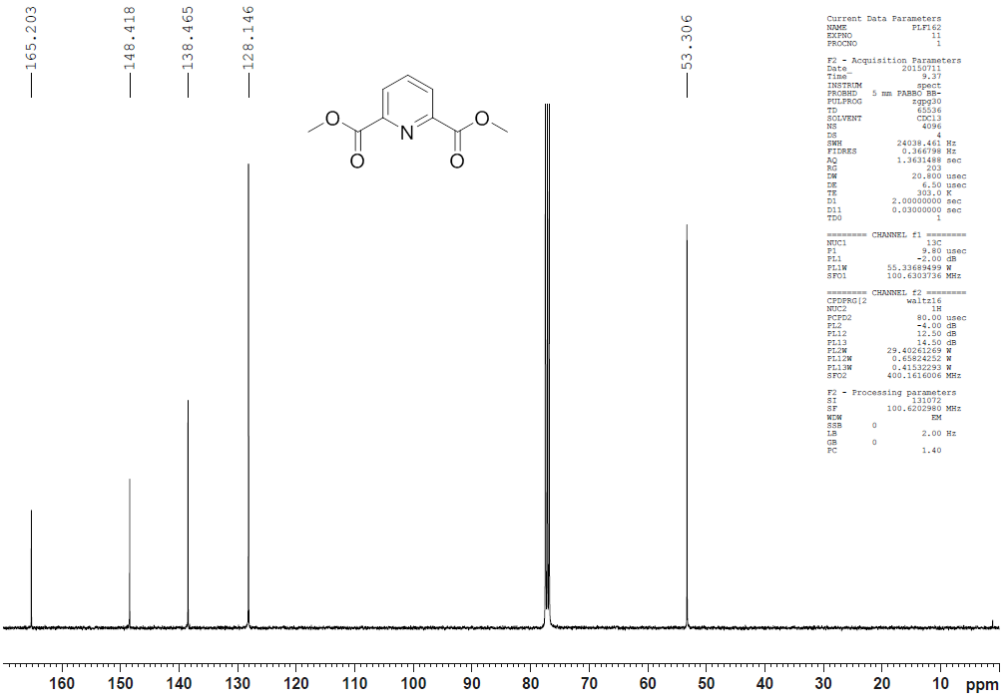

Figure S2: ^{13}C NMR of Dimethyl 2,6-pyridinedicarboxylate in $CDCl_3$

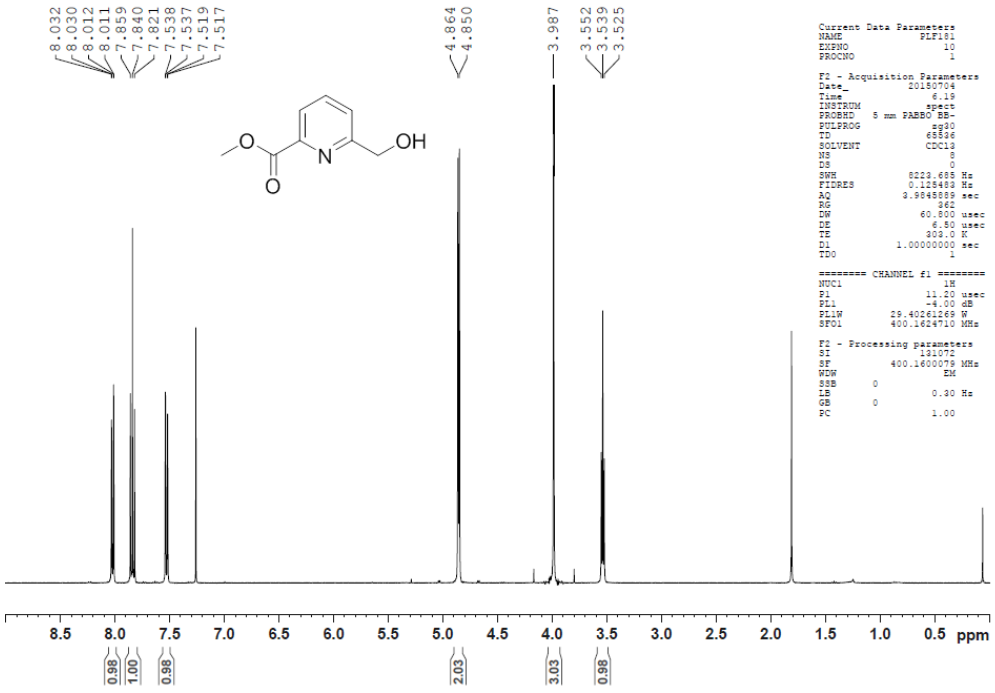

Figure S3: ^{1}H NMR of Methyl 6-(hydroxymethyl)picolinate in $CDCl_3$

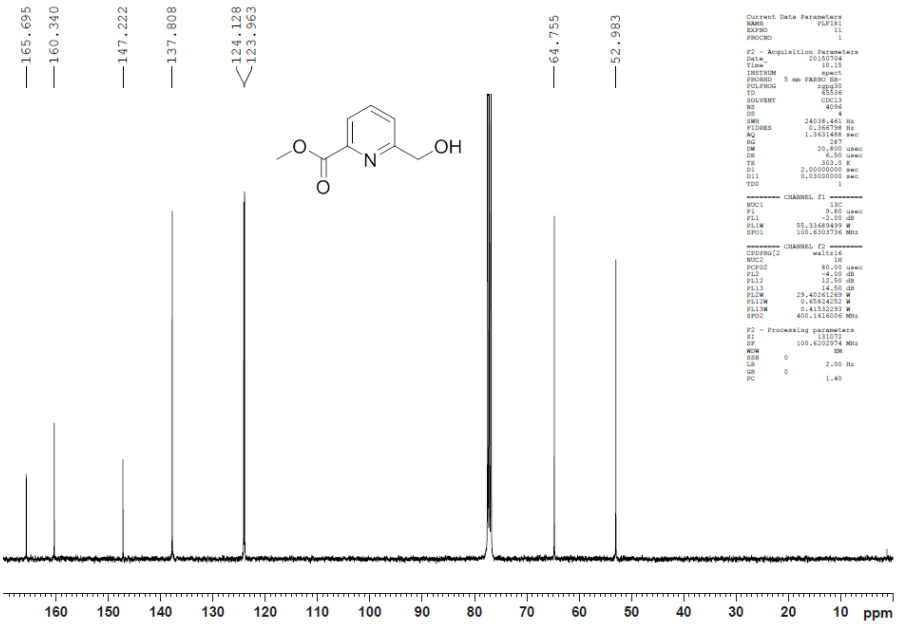

Figure S4: ^{13}C NMR of Methyl 6-(hydroxymethyl)picolinate in $CDCl_3$

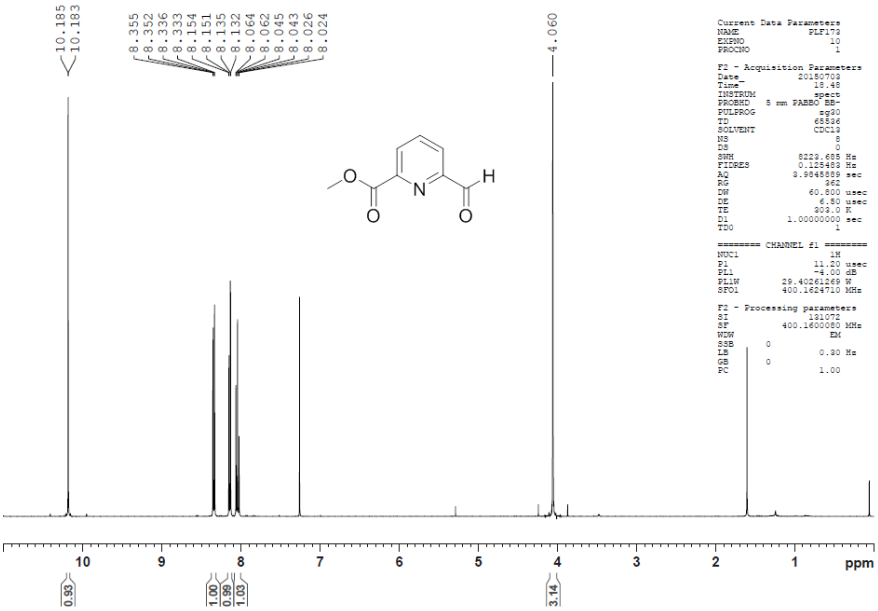

Figure S5: ^{1}H NMR of Methyl 6-formylpicolinate (**B**) in $CDCl_3$

III

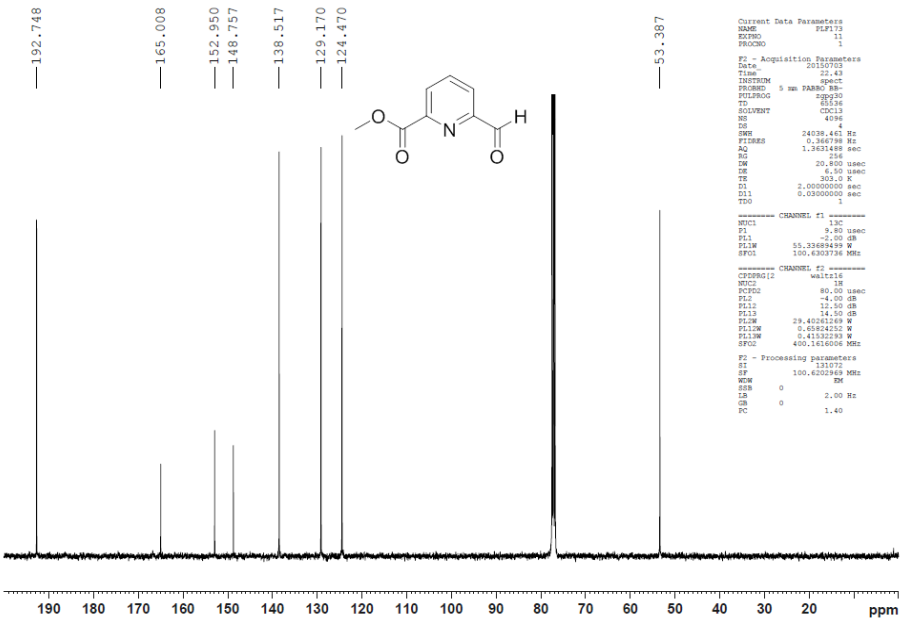

Figure S6: ^{13}C NMR of Methyl 6-formylpicolinate (**B**) in $CDCl_3$

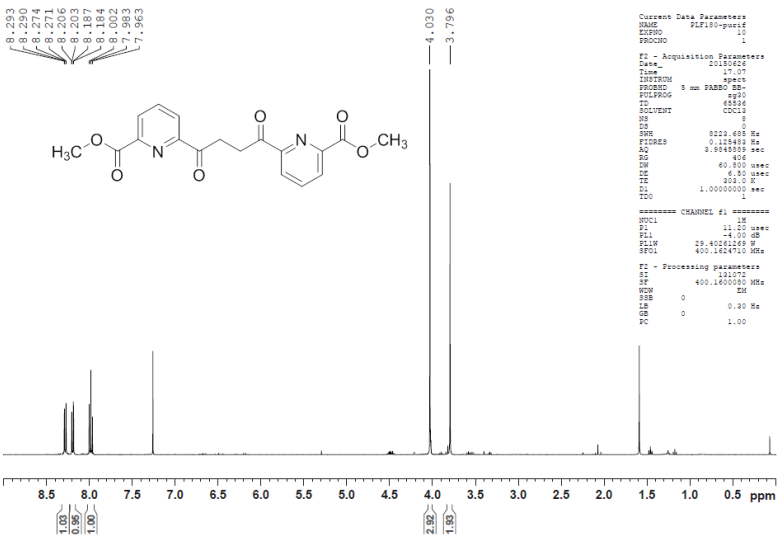

Figure S7: ^{1}H NMR of Dimethyl-6,6'-succinyldipicolinate (**C**) in $CDCl_3$

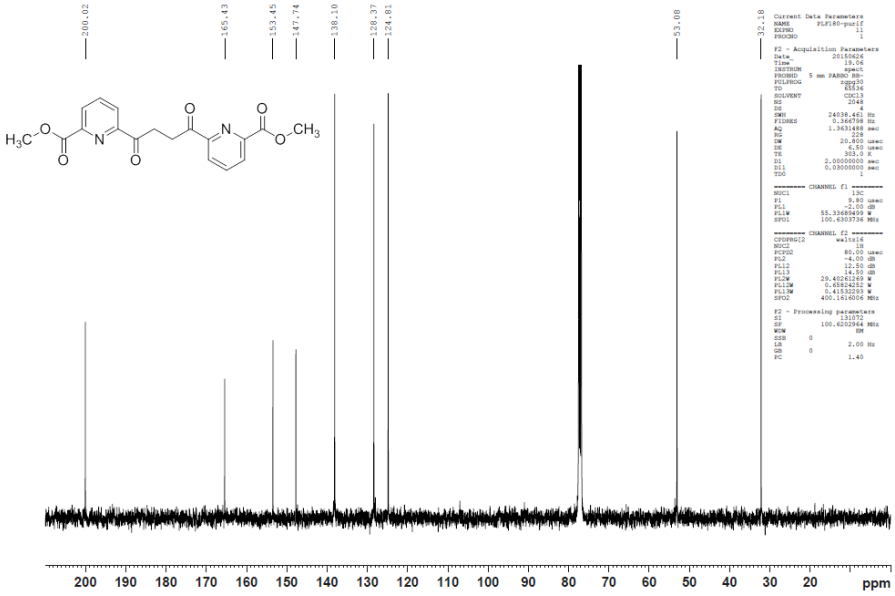

Figure S8: ^{13}C NMR of Dimethyl-6,6'-succinyldipicolinate (**C**) in $CDCl_3$

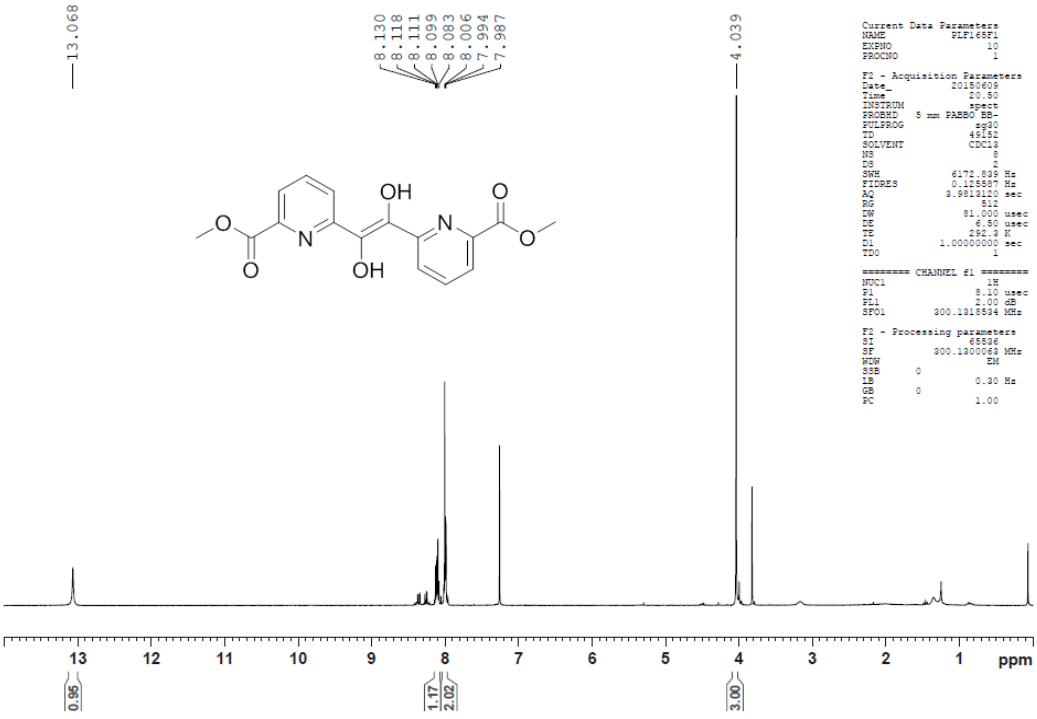

Figure S9: ^{1}H NMR of Dimethyl-6,6'-(1,2-dihydroxyethene-1,2-diyl)-dipicolinate in $CDCl_3$

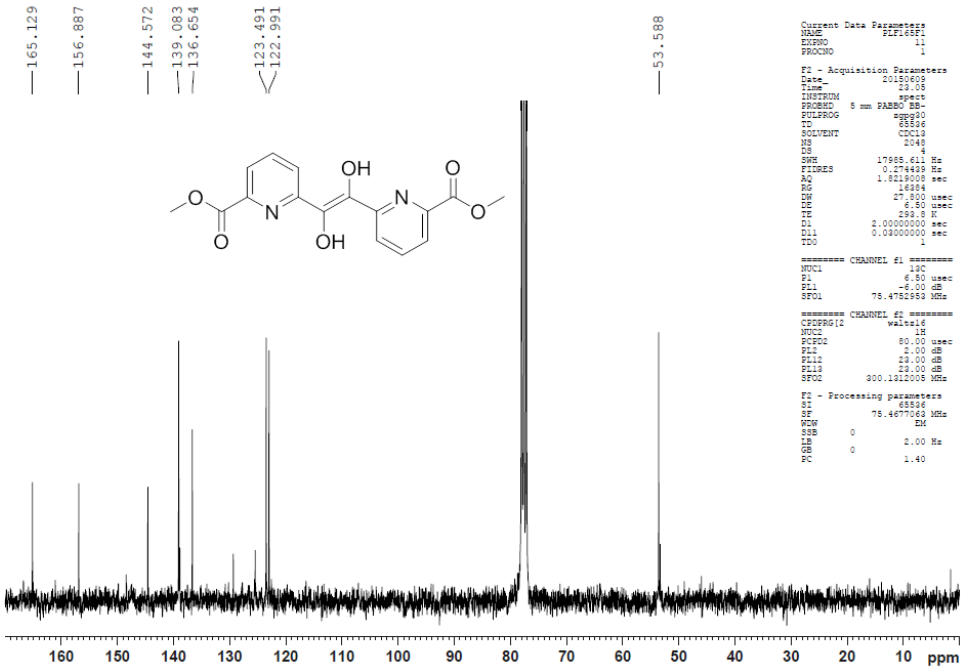

Figure S10: ^{13}C NMR of Dimethyl-6,6'-(1,2-dihydroxyethene-1,2-diyl)-dipicolinate in $CDCl_3$

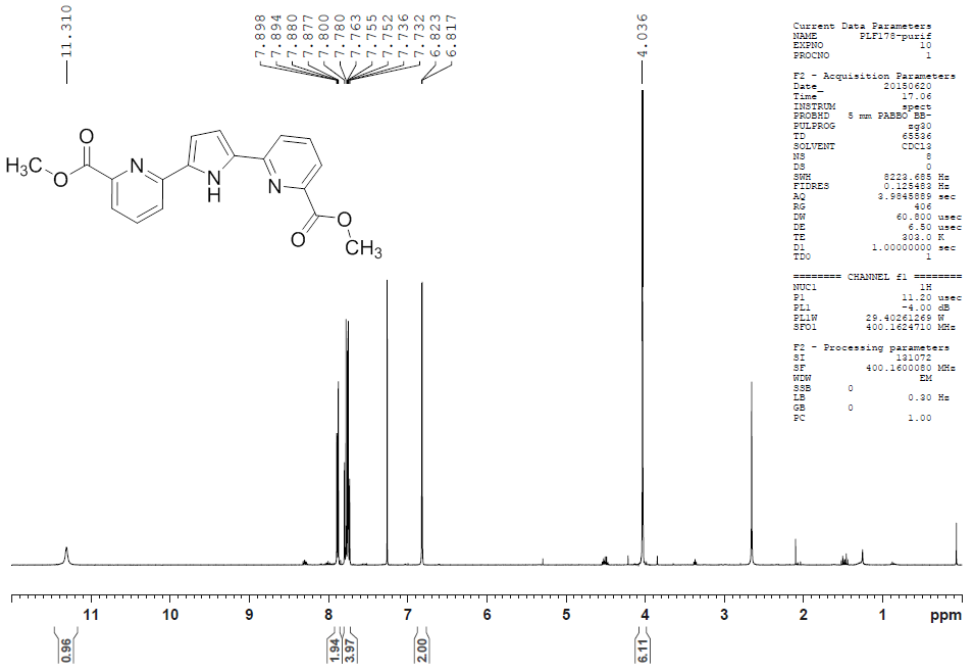

Figure S11: ^{1}H NMR of Dimethyl 6,6'-(1*H*-pyrrole-2,5-diyl)dipicolinate (**D**) in $CDCl_3$

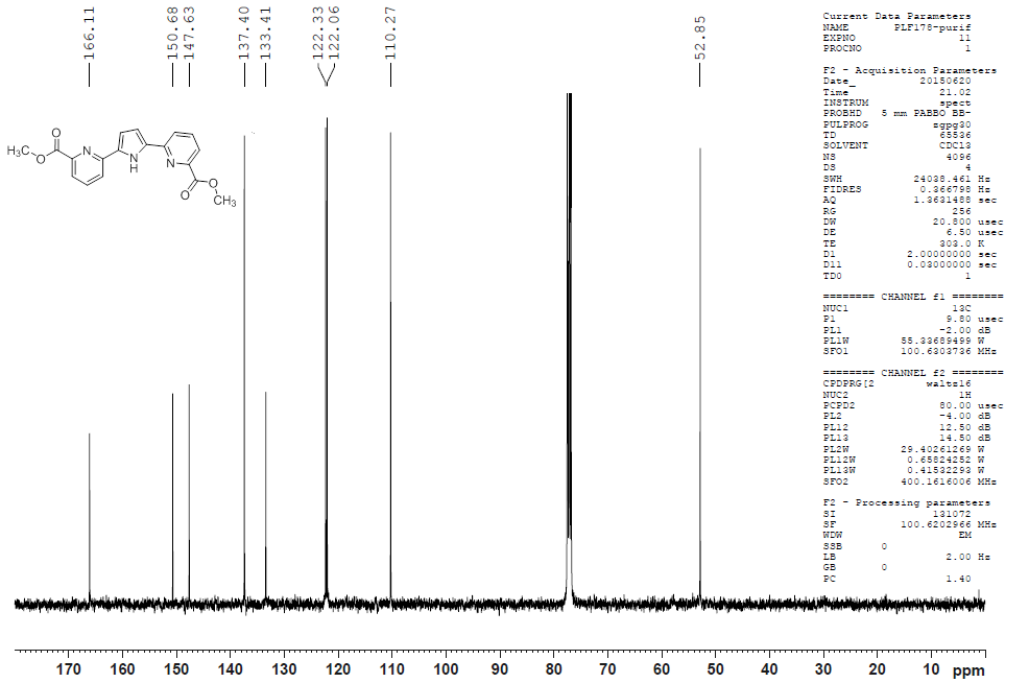

Figure S12: ^{13}C NMR of Dimethyl 6,6'-(1*H*-pyrrole-2,5-diyl)dipicolinate (**D**) in $CDCl_3$

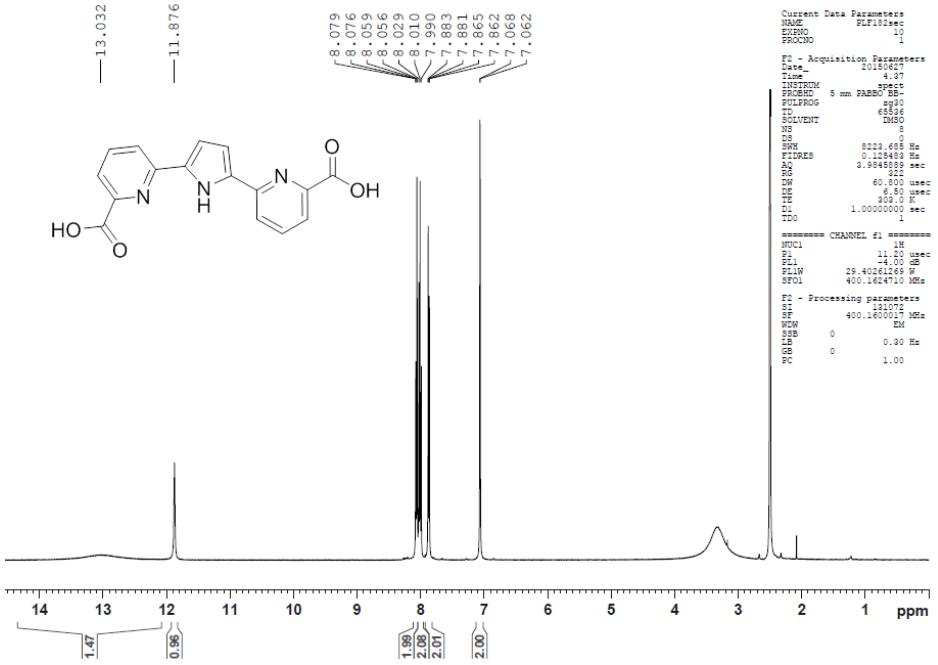

Figure S13: ^{1}H NMR of 6,6'-(1H-pyrrole-2,5-diyl)dipicolinic acid (**H_3t5a**) in DMSO-d6

III

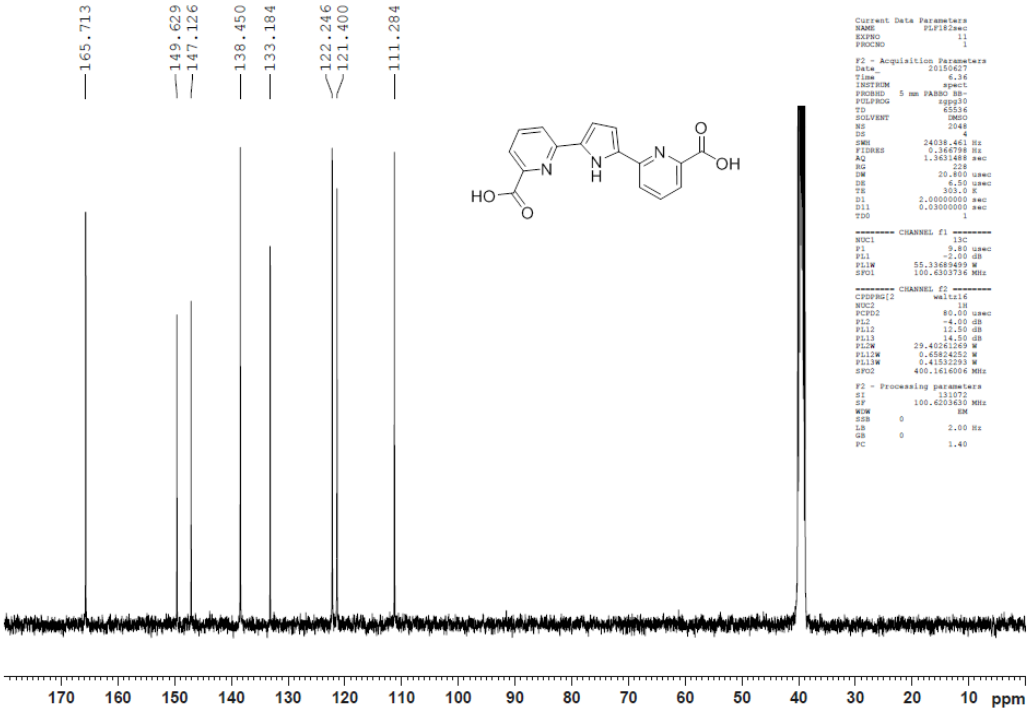

Figure S14: ^{13}C NMR of 6,6'-(1H-pyrrole-2,5-diyl)dipicolinic acid (**H$_3$t5a**) in DMSO-d6

*Characterization complexes **1**H^{II}(κ-N^{2}O), **2**^{III}(κ-N^{3}O$^{1.5}$) and {**2**^{IV}(κ-N^{3}O^2)}$^+$*

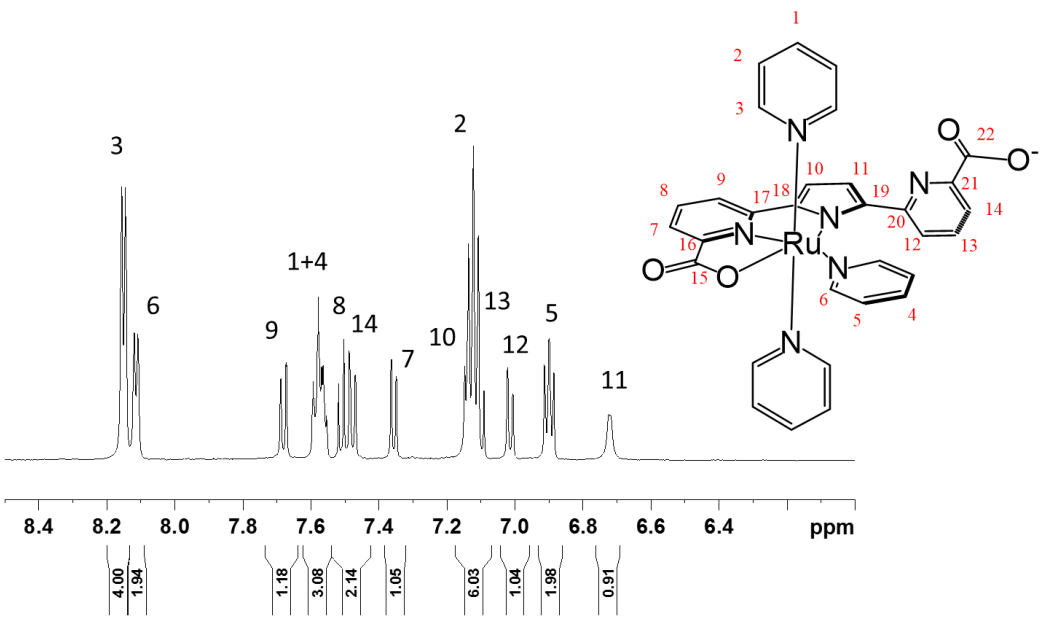

Figure S15: ^{1}H NMR of **1**H^{II}(κ-N^{2}O) in methanol-d4.

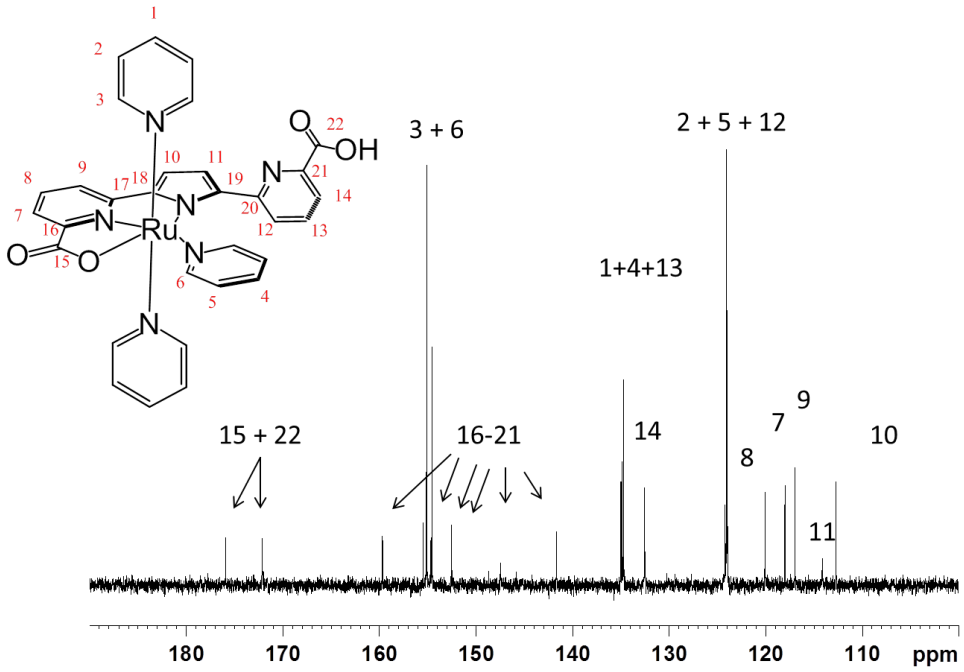

Figure S16: ^{13}C NMR of **1**H^{II}(κ-N^{2}O)in methanol-d4

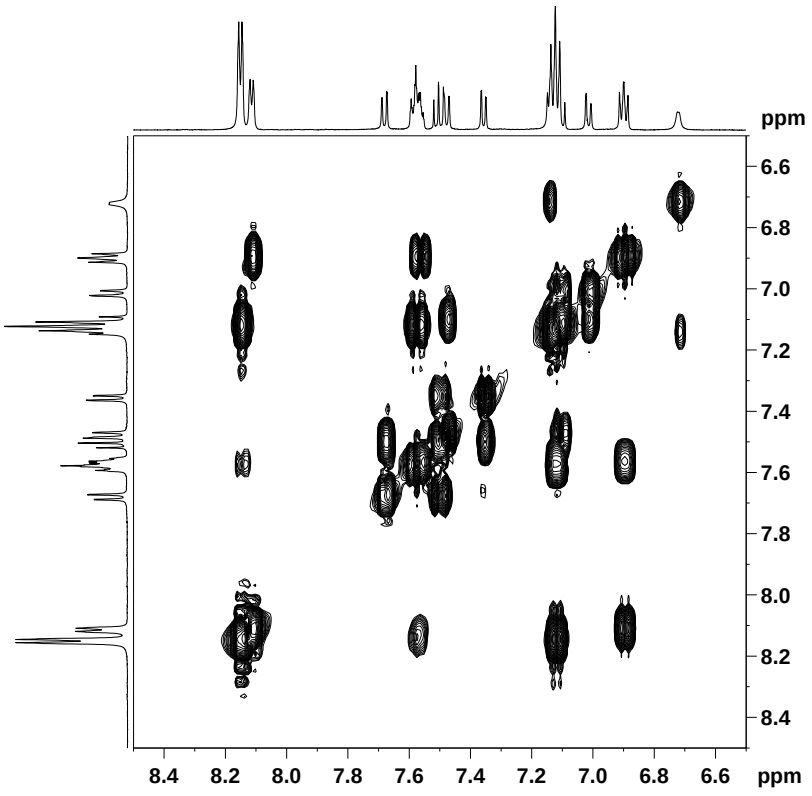

Figure S17: ^{1}H-^{1}H COSY NMR of **1**H^{II}(κ-N^{2}O) in methanol-d4

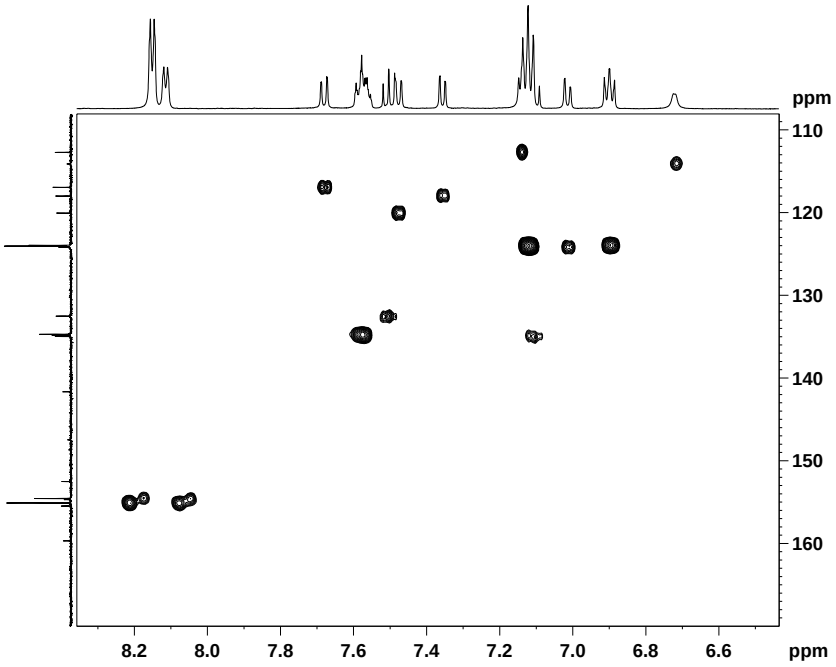

Figure S18: ^{1}H-^{13}C HSQC NMR of **1**H^{II}(κ-$N^{2}O$) in methanol-d4

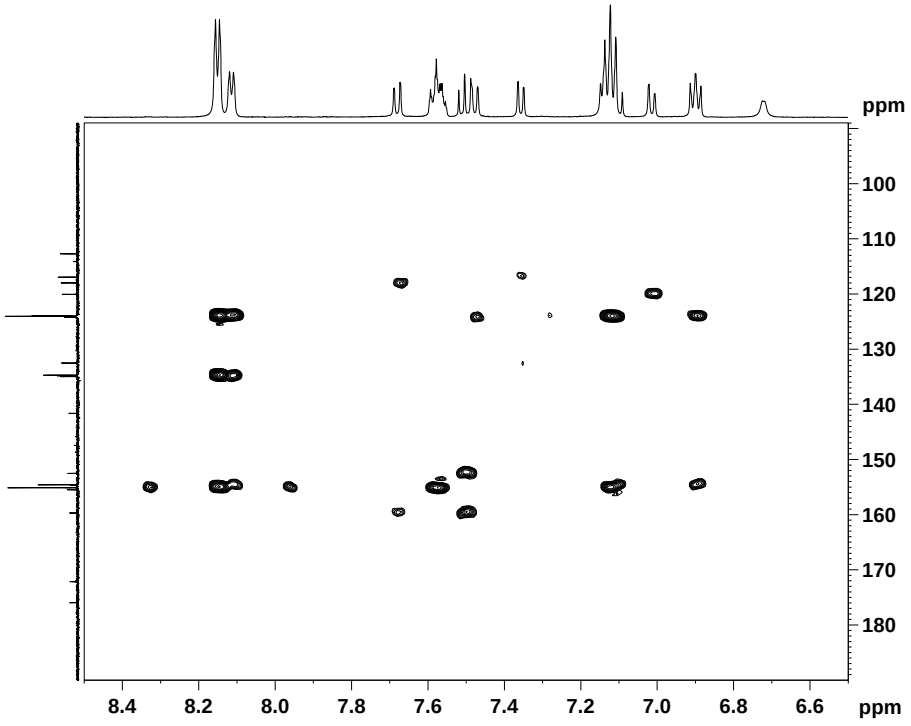

Figure S19: ^{1}H-^{13}C HMBC NMR of **1**H^{II}(κ-$N^{2}O$) in methanol-d4

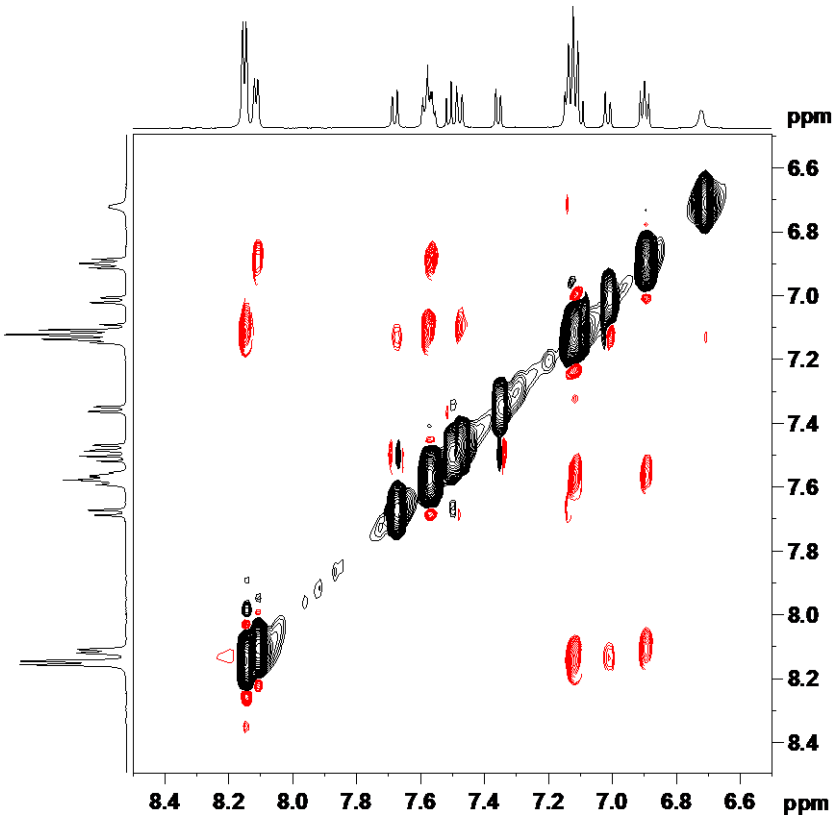

Figure S20: ^{1}H-^{1}H NOESY NMR of **1**H^{II}(κ-N^{2}O) in methanol-d4

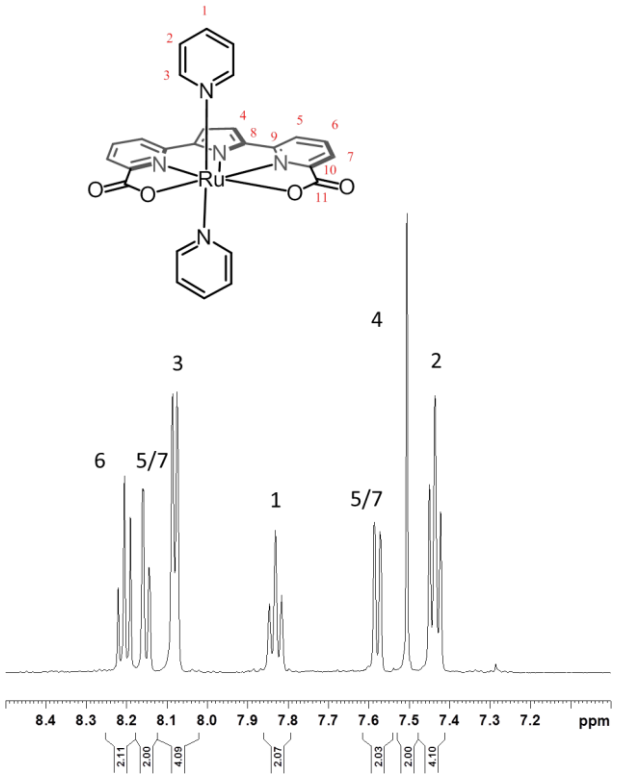

Figure S21: ^{1}H NMR of {**2**^{IV}(κ-N^{3}O^{2})}$^{+}$ in methanol-d4

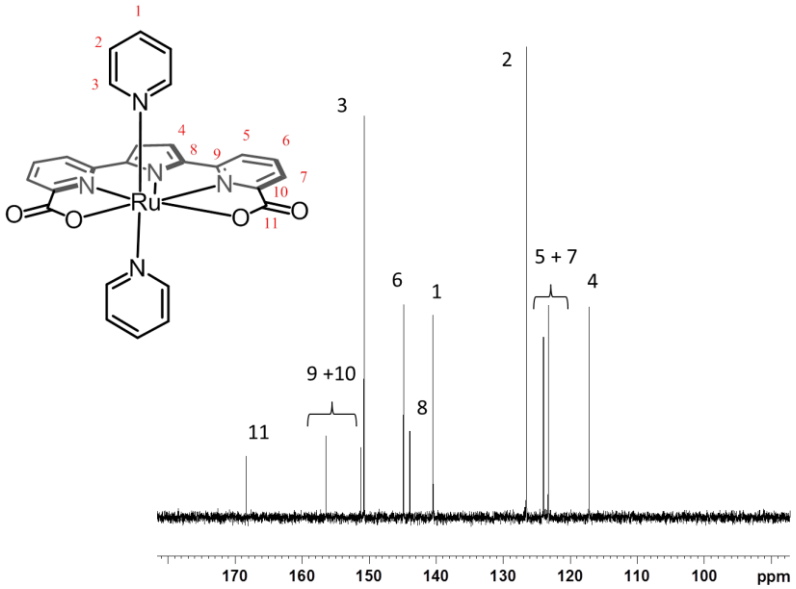

Figure S22: ^{13}C NMR of $\{\mathbf{2}^{IV}(\kappa\text{-}N^3O^2)\}^+$ in methanol-d4

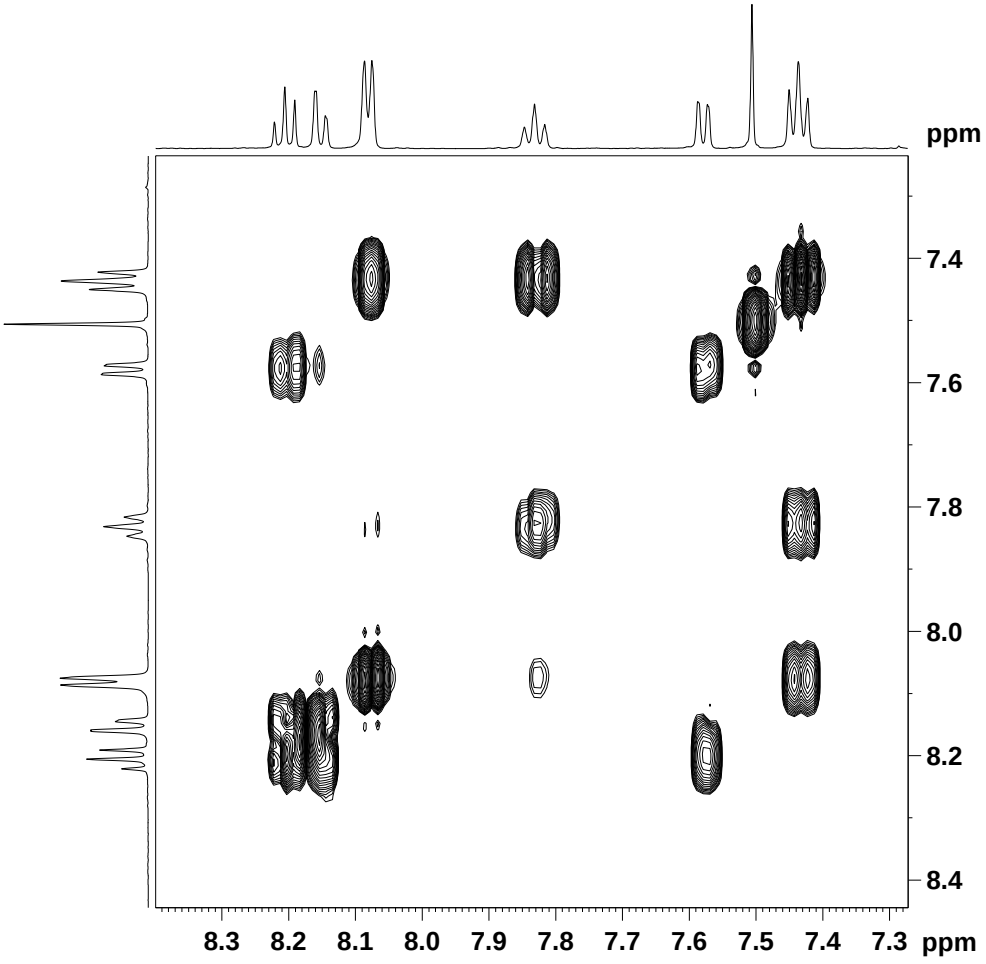

Figure S23: ^1H-^1H COSY NMR of $\{\mathbf{2}^{IV}(\kappa\text{-}N^3O^2)\}^+$ in methanol-d4

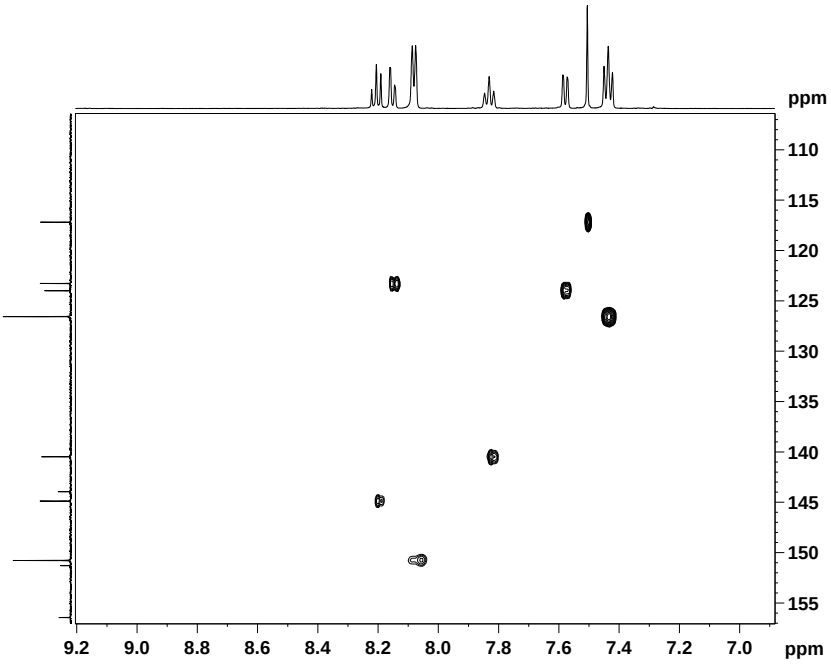

Figure S24: ^{1}H-^{13}C HSQC NMR of {**2**^{IV}(κ-N^3O^2)}$^{+}$ in methanol-d4

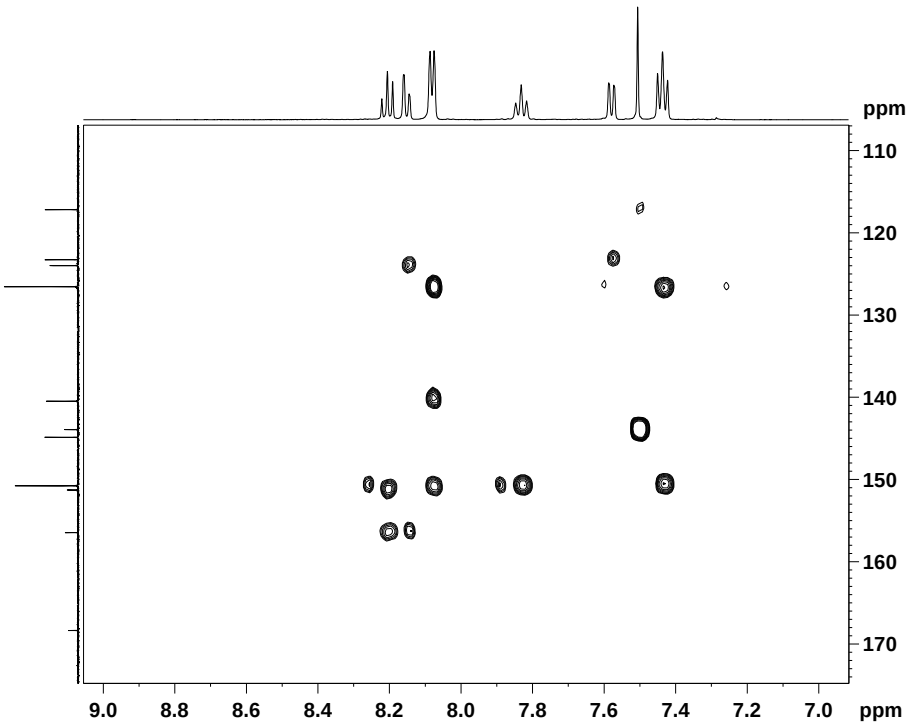

Figure S25: ^{1}H-^{13}C HMBC NMR of {**2**^{IV}(κ-N^3O^2)}$^{+}$ in methanol-d4

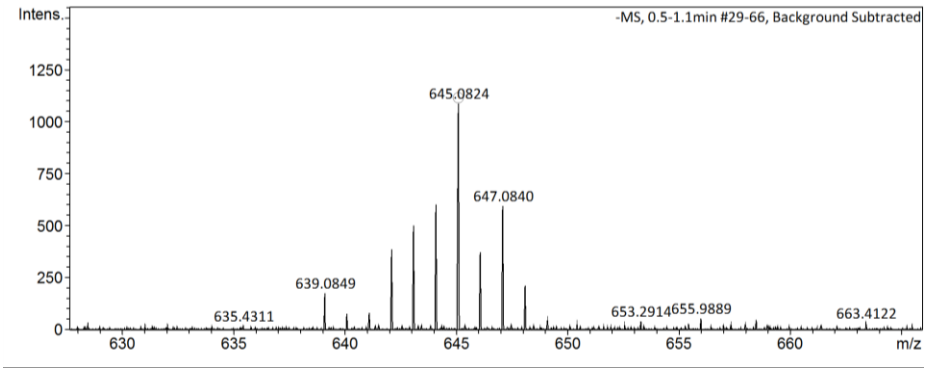

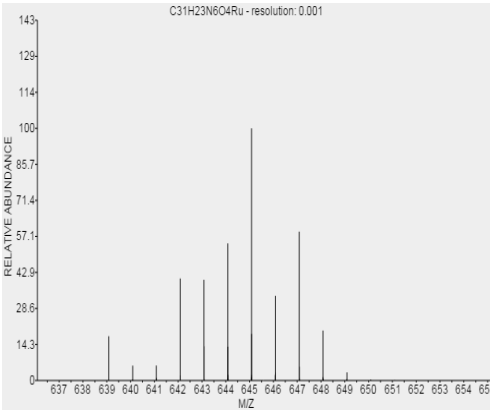

Figure S26: HR-MS of $\{\mathbf{1}^{\mathbf{II}}\}^-$ (ESI^-, top) and simulated pattern (Bottom)

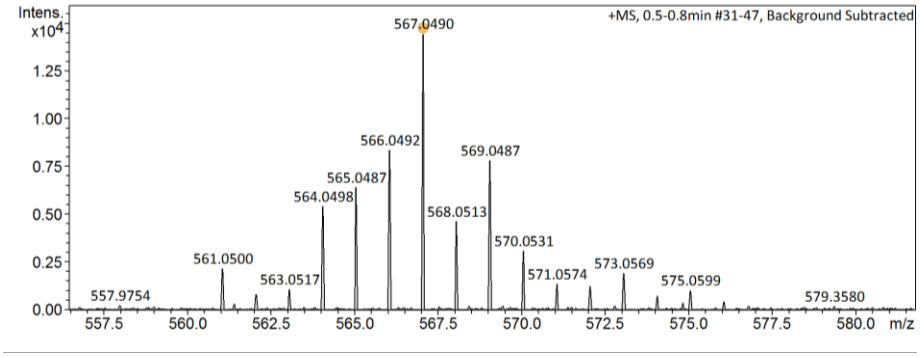

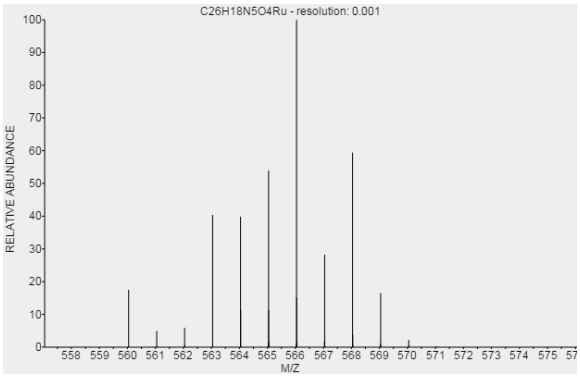

Figure S27: HR-MS of $\{\mathbf{2}^{\mathbf{IV}}(\kappa\text{-}N^3O^2)\}^+$ (ESI^+, top) and simulated pattern (Bottom)

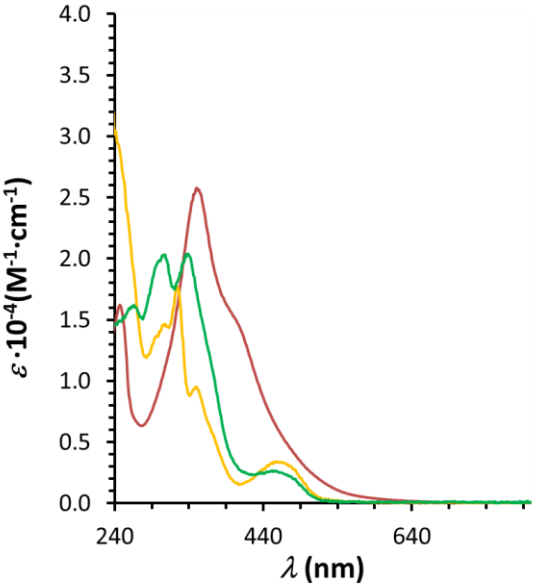

Figure S28: UV VIS of complex **1**H^{II}(κ-N^2O) (72 μM, red solid line), **2**^{III}(κ-$N^3O^{1.5}$) (66 μM, green solid line) and {**2**^{IV}(κ-N^3O^2)}$^+$ (46 μM, orange solid line) in methanol.

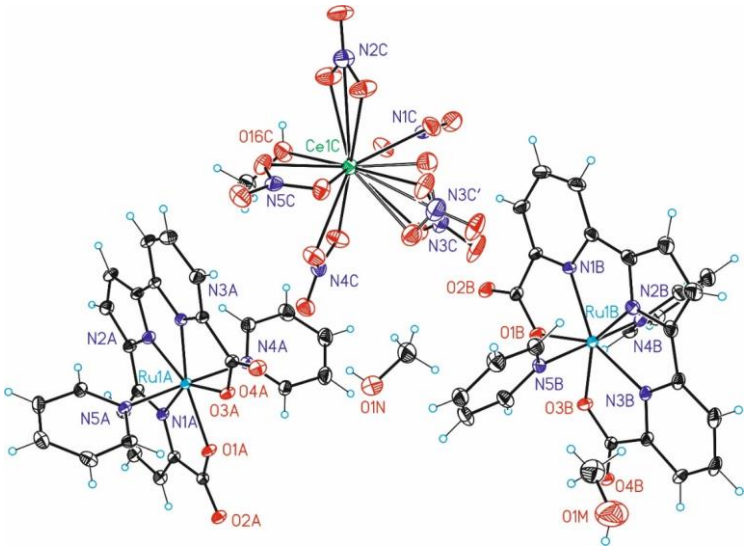

Figure S29 ORTEP plot (ellipsoids 50% of probability) for {**2**^{IV}(κ-N^3O^2)}{$Ce(MeOH)(NO_3)_5$}$_{0.5}$. Color codes: Ru, cyan; N, blue; O, red; C, black; Ce; green; C, black; and H, white.

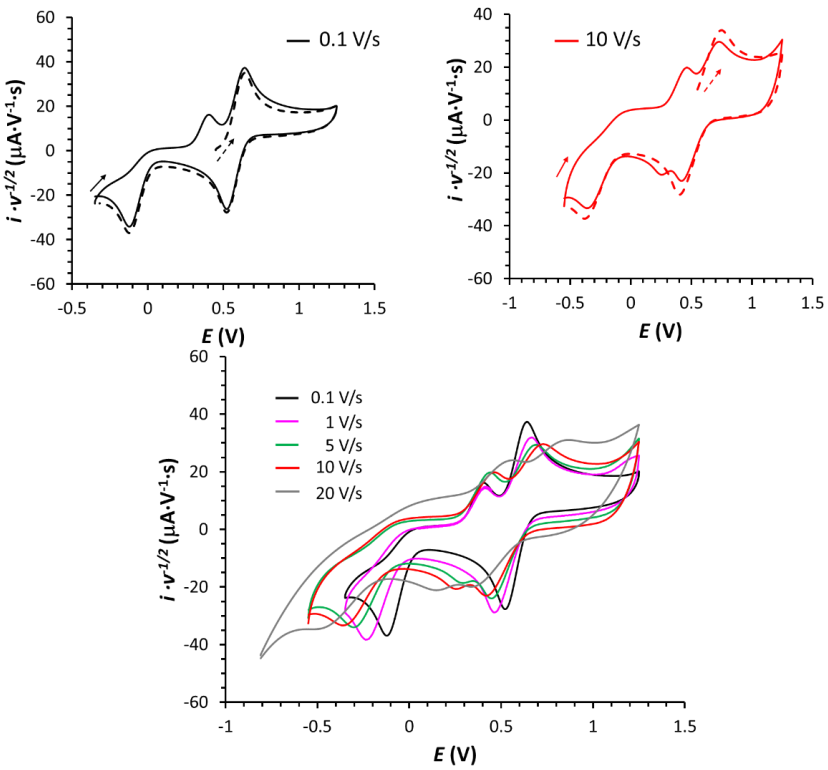

Figure S30: Cyclic Voltammetry (CV) measurements showing the squared mechanism of complex **2**^{III}(κ-N^{3}O$^{1.5}$) (1 mM) at low oxidation states in methanol (0.1 M TBAP). All CVs are normalized by the square root of the scan rate and solutions were purged with N_2 before measuring. **Top**, two-consecutive CV measurements of complex **2**^{III}(κ-N^{3}O$^{1.5}$) at scan rates of 0.1 V/s (top left) and 10 V/s (top right). The two consecutive cycles are represented with dashed (1st cycle) and solid lines (2nd Cycle). The dashed and solid line arrows represent the start of the first and second cycles respectively. **Bottom**, second cycle of the CV of complex **2**^{III}(κ-N^{3}O$^{1.5}$) at different scan rates: 0.1 V/s**,** black line; 1 V/s, pink solid line; 5 V/s, green solid line; 10 V/s, red solid line; and 20 V/s, grey solid line.

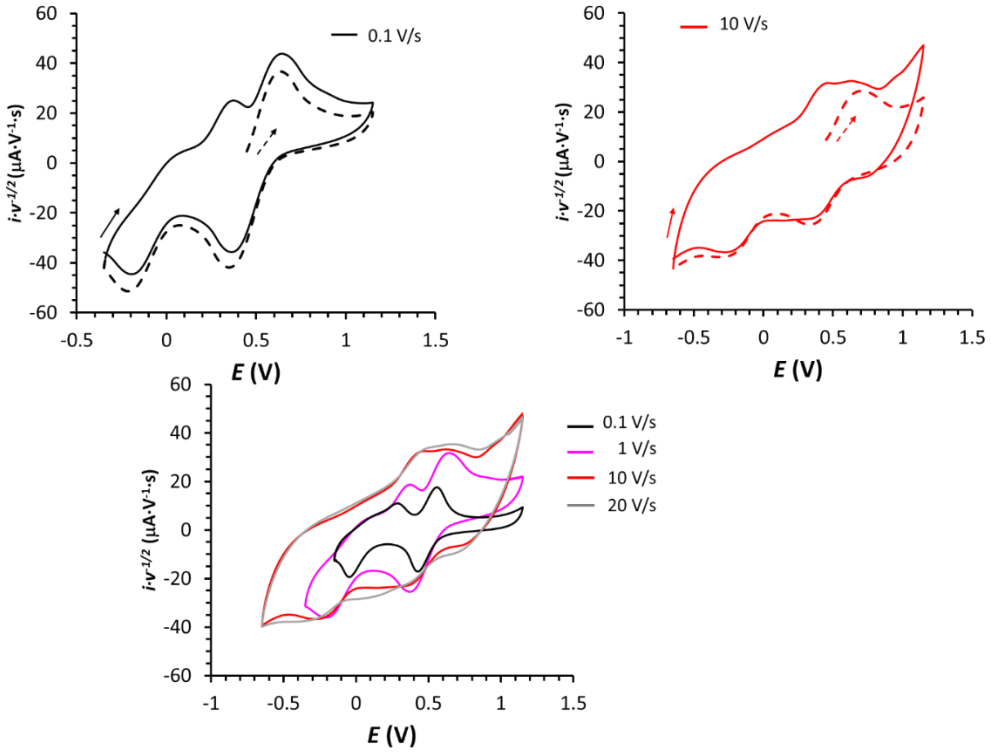

Figure S31 Cyclic Voltammetry experiments showing the squared mechanism of complex **2**^{III}(κ-N^{3}O$^{1.5}$) (1 mM) at low oxidation states at *pH* = 7.0. Measurements were performed under N_2 and CVs are normalized by the square root of the scan rate. **Top**, two-consecutive CV measurements of complex **2**^{III}(κ-N^{3}O$^{1.5}$) at scan rates of 0.1 V/s (top left) and 10 V/s (top right). The two consecutive cycles are represented with dashed (1st cycle) and solid lines (2nd Cycle). The dashed and solid line arrows represent the start of the first and second cycles respectively. **Bottom**, second cycle of the CV of complex **2**^{III}(κ-N^{3}O$^{1.5}$) at different scan rates: 0.1 V/s**,** black line; 1 V/s, pink solid line; 5 V/s, green solid line; 10 V/s, red solid line; and 20 V/s, grey solid line.

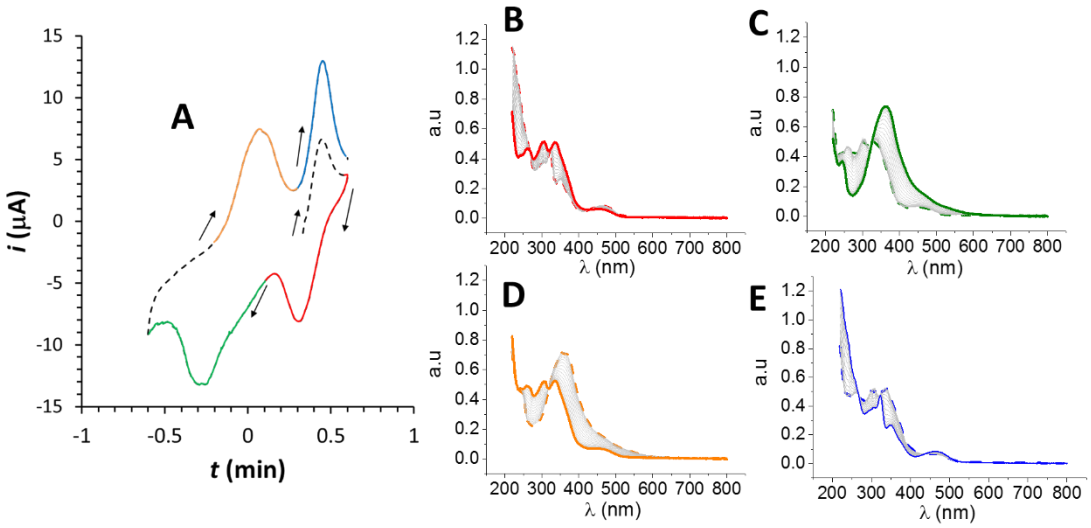

Figure S32 Spectroelectrochemistry experiment for complex **2**^{III}(κ-N^{3}O$^{1.5}$) (0.5 mM) at *pH* = 7.0 in an OTTLE cell. **(A)** CV of complex **2**^{III}(κ-N^{3}O$^{1.5}$) performed during the spectroelectrochemistry experiment at 2 mV/s with Pt mesh working and counter electrodes and a silver wire pseudo reference electrode (approximately - 0.2 V versus NHE). The arrows indicate the scan direction of the experiment. UV-vis spectra were recorded while performing CV (19.5 mV/scan) at four different regions: 0.60 V – 0.10 V, 25 scans in Figure **S32B**; 0.10 V – -0.6 V, 35 scans in Figure **S32C**; **-** 0.20 V – 0.30 V**,** 25 scans in Figure **S32D**; and 0.30 V – 0.60 V, 15 scans in Figure **S32E.** The 1st UV-vis spectrum at each region is a dashed line, the last is a solid line and the intermediate spectra are light grey solid lines.

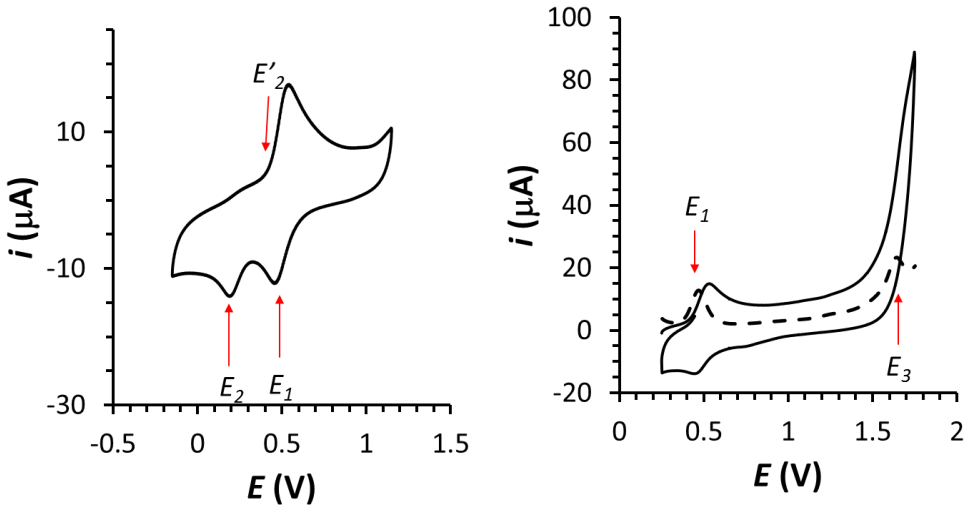

Figure S33: CVs (black solid line) and DPVs (black dashed line) of complex **2**^{III}(κ-N^{3}O$^{1.5}$) (1 mM) at *pH* = 1.0. Measurements were done under N_2. Red arrows indicate the processes indicated in Scheme 2 of the ms.

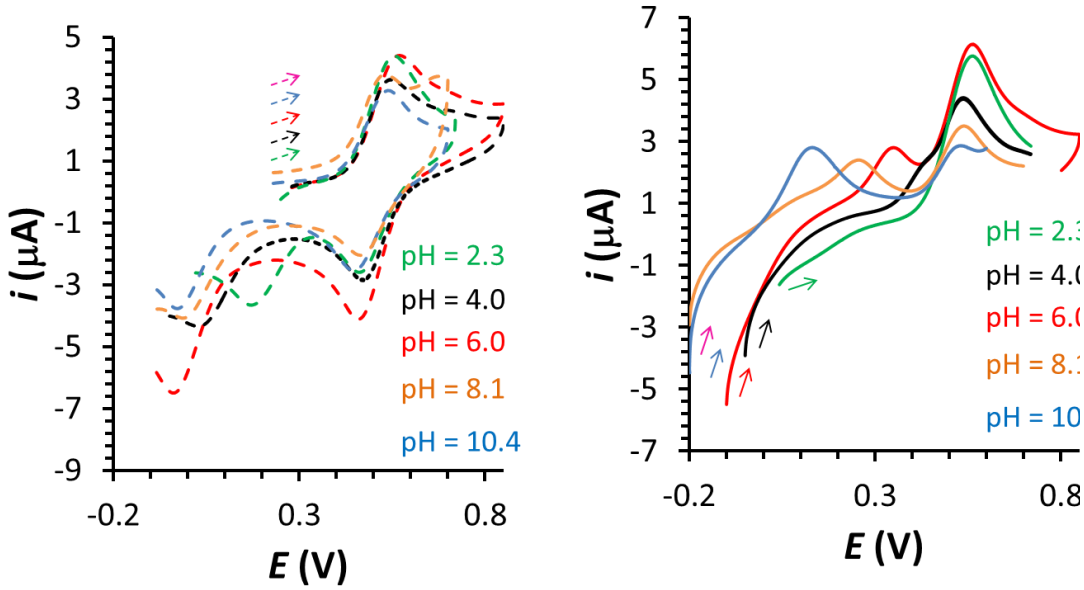

Figure S34: CVs of complex $\mathbf{2}^{\mathbf{III}}(\kappa\text{-}N^3O^{1.5})$ (0.5 mM) at different *pHs* (2.3, green; 4.0, black; 6.0, red; 8.1, orange; and 10.4, blue) in the first cycle (dashed lines, left figure) and in the second cycle (solid line, right figure).

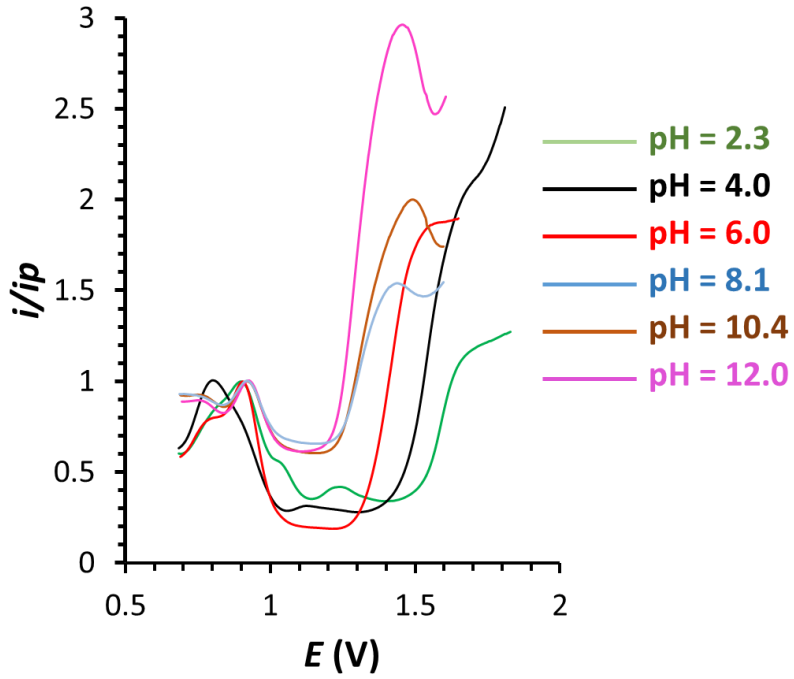

Figure S35: i_p normalized DPVs of a solution containing complexes $\{\mathbf{2}^{\mathbf{IV}}(\kappa\text{-}N^3O^2)\}^+$ and $\mathbf{2}^{\mathbf{IV}}(OH)(\kappa\text{-}N^2O)$ after 50 CV cycles of a $\mathbf{2}^{\mathbf{III}}(\kappa\text{-}N^3O^{1.5})$ (0.5 mM) solution - see Experiment in Figure 3C in the main Section. The 50-repetitive experiment and the subsequent DPV were

performed at the following *pH values*: 2.3, green; 4.0, black; 6.0, red; 8.1, blue; 10.4, brown; and 12.0, pink.

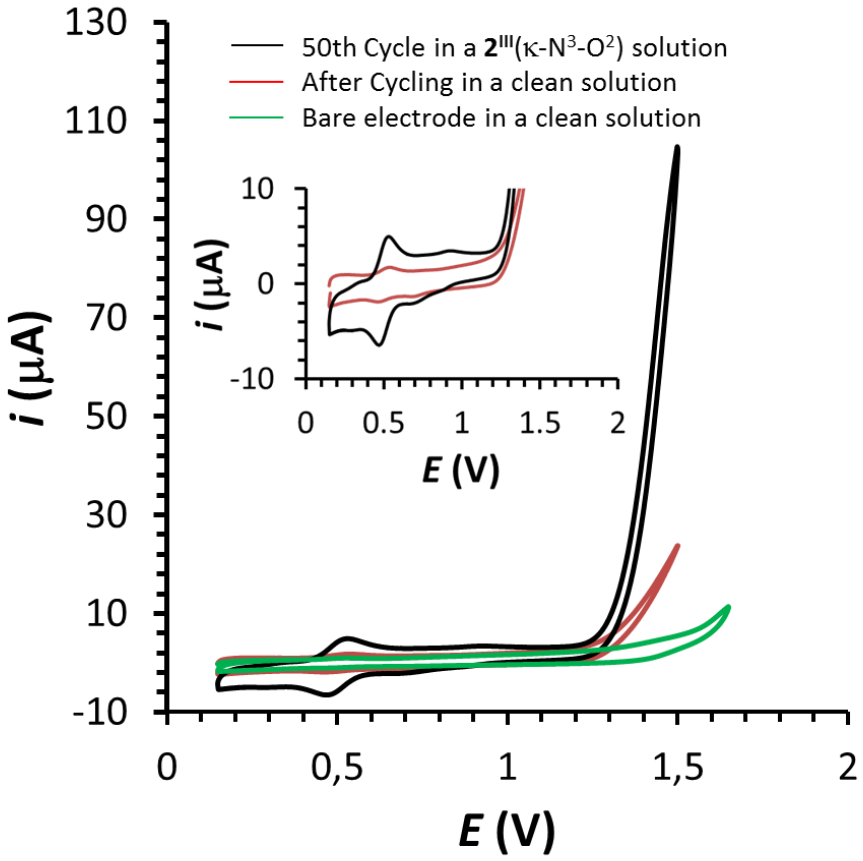

Figure S36: CV experiment that shows the absorption of complex **2**^{III}(κ-N^{3}O$^{1.5}$) on the glassy carbon electrode at *pH* = 7.0 after 50 cycles. The 50th cycle of the 50-repetitive CV experiment in a **2**^{III}(κ-N^{3}O$^{1.5}$) solution (0.5 mM) is plotted together with the electrode after the 50 cycles in a clean *pH* = 7.0 solution with no Ru in solution (red line) and bare electrode in a clean *pH* = 7.0 solution with no Ru in solution (green line).

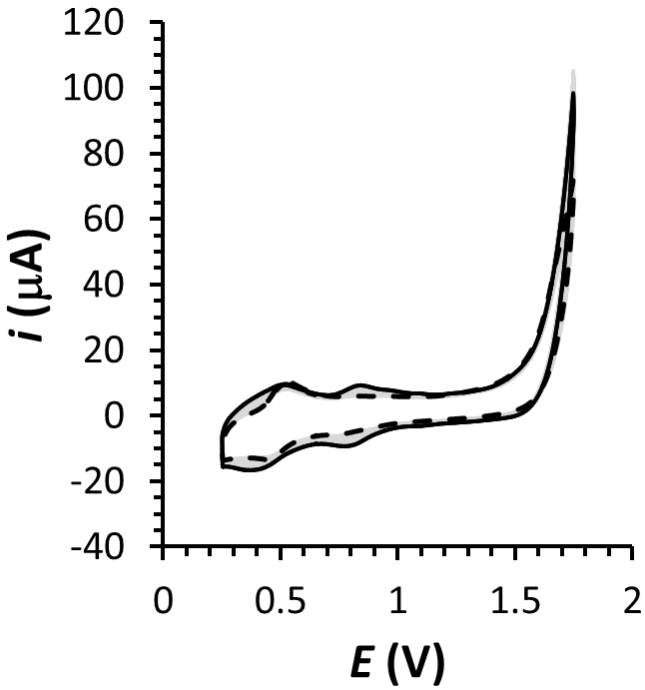

Figure S37: 50-repetive scans CV of **2**^{III}(κ-N^{3}O$^{1.5}$) (1 mM) at *pH* = 1.0: dashed black line, 1st Cycle; grey lines, 2nd - 49th cycles; and solid black line, 50th cycle.

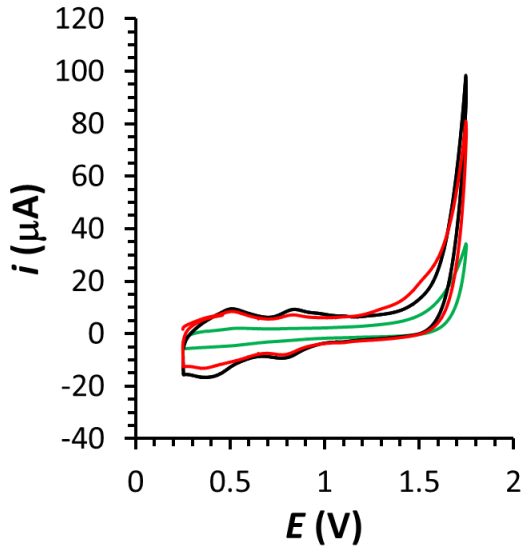

Figure S38: CV experiment that shows the absorption of complex **2**^{III}(κ-N^{3}O$^{1.5}$) on the glassy carbon electrode at *pH* = 1.0 after 50 Cycles. The 50th Cycle of the 50-repetitive CV experiment in a **2**^{III}(κ-N^{3}O$^{1.5}$) solution (1 mM) is plotted together with the electrode after the 50 cycles in

a fresh *pH* = 1.0 solution without Ru in solution (red line) and the polished electrode in a fresh *pH* = 1.0 solution (green line).

Table S1: Selected metric parameters for XRD structures of complexes **1**H^{II}(κ-N^2O), **2**^{III}(κ-$N^3O^{1.5}$) and **2**^{IV}(κ-N^3O^2)$^+$ in Å together with calculated structures at M06-L level of theory.

	$\{Ru^{II}(Ht5a\text{-}\kappa\text{-}N^2O)(py)_3\}^+$ **1**H^{II}(κ-N^2O)	$Ru^{III}(t5a\text{-}\kappa\text{-}N^3O^{1.5})(py)_2$ **2**^{III}(κ-$N^3O^{1.5}$)	$Ru^{III}(t5a\text{-}\kappa\text{-}N^{2.5}O^2)(py)_2$ **2**^{III}(κ-$N^{2.5}O^2$)	$\{Ru^{IV}(t5a\text{-}\kappa\text{-}N^3O^2)(py)_2\}^+$ $\{$**2**^{IV}(κ-N^3O^2)$\}^+$	
	XRD	**XRD**	**M06-L**	**XRD**	**M06-L**
Ru-^{t5a}O1	2.13	2.22	2.06	2.04	2.03
Ru-^{t5a}O2	2.30	2.31	2.13	2.10	2.03
Ru-^{t5a}N1	1.97	2.11	2.50	2.02	2.16
Ru-^{t5a}N2	2.09	1.97	2.14	2.13	2.03
Ru-^{t5a}N3	3.90	2.21	2.06	2.02	2.16
Ru-^{py}N	2.09, 2.10, 2.08	2.11, 2.09	2.09, 2.09	2.11, 2.10	2.12, 2.12

Table S2: Relative free energies at M06 level of theory for complexes **2**^{II}(κ-N$^{2.5}$O), **2**^{II}(κ-N^{3}O$^{1.5}$), **2**^{III}(κ-N$^{2.5}$O) and **2**^{III}(κ-N$^{2.5}$O^{2}) together with their optimized structures.

	II Oxidation State		III Oxidation State	
	2^{II}(κ-N$^{2.5}$O)	**2**^{II}(κ-N^{3}O$^{1.5}$)	**2**^{III}(κ-N$^{2.5}$O)[a]	**2**^{III}(κ-N$^{2.5}$O^{2})
ΔG	0.0	6.9	5.0	0.0

[a] An optimized structure for **2**^{III}(κ-N$^{2.5}$O) could not be obtained and free energy is estimated via single point calculation at oxidation state III on **2**^{II}(κ-N$^{2.5}$O) structure.

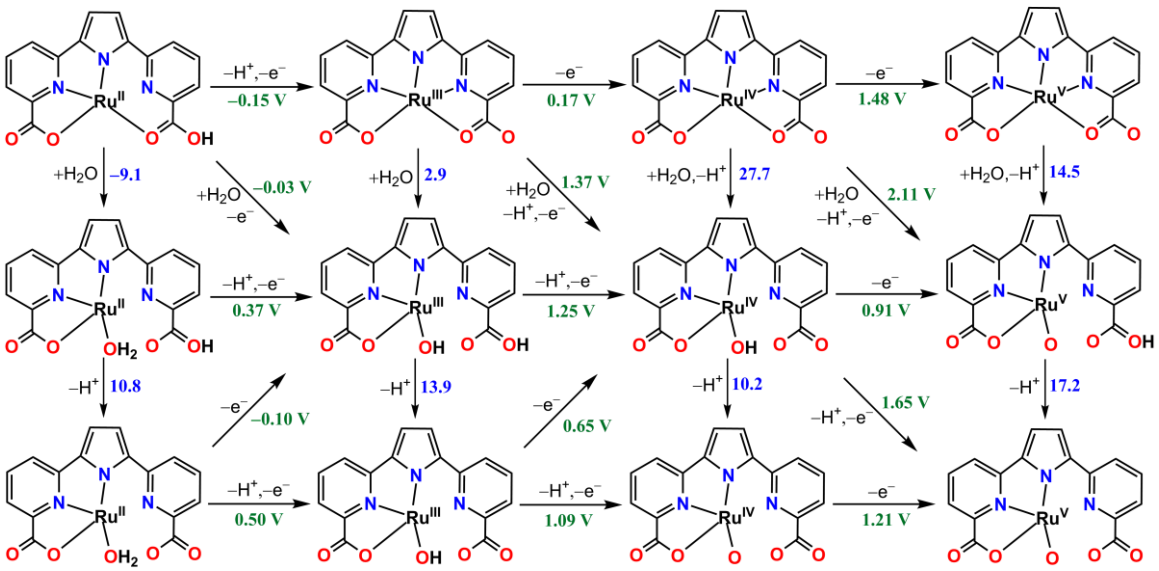

Scheme S2. Relative free energies (ΔG in blue) in units of kcal/mol and redox potentials (E in green) in units of volts at *pH* = 0 at M06 level of theory for the activation of the catalyst starting from **[Ru^{II}(HT5a-κ-N$^{2.5}$O)(py)$_2$]** upper left corner to **[Ru^{V}(T5a-κ-N^{2}O)(py)$_2$(O)]** in lower right corner.

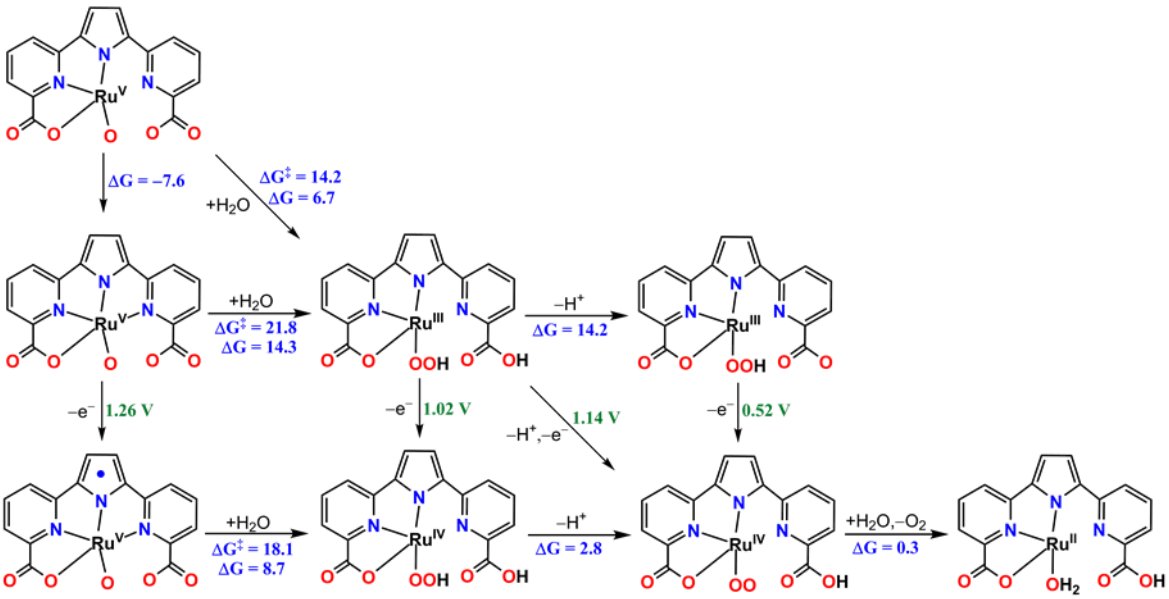

Scheme S3. Relative free energies (ΔG in blue) in units of kcal/mol and redox potentials (E in green) in units of volts at pH = 0 at M06 level of theory for mechanism of oxygen evolution starting from **[Ru^{V}(T5a-κ-N^{2}O)(O)]**

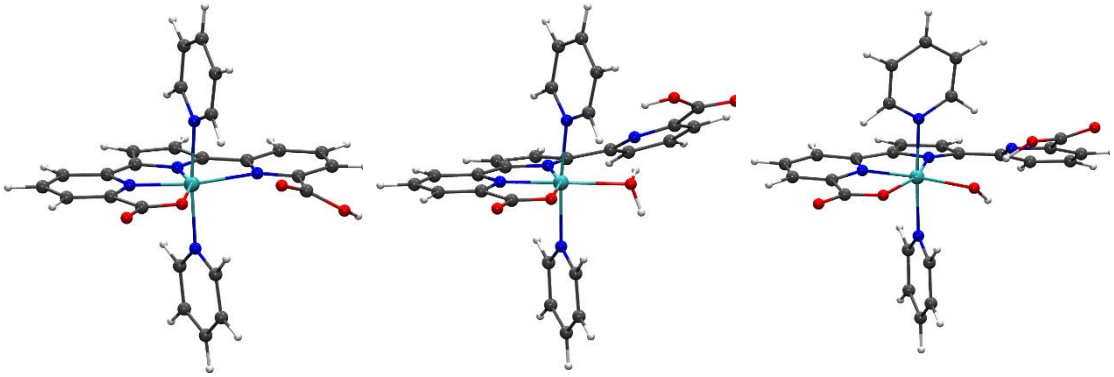

[Ru^{II}(HT5a-κ-N$^{2.5}$O)(py)$_2$]

[Ru^{II}(HT5a-κ-N^{2}O)(py)$_2$(H$_2$O)]

[Ru^{II}(HT5a-κ-N^{2}O)(py)$_2$(OH)]$^{-}$

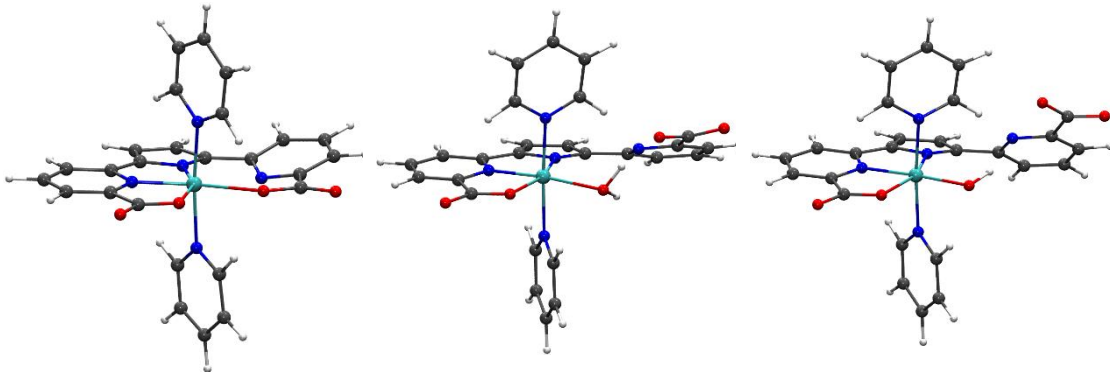

[Ru^{II}(T5a-κ-N^{2}O^{2})(py)$_2$]□

[Ru^{II}(T5a-κ-N^{2}O)(py)$_2$(H$_2$O)]$^{-}$

[Ru^{II}(T5a-κ-N^{2}O)(py)$_2$(OH)]$^{2-}$

Figure S40. Optimized structures at M06-L level of theory for complexes at Ru(II) oxidation state. Color code: Ru, cyan; N, blue; O, red; C, gray; and H, white

Table S3. Selected bond lengths for optimized structures at M06-L level of theory for complexes at Ru(II) oxidation state (see Figure S40 above).

	$[Ru^{II}(HT5a)(py)_2]$			$[Ru^{II}(T5a)(py)_2]$		
	κ-$N^{2.5}O$	κ-N^2O (H_2O)	κ-N^2O (OH)	κ-N^2O^2	κ-N^2O (H_2O)	κ-N^2O (OH)
Ru-N_1	1.95	1.94	1.96	1.96	1.94	1.97
Ru-N_2	1.94	2.11	2.13	2.15	2.13	2.11
Ru-N_3	2.46	3.62	3.55	2.83	3.56	3.78
Ru-N_4 (axial)	2.09	2.07	2.08	2.06	2.08	2.09
Ru-N_5 (axial)	2.08	2.09	2.05	2.06	2.06	2.04
Ru-O_1	2.19	2.12	2.15	2.13	2.14	2.18
Ru-O_2	3.12	4.53	4.25	2.28	4.29	5.02
Ru-O_3 (water)	–	2.23	2.13	–	2.21	2.03

Table S4. Relative free energies (ΔG) in units of kcal/mol at M06-L, M06 and B3LYP-D3 levels of theory for complexes at Ru(II) oxidation state (see Figure S40 above).

	M06-L		M06		B3LYP-D3	
	pH 0.0	pH 7.0	pH 0.0	pH 7.0	pH 0.0	pH 7.0
$[Ru^{II}(HT5a\text{-}\kappa\text{-}N^{2.5}O)(py)_2]$	0.0	0.0	0.0	0.0	0.0	0.0
$[Ru^{II}(HT5a\text{-}\kappa\text{-}N^2O)(py)_2(H_2O)]$	–7.4	–7.4	–9.1	–9.1	–9.3	–9.3
$[Ru^{II}(HT5a\text{-}\kappa\text{-}N^2O)(py)_2(OH)]^+$	12.2	2.7	10.6	1.0	10.8	1.3
$[Ru^{II}(T5a\text{-}\kappa\text{-}N^2O^2)(py)_2]^+$	12.3	2.8	11.4	1.8	13.5	3.9
$[Ru^{II}(T5a\text{-}\kappa\text{-}N^2O)(py)_2(H_2O)]^+$	4.4	–5.1	1.7	–7.8	3.0	–6.5
$[Ru^{II}(T5a\text{-}\kappa\text{-}N^2O)(py)_2(OH)]^{2+}$	34.1	15.0	29.3	10.3	34.4	15.4

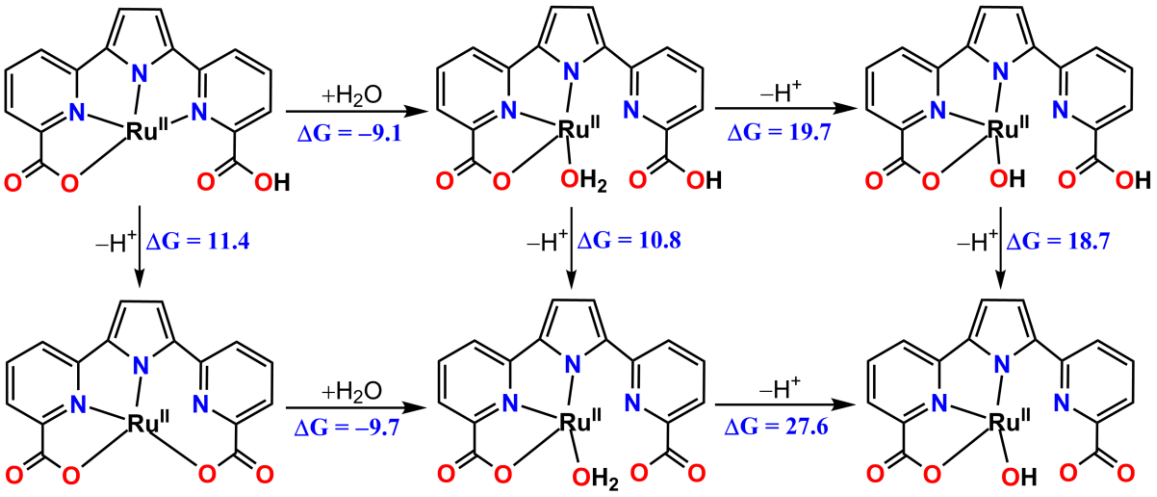

Scheme S4. Relative free energies (ΔG) in units of kcal/mol at *pH* = 0 at M06 level of theory for complexes at Ru(II) oxidation state.

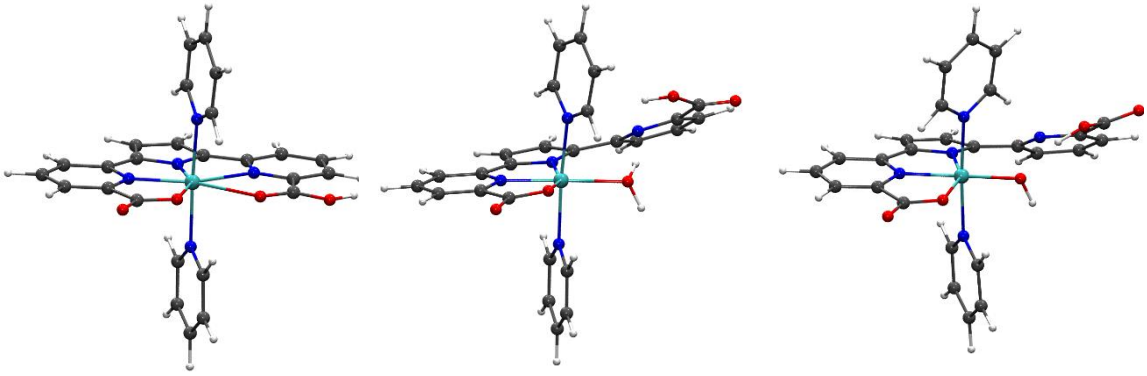

[Ru^{III}(HT5a-κ-N$^{2.5}$O)(py)$_2$]$^+$ **[Ru^{III}(HT5a-κ-N^{2}O)(py)$_2$(H$_2$O)]$^+$** **[Ru^{III}(HT5a-κ-N^{2}O)(py)$_2$(OH)]**

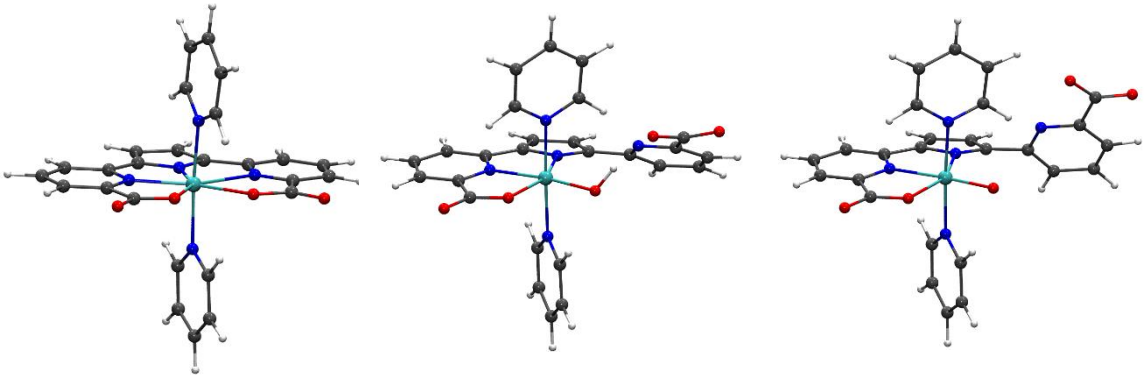

[Ru^{III}(T5a-κ-N$^{2.5}$O^2)(py)$_2$] **[Ru^{III}(T5a-κ-N^{2}O)(py)$_2$(OH)]$^{\square}$** **[Ru^{III}(T5a-κ-N^{2}O)(py)$_2$(O)]$^{2\square}$**

Figure S41. Optimized structures at M06-L level of theory for complexes at Ru(III) oxidation state. Color code: Ru, cyan; N, blue; O, red; C, gray; and H, white.

Table S5. Selected bond lengths for optimized structures at M06-L level of theory for complexes at Ru(III) oxidation state (see Figure S41 above).

	$[Ru^{III}(HT5a)(py)_2]$			$[Ru^{III}(T5a)(py)_2]$		
	κ-$N^{2.5}O$	κ-N^2O (H_2O)	κ-N^2O (OH)	κ-$N^{2.5}O^2$	κ-N^2O (OH)	κ-N^2O (O)
Ru-N_1	2.02	1.96	2.03	2.06	2.04	2.04
Ru-N_2	2.01	2.06	2.12	2.14	2.12	2.11
Ru-N_3	2.38	3.61	3.56	2.50	3.48	3.93
Ru-N_4 (axial)	2.11	2.11	2.10	2.09	2.10	2.10
Ru-N_5 (axial)	2.11	2.12	2.10	2.09	2.08	2.07
Ru-O_1	2.07	2.03	2.07	2.06	2.11	2.17
Ru-O_2	2.48	4.56	4.34	2.13	4.17	5.40
Ru-O_3 (water)	–	2.18	1.96	–	1.92	1.82

Table S6. Relative free energies (ΔG) in units of kcal/mol at M06-L, M06 and B3LYP-D3 levels of theory for complexes at Ru(III) oxidation state (see Figure S41 above).

	M06-L		M06		B3LYP-D3	
	pH 0.0	pH 7.0	pH 0.0	pH 7.0	pH 0.0	pH 7.0
$[Ru^{III}(HT5a\text{-}\kappa\text{-}N^{2.5}O)(py)_2]^+$	0.0	0.0	0.0	0.0	0.0	0.0
$[Ru^{III}(HT5a\text{-}\kappa\text{-}N^2O)(py)_2(H_2O)]^+$	–0.4	–0.4	–3.9	–3.9	–3.1	–3.1
$[Ru^{III}(HT5a\text{-}\kappa\text{-}N^2O)(py)_2(OH)]$	6.4	–3.2	2.2	–7.3	4.5	–5.0
$[Ru^{III}(T5a\text{-}\kappa\text{-}N^{2.5}O^2)(py)_2]$	0.7	–8.8	–0.7	–10.2	1.4	–8.1
$[Ru^{III}(T5a\text{-}\kappa\text{-}N^2O)(py)_2(OH)]^{\square}$	21.6	2.5	16.1	–3.0	20.7	1.6
$[Ru^{III}(T5a\text{-}\kappa\text{-}N^2O)(py)_2(O)]^{2\square}$	64.3	35.7	58.7	30.2	66.4	37.8

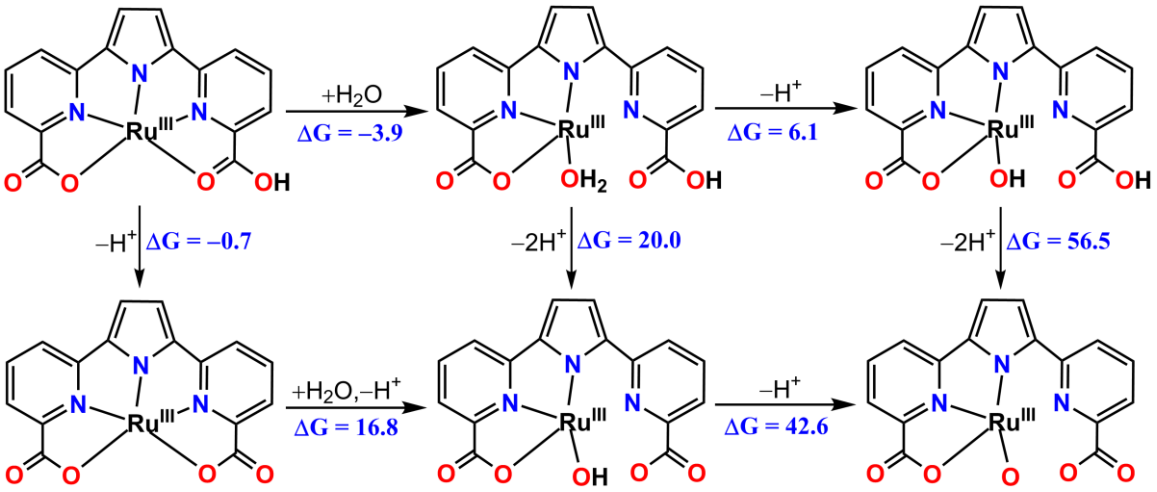

Scheme S5. Relative free energies (ΔG) in units of kcal/mol at *pH* = 0 at M06 level of theory for complexes at Ru(III) oxidation state.

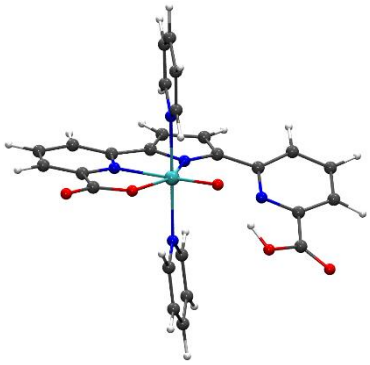

[Ru^{IV}(HT5a-κ-N^{2}O)(py)$_2$(O)]

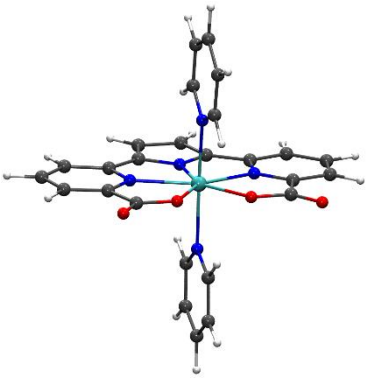

[Ru^{IV}(T5a-κ-N^{3}O^{2})(py)$_2$]$^{+}$

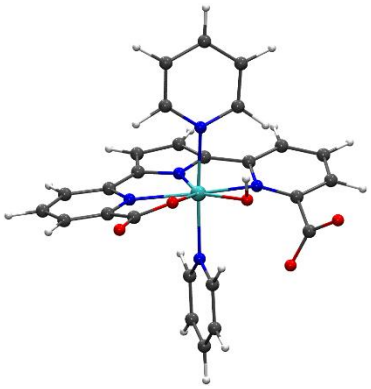

[Ru^{IV}(T5a-κ-N$^{2.5}$O)(py)$_2$(OH)]

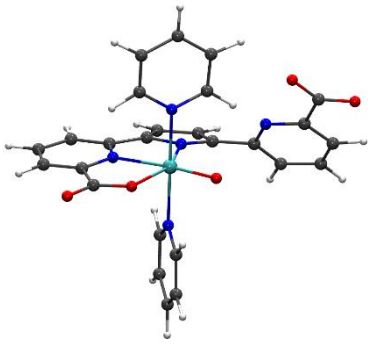

[Ru^{IV}(T5a-κ-N^{2}O)(py)$_2$(O)]□

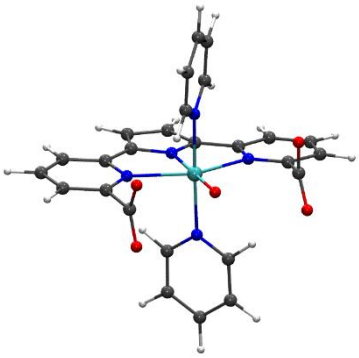

[Ru^{IV}(T5a-κ-N^{3})(py)$_2$(O)]□

Figure S42. Optimized structures at M06-L level of theory for complexes at Ru(IV) oxidation state. Color code: Ru, cyan; N, blue; O, red; C, gray; and H, white.

Table S7. Selected bond lengths for optimized structures at M06-L level of theory for complexes at Ru(IV) oxidation state (see Figure S42 above).

	$[Ru^{IV}(HT5a)(py)_2]$		$[Ru^{IV}(T5a)(py)_2]$		
	κ-N^2O (O)	**κ-N^3O^2**	**κ-$N^{2.5}O$ (OH)**	**κ-N^2O (O)**	**κ-N^3 (O)**
Ru-N_1	2.10	2.16	2.18	2.10	2.21
Ru-N_2	2.13	2.03	2.08	2.11	2.02
Ru-N_3	3.40	2.16	2.38	3.76	2.21
Ru-N_4 (axial)	2.12	2.12	2.12	2.10	2.11
Ru-N_5 (axial)	2.12	2.12	2.08	2.13	2.11
Ru-O_1	2.10	2.03	2.09	2.13	3.90
Ru-O_2	4.00	2.03	3.70	5.12	3.78
Ru-O_3 (water)	1.78	–	1.90	1.77	1.78

Table S8. Relative free energies (ΔG) in units of kcal/mol at M06-L, M06 and B3LYP-D3 levels of theory for complexes at Ru(IV) oxidation state (see Figure S42 above).

	M06-L		**M06**		**B3LYP-D3**	
	pH 0.0	**pH 7.0**	**pH 0.0**	**pH 7.0**	**pH 0.0**	**pH 7.0**
$[Ru^{IV}(T5a\text{-}\kappa\text{-}N^3O^2)(py)_2]^+$	0.0	0.0	0.0	0.0	0.0	0.0
$[Ru^{IV}(HT5a\text{-}\kappa\text{-}N^2O)(py)_2(O)]$	28.0	18.5	24.4	14.9	26.9	17.4
$[Ru^{IV}(T5a\text{-}\kappa\text{-}N^{2.5}O)(py)_2(OH)]$	30.9	21.4	27.7	18.2	33.2	23.7
$[Ru^{IV}(T5a\text{-}\kappa\text{-}N^2O)(py)_2(O)]$□	45.2	26.2	37.9	18.8	43.3	24.2
$[Ru^{IV}(T5a\text{-}\kappa\text{-}N^3)(py)_2(O)]$□	46.8	27.8	40.0	20.9	44.0	25.0

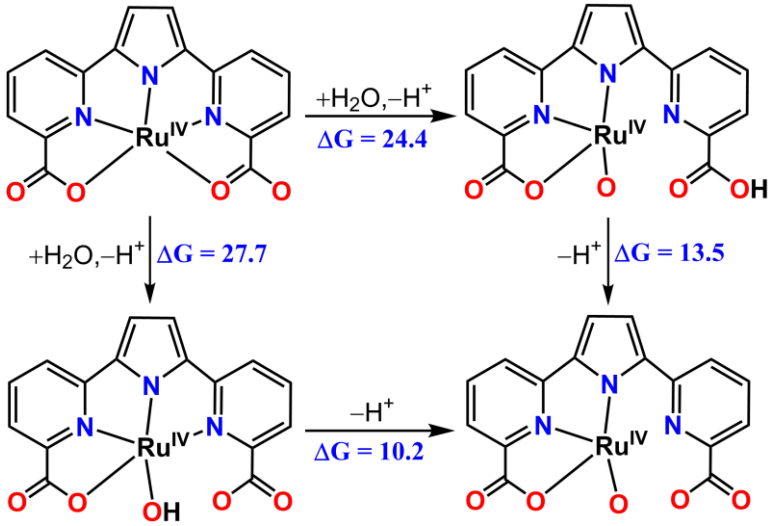

Scheme S6. Relative free energies (ΔG) in units of kcal/mol at *pH* = 0 at M06 level of theory for complexes at Ru(IV) oxidation state.

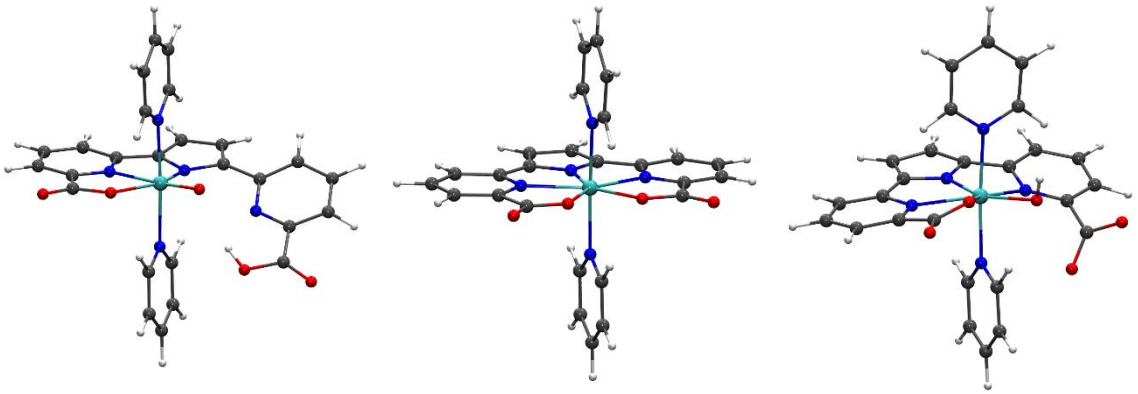

[Ru^{V}(HT5a-κ-N^{2}O)(py)$_2$(O)]$^{+}$ **[Ru^{V}(T5a-κ-N^{3}O^{2})(py)$_2$]$^{2+}$** **[Ru^{V}(T5a-κ-N$^{2.5}$O)(py)$_2$(OH)]$^{+}$**

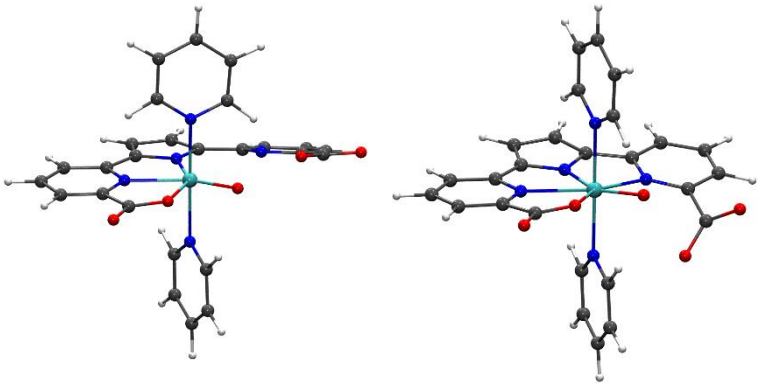

[Ru^{V}(T5a-κ-N^{2}O)(py)$_2$(O)] **[Ru^{V}(T5a-κ-N$^{2.5}$O)(py)$_2$(O)]**

Figure S43. Optimized structures at M06-L level of theory for complexes at Ru(V) oxidation state. Color code: Ru, cyan; N, blue; O, red; C, gray; and H, white.

Table S9. Selected bond lengths for optimized structures at M06-L level of theory for complexes at Ru(V) oxidation state (see Figure S43 above).

	$[Ru^{V}(HT5a)(py)_2]$		$[Ru^{V}(T5a)(py)_2]$		
	κ-N^2O (O)	**κ-N^3O^2**	**κ-$N^{2.5}O$ (OH)**	**κ-N^2O (O)**	**κ-$N^{2.5}O$ (O)**
Ru-N_1	2.16	2.16	2.18	2.15	2.28
Ru-N_2	2.08	2.04	2.06	2.13	2.12
Ru-N_3	3.38	2.16	2.35	3.16	2.38
Ru-N_4 (axial)	2.14	2.13	2.13	2.11	2.15
Ru-N_5 (axial)	2.13	2.13	2.10	2.13	2.09
Ru-O_1	2.00	2.01	2.05	2.10	2.13
Ru-O_2	4.08	2.01	3.75	3.77	3.51
Ru-O_3 (water)	1.70	–	1.91	1.71	1.72

Table S10. Relative free energies (ΔG) in units of kcal/mol at M06-L, M06 and B3LYP-D3 levels of theory for complexes at Ru(V) oxidation state (see Figure S43 above).

	M06-L		**M06**		**B3LYP-D3**	
	pH 0.0	**pH 7.0**	**pH 0.0**	**pH 7.0**	**pH 0.0**	**pH 7.0**
$[Ru^{V}(T5a\text{-}\kappa\text{-}N^3O^2)(py)_2]^{2+}$	0.0	0.0	0.0	0.0	0.0	0.0
$[Ru^{V}(HT5a\text{-}\kappa\text{-}N^2O)(py)_2(O)]^{+}$	13.8	4.3	14.5	5.0	17.1	7.6
$[Ru^{V}(T5a\text{-}\kappa\ N^{2.5}O)(py)_2(OH)]^{+}$	24.1	14.6	21.3	11.8	26.6	17.0
$[Ru^{V}(T5a\text{-}\kappa\text{-}N^2O)(py)_2(O)]$	30.0	11.0	31.7	12.7	36.9	17.8
$[Ru^{V}(T5a\text{-}\kappa\text{-}N^{2.5}O)(py)_2(O)]$	23.9	4.8	24.1	5.0	31.3	12.2

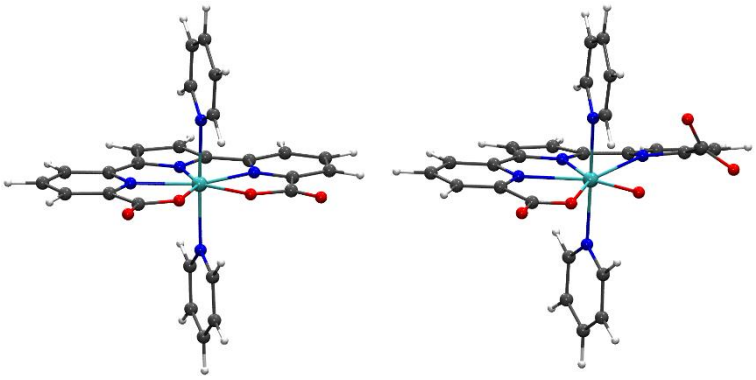

$[Ru^{VI}(T5a\text{-}\kappa\text{-}N^3O^2)(py)_2]^{3+}$ $[Ru^{VI}(T5a\text{-}\kappa\text{-}N^{2.5}O)(py)_2(O)]^{+}$

III

Figure S44. Optimized structures at M06-L level of theory for complexes at Ru(VI) oxidation state. Color code: Ru, cyan; N, blue; O, red; C, gray; and H, white.

Table S11. Selected bond lengths for optimized structures at M06-L level of theory for complexes at Ru(VI) oxidation state (see Figure S44 above).

	$[Ru^{VI}(T5a)(py)_2]^{3+}$	
	κ-N^3O^2	**κ-$N^{2.5}O$ (O)**
Ru-N_1	2.18	2.27
Ru-N_2	2.01	2.12
Ru-N_3	2.18	2.43
Ru-N_4 (axial)	1.97	2.10
Ru-N_5 (axial)	1.97	2.16
Ru-O_1	2.15	2.08
Ru-O_2	2.15	3.66
Ru-O_3 (water)	–	1.71

Table S12. Relative free energies (ΔG) in units of kcal/mol at M06-L, M06 and B3LYP-D3 levels of theory for complexes at Ru(VI) oxidation state (see Figure S44 above).

	M06-L		**M06**		**B3LYP-D3**	
	pH 0.0	**pH 7.0**	**pH 0.0**	**pH 7.0**	**pH 0.0**	**pH 7.0**
$[Ru^{VI}(T5a\text{-}\kappa\text{-}N^3O^2)(py)_2]^{3+}$	0.0	0.0	0.0	0.0	0.0	0.0
$[Ru^{VI}(T5a\text{-}\kappa\text{-}N^{2.5}O)(py)_2(O)]^{+}$	–4.3	–23.3	–10.8	–29.8	–2.6	–21.6

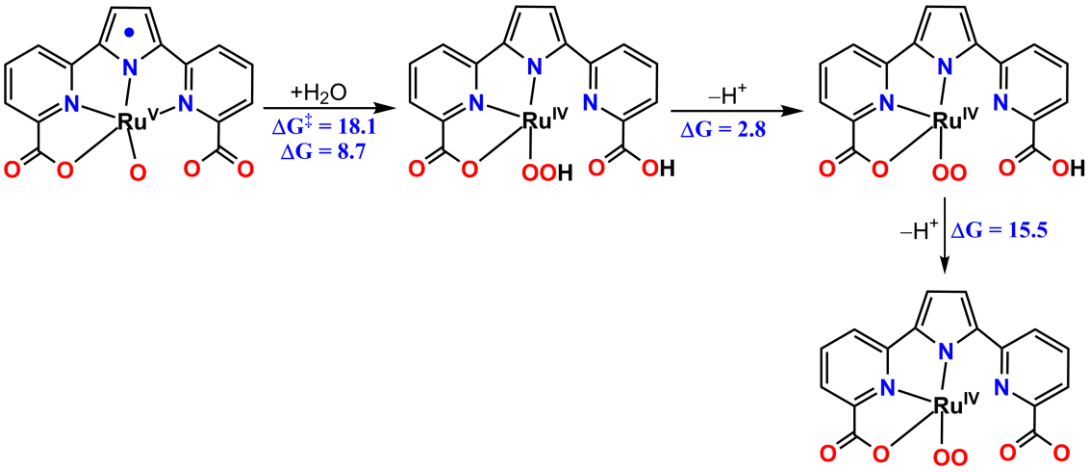

Scheme S7. Relative free energies (ΔG) in units of kcal/mol at pH 0 at M06 level of theory for complexes which form upon water nucleophilic attack on **[Ru^{V}(T5a-κ-N^{3}O•)(py)$_2$(O)]$^{+}$** species.

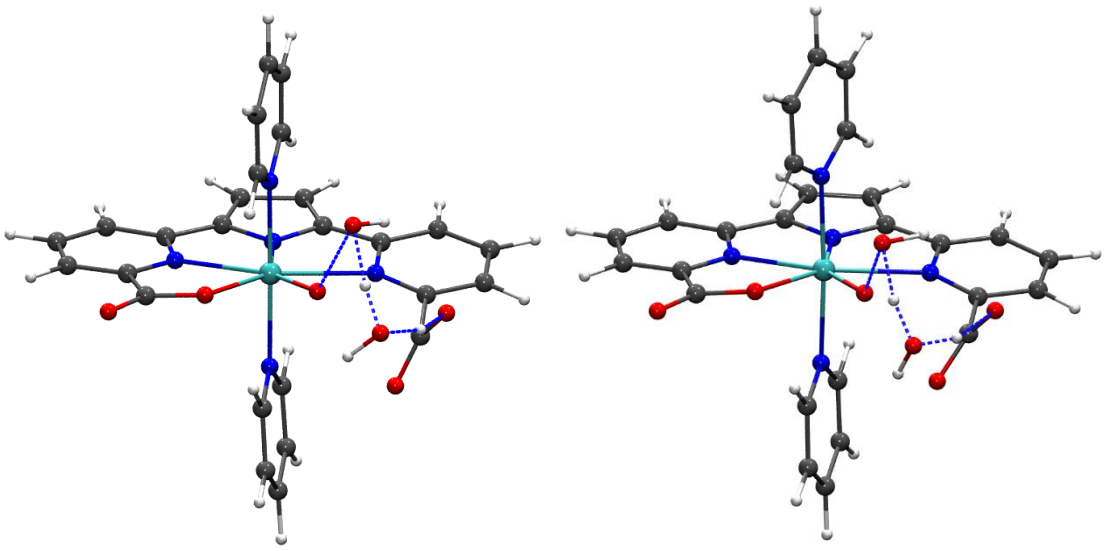

(a) **(b)**

Figure S45. Optimized water nucleophilic attack (WNA) transition state structures for **(a) [Ru^{V}(T5a-κ-N$^{2.5}$O)(O)] + 2 H$_2$O** and **(b) [Ru^{VI}(T5a-κ-N$^{2.5}$O)(O)] + 2 H$_2$O**

References

S1 Data collection with APEX II version v2013.4-1. Bruker (2007). Bruker AXS Inc., Madison, Wisconsin, USA.

S2 Data reduction with Bruker SAINT version V8.30c. Bruker (2007). Bruker AXS Inc., Madison, Wisconsin, USA.

S3 SADABS: V2012/1 Bruker (2001). Bruker AXS Inc., Madison, Wisconsin, USA. Blessing, Acta Cryst. **1995**, A51, 33-38.

S4 Data collection with CrystalClear-SM Expert 2.1 b29. Rigaku 2013.

S5 Data reduction with CrysAlisPro 1.171.38.37f (Rigaku OD, 2015).

S6 Empirical absorption corrrection using sperical harmònics implemented in Scale3 Abspack scaling algorithm, CrysAlisPro 1.171.38.37f (Rigaku OD, 2015).

S7 SHELXT; V2014/4 (Sheldrick 2014). Sheldrick, G.M. *Acta Cryst*. **2015**, A71, 3-8.

S8 SHELXle; C.B. Huebschle, G.M. Sheldrick & B. Dittrich; J. Appl. Cryst. **2011**, 44, 1281-1284.

S9 SHELXL; SHELXL-2014/7 (Sheldrick 2014). Sheldrick, G.M. *Acta Cryst*. **2015**, C71, 3-8.

S10 Platon: A Multipurpose Crystallographic Tool Utrecht University, Utrecht, The Netherlands, A.L. Spek 2011. Spek, A.L. Acta Cryst. **2009**, D65, 148-155.

S11 Matheu, R.; Neudeck, S.; Meyer, F.; Sala, X.; Llobet, A. *ChemSusChem* **2016**, *9*, 3361-3369.

S12 Domingos, S. R.; Luyten, H.; Anrooij, F. v.; Sanders, H. J.; Bakker, B. H.; Buma, W. J.; Hartl, F.; Woutersen, S. *Rev. Sci. Instrum.* **2013**, *84*, 033103

S13 Zhao, Y.; Truhlar, D. G. *Journal of Chemical Physics* **2006**, *125*.

S14 Andrae, D.; Häußermann, U.; Dolg, M.; Stoll, H.; Preuß, H. *Theoretica chimica acta*, *77*, 123.

S15 Hehre, W. J. *AB INITIO Molecular Orbital Theory*; Wiley, 1986.

S16 Frisch, M. J.; Trucks, G. W.; Schlegel, H. B.; Scuseria, G. E.; Robb, M. A.; Cheeseman, J. R.; Scalmani, G.; Barone, V.; Mennucci, B.; Petersson, G. A.; Nakatsuji, H.; Caricato, M.; Li, X.; Hratchian, H. P.; Izmaylov, A. F.; Bloino, J.; Zheng, G.; Sonnenberg, J. L.; Hada, M.; Ehara, M.; Toyota, K.; Fukuda, R.; Hasegawa, J.; Ishida, M.; Nakajima, T.; Honda, Y.; Kitao, O.; Nakai, H.; Vreven, T.; Montgomery Jr., J. A.; Peralta, J. E.; Ogliaro, F.; Bearpark, M. J.; Heyd, J.; Brothers, E. N.; Kudin, K. N.; Staroverov, V. N.; Kobayashi, R.; Normand, J.; Raghavachari, K.; Rendell, A. P.; Burant, J. C.; Iyengar, S. S.; Tomasi, J.; Cossi, M.; Rega, N.; Millam, N. J.; Klene, M.; Knox, J. E.; Cross, J. B.; Bakken, V.; Adamo, C.; Jaramillo, J.; Gomperts, R.; Stratmann, R. E.; Yazyev, O.; Austin, A. J.; Cammi, R.; Pomelli, C.; Ochterski, J. W.; Martin, R. L.; Morokuma, K.; Zakrzewski, V. G.; Voth, G. A.; Salvador, P.; Dannenberg, J. J.; Dapprich, S.; Daniels, A. D.; Farkas, Ö.; Foresman, J. B.; Ortiz, J. V.; Cioslowski, J.; Fox, D. J.; Gaussian, Inc.: Wallingford, CT, USA, 2009.

S17 Cramer, C. J. *Essentials of Computational Chemistry: Theories and Models*; Wiley, 2013.

S18 Zhao, Y.; Truhlar, D. G. *Theoretical Chemistry Accounts* **2008**, *120*, 215.

S19 Zhao, Y.; Truhlar, D. G. *Accounts of Chemical Research* **2008**, *41*, 157.

S20 Becke, A. D. *Journal of Chemical Physics* **1993**, *98*, 5648.

S21 Grimme, S.; Ehrlich, S.; Goerigk, L. *Journal of Computational Chemistry* **2011**, *32*, 1456.

S22 Marenich, A. V.; Cramer, C. J.; Truhlar, D. G. *J Phys Chem B* **2009**, *113*, 6378.

S23 Tissandier, M. D.; Cowen, K. A.; Feng, W. Y.; Gundlach, E.; Cohen, M. H.; Earhart, A. D.; Coe, J. V.; Tuttle, T. R. *Journal of Physical Chemistry A* **1998**, *102*, 7787.

S24 Camaioni, D. M.; Schwerdtfeger, C. A. *Journal Of Physical Chemistry A* **2005**, *109*, 10795.

S25 Kelly, C. P.; Cramer, C. J.; Truhlar, D. G. *J Phys Chem B* **2006**, *110*, 16066.

S26 Bryantsev, V. S.; Diallo, M. S.; Goddard, W. A. *Journal of Physical Chemistry B* **2008**, *112*, 9709.

S27 Lewis, A.; Bumpus, J. A.; Truhlar, D. G.; Cramer, C. J. *Journal of Chemical Education* **2004**, *81*, 596.

S28 Winget, P.; Cramer, C. J.; Truhlar, D. G. *Theoretical Chemistry Accounts* **2004**, *112*, 217.

S29 Ziegler, T.; Rauk, A.; Baerends, E. J. *Theoretica Chimica Acta* **1977**, *43*, 261.

S30 Noodleman, L. *Journal of Chemical Physics* **1981**, *74*, 5737.

S31 Cramer, C. J.; Truhlar, D. G. *Physical Chemistry Chemical Physics* **2009**, *11*, 10757.

S32 Yamaguchi, K.; Jensen, F.; Dorigo, A.; Houk, K. N. *Chemical Physics Letters* **1988**, *149*, 537.

S33 Soda, T.; Kitagawa, Y.; Onishi, T.; Takano, Y.; Shigeta, Y.; Nagao, H.; Yoshioka, Y.; Yamaguchi, K. *Chemical Physics Letters* **2000**, *319*, 223.

UNIVERSITAT ROVIRA I VIRGILI
SEVEN-COORDINATE COMPLEXES FOR WATER OXIDATION CATALYSIS: FROM MOLECULAR CHARACTERIZATION TO SOLID STATE PHOTOCATALYSIS
Roc Matheu Montserrat

Chapter 4

Tuning the water oxidation catalysis in seven-coordinate Ru complexes: quantification of the pi-pi stacking effect and intramolecular H bonding

New seven-coordinate Ru-bda and Ru-tda complexes are developed in this work to quantify the factors that determine their performance in water oxidation catalysis. In the first subchapter, new Ru-bda complexes bearing axial ligands that favor or disfavor intermolecular pi-pi stacking interactions are synthetized and tested as water oxidation catalysts.

In the second and third subchapters, Ru-tda complexes with one or two Ru-OH_2 group that does not promote intramolecular H bonding are prepared. The comparison of the electrochemical and catalytic data obtained allows quantifying the role of the intramolecular H bonding in the water oxidation catalysis with Ru-tda complexes.

IV

The chapter consist of the following indendependent papers:

PAPER C Paper C: Richmond, C. J.; Matheu, R.; Poater, A.; Falivene, L.; Benet-Buchholz, J.; Sala, X.; Cavallo, L.; Llobet, A. *Chem. Eur. J.* **2014**, *20*, 17282-17286

PAPER D Matheu, R.; Ertem, M. Z.; Gimbert-Suriñach, C.; Benet-Buchholz, J.; Sala, X.; Llobet, A. *ACS Catal.* **2017**, *7*, 6525–6532

PAPER E Matheu, R.; Benet-Buchholz, J.; Sala, X.; Llobet, A.; **2017**, *submitted*

PAPER C Supramolecular Water Oxidation with Ru-bda Based Catalysts

Richmond, C. J.; Matheu, R.; Poater, A.; Falivene, L.; Benet-Buchholz, J.; Sala, X.; Cavallo, L.; Llobet, A. *Chem. Eur. J.* **2014**, *20*, 17282-17286.

IV

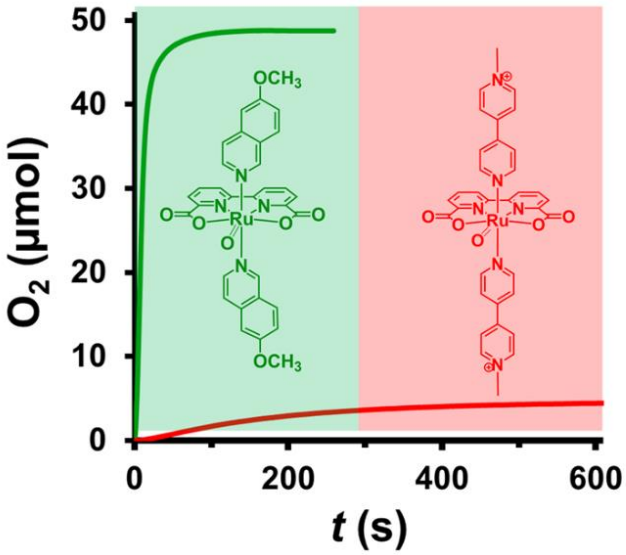

Abstract

Extremely slow and extremely fast new water oxidation catalysts based on the Ru-bda systems are reported with turnover frequencies in the range of 1 and 900 cycles/s respectively. Detailed analyses of the main factors involved in the water oxidation reaction have been carried out and are based on a combination of reactivity tests, electrochemical experiments and DFT calculations. These analyses, give a convergent interpretation that generates a solid understanding of the main factors involved in the water oxidation reaction, which in turn allows the design of catalysts with very low energy barriers in all the steps involved in the water oxidation catalytic cycle. We show that for this type of system π-stacking interactions are the key factors that influence reactivity and by adequately controlling them we can generate exceptionally fast water oxidation catalysts.

Contribution

Roc Matheu synthetized and characterized the new compounds, designed and discussed the manometic experiments and prepared the manuscript.

C 1 Introduction

Today a transition from fossil to solar fuels is needed in order to provide us with a clean and sustainable energy model. A viable option to achieve this challenge is to split water with sun light, however, before this can be realized, one of the key issues that needs to be understood and mastered is water oxidation catalysis. In this respect significant progress has been accomplished over the last five years, mainly based on molecular transition metal complexes.[1] Among the best water oxidation catalysts (WOCs) reported today are dinuclear Ru complexes that make O-O bonds via a water nucleophilic attack mechanism (WNA)[2] and a family of mononuclear Ru complexes based on the tetradentate ligand [2,2'-bipyridine]-6,6'-dicarboxylic acid (H_2bda; see Scheme 1 for the ligand structures described in this paper) that make O-O bonds via a bimolecular Ru-oxo coupling mechanism (I2M).[3] Spectacular performances both in terms of maximum turnover frequencies (TOF_{max}) and turnover numbers (*TON*s) have been reported, with [Ru(bda)(isoq)$_2$], **1**, (isoq = isoquinoline), which has a $TOF_{max} \approx 300\ s^{-1}$, comparable to that of the oxygen evolving systems of photosystem II (OEC-PSII). Complex **1** has been modified by introducing additional functionalities at the axial monodentate pyridyl ligands, allowing it to be anchored on carbon nano-tubes or oxide surfaces, both of which have proved to be useful methods to create efficient photoanodes for electrochemical cells.[4] For the success of the latter it is crucial that the water oxidation catalysis is sufficiently fast so that it can compete favorably with the potential non-productive and deactivating reactions. Thus a detailed mechanistic analysis at a molecular level is essential in order to gain knowledge about the origin of the activation barriers that are responsible for the rate determining step (rds). For the particular case of [Ru(bda)(Isoq)$_2$], **1**, it was found that the rds, under catalytic conditions at pH = 1.0, involves the dimerization of the complex at the formal oxidation state V generating a peroxo dinuclear complex, thus following a mechanism that involves the interaction of two M-O units (I2M). Further one electron oxidation of the peroxide generates the species responsible for the dioxygen release.[3b]

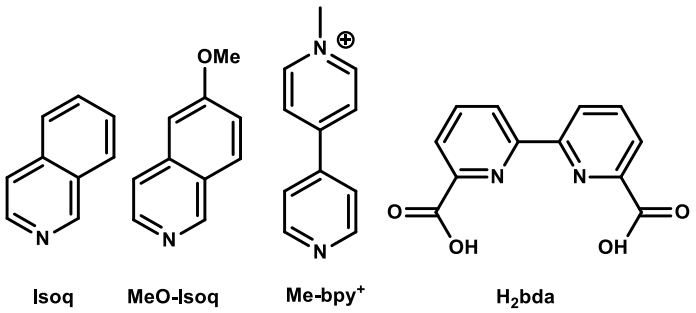

Scheme 1. Ligand structures and abbreviations.

IV

Attempts to improve the performance of Ru-bda complexes include the exertion of electronic perturbations at the metal site via sigma and π-interactions through substituents at the 4-position of the axial groups.[3] For example, the complex containing ethyl isonicotinate, [Ru(bda)(4-COOEt-py)$_2$], **2**, is significantly faster than the 4-methyl pyridine complex [Ru(bda)(4-Me-py)$_2$], **3**, with an impressive TOF_{max} of 119 s^{-1}. Another important factor that improves reaction rates is the π–stacking interaction of the axial ligands, as can be deduced by comparing the TOF_{max} of **1** (*c.a.* 300 s^{-1}) with that of **3** (*c.a.* 32 s^{-1}), which under similar conditions is about one order of magnitude slower.

In this work two new Ru-bda complexes; [Ru(bda)(L)$_2$]$^{n+}$, (L = MeO-isoq, n = 0, **4**; L = Me-bpy$^+$, n = 2, **5**(PF$_6$)$_2$) are reported in order to further explore the benefit of the π-stacking interaction for this type of catalyst. Whilst the complex containing the MeO-isoq was expected to lead to favorable π-stacking effects in water, the opposite was expected for that containing the Me-bpy$^+$ ligand due to its cationic nature and the non-parallel orientation of the pyridyl rings.

C 2 Results and discussion

Ru(bda) WOCs **4** and **5** were synthesized following the previously reported one-pot method,[3a,4b] mixing [RuCl$_2$(DMSO)$_4$] with the aryl axial ligands and bda^{2-} in MeOH and heating to reflux. The as prepared compounds were characterized by standard electrochemical and spectroscopic techniques (for full experimental details and spectra see ESI). An X-ray structure of **4** is presented in Figure 1, the bonding parameters are typical for a Ru(II) d^6 low spin complex,[5] however, the most interesting feature of the X-ray analysis is its 3D packing, where strong π-stacking interactions can be clearly observed between the isoquinoline ligands (See Figure 1). Spiraling columns of three separate molecules form, with distances between π-systems in the range of

3.4-3.7 Å, thus providing precedence for the stacking interactions also proposed to be present during the catalytic cycle.

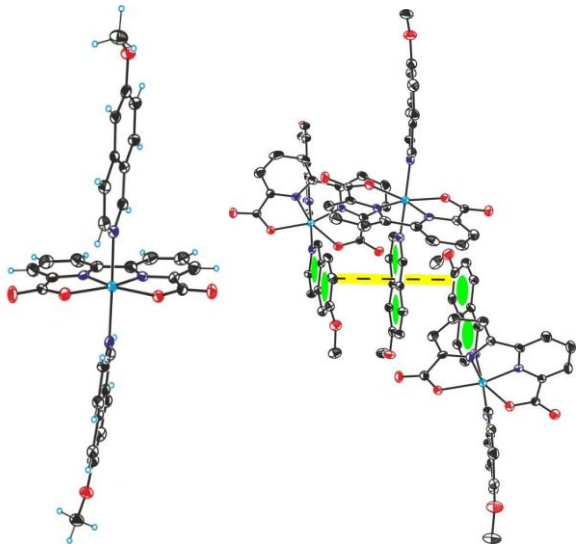

Figure 1. Left, Ortep view for the molecular X-ray structure of **4**. Ellipsoids are plotted at 50 % probability. Color codes: Ru, cyan; N, blue; O, red; C, black; H, light blue. Right, representation of the π-stacking observed in groups of three molecules. The distance between the aromatic rings is in the range 3.4-3.5 Å.

The electrochemical properties of **1**, **4** and **5** were investigated by means of cyclic voltammetry (CV) and differential pulse voltammetry (DPV) using the Hg/Hg_2SO_4 as a reference electrode with the results shown in Figure 2 and Table 1 and the supporting information. From these experiments it is found that the III/II redox potential is the one that suffers the strongest shift due to the electronic effects exerted by the axial ligands. On the other hand the IV/III and V/IV redox potentials are slightly modified. Ironically the most affected redox potential is irrelevant for the catalysis kinetics since the oxidation state II is not involved in the catalytic cycle, it acts only as a catalyst precursor to the oxidation state III that is the lowest oxidation stated involved in the catalytic cycle.[3a] For complex **4**, the V/IV wave is associated with a large electrocatalytic current, as can be observed in the CV of Figure 2, whereas for complex **5** the current is practically identical to the blank, indicating that for the latter the catalysis, if it exists, is very slow. Since the potentials for the redox couples correlated to the catalytic cycles of both **4** and **5** are very similar to each other, it seems probable that the large difference in their reactivity is relevant to the intermolecular stacking associations.

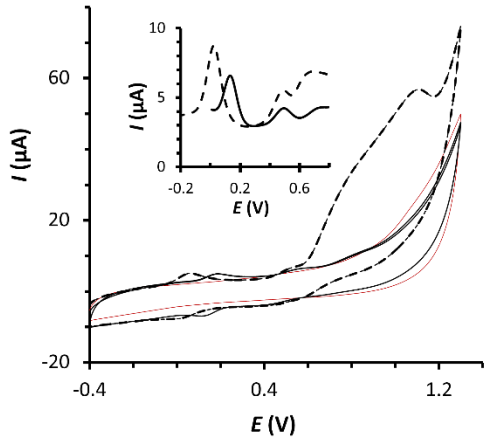

Figure 2. Cyclic voltammograms and DPV (inset) of **4** (dashed line, 0.32 mM), **5** (solid line, 0.32 mM) and bare glassy carbon electrode (red line) in a 0.1 M triflic acid solution containing 25% TFE. The scan rate was 100 mV/s and a glassy carbon electrode (0.07 cm^2) was used as working, Pt mesh was used as counter and Hg/Hg_2SO_4 (MSE) as reference electrodes.

IV

The assessment of the complexes' activity towards water oxidation was further investigated chemically using Ce(IV) as a sacrificial oxidant at pH = 1.0, the results are reported in Figure 3 and Table 1. Manometric gas measurements were used to assess the activity for both the individual catalysts (**1**, **4** and **5**) and 1:1 mixtures of **4** and **5**. Online mass spectrometry and headspace analysis with a Clark electrode were used to confirm O_2 as the only component of the gas produced (see ESI Figures S27-28)

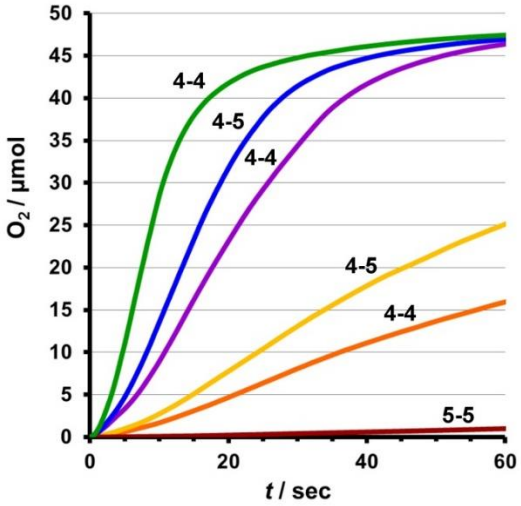

Figure 3. Oxygen evolution profile for Ru-bda catalysts **4** and **5** in varying catalyst ratios and concentrations, [CAN] = 0.1 M, in 2.0 mL 0.1 M triflic acid at 25 °C; [**4**] = 5.0 μM green, [**4**] = [**5**] = 2.5 μM blue, [**4**] = 2.5 μM purple, [**4**] = [**5**] = 1.25 μM yellow, [**4**] = 1.25 μM orange, [**5**] = 5.0 μM red.

Table 1 shows the impressive performance of the Ru-bda family of catalysts under different conditions at pH = 1.0. For instance in entry 3, complex **4** 5.0 µM/Ce(IV) 100 mM (1/20000) generates oxygen at a maximum velocity (v_{max}) of 3.81 µmols/s (TOF_{max} = 381 s^{-1}) with basically 100% oxidative efficiency that illustrates the ruggedness of this family of catalysts.

Table 1. Reactivity and electrochemical parameters for Ru-bda catalysts.

Entry[a]	WOC	[WOC] / µM	[CeIV] / mM	v_{max} / µmol s^{-1} [c]	TOF_{max} / s^{-1} [c]	$E_{1/2}$ vs. NHE [d]
1	4	1.25	100	0.320 ±0.005	130 ±2	0.67 1.14 1.35
2	4	2.5	100	1.26 ±0.01	252 ±2	
3	4	5.0	100	3.81 ±0.16	381 ±16	
4[b]	4	50	350	23.07 ±0.08	923 ±3	
5	5	2.5	100	0.0055±0.0002	1.10 ±0.02	0.78 1.15 1.37
6	5	5.0	100	0.0200±0.0002	2.00 ±0.02	
7	5	20	100	0.350 ±0.008	8.8 ±0.2	
8	1	1.25	100	0.104 ±0.001	41.8 ±0.4	
9	1	2.5	100	0.637 ±0.006	127 ±1	0.70 1.17 1.38
10	1	5.0	100	2.56 ±0.01	256 ±1	
11	4+5	1.25+1.25	100	0.52 ±0.07	103 ±3	
12	4+5	2.5+2.5	100	2.01 ±0.07	201 ±7	

[a] Headspace = 8.5 mL, Temperature = 25 °C, solvent = 3% TFE in 0.1 M triflic acid (2.0 mL), [CAN] = 0.1 M. [b] Headspace = 27.0 mL, Temperature = 25 °C, solvent = 3% TFE in 0.1 M triflic acid (0.5 mL), [CAN] = 0.35 M. [c] Calculations based on averaged data obtained from duplicate reactions. [d] III/II, IV/III and V/IV redox potentials respectively in V *vs*. NHE. Potentials converted from MSE. [e] data from reference 3b.

A kinetic analysis (see ESI Figure S24 and S25) of the reactivity of complexes **4** and **5** based on initial rates, maintaining the Ce(IV) concentration constant and varying the concentration of **4** and **5**, gives a second order behavior, which is again consistent with the fact that the stacking interactions are involved in the rate determining step.

It is also very interesting to point out that under identical conditions (entries 1-3 *vs.* 8-10), complex **4** containing the MeO substituted isoquinoline is about two to three times faster than the non-substituted isoquinoline complex, **1**. This can be attributed to a better stacking match in rds transition state (TS), due to the offset of the two Ru-bda moieties. In sharp contrast, under

identical conditions, complex **5** containing the Me-bpy$^+$ ligand has maximum velocities that are 190 and 128 times slower than **4** and **1** respectively (see entries 3, 6 and 10). Clearly here the positive charge around the Me-bpy$^+$ ligand outweighs the stacking effect and as a consequence lacks the low energy pathway for oxygen formation provided by the bimolecular mechanism is less favorable.

In order to extract further evidence regarding the nature of the π-stacking interaction 1:1 mixtures of complexes **4** and **5** were evaluated (see Figure 3. and Table 1 entries 11-12). Entry 11 shows that a 1.25 µM:1.25 µM combination of **4**:**5** and 100 mM Ce(IV) gives a maximum velocity of 0.52 µmols/s. Combining this data with the rest of the table, the following considerations and conclusions can be extracted: i) Following a bimolecular pathway, three types of interactions can contribute to reach this rate; the **4**:**4**, the **4**:**5** or the **5**:**5**. The latter, as we have shown previously, is more than 2 orders of magnitude slower than the **4**:**4** and thus cannot significantly contribute to the final velocity observed; ii) If there was only the **4**:**4** type of interaction then the rate obtained should be 0.32 µmols s^{-1}, similar to entry 1 of the Table. The fact that the rate observed is 0.52 µmols/s clearly manifests the existence of a **4**:**5** interaction; iii) Assuming no contribution from the **4**:**4** interaction, then the maximum velocity for the **4**:**5** (1.25 µM:1.25 µM) interaction would be 0.52 µmols/s, and hence a TOF_{max} of 103 s^{-1}; iv) For the **4**:**4** (1.25 µM:1.25 µM) interaction under these conditions (entry 2) a rate of 1.26 µmols s^{-1} is observed, resulting in a TOF_{max} of 252 s^{-1}.

IV

If the activation energy in the rds is inversely proportional to the strength of the stacking interaction, then the rate of oxygen production should also follow this trend, which is what was observed for 1.25 µM:1.25 µM pairs of **4** and **5**, **4**:**4** > **4**:**5** >> **5**:**5** (1.26 > 0.52 >> --). A similar analysis with identical conclusions can be carried out by comparing the 2.5 µM combination (entry 12, 3 and 6) giving the same trend, **4**:**4** > **4**:**5** >> **5**:**5** (3.81 > 2.01 >> 0.02).

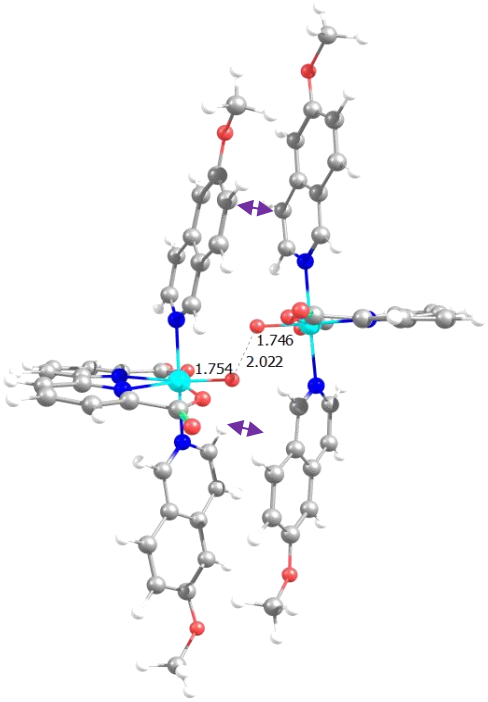

Figure 4. Calculated TS structure for the **4**:**4** dimer (distances in Å).

DFT calculations were performed to support the scenarios emerging from the experiments. Focusing on the O-O bond formation step, the free energy barrier, calculated as the free energy difference between the dimeric [Ru-O - - O-Ru]$^{2+}$ TS and two separated [Ru(V)=O]$^{+}$ species, increases from 18.0 kcal/mol for **4:4** (see Figure 4), to 20.7 kcal/mol for **1:1**, to 24.5 kcal/mol for **4:5**, in very good qualitative agreement with the experimental trend. Transition state structural analysis of **1:1** and **4:4** also evidences shorter distances between the tips of the axial ligands in the **4:4** TS (3.24 Å) compared to the **1:1** TS (3.54 Å), suggesting that stronger stacking, stabilizes the **4:4** TS relative to the **1:1** TS (see Figure S30.). To have additional support for this hypothesis, the stacked axial ligands were rigidly extracted from **4:4** TS and **1:1** TS, and their interaction energy was calculated. This results in a stacking interaction energy of 6.5 kcal/mol for the MeO-Isoq dimer, while for the unsubstituted Isoq dimer the stacking energy amounts to 3.5 kcal/mol only. Natural population analysis indicates that the increased stacking energy of the MeO-Isoq dimer is due to stabilizing electrostatic interaction between the positively charged C atom bearing the OMe substituent on one MeO-Isoq ligand, and negatively charged C atoms of the other MeO-Isoq ligand, see Figure S31. This arrangement therefore has a favorable off-center-parallel stacking geometry between aromatic units.[6] In addition, analysis of the steric maps of the monomeric species [Ru(V)=O]$^{+}$, see Figure S32, clearly indicates that the Me-bpy^{+} ligands in **5**, are also destabilized by the higher steric hindrance between the Me-bpy^{+} ligands. Steric hindrance is instead negligible in the [Ru(V)=O]$^{+}$ species **1** and **4**, see again Figure S32.

Finally under extreme conditions (entry 4, Table 1) the system **4** 50 µM/Ce(IV) 350 mM, yields an impressive maximum velocity of oxygen generation of 23.07 µmols s^{-1} which implies a TOF_{max} of 923 cycles/s, which is among the highest reported for a molecular WOC.[7]

C 3 Conclusions

In conclusion convergent chemical, electrochemical and DFT experiments involving Ru-bda type catalysts generates a solid knowledge on these systems regarding the key factors that influence their reactivity. This knowledge in turn allows the judicial design of systems for extremely fast water oxidation reactivity, as is the case of **4**, which is vital for the building up of efficient photoanodes.

IV

C 4 Experimental Section

Materials: $RuCl_3 \cdot 3H_2O$ and 6-methoxyisoquinoline were supplied by Precious Metals Online PMO Pty Ltd and Apollo Scientific. All other reagents were purchased from Sigma-Aldrich. 6,6'-Dicarbonixilic acid-2,2'-dipyridyl (H_2bda),[4] $[RuCl_2(DMSO)_4]$[8] and [1-Methyl-4,4'-bipyridinium]PF_6 (Me-bpy(PF_6))[9] were prepared according to the reported procedures. Methanol (MeOH) was distilled over Mg/I_2. All synthetic manipulations under N_2/Ar were performed using standard Schlenk tubes and vacuum-line techniques.

Synthesis of 4: The procedure was modified from a previously reported procedure.[4] $[RuCl_2(DMSO)_4]$ (100 mg, 0.21 mmol), 6,6'-dicarbonixilic acid-2,2'-dipyridyl (H_2bda) (59.50 mg, 0.2 mmol) and Et_3N (0.1 mL) were dissolved in anhydrous MeOH (10 mL) and heated to reflux for 3 hours under Ar. 6-methoxyisoquinoline (65 mg, 0.41 mmol) was subsequently added to the solution and the reaction was then heated to reflux overnight. The product precipitated as a brown powder, which was filtered, washed with acetone (3 x 15 mL) and diethyl ether (3 x 15 mL) and dried under vacuum (20 mg, 18% yield based on Ru). ^{1}H NMR (400 Hz, [d4]-methanol): δ= 3.91 (6H, s), 7.19 (2H, d, J=2.3 Hz), 7.23 (2H, dd, J=2.3, 9.0 Hz), 7.50 (4H, q, J=7.58 Hz), 7.75 (2H, d, J=9.0 Hz), 7.92 (2H, t, J=7.9 Hz), 8.05 (2H, dd, J=0.9, 7.9 Hz), 8.42 (2H, s), 8.66 (2H, dd, J=0.9, 7.9 Hz). ^{13}C NMR (500Hz, [d4]-methanol) δ = 28.0, 102.5, 119.5, 120.4, 123.2, 123.6, 124.4, 127.5, 130.1, 136.1, 141.4, 153.2, 154.8, 159.1, 161.4, 172.7. UV-vis [λ_{max}, nm (ε, M^{-1} cm^{-1})]: 237 (122000), 300 (37000) and 400 (16000). $E_{1/2}$ (MeOH/Acetone 1:1, 0.1M $TBAPF_6$): 0.10 V vs Hg/Hg_2SO_4. MALDI$^+$-HRMS m/z: Calc for $\{(MeOIsoq)_2Ru(bda)\}^+$: 662.0734, found: 662.0811 (12 ppm). *Anal.* Calc. for **4**$\cdot 3.5H_2O$ ($C_{32}H_{31}N_4O_{9.5}Ru$): C, 53.04%; H, 4.31%; N, 7.73%. Found: C, 52.96%; H, 3.97%; N, 7.61%.

Synthesis of 5: The procedure was modified from a previously reported procedure.[4] $[RuCl_2(DMSO)_4]$ (75 mg, 0.17 mmol), 6,6'-dicarbonixilic acid-2,2'-dipyridyl (H_2bda) (50.6 mg, 0.17 mmol) and Et_3N (0.1 mL) were dissolved in anhydrous MeOH (6 mL) and heated to reflux for 3 hours under Ar. [1-Methyl-4,4'-bipyridinium]PF_6 ([Me-bpy]PF_6) (100 mg, 0.31 mmol) was subsequently added to the solution and then heated to reflux overnight. A brown solid (95mg) precipitated as a brown powder, which was filtered, washed with MeOH (3 x 5 mL) and diethyl ether (3 x 15mL) and allowed to dry in air. The dry precipitated was dissolved in 80 mL of 1:1 MeOH/acetone and evaporated to a final volume of 10 mL. Then 40 mL of

MeOH were added and the solvent evaporated until precipitation occurred. The suspension was filtered and the solid washed with MeOH (10 mL) and diethyl ether (3 x 15 mL) and finally dried under vacuum (45 mg, 27% yield based on Ru). ^{1}H NMR (400Hz, [d4]-methanol): δ=7.92 (4H, dd, J=1.5, 5.4 Hz), 8.15 (4H, m), 8.32 (4H, dd, J=1.36, 5.4 Hz), 8.55 (4H, d, J=6.8 Hz), 8.86 (2H, dd, J=1.5, 7.5 Hz), 9.17 (4H, d, J=6.8 Hz). ^{13}C NMR (500Hz, [d4]-methanol) δ = 46.1, 121.5, 124.1, 124.3, 124.6, 131.6, 140.3, 144.95, 150.6, 152.5, 154.7, 158.5, 171.9. UV-vis [λ_{max}, nm (ε, M^{-1} cm^{-1})]: 250 (50000), 300 (29000), 510 (16800). $E_{1/2}$ (MeOH/acetone 1:1, 0.1 M $TBAPF_6$): 0.17 V vs Hg/Hg_2SO_4. MALDI$^+$-HRMS m/z: Calc. for {[Ru(bda)(MeBpy)$_2$]PF_6-dctb}$^+$: 1081.2322, found: 1081.2314 (1ppm). *Anal.* Calc. for **5**·2H_2O ($C_{34}H_{32}F_{12}N_6O_6P_2Ru$): C, 40.37%; H, 3.19%; N, 8.31%. Found: C, 40.14%; H, 2.76 %; N, 8.11 %.

C 5 Acknowledgements

CR thanks the European Commission and Marie Curie Actions for an Intra-European Fellowship. AL thanks MINECO CTQ-2013-49075-R and "La Caixa" foundation for financial support. M.R. thanks "La Caixa" foundation for a PhD grant. XS thanks MINECO CTQ2011-26440 for financial support. LC thanks King Abdullah University of Science and Technology for financial support. AP thanks the Spanish MINECO for a Ramón y Cajal contract (RYC-2009-05226) and European Commission for a Career Integration Grant (CIG09-GA-2011-293900).

IV

C 6 References

1 "Molecular Water Oxidation Catalysis: A Key Topic for New Sustainable Energy Conversion Schemes." Edited by A. Llobet. **2014** John Wiley and Sons Ltd. ISBN: 9781118413371.

2 a) S. Neudeck, S. Maji, I. Lopez, S. Meyer, F. Meyer, A. Llobet, *J. Am. Chem. Soc.* **2014**, *136*, 24-27. (b) I. López, M. Z. Ertem, S. Maji, J. Benet-Buchholz, A. Keidel, U. Kuhlmann, P. Hildebrandt, C. J. Cramer, V. S. Batista, A. Llobet, A. *Angew. Chem. Int. Ed.* **2014,** *53*, 205-210.

3 a) L. Duan, L. Wang, A. K. Inge, A. Fischer, X. Zou, L. Sun, *Inorg. Chem.* **2013**, *52*, 7844-7852. b) L. Duan, F. Bozoglian, S. Mandal, B. Stewart, T. Privalov, A. Llobet, L. Sun, *Nat. Chem.* **2012**, *4*, 418-423.

4 a) Y. Gao, X. Ding, J. Liu, L. Wang, Z. Lu, L. Li, L. Sun, *J. Am. Chem. Soc.* **2013**, *135*, 4219-4222; b) F. Li, B. Zhang, X. Li, Y. Jiang, L. Chen, Y. Li, L. Sun, *Angew. Chem. Int. Ed.* **2011**, *50*, 12276-12279; *Angew. Chem.* **2011**, *123*, 12484-12487.

5 a) C. Di Giovanni, L. Vaquer, X. Sala, J. Benet-Buchholz, A. Llobet, *Inorganic Chemistry* **2013**, *52*, 4335-4345; b) N. Planas, G. Christian, S. Roeser, E. Mas-Marza, M.-R. Kollipara, J. Benet-Buchholz, F. Maseras, A. Llobet, *Inorg. Chem.* **2012**, *51*, 1889-1901.

6 C. R. Martinez, B. L. Iverson, *Chem. Sci.* **2012**, *3*, 2191-2201.

7 (a) H. Lv, J. Song, Y. V. Geletii, J. W. Vickers, J. M. Sumliner, D. G. Musaev, P. Kögerler, P. F. Zhuk , J. Bacsa, G. Zhu, C. L. Hill, *J. Am. Chem. Soc.* **2014**, 136, 268–9271. (b) L. Wang, L. Duan, Y. Wang, M. Ahlquist, L. Sun, *Chem. Commun*. **2014**, *50*, 12947-12950.

8 I. P. Evans, A. Spencer, G. Wilkinson, *J. Chem. Soc., Dalton Trans.* **1973**, 204-209.

9 E. H. Yonemoto, R. L. Riley, Y. I. Kim, S. J. Atherton, R. H. Schmehl, T. E. Mallouk, *J. Am. Chem. Soc.* **1992**, *114*, 8081-8087.

C 7 Supporting Information

Paper C: Supramolecular Water Oxidation with Ru-bda Based Catalysts

Outline

IV

Methods and instrumentation

All electrochemical experiments were performed on a PAR 263A EG&G potentiostat or on an IJ-Cambria HI-660 potentiostat, using a three-electrode cell. Glassy carbon (S = 0.07 cm^2) as working electrode, platinum mesh as counter electrode, and Hg/Hg_2SO_4 (saturated K_2SO_4 solution) as reference electrode unless otherwise indicated. $E_{1/2}$ values reported in this work were estimated from Cyclic Voltammetry (CV) experiments as the average of the oxidative and reductive peak potentials or by DPV when indicated. Differential Pulse Voltammetries (DPV) were performed with a pulse amplitudes of 0.05 V, pulse widths of 0.05 s, sampling width of 0.02 s, and a pulse period of 0.1 s.

Matrix-assisted laser desorption ionization (MALDI) mass spectrometry (MS) experiments were performed on a Bruker Daltonics Autoflex equipped with a nitrogen laser (337 nm).

UV–Vis spectroscopy was performed on a Cary 50 Bio (Varian) UV–Vis spectrophotometer with 1 cm quartz cells.

A 400 MHz Bruker Avance II spectrometer and a Bruker Avance 500 MHz were used to carry out NMR spectroscopy. FT-IR measurements carried out on a Bruker Optics FTIR Alpha spectrometer equipped with a DTGS detector, KBr beamsplitter at 4 cm^{-1} resolution.

Elemental analysis was performed by the Elemental Analysis Unit at the University of Santiago de Compostela (Spain) on an EA-1108, CHNS-O elemental analyser from Fisons Instruments.

Manometric measurements were carried out with a Testo 521 differential pressure manometer, with an operating range of 1-100 hPa and an accuracy of within 0.5% of the measurement, coupled to thermostatted reaction vessels for dynamic monitoring of the headspace pressure above each reaction. A 0.1 M triflic acid solution (pH 1.0, 0.45−3.2 mL) was added to the sample vessel containing $Ce(NH_4)_2(NO_3)_6$ under stirring and the equivalent volume added to the reference vessel. Once the CAN was dissolved, the pressures were equalised and a blank solution of triflic acid (50−100 µL) was injected into the reference cell and a trifluoroethanol/triflic acid (1:2 by volume) solution of catalyst (50−100 µL) was then injected into the sample cell with continued stirring and the pressure difference was recorded vs. time. The composition of the gas evolved was determined by online mass-spectrometry and Clark electrode experiments.

Online MS monitoring of the gas evolution was performed on a Pfeiffer Ominstar GSD 301C mass spectrometer. Typically, 16.04 mL vials containing a solution of CAN (0.175 M) in 0.1 M triflic acid (1.0 mL) were degassed with nitrogen then connected to the apparatus capillary tubing. Subsequently, a previously degassed solution of catalyst (0.2-0.4 mM, 50-100 µL) was introduced using a Hamilton gastight syringe, and the headspace gas was dynamically monitored.

Oxygen detection was also carried out by inserting a gas-phase Clark-type electrode (Unisense Ox-N needle microsensor) in the headspace of the manometric reaction vessel and simultaneously measuring oxygen concentration *vs*. time and pressure difference *vs*. time

X-ray Crystal Structure Determination. Complex **4** was dissolved in methanol and water and under slow evaporation at room temperature suitable crystals were obtained. The measured crystals were prepared under inert conditions immersed in perfluoropolyether as protecting oil for manipulation.

Data collection: Crystal structure determination for **4** was carried out using a Apex DUO Kappa 4-axis goniometer equipped with an APPEX 2 4K CCD area detector, a Microfocus Source E025 IuS using MoK_α radiation, Quazar MX multilayer Optics as monochromator and a Oxford Cryosystems low temperature device Cryostream 700 plus (T = -173 ˚C). Full-sphere data collection was used with ω and φ scans. *Programs used:* Data collection APEX-2, data reduction Bruker Saint V/.60A and absorption correction SADABS.

IV

Structure Solution and Refinement: Crystal structure solution was achieved using direct methods as implemented in SHELXTL and visualized using the program XP. Missing atoms were subsequently located from difference Fourier synthesis and added to the atom list. Least-squares refinement on F^2 using all measured intensities was carried out using the program SHELXTL. All non hydrogen atoms were refined including anisotropic displacement parameters.

Comments to the structure: The asymmetric unit contains two independent molecules of the metal complex, six water molecules and two methanol molecules. This compound crystallizes in the chiral space group $P2_1$. The water molecules and the methanol molecules are generating a network of hydrogen bonds with the carboxylate groups of the metal complex. In the crystal packing π-stacking can be observed in groups of three molecules. The distance between aromatic rings is in the range 3.4-3.7 Å.

Computational Details:

All the DFT static calculations were performed at the GGA level with the Gaussian09 set of programs,[S1] using the M06L functional.[S2] During the geometry optimizations, the electronic configuration of the molecular systems was described with the standard split-valence basis set with a polarization function of Ahlrichs and co-workers for H, C, N, O, and Cl (SVP keyword in Gaussian).[S3] For Ru we used the small-core, quasi-relativistic Stuttgart/Dresden effective core potential, with an associated valence basis set contracted (standard SDD keywords in gaussian09).[S4] The geometry optimizations were performed without symmetry constraints, and the characterization of the located stationary points was performed by analytical frequency calculations. The reported energies have been refined via single point calculations on the M06L geometries with triple ζ valence plus polarization (TZVP keyword in Gaussian) using the M06 functional,[S5] however estimating solvent effects with the polarizable continuum solvation model PCM using water as solvent.[S6]

Since in this work we had to describe the interaction between two moieties in the reaction mechanism, careful treatment of the entropic contribution to the free energy was fundamental. In this respect, it is clear that the contribution calculated in the gas phase (p = 1 atm) most likely exaggerates the entropic contribution.[S7] Thus, some kind of correction is needed and various recipes have been proposed in the literature, like using only a fraction of the gas-phase entropy, or using a higher pressure that would represent better the liquid state. In the present work we adopted the latter, and all the thermochemical analysis was performed at p = 1354 atm, as suggested by Martin et al.[S7a]

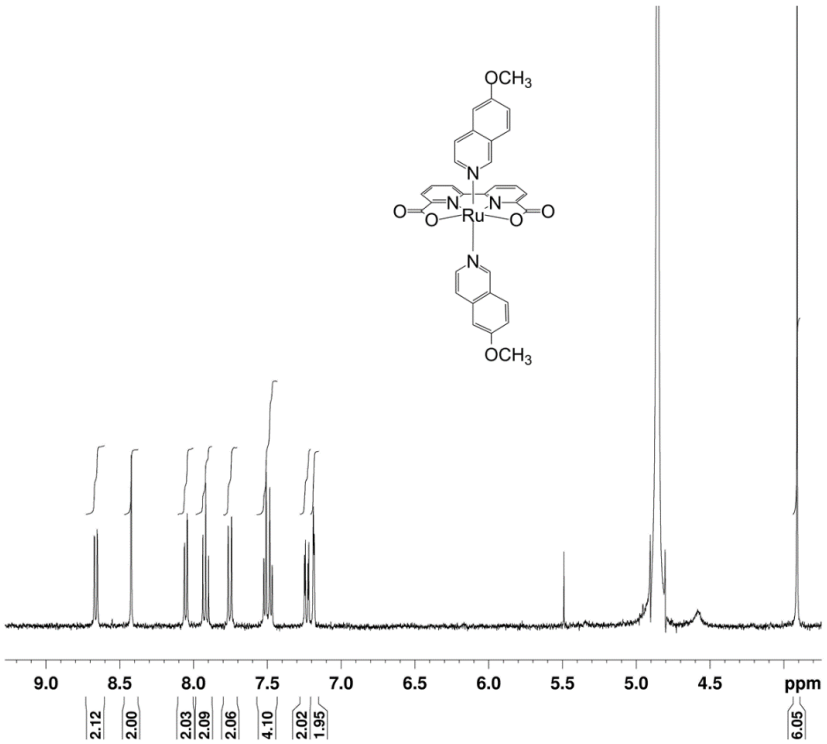

Figure S1: ^{1}H NMR of **4** in [d4]-Methanol/[d6]-acetone 1:1 mixture.

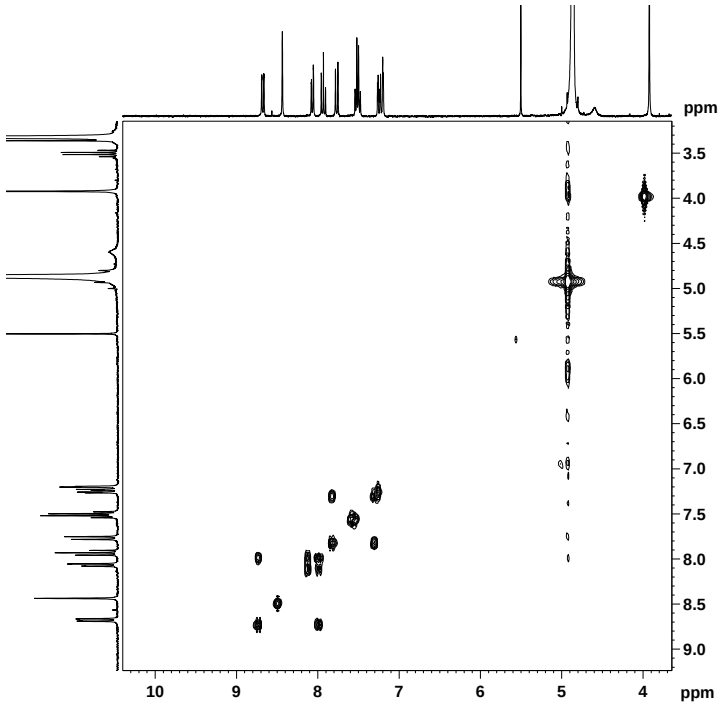

Figure S2: ^{1}H-^{1}H COSY NMR of **4** in [d4]-Methanol/[d6]-acetone 1:1 mixture.

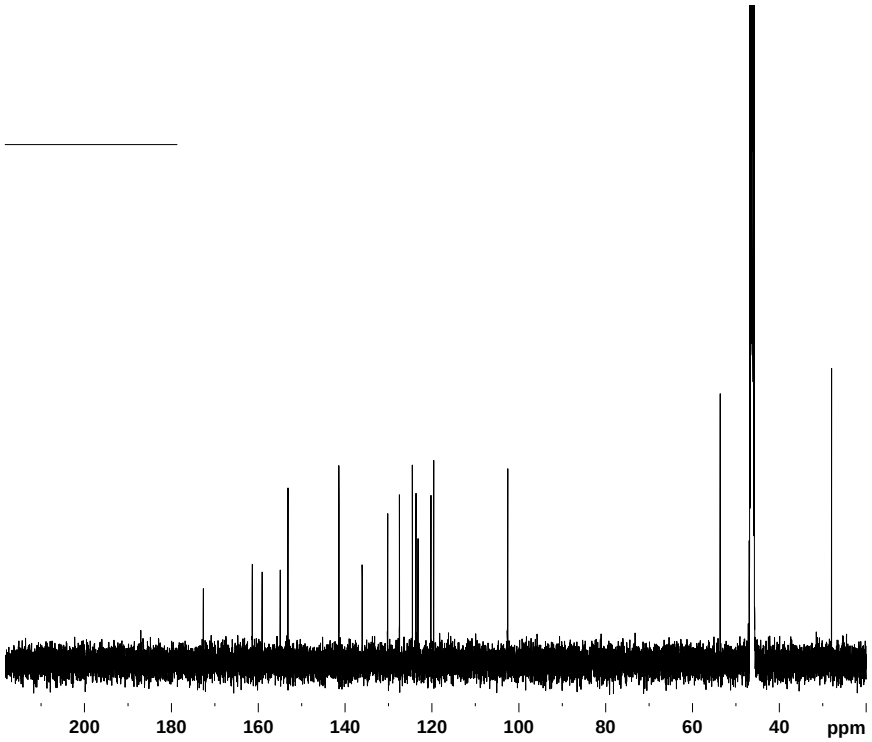

Figure S3: $^{13}C\{H\}$ NMR of **4** in [d4]-Methanol/[d6]-acetone 1:1 mixture.

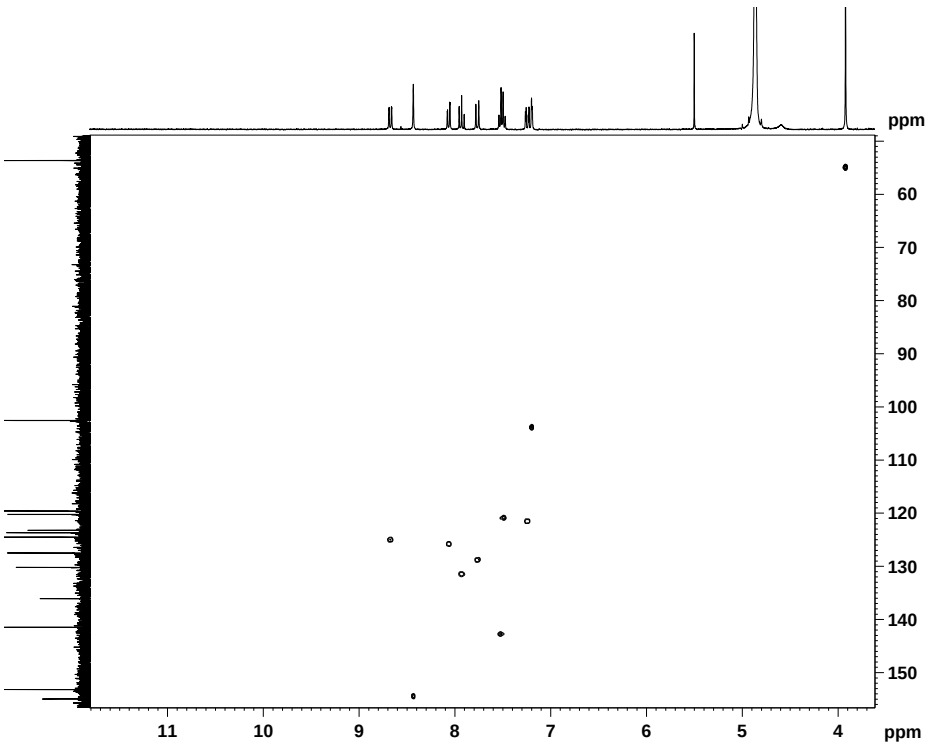

Figure S4: ^{1}H-^{13}C HSQC NMR of **4** in [d4]-Methanol/[d6]-acetone 1:1 mixture.

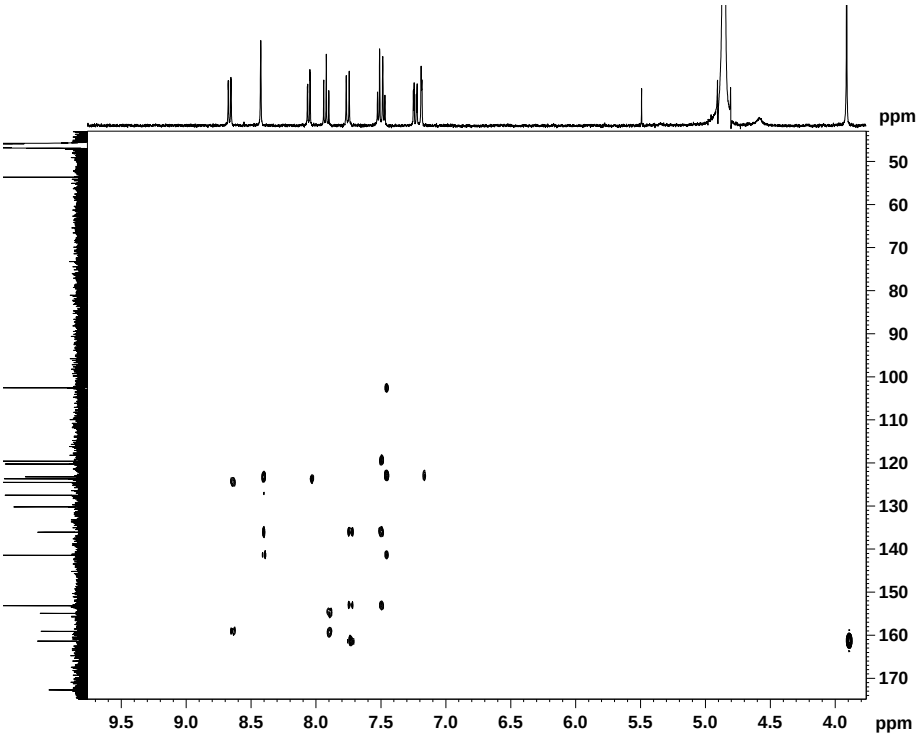

IV

Figure S5: ^{1}H-^{13}C HMBC NMR of **4** in [d4]-Methanol/[d6]-acetone 1:1 mixture.

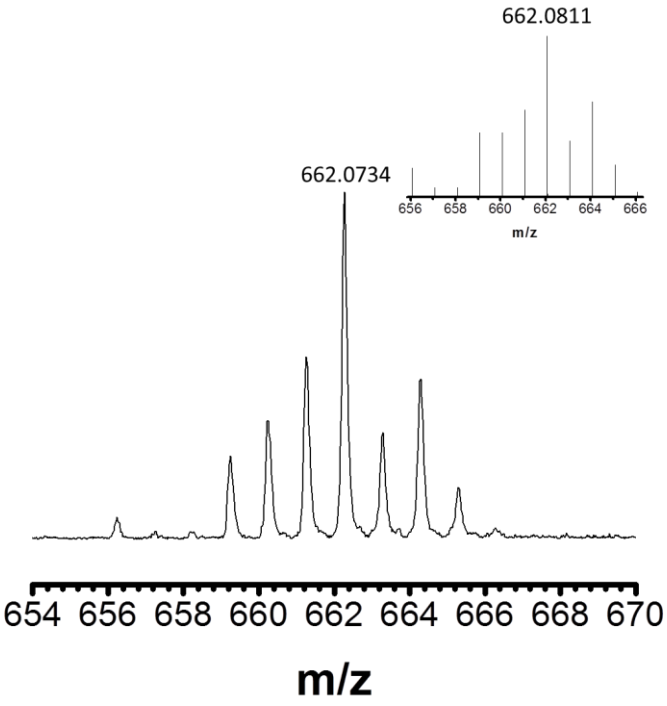

Figure S6: High Resolution Mass Spectrum of compound **4** in a MALDI^{+} dctb matrix**.** The molecular peak was found as **4**$^{+}$. Inset shows simulated m/z pattern.

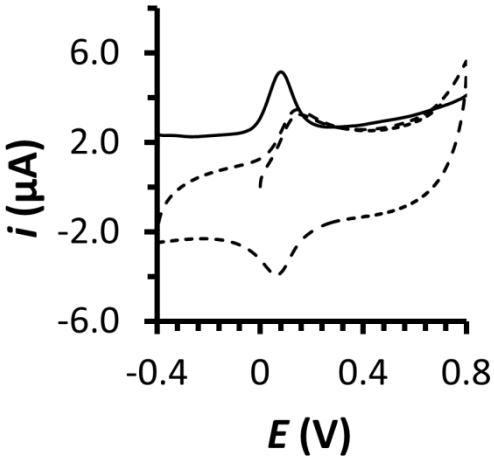

Figure S7: Cyclic voltammogram (dashed line) and DPV (solid line) of **4** (0.5 mM) in 0.1 M n-Bu_4NPF_6 MeOH/acetone 1:1 mixture. The scan rate was 100 mV/s and a glassy carbon electrode (0.07 cm^2) was used as working, Pt mesh was used as counter and Hg/Hg_2SO_4 as reference electrodes.

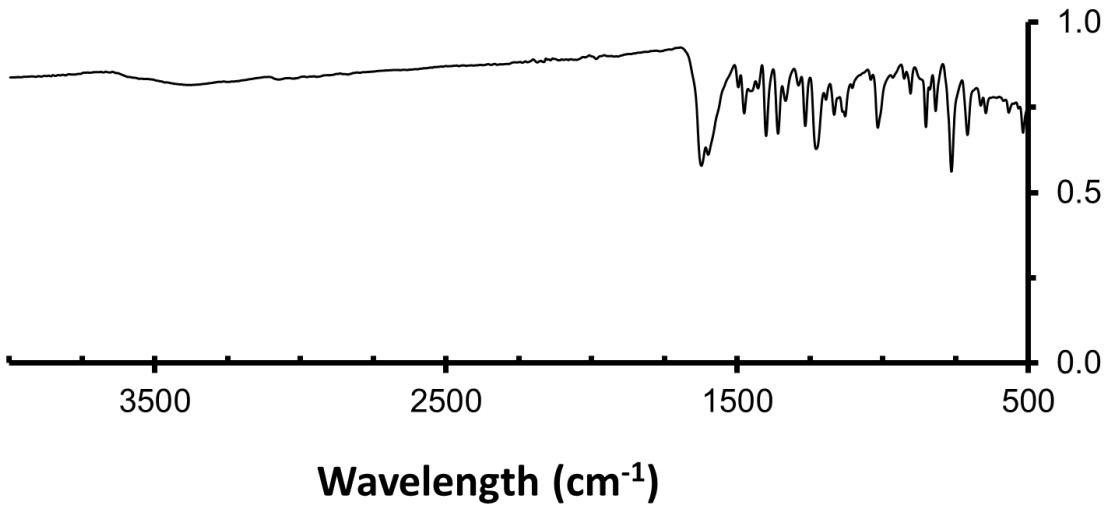

Figure S8: FT-IR spectrum of **4** (powder).

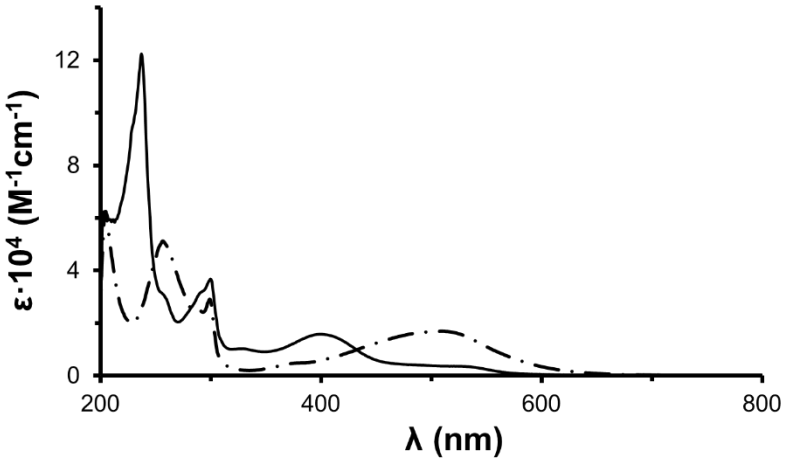

Figure S9: UV-vis spectra of **4** (dashed line, 14.9 µM) and **5**$[PF_6]_2$ (solid line, 22.5 µM) in MeOH.

IV

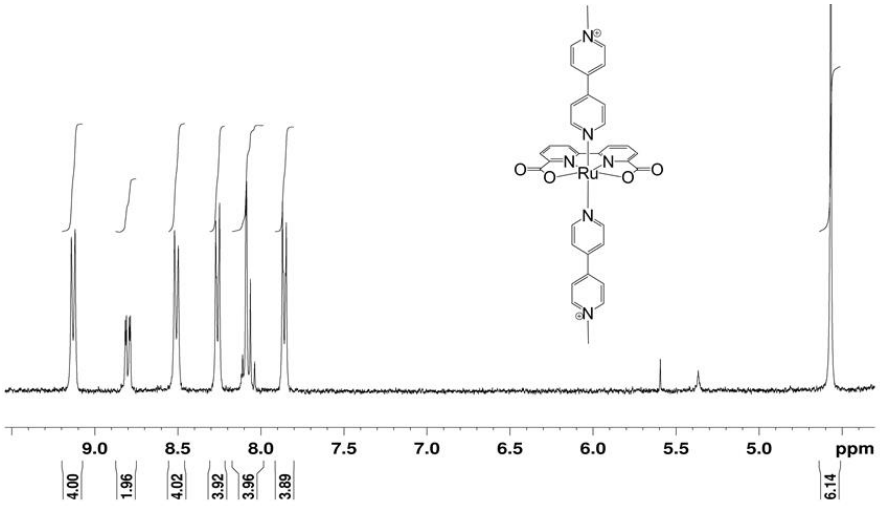

Figure S10: ^1H NMR of **5**$[PF_6]_2$ in [d4]-Methanol/[d6]-acetone 1:1 mixture.

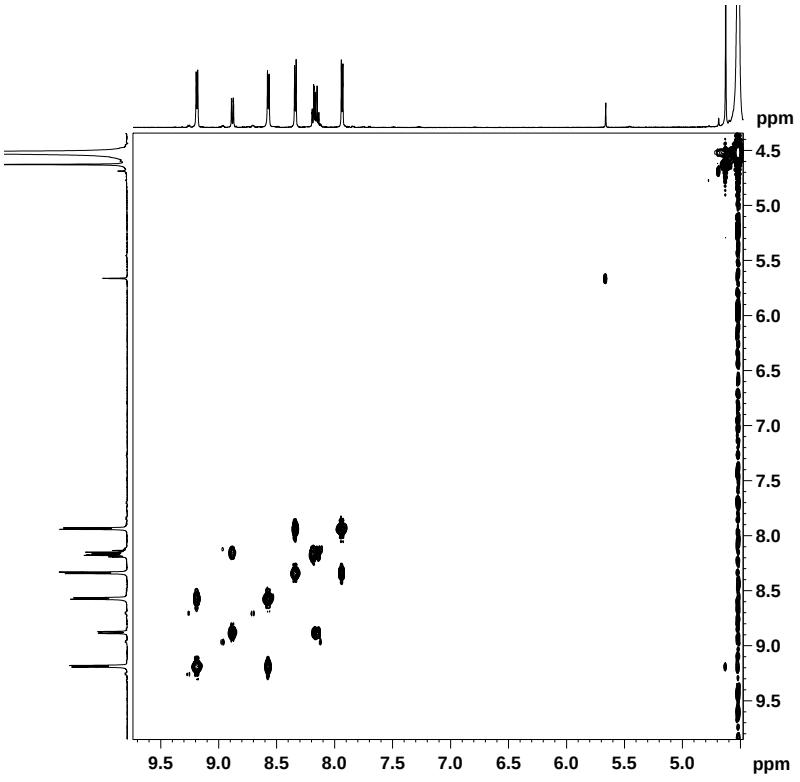

Figure S11: ^{1}H-^{1}H COSY NMR of **5**$[PF_6]_2$ in [d4]-Methanol/[d6]-acetone 1:1 mixture.

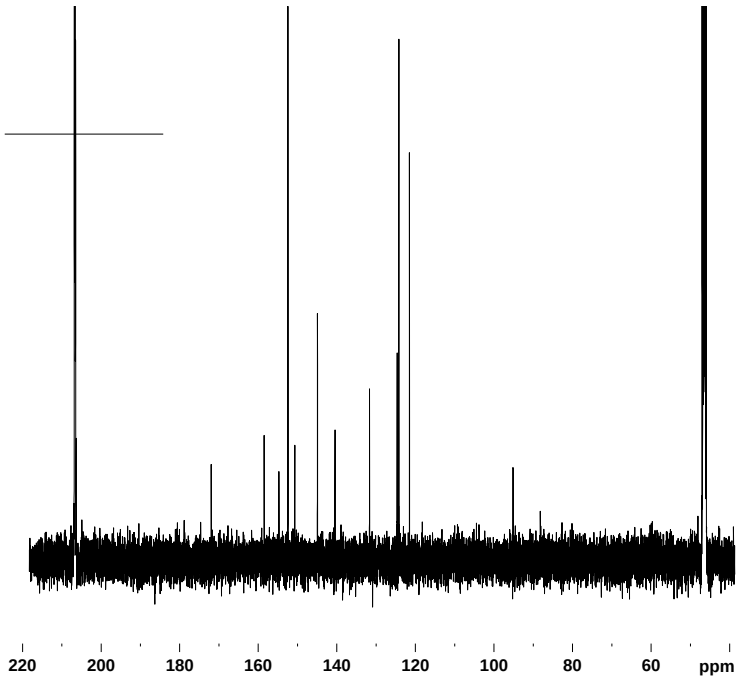

Figure S12: $^{13}C\{H\}$ NMR of **5**$[PF_6]_2$ in [d4]-Methanol/[d6]-acetone 1:1 mixture.

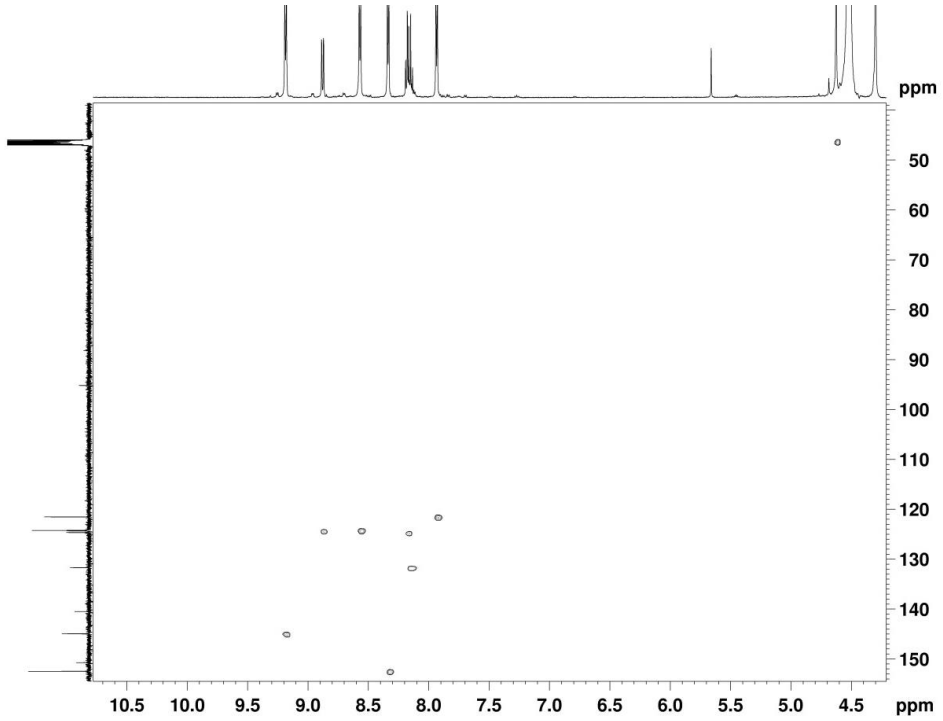

Figure S13: ^{1}H-^{13}C HSQC NMR of **5**$[PF_6]_2$ in [d4]-Methanol/[d6]-acetone 1:1 mixture.

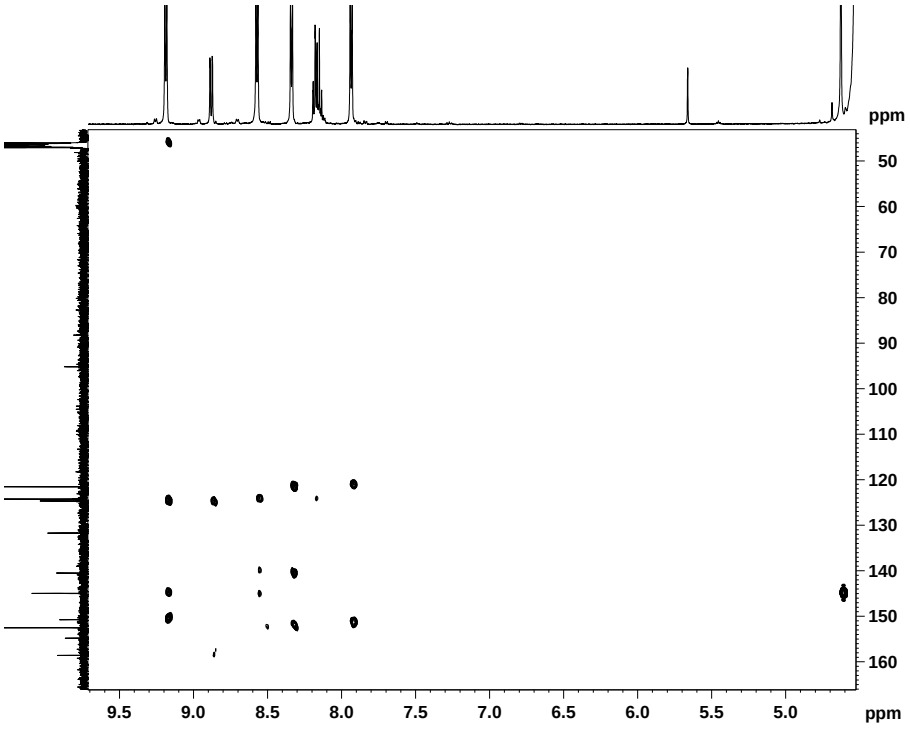

Figure S14: ^{1}H-^{13}C HMBC NMR of **5**$[PF_6]_2$ in [d4]-Methanol/[d6]-acetone 1:1 mixture.

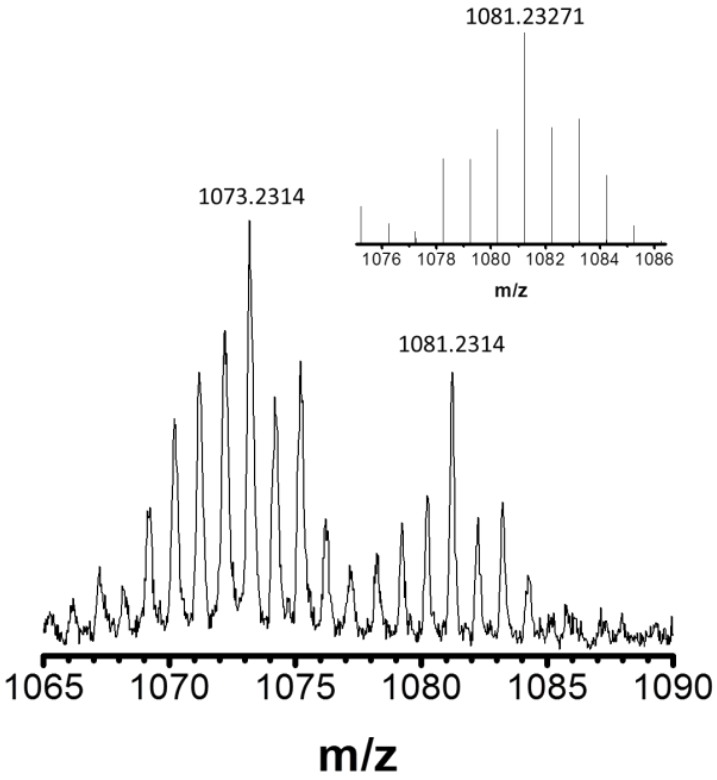

Figure S15: High Resolution Mass Spectrum of compound **5**$[PF_6]_2$ in a MALDI$^+$ *trans*-2-[3-(4-*tert*-butylphenyl)-2-methyl-2-propenylidene]malononitrile (dctb) matrix**.** The molecular peak was found as $\{[(MeBpy)_2Ru(bda)](PF_6)(dctb)\}^+$. Inset shows simulated m/z pattern for $\{[(MeBpy)_2Ru(bda)](PF_6)(dctb)\}^+$.

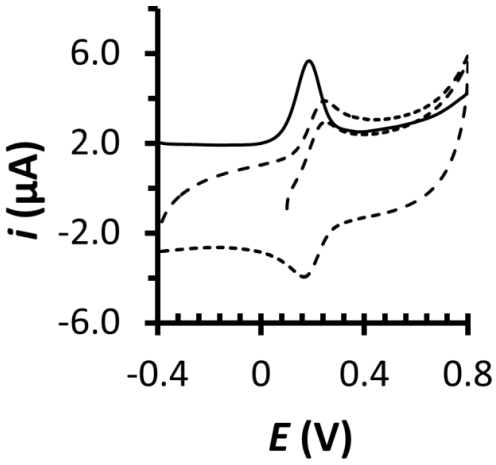

Figure S16: Cyclic voltammogram (dashed line) and DPV (solid line) of **5**$[PF_6]_2$ (0.5 mM) in 0.1 M n-Bu_4NPF_6 Acetone/MeOH 1:1 mixture. The scan rate was 100 mV/s and a glassy carbon electrode (0.07cm^2) was used as working, Pt mesh was used as counter and Hg/Hg_2SO_4 as reference electrodes.

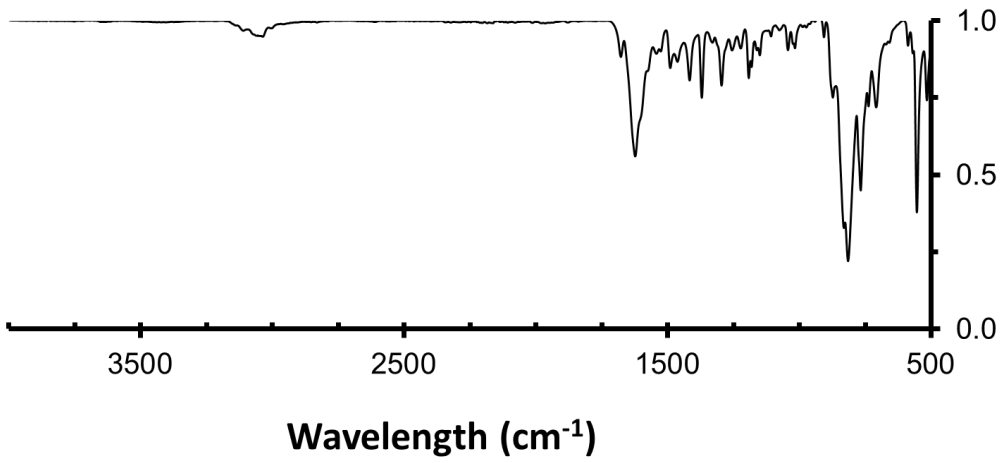

Figure S17: FT-IR spectrum of **5**$[PF_6]_2$ (powder).

IV

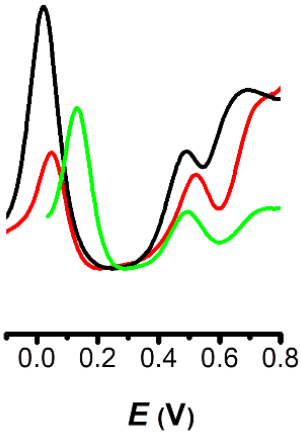

	4	1	5
III/II	0.02	0.05	0.13
IV/III	0.49	0.52	0.5
V/IV	0.70	0.73	0.72

Figure S18: Left: Normalized DPVs of **4** (black)**, 1** (red) and **5** (green) in 0.1 M triflic acid solution with 25 % of TFE. A glassy carbon electrode (0.07cm^2) was used as working, Pt mesh was used as counter and Hg/Hg_2SO_4 as reference electrodes. Right: measured $E_{1/2}$ (V) vs Hg/Hg_2SO_4 of complex **4**, **1** and **5** from DPV.

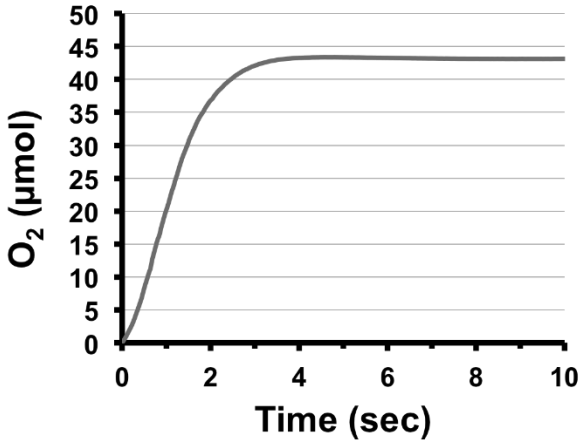

Figure S19: Manometry data plot for WOC **4**, [**4**] = 50 µM. Headspace = 27.0 mL, Temperature = 25°C, solvent = 3% TFE in 0.1 M triflic acid (0.5 mL), [CAN] = 0.1 M. TOF=923 s^{-1}

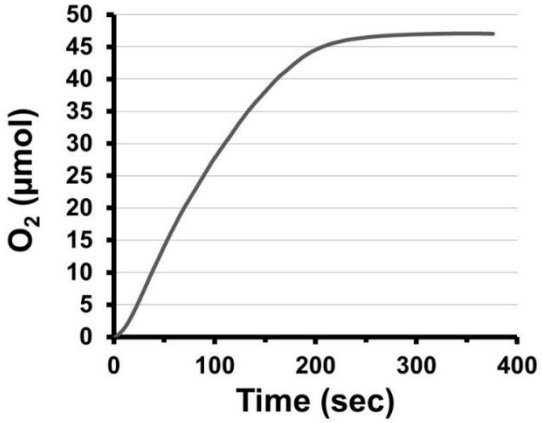

Figure S20: Manometry plot for WOC **5**, [**5**]=20 µM. Headspace = 8.5 mL, Temperature = 25°C, solvent = 3% TFE in 0.1 M triflic acid (2.0 mL), [CAN] = 0.1 M

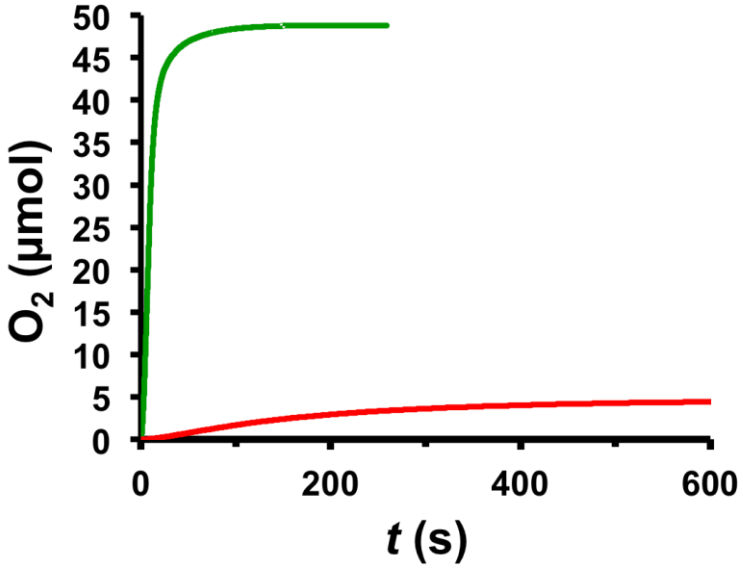

Figure S21: Manometry data plot for WOC **4** (green line) and WOC **5** (red line), [**4**] = [**5**] = 5.0 µM]. Headspace = 8.5 mL, Temperature = 25°C, solvent = 3% TFE in 0.1 M triflic acid (2.0 mL), [CAN] = 0.1 M

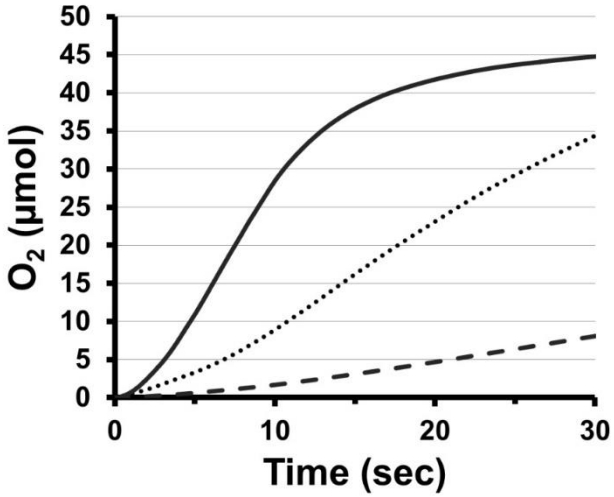

Figure S22: Manometry plots for WOC **4** at concentrations [**4**] = 5.0 µM, solid line; [**4**] = 2.5 µM, dotted line; and [**4**] = 1.25 µM, dashed line. Headspace = 8.5 mL, Temperature = 25°C, solvent = 3% TFE in 0.1 M triflic acid (2.0 mL), [CAN] = 0.1 M.

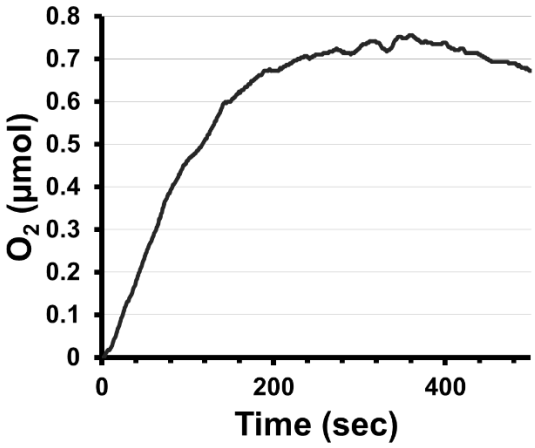

Figure S23: Manometry plot for WOC **5**, [**5**]=2.5 µM. Headspace = 8.5 mL, Temperature = 25°C, solvent = 3% TFE in 0.1 M triflic acid (2.0 mL), [CAN] = 0.1 M

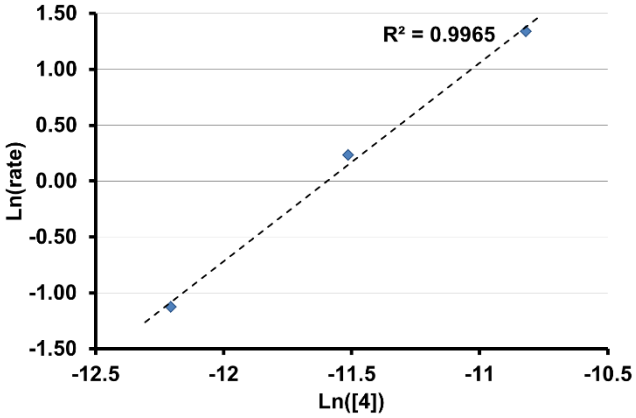

Figure S24: Plot of Ln(rate) versus Ln([**4**]). The linear fitting gives a slope of 1.78 ± 0.18, indicating second order in catalyst **4**.

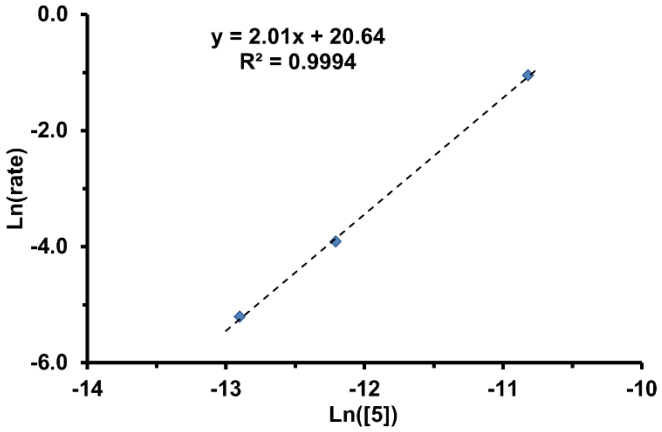

IV

Figure S25: Plot of Ln(rate) versus Ln([**5**]). The linear fitting gives a slope of 2.01 ± 0.11, indicating second order in catalyst **5**.

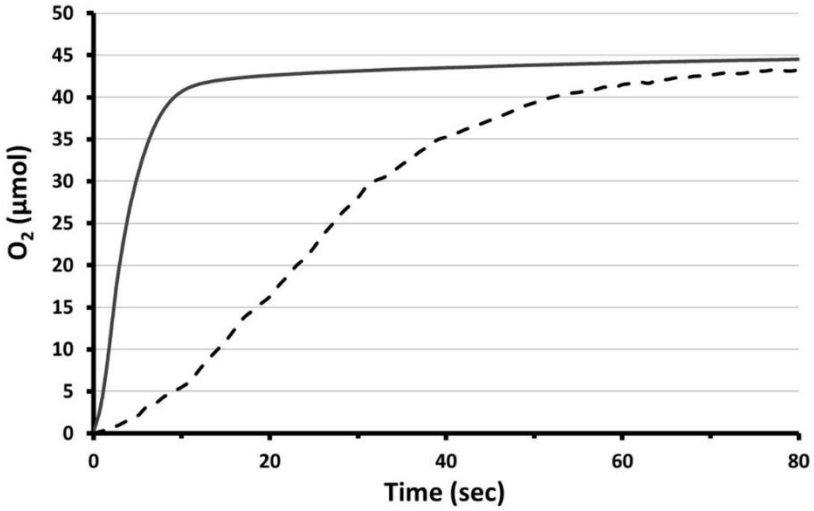

Figure S26: Plots of oxygen gas production of WOC **4** measured simultaneously by manometry (solid line) and Clark electrode (dashed line). Headspace = 27 mL, Temperature = 25°C, solvent = 3% TFE in 0.1 M triflic acid (0.5 mL), [CAN] = 0.35 M.

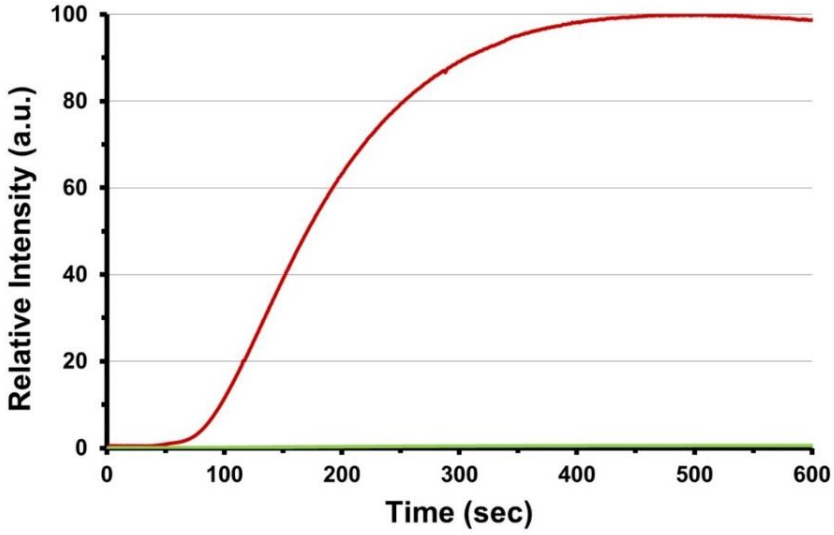

Figure S27: Plots of gas production or WOC **4** measured by online MS. Oxygen (red line), Carbon dioxide (green line). Solvent = 3% TFE in 0.1 M triflic acid (1.0 mL), [**4**] = 10 µM, [CAN] = 0.175 M

.

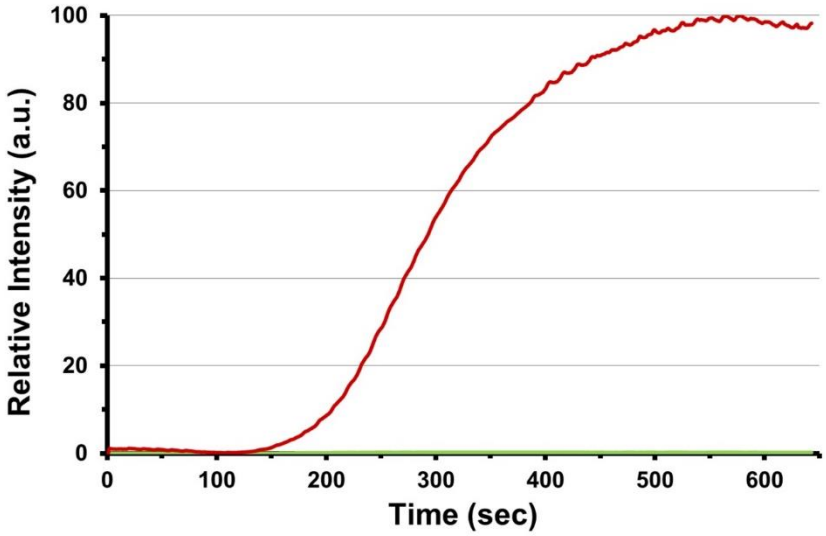

Figure S28: Plots of gas production or WOC **5** measured by online MS. Oxygen (red line), Carbon dioxide (green line). Solvent = 3% TFE in 0.1 M triflic acid (1.0 mL), [**5**] = 40 µM, [CAN] = 0.175 M.

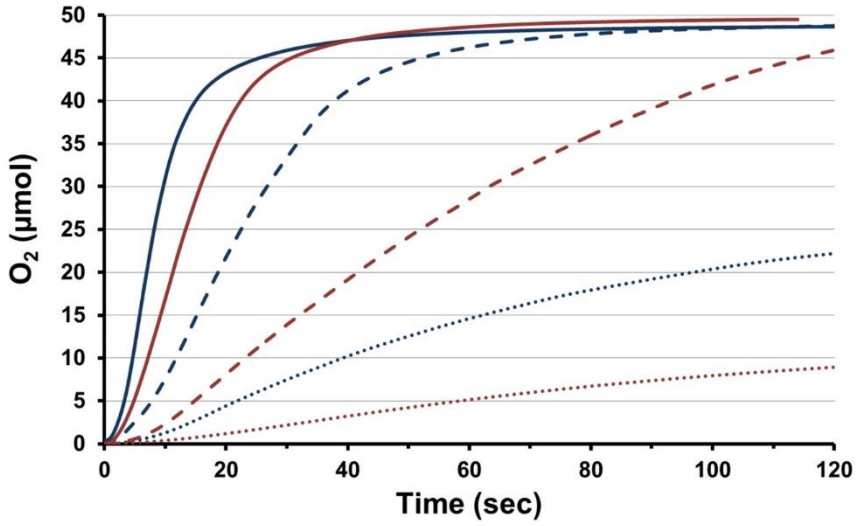

IV

Figure S29: Manometry plots for WOC **4** (dark blue lines) and **1** (red lines) at concentrations; 5.0 µM, solid lines; 2.5 µM, dashed lines; and 1.25 µM, dotted lines. Headspace = 8.5 mL, Temperature = 25°C, solvent = 3% TFE in 0.1 M triflic acid (2.0 mL), [CAN] = 0.1 M.

Table S1: Crystal data and structure refinement for **4**

Identification code	**4**	
Empirical formula	C33 H34 Cl0 N4 O10 Ru	
Formula weight	747.71	
Temperature	100(2) K	
Wavelength	0.71073 Å	
Crystal system	Monoclinic	
Space group	P2(1)	
Unit cell dimensions	a = 14.1998(7)Å	α= 90°.
	b = 14.1439(6)Å	β = 99.348(2)°.
	c = 15.9244(7)Å	γ = 90°.
Volume	3155.8(2) $Å^3$	
Z	4	
Density (calculated)	1.574 Mg/m^3	
Absorption coefficient	0.563 mm^{-1}	
F(000)	1536	
Crystal size	0.01 x 0.01 x 0.01 mm^3	
Theta range for data collection	1.296 to 31.247°.	
Index ranges	-17<=h<=20,-20<=k<=11,-16<=l<=22	
Reflections collected	26818	
Independent reflections	11396[R(int) = 0.0239]	
Completeness to theta =31.247°	84.1%	
Absorption correction	Empirical	
Max. and min. transmission	0.994 and 0.859	
Refinement method	Full-matrix least-squares on F^2	
Data / restraints / parameters	11396/ 23/ 890	
Goodness-of-fit on F^2	1.167	
Final R indices [I>2sigma(I)]	R1 = 0.0461, wR2 = 0.1389	
R indices (all data)	R1 = 0.0550, wR2 = 0.1782	
Flack parameter	x =-0.013(19)	
Largest diff. peak and hole	3.383 and -0.858 $e.Å^{-3}$	

IV

DFT data

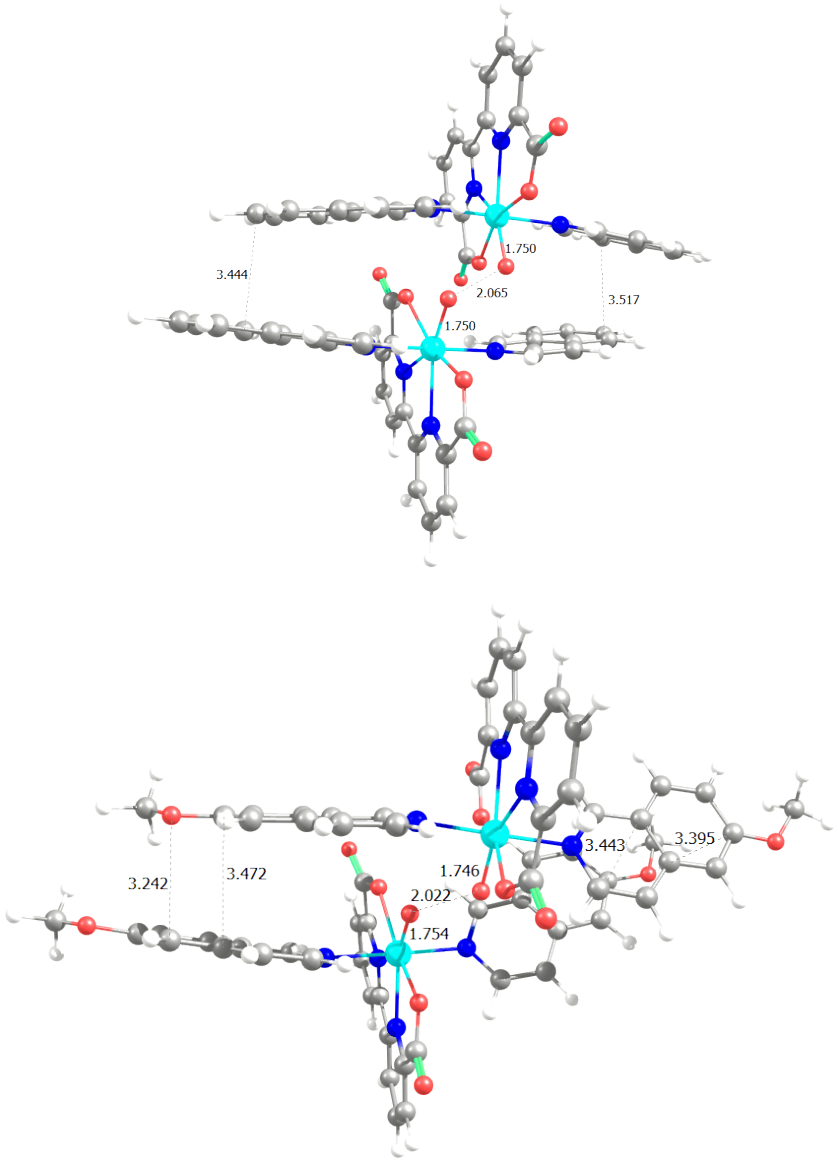

Figure S30: Geometry of the **1**:**1** and **4**:**4** TS. Key distances in Å.

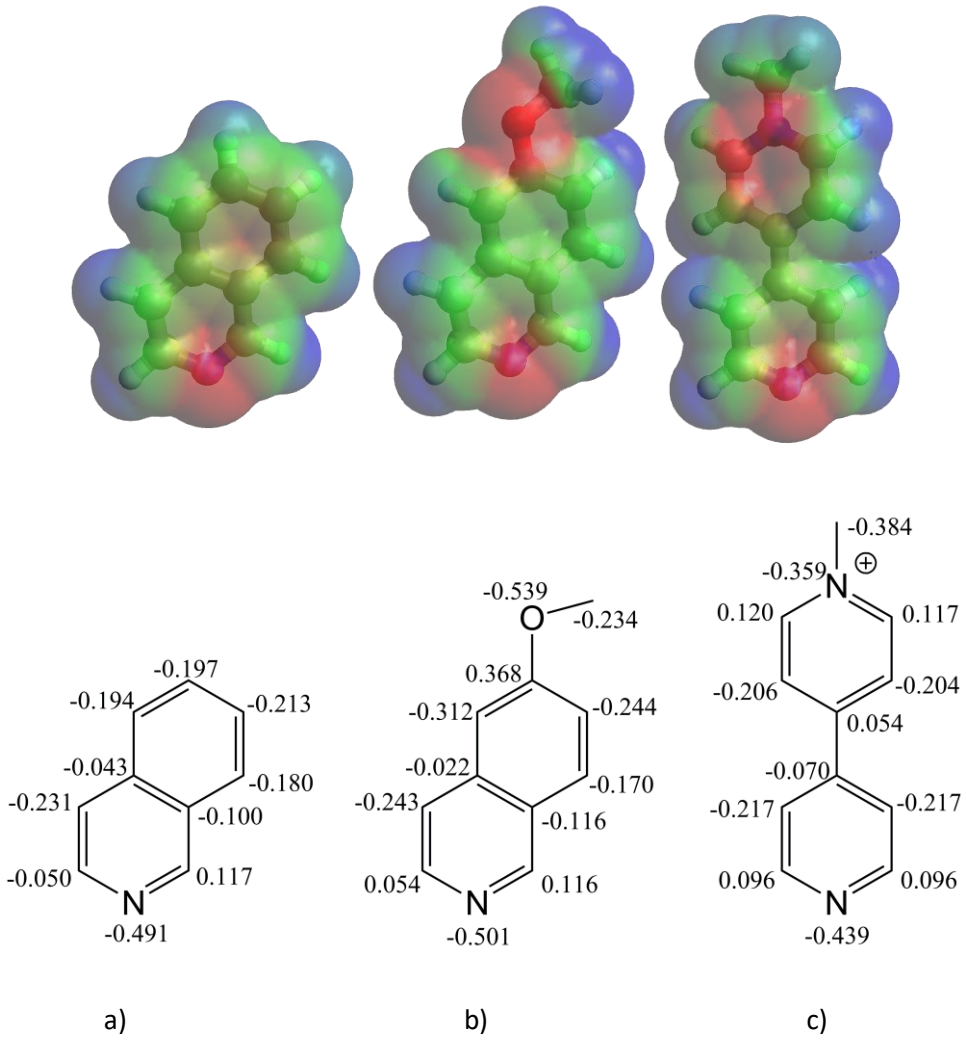

Figure S31: NPA charges and 3D representation of the electrostatic potential of a) Isoq, b) OMe-Isoq and c) Me-bpy ligand. Bottom row, NPA charges.

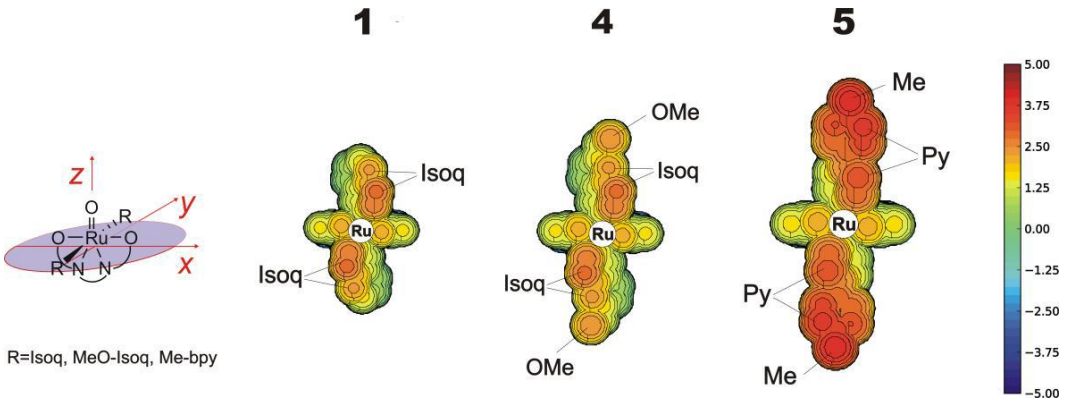

Figure S32: Steric maps of the [Ru(V)=O]+ species of **1**, **4** and **5**.

References

S1 Frisch, M. J.; Trucks, G. W.; Schlegel, H. B.; Scuseria, G. E.; Robb, M. A.; Cheeseman, J. R.; Scalmani, G.; Barone, V.; Mennucci, B.; Petersson, G. A.; Nakatsuji, H.; Caricato, M.; Li, X.; Hratchian, H. P.; Izmaylov, A. F.; Bloino, J.; Zheng, G.; Sonnenberg, J. L.; Hada, M.; Ehara, M.; Toyota, K.; Fukuda, R.; Hasegawa, J.; Ishida, M.; Nakajima, T.; Honda, Y.; Kitao, O.; Nakai, H.; Vreven, T.; Montgomery, J. A.; Peralta, J. E.; Ogliaro, F.; Bearpark, M.; Heyd, J. J.; Brothers, E.; Kudin, K. N.; Staroverov, V. N.; Kobayashi, R.; Normand, J.; Raghavachari, K.; Rendell, A.; Burant, J. C.; Iyengar, S. S.; Tomasi, J.; Cossi, M.; Rega, N.; Millam, J. M.; Klene, M.; Knox, J. E.; Cross, J. B.; Bakken, V.; Adamo, C.; Jaramillo, J.; Gomperts, R.; Stratmann, R. E.; Yazyev, O.; Austin, A. J.; Cammi, R.; Pomelli, C.; Ochterski, J. W.; Martin, R. L.; Morokuma, K.; Zakrzewski, V. G.; Voth, G. A.; Salvador, P.; Dannenberg, J. J.; Dapprich, S.; Daniels, A. D.; Farkas; Foresman, J. B.; Ortiz, J. V.; Cioslowski, J.; Fox, D. J. Wallingford CT, 2009.

IV

S2 Y. Zhao, D. G. Truhlar, *J. Chem. Phys.* **2006**, *125*, 194101-194118.

S3 Schafer, A.; Horn, H.; Ahlrichs, R. *J. Chem. Phys.* **1992**, *97*, 2571-2577.

S4 (a) Kuchle, W.; Dolg, M.; Stoll, H.; Preuss, H. *J. Chem. Phys.* **1994**, *100*, 7535-7542; (b) Leininger, T.; Nicklass, A.; Stoll, H.; Dolg, M.; Schwerdtfeger, P. *J. Chem. Phys.* **1996**, *105*, 1052-1059; (c) Häussermann, U.; Dolg, M.; Stoll, H.; Preuss, H.; Schwerdtfeger, P.; Pitzer, R. M. *Theor. Chem. Acc.* **1993**, *78*, 1211-1224.

S5 Zhao, Y.; Truhlar, D. *Theor. Chem. Acc.* **2008**, *120*, 215-241.

S6 (a) Barone, V.; Cossi, M. *J. Chem. Phys. A* **1998**, *102*, 1995-2001; (b) Tomasi, J.; Persico, M. *Chem. Rev.* **1994**, *94*, 2027-2094.

S7 Martin, R. L.; Hay, P. J.; Pratt, L. R. *J. Phys. Chem. A* **1998**, *102*, 3565-3573; (b) Margl, P. *Can. J. Chem.* **2009**, *87*, 891-903; (c) Cooper, J.; Ziegler, T. *Inorg. Chem.* **2002**, *41*, 6614-6622; (d) Rotzinger, F. P. *Chem. Rev.* **2005**, *105*, 2003-2038; (e) Leung, B. O.; Reid, D. L.; Armstrong, D. A.; Rauk, A. *J. Chem. Phys. A* **2004**, *108*, 2720-2725; (f) Ardura, D.; López, R.; Sordo, T. L. *J. Chem. Phys. B* **2005**, *109*, 23618-23623; (g) Raynaud, C.; Daudey, J.-P.; Jolibois, F.; Maron, L. *J. Chem. Phys. A* **2005**, *110*, 101-105; (h) Solans-Monfort, X.; Copéret, C.; Eisenstein, O. *Organometallics* **2012**, *31*, 6812-6822.

PAPER D Hydrogen Bonding Rescues Overpotential in Seven Coordinated Ru Water Oxidation Catalysts

Matheu, R.; Ertem, M. Z.; Gimbert-Suriñach, C.; Benet-Buchholz, J.; Sala, X.; Llobet, A.;
ACS Catal. **2017**, *7*, 6525–6532

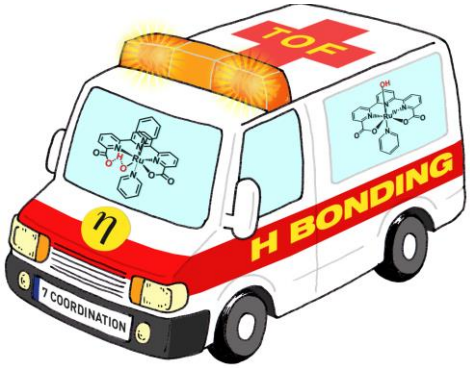

IV

Abstract

In this work we describe the synthesis, structural characterization and redox properties of two new Ru complexes containing the dianionic potentially pentadentate [2,2':6',2''-terpyridine]-6,6''-dicarboxylate (tda^{2-}) ligand that coordinates Ru at the equatorial plane and with additional pyridine or dmso acting as monondentate ligand in the axial positions: $[Ru^{II}(tda\text{-}\kappa\text{-}N^3O)(py)(dmso)]$, **1^{II}** and $[Ru^{III}(tda\text{-}\kappa\text{-}N^3O^2)(py)(H_2O)^{ax}]^+$, **2^{III}(H$_2$O)$^+$**. Complex **1^{II}** has been characterized by single crystal XRD in the solid state and in solution by NMR spectroscopy. The redox properties of **1^{II}** and **2^{III}(H$_2$O)$^+$** have been thoroughly investigated by means of cyclic voltammetry (CV) and differential pulse voltammetry (DPV). Complex **2^{II}(H$_2$O)** displays catalytic activity with regard to the oxidation of water to dioxygen and its properties have been analyzed based on foot of the wave analysis (FOWA) and catalytic Tafel plots. The activity of **2^{II}(H$_2$O)** has been compared with related water oxidation catalysts (WOCs) previously described in the literature. Despite its moderate activity, **2^{II}(H$_2$O)** constitutes the cornerstone for the rationalization of the different factors that govern overpotentials as well as efficiencies in molecular water oxidation catalysts (WOCs). The present work uncovers the interplay between different parameters namely, coordination number, number of anionic groups bonded to the first coordination sphere of the metal center, water oxidation catalysis overpotential, pK_a and hydrogen bonding and the performance of a given WOC. It thus establishes the basic principles for the design of efficient WOCs operating at low overpotentials.

Contribution

Roc Matheu synthetized and characterized the new compounds, performed the electrochemical experiments and prepared the manuscript.

D 1 Introduction

Water oxidation catalysis is a field that has exhibited significant progress over the last ten years mainly powered by the promise of generation of sustainable carbon neutral fuel, based on water splitting.[1,2]Particularly impressive has been the development of water oxidation catalysts based on transition metal complexes and the understanding of their mechanisms at a molecular level. For the latter the main contribution has been led by Ru complexes where electrochemical, spectroscopic and reactivity studies together with the characterization of some reaction intermediates has generated a significant amount of knowledge in this topic.[3]

The main challenge today in this field is to design and develop rugged and fast catalysts that can be incorporated into a device for overall water splitting at neutral to acidic pHs. To achieve this goal, it is imperative to further understand the factors that govern the catalyst's performance at a molecular level as well as the deactivation pathways that operate in parallel so that they can be avoided.[4] Molecular transition metal complexes constitute an excellent platform to examine these factors since significant information based on an arsenal of spectroscopic, electrochemical and analytical techniques can be used together with the valuable complementary information provided by computational studies.[5-14]

IV

The best water oxidation catalysts reported today are based on seven coordinated Ru complexes containing dianionic ligands such as [2,2'-bipyridine]-6,6'-dicarboxylato (bda^{2-}) [15-17]and [2,2':6',2''-terpyridine]-6,6''-dicarboxylato (tda^{2-}) (see Figure 1 for drawn structures of these ligands). Particularly impressive is the seven coordinate complex $[Ru^{IV}(tda\text{-}\kappa\text{-}N^3O)(py)_2(O)^{eq}]$, **$4^{IV}(O)$**, (the superscript in roman numbers indicates the formal oxidation state of Ru; py is pyridine; the "eq" superscript means equatorial) that is capable of oxidizing water to dioxygen at maximum turnover frequencies (TOF_{MAX}) of 7.700 s^{-1} and 50.000 s^{-1} at pH = 7.0 and pH = 10.0 respectively.[18] In addition, this catalyst achieves turnover numbers (TONs) above one million when anchored into graphitic solid electrodes.[19] One of the key features for the unprecedented performance of this catalyst is the presence of a non-coordinated carboxylate that acts as an intramolecular proton acceptor at the O-O bond formation step, which decreases the energy requirement for the rate determining step.[18]

In an attempt to shed more light into the different factors that influence WOC performance and to come up with a consistent, integrative and unified model, we have prepared new Ru complexes based on the tda^{2-} ligand $[Ru^{II}(tda\text{-}\kappa\text{-}N^3O)(py)(dmso)]$, **$1^{II}$**, and $[Ru^{III}(tda\text{-}\kappa\text{-}N^3O^2)(py)(H_2O)^{ax}]^+$, **$2^{III}(H_2O)^+$**. We have thoroughly described their redox properties and compared them with relevant complexes previously described in the literature. We have further

performed density functional theory (DFT) calculations to offer a complete view of the catalytic mechanism of this new water oxidation catalyst and to examine the role of coordination number, number of anionic groups bonded to the first coordination sphere of the metal center and pK_as on water oxidation catalysis overpotential of a set of relevant complexes.

D 2 Results

D 2.1 Synthesis and structure

$[Ru^{II}Cl_2(dmso)_4]$ is used as a starting material to prepare $[Ru^{II}(tda\text{-}\kappa\text{-}N^3O)(py)(dmso)]$, $\mathbf{1^{II}}$, that when treated with neat triflic acid and water under an open atmosphere generates $[Ru^{III}(tda\text{-}\kappa\text{-}N^3O^2)(py)(H_2O)^{ax}]^+$, $\mathbf{2^{III}(H_2O)^+}$, as indicated in equations 1-2.

$$[Ru^{II}Cl_2(dmso)_4] \xrightarrow[2)\ Py,\ T = 25^{\circ}C]{1)\ H_2tda,\ Et_3N,\ MeOH} [Ru^{II}(tda\text{-}\kappa\text{-}N^3O)(py)(dmso)] \quad \mathbf{1^{II}} \qquad (1)$$

$$[Ru^{II}(tda\text{-}\kappa\text{-}N^3O)(py)(dmso)]\ \mathbf{1^{II}} \xrightarrow[2)\ H_2O]{1)\ neat\ CF_3SO_3H,\ O_2} [Ru^{III}(tda\text{-}\kappa\text{-}N^3O^2)(py)(OH_2)^{ax}]^+\ \mathbf{2^{III}(H_2O)^+} \qquad (2)$$

Complex $\mathbf{1^{II}}$ has been structurally characterized in solution by NMR spectroscopy and in the solid state by single crystal X-ray diffraction analysis. An Ortep plot is presented in Figure 1 where the metal center shows a distorted octahedral geometry with the tda^{2-} ligand acting in κ-N^3O fashion in the equatorial zone with one non-coordinated carboxylate group. Finally, a pyridyl and a dmso ligands complete the axial positions. NMR spectroscopy corroborates that the solid state structure is basically maintained in solution. A one electron reduction of $\mathbf{2^{III}(H_2O)^+}$ generates $\mathbf{2^{II}(H_2O)}$ *in situ* and its ^{1}H-NMR spectrum shows symmetrical features for the tda^{2-} resonances indicating the existence of a fast dynamic process where the two carboxylato groups of the tda^{2-} ligand coordinate and decoordinate very fast in a synchronized manner at room temperature (all the NMR spectra are presented in the SI). The optimized structures at M06 level of theory [20,21] indicate that κ-N^3O binding is favored for $\mathbf{2^{II}(H_2O)}$ supporting the dynamic nature of coordination of carboxylato groups. On the other hand for $\mathbf{2^{III}(H_2O)^+}$ a κ-N^3O^2 mode is favored by DFT with a Ru-N distance of 2.50 Å for the central pyridyl group of the trpy ligand, that suggests an overall "6.5" coordination number as has been previously reported in related complexes [18] (see Figure 1C-D).

IV

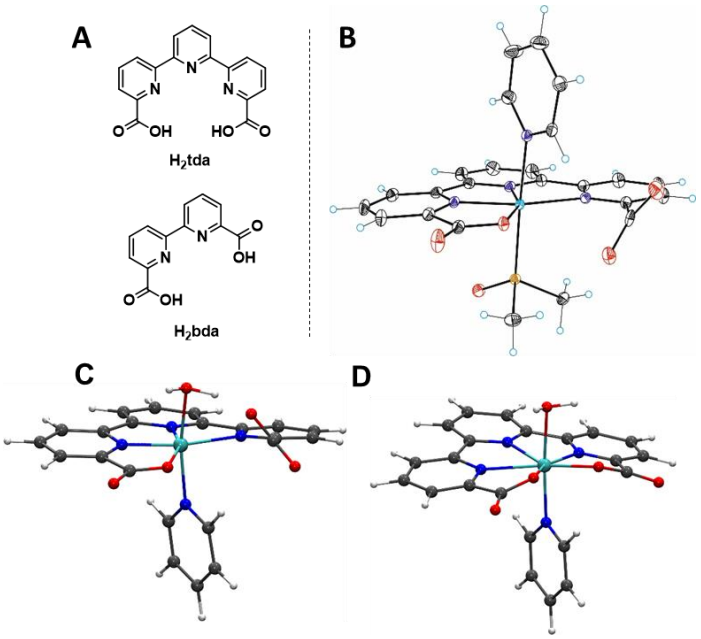

Figure 1: **A**, Drawing of protonated bda^{2-} and tda^{2-} ligands. **B,** ORTEP plot for complex $\mathbf{1^{II}}$ with ellipsoids at 50% probability. Color code: Ru, cyan; N, purple; O, red; C, black; S, orange; and H, colorless. **C**, Optimized structures at M06 level of theory for $[Ru^{II}(tda\text{-}\kappa\text{-}N^3O)(py)(H_2O)^{ax}]$ and **D,** for $[Ru^{III}(tda\text{-}\kappa\text{-}N^3O^2)(py)(H_2O)^{ax}]^+$. Color code: Ru, cyan; N, blue; O, red; C, gray; and H, white.

D 2.2 Redox Properties and water oxidation catalysis

The redox properties of the complexes reported here have been investigated based on cyclic voltammetry (CV) and differential pulse voltammetry (DPV) techniques using a three electrode configuration with a glassy carbon disk as a working electrode, a Pt wire as auxiliary electrode and a Hg/Hg_2SO_4 as a reference electrode. All potentials were converted to NHE by adding 0.65 V.

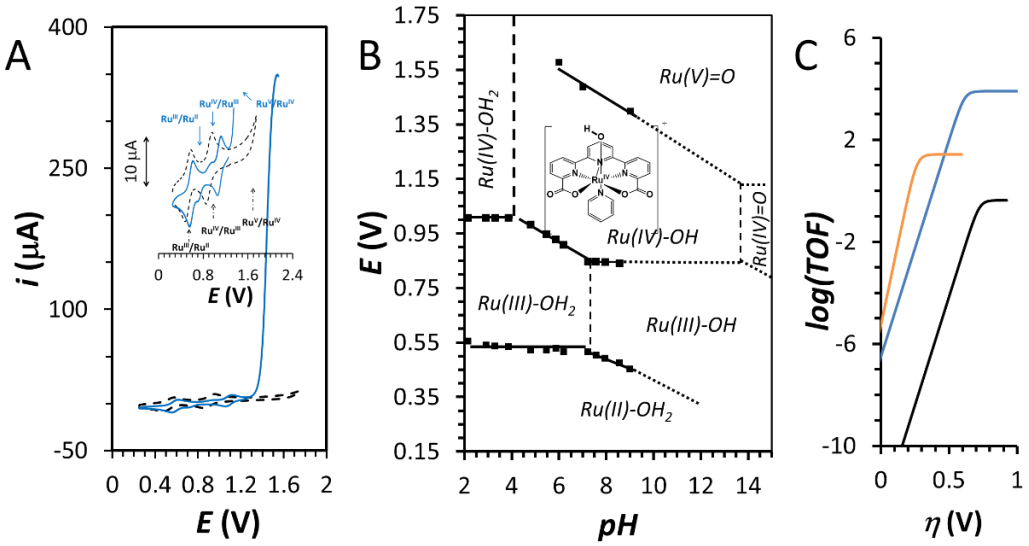

Figure 2: **A**, blank corrected Cyclic Voltammetry (CV) at pH =7.0 for **2^{IV}(O)** (black dashed line) and **$4^{IV,2+}$/4^{IV}(O)** 0.75 mM/0.37 mM (blue solid line) at pH = 7.0. Inset: enlargement of the y-axis and assignment of redox couples. **B**, Pourbaix diagram of **2^{III}(H_2O)$^+$** indicating the predominant species in the different *E*-pH zones. Auxiliary ligand tda^{2-} and py are not shown for simplicity. Vertical lines indicate pK_as. Dotted lines indicate redox potentials extrapolated using the Nernst equation. **C,** catalytic Tafel plot for complexes **2^{IV}(O)** (black line), **3^{IV}(O)** (0.5 mM, orange line) and **4^{IV}(O)** (blue line) at pH = 7.0.

At pH = 7.0 the blank corrected CV for the Ru-aqua complex **2^{II}(H_2O)** shows two one-electron chemically reversible waves that are associated with the IV/III and III/II redox couples and a small increase on current density in the 1.3-1.5 V zone that is associated with the V/IV couple and water oxidation catalysis as exhibited in Figure 2A. In addition, the electrochemical response of its homologue, **4^{IV}(OH)**$^+$ that we have reported earlier, is also shown for comparative purposes. Note that **4^{IV}(OH)**$^+$ is generated from $[Ru^{IV}(tda\text{-}\kappa\text{-}N^3O^2)(py)_2]^{2+}$, **$4^{IV,2+}$**, that has no hydroxido species bonded to Ru, and that both species are present in solution as can be seen in Figure 2A.[18]

A complete Pourbaix diagram is offered in Figure 2B where the zones of predominant species derived from **2^{II}(H_2O)** with different electron/proton content are shown. An interesting feature of the Pourbaix diagram for **2^{IV}(OH)**$^+$ is the pH 10-14 zone, that has been built by extrapolating the values of the V/IV couple at this pH and by assuming that the redox potential for the Ru^V=O/Ru^{IV}=O couple for $[Ru^{IV}(bda)(Me\text{-}py)_2(O)^{eq}]$, **$3^{IV}$(O)** (1.12 V),[15] is the same as for **2^{IV}(O)**. This assumption is based on Lever's approach[22-24]where it is shown that the Ru^{III}/Ru^{II} couple for a set of complexes can be calculated based on additive contribution of their respective ligands bonded to the first coordination sphere. In the present case, complexes **2^{IV}(O)** and **3^{IV}(O)** can be

IV

considered as "pseudo isomers" since in both cases the first coordination sphere is occupied by 4 pyridyl groups, two carboxylato and one terminal oxo ligand (see drawn structures in Figure 4B). Using this value for the V/IV redox potential and assuming a Nernstian behavior we could determine the pK_a for the Ru^{IV}-OH/Ru^{IV}-O couple as 13.5, at the E^o(V/IV) slope change as shown in Figure 2B. These assumptions are further supported by computed oxidation potentials and pK_as (Table 1). Firstly, the computed potentials at pH 0 for Ru^{III}-OH_2/Ru^{II}-OH_2 (0.43 V) and Ru^{IV}-OH_2/Ru^{III}-OH_2 (0.79 V) couples for **$2^{II}(H_2O)$** are within ≅ 0.2 V compared to those reported in experimental Pourbaix diagram in Figure 2B. The computed potentials for Ru^{V}-O/Ru^{IV}-OH (at pH = 0) and Ru^{V}-O/Ru^{IV}-O are 1.67 V and 0.97 V respectively, in line with the predicted potentials with Lever's approach as described above. Finally, the computed pK_a for Ru^{IV}-OH/Ru^{IV}-O couple is 11.8, again in good agreement with experimental estimation (Table 1).

A quantitative evaluation of the catalytic properties of **$2^{IV}(O)$** was carried out based on the Foot of the Wave Analysis (FOWA).[25] Using this methodology we obtain a TOF_{max} = 0.4 s^{-1} for **$2^{IV}(O)$** whereas for **$4^{IV}(O)$** under the same conditions and at nearly the same overpotential we get a TOF_{max} = 7.900 s^{-1}, that is more than 4 orders of magnitude higher. A catalytic Tafel plot is also reported in Figure 2C for **$2^{IV}(O)$**, **$3^{IV}(O)$** and **$4^{IV}(O)$** for comparative purposes. A catalytic cycle based on DFT calculations has been carried out for **$2^{IV}(O)$**, that agrees with the available experimental data and parallels that of **$4^{IV}(O)$**.[18] DFT calculations were performed at M06 level of theory [20] with SMD aqueous continuum solvation model [21] to account for bulk solvation effects and optimized transition state structures for O-O bond formation. The main features of this catalytic cycle are shown in Figure 3, and further details are presented in the supporting information (SI).

The main difference between the catalytic cycle for **$4^{IV}(O)$** and **$2^{IV}(O)$** is the fact that for the latter the Ru^{V}-O active group is situated in the axial position and thus has no access to efficient intramolecular hydrogen bonding at the critical O-O bond formation step as can be seen in optimized TS (Figure 3). The computed free energy of activation ($\Delta G^{\ddagger}$) for O-O bond formation step is now 31.0 kcal/mol for catalyst **$2^{IV}(O)$**, which is 5.2 kcal/mol higher than for **$4^{IV}(O)$**, in line with their relative rates of water oxidation. Again these results manifest the facilitating role of a pendant base as a proton acceptor in O-O bond formation via water nucleophilic attack (WNA) pathway.

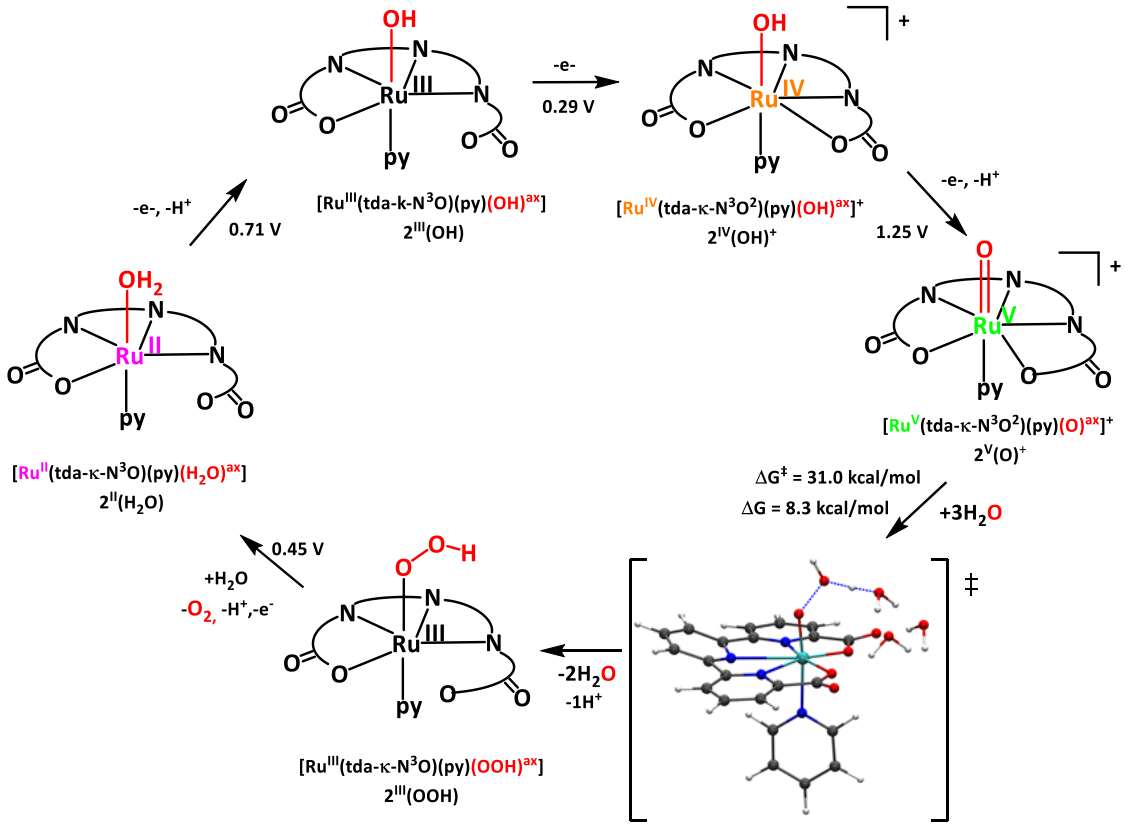

Figure 3. Catalytic water oxidation cycle based on DFT calculations for **$2^{III}(OH)^+$** at pH = 7.0. The arcs connecting N and O atoms represent the tda^{2-} ligand. Color code for the transition state: Ru, cyan; N, blue; O, red; C, gray; and H, white.

D 3 Discussion

D 3.1 The Ru^V=O/Ru^{IV}=O redox couple and the anionic nature of the ligands.

Mononuclear mono-aqua Ru complexes containing polypyridyl type of ligands such as **$2^{II}(H_2O)$**, can undergo a series of electron transfer and/or PCET processes to reach high oxidation states that are capable of promoting the oxidation of water to dioxygen. In most cases the active species are based on the Ru^V=O/Ru^{IV}=O couple or the corresponding Ru^{IV}-OH species depending on the pH. It is thus of fundamental importance to understand how to influence the redox potential of this couple so that efficient catalysts can be designed with overpotentials close to the thermodynamic value of the $4H^+/4e^-$ water oxidation pathway. Intuitively, the electronic perturbation of the metal center can be achieved directly with ligands containing anionic groups that occupy the first coordination sphere of the metal center or in a remote manner by adding electron donating or withdrawing groups attached at the pyridyl backbone of the auxiliary ligands. The latter strategy has been developed in a number of occasions,[16,26,27] but the results obtained in terms of potential change in high oxidation states are very poor as well as on improving TOFs. On the other hand, the first strategy has proven to be very successful especially

IV

using additional carboxylato groups attached to the pyridyl backbone that can directly coordinate to the metal center when compared to auxiliary ligands containing pyridyl groups only.

Figure 4A shows the correlation that can be established for 6 coordinated (CN6) octahedral Ru complexes between the Ru^{V}/Ru^{IV} redox couple and the number of anionic units contained in the auxiliary ligands of the complex, defined as "n^{-}". Indeed the redox potential of this couple decreases by roughly 250 mV per anionic charge as can be observed for $[Ru^{IV}(trpy)(bpy)(OH)]^{3+}$, $\mathbf{6^{IV}(OH)}^{3+}$ (zero charges, $n^{-} = 0$), [27] $[Ru^{IV}(trpy)(ppc)(OH)]$, $\mathbf{7^{IV}(OH)}^{2+}$ (Hppc = ethyl 3-(pyridin-2-yl)-1*H*-pyrazole-5-carboxylate, $n^{-} = 1$),[28] $[Ru^{IV}(bca)(py)_2(OH)]^{2+}$, $\mathbf{8^{IV}(OH)}^{2+}$ (Hbca = 2,2'-bipyridne-6-carboxylic acid; $n^{-} = 1$)[29] and *trans*-$[Ru^{IV}(pdc)(Me\text{-}py)_2(OH)]^{+}$, $\mathbf{9^{IV}(OH)}^{+}$ (H_2pdc = pyridine-2,6-dicarboxylic acid; $n^{-} = 2$).[30] (see Figure 4B for a drawing of these complexes). The computed potentials for Ru^{V}=O/Ru^{IV}=O couples at M06 level of theory exhibit a similar trend and are shown in parenthesis in Table 1. The same trend can be observed for seven coordinated (CN7) complexes in the cases of $[Ru(trpc)(Me\text{-}py)_2(OH)]$, $\mathbf{5^{IV}(OH)}^{2+}$ (Htrpc = 2,2':6',2''-terpyridine-6-carboxylate; $n^{-} = 1$),[31] $\mathbf{4^{IV}(OH)}^{+}$ ($n^{-} = 1$), $\mathbf{3^{IV}(OH)}^{+}$ ($n^{-} = 2$) and $\mathbf{2^{IV}(OH)}^{+}$ ($n^{-} = 2$), but with a decrease of approx. 200 mV with regard to their corresponding CN6 counterparts due to the addition of one more ligand at the first coordination sphere of Ru. The trend is similar for computed potentials for CN7 complexes and even the shift from CN6 counterparts are well reproduced with the exception of $\mathbf{9^{IV}(OH)}^{+}$ for which the difference between experiment and theory is the largest, a fact that is not well understood at present (Table 1). The 2,2':6',2'':6'',2'''-quaterpyridine (qtpy) complex $[Ru^{II}(qtpy)(py)_2]^{2+}$, is potentially an example of CN7, $n^{-} = 0$. However, a recent report indicates that it undergoes multiple pyridyl oxidation forming the corresponding N-oxide and thus is not considered in this work.[32]

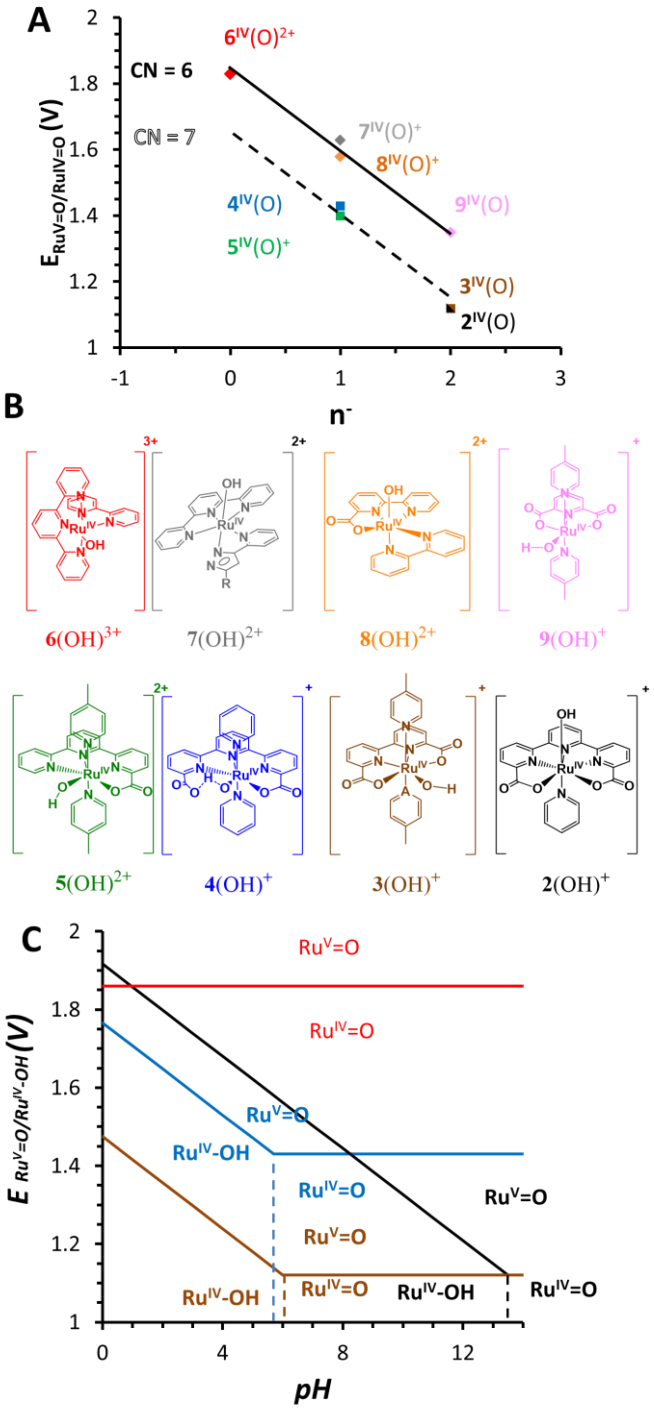

Figure 4. **A**, Correlation between Ru(V)=O/Ru(IV)=O redox potential and the number of anionic charges, ***n***$^{-}$, contained in the auxiliary ligands bonded to metal center, both for 6 (solid black line) and 7 coordinated catalysts (dashed black line). **B**, drawn structures for complex $\mathbf{2^{IV}(OH)^{+}}$, $\mathbf{3^{IV}(OH)^{+}}$, $\mathbf{4^{IV}(OH)^{+}}$, $\mathbf{5^{IV}(OH)^{3+}}$, $\mathbf{6^{IV}(OH)^{3+}}$, $\mathbf{7^{IV}(OH)^{2+}}$, $\mathbf{8^{IV}(OH)^{2+}}$, and $\mathbf{9^{IV}(OH)^{+}}$. **C,** Overlaid Pourbaix diagrams for the V/IV redox couple for complexes $\mathbf{2^{IV}(OH)^{+}}$ (black), $\mathbf{3^{IV}(OH)^{+}}$ (brown), $\mathbf{4^{IV}(OH)^{+}}$ (blue) and $\mathbf{6^{IV}(O)^{+}}$ (red).

D 3.2 The pH dependency of the Ru^{V}=O/Ru^{IV}=O redox couple and WOC overpotential.

The pH-dependency of the Ru^{V}/Ru^{IV} couple is shown in Figure 4C for representative water oxidation catalysts **$2^{IV}(OH)^{+}$**, **$3^{IV}(OH)^{+}$**, **$4^{IV}(OH)^{+}$** and **$6^{IV}(OH)^{3+}$**. The Ru^{V}-OH species is very acidic for the complexes discussed here and thus their pK_a is always lower than zero. In sharp contrast, for these complexes in oxidation state IV their pK_a drastically changes from values lower than zero all the way up to 13.5 as shown in Table 1 and Figure 4C. Thus, the value of the V/IV redox couple over pH is strongly influenced by the acidity of the Ru^{IV}-OH group that is by its pK_a. Two extreme cases shown in Figure 4C illustrate this point. For complex **$6^{IV}(OH)^{3+}$** the $pK_a < 0$ ($pK_a^{calc} = -8.9$) and thus the predominant species over the whole 0-14 pH-range is the Ru^{IV}=O. Therefore, the couple is pH independent (see red line in Figure 4C) and only an electron transfer process occurs in this case. On the other hand, for complex **$2^{IV}(OH)^{+}$** the pK_a is 13.5 (pK_a^{calc} = 11.8) and thus for this complex the Ru^{IV}-OH is the predominant species over the pH range 0-13.5 (black line Figure 4C). As a consequence of this, within this pH range the electron transfer is accompanied with proton removal in a typical PCET process with 59 mV per pH-unit decrease according to the Nernst equation. This situation produces a radically different scenario with regard to water oxidation overpotential for these couples as a function of pH. For instance, at pH = 0, **$6^{IV}(O)^{2+}$** has an overpotential of 590 mV whereas for **$2^{IV}(OH)^{+}$** this increases up to 680 mV. On the other hand, shifting the pH up to 13.5 does not change the overpotential for **$2^{IV}(OH)^{+}$** but in sharp contrast that of **$6^{IV}(O)^{2+}$** increases all the way to 1400 mV.

IV

Table 1: Selected Redox Potentials and pK_a values for Complex **$2^{IV}(OH)^{+}$** and Related Complexes

Complex	$2^{IV}(OH)^{+}$	$3^{IV}(OH)^{+}$	$4^{IV}(OH)^{+}$	$5^{IV}(O)^{2+}$	$6^{IV}(O)^{2+}$	$7^{IV}(O)^{+}$	$8^{IV}(O)^{+}$	$9^{IV}(O)$
Ru^{IV}-OH Coord. Environment[a]	4py, $2COO^{-}$	4py, $2COO^{-}$	5py, $1COO^{-}$	5py, $1COO^{-}$	5py	4py, $1pyr^{-}$	4py, $1COO^{-}$	3py, $2COO^{-}$
Coord. Number	7	7	7	7	6	6	6	6
pK_a; *Ru^{IV}-OH/Ru^{IV}-O (Calc.)*[b]	13.5[c] (11.8)	6.0 (6.8)	5.7 (5.4)	na[d]	<1.0 (-8.9)	< 1.0 (-7.7)	< 1.0 (-2.6)	na[d] (2.9)
E^0 Ru^{V}=O/Ru^{IV}=O (V) (Calc.)[b]	1.12[c] (0.97)	1.12 (1.04)	1.43 (1.26)	1.40[e]	1.86 (1.76)	1.59 (1.60)	1.59 (1.33)	1.35[f] (0.95)[d]
Reference	tw[d]	15	18	31	27	28	29	30

a. In this row, py represents the monodentate pyridyl ligand or a pyridyl group of an auxiliary ligand while COO^{-} represents the carboxylato group of the corresponding ligand. The abbreviation pyr^{-} is for the pyrazolato group.b. Calculated based on DFT.c. The E^{o} of the Ru^{V}=O/Ru^{IV}=O redox couples of complexes **$2^{IV}(OH)^{+}$** and **$3^{IV}(OH)^{+}$** are assumed

to be identical and the pK_a was extrapolated from the Pourbaix diagram. See Figure 2B.d. tw, means this work; na, means not available.e. Data estimated from the foot of the catalytic wave in Figure 10 in reference 31. f. Data estimated from the catalytic wave in Figure 1 in reference 30.

Another interesting feature that can be observed in Figure 4C is the effect of the number of anionic groups coordinated to the metal center in seven coordinated complexes that have the same pK_a, that is comparing complex **3^{IV}(OH)**$^+$ and **4^{IV}(OH)**$^+$, brown and blue lines in Figure 4C respectively. In this case the potentials are virtually parallel to one another and thus the overpotential is 300 mV lower for **3^{IV}(OH)**$^+$ than for **4^{IV}(OH)**$^+$ over the whole pH range.

Finally, it is also worth comparing complexes **2^{IV}(OH)**$^+$ and **3^{IV}(OH)**$^+$ (pK_a^{calc} = 6.8) that have the same Ru(V/IV) potentials at pH 13.5, because they are pseudo-isomers, but that have radically different pK_a values (see black and brown lines respectively in Figure 4C). At pH 13.5 they have identical overpotentials of 720 mV but at pH 6, **3^{IV}(OH)**$^+$ decreases its overpotential by 390 mV with regard to **2^{IV}(OH)**$^+$ that keeps constant up to the whole pH-range.

IV

D 3.3 The pK_a of the Ru^{IV}-OH/Ru^{IV}=O couple.

In the previous sections, we have put forward the importance of increasing the coordination number as well as the number of anionic groups contained in the auxiliary ligands in order to reduce the redox potentials of the V/IV couple. However, strongly increasing the electron density at the metal center in this manner not only reduces the redox potential but also drastically decreases the acidity of Ru^{IV}-OH and thus increases its pK_a. A paradigmatic example of the interplay between redox potential and pK_a is the comparison of redox potentials discussed above for **6^{IV}(O)** $^{2+}$ and **2^{IV}(OH)**$^+$. At pH 13.5 for **2^{IV}(OH)**$^+$ the redox potential is drastically reduced compared to **6^{IV}(O)**$^{2+}$, but at pH = 0 its redox potential is actually higher than that of **6^{IV}(O)**$^{2+}$. Thus, a key question that arises here is which are the factors that influence the pK_a of this couple and how can they be manipulated given its key role on the overpotential in WOCs. In other words, how can we strongly decrease redox potentials but without increasing the pK_a? The answer to this apparently contradictory question is the key to access efficient WOCs with low overpotentials at low pH.

In Table 1 are gathered the experimental and computed pK_a values for the Ru^{IV}-OH species for the complexes studied here and for some other related complexes relevant for the present discussion. A few conclusions can be extracted from this Table,

- For six coordinated complexes **6^{IV}(O)**$^{2+}$ and **7^{IV}(O)**$^+$ with zero and one anionic charge respectively, their Ru^{IV}-OH species are highly acidic with pK_a's < 0 and thus their V/IV couple is pH independent over the whole pH range. Theory also predicts pK_a's < 0 for complexes with zero

and one anionic charges $\mathbf{6^{IV}(OH)^{3+}}$, $\mathbf{7^{IV}(OH)^{2+}}$ and $\mathbf{8^{IV}(OH)^{2+}}$, whereas the six coordinated complex with a dianionic ligand, $\mathbf{9^{IV}(OH)^{+}}$, is predicted to be less acidic with a pK_a^{calc} = 2.9.

- The six coordinated complex, $\mathbf{6^{IV}(OH)^{3+}}$, with zero charge on the ligand is predicted to be very acidic with a pK_a^{calc} = - 8.9, but for $\mathbf{2^{IV}(OH)^{+}}$, that contains two anionic charges with an aqua ligand positioned axially, the pK_a spectacularly increases up to 13.5 (pK_a^{calc} = 11.8).

- For $\mathbf{3^{IV}(OH)^{+}}$ with two anionic charges and CN7 but with significant intramolecular H-bonding at the equatorial zone between the Ru-OH group and the neighboring Ru-carboxylato group ($d_{O\text{-}H\text{----}O carboxylato}$ = 2.174 Å; $\wedge_{HO\text{-}Ru\text{-}O carboxylato}$ = 73.8°),[33] displays a pK_a = 6.0 (pK_a^{calc} = 6.8). This is in sharp contrast with its pseudo isomer $\mathbf{2^{IV}(OH)^{+}}$, that has the same number of anionic charges but no intramolecular H-bonding with a pK_a = 13.5 (pK_a^{calc} = 11.8). Thus the hydrogen bonding here is responsible for increasing the acidity by more than 7 orders of magnitude. This pK_a shift is then responsible for the stabilization of the V/IV redox potential at low pH which is important since there are very few WOCs operative at low overpotentials in such acidic conditions.

- Finally, for the seven coordinated complex $\mathbf{4^{IV}(OH)^{+}}$ with one anionic donor group but with intramolecular hydrogen bonding has a pK_a of 5.7 (pK_a^{calc} = 5.4). similar to $\mathbf{3^{IV}(OH)^{+}}$.

D 3.4 Catalysis

In the previous section, we have uncovered the role of hydrogen bonding in increasing the pK_a of the Ru(IV)-OH species, a thermodynamic effect. Further, it is interesting to see here that for $\mathbf{2^{IV}(OH)^{+}}$ at pH = 7, the overpotential is about 100 mV higher than for $\mathbf{4^{IV}(OH)^{+}}$, yet the latter oxidizes water to dioxygen 3 orders of magnitude faster than the former, as can be graphically observed in the Tafel plot in Figure 2B. This has been associated with the role of the dangling carboxylate that acts as intramolecular base accepting a proton from the incoming water molecule at the O-O bond formation step and thus reducing the energy of activation, a kinetic effect (Figure 3). Thus the dangling carboxylate in complex $\mathbf{4^{IV}(OH)^{+}}$ has a dual role of favoring both thermodynamics and kinetics. In the same line, it is also interesting to realize that $\mathbf{6^{IV}(O)^{2+}}$ at pH = 7 has an overpotential of 650 mV and a TOF of 0.05 s^{-1} (measured at pH = 1.0).[27]This is in sharp contrast to $\mathbf{4^{IV}(OH)^{+}}$ that even with a lower η of 450 mV has a TOF_{max} of 7.900 s^{-1}, that is more than 5 orders of magnitude faster than that of $\mathbf{6^{IV}(O)^{2+}}$, again a consequence of the absence of intramolecular hydrogen bonding and a pendant base in the latter.

Finally, at pH 7, $\mathbf{3^{IV}(OH)^{+}}$ has an overpotential of 300 mV that is the lowest of all complexes discussed here. Under these conditions, $\mathbf{3^{IV}(OH)^{+}}$ reaches a TOF_{max} of 25 s^{-1} as shown in the Tafel plot in Figure 2. For this complex, however it is not possible to establish a direct comparison

since it follows an I2M mechanism whereas the rest of the complexes generate the O-O bond formation via a water nucleophilic attack (WNA) mechanism.

D 4 Conclusions

Complex $[Ru^{IV}(tda)(py)(OH^{ax})]^{+}$, $\mathbf{2^{IV}(OH)^{+}}$, with one pyridyl and one hydroxido ligand at the axial positions displays a moderate activity with regard to its capacity to oxidize water to dioxygen catalytically. However, it is extremely important because it constitutes the *cornerstone* that allows rationalization of the different factors involved in both six and seven coordination Ru WOCs with polypyridyl and related ligands described in the literature. From a thermodynamic perspective these factors include the influence of six and seven coordination on the Ru^{V}/Ru^{IV} redox couple and the pK_a of the Ru^{IV}-OH/Ru^{IV}-O species. The latter is strongly influenced by their access to intramolecular hydrogen bonding that is in turn controlled by the relative position of the hydroxido ligand with regard to the auxiliary tda^{2-} ligand. In complex $\mathbf{2^{IV}(OH)^{+}}$, the axial position of the hydroxido ligand precludes the presence of intramolecular hydrogen bonding and thus allows quantifying the combined effect of anionic ligands and coordination number when compared to related complexes described in the literature. From a kinetic perspective it is impressive to see the contrast in TOF= 0.4 s^{-1} for $\mathbf{2^{IV}(OH)^{+}}$ with no H-bonding and TOF= 7900 s^{-1} for $\mathbf{4^{IV}(OH)^{+}}$, at pH = 7. For the latter complex the hydroxido ligand is situated in the equatorial plane and is responsible for the O-O bond formation with an incoming solvent water molecule that can transfer a proton to the dangling carboxylate in an intramolecular manner.

As a summary, the present work shows how the different factors involved in Ru-WOC can be controlled by the auxiliary ligands and thus pave the way for the design of efficient transition metal based catalysts at low pH and low overpotentials.

D 5 Acknowledgments

R.M. thanks “La Caixa” foundation for a PhD grant. A.L. thanks MINECO and FEDER (CTQ-2016-80058-R, SEV-2013-0319; CTQ-2014-52974-REDC) and “La Caixa” foundation for financial support. The work carried out at Brookhaven National Laboratory (M.Z.E.) was supported by the U.S. Department of Energy, Office of Science, Division of Chemical Sciences, Geosciences

D 7 References

1 Lewis, N. S. *Science* **2016**, *351*, aad19201-aad19209.
2 Llobet, A.; Meyer, F. *Angew. Chem. Int. Ed.,* **2011**, *50*, A30-33.
3 (a) X. Sala, S. Maji, R. Bofill, J. Garcia-Anton, L. Escriche and A. Llobet, *Acc. Chem. Res.*, 2014, **47**, 504-516. (b) Keidel, A.; López, I.; Staffa, J.; Kuhlmann, U.; Bozoglian, F.;

Gimbert-Suriñach, C.; Benet-Buchholz, J.; Hildebrandt, P.; Llobet, A. *ChemSusChem*, **2017**, *10*, 551-561.

4 Molecular Water Oxidation Catalysis: A Key Topic for New Sustainable Energy Conversion Schemes. Edited by A. Llobet. **2014** John Wiley and Sons Ltd. ISBN: 9781118413371.

5 Barnett, S. M.; Goldberg, K. I.; Mayer, J. M. *Nat. Chem.* **2012**, *4*, 498-502.

6 Okamura, M.; Kondo, M.; Kuga, R.; Kurashige, Y.; Yanai, T.; Hayami, S.; Praneeth, V. K. K.; Yoshida, M.; Yoneda, K.; Kawata, S.; Masaoka, S. *Nature* **2016**, *530*, 465-468.

7 Sens, C.; Romero, I.; Rodriguez, M.; Llobet, A.; Parella, T.; Benet-Buchholz, J. *J. Am. Chem. Soc.* **2004**, *126*, 7798-7799.

8 Concepcion, J. J.; Tsai, M. K.; Muckerman, J. T.; Meyer, T. J. *J. Am. Chem. Soc.* **2010,** *132*, 1545-1557.

9 Neudeck, S.; Maji, S.; Lopez, I.; Meyer, S.; Meyer, F.; Llobet, A. *J. Am. Chem. Soc.* **2014**, *136*, 24-27.

10 Wasylenko, D. W.; Ganesamoorthy, C.; Henderson, M.; Koivisto, B. D.; Osthoff, H.; Berlinguette, C. P. *J. Am. Chem. Soc*. **2010**, *132*, 16094-16106.

11 D. E. Polyansky, J. T. Muckerman, J. Rochford, R. Zong, R. P. Thummel and E. Fujita, *J. Am. Chem. Soc.* **2011**, *133*, 14649-14665.

12 Shaffer, D. W.; Xie, Y.; Szalda, D. J.; Concepcion, J. J. *Inorg. Chem.* **2016**, *55*, 12024-12035.

13 Schulze, M.; Kunz, V.; Frischmann, P. D.; Würthner, F. *Nat. Chem.* **2016**, *8*, 576-583.

IV

14 Gimbert-Suriñach, C.; Moonshiram, D.; Francas, L.; Planas, N.; Bernales, V.; Bozoglian, F.; Guda, A.; Mognon, L.; López, I.; Hoque, Md A.; Gagliardi, L.; Cramer, C. J.; Llobet, A. *J. Am. Chem. Soc.* 2016, **138**, 15291-15294.

15 Duan, L.; Bozoglian, F.; Mandal, S.; Stewart, B.; Privalov, T.; Llobet, A.; Sun, L. *Nat. Chem.* **2012,** *4,* 418-423.

16 Richmond, C. J.; Matheu, R.; Poater, A.; Falivene, L.; Benet-Buchholz, J.; Sala, X.; Cavallo, L.; Llobet, A. *Chem. Eur. J.* **2014**, *20*, 17282–17286.

17 Wang, L.; Duan, L.; Wang, Y.; Ahlquist, M. S. G.; Sun, L. *Chem. Commun.* **2014**, *50*, 12947-12950.

18 Matheu, R.; Ertem, M. Z.; Benet-Buchholz, J.; Coronado, E.; Batista, V. S.; Sala, X.; Llobet, A. *J. Am. Chem. Soc.* **2015**, *137,* 10786-10795.

19 Creus, J.; Matheu, R.; Peñafiel, I.; Moonshiram, D.; Blondeau, P.; Benet-Buchholz, J.; García-Antón, J.; Sala, X.; Godard, C.; Llobet, A. *Angew. Chem. Int. Ed*. **2016**, *55*, 15382-15386.

20 (a) Zhao, Y.; Truhlar, D. G. *Theor. Chem. Acc.* **2008**, *120*, 215-215. (b) Zhao, Y.; Truhlar, D. G. *Acc. Chem. Res.* **2008**, *41*, 157-157.

21 Marenich, A. V.; Cramer, C. J.; Truhlar, D. G. *J. Phys. Chem. B* **2009**, *113*, 6378-6378.

22 Lever, A.B.P. *Inorg. Chem*., **1990**, *29*, 1271-1285.

23 A. B. P. Lever and E. S. Dodsworth, in Comprehensive Coordination Chemistry, II, Vol. 2 Edited by A. B. P. Lever, Elsevier Publishers**, 2004**.

24 Masllorens, E.; Rodriguez, M.; Romero, I.; Roglans, A.; Parella, T.; Benet-Buchholz, J.; Poyatos, M.; Llobet, A. *J. Am. Chem. Soc* **2006**, *128*, 5306-5307.

25 Matheu, R.; Neudeck, S.; Meyer, F.; Sala, X.; Llobet, A. *ChemSusChem* **2016**, *9*, 3361-3369.

26 Roeser, S.; Bozoglian, F.; Richmond, C. J.; League, A. B.; Ertem, M. Z.; Francas, L.; Miro, P.; Benet-Buchholz, J.; Cramer, C. J.; Llobet, A *Cat. Sci. Technol*., **2016**, *6*, 5088-5101.

27 Wasylenko, D. J.; Ganesamoorthy, C.; Henderson, M. A.; Berlinguette, C. P. *Inorg. Chem.* **2011**, *50*, 3662-3672.
28 Mognon, L.; Benet-Buchholz, J.; Llobet, A. *Inorg. Chem.* **2015**, *54*, 11948-11957.
29 Tong, L.; Inge, A. K.; Duan, L.; Wang, L.; Zou, X.; Sun, L. *Inorg. Chem* .**2013**, *52*, 2505-2518.
30 Li, F.; Li, L.; Tong, L.; Daniel, Q.; Gothelid, M.; Sun, L. *Chem. Commun.* **2014**, *50*, 13948-13951.
31 Fan, T.; Duan, L.; Huang, P.; Chen, H.; Daniel, Q.; Ahlquist, M. S. G.; Sun, L. *ACS Catal.* **2017***, 7,* 2956−2966.
32 Liu, Y.; Ng, S.-M.; Yiu, S.-M.; Lam, W. W. Y.; Wei, X.-G.; Lau, K.-C.; Lau, T.-C. *Angew. Chem. Int. Ed*. **2014**, *53*, 14468-14471.
33 Duan, L.; Fischer, A.; Xu, Y.; Sun, L. *J. Am. Chem. Soc.* **2009**, *131*, 10397-10399.

D 7 Supporting Information

Paper D: Hydrogen Bonding Rescues Overpotential in Seven Coordinated Ru Water Oxidation Catalysts

Outline

IV

1. Materials.

All materials were provided by Sigma-Aldrich unless indicated. [2,2':6',2''-terpyridine]-6,6''-dicarboxylic acid (H_2tda),[S1] [Ru^{II}(tda-κ-N^3O)$(py)_2$] (complex **4^{II}**),[S2] [Ru^{IV}(tda-κ-N^3O)$(py)_2(O)^{ax}$] (complex **4^{IV}(O)**) [S2] and [$RuCl_2dmso_4$][S3] were synthesized according to the literature. High-purity deionized water was obtained by passing distilled water through a nanopure Milli-Q water purification system.

Synthesis of [Ru(tda-κ-N^3O)(dmso)(py)], 1^{II}. A sample of [$RuCl_2dmso_4$] (150 mg, 0.30 mmol), 2',2'':6',2''-terpyridine-6',6''-dicarboxylic acid (H_2tda) (99 mg, 0.31 mmol) and Et_3N (0.3 mL) were dissolved in degassed dry MeOH (6 mL), refluxed for 6 hours and cooled down to RT. A brown solid (approx. 100 mg) appears in the reaction mixture and is filtered, washed with MeOH and diethyl ether. The solid was then suspended in water (5 mL) and pyridine (15 mL) and stirred for 4 days at room temperature. This generated a brown solution was that was extracted with DCM (3 x 100 mL). The volume of the aqueous fraction was then reduced to dryness. A brown solid was obtained in this way that was dissolved in MeOH and precipitated with diethyl ether (90 mg, 0.14 mmol, 45 % yield). Crystals suitable for XRD were obtained from a slow evaporation of a saturated methanol solution. ^{1}H-NMR (400Hz, [d4]-methanol), δ: 2.92 (6H, s), 7.28 (2H, t, J = 7.7 Hz), 7.76 (1H, tt, J = 1.5 and 7.7 Hz), 8.10 (2H, dd, J = 7.7 and 1.5 Hz), 8.13 (2H, dd, J = 1.1 and 7.9 Hz), 8.23 (2H, t, J = 7.9 Hz), 8.29 (1H, t, J = 8.1 Hz), 8.56 (2H, dd, J = 1.1 and 7.9 Hz), 8.66 (2H, d, J = 8.1 Hz). ^{13}C-NMR (500Hz, [d4]-methanol) δ:42.0, 123.9, 124.2, 125.4, 126.4, 135.8, 138.0, 138.3, 150.9, 157.8, 158.1, 160.5, 171.1. MALDI$^+$-HRMS m/z: calc. for [**1^{II}** + Na^+] ($C_{24}H_{20}N_4NaO_5RuS^+$): 601.00901, found m/z: 601.0103 (0.7 ppm). Anal. Calc.: [**1^{II}** + 3.5·H_2O] ($C_{24}H_{27}N4O_{8.5}RuS$): C, 45.00 %; H, 4.25 %; N, 8.75 %; S, 5.01 %. Found: C, 45.01 %; H, 4.16 %; N, 8.75 %; S, 5.15 %.

Synthesis of [Ru(tda-κ-N^3O)(py)$(OH_2)^{ax}$](PF_6), [$2^{III}(OH)_2$](PF_6). Complex **1^{II}** (100 mg, 0.2 mmol) was dissolved in 0.3 mL of *neat* triflic acid and stirred for 4 hours. The solution was then added to 3.6 mL of saturated solution KPF_6. A brown precipitate was filtered and allowed to dry (95 mg, 65 %). ^{1}H-NMR (500 Hz, D_2O + Sodium ascorbate) δ: 6.87 (2 H, t, J = 7.1 Hz), 7.38 (1 H, t, J = 7.1 Hz), 7.65 (2 H, d, J = 7.1 Hz), 7.87 (1 H, t, J = 8.0 Hz), 7.94 (2 H, d, J = 7.8 Hz), 8.00 (2 H, t, J = 7.8 Hz), 8.33 (2 H, d, J = 7.8 Hz), 8.36 (2 H, d, J = 8.0 Hz).^{13}C-NMR (500 Hz, D_2O): 123.2, 123.7, 124.6, 125.6, 132.9, 136.2, 137.3, 153.2, 157.5, 159.0, 162.4, 173.9, 177.1. MALDI$^+$-HRMS m/z: calc. for [**2^{III}**-py] ($C_{17}H_9N_3O_4Ru$): 420.96366, found m/z: 420.9649 (2.9 ppm). Anal. Calc.: {[**$2^{III}(OH)_2$**](PF_6) + 0.1·CF_3SO_3H + 2·H_2O} ($C_{22.1}H_{20.1}F_{6.3}N_4O_{7.3}PRuS_{0.1}$): C, 37.20 %; H, 2.84 %; N, 7.85 %; S, 0.45 %. Found: C, 37.20 %; H, 2.77 %; N, 7.68 %; S, 0.5 %.

IV

2. Methods and Instrumentation.

Matrix-assisted laser desorption ionization (MALDI) mass spectrometry (MS) experiments were performed on a Bruker Daltonics Autoflex equipped with a nitrogen laser (337 nm). A Bruker Avance 500 MHz or 400 MHz were used to carry out NMR spectroscopy. The pH of the solutions was determined by a pHmeter (CRISON, Basic 20^{+}) calibrated before measurements through standard solutions at pH = 4.01, 7.00 and 9.21.

Electrochemical methods

General considerations

All electrochemical experiments were performed in an IJ-Cambria HI-730 bipotentiostat, using a three-electrode cell. The Reference Electrode (RE) was Hg/Hg_2SO_4 (K_2SO_4 saturated) unless indicated and potentials were converted to NHE by adding 0.65 V.

Cells: A 20 mL vial was used as an electrochemical cell for CV measurements. A Teflon-made with holes for the three electrodes was used as a lid to ensure a reproducible distance between the electrodes. A two compartments cell (25 mL per compartment) with a separation frit was used for Bulk Electrolysis Experiments.

Cyclic voltammetry (CV) and Differential Pulse Voltammetry

Glassy carbon disk (ϕ = 0.3 cm, S = 0.07 cm^2), Pt disk and Hg/Hg_2SO_4 (K_2SO_4 saturated) were used as Working Electrode (WE), Counter Electrode (CE) and Reference Electrode (RE) respectively, unless explicitly mentioned. Glassy carbon electrodes were polished with 0.05 µm alumina (Al_2O_3) and rinsed with water. CVs and DPVs were iR compensated by the potentiostat in all the measurements unless indicated. Cyclic Voltammograms (CV) were recorded at 100 $mV{\cdot}s^{-1}$ scan rate, unless explicitly expressed. The DPV parameters were ΔE = 4 mV, Amplitude = 0mV, Pulse width = 5 s, Sampling width = 0.0167 s, Pulse period = 5 s unless explicated.

Pourbaix diagram

For the construction of the Pourbaix Diagram solutions of complex $\mathbf{2^{III}(H2O)^{+}}$ 0.5 mM, in *I* = 0.1 M phosphate buffer solutions were used at the desired pH. For the IV/III and III/II redox couples the $E_{1/2}$ was estimated from the their corresponding $E_{p,c}$ and $E_{p,a}$ values ($E_{1/2} = 1/2(E_{p,c} + E_{p,a})$) in the CV. For the V/IV redox couple the $E^{o'}$ was estimated at the onset of the catalytic current.

Foot of the Wave Analysis (FOWA)

Peak current intensity (i_p) and standard potential (E^0) determination

a) i_p was estimated from the peak cathodic current intensity of the Ru^{III}/Ru^{II} redox couple.

b) E^0 was extracted from DPV for complex $\mathbf{4^{IV}(O)}$. For complex $\mathbf{2^{IV}(OH)^+}$ E^0 was estimated as the inset of the catalytic current as shown in Figure S15.

TOF_{MAX} and k_{WNA} *determination*

The global kinetic constant of the catalytic oxidation of water (k_{WNA}, s^{-1}) was extracted from the linear fit at the foot of the wave of the i/i_p *vs.* $[1+e((E^0-E)\cdot(F/RT))]$ plot assuming a WNA mechanism. k_{WNA} is equal to TOF_{MAX}, which is a particular case of the Turn Over Frequency (TOF) where TOF is calculated for potentials much higher than the corresponding E^o.

Catalytic Tafel plots

The catalytic Tafel plots were drawn by applying the formula ($\mathrm{TOF} = \frac{k_{WNA}}{1+e^{\left(\frac{F(E^0-E)}{RT}\right)}}$) where E^0 is the standard potential, E is the applied potential, R is the gas constant and T is the temperature.

Single-Crystal XRD Methods

X-ray Crystal Structure Determinations

The measured crystals were prepared under inert conditions immersed in perfluoropolyether as protecting oil for manipulation.

Data collection

Crystal structure determinations for $\mathbf{1^{II}}$ was carried out using a Apex DUO diffractometer equipped with a Kappa 4-axis goniometer, an APEX II 4K CCD area detector, a Microfocus Source E025 IuS using MoK_α radiation, Quazar MX multilayer Optics as monochromator and an Oxford Cryosystems low temperature device Cryostream 700 plus (T = -173 ˚C). Full-sphere data collection was used with ω and φ scans. The structure has been deposited at CCDC with reference number 1545291.

Programs used

Data collection with APEX-2,[S4] data reduction with Bruker Saint [S5] and absorption correction with SADABS.[S6]

Structure Solution and Refinement

Crystal structure solution was achieved using direct methods as implemented in SHELXTL[S7] and visualized using the program XP. Missing atoms were subsequently located from difference Fourier synthesis and added to the atom list. Least-squares refinement on F^2 using all measured intensities was carried out using the program SHELXTL. All non-hydrogen atoms were refined including anisotropic displacement parameters.

Comments to the structures

Complex **1**^{II} crystallizes with one molecule of the metal complex and two molecules of methanol in the asymmetric unit. One of the methanol molecules is disordered in two positions (ratio 59:41).

Computational Methods

Density functional theory

Geometry optimizations were performed at M06-L[S8] and M06 [S9,S10] levels of density functional theory using the Stuttgart [8s7p6d2f | 6s5p3d2f] ECP28MWB contracted pseudopotential basis set[S11] on Ru and the 6-31G(d) basis set[S12] on all other atoms. Non-analytical integral evaluations made use of a pruned grid having 99 radial shells and 590 angular points per shell and an automatically generated density-fitting basis set was used within the resolution-of-the-identity approximation to speed the evaluation of Coulomb integrals as implemented in Gaussian 09 software package. [S13] The nature of all stationary points was verified by analytic computation of vibrational frequencies, which were also used for the computation of zero-point vibrational energies, molecular partition functions (with all frequencies below 50 cm^{-1} replaced by 50 cm^{-1} when computing free energies), and for determining the reactants and products associated with each transition-state structure (by following the normal modes associated with imaginary frequencies). Partition functions were used in the computation of 298 K thermal contributions to free energy employing the usual ideal-gas, rigid-rotator, harmonic oscillator approximation.[S14] For M06-L optimized structures, free energy contributions were added to single-point M06-L, M06 [S9,S10] and B3LYP[S15](with the D3 version of Grimme's dispersion with Becke-Johnson

damping[S16]) electronic energies computed with SMD aqueous continuum solvation model[S17]and the SDD basis set on ruthenium and the 6-311+G(2df,p) basis set on all other atoms to arrive at final composite free energies. For M06 optimized structures, M06 electronic energies computed with SMD aqueous continuum solvation model [S17] and the SDD basis set on ruthenium and the 6-311+G(2df,p) basis set on all other atoms to arrive at final composite free energies. The optimization of water nucleophilic attack transition state structures were performed at M06 level of theory in the presence of SMD aqueous continuum solvation model instead of gas phase optimizations.

Solvation and standard reduction potentials

As stated above, solvation effects associated with water as solvent were accounted for using the SMD continuum solvation model. A 1 M standard state was used for all species in aqueous solution except for water itself, for which a 55.6 M standard state was employed. Thus, for all molecules but water, the free energy in aqueous solution is computed as the 1 atm gas-phase free energy, plus an adjustment for the 1 atm to 1 M standard-state concentration change of *RT* ln (24.5), or 1.9 kcal/mol, plus the 1 M to 1 M transfer (solvation) free energy computed from the SMD model. In the case of water, the 1 atm gas-phase free energy is adjusted by the sum of a 1 atm to 55.6 M standard-state concentration change, or 4.3 kcal/mol, and the experimental 1 M to 1 M solvation free energy, –6.3 kcal/mol. The 1 M to 1 M solvation free energy of the proton was taken from experiment as –265.9 kcal/mol.[S18-S21]

Standard reduction potentials were calculated for various possible redox couples. For a redox reaction of the form

$$O_{(aq)} + n\,e^-_{(g)} \rightarrow R_{(aq)} \quad \text{(S1)}$$

where *O* and *R* denote the oxidized and reduced states of the redox couple, respectively, and *n* is the number of electrons involved in redox reaction, the reduction potential $E^0_{O/R}$ relative to NHE was computed as

$$E^{\circ}_{O|R} = -\frac{\Delta G^{\circ}_{O|R} - \Delta G^{\circ}_{\mathrm{NHE}}}{nF} \quad \text{(S2)}$$

where $\Delta G^0_{O/R}$ is the free energy change associated with eq. 1 (using Boltzmann statistics for the electron), ΔG^0_{NHE} is the free energy change associated with

$$H^{+}_{(aq)} + e^{-}_{(g)} \rightarrow \frac{1}{2}H_{2(g)} \quad \text{(S3)}$$

which is –4.28 eV with Boltzmann statistics for the electron,[S6,S22,S23] and *F* is the Faraday constant.

Non-single-determinantal state energies

Several possible intermediates in the water oxidation mechanism have electronic structures that are not well described by a single determinant. In such instances, standard Kohn-Sham DFT is not directly applicable,[S14,S24-S26] and we adopt the Yamaguchi broken-spin-symmetry (BS) procedure [S27,S28] to compute the energy of the spin-purified low-spin (LS) state as

$$^{LS}E = \frac{^{BS}E\left(\left\langle S^2\right\rangle - {}^{LS}\left\langle S^2\right\rangle\right) - {}^{HS}E\left(\left\langle S^2\right\rangle - {}^{LS}\left\langle S^2\right\rangle\right)}{{}^{HS}\left\langle S^2\right\rangle - {}^{BS}\left\langle S^2\right\rangle} \quad \text{(S4)}$$

where HS refers to the single-determinantal high-spin coupled state that is related to the low-spin state by spin flip(s) and < *S*2 > is the expectation value of the total spin operator applied to the appropriate determinant.

IV

3. Characterization of complexes 1^{II} and $2^{III}(OH_2)^+$

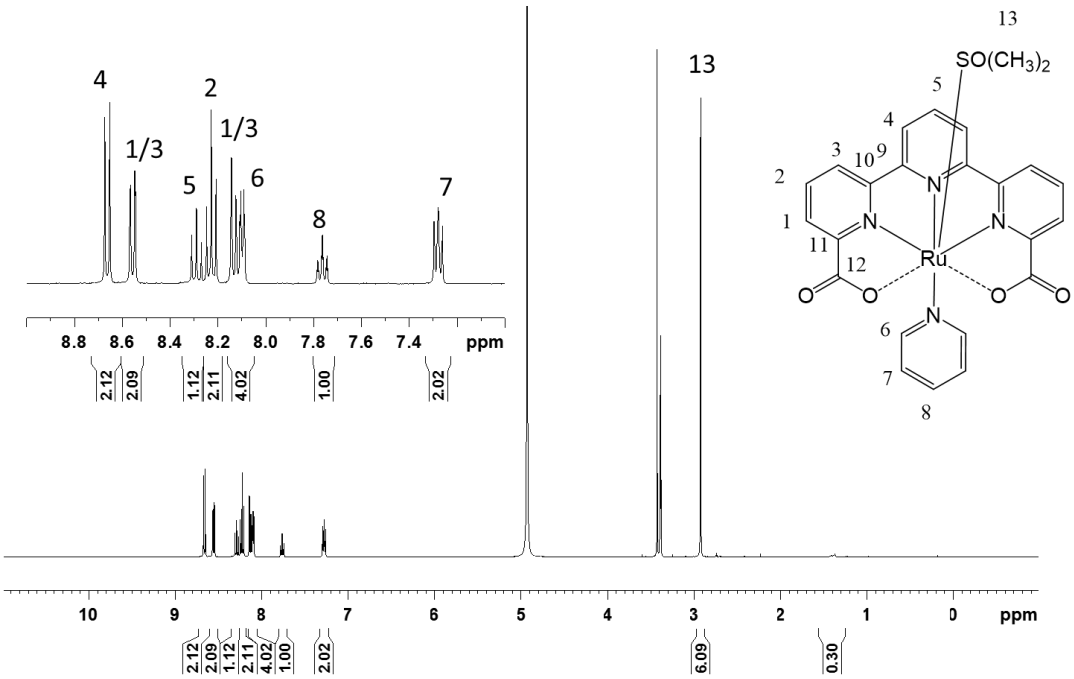

Figure S1: ^{1}H of $\mathbf{1^{II}}$ in [d4]-methanol.

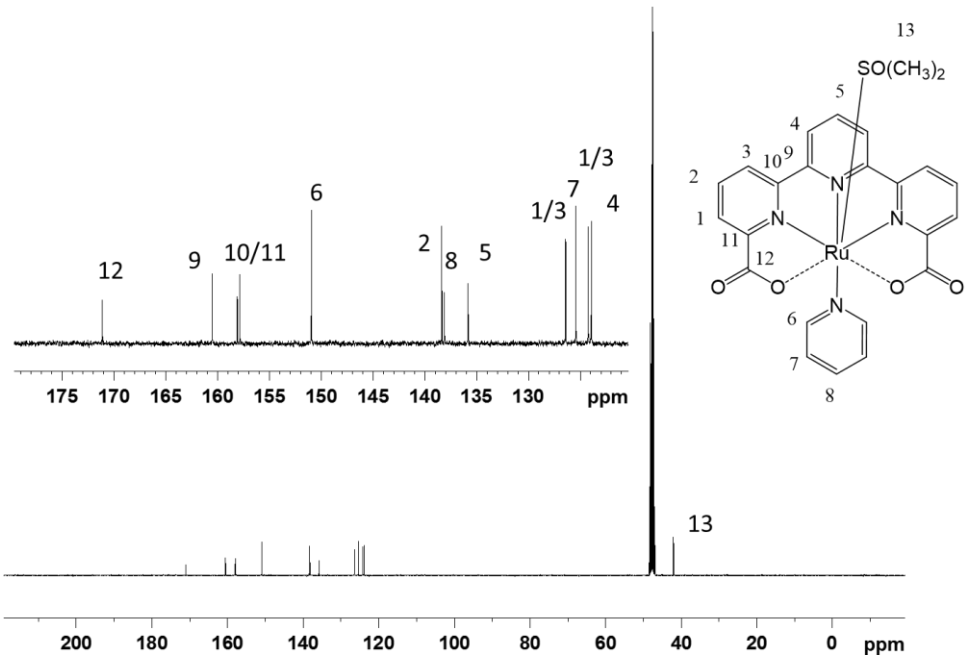

Figure S2: ^{13}C of $\mathbf{1^{II}}$ in [d4]-methanol.

IV

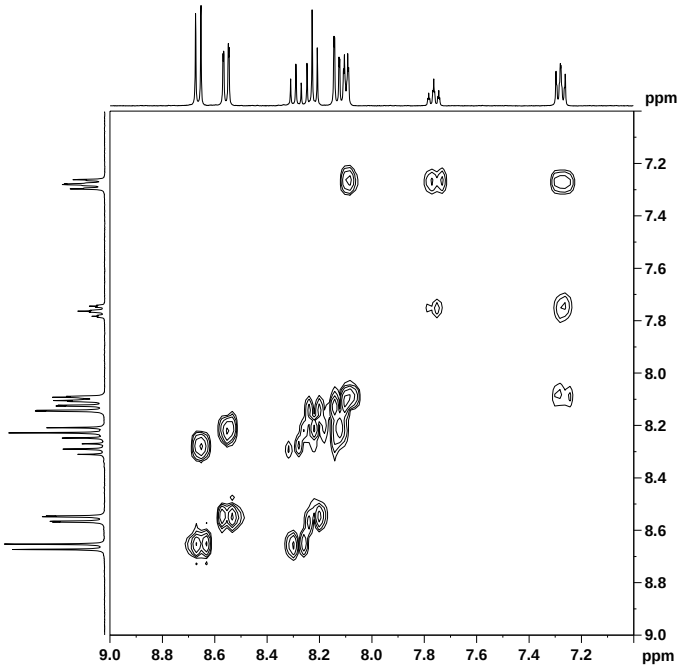

Figure S3: ^{1}H-^{1}H COSY of **1^{II}** in [d4]-methanol.

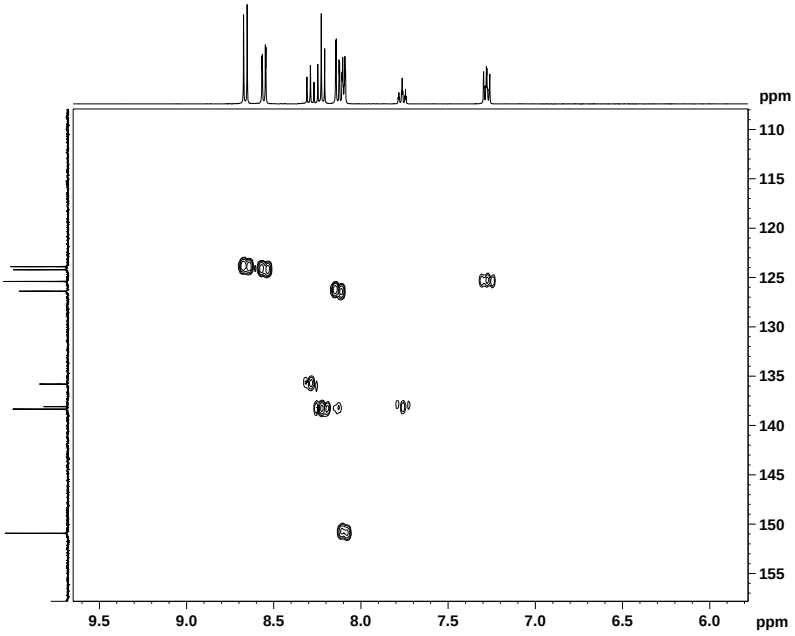

Figure S4: ^{1}H-^{13}C HSQC of **1^{II}** in [d4]-methanol.

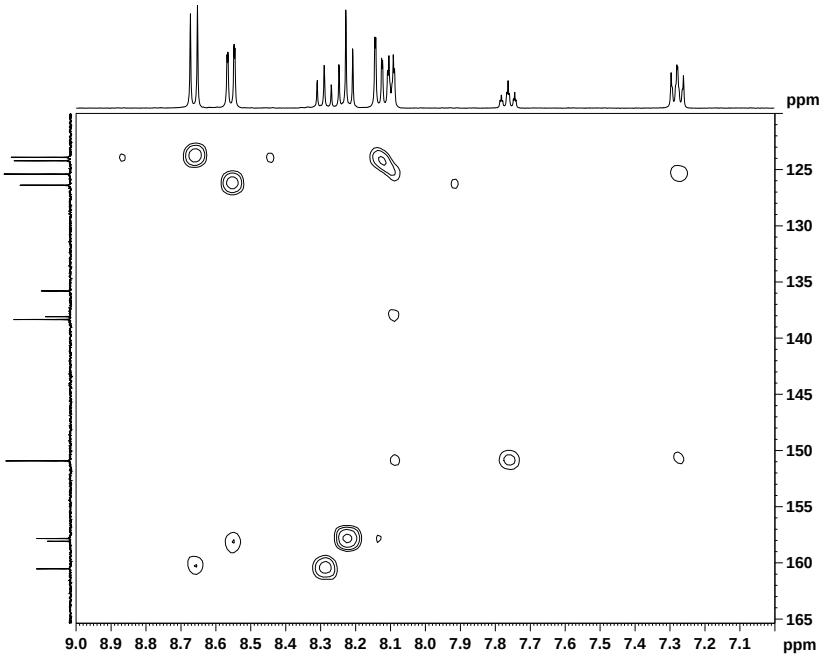

Figure S5: ^{1}H-^{13}C HMBC of **1**^{II} in [d4]-methanol.

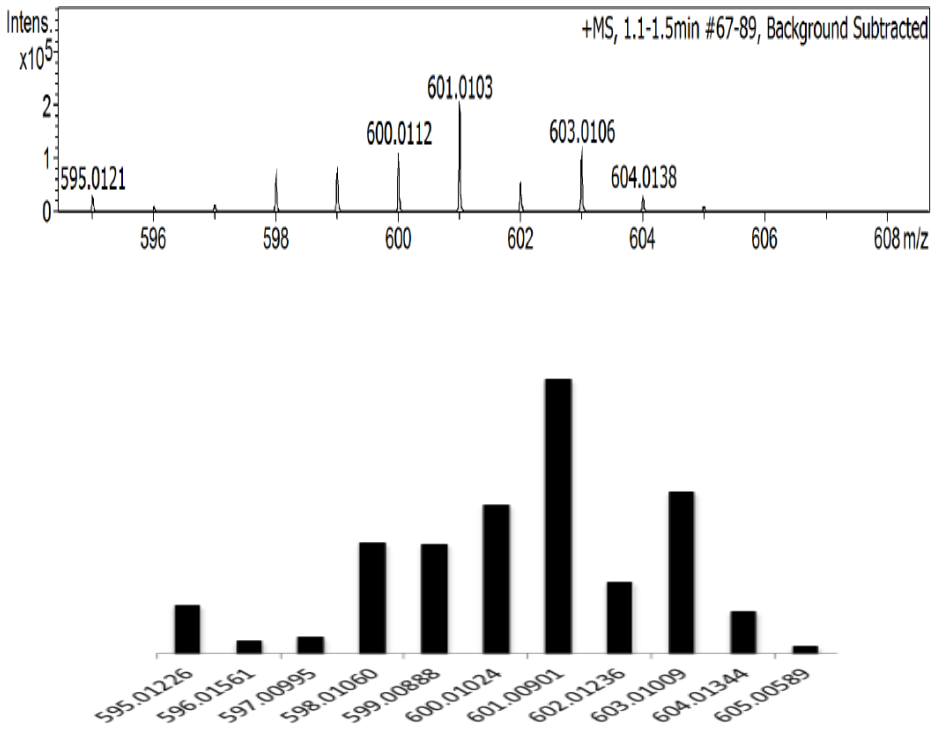

Figure S6: Measured HR-MS for $(\mathbf{1}^{III})^{+}$ (top) and simulated HR-MS for $(\mathbf{1}^{III})^{+}$ (bottom).

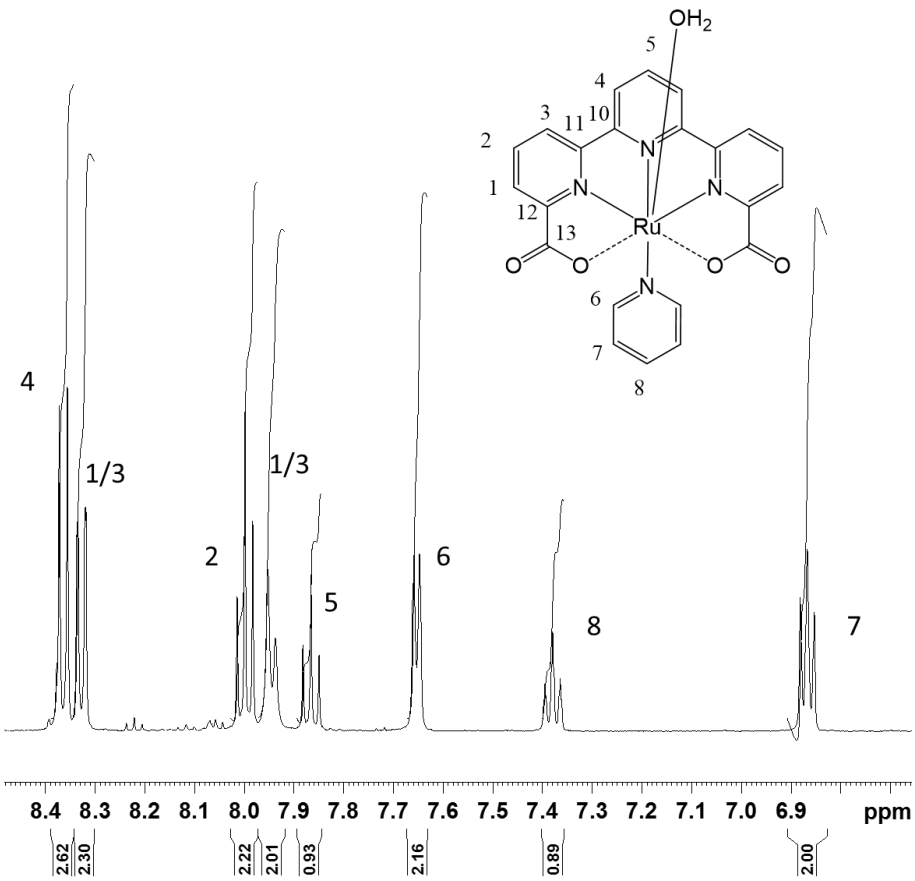

Figure S7: ^{1}H of $\mathbf{2^{II}(OH_2)}$ in D_2O with sodium ascorbate as reducing agent.

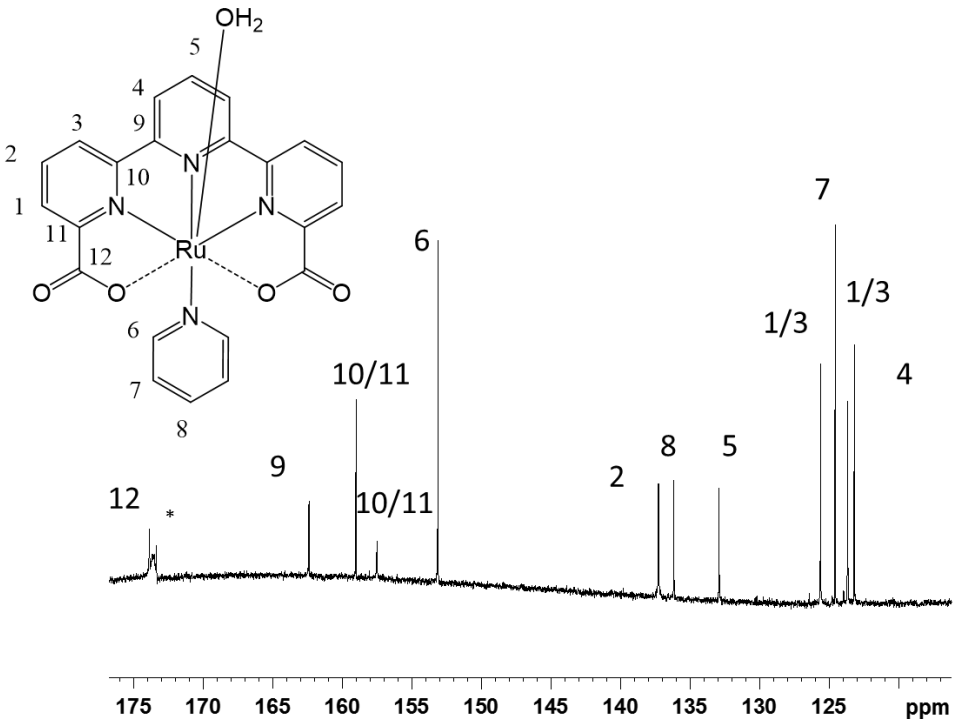

Figure S8: ^{13}C of **$2^{II}(OH_2)$** in D_2O with sodium ascorbate as reducing agent.

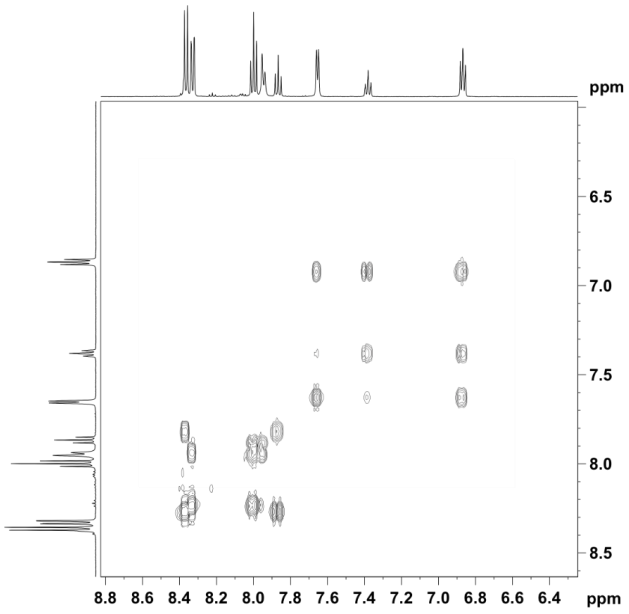

Figure S9: ^{1}H-^{1}H COSY of **$2^{II}(OH_2)$** in D_2O with sodium ascorbate as reducing agent.

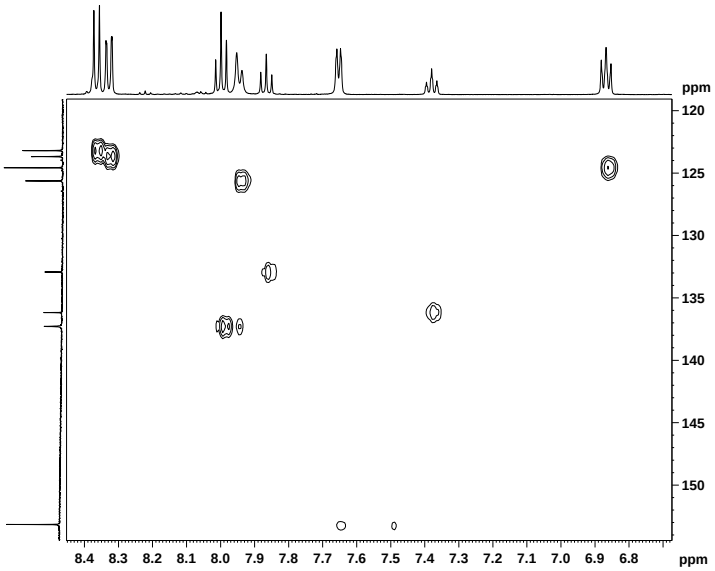

IV

Figure S10: ^{13}C-^{1}H HSQC of **$2^{II}(OH_2)$** in D_2O with sodium ascorbate as reducing agent.

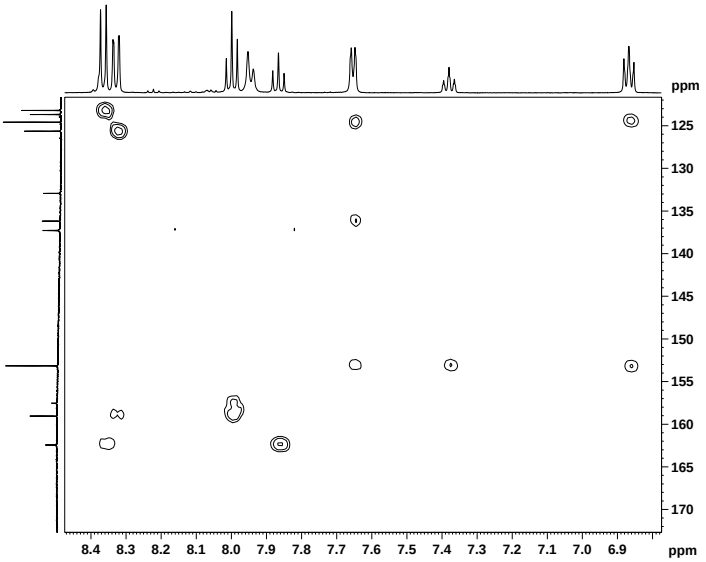

Figure S11: ^{13}C-^{1}H HMBC of **$2^{II}(OH_2)$** in D_2O with sodium ascorbate as reducing agent.

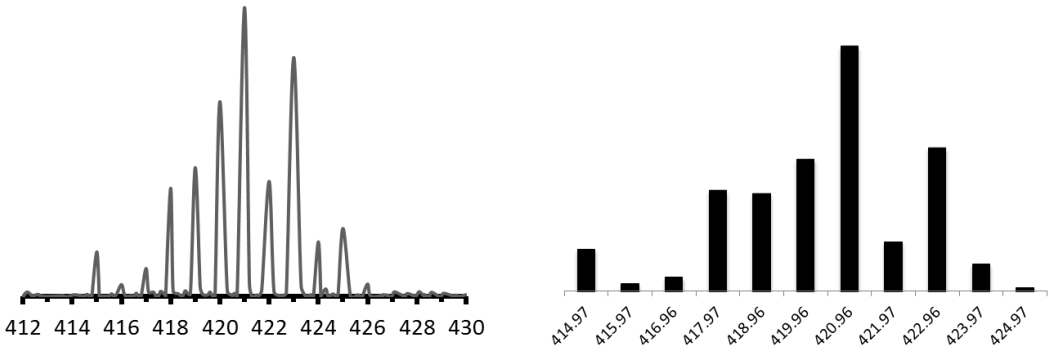

Figure S12: Measured HR-MS of $(\mathbf{2}^{III}\text{-py})^+$ (left) and simulated HR-MS of $(\mathbf{2}^{III}\text{-py})^+$ (right)

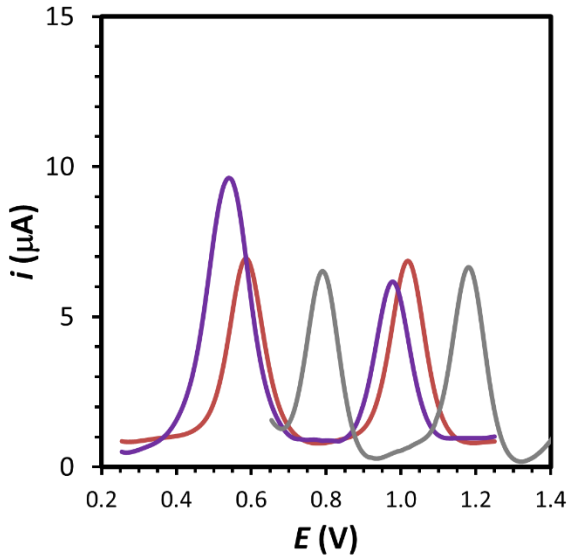

Figure S13: Diffential Pulse Voltammetry of complex $\mathbf{1}^{II}$ (grey line), $\mathbf{2}^{III}\mathbf{(OH_2)}^+$(purple line) and $\mathbf{4}^{II}$ (red line) at pH = 1.

4. Metric parameters for single-crystal XRD structure of complex 1^{II}

Table S1: Metric parameters of $\mathbf{1}^{II}$.

Ru-N^{tda}1	2.17 Å
Ru-N^{tda}2	1.96 Å
Ru-N^{tda}3	1.97 Å
Ru-O^{tda}1	2.17 Å
Ru-O^{tda}2	3.32 Å
Ru-S^{dmso}1	2.25 Å

IV

Electrochemical data

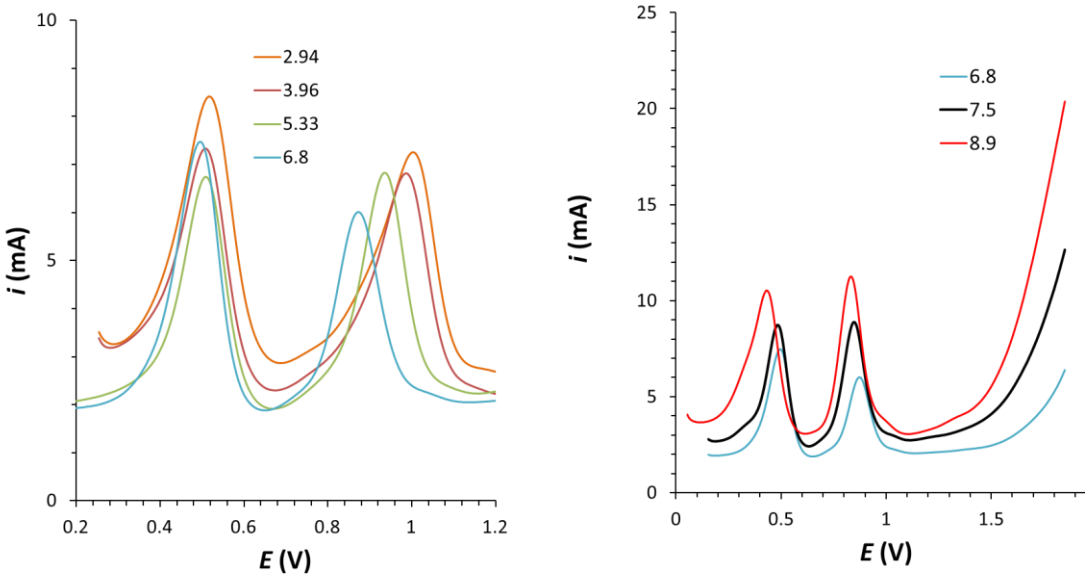

Figure S14: DPVs for $\mathbf{2^{III}(OH_2)}^{+}$ at different pHs.

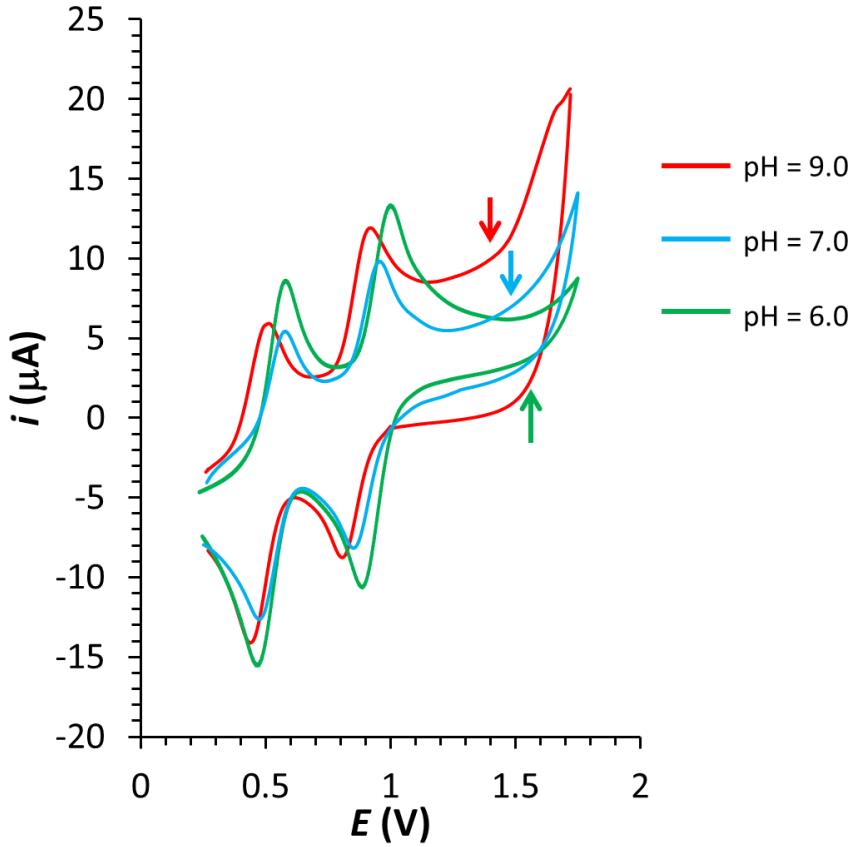

Figure S15: Blank-corrected CVs of $\mathbf{2^{III}(OH_2)^+}$ at pH 6.0, 7.0 and 9.0. Arrows indicate the potential used for the Ru^{V}/Ru^{IV} redox couple in the Pourbaix diagram.

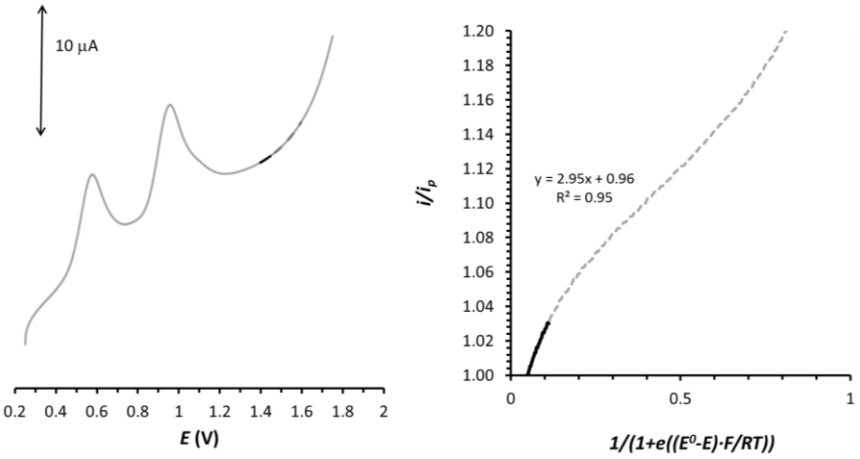

IV

Figure S16: Left, grey solid line shows a blank-corrected CV of **2^{IV}(OH)**$^{+}$ solution at pH = 7.0 (**2^{IV}(OH)**$^{+}$] = 0.5 mM). Right, *i/i$_p$ vs*. [1/(1+e((*E^0-E)(F/RT*)))] plot assuming a WNA mechanism. The grey dashed line indicates the data points used to for the FOWA and the black solid represents the points used in the lineal fit. *E^0* = 1.50 V was used and TOF_{MAX} = 0.4 s^{-1} was extracted from the analysis.

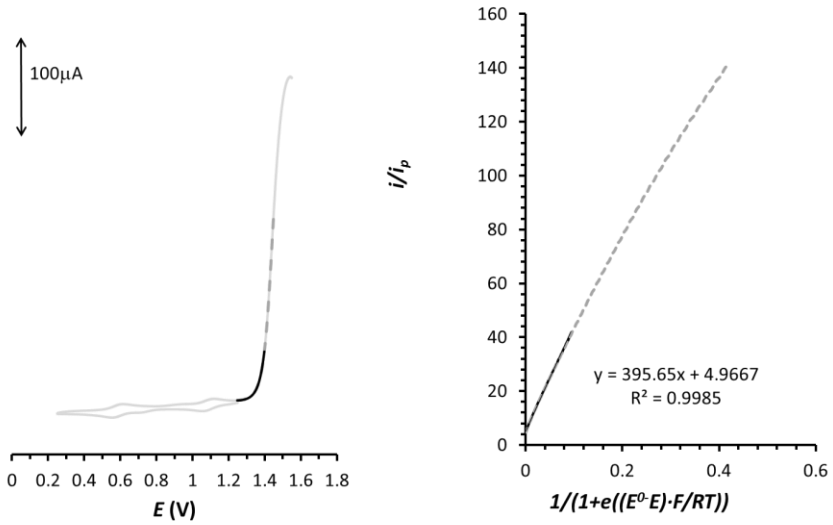

Figure S17: Left, grey solid line shows a blank-corrected CV of a **4^{IV}** and **4^{IV}(O)** solution at pH = 7.0 (**[4^{IV}]** = 0.75 mM and [**4^{IV}(O)**] = 0.37 mM). Right, *i/i$_p$ vs*. [1/(1+e((*E^0-E)(F/RT*)))] plot assuming a WNA mechanism.The grey dashed line indicates the data points used to for the FOWA and the black solid represents the points used in the lineal fit. *E^0* = 1.50 V was used and TOF_{MAX} = 0.4 s^{-1} was extracted from the analysis. *E^0* = 1.43 V was used and TOF_{MAX} = 7.9 10^3 s^{-1} was extracted from the analysis.

6. Computational data

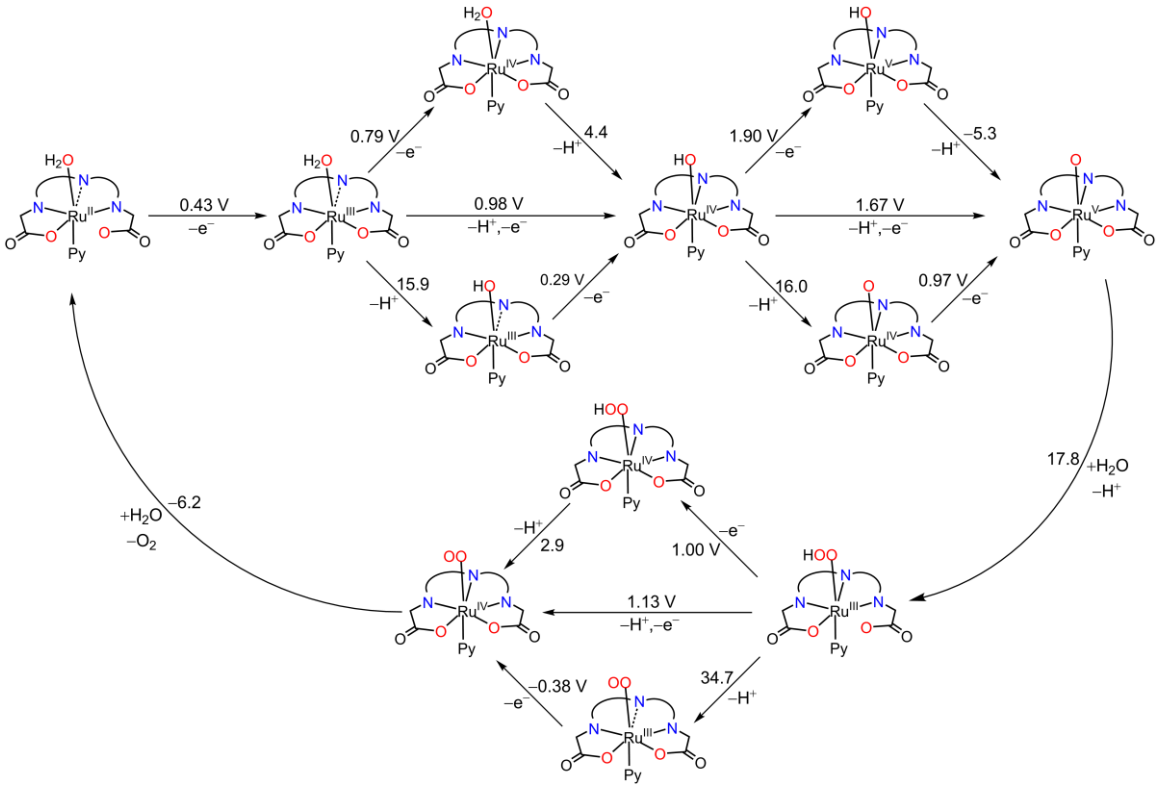

Scheme S1. Proposed catalytic cycle for water oxidation by 2IV(OH)+ complex at M06 level of theory. The computed redox potentials are reported in units of volts vs NHE and free energy changes are reported in units of kcal/mol at pH 0. Only the backbone of tda ligand is shown for the sake of clarity.

IV

Table S2. Computed redox potentials and pKa values for complex 2IV(OH)+ and related complexes at M06-L (in black), M06 (in blue) and B3LYP-D3 (in red) level of theories obtained via single point calculations on optimized geometries at M06-L level of theory.[a]

	pK_a	**E vs NHE (pH 0)**	
	[Ru^{IV}-OH]/ [Ru^{IV}-O]	**[Ru^{IV}-OH]/ [Ru^{V}-O]**	**[Ru^{IV}-O]/ [Ru^{V}-O]**
$[Ru^{IV}(trpy)(bpy)(OH)]^{3+}$	–8.4	1.00	1.50
$6^{IV}(OH)^{3+}$	–9.6	1.20	1.77
$[Ru^{IV}(trpy)(ppc)(OH)]^{2+}$	–5.9	0.92	1.26
$7^{IV}(OH)^{2+}$	–7.7	1.16	1.61
$[Ru^{IV}(bca)(bpy)(OH)]^{2+}$	–1.7	0.93	1.04
$8^{IV}(OH)^{2+}$	–2.8	1.18	1.35
trans-$[Ru^{IV}(pdc)(py)_2(OH)]^{+}$	5.0	0.86	0.57
$9^{IV}(OH)^{+}$	2.4	1.12	0.98
$[Ru^{IV}(tda\text{-}\kappa\text{-}N^3O)(py)_2(OH)^{eq}]^{+}$	6.4	1.30	0.91
	4.1	1.62	1.38
$[Ru^{IV}(bda)(py)_2(OH)^{eq}]^{+}$	12.2	1.19	0.47
$3^{IV}(OH)^{+}$	9.4	1.47	0.91
$[Ru^{IV}(tda\text{-}\kappa\text{-}N^2O^2)(py)(OH)^{ax}]^{+}$	13.9	1.34	0.52
	11.8	1.71	1.01

a. See computational methods for details

Table S3: Computed redox potentials and pK_a values for complex **2^{IV}(OH)$^+$** and related complexes at M06 level of theory[a]

	pK_a	**E vs NHE (pH 0)**	
	[Ru^{IV}-OH]/	**[Ru^{IV}-OH]/**	**[Ru^{IV}-O]/**
	[Ru^{IV}-O]	**[Ru^{V}-O]**	**[Ru^{V}-O]**
[Ru^{IV}(trpy)(bpy)(OH)]$^{3+}$	–8.9	1.23	1.76
[Ru^{IV}(trpy)(ppc)(OH)]$^{2+}$	–7.7	1.15	1.60
[Ru^{IV}(bca)(bpy)(OH)]$^{2+}$	–2.6	1.18	1.33
trans-[Ru^{IV}(pdc)(py)$_2$(OH)]$^+$	2.9	1.12	0.95
[Ru^{IV}(tda-κ-N^{3}O)(py)$_2$(OH)^{eq}]$^+$	5.4	1.57	1.26
[Ru^{IV}(bda)(py)$_2$(OH)^{eq}]$^+$	6.8	1.47	1.04
[Ru^{IV}(tda-κ-N^{2}O^2)(py)(OH)^{ax}]$^+$	11.8	1.67	0.97

a. See computational methods for details

7. References

S1 Galaup, C.; Couchet, J.-M.; Bedel, S.; Tisnès, P.; Picard, C. *J. Org. Chem.* **2005**, *70*, 2274-2284.

S2 Matheu, R.; Ertem, M. Z.; Benet-Buchholz, J.; Coronado, E.; Batista, V. S.; Sala, X.; Llobet, A. *J. Am. Chem. Soc.* **2015**, *137*, 10786-10795.

S3 Evans, I. P.; Spencer A.; Wilkinson, G.; *J. Chem. Soc., Dalton Trans.* **1973**, 204-209.

S4 Data collection with APEX II version v2013.4-1. Bruker (2007). Bruker AXS Inc., Madison, Wisconsin, USA.

S5 Bruker SAINT version V8.30c. Bruker (2007). Bruker AXS Inc., Madison, Wisconsin, USA.

S6 SADABS: V2012/1 Bruker (2001). Bruker AXS Inc., Madison, Wisconsin, USA. Blessing, Acta Cryst. (1995) A51 33-38.

S7 Sheldrick, G.M. *Acta Cryst*. **2008** A64, 112-122. SHELXTL version V6.14.

S8 Zhao, Y.; Truhlar, D. G. *J. Chem. Phys.* **2006**, *125*, 194101-194119.

S9 Zhao, Y.; Truhlar, D. G. *Theor. Chem. Acc.* **2008**, *120*, 215–241.

S10 Zhao, Y.; Truhlar, D. G. *Acc. Chem. Res.* **2008**, *41*, 157-167.

S11 Andrae, D.; Häußermann, U.; Dolg, M.; Stoll, H.; Preuß, H. *Theor. Chim. Acta. 77*, 123-141.

S12 Hehre, W. J. *AB INITIO Molecular Orbital Theory*; Wiley, 1986.

S13 Frisch, M. J.; Trucks, G. W.; Schlegel, H. B.; Scuseria, G. E.; Robb, M. A.; Cheeseman, J. R.; Scalmani, G.; Barone, V.; Mennucci, B.; Petersson, G. A.; Nakatsuji, H.; Caricato, M.; Li, X.; Hratchian, H. P.; Izmaylov, A. F.; Bloino, J.; Zheng, G.; Sonnenberg, J. L.; Hada, M.; Ehara, M.; Toyota, K.; Fukuda, R.; Hasegawa, J.; Ishida, M.; Nakajima, T.; Honda, Y.; Kitao, O.; Nakai, H.; Vreven, T.; Montgomery Jr., J. A.; Peralta, J. E.; Ogliaro, F.; Bearpark, M. J.; Heyd, J.; Brothers, E. N.; Kudin, K. N.; Staroverov, V. N.; Kobayashi, R.; Normand, J.; Raghavachari, K.; Rendell, A. P.; Burant, J. C.; Iyengar, S. S.; Tomasi, J.; Cossi, M.; Rega, N.; Millam, N. J.; Klene, M.; Knox, J. E.; Cross, J. B.; Bakken, V.; Adamo, C.; Jaramillo, J.; Gomperts, R.; Stratmann, R. E.; Yazyev, O.; Austin, A. J.; Cammi, R.; Pomelli, C.; Ochterski, J. W.; Martin, R. L.; Morokuma, K.; Zakrzewski, V. G.; Voth, G. A.; Salvador, P.; Dannenberg, J. J.; Dapprich, S.; Daniels, A. D.; Farkas, Ö.; Foresman, J. B.; Ortiz, J. V.; Cioslowski, J.; Fox, D. J.; Gaussian, Inc.: Wallingford, CT, USA, 2009.

S14 Cramer, C. J. *Essentials of Computational Chemistry: Theories and Models*; Wiley, 2013.

S15 Becke, A. D. *J. Chem. Phys.* **1993**, *98*, 5648-5652.

S16 Grimme, S.; Ehrlich, S.; Goerigk, L. *J. Comput. Chem.* **2011**, *32*, 1456-1465.

S17 Marenich, A. V.; Cramer, C. J.; Truhlar, D. G. *J. Phys. Chem. B* **2009**, *113*, 6378-6396.

S18 Tissandier, M. D.; Cowen, K. A.; Feng, W. Y.; Gundlach, E.; Cohen, M. H.; Earhart, A. D.; Coe, J. V.; Tuttle, T. R. *J. Phys. Chem. A* **1998**, *102*, 7787-7794.

S19 Camaioni, D. M.; Schwerdtfeger, C. A. *J. Phys. Chem. A* **2005**, *109*, 10795-10797.

S20 Kelly, C. P.; Cramer, C. J.; Truhlar, D. G. *J. Phys. Chem. B* **2006**, *110*, 16066-16081.

S21 Bryantsev, V. S.; Diallo, M. S.; Goddard, W. A. *J. Phys. Chem. B* **2008**, *112*, 9709-9719.

S22 Lewis, A.; Bumpus, J. A.; Truhlar, D. G.; Cramer, C. J. *J. Chem. Ed.* **2004**, *81*, 596-604.

S23 Winget, P.; Cramer, C. J.; Truhlar, D. G. *Theor. Chem. Acc.* **2004**, *112*, 217-232.

S24 Ziegler, T.; Rauk, A.; Baerends, E. J. *Theor. Chem. Acta* **1977**, *43*, 261-271.

S25 Noodleman, L. *J. Chem. Phys.* **1981**, *74*, **5737**–5743.

S26 Cramer, C. J.; Truhlar, D. G. *Phys. Chem. Chem. Phys.* **2009**, *11*, 10757-10816.

S27 Yamaguchi, K.; Jensen, F.; Dorigo, A.; Houk, K. N. *Chem. Phys. Lett.* **1988**, *149*, 537-542.

S28 Soda, T.; Kitagawa, Y.; Onishi, T.; Takano, Y.; Shigeta, Y.; Nagao, H.; Yoshioka, Y.; Yamaguchi, K. *Chem. Phys. Lett.* **2000**, *319*, 223-230.

PAPER E Synthesis, characterization and electrochemical analysis of a Ru *trans*-di-aquo complex with a seven-coordinate environment

Matheu, R.; Benet-Buchholz, J.; Sala, X.; Llobet, A.; **2017**, *submitted*

IV

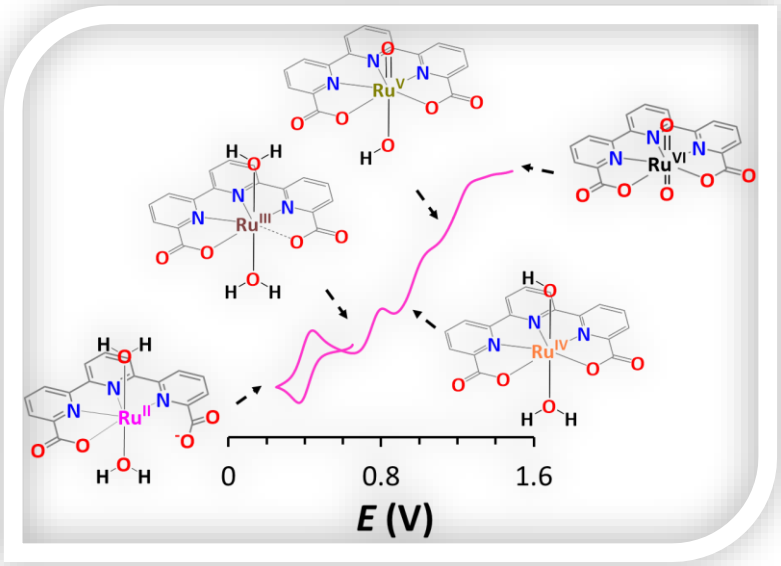

Abstract

In this work we prepare and characterize Ru complexes that contain the tda^{2-} ligand in the equatorial plane (tda^{2-} = [2,2':6',2''-terpyridine]-6,6''-dicarboxylate) including a complex that bear two aqua groups in *trans* position, complex [*trans*-Ru^{III}(tda-κ-N^3O)$(OH_2^{ax})_2]^+$, **3^{III}**$(OH_2)_2^+$ and a useful synthetic intermediate complex [Ru^{II}(tda-κ-N^3O)(dmso)(OH_2^{ax})], **4^{II}.** The synthetic intermediate **4^{II}** is further used to prepare complexes [Ru^{II}(tda-κ-N^3O)$(py)_2$] , **5^{II}**, and complex [Ru^{II}(tda-κ-N^3O)(dmso)(py)] , **6^{II}**, that bear one and two pyridyl ligands (py) in the axial positions. The single-crystal X-ray Diffraction of the novel Ru-tda complexes allows studying the effect of the tda^{2-} in the equatorial first coordination sphere in the low oxidation states. The κ-N^3O coordination mode of the tda^{2-} ligand distorts the typical octahedral geometry in the equatorial plane and provides a large opening in the ORuN angle (125^0) that induces phenomena such as dynamic behavior and additional coordination. In addition, the electrochemical properties of the Ru-tda complexes are assessed by Cyclic Voltammetry (CV) and Differential Pulse Voltammetry (DPV). The dmso ligand stabilize the potentials of the IV/III and III/II redox couples by 200-250 mV when compared to py or aqua ligands. By contrast, the substitution of a py ligand by an aqua ligand only reduces the redox potential by 20-50 mV. Finally, complex **3^{III}**$(OH_2)_2^+$ show a very rich electrochemistry that involves V and VI oxidation states. A Pourbaix diagram of complex **3^{III}**$(OH_2)_2^+$ is constructed and compared to related complexes in the literature. Electrochemical properties of the complex show the importance of the seven coordination and the H bonding in stabilizing high oxidation states.

Contribution

Roc Matheu synthetized and characterized the new compounds, performed the electrochemical experiments and prepared the manuscript.

E 1 Introduction

Ruthenium complexes constitute one of the richest family of coordination compounds partly thanks to the large number of formal oxidation states that Ru can access that range from -3 up to +8.[1] These complexes have a myriad of applications in many fields including, photochemistry and photophysics,[2,3] bioinorganic chemistry [4,5] and catalysis. From a catalytic perspective, Ru complexes are active in a large number of reactions involving C-C coupling,[6] C-H insertions[7] and especially in redox catalysis with organic transformations. The latter includes the oxidation of alkenes to epoxides, sulfides to sulfoxides, alcohols to aldehydes and carboxylic acid. [8] Particularly interesting is the catalytic oxidation of water to dioxygen because of its implications in new clean and renewable energy conversion schemes.[9,10]

For redox catalysis, one of the unavoidable requirements to display significant redox activity is the presence of a Ru-OH_2 group within the complex.[11-14] This allows to reach reactive higher oxidation states via proton-coupled electron transfer at a relatively low energy.[15] For the particular case of the water oxidation catalysis, the best catalysts described so far involve the formation of seven coordinate complexes at high oxidations states, stabilized by sigma donor groups such as carboxylates.[16-18]

A good example of this family of catalysts is the $[Ru^{IV}(tda\text{-}\kappa\text{-}N^3O)(py)_2(OH^{eq})]^+$ complex, $\mathbf{1^{IV}(OH)^+}$, where tda^{2-} is the pentadentate ligand ([2,2':6',2''-terpyridine]-6,6''-dicarboxylate), py is pyridine and OH^{eq} is a hydroxido ligand bonded to the metal center at the equatorial position, see Chart 1 and 2. Complex $\mathbf{1^{IV}(OH)^+}$ is today the fastest water oxidation catalysts reported achieving maximum turnover frequencies (TOF_{max}) of 50 000 s^{-1} at pH = 10.0.[17] In sharp contrast, the $[Ru^{IV}(tda\text{-}\kappa\text{-}N^3O)(py)(OH^{ax})]$ complex, $\mathbf{2^{IV}(OH)^+}$, where the hydroxido group is placed at the axial position, is a poor catalyst.[19]

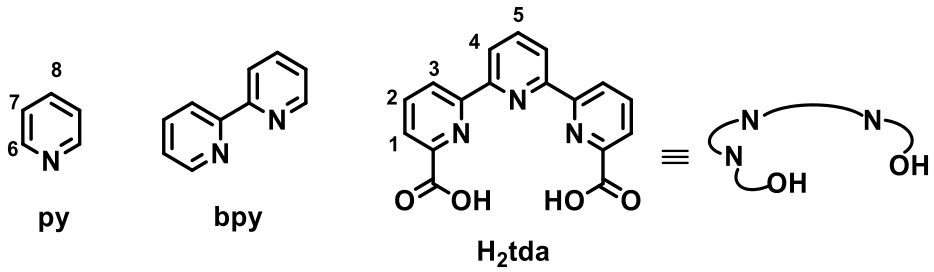

Chart 1. Ligands used and/or discussed in this work together with the labelling and numbering schemes.

Here on we report the synthesis and spectral and redox properties of a new member of the Ru-tda family of complexes, *trans*-[Ru^{III}(tda-κ-N^3O)(H_2O^{ax})$_2$], **$3^{III}(H_2O)_2^+$**. The properties of the complex are compared with the rest of the members of the family and with other relevant complexes previously described in the literature. In addition, we report a new complex [Ru^{II}(tda-κ-N^3O)(dmso)(H_2O)], **4^{II}**, that is an excellent synthetic intermediate for the preparation of all the family of Ru-tda complexes.

E 2 Experimental Section

E 2.1 Materials

General Materials

IV

Solvents and products were provided by Sigma-Aldrich unless indicated. [2,2':6',2''-terpyridine]-6,6''-dicarboxylic acid (H_2tda)[20] and [$RuCl_2dmso_4$][21] were synthesized and purified according to the literature. High-purity deionized water was obtained by passing distilled water through a nanopure Milli-Q water purification system.

Synthesis of [Ru(tda-κ-N^3O)(dmso)(OH_2^{ax})], **4^{II}.** [$RuCl_2dmso_4$] (150 mg, 0.31 mmol), 2',2'':6',2''-terpyridine-6',6''-dicarboxylic acid (H_2tda) (99 mg, 0.31 mmol) and Et_3N (0.3 mL) were degassed in dry methanol (6 mL), refluxed for 6 hours and cooled down to RT. A brown solid (100 mg) appeared in the reaction mixture and was filtered, washed with methanol and diethyl ether. The solid was dissolved in water (30 mL) and the mixture was heated at 60 ^{0}C until all the solid was completely dissolved. The solvent was then reduced to dryness and the solid obtained was washed with acetone and diethyl ether and dried under vacuum (90 mg, 50 % yield). Crystals suitable for single-crystal X-Ray Diffraction (XRD) were collected by slow evaporation of a **4^{II}** solution at *pH* = 1.0 (≈ 1mM). ^{1}H NMR (500 MHz, D_2O) δ: 2.63 (6H, s), 8.13 (1 H, t, *J* = 8.1 Hz), 8.27 (2 H, t, *J* = 7.8 Hz), 8.32 (4 H, dd, *J* = 7.8, 1.3 Hz), 8.40 (2 H, d, *J* = 8.1 Hz), 8.47 (2 H, dd, *J* = 7.8, 1.3 Hz,). ^{13}C NMR (500 Hz, D_2O) δ: 42.7, 115.8, 118.3, 120.8, 123.4, 123.6, 124.4, 126.2, 128.2, 137.6, 140.1, 152.7, 158.8, 160.3, 170.0. HRMS m/z: Calc. for [**4**-H_2O+Na]$^+$ ($C_{19}H_{15}N_3NaO_5RuS^+$): 521.9668. Found m/z: 521.9672. *Anal.* Calc. for [**4**+H_2O]: C, 42.7 %; H, 3.6 %; N, 7.9; S: 5.9 %. Found: C, 42.4 %; H, 3.2 %; N, 7.7%; S, 5.9.

Synthesis of [*trans*-Ru(tda-κ-N^3O)(OH_2^{ax})$_2$](PF_6)$_{0.5}$(SO_3CF_3)$_{0.5}$, **$3^{III}(OH_2)_2(PF_6)_{0.5}(SO_3CF_3)_{0.5}$.** Complex **$4^{II}$** (100 mg, 0.19 mmol) was dissolved in 0.3 mL of *neat* triflic acid and heated to 100 ^{0}C for 4 hours and cooled to room temperature. To this solution 3.6 mL of a saturated KPF_6 solution was added and kept in the fridge for 2 hours. During this period, crystals suitable for XRD appeared (90 mg, 75 %). ^{1}H-NMR (500 Hz, D_2O + ascorbic acid) δ: 7.73 (1 H, t, J=8.1 Hz), 8.06

(4 H, m), 8.34 (2 H, d, J=8.1 Hz), 8.37 (2 H, d, J=7.9 Hz). ^{13}C-NMR (500 Hz, D_2O + ascorbic acid) 122.3, 123.1, 125.3, 132.0, 137.1, 158.6, 160.2, 164.1, 173.3. HRMS m/z: Calc. for [$\mathbf{3^{III}(OH_2)_2}^+$-$H_2O$] ($C_{17}H_9N_3O_4Ru$): 420.9637, found m/z: 420.9649 (2.9 ppm). *Anal.* Calc.: [$\mathbf{3^{III}(OH_2)_2}^+$+ 0.1·$CF_3SO_3H$ + H_2O] $\{PF_6\}_{0.5}\{SO_3CF_3\}_{0.5}$ ($C_{17.6}H_{15.1}F_{4.8}N_3O_{8.8}P_{0.5}RuS_{0.6}$): C, 33.2 %; H, 2.4 %; N, 6.6 %; S, 3.0 %. Found: C, 33.1 %; H, 2.4 %; N, 6.4 %; S, 3.3 %.

Synthesis of [Ru(tda-κ-N^3O)(py)($SO(CH_3)_2$)], **5^{II}.** The synthesis was adapted from the literature but using complex **4^{II}** as starting material.[19] Complex **4^{II}** (50 mg, 0.1 mmol) was dissolved in water (2.5 mL) and pyridine (7.5 mL) and stirred for 2 days at room temperature. The brown solution was extracted with dichloromethane (3 x 100 mL) and the organic phase was discarded. Then aqueous solution was reduced to dryness under low pressure. The brown solid obtained in this way was redissolved in methanol. Upon addition of diethyl ether a brown solid appeared that was filtered and dried under vacuum (44 mg, 0.14 mmol, 75 % yield). The purity of the product was confirmed by ^{1}H NMR and electrochemistry.[19]

Synthesis of [Ru(tda-κ-N^3O)($py)_2$], **6^{II}.** The synthesis was adapted from the literature using complex **4^{II}** as starting material. Complex **4^{II}** (50 mg, 0.1 mmol) was dissolved in water (2.5 mL) and pyridine (7.5 mL) and stirred overnight at reflux. The brown solution was extracted with dichloromethane (3 x 100 mL) and the organic phase was discarded. Then aqueous solution was reduced to dryness under low pressure. The brown solid obtained in this way was redissolved in methanol. Upon addition of diethyl ether a brown solid appeared that was filtered and dried under vacuum (40 mg, 70 % yield). The purity of the product was confirmed by ^{1}H NMR and electrochemistry. [17]

Solutions at pH = 1.0, pH = 7.0 and pH = 12.0. A pH = 1.0 triflic acidic solution with 0.1M ionic strenght. A sample of neat triflic acid (10 g, 0.0663 mols) was diluted with 662 mL of deionised water. A pH = 7.0 phospahte buffered solution with 0.1 M ionic strenght. A sample of NaH_2PO4 (2.31 g, 0.0193 M) and Na_2HPO_4 (3.77 g, 0.0266 M) were dissolved in deionised water up to 1 L. A pH = 12.0 phosphate buffer soltion with 0.1 M ionic strenght. A sample of Na_2HPO_4 (10.293 g, 0.0073 M) and Na_3PO_4 (2.06 g, 0.0126 M) were dissolved with deionised water up to 1 L.

E 2.2 Instrumentation and Methods

General Instrumentation and Methods. Electrospray ionization (ESI)) mass spectrometry (MS) experiments were performed on a Waters Micromass LCT Premier equipment. A Bruker Avance 500 MHz were used to carry out NMR spectroscopy. The *pH* of the solutions was determined by

a *pH*-meter (CRISON, Basic 20$^+$) calibrated before measurements through standard solutions at *pH* = 4.01, 7.00 and 9.21.

Electrochemical methods. All electrochemical experiments were performed in an IJ-Cambria HI-730 bipotentiostat, using a three-electrode cell. A 20 mL vial was used as an electrochemical cell. A Teflon-made with holes for the three electrodes was used as a lid to ensure a reproducible distance between the electrodes. Glassy carbon disk (ϕ = 0.3 cm, S = 0.07 cm^2) and Pt disk were used as Working Electrode (WE) and Counter Electrode (CE) respectively. Glassy carbon electrodes were polished successively with 0.05 µm alumina (Al_2O_3) and washed with water. The Reference Electrode (RE) was Hg/Hg_2SO_4 (K_2SO_4 saturated) unless indicated and potentials were converted to NHE by adding 0.65 V. CVs and DPVs were iR compensated (90%). Cyclic Voltammograms (CV) were recorded at 100 mV·s^{-1} scan rate. The DPV parameters were ΔE = 4 mV, Pulse width = 5 s, Sampling width = 0.0167 s, Pulse period = 5 s.

IV

Pourbaix diagram. Three solutions of **3^{III}(OH$_2$)$_2$**(≈ 0.5 mM) were prepared at pH = *1.0*, pH = *7.0* and at *pH* = 12.0. The three solutions contained an ionic strength of 0.1 M. The three solutions containing complex **3^{III}(OH$_2$)$_2$** were mixed in order to obtain the desired *pH*, which was measured by the use of a *pH*meter. CV and DPV experiments were performed to analyze the solution at each *pH*. Due to the irreversibility of the VI/V and V/IV redox couple, DPV was used to extract the $E_{1/2}$ values for the Pourbaix diagram.

Single-Crystal XRD Methods. The measured crystals were prepared under inert conditions immersed in perfluoropolyether as protecting oil for manipulation. Crystal structure determinations for **8(4^{II}+7^{II})$^+$** and **3^{III}(OH$_2$)$_2^+$** were carried out using a Apex DUO diffractometer equipped with a Kappa 4-axis goniometer, an APEX II 4K CCD area detector, a Microfocus Source E025 IuS using MoK_α radiation, Quazar MX multilayer Optics as monochromator and an Oxford Cryosystems low temperature device Cryostream 700 plus (*T* = -173 ˚C). Full-sphere data collection was used with ω and φ scans. Data collection with APEX-2[22], data reduction with Bruker Saint [23] and absorption correction with SADABS[24].Crystal structure solution was achieved using direct methods as implemented in SHELXTL[25] and visualized using the program XP. Missing atoms were subsequently located from difference Fourier synthesis and added to the atom list. Least-squares refinement on F^2 using all measured intensities was carried out using the program SHELXTL. All non-hydrogen atoms were refined including anisotropic displacement parameters. Complex **3^{III}(OH$_2$)$_2^+$** crystallizes with water molecule, half triflate anion and half hexafluorophosphate anion in the asymmetric unit. The triflate and hexafluorophosphate anions are located on a mirror plane shared with the neighbouring asymmetric unit. Both anions are

showing large ellipsoids due to a disorder around the mirror plane which could not be properly refined. The asymmetric unit in the crystal structure of compound **8(4^{II}+7^{II})$^{+}$** contains a molecule of **4^{II}** and one of **7$^{II,+}$**, where one of the carboxylato groups is protonated.

E 3 Results and Discussion

E 3.1 Synthesis and solid-state structure

The strategy for the preparation of the Ru-tda complexes is summarized in Scheme 1. Reaction of [Ru^{II}Cl$_2$(dmso)$_4$] with tda^{2-} in methanol at reflux temperature for six hours yields a brown precipitate. Upon dissolving the solid in water the neutral complex [Ru^{II}(tda-κ-N^{3}O)(dmso)(OH$_2$)], **4^{II}**, is generated in reasonable good yields (50 %). Complex **4^{II}** has been characterized in solution by spectroscopic and electrochemical techniques and in the solid state by single-crystal X-ray Diffraction (XRD). Crystals suitable for XRD were collected upon slow evaporation of a **4^{II}** solution in water. The unit cell contains two different complexes that include the initial **4^{II}** complex together with its aquated derivative [Ru^{II}(tda-κ-N^3)(dmso)(OH$_2^{ax}$)(OH$_2^{eq}$)]$^{+}$, **7$^{II,+}$** (with one craboxylato group protonated), forming a dinuclear complex **8(4^{II}+7^{II})$^{+}$** according to equation 1. Complexes **4^{II}** and **7$^{II,+}$** are strongly interacting via extensive hydrogen bonding described in Figure 1.

2 [Ru^{II}(tda-κ-N^{3}O)(dmso)(OH$_2^{ax}$)] + H$_2$O + H^{+} ->

4^{II}

{[Ru^{II}(tda-κ-N^{3}O)(dmso)(OH$_2^{ax}$)][Ru^{II}(tda-κ-N^3)(dmso)(OH$_2^{ax}$)(OH$_2^{eq}$)]}$^{+}$ (1)

8(4^{II}+7^{II})$^{+}$

An ORTEP plot of **4^{II}** is depicted in Figure 1 and shows a pseudo-octahedral geometry around the Ru metal center expected for a d^6 Ru(II) metal ion. In the structure, the tda^{2-} ligand acts in a tetradentate manner occupying the equatorial positon of the Ru center, with the three pyridyl moieties and one carboxylate group bonded to the Ru center and one non-bonded dangling carboxylate. Finally, the axial positons are occupied by an aquo and dmso ligand. An ORTEP plot of **7$^{II,+}$** is also illustrated in Figure 1 where the tda^{2-} ligand acts as meridional tridentate ligand through the N atoms of the pyridyl groups whereas the two carboxylates are not bonded to the metal center, with one of the two carboxylate groups protonated. Instead an aquo ligand is coordinated to Ru in the free equatorial position and thus is situated *cis* with regard to the axial aqua and dmso ligands that complete the octahedral coordination. Here, it is interesting to note the geometrical distortion imposed by the tda^{2-} ligand. Scheme 2 shows the NRuN, NRuO and ORuO angles in the equatorial plane for **4^{II}** and **7$^{II,+}$**. For **4^{II}** it is striking to see 125^{o} NRuO angle,

that deviates by 35º from the ideal 90º for an octahedral coordination. When the carboxylato coordination atom is replaced by the monodenate aqua ligand in $\mathbf{7}^{II,+}$, the geometrical restriction imposed by the now $(tda\text{-}\kappa\text{-}N^3)^{2-}$ ligand is released as indicated by the two ORuN angles down to 100º and 99º.

Scheme 1. Synthetic strategy for the preparation of the complexes described in this work (colored) and nomenclature used. Key axial and equatorial ligands are indicated with a "ax" or "eq" super index respectively.

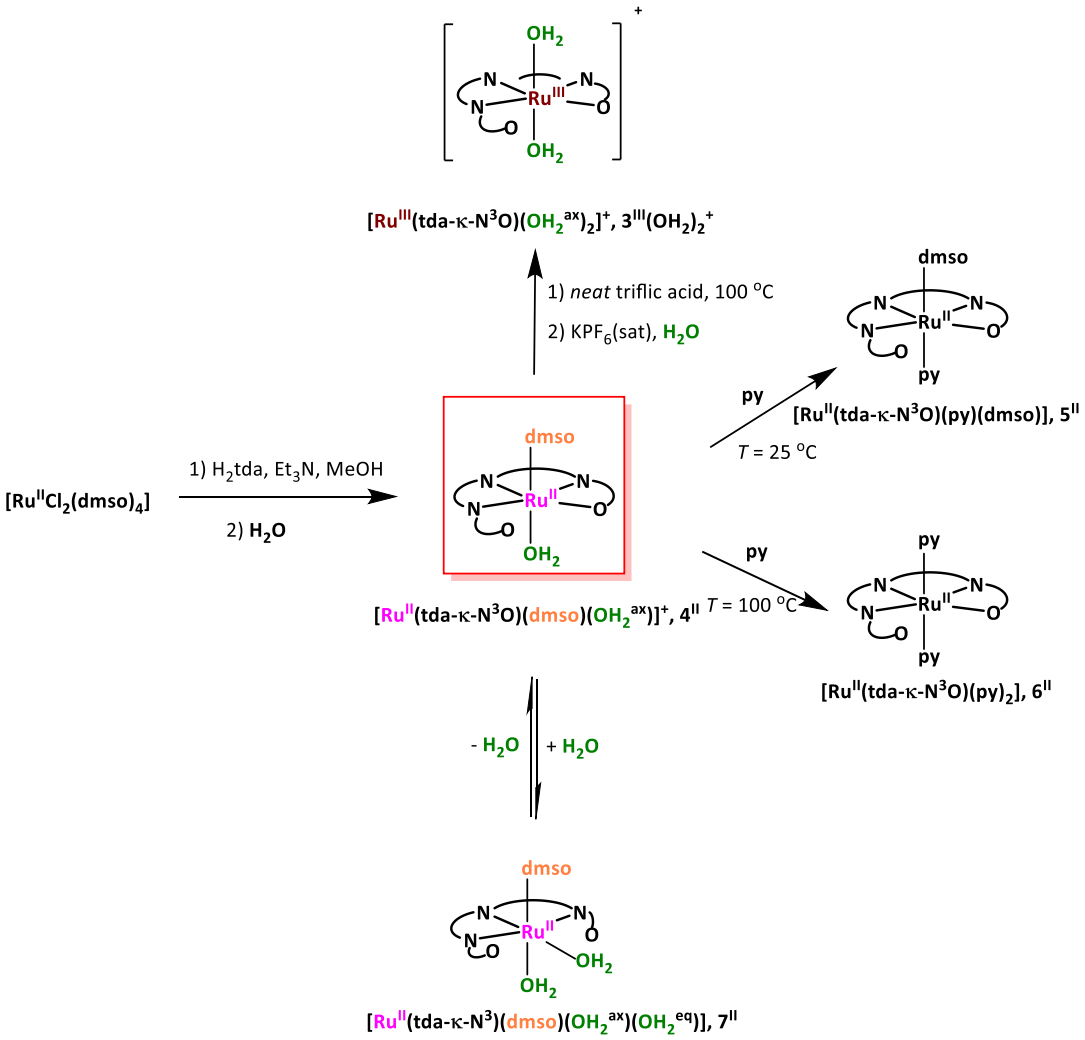

The strong geometric distortion imposed by the tda^{2-} ligand has significant consequences in the Ru-tda complexes depending on the oxidation state of the Ru center. At oxidation state II it fosters a dynamic behavior in solution whereas at oxidation state III and above it favors the

formation of six and a half and seven coordinated Ru complexes. Both phenomena will be described below.

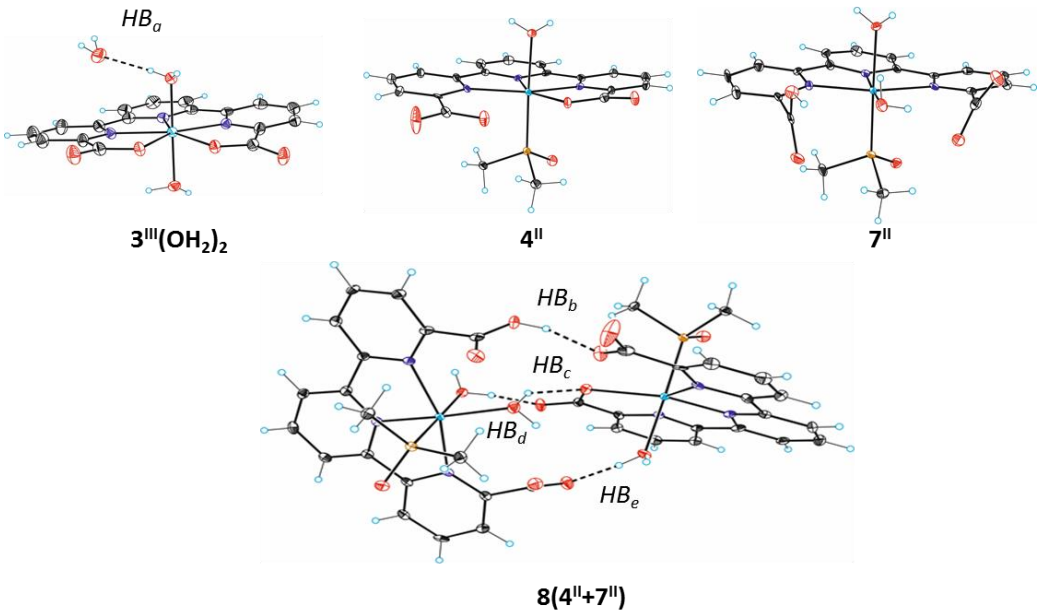

Figure 1. ORTEP plot for complexes **3^{III}(OH$_2$)$_2$$^{+}$**, **4^{II}**, **7$^{II,+}$** and **8(4^{II}+7^{II})$^{+}$**. Ellipsoids are plotted at 50% probability. Dashed lines indicate contacts. Color codes: Ru, cyan; N, purple; O, red; C, black and H; colorless. Hydrogen bond distances (O-H-O): *HB$_a$*, $d_{O\text{-}H\text{-}O}$ = 2.6 Å, $d_{O\text{-}H}$ = 0.7 Å, $d_{O\text{-}H}$ = 1.9 Å; angle O-H-O = 186°; *HB$_b$*, $d_{O\text{-}H\text{-}O}$ = 2.5 Å, $d_{O\text{-}H}$ = 0.9 Å, $d_{O\text{-}H}$ = 1.7 Å; angle O-H-O = 153°; *HB$_c$*, $d_{O\text{-}H\text{-}O}$ = 2.8 Å, $d_{O\text{-}H}$ = 0.9 Å, $d_{O\text{-}H}$ = 2.0 Å; angle O-H-O = 143°; *HB$_d$*, 2.5 Å, $d_{O\text{-}H}$ = 0.9 Å, $d_{O\text{-}H}$ = 1.65 Å; angle O-H-O = 171°; *HB$_e$*, 2.5 Å. $d_{O\text{-}H}$ = 0.9 Å, $d_{O\text{-}H}$ = 1.66 Å; angle O-H-O = 152°

Complex **4^{II}** is used as a versatile synthetic intermediate to prepare the rest of the complexes described in this work. The versatility of this complex as intermediate arises from the different degree of bonding strength of the three ligands in **4^{II}** namely: the tda^{2-}, the dmso and the aqua ligands. The tda^{2-} ligand here acts in a tetradentate-κ-N^{3}O manner and coordinates in the equatorial position very strongly. In sharp contrast, the axial aquo ligand is a very labile ligand that will be easily replaced by other monodentate ligands. Finally, the dmso ligand is situated in an intermediate coordination strength between the tda^{2-} and aqua ligand.

Consequently, treatment of complex **4^{II}** with pyridine under *mild conditions* (stirring at RT), generates complex **5^{II}** according to the following equation,

$[Ru^{II}(tda\text{-}\kappa\text{-}N^3O)(dmso)(OH_2^{ax})]$ + py -> $[Ru^{II}(tda\text{-}\kappa\text{-}N^3O)(dmso)(py)]$ + H_2O (2)

4^{II} **5^{II}**

Where the initial aqua ligand has been substituted by pyridine. Under *harsher conditions,* at 100 ^oC, with excess pyridine both the dmso and aquo ligands are substituted generating the bis pyridine complex **6^{II},**

$[Ru^{II}(tda\text{-}\kappa\text{-}N^3O)(dmso)(OH_2^{ax})]$ + 2 py -> $[Ru^{II}(tda\text{-}\kappa\text{-}N^3O)(py)_2]$ + dmso + H_2O (3)

4^{II} **6^{II}**

The isolated yields for **5^{II}** and **6^{II}** are above 70% although both reactions (equations 2 and 3) proceed virtually in a quantitative manner as evidenced electrochemically.

IV

Further, the solubilization of **4^{II}** in *neat* triflic acid (CF_3SO_3H), followed by heating at 100 ^oC for four hours in an open atmosphere, produces the removal of the pyridine and an dmso axial ligands, presumably by triflate anions and the aerial oxidation of Ru(II) to Ru(III), as indicated in equation 4,

$[Ru^{II}(tda\text{-}\kappa\text{-}N^3O)(dmso)(OH_2^{ax})]$ + 2 $CF_3SO_3^-$ - $1e^-$ ->

4^{II}

$[Ru^{III}(tda\text{-}\kappa\text{-}N^3O)(CF_3SO_3)_2]^-$ + dmso + H_2O (4)

In aqueous solution the labile triflato ligands are easily substituted by aquo ligands forming the *trans*-bis-aquo-Ru complex indicated in equation 5,

$[Ru^{III}(tda\text{-}\kappa\text{-}N^3O)(CF_3SO_3)_2]^-$ + 2 H_2O -> $[trans\text{-}Ru^{III}(tda\text{-}\kappa\text{-}N^3O)(OH_2^{ax})_2]^+$ + 2 $CF_3SO_3^-$ (5)

$3^{III}(OH_2)_2^+$

Addition of PF_6^- to this solution precipitates the complex with a mixing of counter anions **$\{[3(OH_2)_2](PF_6)_{0.5}(CF_3SO_3)_{0.5}\}$**, in 75% isolated yield. This complex has also been characterized in the solid state by the XRD and an ORTEP plot of its hydrated cation is illustrated in Figure 1. The Ru(III) center displays a distorted pentagonal bipyramid geometry where the axial positions are occupied by the two aqua groups and the five equatorial positions are occupied by the bonding atoms of the tda^{2-} ligand. Here the three N and one O have the typical Ru(III)-N and Ru(III)-O bonding distances[17-19,26] while one of the Ru-O carboxylates appears at 2.4 Å, and thus is basically a contact. Therefore, since Ru(III) is d^5 ion it cannot be seven coordinated but the geometrical

nature of the ligand clearly forces the metal coordination towards a pentagonal bipyramid geometry as can be seen in Figure 1 and Scheme 2. We named this coordination as 6.5.

Scheme 2. Selected angles for the equatorial first coordination sphere of complexes $\mathbf{4^{II}}$, $\mathbf{7^{II,+}}$ and $\mathbf{3^{III}(OH_2)_2^+}$. Axial ligands are omitted for clarity. Dashed line indicates contact.

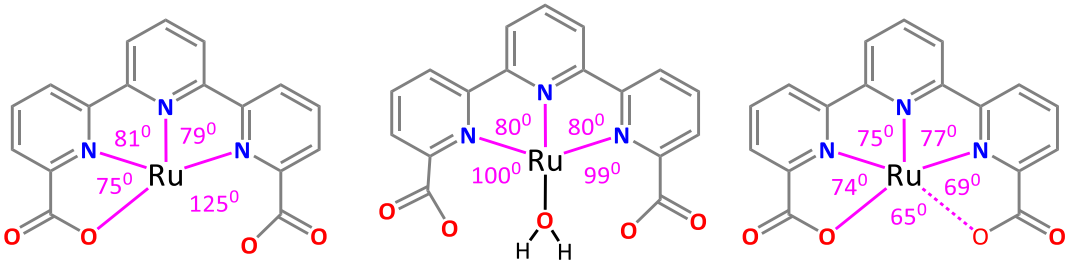

$\mathbf{4^{II}}$ $\mathbf{7^{II,+}}$ $\mathbf{3^{III}(OH_2)_2^+}$

IV

E 3.2 Solution behavior

Complexes $\mathbf{4^{II}}$, $\mathbf{5^{II}}$ and $\mathbf{6^{II}}$ are all diamagnetic Ru(II) low spin d^6 ions and were characterized by NMR spectroscopy in a D_2O solution containing 0.1 M CF_3SO_3D (*pD* = 1.0). The Ru(III) complex $\mathbf{3^{III}(OH_2)_2^+}$ was reduced in situ with ascorbic acid to generate the corresponding diamagnetic complex $\mathbf{3^{II}(OH_2)_2}$ and their NMR spectra are presented in Figure 2.

Complexes $\mathbf{5^{II}}$ and $\mathbf{6^{II}}$ contain axial pyrdiyl ligands and the resonances of the pyrdyl ligands appear in the 6.5-8.1 ppm region whereas those of the tda^{2-} ligand appear at lower fields. Besides, it is interesting to realize that the tda^{2-} resonances appear as if the ligand was coordinated in a symmetrical manner. This is due to the fast dynamic behavior that exists in these complexes where the bonded and dangling carboxylate synchronically decoordinate and coordinate respectively, as displayed graphically in the upper part of Scheme 3. This dynamic behavior is fostered by the geometrical constrains imposed by the tda^{2-} ligand that strongly distorts from an ideal octahedral geometry and at the same time provides for an additional bonding carboxylate site in very close proximity and symmetrical to the bonded one.

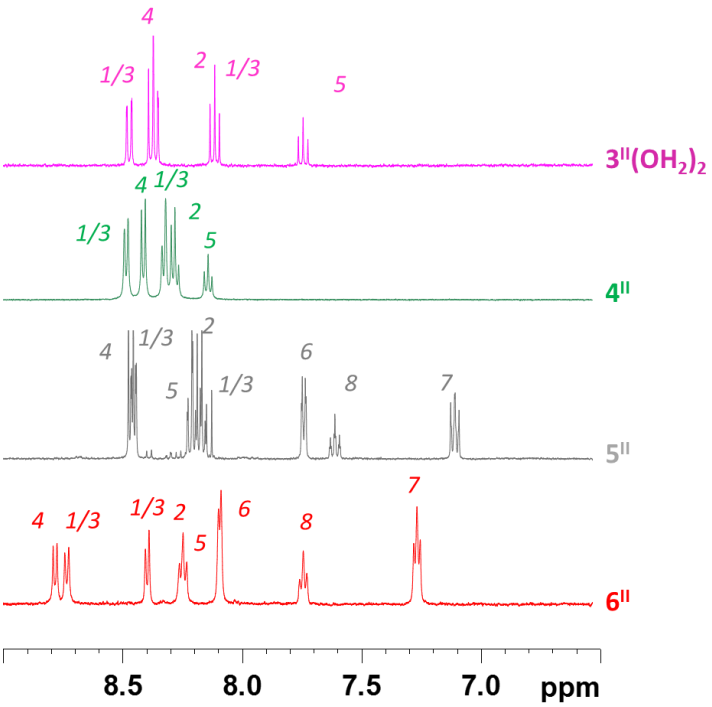

Figure 2. ^{1}H NMR for **$3^{II}(OH_2)_2$**, **4^{II}**, **5^{II}** and **6^{II}** at *pD* = 1.0 solution. See Chart 1 for the numbering scheme.

Further in water as solvent, this dynamic behavior is also in equilibrium with the coordination of a solvent water in the equatorial position as indicated in the lower part of Scheme 3. This is clearly evidenced in the case of **4^{II}** where in the crystallization process generates **$7^{II,+}$**. However, in solution this species is clearly very minor as evidenced electrochemically based on their respective redox potentials. It thus points out that the isolation of **$7^{II,+}$** is accomplished thanks to a lower solubility of the crystallized species **$8(4^{II}+7^{II})^{+}$** with regard to that of **4^{II}** alone.

This behavior in the Ru(II) oxidation state is radically different to the behavior of the Ru-tda complexes at Ru(IV) oxidation state. Here the tda^{2-} ligands in low coordinating organic solvents, favors a seven coordination environment for this d^4 ion, with a pentagonal bipyramid geometry and with the tda^{2-} ligands acting in κ-N^3O^2 fashion, as previously described.[17] Further in aqueous solution at *pH* = 7.0 or in basic solution, one bonded carboxylate can be replaced by a hydroxido ligand generating the seven coordinated active catalyst **$1^{IV}(OH)^{+}$**, depicted in Chart 2.[17]

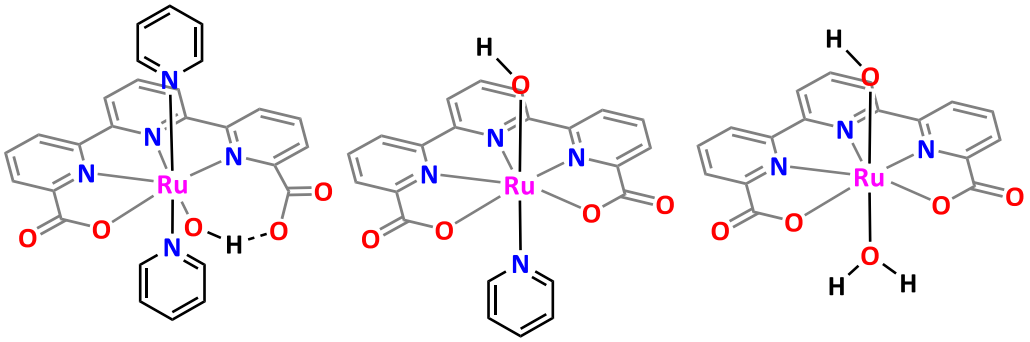

$\mathbf{1}^{IV}(OH)^+$ $\mathbf{2}^{IV}(OH)^+$ $\mathbf{3}^{IV}(OH)(OH_2)^+$

Chart 2. Ru hydroxido-pyridine complexes based on the tda^{2-} ligand. Complexes $\mathbf{2}^{IV}(OH)^+$ and $\mathbf{3}^{IV}(OH)(OH_2)^+$ are the one-electron oxidized forms of $\mathbf{2}^{III}(OH)_2^+$ and $\mathbf{3}^{III}(OH_2)_2^+$ at pH > 4.

IV

Scheme 3. Reaction pathways leading to a combination of equilibria involved in dynamic behaviour of Ru-tda complexes in water. The dashed lines indicate bonds that are simultaneously formed and broken in the transition state. L-Ax represents the axial ligands py, dmso or aquo.

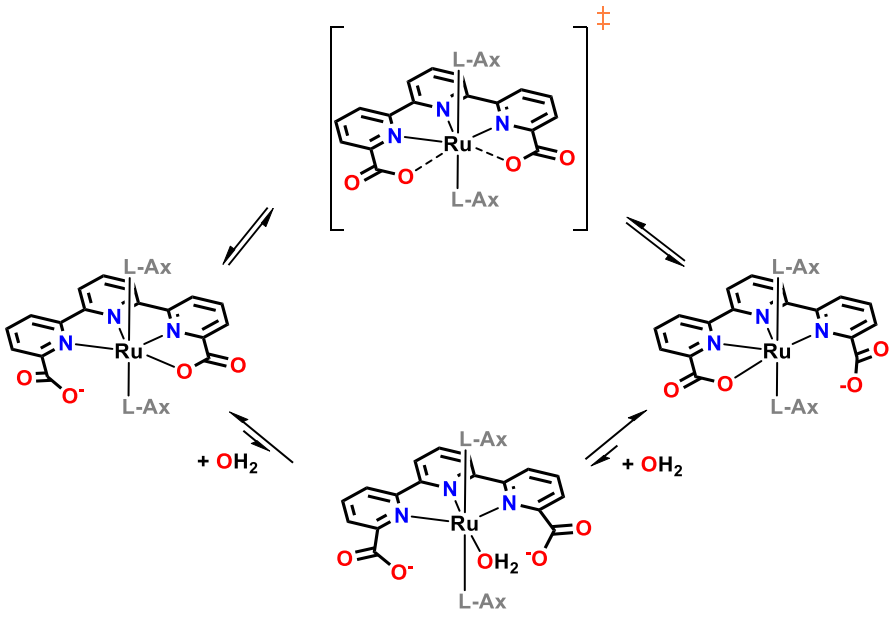

E 3.3 Electrochemical properties

The electrochemical properties of the Ru-tda complexes were investigated by Cyclic Voltammetry (CV) and Differential Pulse Voltammetry (DPV) techniques by using a Glassy Carbon as a working electrode and Hg/Hg_2SO_4 as a reference electrode. All potentials were converted to NHE by adding 0.65 V.

The CV of complex $\mathbf{3^{III}(OH_2)_2^+}$ at *pH* = 1.0 is shown in Figure 3 left, and shows two reversible waves at E^0 = 0.52 V (ΔE = 60 mV) and at E^0 = 0.94 V (ΔE = 60 mV). These redox events correspond to single outer sphere electron transfer processes associated with the III/II and IV/III redox couples respectively. No proton transfer is associated to these couples as evidenced by the Pourbaix diagram shown in Figure 4, right. Figure 3 right shows the DPV of complexes $\mathbf{3^{III}(OH_2)_2^+}$, $\mathbf{4^{II}}$, $\mathbf{5^{II}}$ and $\mathbf{6^{II}}$ at *pH* = 1.0 together with the related complex $\mathbf{2^{III}(OH)^+}$. The $E_{1/2}$ for these complexes are presented in Table 1, together with other redox and thermodynamic data of related Ru polypyridyl complexes for comparison purposes. The DPV for all complexes exhibit a couple of waves associated with the III/II and IV/III redox couples (see entries 1-5 Table 1). Here, it is interesting to see that complexes $\mathbf{4^{II}}$ and $\mathbf{5^{II}}$, which contain the DMSO ligand, have redox potentials about 200-250 mV higher than complexes $\mathbf{2^{III}(OH_2)_2^+}$, $\mathbf{3^{III}(OH_2)_2^+}$ and $\mathbf{6^{II}}$, which only contain py and aquo ligands. The increase of potential is associated with the electron withdrawing character of the dmso ligand as has been previously documented.[27] On the other hand, the electronic effect exerted by the pyridyl ligand compared to the aquo ligands can be nicely observed by comparing complexes $\mathbf{2^{III}(OH)^+}$, $\mathbf{3^{III}(OH_2)_2^+}$ and $\mathbf{6^{II}}$ (entries 4, 5 and 3 respectively). where the π-acceptor character of pyridine cathodically shifts the $E_{1/2}$ values by approximately 30 mV in both couples.

IV

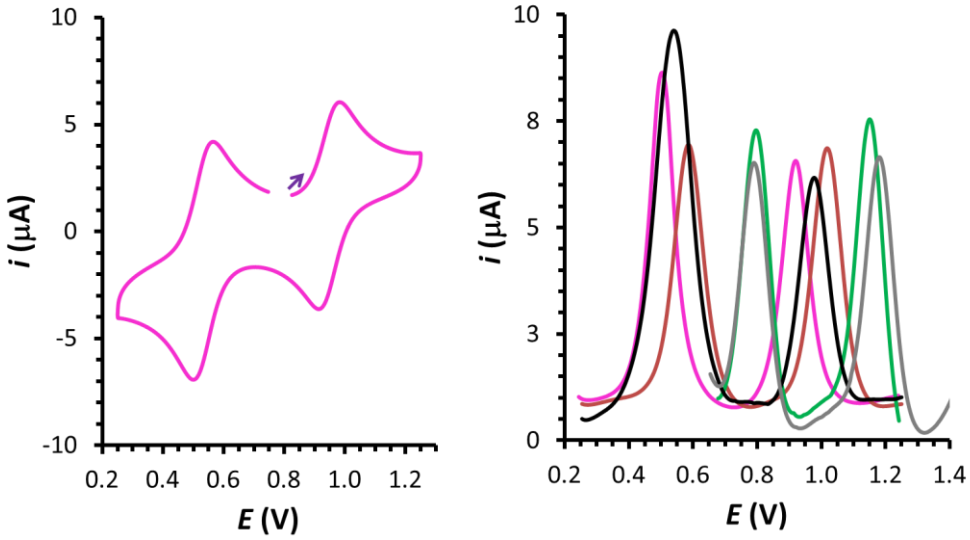

Figure 3. Left, CV of complex $\mathbf{3^{III}(OH_2)_2^+}$ at *pH* = 1.0. Right, DPV of complexes $\mathbf{2^{III}(OH_2)^+}$ (black line), $\mathbf{3^{III}}(OH_2)_2^+$ (pink line), $\mathbf{4^{II}}$ (green line), $\mathbf{5^{II}}$ (grey line), $\mathbf{6^{II}}$ (brown line) at *pH* = 1.0. *E* is reported *vs*. NHE.

It is also interesting to compare the potentials of the IV/III and III/II redox couples for $\mathbf{3^{III}(OH_2)_2^+}$ with those of other related Ru complexes containing polypyridyl ligands such as $[Ru^{II}(bpy)_3]^{2+}$, $\mathbf{9^{II,2+}}$ ($E_{1/2}$ (III/II) = 1.26 V; bpy is 2,2'-bipyridine; Table 1, entry 6).[28] For $\mathbf{9^{II,2+}}$ the III/II couple is

anodically shifted by 460 mV with regard to that of **$3^{III}(OH_2)_2^{+}$** which is due to strong sigma-donation effect exerted by the carboxylates of the tda^{2-} ligands. Further, it is interesting to note that the potential for the second oxidation to reach Ru(IV) is out of solvent limits and it has never been measured. In sharp contrast, the second wave of **$3^{III}(OH_2)_2^{+}$**, the IV/III couple, is only 420 mV above the III/II due to the formation of a seven coordinated complex $[Ru^{IV}(tda\text{-}\kappa\text{-}N^3O^2)(OH_2^{ax})_2]^{+}$ where the tda^{2-} acts now as pentadentate k-N^3O^2 ligand.

Table 1. Thermodynamic properties for complexes **$3^{III}(OH_2)_2^{+}$**, **4^{II}** and other relevant Ru complexes described previously. a, measured at *pH* = 1.0, b Calculated from the VI/V and V/IV redox couples.

Entry	Complex	E^o (V *vs*. NHE)[a]			pK$_a$			Ref.
		III/II	IV/III	VI/IV	$Ru^{IV}OH_2$	$Ru^{IV}(OH_2)_2$	$Ru^{IV}(OH_2)(OH)$	
1	$[Ru^{III}(tda\text{-}\kappa\text{-}N^3O)(dmso)(OH_2^{ax})]$ **4^{II}**	0.80	1.15	---	---	---	---	t.w.
2	$[Ru^{III}(tda\text{-}\kappa\text{-}N^3O)(dmso)(py)]$ **5^{II}**	0.59	1.02	---	---	---	---	t.w., 19
3	$[Ru^{III}(tda\text{-}\kappa\text{-}N^3O)(py)_2]$ **6^{II}**	0.80	1.18	---	---	---	---	t.w., 17
4	$[Ru^{III}(tda\text{-}\kappa\text{-}N^3O)(py)(OH_2^{ax})]^{+}$ **$2^{III}(OH_2)^{+}$**	0.54	0.97	---	3.9	---	---	19
5	$[trans\text{-}Ru^{III}(tda\text{-}\kappa\text{-}N^3O)(OH_2^{ax})_2]^{+}$ **$3^{III}(OH_2)_2^{+}$**	0.52	0.94	> 1.75	---	4.0	> 8	t.w.
6	$[Ru^{II}(bpy)_3]^{2+}$ **$9^{II,2+}$**	1.26	---	---	---	---	---	27
7	$[Ru^{II}(trpy)(bpy)(OH_2)]^{2+}$ **$10^{II}(OH)^{2+}$**	1.04	1.23	1.80	< 1.0	---	---	28
8	$[trans\text{-}Ru^{II}(bpy)_2(OH_2^{ax})_2]^{2+}$ **$11^{II}(OH_2)_2^{2+}$**	0.69	1.13	1.26 [b]	---	< 1.0	< 1.0	29
9	$[cis\text{-}Ru^{II}(bpy)_2(OH_2^{ax})_2]^{2+}$ **$12^{II}(OH_2)_2^{2+}$**	0.80	1.15	1.42 [b]	---	< 1.0	< 1.0	29

It is also interesting to compare the potentials of the IV/III and III/II redox couples for **$3^{III}(OH_2)_2^{+}$** with those of other related Ru-aquo complexes containing polypyridyl ligands at *pH* = 1.0 such as $[Ru^{II}(trpy)(bpy)(OH_2)]^{2+}$, **$10(OH_2)^{2+}$** ($E_{1/2}$ (III/II) = 1.04 V, $E_{1/2}$ (IV/III) = 1.23 V; trpy is 2,2':2",6'-terpyridine; Table 1, entry 7).[29] Here the potentials for **$10(OH_2)^{2+}$** are significantly lower than **$9^{II,2+}$** but still above those of **$3^{III}(OH_2)_2^{+}$**, as a consequence of the absence of anionic strong sigma donating ligands and the presence of Ru-aqua groups that enables proton coupled electron transfer (PCET) processes.

The redox properties of complex $\mathbf{3^{III}(OH_2)_2^+}$ were also studied as a function of the *pH* and its Pourbaix diagram is depicted in Figure 4 right. The CV of $\mathbf{3^{III}(OH_2)_2^+}$ at *pH* = 7.0 is shown in Figure 4 left where four one-electron redox process occur in the 0.4 - 1.2 V range. The degree of proton content of the different generated species is inferred from its Pourbaix diagram. Thus in this particular case at *pH* = 7.0 the III/II couple involves also a proton transfer (approx. 60 mV/pH slope) whereas the IV/III involves only a single electron transfer (0 mV/*pH* slope). Further, the V/IV now involves a one-electron two-protons transfer (approx. 120 mV/*pH* slope) and finally the VI/V wave is a one-electron one-proton transfer with an approx. 60 mV/*pH* slope. The access to five different oxidation states thanks to PCET mechanisms is exceptional for complexes containing just a single metal center.[15] This extremely rich redox chemistry of $\mathbf{3^{III}(OH_2)_2^+}$ parallels that of [*trans*-$Ru^{II}(bpy)_2(OH_2^{ax})_2]^{2+}$ complex, $\mathbf{11^{II}(OH_2)_2^{2+}}$, and [*cis*-$Ru^{II}(bpy)_2(OH_2^{ax})_2]^{4+}$ complex, $\mathbf{12^{II}(OH_2)_2^{2+}}$, reported earlier (see Table 1, entries 8 and 9 for selected values and Figure S16 for their Pourbaix diagrams).[30] The redox potential values and the shape of the diagram differ from those of $\mathbf{3^{III}(OH_2)_2^+}$ due to the different electronic and geometrical effects exerted by tda^{2-} compared to bpy. The tda^{2-} increases the electron density around the metal center in comparison to bpy and on also provides access to seven coordination. In addition, this increase in electron density also reflected in an increase of basicity for the Ru species that contain aquo, hydroxido or oxo groups. This is clearly observed when comparing the first and second pK_as for the $Ru^{IV}(OH_2)_2$ species in **3** and **11** (entries 5 and 8 in Table 1). The first pK_a = 4 for **3** and lower than 1 for **11,** and the second pK_a is higher than 8 for **3** and lower than 1 for **11**. Thus the dicarboxylato ligand tda^{2-}, renders the Ru(IV) species at least 10 million times more basic than the bpy ligand.

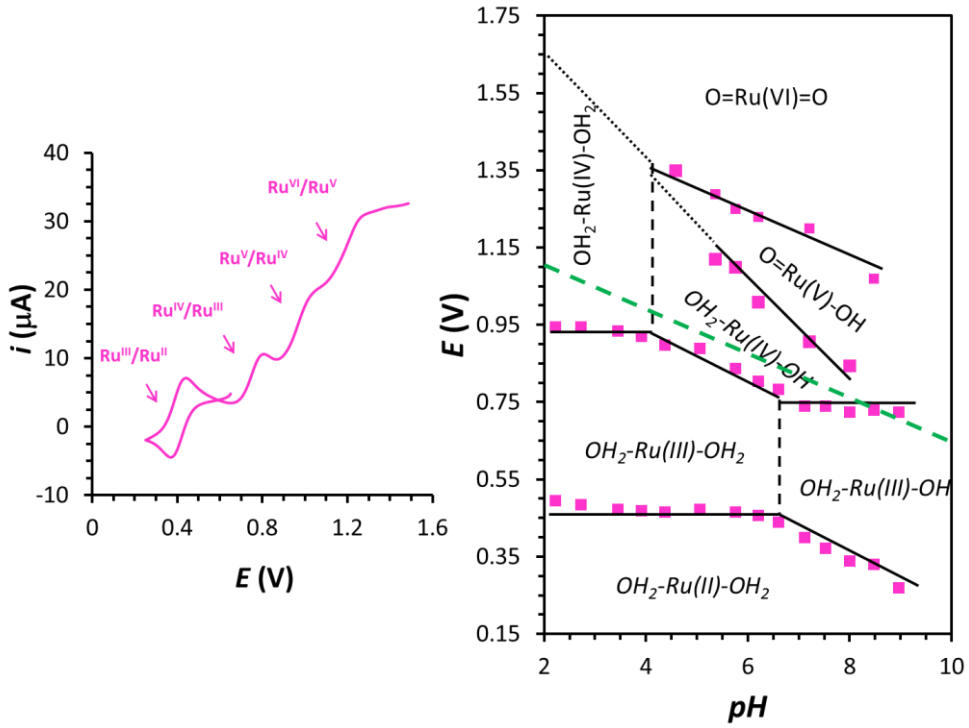

Figure 4. Left, blank corrected Cyclic Voltammetry (CV) for 0.5 mM $\mathbf{3^{III}(OH_2)_2^+}$ at *pH* = 7.0. The arrows indicate the redox couples involved in the redox events. Right, Pourbaix diagram of $\mathbf{3^{III}(OH_2)_2^+}$, showing the zone of predominance of the different species as function of potential and *pH* (the tda^{2-} ligand is omitted for clarity). Vertical dashed lines indicate pK_a values. The green dashed line indicates the thermodynamic potential for O_2/H_2O redox couple.

These considerations are important because it underlines the opposite effects an electronic perturbation exerts into the redox potentials of Ru-aquo type of complexes. That is, the increase in electron density lowers the redox potential but also increase the pK_a. Thus at *pH*s lower than the pK_a, the expected decrease in redox potential exerted by an electron donating group might be cancelled due to the increase of the pK_a.

Interestingly, the Pourbaix diagram of complex $\mathbf{3^{III}(OH_2)_2^+}$ shows that the potentials for the III/II and IV/III couples are very similar to the ones reported earlier for $\mathbf{2^{III}(OH_2)^+}$**.** The similarity is a consequence of the fact that the replacement of one of the aqua ligands by a pyridyl maintains almost unchanged the potentials and the *pKa* at oxidation state II, III and IV (see Table 1 for the values and Figure S15 for the Pourbaix diagram of $\mathbf{2^{III}(OH_2)^+}$). However, the Pourbaix diagram of complex $\mathbf{3^{III}(OH_2)_2^+}$ strongly differs from that of $\mathbf{2^{III}(OH_2)^+}$ at higher oxidation states than Ru(IV). While complex $\mathbf{2^{III}(OH_2)^+}$ only undergoes a single electron transfer beyond oxidation state IV, complex $\mathbf{3^{III}(OH_2)_2^+}$ can access all the way up to Ru(VI) forming the *trans*-Ru-dioxo species. This

IV

difference is again due to the higher number of protons that can be lost in $\mathbf{3^{III}(OH_2)_2}^{+}$ with two Ru-aquo groups as compared to $\mathbf{2^{III}(OH_2)}^{+}$ with only one Ru-aquo group.

Finally, it is interesting to notice that the VI/V couple for $\mathbf{3^{VI}(O)_2}$ is well above the thermodynamic potential of water to dioxygen and thus could potentially act as a water oxidation catalyst. Unfortunately, decomposition reactions possibly involving polymeric oxo-bridged type of species such as the ones described for $\mathbf{10^{IV}(OH)}^{3+}$ (see Figure S14), compete with the catalytic reaction.[31,32]

E 3.4 Implications for water oxidation catalyst design

The present work reports the synthesis and characterization of $\mathbf{3^{III}(OH_2)_2}^{+}$ that completes the family of seven coordinated Ru-tda complexes bearing different aqua/pyridine ligands in the axial position as drawn in Chart 2. While $\mathbf{1^{IV}(OH)}^{+}$ is a spectacular catalyst reaching maximum TOF in the order of 50 000 s^{-1}, the replacement of one pyridine by a hydroxido to generate $\mathbf{2^{IV}(OH)}^{+}$ renders this complex still a catalyst but very poor due to the lack of access to hydrogen bonding. Additional replacement of the pyridine ligand by a second hydroxido ligand generates the bis-hydroxido complex $\mathbf{3^{IV}(OH)_2}^{+}$ that even though has the right redox potential for water oxidation unfortunately decomposes quickly towards the formation of polymeric oxo-bridged species. It thus suggests the need of non-aqua ligands or non-labile ligands to block the formation of highly stable oxo-bridged Ru complexes.

Thus the present work enlarges the landscape of Ru-tda complexes and uncovers additional factors that influence the water oxidation catalysis namely, the presence of one or two Ru-aqua groups, the seven coordination and the presence of anionic ligands and their implication in both *pKa* and redox potentials, the capacity to generate the proper intramolecular hydrogen bonding and the avoidance of oxo-bridged formation.

E 4 Conclusions

In summary, we synthesized and characterized two Ru-tda complexes that generate a complete synthetic picture. In particular, complex $\mathbf{4^{II}}$ is the synthetic precursor that can be used for the preparation of most Ru-tda complexes. The characterization of complex $\mathbf{4^{II}}$ together with the other Ru-tda complexes by means of NMR, single-crystal XRD shows common structural trends regardless of the axial ligands: the Ru center in the II oxidation state coordinates the tda^{2-} ligand in the κ-N^3O mode in the solid-state and in solution. In the III oxidation state, complex $\mathbf{3^{III}(OH_2)_2}^{+}$ is 6.5 coordinated that represents the half way between the six coordination and the seven coordination.

All Ru-tda complexes studied in this work access to the III and IV oxidation state electrochemically. The potential for the process strongly depends on the axial ligand: while dmso increases the redox potential by 200-250 mV compared to OH_2 ligand, the replacement of py by an aqua ligand only cathodically shifts the potential by 20-50 mV. Finally, complex $[\mathbf{3^{III}(OH_2)_2}]^+$ reaches oxidation V and VI thanks to the two OH_2 groups situated in trans position as related *trans*-aqua complexes. The electrochemical features of the complex reveal the need to provide H bonding to stabilize high oxidation states in Ru(OH)-tda complexes.

E 5 Acknowledgments

R.M. thanks "La Caixa" foundation for a PhD grant. A.L. thanks MINECO (CTQ-2013-49075-R, SEV-2013-0319; CTQ-2014-52974-REDC), COST actions (CM1202) and "La Caixa" foundation for financial support.

E 6 References

1 Bruneau, C. *Ruthenium catalysts and fine chemistry*; Springer-Verlag: Berlin, **2004**.
2 Pal, A. K.; Hanan, G. S. *Chem. Soc. Rev.* **2014**, *43*, 6184-6197.
3 Colasson, B.; Credi, A.; Ragazzon, G. *Coord. Chem. Rev.* **2016**, *325*, 125-134.
4 Jiang, C. W.; Chao, H.; Hong, X. L.; Li, H.; Mei, W. J.; Ji, L. N. *Inorg. Chem. Commun.* **2003**, 6, 773-775.
5 Ossipov, D.; Gohil, S.; Chattopadhyaya, J. *J. Am. Chem. Soc.* **2002**, 124, 13416-13433.
6 Giri, R.; Thapa, S.; Kafle, A. *Adv. Synth. Catal.* **2014**, *356*, 1395-1411.
7 Doyle, M. P.; Duffy, R.; Ratnikov, M.; Zhou, L. *Chem. Rev.* **2010**, *110*, 704-724.
8 Punniyamurthy, T.; Velusamy, S.; Iqbal, *J. Chem. Rev.* **2005**, *105*, 2329-2364.
9 Garrido-Barro, P.; Gimbert-Suriñach, C.; Matheu, R.; Sala, X.; Llobet, A. *Chem. Soc. Rev.* **2017**, *in press.*
10 Blakemore, J. D.; Crabtree, R. H.; Brudvig, G. W. *Chem. Rev.* **2015**, *115*, 12974-13005.
11 Gersten, S. W.; Samuels, G. J.; Meyer, T. J. *J. Am. Chem. Soc.* **1982**, *104*, 4029–4030.
12 Sens, C.; Romero, I.; Rodriguez, M.; Llobet, A.; Parella, T.; Benet-Buchholz, J. *J. Am. Chem. Soc.* **2004**, *126*, 7798-7799.
13 Concepcion, J. J.; Tsai, M. K.; Muckerman, J. T.; Meyer, T. J. *J. Am. Chem. Soc.* **2010,** *132*, 1545-1557.
14 Nyhlén, J.; Duan, L.; Åkermark, B.; Sun, L.; Privalov, T. *Angew. Chem. Int. Ed.* **2010**, *49*, 1773-1777.
15 Gagliardi, C. J.; Vannucci, A. K.; Concepcion, J. J.; Chen, Z.; Meyer, T. J. *Energy Environ. Sci.* **2012**, *5*, 7704-7717.
16 Duan, L.; Fischer, A.; Xu, Y.; Sun, L. *J. Am. Chem. Soc*. **2009**, *131*, 10397-10399.
17 Matheu, R.; Ertem, M. Z.; Benet-Buchholz, J.; Coronado, E.; Batista, V. S.; Sala, X.; Llobet, A. *J. Am. Chem. Soc.* **2015**, *137,* 10786-10795.
18 Matheu, R.; Ertem, M. Z.; Pipelier, M.; Lebreton, J.; Dubreuil, D.; Benet-Buchholz, J.; Sala, X.; Tessier, A.; Llobet, A.; **2017***, submitted.*
19 Matheu, R.; Ertem, M. Z.; Gimbert-Suriñach, C.; Benet-Buchholz, J.; Sala, X.; Llobet, A.; **2017**, *submitted.*
20 Galaup, C.; Couchet, J.-M.; Bedel, S.; Tisnès, P.; Picard, C. *J. Org. Chem.* **2005**, *70*, 2274-2284.
21 Evans, I. P.; Spencer A.; Wilkinson, G.; *J. Chem. Soc., Dalton Trans.* **1973**, 204-209.

22 Data collection with APEX II version v2013.4-1. Bruker (2007). Bruker AXS Inc., Madison, Wisconsin, USA.
23 Bruker SAINT version V8.30c. Bruker (2007). Bruker AXS Inc., Madison, Wisconsin, USA.
24 SADABS: V2012/1 Bruker (2001). Bruker AXS Inc., Madison, Wisconsin, USA. Blessing, Acta Cryst. (1995) A51 33-38.
25 Sheldrick, G.M. *Acta Cryst*. **2008** A64, 112-122. SHELXTL version V6.14.
26 Richmond, C. J.; Matheu, R.; Poater, A.; Falivene, L.; Benet-Buchholz, J.; Sala, X.; Cavallo, L.; Llobet, A. *Chem. Eur. J.* **2014**, *20*, 17282-17286.
27 Mognon, L.; Benet-Buchholz, J.; Llobet, A. *Inorg. Chem.* **2015**, *54*, 11948-11957.
28 Berardi, S.; Francas, L.; Neudeck, S.; Maji, S.; Benet-Buchholz, J.; Meyer, F.; Llobet, A. *ChemSusChem* **2015**, *8*, 3688-3696.
29 Wasylenko, D. W.; Ganesamoorthy, C.; Henderson, M.; Koivisto, B. D.; Osthoff, H.; Berlinguette, C. P. *J. Am. Chem. Soc*. **2010**, *132*, 16094-16106.
30 Dobson, J. C.; Meyer, T. J. *Inorg. Chem.* **1988**, *27*, 3283-3291.
31 López, I.; Maji, S.; Benet-Buchholz, J.; Llobet, A. *Inorg. Chem.* **2015**, *54*, 658-666.
32 López, I.; Ertem, M. Z.; Maji, S.; Benet-Buchholz, J.; Keidel, A.; Kuhlmann, U.; Hildebrandt, P.; Cramer, C. J.; Batista, V. S.; Llobet, A. *Angew. Chem. Int. Ed.* **2014**, *53*, 205-209.

IV

E 7 Supporting Information

Supporting information for:

Paper E: Synthesis, characterization and electrochemical analysis of a Ru *trans*-di-aquo complex with a seven-coordinate environment

Outline

IV

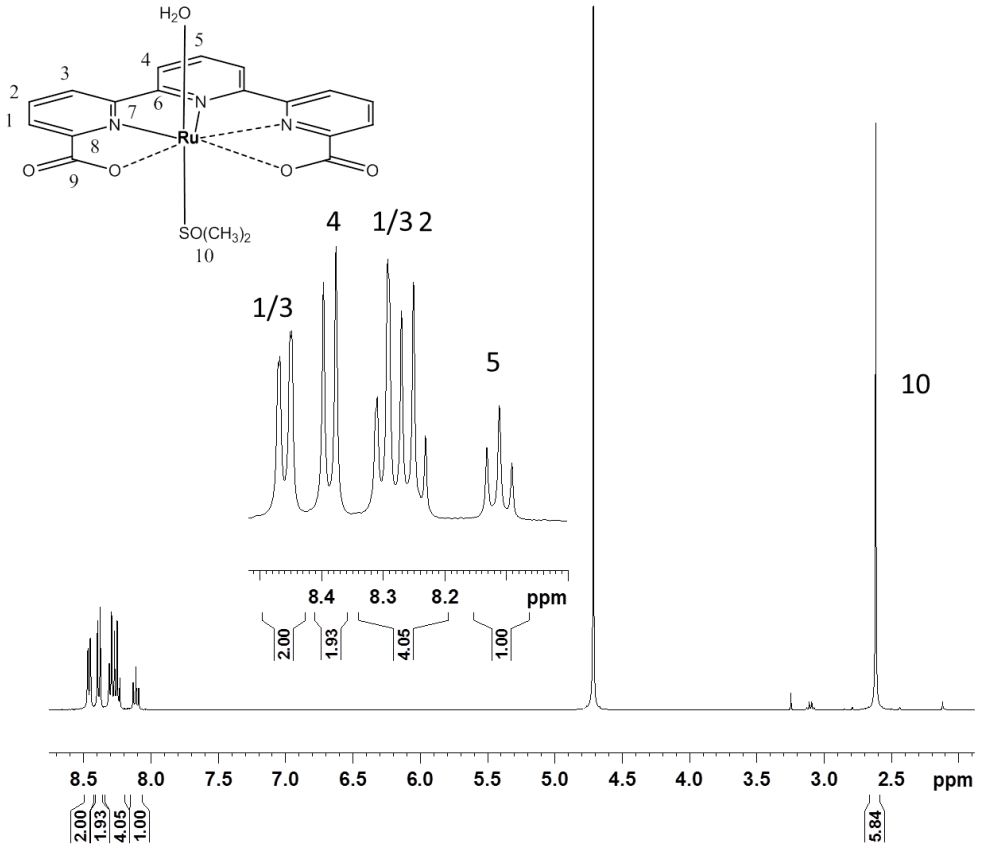

Figure S1: ^{1}H of **4^{II}** in D_2O (0.1 M CF_3SO_3D).

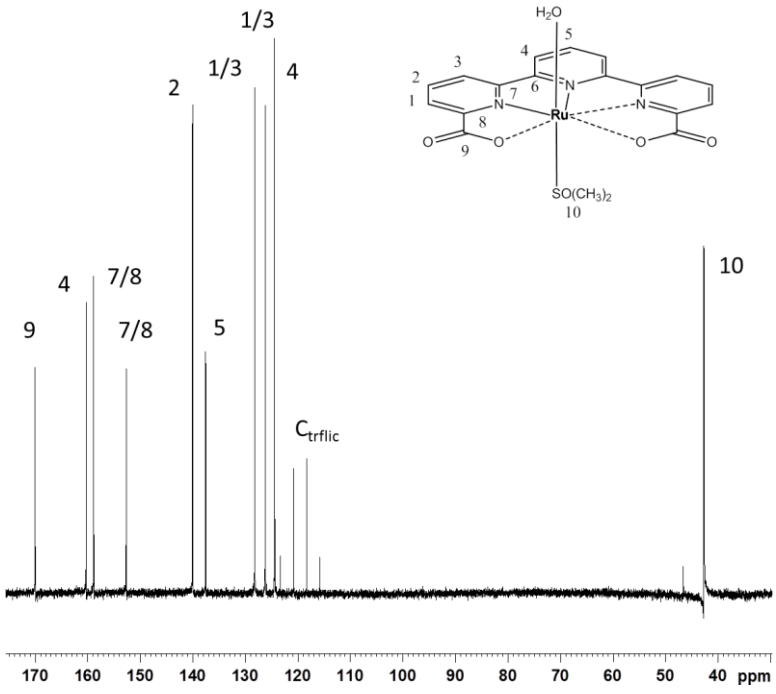

Figure S2: ^{13}C of **4^{II}** in D_2O (0.1 M CF_3SO_3D).

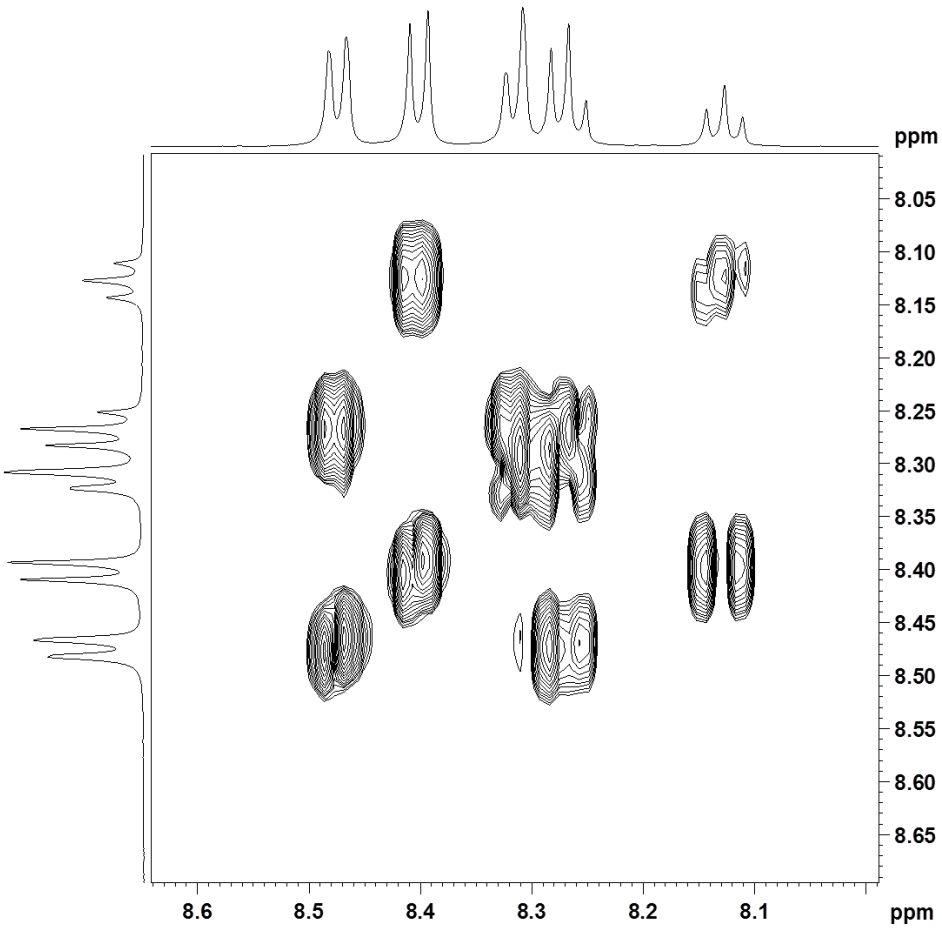

Figure S3: ^{1}H- ^{1}H COSY of **4^{II}** in D_2O (0.1 M CF_3SO_3D).

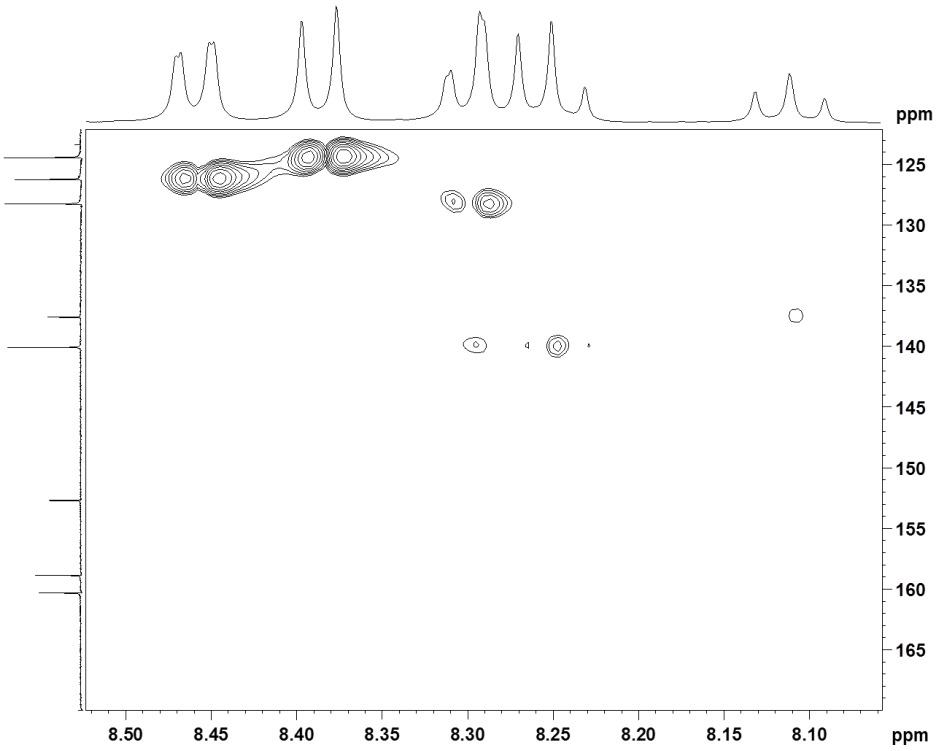

Figure S4: ^{13}C-^{1}H HSQC of **4^{II}** in D_2O (0.1 M CF_3SO_3D).

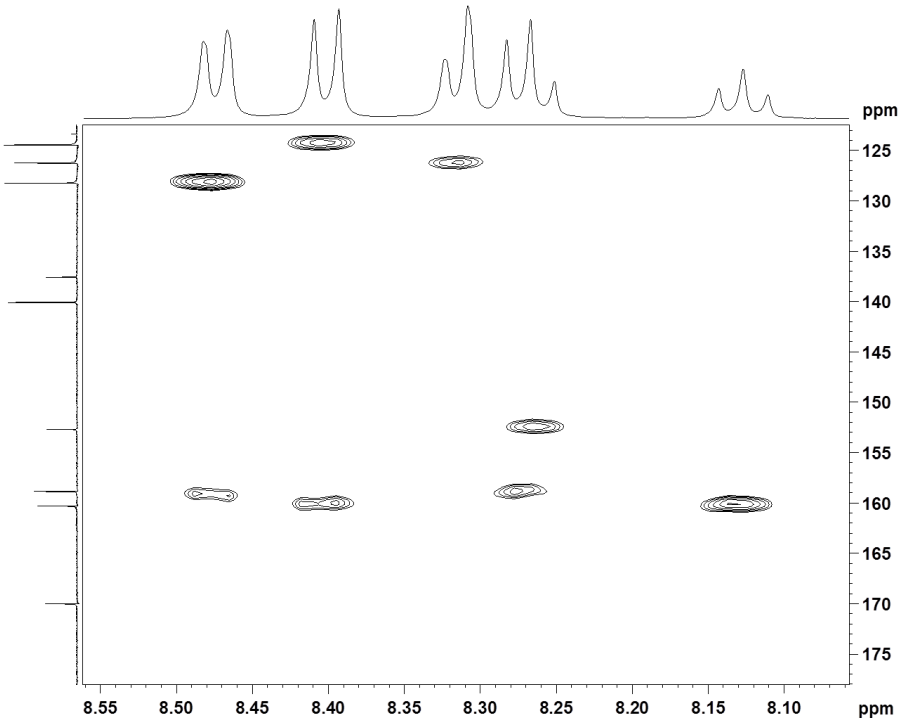

Figure S5: ^{13}C-^{1}H HMBC of **4^{II}** in D_2O (0.1 M CF_3SO_3D).

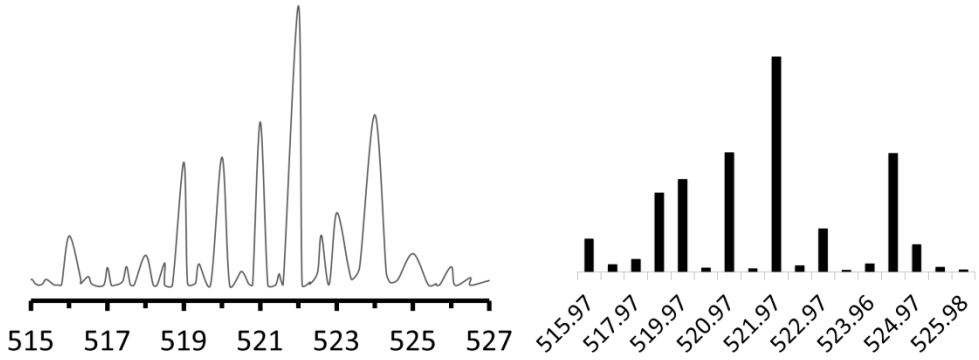

Figure S6: Measured HR-MS of [$\mathbf{4^{II}}$-H_2O+Na^+] (left) and simulated spectra for [$\mathbf{4^{II}}$-H_2O+Na^+] (right)

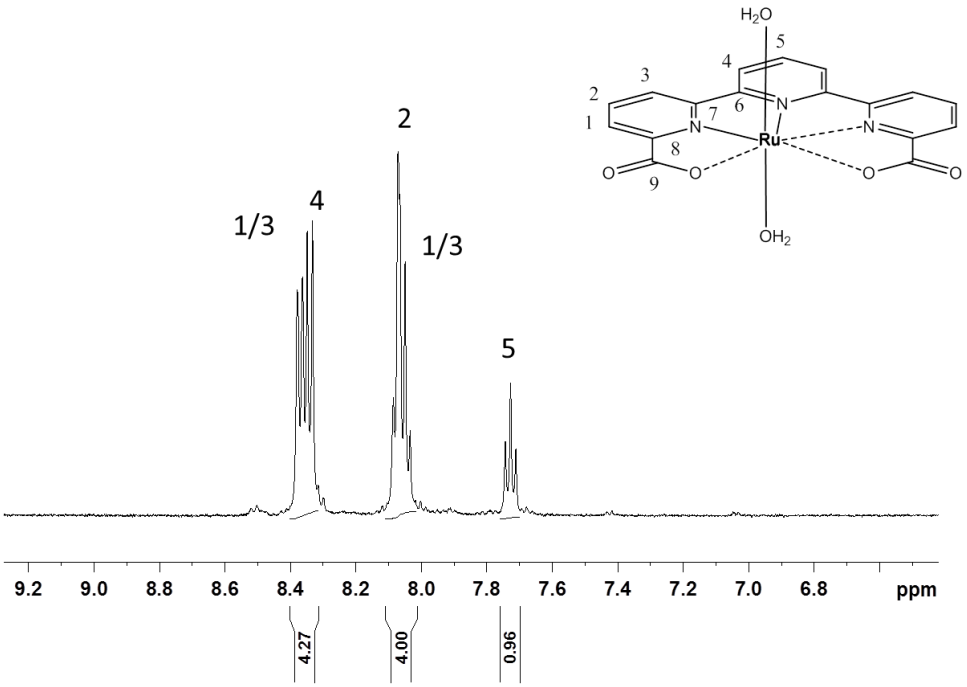

Figure S7: ^1H of $\mathbf{3^{II}(OH_2)_2}$ in D_2O with ascorbic acid as reducing agent.

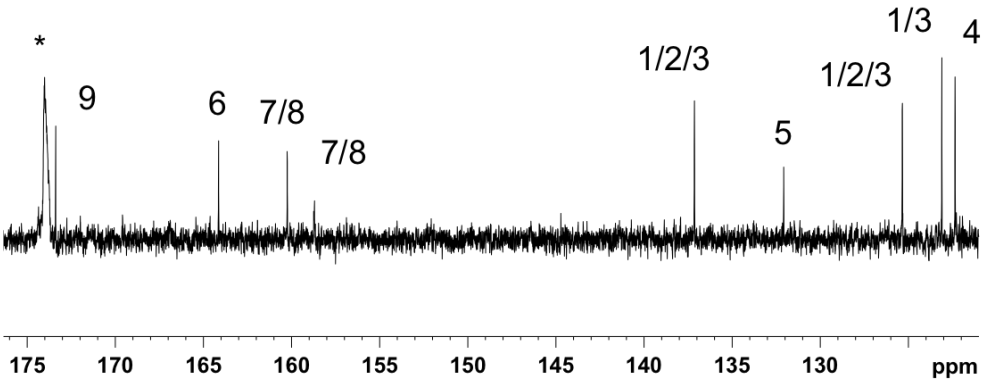

IV

Figure S8: ^{13}C of $\mathbf{3^{II}(OH_2)_2}$ in D_2O with ascorbic acid as reducing agent. Asterisc indicates a ^{13}C resonance of ascorbic acid

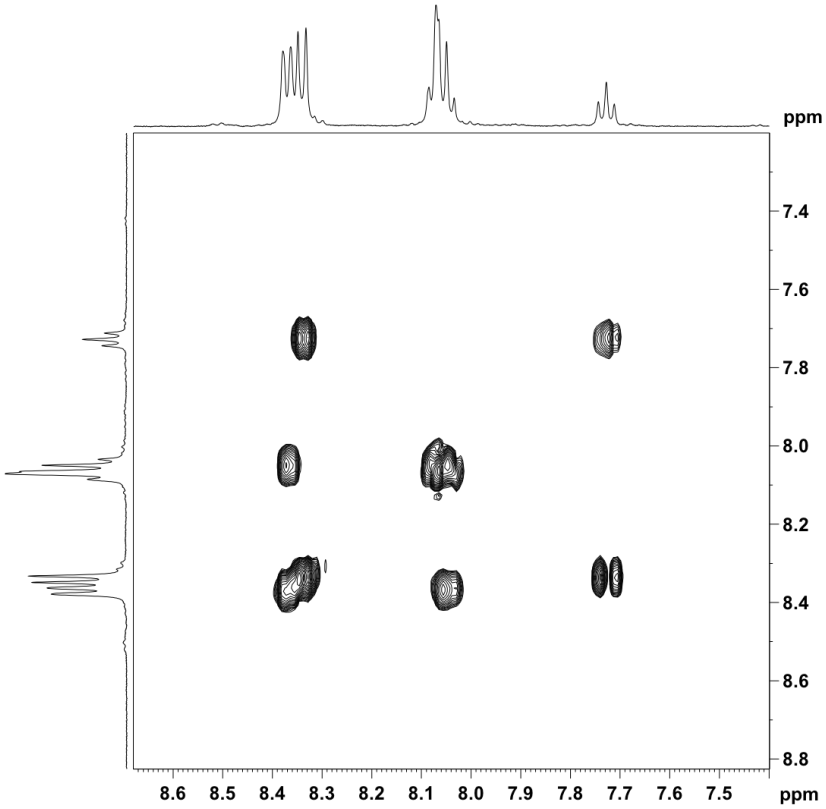

Figure S9: ^{1}H-^{1}H COSY of $\mathbf{3^{II}(OH_2)_2}$ in D_2O with ascorbic acid as reducing agent.

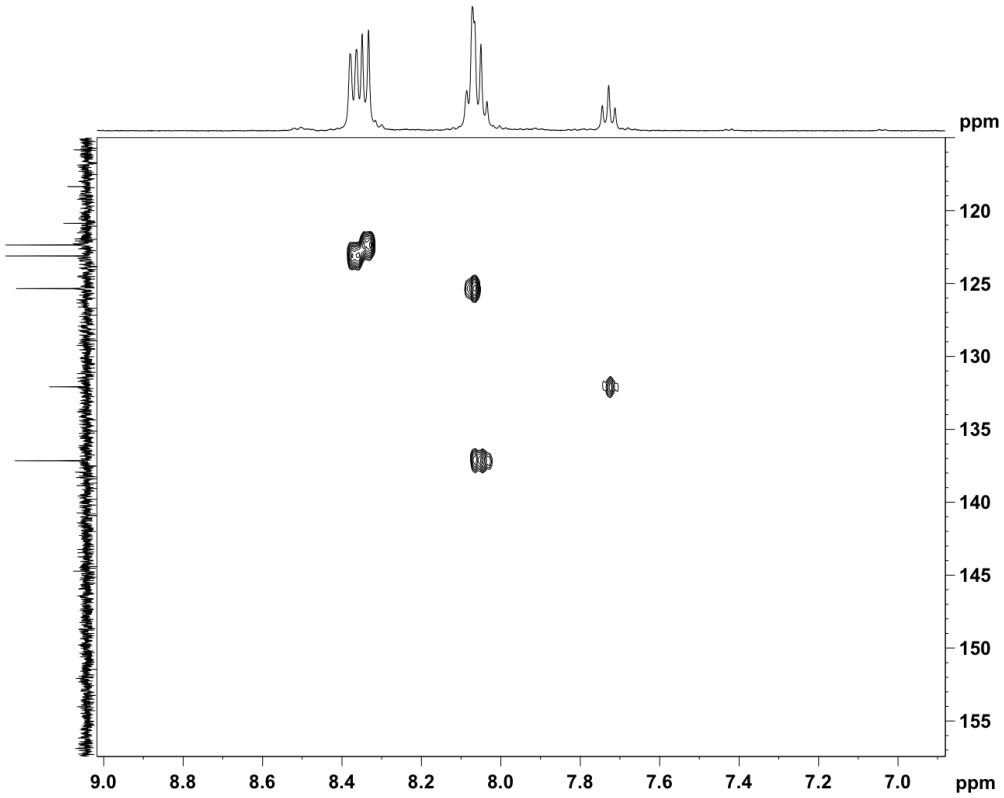

Figure S10: ^{13}C-^{1}H HSQC of **$3^{II}(OH_2)_2$** in D_2O with ascorbic acid as reducing agent.

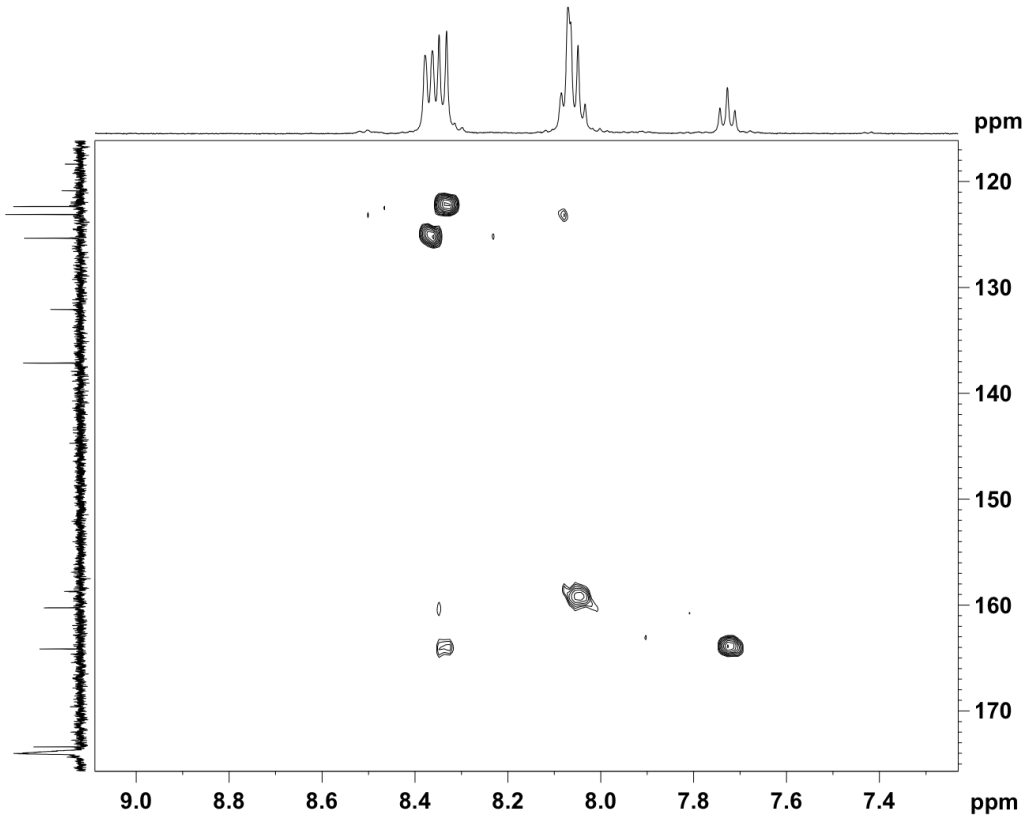

Figure S11: ^{13}C-^{1}H HMBC of **$3^{II}(OH_2)_2$** in D_2O with ascorbic acid as reducing agent.

Table S1: Metric parameters of $\mathbf{3^{III}(OH_2)_2^+}$, $\mathbf{4^{II}}$, $\mathbf{5^{II}}$, $\mathbf{6^{II}}$ and $\mathbf{7^{II,+}}$ in Å.

		$\mathbf{3^{III}(OH_2)_2^+}$	$\mathbf{4^{II}}$	$\mathbf{5^{II}}$	$\mathbf{6^{II}}$	$\mathbf{7^{II,+}}$
Equatorial coordination	Ru-OH_2	---		---	---	2.2
	Ru-N1	2.0	2.0	2.2	2.0	2.1
	Ru-N2	2.0	1.9	2.0	1.9	1.9
	Ru-N3	2.1	2.2	2.0	2.1	2.1
	Ru-O1	2.2	2.3	2.2	2.2	3.5
	Ru-O2	2.4	3.1	3.3	---	3.7
Axial coordination	Ru-N4	---	---	2.1	2.1	---
	Ru-N5	---	---	---	2.1	---
	Ru-$O3H_2$	2.1	2.1	---	---	2.1
	Ru-$O4H_2$	2.1	---	---	---	---
	Ru-S1	---	2.2	2.2	---	2.2
Ox. State		II	II	II	II	III
Reference		This work	This work	1	2	This work

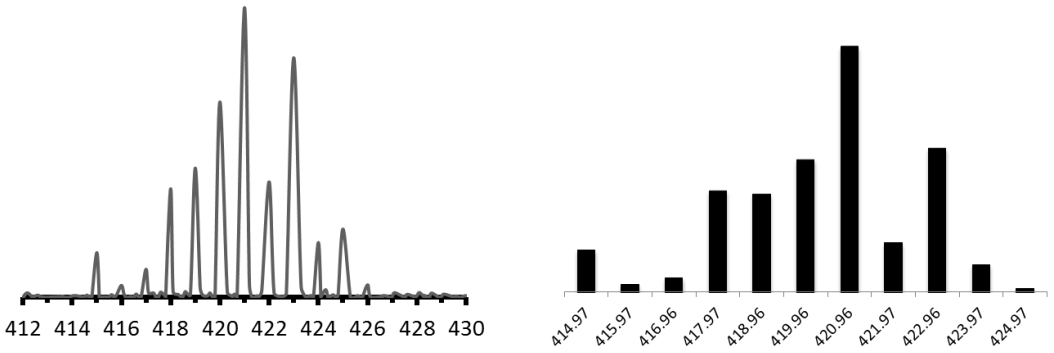

Figure S12: Measured HR-MS of $[\mathbf{3^{III}(OH_2)_2}\text{-}2\cdot H_2O]^+$ (left) and simulated HR-MS of $[\mathbf{3^{III}(OH_2)_2}\text{-}2\cdot H_2O]^+$ (right)

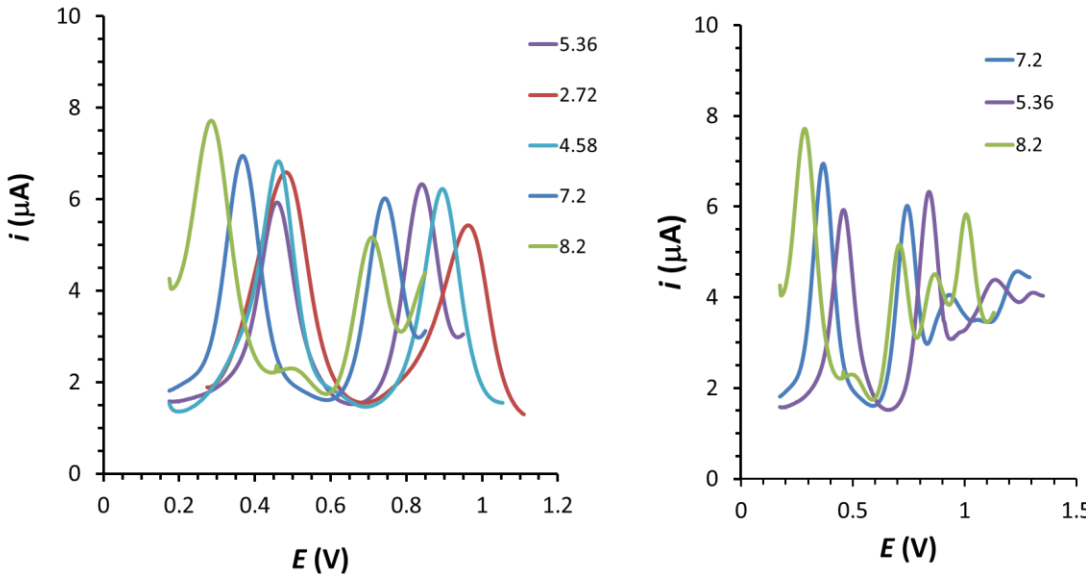

Figure S13: DPVs of $\mathbf{3^{III}(OH_2)_2^+}$ at pH from 2.72 to 8.20.

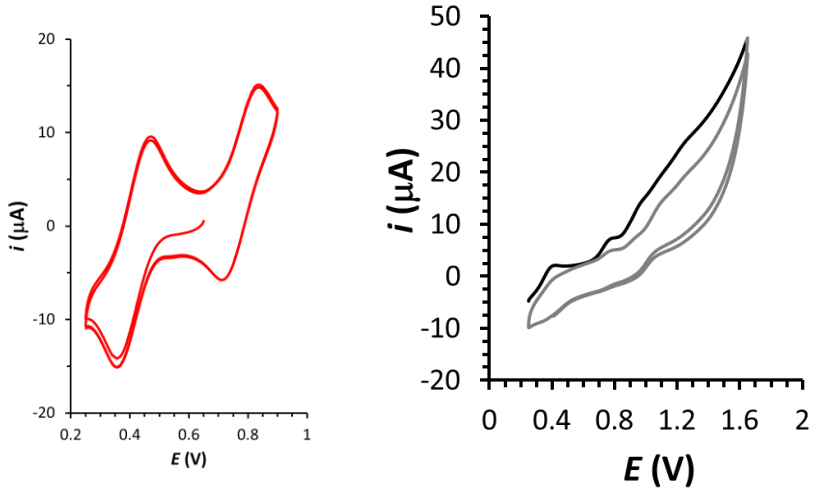

Figure S14: Left, two consecutive CVs of $\mathbf{3^{III}(OH_2)_2^+}$ at pH = 7.0 cycled from 0.2 V to 0.9 V (red line). Right, two consecutive CVs of $\mathbf{3^{III}(OH_2)_2^+}$ cycled between 0.2 and 1.9 V (black line first segment and grey the rest).

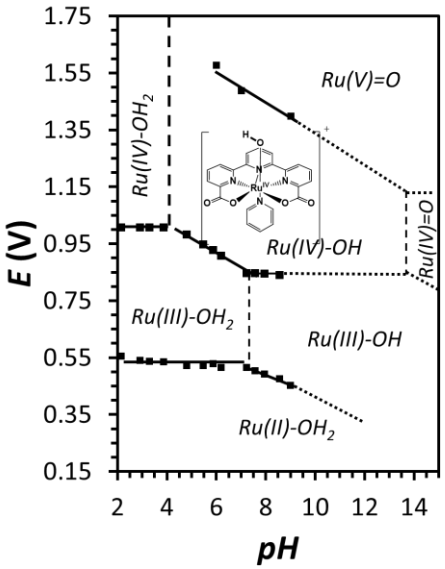

IV

Figure S15. Pourbaix diagram for complexes for complex $\mathbf{2^{III}(OH)^{+}}$.Reprinted from reference 1.

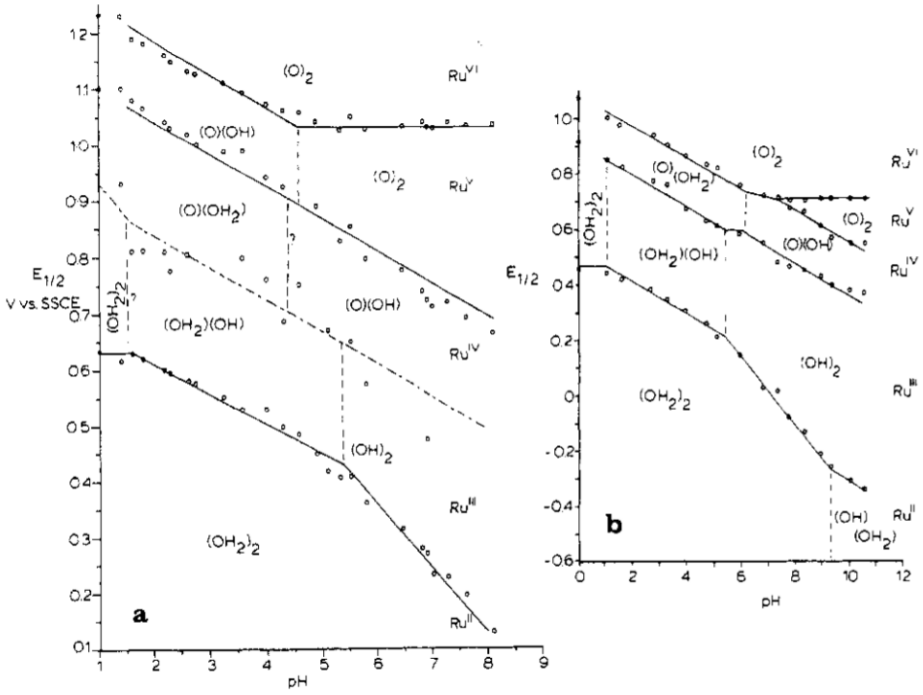

Figure S16. Pourbaix diagram for complexes for complex $\mathbf{12^{II}(OH_2)_2^{2+}}$ (**a**) and $\mathbf{11^{II}(OH_2)_2^{2+}}$ (**b**). Reprinted from reference 3. Potential vs SSCE.

REFERENCES

S1 Matheu, R.; Ertem, M. Z.; Gimbert-Suriñach, C.; Benet-Buchholz, J.; Sala, X.; Llobet, A.; **2017**, *submitted*

S2 Matheu, R.; Ertem, M. Z.; Benet-Buchholz, J.; Coronado, E.; Batista, V. S.; Sala, X.; Llobet, A. *J. Am. Chem. Soc.* **2015**, *137,* 10786-10795

S3 Dobson, J. C.; Meyer, T. J. *Inorg. Chem.* **1988**, *27*, 3283-3291

Chapter 5

Foot of the Wave Analysis for Mechanistic Elucidation and Benchmarking Applications in Molecular Water Oxidation Catalysis

The mathematical description for the foot of the wave analysis (FOWA) applied to the electrocatalytic oxidation of water to dioyxen is reported either for water oxidation catalysts (WOCs) working through the water nucleophilic attack or the interaction of two M-O units. Further, the application of the FOWA at different catalyst concentrations allows elucidating the reaction mechanism that operates in each case. This has been used in one hand to corroborate the operating mechanim in previously reported WOCs and to elucidate the mechanism of new seven-coordinate Ru catalysts. Finally we show how catalytic Tafel plots provide a perfect tool for benchmarking water oxidation catalysts under comparable conditions, for the first time.

V

The chapter consist of the following indendendent paper:

PAPER F Matheu, R.; Neudeck, S.; Meyer, F.; Sala, X.; Llobet, A. *ChemSusChem* **2016**, *9*, 3361-3369.

PAPER F Foot of the Wave Analysis for Mechanistic Elucidation and Benchmarking Applications in Molecular Water Oxidation Catalysis

Matheu, R.; Neudeck, S.; Meyer, F.; Sala, X.; Llobet, A. *ChemSusChem* **2016**, *9*, 3361-3369.

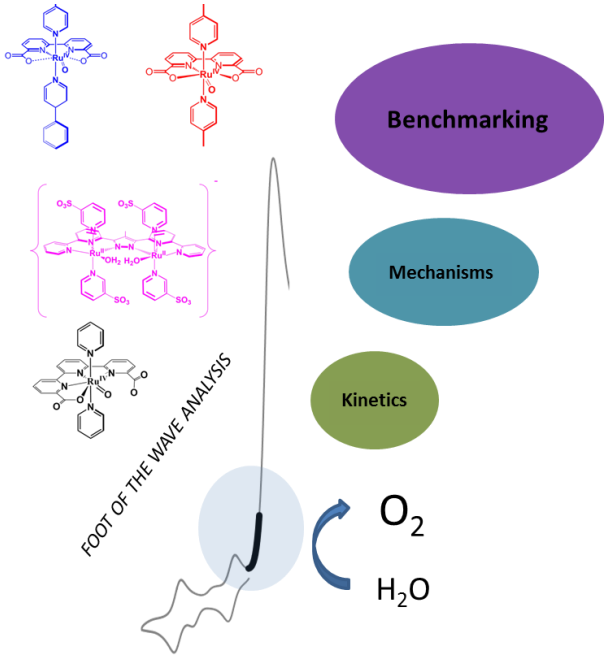

V

Abstract

The description of the foot of the wave analysis (FOWA) applied to the electrocatalytic oxidation of water to dioxygen is reported for cases where the rate determining step is first order and second order with regard to catalyst concentration. This coincides with the so called water nucleophilic attack (WNA) and interaction of two M-O units (I2M) mechanism, respectively. The newly adapted equations are applied to a range of relevant *molecular* catalysts both in homogeneous and heterogeneous phase, and the kinetic parameters, including apparent rate constants and turnover frequencies, are determined. In this respect the application of FOWA at different catalyst concentrations allows elucidating the reaction mechanism that operates in each case. In addition catalytic Tafel plots are used for assessing the performance of several *molecular* water oxidation catalysts (WOCs) as a function of overpotential under analogous conditions, and such analysis is valuable for benchmarking purposes. While this had been earlier carried out for oxide based WOCs, now it is the first time reported for molecular WOCs.

Contribution

Roc Matheu contributed to all the parts of this paper.

F 1 Introduction

Hydrogen generated by water splitting with sunlight is today considered as one of the most promising energy vectors for replacing fossil fuels. [1-3] This can be achieved using photoelectrochemical cells where water oxidation is occurring at the anode and proton reduction at the cathode, driven by sunlight.[4] The H_2 obtained in this way is generally termed *solar fuel*, generated by an *artificial photosynthetic device,* in analogy with the main mode of action of photosynthesis in green plants and algae.[5] The anodic water oxidation reaction is one of the key reactions involved in these processes common to both water splitting with sunlight and natural photosynthesis, and thus it is essential for the construction of functional devices[6,7] as well as for the comprehension of the reactions involved in natural photosynthesis.[8] In addition, the water oxidation anodic reaction can be potentially coupled to other interesting reactions such as CO_2 or N_2 reduction reactions to build artificial photosynthetic devices for instance for the generation of MeOH or NH_3 respectively.[9-11] The water oxidation reaction thus emerges as the key partner for various reduction reactions for energy and industrially relevant applications in the near future. For this reason it is imperative to understand the main pathways involved in the catalytic water oxidation reaction as well as the pathways that deactivate the catalyst.[12-14] In this respect water oxidation catalyzed by molecular transition metal complexes represent an ideal ground because of the ligand engineering possibilities for modulating the electronic and steric properties of the catalyst.[15]

V

While the capacity of transition metal oxides to perform water oxidation to dioxygen has been known for a long time [16-19] and has recently been benchmarked,[20-22] that of molecular transition metal complexes is more recent and has boomed only over the last 10 years.[12,23-30] There is nowadays a variety of transition metal complexes that have been reported to very efficiently oxidize water to dioxygen. However the conditions under which the catalysis is carried out differ from one another and hamper a meaningful comparison. In addition precise electrochemical methods are not available when S-shape catalytic responses are not obtained.[31-34]

There is thus a need to develop techniques to benchmark water oxidation catalysis with molecular systems in order to be able to identify the best catalyst for a given application. For this purpose we have *adapted* the so called “Foot of the Wave Analysis” (FOWA) for water oxidation catalysts that can be applied even when an ideal S-shape response is not obtained in cyclic voltammetry. The methodology is based on the analysis of the first data points of the catalysis, where the catalytic response is unperturbed by side phenomena that usually prevents the extraction of the kinetic information. The methodology was first reported by Costentin,

Robert, Saveant et al. [35] and was applied to the electrocatalytic reduction of protons and carbon dioxide.[36-41] Recently, Mayer et al.[42] have also shown a very nice agreement between apparent rate constants derived spectroscopically by UV-vis and based on FOWA for the catalytic oxygen reduction, which further validates this methodology.

Herein we extend the FOWA concept to catalytic water oxidation by *molecular* transition metal complexes. We thus report the FOWA mathematical equations adapted for electrocatalytic water oxidation reactions and their applications to some of the most relevant examples reported so far in the literature.[43-47] Chart 1 shows schematic structures and general nomenclature of the water oxidation catalysts discussed in the present work. In addition, the FOWA methodology is used as a tool for the elucidation of reaction mechanisms for these molecular water oxidation catalysts (WOCs), in particular with respect to the O-O bond formation. Finally, based on the FOWA results catalytic Tafel plots are reported for all these WOCs under similar conditions, allowing for a fair comparison among them.

V

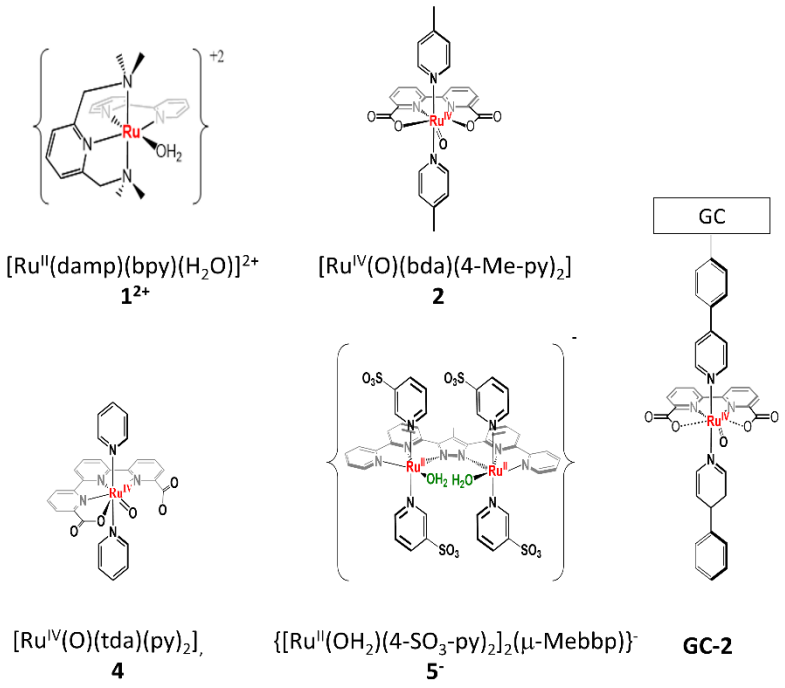

$[Ru^{II}(damp)(bpy)(H_2O)]^{2+}$ **1^{2+}**

$[Ru^{IV}(O)(bda)(4\text{-}Me\text{-}py)_2]$ **2**

$[Ru^{IV}(O)(tda)(py)_2]$ **4**

$\{[Ru^{II}(OH_2)(4\text{-}SO_3\text{-}py)_2]_2(\mu\text{-}Mebbp)\}^{-}$ **5^{-}**

GC-2

Chart 1. Schematic structures of the complexes discussed in this work.

F 2 Results

F 2.1 Main mechanistic scenarios described for molecular water oxidation catalysts

Scheme 1 shows the reaction mechanism proposed for complex $[Ru^{II}(damp)(bpy)(H_2O)]^{2+}$, **$1^{2+}$** (damp is 2,6-bis(dimethylaminomethyl)-pyridine and bpy is 2,2'-bipyridine; see Chart 1) [43] and the seven coordinated complex $[Ru^{IV}(O)(bda)(4\text{-}Me\text{-}py)_2]$, **2** (pKa ($Ru^{IV}$-OH/$Ru^{IV}$-O) = 5.9; bda^{2-} is

2,2'-bipyridine-6,6'-dicarboxylate and py is pyridine).[45] These two complexes follow two different O-O bond formation pathways that are representative of the main mechanisms that have been reported in recent years[25,48-50] For the sake of simplicity and easy follow up of electron counting, we will refer only to formal oxidation states at the Ru metal center. This does not neglect the obvious total or partial contribution from the Ru bonded terminal oxido or hydroxido ligands on the removal of electron density especially at high oxidation states. Complex $\mathbf{1}^{2+}$ follows the so-called water nucleophilic attack (WNA) mechanism where the O-O bond formation occurs via a nucleophilic attack of solvent water to an electrophilic Ru^{V}-O group and is the rate determining step (rds), as is also proposed for a number of so called single site catalysts.[51]The rate constants for WNA and the last ET step are also indicated in Scheme 1 and presented as equations 1 and 2 below,

$$[(damp)(bpy)Ru^{IV}\text{-}O]^{2+} - 1e^- \rightarrow [(damp)(bpy)Ru^{V}\text{-}O]^{3+} \quad (1)$$

$$[(damp)(bpy)Ru^{V}\text{-}O]^{3+} + H_2O \rightarrow [(damp)(bpy)Ru^{III}\text{-}OOH]^{2+} + H^+ \quad (2)$$

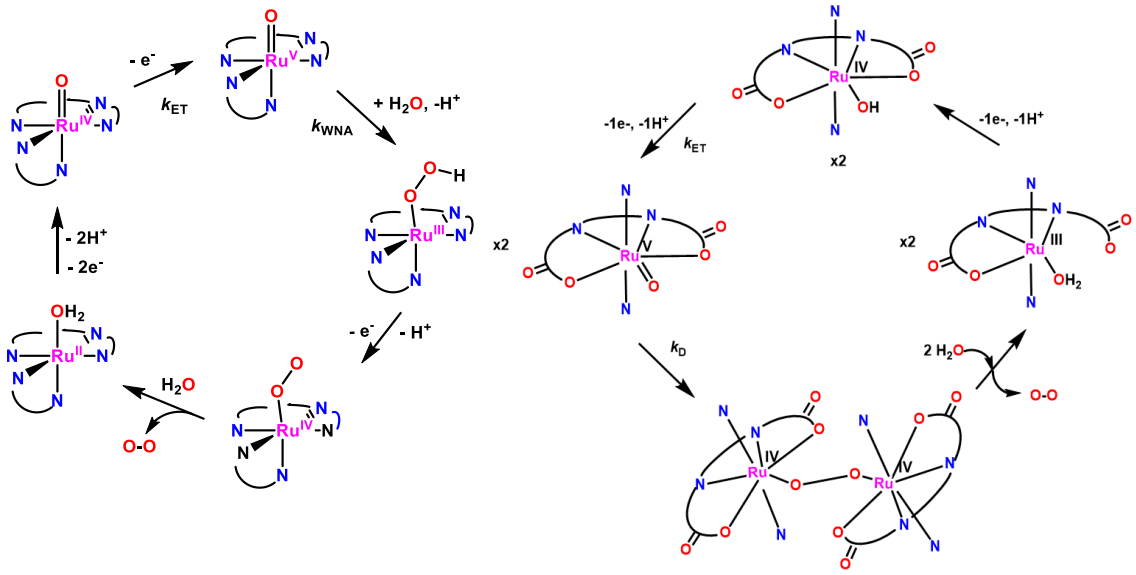

Scheme 1. Main O-O bond formation mechanism described for molecular water oxidation catalysis. Left, WNA mechanism proposed for $[Ru^{II}(damp)(bpy)(H_2O)]^{2+}$, $\mathbf{1}^{2+}$. The 3N and 2N linked by arcs represents the damp and bpy ligands respectively. Right, I2M mechanism proposed for $[Ru^{IV}(O)(bda)(4\text{-Me-py})_2]$, 2. The O and N linked by arcs represent the bda^{2-} ligand whereas the picoline ligand is represented by a single N.

On the other hand the Ru-bda complex **2H$^+$**, at low pH, follows the so-called interaction of two M-O units (I2M) mechanism where the O-O bond formation is proposed to occur via dimerization of two M-O groups.[45]For a mononuclear complex this is an intermolecular reaction but for a dinuclear complex this could potentially occur in an intramolecular manner.[52] In the former case the dimerization is produced upon reaching the Ru(V) state and under stoichiometric conditions the slowest steps are associated with the dimerization process (k_D = 1.1 x 10^5 $M^{-1}s^{-1}$) and the subsequent oxygen ejection (k_{O2} = 5.8 s^{-1}) displayed in equations 3b and 3c respectively and in Scheme 1. In both cases the kinetic processes are independent of the [Ce(IV)] used as chemical oxidant. Given the second and first order nature of k_D and k_{O2} respectively, the rds of the process depends on the initial concentration of Ru. For low [Ru] (below the 5 μM range) the dimerization process (3b) is the rds and above the 0.5 mM range the oxygen ejection (3c) is the rds. However, under excess of Ce(IV) the peroxo complex is proposed to be further oxidized to a superoxo species (4a) that in turn evolves oxygen (4b). Both processes are described to be very fast under these conditions and thus the kinetics again are independent of [Ce(IV)] and the rds is governed by k_D at the μM concentration range of Ru.

V

$$[(bda)(py)_2Ru^{IV}\text{-}OH]^+ - 1e^- \rightarrow [(bda)(py)_2Ru^{V}\text{-}O]^+ + H^+ \quad (3a)$$

$$2\,[(bda)(py)_2Ru^{V}\text{-}O]^+ \xrightarrow{k_D} [(bda)(py)_2Ru^{IV}\text{-}OO\text{-}Ru^{IV}(bda)(py)_2]^{2+} \quad (3b)$$

$$[(bda)(py)_2Ru^{IV}\text{-}OO\text{-}Ru^{IV}(bda)(py)_2]^{2+} + 2\,H_2O \xrightarrow{k_{O2}} 2\,[(bda)(py)_2Ru^{III}(OH_2)]^+ + O_2 \quad (3c)$$

$$[(bda)(py)_2Ru^{IV}\text{-}OO\text{-}Ru^{IV}(bda)(py)_2]^{2+} \xrightarrow{-1\,e^-} [(bda)(py)_2Ru^{IV}\text{-}OO^-\text{-}Ru^{IV}(bda)(py)_2]^{3+} \quad (4a)$$

$$[(bda)(py)_2Ru^{IV}\text{-}OO^-\text{-}Ru^{IV}(bda)(py)_2]^{3+} + 2\,H_2O \rightarrow [(bda)(py)_2Ru^{III}(OH_2)]^+ + [(bda)(py)_2Ru^{IV}(OH)]^+ + H^+ + O_2 \quad (4b)$$

Table 1. Summary of reactions and key equations obtained for the WNA, I2M and hetero-WNA mechanisms including TOF-η relationships and TOF_{MAX} formulas.

WNA		I2M		Hetero-WNA	
$P \rightarrow Q + e^-$ $Q + H_2O \overset{k_1}{\rightarrow} P + O_2$ ($k_1 \cdot [H_2O] = k_{WNA}$)	5	$P \rightarrow Q + e^-$ $Q + Q \overset{k_D}{\rightarrow} 2P$	6	$het-P \rightarrow het-Q + e^-$ $het-Q + H_2O \overset{k_1}{\rightarrow} het-P + O_2$	7
$\frac{i}{i_p} = \frac{4 \cdot 2.24\sqrt{\frac{R \cdot T}{F \cdot \nu} \cdot k_{WNA}}}{1 + e\left(\frac{F(E^0 - E)}{RT}\right)}$	8	$\frac{i}{ip} = \frac{4 \cdot 2.24 \cdot \sqrt{\frac{R \cdot T}{3 \cdot F \cdot \nu} \cdot k_D \cdot C^0_{Cat}}}{\left(1 + e\left(\frac{F(E^0 - E)}{RT}\right)\right)^{3/2}}$	9	$\frac{i}{Q_{Ru}} = \frac{k_{WNA}}{1 + e\left(\frac{F(E^0 - E)}{RT}\right)}$	10
$TOF = \frac{k_{WNA}}{1 + e\left(\frac{F(E^0 - E_{H_2O/O_2} - \eta)}{RT}\right)}$	11	$TOF = \frac{\frac{1}{3} \cdot k_D \cdot C^0_{Cat}}{\left(1 + e\left(\frac{F(E^0 - E_{H_2O/O_2} - \eta)}{RT}\right)\right)^{3/2}}$	12	$TOF = \frac{k_{WNA}}{1 + e\left(\frac{F(E^0 - E_{H_2O/O_2} - \eta)}{RT}\right)}$	13
$TOF_{MAX} = k_{WNA}$	14	$TOF_{MAX} = 1/3 \cdot k_D \cdot C^0_{Cat}$	15	$TOF_{MAX} = k_{WNA}$	16

Abbreviations used: C^0_{cat} *or* [Ru], initial bulk concentration of catalyst; E^o, standard potential for the P and Q Couple; $E_{H2O/O2}$, standard potential of oxidation of water at the working pH; *F,* Faradaic constant; η, overpotential; *i,* CV current intensity; i_p, peak current intensity of one-electron redox process of the catalyst; k_1, apparent WNA rate constant; k_{WNA}, apparent WNA pseudo-rate constant ($k_1 \cdot [H_2O]$); k_D, apparent dimerization constant; Q_{Ru}, *m*oles of electrons associated with a 1 electron transfer process of the immobilized catalyst; *R,* gas constant; *T*, temperature; TOF, turn over frequency; *x,* distance from the electrode surface.

F 2.2. The FOWA equations for water oxidation catalysis.

We have adapted the FOWA methodology[35-39] using the equations 5 and 6 (see Table 1) for the WNA and I2M mechanisms, respectively, in homogeneous phase. Therefore, we used the generic "P" and "Q" labels that correspond to equations 1-2 and 3a-3b, respectively, just described above for catalyst $\mathbf{1}^{2+}$ and **2**. In both cases, we are assuming that the O-O bond formation is the rds. Other scenarios for water oxidation catalysis with different rds steps are not considered in the present work; however, systems where the rds is first order with regard to [Ru] will also be comprised within the equations of the WNA mechanisms[49] as will be the intramolecular O-O bond formation in dinuclear complexes.[47,53-54]

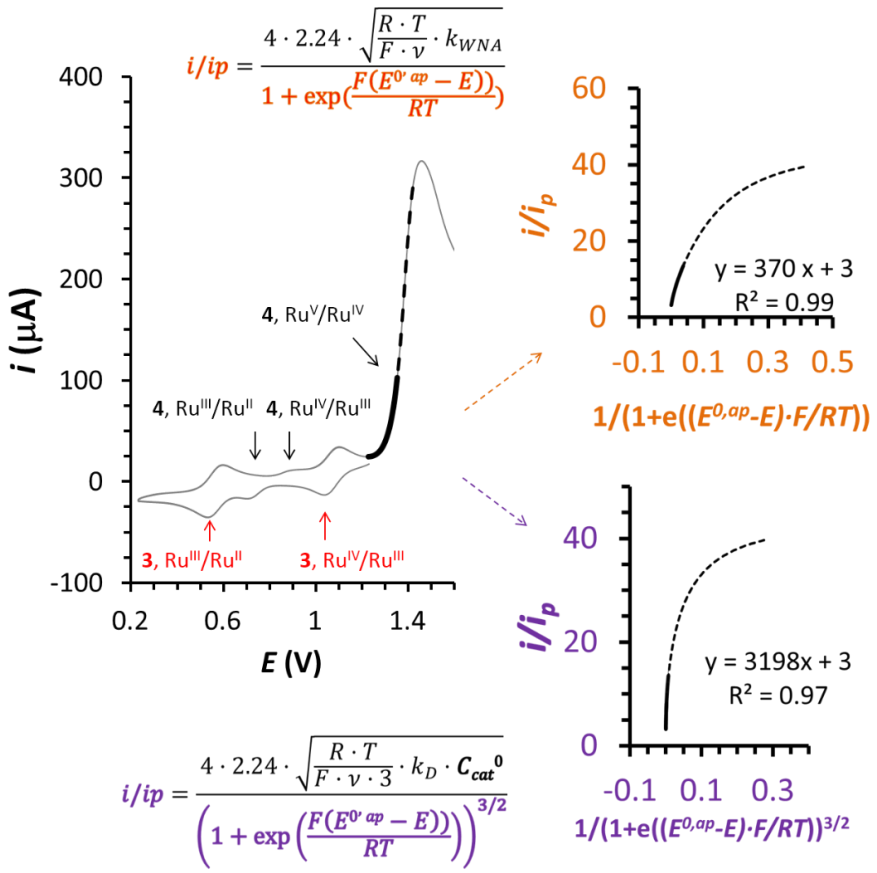

V

Figure 1: Left, grey solid line shows a CV of a **3**/**4** mixture (3.0 mM/1.5 mM) at pH = 7.0. The black dashed line indicates the data points used for the FOWA. The black solid arrows indicate the one-electron processes of complexes **3** and **4**.[44] Top right, i/i_p *vs*. [1/(1+e(($E^{o,ap}$-*E*)(*F*/*RT*)))] plot assuming a WNA mechanism and the used equation. Bottom right, i/i_p *vs*. [1/(1+e(($E^{o,ap}$-*E*)(*F*/*RT*)))$^{3/2}$] plot assuming an I2M mechanism and its equation. The fitting points for the extraction of rate constants at the foot of the wave are represented as a black solid line in the three graphs.

A complete mathematical description of the FOWA equations is presented in the SI and the most relevant equations are listed in Table 1. It is worth mentioning that for the WNA mechanism, k_{WNA} is an apparent pseudo-rate constant defined as $k_{WNA} = k_1 \cdot [H_2O]$ (see Table 1) that is associated with the chemical reaction (equation 2) following electron transfer. In a similar manner k_D correspond to the dimerization process (equation 3b) that occurs after electron transfer in the I2M mechanism. A related bimolecular mechanism had been previously considered by Costentin and Saveant.[55] Within this framework it is important to realize that the key features that distinguish the FOWA equations for the WNA vs. I2M mechanisms are the different dependences of "i/i_p" on catalyst concentration (where "*i*", is the current intensity at the CV and "i_p" is the peak current intensity of a one electron redox process of the catalyst; see equations 8 and 9 in Table 1). This concentration dependence is an intrinsic property of each mechanism that will be used for the subsequent discussions. Further the turnover frequency

(TOF) and its maximum value, TOF_{MAX}, are two key features for the proper catalyst characterization, whose equations (11-14) are displayed in Table 1 for both the WNA and I2M mechanisms.

We also have applied the FOWA formalisms to **GC-2**, which is a homologue of catalyst **2** attached to the surface of an electrode, under severely restricted translational mobility conditions, and thus with basically no diffusion. We have used the chemical equations 7 (Table 1) with the generic terminology "het-P" and "het-Q" to denote the heterogeneous phase nature for the anchored catalyst, under different oxidation states, and we deduced its corresponding TOF and TOF_{MAX} equations 13 and 16.

*F 2.3 The FOWA methodology applied to $[Ru^{IV}(O)(tda)(py)_2]$, **4**, and $\{[Ru^{II}(OH_2)(4\text{-}SO_3\text{-}py)_2]_2(\mu\text{-}Mebbp)\}^-$, **5**$^-$, complexes.*

Under neutral and basic condition the seven coordinate complex $[Ru^{IV}(tda)(py)_2]^{2+}$, $\mathbf{3}^{2+}$ (tda^{2-} is [2,2':6',2''-terpyridine]-6,6''-dicarboxylate), has recently been reported to undergo hydroxide substitution with concomitant proton loss (pK_a [Ru(OH)/Ru(O)] = 5.6) to form $[Ru^{IV}(O)(tda)(py)_2]$, **4**,[44] containing a pendant carboxylate that coexists with $\mathbf{3}^{2+}$. Complex **4** has been shown to display a spectacular activity with regard to the catalytic oxidation of water with maximum turnover frequencies ranging from 8.000 to 50.000 cycles per second depending on the pH and thanks to the pendant group that acts as an intramolecular proton acceptor. From a mechanistic perspective, a WNA mechanism has been proposed based on DFT upon reaching the $[Ru^{V}\text{-}O]$ state, with O-O bond formation via a water nucleophilic attack by a solvent water molecule in an analogous manner as described for $\mathbf{1}^{2+}$ in equations 1-2.[44]

Figure 1 shows a cyclic voltammogram of a mixture of 3.0 mM $\mathbf{3}^{2+}$ and 1.5 mM **4** at pH = 7.0 with a large electrocatalytic activity in the 1.3-1.6 V range that is associated with the generation of the corresponding $[Ru^{V}]$ complex whose Ru^{V}/Ru^{IV} apparent potential occurs at $E^{o,ap}$ = 1.43 V. This apparent potential is obtained by Differential Pulse Voltammety (DPV) although it has its intrinsic limitations, see supporting information for more details.

All the potentials in this work are measured vs. the mercury/mercurous sulfate (MSE, K_2SO_4 saturated at 25 °C) reference electrode but are reported vs. NHE by adding 0.65 V. We consider the peak current intensity of the wave associated with the background corrected (i.e., blank current subtracted) Ru^{III}/Ru^{II} couples as the "i_p" of the Ru^{V}/Ru^{IV} couple. Here it is important to mention that FOWA considers that the electron transfer kinetics of the process coupled to the catalytic reaction is infinitely fast and thus assumes a reversible Nernstian behavior. Compelling

evidence that advocates for Nernstian behavior in our complexes is suggested by the 59 mV anodic-cathodic peak separation in the redox waves of **3** within the 50-500 $mV \cdot s^{-1}$ range (see Figure S1).[44-47] We thus assume Nernstian behavior in all the complexes **1** – **5** studied in this work. While this estimation of the standard potential of the redox couple is certainly not ideal, it is actually the only way to calculate it for the water oxidation catalysis. Therefore it constitutes an intrinsic limitation of FOWA applied to water oxidation catalysis.

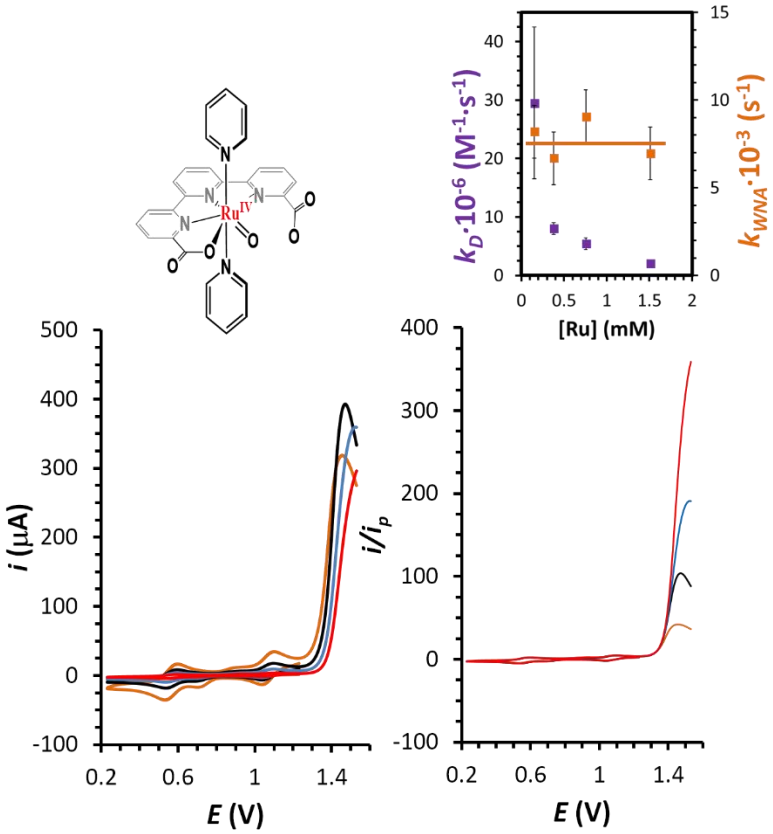

Figure 2: Left, CV of a **3**/**4** mixture at pH=7 at different concentrations (3.00 mM/1.50 mM; orange solid line, 1.50 mM/0.75 mM; black solid line, 0.75 mM/0.37 mM; blue solid line and 0.30 mM/0.15 mM; red solid line respectively). Right, i_p normalized CVs. Inset, plot of calculated k_D and k_{WNA} vs. [**4**]. The standard deviation of each data point is represented with vertical lines. The solid orange line indicates the trend for the WNA mechanism.

For complex **4**, the FOWA equations 8 and 9 in Table 1 were applied for the WNA and the I2M mechanisms respectively giving acceptable mathematical simulations in both cases as can be seen in the right hand side of Figure 1 where a plot of "i/i_p" vs. "$1/(1+e((E^{0,ap}-E)\cdot(F/RT)))$" and vs. "$1/(1+e((E^{o,ap}-E)\cdot(F/RT)))^{3/2}$" is presented.[56] To discern between the two mechanisms the FOWA methodology was applied at different [Ru]. A set of CVs within the 0.15-1.50 mM concentration range was recorded for **4** as shown in Figure 2 left, together with their i_p normalized CV on the

right hand side. The latter clearly shows that the slope ("i/i_p" vs. E) at the foot of the wave zone for all the normalized CVs is identical and thus clearly points out to a WNA mechanism. Indeed the extraction of the apparent rate constants k_{WNA} and k_D values (FOWA equations 8 and 9 respectively) show that while for the former they are constant with a value of $(7.7\pm1.5)\cdot10^3\ s^{-1}$, for the latter they decrease as the [Ru] increases. A plot of the k values vs. [Ru] (see inset Figure 2) graphically shows this point and thus unambiguously confirms the WNA nature of the mechanism operating in this case. It is important to emphasize here that the dependence of the rate constant on catalyst concentration is the key tool to determine the reaction mechanism and on the other hand the consistency of the concentration dependence results obtained further reveals the virtue of the methodology used. The preference of this mechanism is readily explained by the intramolecular proton abstraction by the dangling carboxylate and by the steric hindrance that any potential mechanism based on a dimerization process will suffer for this particular complex. All the kinetic data obtained for this complex and all the other complexes described in this work are reported in Table 2.

Another interesting asset of the FOWA methodology is the fact that since the measurement is done at the foot of the wave, at the very beginning of the catalytic reaction, a number of undesired reactions or effects are either suppressed or minimized.[38] In the case of Ru-tda complex **4**, the water oxidation catalysis is so fast that significant changes of the local pH at the electrode surface are evidenced by an anodic shift of the Ru-OH_2 waves after catalysis.[44]For this reason the value obtained with the classical Shain et al. methodology[33] based on plotting "i/i_p" vs. the "$\nu^{-1/2}$" even under pure kinetic control, would not give the correct apparent rate constant.

The same FOWA treatment was also applied for complex $\{[Ru^{II}(OH_2)(4\text{-}SO_3\text{-}py)_2]_2(\mu\text{-Mebbp})\}^-$, **5**$^-$, (Mebpp is 3,5-di([2,2'-bipyridin]-6-yl)-4-methylpyrazolate) that has been recently reported to undergo a WNA mechanism at pH = 1.0 with Ce(IV) as a chemical oxidant, based on $H_2{}^{18}O$ labeling experiments. The FOWA at different [**5**$^-$] further confirms the proposed WNA nature of the mechanism as can be observed in the corresponding "i/i_p" plots shown in Figure S5 in the SI. A constant value of $TOF_{MAX} = 50 \pm 10\ s^{-1}$ is obtained for this complex at different concentrations, and all the related kinetic data is also presented in Table 2.

Table 2. Kinetic, thermodynamic data and experimental conditions for the complexes studied in the present work.

Complex	*pH*	*Mec. FOWA*[a] *(Mec. Lit)*[b]	TOF_{MAX} s^{-1}	$TOF_{E_{Ce}}$[c] *(TOFlit)*[d] s^{-1}	$k_D \cdot 10^{-3}$ $s^{-1}M^{-1}$	$E^{o,ap}$ V[e]	*[Ru]*[f] *mM*
4	7.0	WNA	$(7.7\pm1.5)\cdot10^3$	0.37	---	1.43	0.15 - 1.5
5$^-$	1.0	WNA (WNA)[g]	50 ± 10	0.07 (0.07)[h]	---	1.71	0.08 – 0.79
2	1.0	I2M (I2M)[i]	11 ± 3[j]	11[j] (30)[k]	170 ± 50	1.39	0.2
2	7.0	I2M	11 ± 3[j]	11	160 ± 30	1.08	0.12 – 0.84
2	12.0	I2M	11 ± 3[j]	11	170 ± 40	1.08	0.14 – 0.94
GC-2	7.0	WNA	1.9[l]	1.9[l]	---	1.08	0.05 - 0.4[m]

a) Mechanism established in this work, b) Mechanism established in the literature, c) TOF_{ECe} stands for estimated TOF obtained by FOWA at a 1.55 V applied potential; that is the Ce(IV)/Ce(III) standard potential calculated with the FOWA equations based on the kinetics obtained for complex **5**$^-$ using Ce(IV) as oxidant, under the conditions used here. See text for more information and reference 68, d) Calculated TOF using Ce(IV) as a sacrificial oxidant in the literature, e) Apparent potential of the redox couple extracted from DPV in this work, f) Concentration range used in this work, g) The mechanism was elucidated based on isotope labeling experiments,[47]h) Experimental conditions: $[CF_3SO_3H]$ = 0.1 M, $[Ce(NH_4)_2(NO_3)_6]$ = 0.1 M and [Ru] = 1 mM,[47]i) Mechanism stablished thought kinetic studies,[45] j) Calculated TOF_{MAX} with [2] = 0.2 mM, k) Experimental conditions: $[CF_3SO_3H]$ = 0.1 M, $[Ce(NH_4)_2(NO_3)_6]$ = 0.538 M and [Ru] = 0.2 mM,[45]l) Calculated from the average of CVs from **GC-2** electrodes at low superficial concentration (Γ= 0.10 and 0.06 nmol/cm^2), m) Superficial concentration range (nmol/cm^2).

*F 2.4 The FOWA methodology applied to the [Ru^{IV}(O)(bda)$(py)_2$], **2**, complex.*

As shown in the previous section the WNA mechanism operates in case of catalysts **4** and $\mathbf{5}^-$. We thus focused our endeavors on catalyst **2**, that had previously been shown to undergo an I2M type of mechanism at pH 1.0 using Ce(IV) as a chemical oxidant.[45] We carried out the analogous FOWA analysis at pH 7.0 and 12.0; the results are shown in the supporting information (Figures S8-S13), in Figure 3 and in Table 2. Figure 3 shows the cyclic voltammograms of complex **2** at pH = 7.0 at four different concentrations of Ru (in the 0.12-0.84 mM range). As can be observed upon reaching the wave associated with the Ru^V/Ru^{IV} couple a large electrocatalytic current emerges at approximately 1.1 V, that increases with increasing concentration of the Ru catalyst. Figure 3 (right) shows the normalized "i/i_p" voltammograms that now clearly reveals that the slope ("i/i_p" vs. E) at the foot of the catalytic current increases with [Ru], pointing towards an I2M type of mechanism. Indeed using equations 8 and 9 in Table 1 the apparent k_{WNA} and k_D were extracted and are plotted in the inset versus catalyst concentration. In sharp contrast with complex **4** the calculated $k_D = (160 \pm 40)\cdot 10^3$ $M^{-1}\cdot s^{-1}$ is independent of the catalyst concentration whereas the calculated k_{WNA} is dependent. Thus, these experiments unambiguously show that the mechanism operative at pH 7.0 for Ru-bda complex **2** is the I2M. Finally, k_D was determined to estimate the TOF and TOF_{MAX} using equation 12 and 15 in Table 1 at 0.2 mM concentration. This concentration value was used to compare the electrochemical TOFs at all pHs as well as with the ones obtained using CAN as sacrificial oxidant at pH = 1.0 in homogeneous phase. The same FOWA methodology was applied at pH 12 for this catalyst, giving very similar results (see SI Figure S11-S13 and Table 2) and confirming the I2M nature of the mechanism operating at this pH. Very similar k_D values were obtained at pH 7.0 and 12.0 in a comparable range of concentrations confirming once again the independence of the rds on the concentration of OH^-

At pH 1.0 the solubility of the catalyst precursor, **2**, is very low preventing a complete kinetic analysis using FOWA within a reasonable range of concentrations. For this reason we carried out the FOWA analysis for a single catalyst concentration, 0.2 mM, and we run the CV at a scan rate of 10 mV/s (all the previous examples described were carried out at 100 mV/s). This gave practically the same k_D values as the ones obtained at higher pH (see SI Figure S19-S21 and Table 2) and thus confirms that for **2** the I2M mechanism operates over the pH range 1.0-12.0.

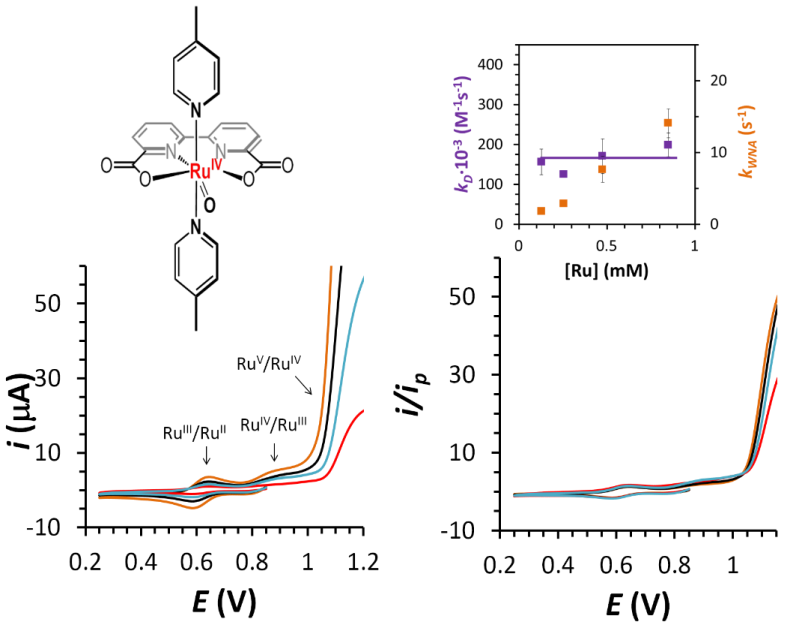

Figure 3. Left, CV of a **2** at 0.84 mM (orange solid line), 0.47 mM (black solid line), 0.25 mM (blue solid line) and 0.12 mM (red solid line) at pH = 7.0. The black solid arrows indicate the one-electron processes of **2**. Right, i_p normalized CVs. Inset, plot of calculated k_D and k_{WNA} vs. [**2**]. The standard deviation of each data point is represented with vertical lines. The solid purple line indicates the trend for the I2M mechanism.

Finally, we proceeded to evaluate catalyst **2** under restricted translational mobility conditions by anchoring it on a glassy carbon electrode. Under these conditions complex **2** cannot undergo a bimolecular dimerization and thus needs to change the reaction mechanism for water oxidation catalysis. We anchored a related Ru-NO catalyst precursor, {[Ru(NO)(bda)(PyPh-N_2^+)$_2$][PF_6]$_3$}, **6**, (PyPh-N_2^+ is 4-(pyridin-4-yl)benzenediazonium), on the surface of the electrode following the reduction of its diazonium salt as has been recently described.[46] In this way we generate a Ru-NO species at the surface of the electrode that is converted to **GC-2** after one CV cycling in the range 0.2 V – 1.5 V as described in our previous work and in the SI. [46] The amount of **GC-2** catalyst generated by this protocol ranges from 0.06 to 0.34 nmol/cm^2, and nicely correlates with the initial concentration of **6** used (See Figure S14 in the SI).

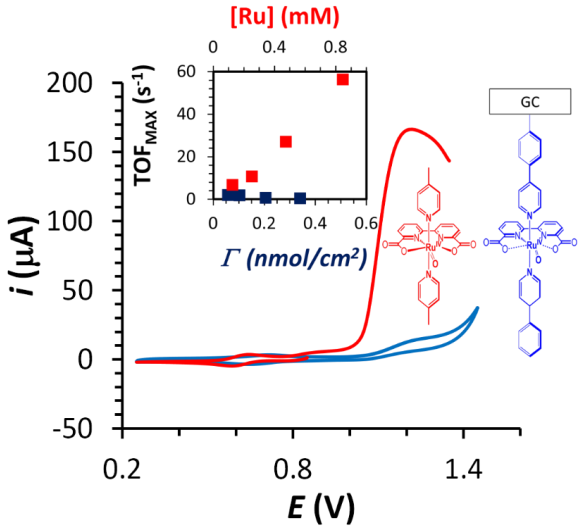

Figure 4. CV of 0.5 mM **2** that generates an i_p= 1.9 μA (red) and **GC-2** with Γ^{o}_{cat} = 0.34 nmol/cm^2 that generates a i_p= 2.6 μA (blue) both at pH = 7.0. Inset, plot of TOF_{MAX} for **2** (red squares) and **GC-2** (blue squares) *vs*. different Ru concentrations (red squares) and the Ru superficial concentrations (blue squares). The relative position of the two horizontal axis in the inset is set so that the i_p values for **2** and **GC-2** are coincident (see figure S18 for the plot of TOF_{max} *vs*. i_p values).

Application of the FOWA methodology at different surface coverage (0.06-0.39 nmol/cm^2 range, see SI Figure S15-S17) in this case using equation 10 in Table 1 gave a k_{WNA} value of 1.9 s^{-1} (see inset Figure 4 and SI, Figure S17). The catalyst concentration independency with regard to the rate constant is clear evidence for the mechanistic change, from I2M to WNA, due to the lack of translation mobility of the active species in **GC-2**. For higher surface coverages of 0.19 and 0.39 nmol/cm^2 the apparent rate decreases to 0.6 s^{-1}, a fact that might be attributed to surface effects associated with the electrode roughness.[57] Further, the TOF_{MAX} of **GC-2** obtained by FOWA is similar to the TOF obtained in previous work with heterogenised catalysts, that were in the range of under heterogeneous conditions (0.03-0.84 s^{-1} with overpotentials in the 0.3-0.8 V range. They were calculated by dividing the electrical charge associated with the O_2 evolution (Q_{O2}) in a bulk electrolysis experiment by the charge associated to the catalyst (Q_{Ru}): TOF = $Q_{O2}/(4 \cdot Q_{Ru})$.[46,58]These similarities thus lend further support to the methodology used here.

V

In addition to the different mechanistic scenarios for **2** and **GC-2**, the physical meaning of i_p in the voltammogram for dissolved species and i_p in the voltammogram for the surface-confined systems is also different, and therefore a direct comparison of apparent rate constants for **2** and **GC-2** is meaningless. However it is very instructive to see the behavior of these two catalysts when their corresponding i_p values are very similar. This can be observed in Figure 4 for [**2**] = 0.5 mM and for **GC-2** with a surface coverage of 0.34 nmol/cm^2, both at pH 7.0. Under these conditions the catalytic current density for **2** is more than one order of magnitude higher than for **GC-2** at E = 1.2 V (2.3 mA/cm^2 vs. 0.2 mA/cm^2).

F 2.5 Catalytic Tafel plots based on FOWA equations.

The catalytic Tafel plots commonly used "electrochemical Tafel plots". The electrochemical Tafel plots define a relationship between the current density and the overpotential with respect to the equilibrium potential.[59,60] On the other hand catalytic Tafel plots used here establish a relationship between the Turn Over Frequency of the catalyst and the applied potential with respect to the standard potential of the reaction.[35,38]

V

Catalytic Tafel graphs were drawn by plotting TOF as a function of overpotential (η) following equations 11, 12 and 13 in Table 1 for the WNA, I2M and hetero-WNA mechanisms respectively.[35] Figure 5 illustrates the catalytic Tafel plots for the complexes discussed in this work, allowing an easy and quick comparison among them. There are three key features that define the shape of the Tafel plot and thus reflect the activity and nature of the catalyst: a) the TOF_{MAX} which is the apparent rate at which the curve reaches a Plateau and that is described by equations 14, 15 and 16 in Table 1 for the WNA, I2M and hetero-WNA mechanisms respectively, b) the lowest value of potential where TOF = TOF_{MAX} and c) the slope that defines the relationship between TOF and overpotential which is a distinctive feature of each mechanism.

F 3 Discussion

The equations reported in this work that are summarized in Table 1 provide a valuable tool for the integral treatment of molecular water oxidation electrocatalysis. The data analysis allows to progress one step forward by unravelling the mechanisms operating for a given catalyst. In addition the detailed kinetic information also allows comparing catalysts under similar conditions. The latter is very important since so far the kinetic values reported were mostly obtained in drastically different conditions and therefore difficult to compare. Furthermore, the variation of the apparent rate constant as a function of overpotential graphically shown by the catalytic Tafel plots offer a comprehensive view of the catalyst performance as a function of the

applied potential. Benchmarking conditions had been recently proposed to compare WOCs based on solid metal oxides.[20,21] On the other hand catalytic Tafel plots have been successfully used to benchmark molecular proton reduction catalysts. [61,62]Here for the first time a comparison under the same conditions over a large span of overpotentials is carried out based on catalytic Tafel plots for molecular water oxidation catalysts.

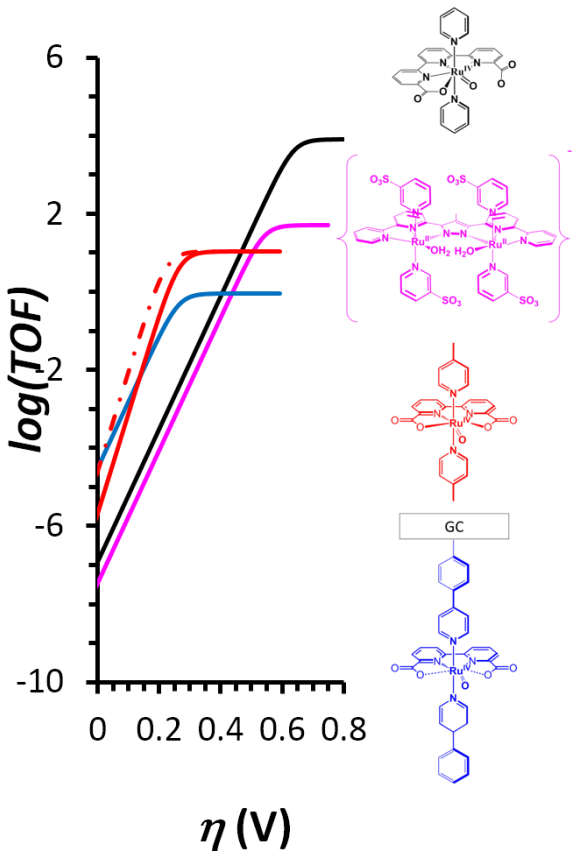

Figure 5: Catalytic Tafel plot of **5**$^{-}$ and **2** at pH 1.0 (pink solid line and red dashed line respectively) and **2**, **4** and **GC-2** at pH 7.0 (red, black and blue solid lines respectively). The green dashed line represents the potential of $E^{o'}(Ce^{IV}/Ce^{III})$ at pH 1.0. For catalyst **2**, a concentration of 0.2 mM was used for the plot.

Figure 5 shows Tafel plots for complexes **2**, **4**, **5**$^{-}$ and **GC-2**, and a number of conclusions can be drawn from the careful examination of this graph. At high overpotentials (η > 0.6 V) complex **4** is the best catalyst with a TOF_{MAX} value of $(7.7\pm1.5)\cdot10^{3}$ s^{-1} that is almost two orders of magnitude higher than that of the naturally occurring reaction in the OEC of photosystem II and three orders of magnitude higher than that of complex **2**, which is one of the best catalysts described so far. Furthermore the WNA mechanism obtained here is consistent with the molecular structure of the catalyst as the dangling carboxylate at the [Ru^{V}=O] oxidation state favors the intramolecular

proton transfer of an approaching water molecule for the critical O-O bond formation step, and thus favors the WNA mechanism. For these reasons catalyst **4** would be an ideal catalyst to anchor at the surface of a semiconductor that generated light induced high energy holes. For instance, semiconductors such as $BiVO_4$ or WO_3 that have very oxidizing valence bands of approximately 2.5 and 3 V respectively,[6] and thus are ideal to be integrated in such a photoanode for a water splitting electrochemical cells.[63,64]

On the other hand, at high overpotentials catalyst **4** has a TOF_{MAX} that is **2** orders of magnitude higher than the dinucleating Ru-Mebbp complex $\mathbf{5}^{-}$. However, at lower overpotentials the TOF of the two complexes differ by less than an order of magnitude and thus would be equally valuable for potential water splitting applications. In addition, the catalytic experiments are carried out at pH 7.0 for **4** and at pH 1.0 for $\mathbf{5}^{-}$. Therefore this leaves us with a couple of excellent WNA type of catalyst at low overpotentials within the pH range 1-7.

V

At η = 0.45 V the plots of catalyst **2** and **4** cross and thus indicates that under this conditions they have identical behavior. Please note that while for the WNA cases the plot is independent of the catalyst concentration for the I2M it depends on the initial catalysts concentration. Here we use [**2**] = 0.2 mM which is close to saturation but is a value reasonably achievable for other molecular WOCs. At lower overpotentials, **2** clearly outperforms **4** in homogeneous phase and is the best catalyst studied in this work. In addition higher TOFs can be obtained for complexes analogous to **2**, by fine tuning the axial ligand reaching TOFs up to 1000 s^{-1} at pH = 1.0 with a huge excess of Ce(IV) as chemical oxidant.[65,66]

It is also interesting to stress the mechanistic O-O bond formation change of catalyst **2** in homogenous phase and anchored on the GC electrode, **GC-2**, from I2M to WNA respectively due to the restricted translation mobility of the latter. This mechanistic change has been proposed earlier but has been demonstrated here for the first time based on the FOWA analysis with different catalyst surface concentrations for **GC-2** and different concentrations for **2**. The absence of a bimolecular path at the anchored **GC-2** catalyst involves access to a path that is obviously higher in energy and produces a decrease of the activity that in addition enables deactivation pathways, ultimately leading to the formation of RuO_2 dispersed at the surface of the electrode as has been shown recently.[46]

Finally, using Ce(IV) at pH = 1.0 an apparent rate constant of 0.07 s^{-1} is obtained for $\mathbf{5}^{-}$ which implies an overpotential of 0.38 V according to equation 11 and assuming that the TOF for $\mathbf{5}^{-}$ in homogeneous phase depends on electron transfer.[47] This would be associated with a $E^{o'}$ for the Ce(IV)/Ce(III) couple of 1.55 V which falls within the 1.46-1.63 V range reported.[67-71]For complex

2 the TOF obtained at pH = 1.0 with Ce(IV) is 30 s^{-1} [45] which compares well with the TOF_{MAX} = 11 s^{-1} value obtained by FOWA assuming also η = 0.38 V at [**2**] = 0.2 mM. However a direct comparison cannot be made since in homogeneous phase at this concentration range the rds depends on both the k_D and k_{O2}, but is independent on Ce(IV).

It is also worth realizing that TOF values are highly dependent on the η and thus the goodness of a catalyst cannot be judged with a single chemical oxidant. For instance in the case of catalysts **2** and $\mathbf{5}^-$, the former is better at low η and the latter at high η.

F 4 Conclusions

In conclusion, we have adapted the electrochemical methodology of the foot of the wave analysis (FOWA) to electrochemical water oxidation. That allows calculating catalytic water oxidation apparent rate constants in a very simple and reliable manner. These equations also allow elucidating the first or second order catalyst dependence on the electrocatalytic peak current at the foot of the wave that is directly related to the O-O bond formation step in the case where this step is the rds. In these cases this allows distinguishing between WNA and I2M type of mechanisms. Finally, the catalytic Tafel plots are used for easily and graphically comparing WOCs under identical conditions and thus are valuable for choosing the right catalyst for a specific application.

V

F 5 Acknowledgements

R.M. thanks “La Caixa” foundation for a PhD grant. A.L. thanks MINECO (CTQ-2013-49075-R, SEV-2013-0319; CTQ-2014-52974-REDC; ENE2014-52280-REDT) and “La Caixa” foundation for financial support. X.S. thanks MINECO/FEDER for financial support (CTQ2015-64261-R). F.M. thanks the DFG (Me 1313/9-1 in the ERA Chemistry framework and SFB 1073, project C01) for financial support, and S.N. thanks the international PhD program *CaSuS* (Catalysis for Sustainable Synthesis) for a PhD fellowship. FEDER and European COST actions, CM1202 and CM1205 are also gratefully acknowledged.

F 6 References

1 N. S. Lewis and D. G. Nocera, *Proc. Natl. Acad. Sci. USA*, **2006**, *103*, 15729-15735.

2 C.-J. Zhong, J. Luo, P. N. Njoki, D. Mott, B. Wanjala, R. Loukrakpam, S. Lim, L. Wang, B. Fang and Z. Xu, *Energy Environ. Sci.* **2008**, *1*, 454-466.

3 N. S. Lewis, *Science* **2016**, *351*, 353.

4 J. Marshall, *Nature,* **2014**, *510,* 22-24.

5 F. Rappaport, M. Guergova-Kuras, P. J. Nixon, B. A. Diner and J. Lavergne, *Biochemistry*, **2002**, *41*, 8518-8527.
6 J. R. McKone, N. S. Lewis and H. B. Gray, *Chem. Mater.* **2014**, *26*, 407-414.
7 J. Luo, J.-H. Im, M. T. Mayer, M. Schreier, M. K. Nazeeruddin, N.-G. Park, S. D. Tilley, H. J. Fan and M. Grätzel, *Science*, **2014**, *345*, 1593-1596.
8 M. Suga, F. Akita, K. Hirata, G. Ueno, H. Murakami, Y. Nakajima, T. Shimizu, K. Yamashita, M. Yamamoto, H. Ago and J.-R. Shen, *Nature*, **2015**, *517*, 99-103.
9 J. J. Concepcion, R. L. House, J. M. Papanikolas and T. J. Meyer, *Proc. Natl. Acad. Sci. USA*, **2012**, *109*, 15560-15564.
10 B. Kumar, M. Llorente, J. Froehlich, T. Dang, A. Sathrum and C. P. Kubiak, *Annu. Rev. Phys. Chem.* **2012**, *63*, 541-569.
11 F.-F. Li and S. Licht, *Inorg. Chem*. **2014**, *53*, 10042–10044.
12 Molecular Water Oxidation Catalysis: A Key Topic for New Sustainable Energy Conversion Schemes. **2014** Edited by A. Llobet. John Wiley and Sons Ltd.
13 L. Francas, X. Sala, E. Escudero-Adan, J. Benet-Buchholz, L. Escriche and A. Llobet, Inorg. Chem. **2011**, *50*, 2271-2781.
14 D. Hong, S. Mandal, Y. Yamada, Y.-M. Lee, W. Nam, A. Llobet and S. Fukuzumi, Inorg. Chem. **2013**, *52*, 9522-9531.
15 A. Singh and L. Spiccia, Coord. Chem. Rev. **2013**, *257*, 2607-2622.
16 A. Coehn, M. Gläser, *Z. Anorg. Chem.* **1902**, *33*, 9-24.
17 A.C.C. Tseung and S. Jasem, *Electrochim. Acta*, **1977**, *22*, 31-34.
18 Y. Matsumoto, E. Sato, *Electrochim. Acta*, **1979**, *24*, 421-423.
19 A. Harriman, I. J. Pickering, J. M. Thomas and P. A. Christensen, *J. Chem. Soc. Faraday Trans.* **1988**, *84*, 2795-2806.
20 C. C. L. McCrory, S. Jung, J. C. Peters and T. F. Jaramillo, *J. Am. Chem. Soc.* **2013**, *135*, 16977-16987.
21 C. C. L. McCrory, S. Jung, I. M. Ferrer, S. M. Chatman, J. C. Peters and T. F. Jaramillo, *J. Am. Chem. Soc.* **2015**, *137*, 4347-4357.
22 S. Jung, C. C. L. McCrory, I. M. Ferrer, J. C. Peters, T. F. Jaramillo, *J. Mater. Chem. A*, **2016**, *4*, 3068-3076.
23 C. Sens, I. Romero, M. Rodriguez, A. Llobet, T. Parella and J. Benet-Buchholz, *J. Am. Chem. Soc*, **2004**, *126*, 7798-7799.
24 R. Zong and R. P. Thummel, *J. Am. Chem. Soc.* **2005**, *127,* 12802-12803.
25 J. J. Concepcion, J. W. Jurss, J. L. Templeton and T. J. Meyer, *J. Am. Chem. Soc.* **2008**, *130,* 16462-16463.
26 H. Lv, J. Song, Y. V. Geletii, J. W. Vickers, J. M. Sumliner, D. G. Musaev, P. Kögerler, P. F. Zhuk, J. Bacsa, G. Zhu and C. L. Hill, *J. Am. Chem. Soc.* **2014**, *136*, 9268-9271.
27 L. Duan, A. Fischer, Y. Xu and L. Sun, *J. Am. Chem. Soc.* **2009**, *131*, 10397-10399.
28 P. Garrido-Barros, I. Funes-Ardoiz, S. Drouet, J. Benet-Buchholz, F. Maseras and A. Llobet, *J. Am. Chem. Soc.* **2015**, *137*, 6758-6761.
29 S. M. Barnett, K. I. Goldberg and J. M. Mayer, *Nat. Chem.* **2012**, *4*, 498-502.

V

30 D. E. Polyansky, J. T. Muckerman, J. Rochford, R. Zong, R. P. Thummel and E. Fujita, *J. Am. Chem. Soc.* **2011**, *133*, 14649-14665.
31 E. S. Rountree, B. D. McCarthy, T. T. Eisenhart and J. L. Dempsey, *Inorg. Chem.* **2014,** *53*, 9983-10002.
32 N. Song, J. J. Concepcion, R. A. Binstead, J. A. Rudd, A. K. Vannucci, C. J. Dares, M. K. Coggins and T. J. Meyer, *Proc. Natl. Acad. Sci. USA*, **2015,** *112*, 4935-4940.
33 R. S. Nicholson, I. Shain, *Anal. Chem*. **1964,** *36*, 706-723.
34 Electrochemical Methods, Fundamentals and Applications. Allen J. Bard and Larry R. Faulkner, John. Wiley & Sons, Inc. 2nd Ed, New York, NY, 2001. See Chapter 12, section 3.5.
35 C. Costentin, S. Drouet, M. Robert and J.-M. Savéant, *J. Am. Chem. Soc.* **2012**, *134*, 11235-11242.
36 C. Costentin, S. Drouet, M. Robert and J.-M. Savéant, *Science*, **2012**, *338*, 90-94.
37 V. Artero and J.-M. Saveant, *Energy Environ. Sci.* **2014**, *7*, 3808-3814.
38 C. Costentin and J.-M. Savéant, *ChemElectroChem*, **2014**, *1*, 1226-1236.
39 C. Costentin, H. Dridi, J.-M. Savéant, *J. Am. Chem. Soc.* **2014**, *136*, 13727-13734.
40 C. Costentin, G. Passard and J.-M. Savéant, *J. Am. Chem. Soc.* **2015**, *137*, 5461-5467.
41 Elements of Molecular and Biomolecular Electrochemistry: An Electrochemical Approach to Electron Transfer Chemistry, J.-M. Savéant, John. John Wiley & Sons, Inc. Hoboken, New Jersey, 2006.
42 D. J. Wasylenko, C. Rodríguez, M. L. Pegis and J. M. Mayer, *J. Am. Chem. Soc.* **2014**, *136*, 12544-12547.
43 L. Vigara, M. Z. Ertem, N. Planas, F. Bozoglian, N. Leidel, H. Dau, M. Haumann, L. Gagliardi, C. J. Cramer and A. Llobet, *Chem. Sci.* **2012**, *3*, 2576-2586.
44 R. Matheu, M. Z. Ertem, J. Benet-Buchholz, E. Coronado, V. S. Batista, X. Sala and A. Llobet, *J. Am. Chem. Soc.* **2015**, *137*, 10786-10795.
45 L. Duan, F. Bozoglian, S. Mandal, B. Stewart, T. Privalov, A. Llobet and L. Sun, *Nat. Chem.* **2012**, *4*, 418-423.
46 R. Matheu, L. Francàs, P. Chernev, M. Z. Ertem, V. Batista, M. Haumann, X. Sala and A. Llobet, *ACS Catal.* **2015**, *5*, 3422-3429.
47 S. Neudeck, S. Maji, I. Lopez, S. Meyer, F. Meyer and A. Llobet, *J. Am. Chem. Soc.* **2014**, *136*, 24-27.
48 X. Sala, S. Maji, R. Bofill, J. Garcia-Anton, L. Escriche and A. Llobet, *Acc. Chem. Res.* **2014**, *47*, 504-516.
49 D. J. Wasylenko, C. Ganesamoorthy, M. A. Henderson, B. D. Koivisto, H. D. Osthoff and C. P. Berlinguette, *J. Am. Chem. Soc.* **2010**, *132*, 16094–16106.
50 S. Maji, L. Vigara, F. Cottone, F. Bozoglian, J. Benet-Buchholz and A. Llobet, *Angew. Chem. Int. Ed.* **2012**, *51*, 5967-5970.
51 S. Roeser, P. Farras, F. Bozoglian,M. Martinez-Belmonte, J. Benet-Buchholz and A. Llobet, *Chem.Sus. Chem*. **2011**, *4*, 197-197.
52 S. Romain, F. Bozoglian, X. Sala, A. Llobet, *J. Am. Chem. Soc*. **2009**, *131*, 2768-2769.
53 Neudeck, S.; Maji, S.; Lopez, I.; Dechert, S.; Benet-Buchholz, J.; Llobet, A.; Meyer, F. *Inorg. Chem.* **2016**, *55*, 2508-2521.

V

54 Berardi, S.; Francas, L.; Neudeck, S.; Maji, S.; Benet-Buchholz, J.; Meyer, F.; Llobet, A. *ChemSusChem* **2015**, *8*, 3688-3696.
55 See page 23 in the supporting information of C. Costentin and J. M. Saveant, *Chem.ElectroChem*, **2014**, *1*, 1226-1236.
56 For the mathematical simulations between 50 and 100 points are systematically used with R factors higher than 0.97.
57 D. Belanger and J. Pinson, *Chem. Soc. Rev.* **2011**, *40*, 3995-4048.
58 F. Li, B. Zhang, X. Li, Y. Jiang, L. Chen, Y. Li and L. Sun, *Angew. Chem. Int. Ed.* **2011**, *123*, 12484-12487.
59 The Tafel equation celebrated the 100th anniversary in 2005. See Ref. 59
60 J. Tafel, K. Schmitz, K. Naremann and B. Emmert: Z. *Phys. Chem*. **1905**, *50*, 713–752.
61 C. Costentin, G. Passard, J.-M. Savéant, *J. Am. Chem. Soc.* **2015**, *137*, 5461-5467.
62 V. Artero, J.-M. Saveant, *Energy Environ. Sci.* **2014**, *7*, 3808-3814.
63 N. Guijarro, M. S. Prevot and K. Sivula, *Phys. Chem. Chem. Phys.* **2015**, *17*, 15655-15674.
64 Y. Ma, S. R. Pendlebury, A. Reynal, F. Le Formal and J. R. Durrant, *Chem. Sci.* **2014**, *5*, 2964-2973.
65 C. J. Richmond, R. Matheu, A. Poater, L. Falivene, J. Benet-Buchholz, X. Sala, L. Cavallo and A. Llobet, *Chem. Eur. J.* **2014**, *20*, 17282-17286.
66 L. Wang, L. Duan, Y. Wang, M. S. G. Ahlquist and L. Sun, *Chem. Commun.* **2014**, *50*, 12947-12950.
67 The standard potential of the Ce(IV/III) couple is highly sensitive to pH, ionic strength, anion nature etc. See references: 59-62.
68 V. Nair, A. Deepthi, *Chem. Rev.* **2007**, *107*, 1862-1891.
69 S. A. Hayes, P. Yu, T. J. O'Keefe, M. J. O'Keefe and J. O. Stoffer *J. Electrochem. Soc.* **2002**, *149*, 623-630.
70 P. Yu, T. J. O'Keefe, *J. Electrochem. Soc.* **2006**, *153*, 80-85.
71 T. N. Bondareva, A. G. Stromberg, *Zh. Obsh. Khim*. **1955**, *25*, 639-642.

V

F 7 Supporting information

Paper F : Foot of the Wave Analysis for Mechanistic Elucidation and Benchmarking Applications in Molecular Water Oxidation Catalysis

Outline

Materials

All materials were provided by Sigma-Aldrich unless indicated. Ligands [2,2'-bipyridine]-6,6'-dicarboxylate (H_2bda),[2,2':6',2''-terpyridine]-6,6''-dicarboxylate (H_2tda) and 3,5-bis([2,2'-bipyridin]-6-yl)-4-methylpyrazol-1-ide (Mebpp) were synthesized according to literature procedures.[S1-S3] Complexes [Ru(bda)(4-Me-py)$_2$], [Ru(tda)(py)$_2$], {Na_3[Ru(OH)(4-SO_3-py)$_2$]$_2$(μ-Mebbp)} and {[Ru(NO)(bda)(PyPh-N_2)$_2$][PF_6]$_3$} (where PyPh-N_2 is 4-(pyridin-4-yl)benzenediazonium) were prepared and purified as reported.[S1, S4-S6] All the reagents, materials and procedures for the preparation of **GC-2** were carried out as described in the literature.[S6] High-purity deionized water was obtained by passing distilled water through a nanopure Milli-Q water purification system.

Preparation of solutions used in this work.

a) A pH = 1.0 triflic acidic solution with 0.1M ionic strenght. A sample of neat triflic acid (10 g, 0.0663 mols) was diluted with 662 mL of deionised water.

b) A pH = 7.0 phospahte buffered solution with 0.1M ionic strenght. A sample of NaH_2PO4 (2.31 g, 0.0193 M) and Na_2HPO_4 (3.77 g, 0.0266 M) were dissolved in deionised water up to 1 L.

c) A pH = 12.0 phosphate buffer soltion with 0.1M ionic strenght. A sample of Na_2HPO_4 (10.293 g, 0.0073 M) and Na_3PO_4 (2.06 g, 0.0126 M) were dissolved with deionised water up to 1 L.

d) A tetrabutylammonium hexafluorophosphate (TBAH) acetone solution with a 0.1 M ionic strength. A sample of TBAH (3.87 g, 0.01 mols) were dissolved in acetone up to 100 mL.

Preparation of complex solutions for electrochemical analysis

3/4 mixtures. A mixture of **3/4** (3.0 mM/1.5 mM respectively) at pH = 7.0 was prepared as described in the literature.[S4] This solution was used to prepare solutions with concentrations of **3**/**4** of 1.50 mM/0.75 mM, 0.75 mM/0.37 mM and 0.30 mM/0.15 mM by diluting with the adequate volume of the pH = 7.0 phosphate buffer solution described above.

5$^-$. A sample of complex {Na_3[Ru(OH)(4-SO_3-py)$_2$]$_2$(μ-Mebbp)·7.5 H_2O} (11.55 mg, 0.0079 mmol) was dissolved in 10 mL of a pH = 1.0 solution (0.79 mM). This solution was then used to

prepare 0.40 mM, 0.20 mM and 0.08 mM solutions of complex **5**$^{-}$ by dilution using the pH = 1.0 solution describe above.

[Ru^{III}(OH)(bda)(4-Me-py)$_2$]. Three solutions at different pHs were prepared for this complex.

Solutions at pH = 7.0. A sample of [Ru^{II}(bda)(Me-py)$_2$] (4.44 mg, 0.0084 mmol) was suspended in 8 mL of a pH = 7.0 solution. The solution was then introduced in one of the compartments of a two-compartment cell separated with a frit. The other compartment was filled with 8 mL of pH = 7.0 solution. A Pt grid was used as a working electrode, another Pt grid as a counter electrode and Hg/Hg_2SO_4 as a reference electrode. A potential of *E* = 0.70 V was applied for 15 minutes to the cell under magnetic stirring upon which the compartment with the initial complex turned from dark brown to dark green. This solution is then transferred to a volumetric flask and filled up to 10 mL with a pH = 7.0 solution, generating a 0.84 mM solution of [Ru^{III}(OH)(bda)(4-Me-py)$_2$]. Solutions of 0.47 mM, 0.25 mM and 0.12 mM were prepared by dilution with the appropriate amount of the pH = 7 phosphate buffer solution.

Solutions at pH = 12.0. At this pH a similar procedure was used as in the previous case. A sample of 5.00 mg of [Ru^{II}(bda)(Me-py)$_2$] was used to prepare a 0.94 mM pH 12.0 solution. Solutions of 0.53 mM, 0.28 mM and 0.14 mM were prepared by dilution with the appropriate amount of the pH = 12.0 phosphate buffer solution

Solution at pH = 1.0. A sample of [Ru^{II}(bda)(4-Me-py)$_2$] (1.08 mg, 0.0020 mmol), was dissolved in 10 mL of the pH = 1.0 solution generating a 0.20 mM solution of [Ru^{III}OH(bda)(Me-py)$_2$].

GC-2. A sample of complex {[Ru(NO)(bda)(PyPh-N_2)$_2$][PF_6]$_3$}, **6**, (6.7 mg, 0.0049 mmol) was dissolved in 10 mL of 0.1M TBAH acetone. This generates a 0.49 M solution of **6** in acetone. Solutions of 0.20 mM, 0.10 mM and 0.05 mM were prepared by dilution with the appropriate amount of the acetone solution. The modified glassy carbon electrodes **GC-2**, were obtained by sweeping the potential between 1.05 V and -0.15 V as indicated in the literature.[S6]

All the solutions described in this section were stored in the fridge between preparation and analysis (< 1 h).

V

Electrochemical Methods

All electrochemical measurements were performed on an IJ-Cambria CHI-620e potentiostat.

Electrodes. A glassy carbon disk was used as a working electrode (S=0.07 cm^2). The glassy carbon disk was polished with alumina 0.05 μm for 60 seconds in different directions prior to any measurement. The electrode was rinsed with abundant water and dried with N_2. A Pt disk was used as a counter electrode and Hg/Hg_2SO_4 (K_2SO_4 saturated) was used as a reference electrode. Potentials were converted to NHE by adding 0.65 V.

Cell. A 20 mL vial was used as an electrochemical cell for cyclic voltammetry (CV) and Differential Pulse Voltammetry (DPV) using a 3 electrode configuration. A Teflon lid with holes for the three electrodes was used to ensure a reproducible distance between the electrodes.

CV and DPV. In all cases iR compensation was applied at 95% of resistance for both techniques. The scan rate for cyclic voltammetry was 100 mV/s unless indicated. CV started at the Open Circuit Potential (OCP) except for the case of **GC-2** where the CV started at 0.25 V. The current intensity of all CVs was corrected by subtracting the current intensity of the blank. The DPV parameters used were: ΔE = 4 mV, Amplitude = 50 mV, Pulse width = 5 s, Sampling width = 0.0167 s, Pulse period = 5 s unless explicitly mentioned. The blank CVs were performed following exactly the same procedure.

Caution must be taken on the determination of the Ru^{V}/Ru^{IV} redox potential since it is well known that the kinetic and thermodynamic parameters of the electron transfer (k^o, E^o, and α, if the Butler-Volmer kinetics are assumed) and those of the chemical reaction are coupled to each other in an intricate manner (see glossary of symbols in Chart S1). As a result, the position of the current peak in DPV is a function of all the parameters mentioned above and can be different from true E^o needed for application of FOWA.

Foot of the Wave Analysis (FOWA)

i_p, $E^{0,ap}$ and Γ^0_{cat} determination

a) i_p was estimated from the peak current intensity of the Ru^{III}/Ru^{II} or the $Ru^{III}Ru^{II}/Ru^{III}Ru^{II}$ wave for mononuclear and dinuclear complexes respectively. The anodic wave was used for $\mathbf{5}^-$ and for the **GC-2**. The cathodic wave was used for **2** and **3/4** mixtures.

b) $E^{0,ap}$ was extracted from DPV. Three replicates were used to determine the $E^{0,ap}$ for each complex.

c) The superficial concentration Γ^0_{cat} (nmol/cm^2) of **GC-2** was estimated by integrating the charge under the III/II wave in a CV of **GC-2** at pH = 7.0 and using equation S1.

$$\Gamma^0_{cat} = \frac{Q_{Ru}}{n \cdot S \cdot F} \qquad \text{(S1)}$$

where, Q_{Ru} is the charge integrated under the wave, *n* is the number of electrons involved in the electron transfer event, S is the electrode surface and F is the Faradaic constant.

k_{WNA} and k_D determination

The apparent kinetic constants (k_{WNA} and k_D) were extracted from the linear fit at the foot of the wave of the i/i_p *vs*. $[1+e((E^{0,ap}-E)\cdot(F/RT))]$ plot assuming a WNA mechanism or i/i_p *vs*. $[(1+e((E^{0,ap}-E)\cdot(F/RT)))^{3/2}]$ plot assuming a I2M mechanism. Five CV replicates were performed and the kinetic constant reported is the average of the constants obtained in each case. The standard deviation of the measurement was calculated based on these five measurements. The linear fit considered the best slope (R > 0.985) that contained a range of 50-100 data points. For the analysis of **GC-2**, three CVs were averaged to extract the kinetic constant.

In all cases the first cycle of the CV was used for FOWA except for **GC-2** where the second cycle was used.

Catalytic Tafel plots

The catalytic Tafel plots were drawn by applying equations 33-35 in table S1. In the case of I2M mechanism the expression of TOF is dependent on the concentration. A value of 0.2 mM was used for **2**.

Mathematical derivation for the estimation of k_{WNA}, k_D and TOF

The mathematical equations derived for the FOWA methodology were based on a kinetic treatment for the electrocatalytic process that involves an electron transfer reaction (ET) followed by a chemical reaction (CR). The ET is defined by the standard potential of the redox couple, E^o, and the CR by its apparent rate that will be labeled k_{WNA} and k_D for the WNA and I2M mechanism respectively. A glossary of all the symbols used for the mathematical treatment is presented in Chart S1. Here we describe the FOWA methodology applied for the water oxidation reactions, following the same methodology described earlier by Saveant et al. [S7] The WNA expression for water oxidation is easily readapted from the H^+ reduction reaction (see equation S5 for the main difference). On the other hand although homolytic schemes for H^+ reduction have been reported before,[S7] the general scheme for the H_2 evolution reaction is different from the I2M general scheme for water oxidation (see table S2 for the comparison of the two general reaction schemes) and thus new equations are needed.

V

Homogenous phase

In homogeneous phase the P and Q species represent the highly oxidized Ru center in their formal oxidation state IV and V respectively. The first step is common to both mechanisms (P - $1e^-$ -> Q) whereas the next step, the CR, is first order in [Ru] for the WNA mechanism and second order for the I2M mechanism. The reaction scheme considers that the catalytic reactions that generate dioxygen (equation S2) are fast, irreversible and with no side phenomena. The consideration is consistent with a scenario where the reaction and diffusion of P and Q have similar rates and therefore a steady-state situation is assumed. The P and Q species are confined in a diffusion-reaction layer that is much thinner than the typical diffusion layer. [S7] The profile of these species in a diffusion-reaction layer, in particular the concentration of Q profile (C_Q), can be derived from the mathematical resolution of the differential equation of the diffusion-reaction layer. This consists of a diffusion term governed by the Fick Law (equation S5) and a kinetic term governed by the reaction scheme. Table S1 presents a summary of the differential equations for the WNA and the I2M mechanisms together with the mathematical resolution of the C_Q profile (see equations S20-S21 for the differential equations and equations S25-S26 for the resolution of the C_Q functions). The obtained C_Q profile comprises the concentration of Q at the electrode surface ($(C_Q)_{x=0,}$ equation S6) which is a function of the potential and can be derived from the Nernst equation (equations S3) and the mass balance equation (equation S4).

$$2\,H_2O \rightarrow O_2 + 4H^+ + 4e^- \quad \text{(S2)}$$

$$e^{(E^0-E)F/RT} = \frac{(C_P)_{x=0}}{(C_Q)_{x=0}} \quad \text{(S3)}$$

$$(C_Q)_{x=0} + (C_P)_{x=0} = C^0_{Cat} \quad \text{(S4)}$$

The C_Q profile is then included into equation S5 which represents a dependence of the catalytic current on the concentration of Q according to Fick's first law, see equations S5 and S6. The expressions for the catalytic current for the WNA and I2M mechanisms are summarized in table S1, equations S27 and S28, and they will be used to determine both the FOWA expressions and TOF-η relationship. m is the number of electrons transferred to a single molecule in a single turn over. In the WNA case m = 4 as all the electron transfers occur at the same molecule and m=2 in the I2M as the four electron transfer occur in two centers.

$$\frac{i}{m \cdot F\,S} = -D\left(\frac{\partial C_Q}{\partial x}\right)_{x=0} \quad \text{(S5)}$$

$$(C_Q)_{x=0} = \frac{C^0_{Cat}}{1+e^{(E^0-E)F/RT}} \quad \text{(S6)}$$

Normalizing i by the peak current intensity in the absence of catalysis, i_p, (equation S7) in the Randles-Sevcik equation yields the FOWA equations for the WNA and I2M reaction schemes, see equations S30 and S31 in table S1.

$$i_p = 0.446 \cdot F \cdot S \cdot C^0_{Cat} \cdot \sqrt{\left(\frac{F \cdot \nu \cdot D}{R \cdot T}\right)} \quad \text{(S7)}$$

Further, the C_Q profile in the reaction-diffusion layer and the catalytic formula allow obtaining the mathematical relationship between turnover frequency (TOF) and overpotential (η) which that are presented as equations S33 and S34 in Table S1. These equations were derived by relating the amount of O_2 produced ($N_{product}$) and the amount of Q in the diffusion-reaction ($N_{active\ cat}$) both at a certain time t as shown in equations S8, S9 and S10. In equation S9 the number of transferred electrons is 4 as the water oxidation reaction regardless of the considered mechanism. Finally the equations for the TOF_{MAX} are also reported for both mechanism in equations S36 and S37. The TOF_{MAX} is a particular case, where the TOF is calculated for potentials much higher than the corresponding E^o.

$$\mathrm{TOF} = \frac{N_{product}}{N_{active\ cat}} \cdot \frac{1}{t} \quad \text{(S8)}$$

$$N_{product} = \frac{i}{4F} \cdot t \quad \text{(S9)}$$

$$N_{active\ cat} = S\left[\int_0^{\infty} C_Q dx\right]_{E \to +\infty} \quad \text{(S10)}$$

Heterogeneous phase

In heterogeneous phase the molecular catalyst is anchored at the surface of an electrode with no translational mobility. Under these conditions the catalyst does not diffuse to the bulk solution and thus greatly simplifies the mathematical treatment. The catalyst concentration at the surface of the electrode is calculated from equation S11, and will be termed "het-P" and "het-Q" for species P and Q anchored on the surface of the electrode respectively.

V

For the WNA mechanism in heterogeneous phase (het-WNA) the catalytic scheme is very similar to that in the homogeneous phase where the concentrations of P and Q are replaced respectively by het-P and het-Q and whose concentration is governed by the adapted Nernst equation S12.

$$\Gamma\left(\frac{\mathrm{mol}}{\mathrm{cm}^2}\right) = \frac{Q_{Ru}}{n \cdot S \cdot F} \quad \text{(S11)}$$

$$\Gamma_Q = \frac{\Gamma^0_{cat}}{1 + e^{(E^0 - E)F/RT}} \quad \text{(S12)}$$

In this case the current intensity (*i*), is only dependent on the apparent rate of reaction (k_{WNA}) and the diffusion of the substrate and the product (H_2O, O_2) between the electrode and the bulk solution. Here it is assumed that the gradient of both H_2O and O_2 are constant as well as the bulk concentration of the substrate (H_2O). This generates equation S29 in table S1 where the catalytic current depends only on the surface coverage of Q and k_{WNA}.

Analogously to the homogeneous case, the FOWA formula for the het-WNA can be obtained by applying the Nernst equation and dividing by the moles of electrons associated with a 1 electron transfer process of the immobilized catalyst Q_{Ru}, (equation S32 in Table S1).

Further, the TOF-η and the TOF_{MAX} equations 35 and 38 are obtained applying equations S14, S15 and S16 similarly to the homogeneous case.

$$C_{O_2}^0 = \frac{k_{WNA} \cdot \Gamma_{cat}^0}{1+e^{(E^{0,ap}-E)F/RT}} \cdot \frac{S}{V} \cdot t \quad \text{(S14)}$$

$$N_{active\ cat} = \Gamma_{cat}^0 \cdot S \quad \text{(S15)}$$

$$N_{product} = C_{O_2}^0 \cdot V = \frac{k_{WNA}}{1+e^{(E^0-E)F/RT}} \cdot S \cdot t \quad \text{(S16)}$$

V

Chart S1: Glossary of symbols used in this work.

i	CV current intensity	C_Q, C_P	Concentration profile of P and Q species as a function of x
i_p	Peak current intensity	C_{Cat}^0 *or* [Ru]	Initial bulk concentration of catalyst
n	Number of electrons transferred at the electron transfer	$C_{O_2}^0$, $C_{H_2O}^0$	Bulk concentration of Oxygen and Water
m	Number of electrons transferred per catalyst molecule in a single turn over.	$(C_Q)_{x=0'}(C_Q)_{x=0}$	Concentration of Q and P at the surface of the electrode
T	Temperature	Γ_P, Γ_Q	Surface concentration of P and Q species
R	Gas constant	Γ_{cat}^0	Initial surface concentration of the immobilized catalyst
F	Faradaic constant	Q_{Ru}	Moles of electrons associated with a 1 electron transfer process of the immobilized Ruthenium catalyst
S	Geometric surface of the electrode	t	Time
ν	Scan rate	TOF	Turn over frequency
D	Diffusion coefficient	$N_{product}$	Number of moles of product generated in a time t.
x	Distance from the electrode surface	$N_{activecat}$	Maximum number of moles of Q in the diffusion-reaction layer in a time t.
V	Volume		
k_1	Apparent WNA rate constant	η	Overpotential
k_{WNA}	Apparent WNA pseudo-rate constant	$E^{0,ap}$	Apparent potential for the P,Q Couple
k^o	Standard rate constant	k^o	Standard rate constant
α	Transfer coefficient	E^o	Standard potential P, Q Couple

Table S1. Summary of key equations obtained for the WNA, I2M and hetero-WNA mechanisms including TOF-η relationships and TOF_{MAX} equations.

	WNA		I2M		Hetero-WNA	
Reaction Scheme	$P \rightarrow Q + e^-$ $Q + H_2O \xrightarrow{k_1} P + O_2$	(S17)	$P \rightarrow Q + e^-$ k_D $Q + Q \rightarrow 2P$	(S18)	$het-P \rightarrow het-Q + e^-$ $het-Q + H_2O \xrightarrow{k_1} het-P + O_2$	(S19)
Differential equation in the diffusion-reaction layer	$\frac{\partial C_Q}{\partial t} = D\frac{\partial {C_Q}^2}{\partial x^2} - k_1 C_Q C_A^0$	(S20)	$\frac{\partial C_Q}{\partial t} = D\frac{\partial {C_Q}^2}{\partial x^2} - 2\cdot k_D \cdot C_Q^2$	(S21)	---	
Observed kinetic constant	$k_{WNA} = k_1 \cdot C_{H_2O}^0$	(S22)	k_D	(S23)	$k_{WNA} = k_1 \cdot C_{H_2O}^0$	(S24)
Q profile in diffusion-reaction layer	$C_Q = (C_Q)_{x=0}\, e^{-\sqrt{\frac{k_{WNA}}{D}}x}$	(S25)	$C_Q = \frac{1}{\left(\sqrt{\frac{k_D}{3\cdot D}}\cdot x + \frac{1}{\sqrt{(c_Q)_{x=0}}}\right)^2}$	(S26)	---	
Current intensity at the foot of the wave	$i = \frac{4\cdot F\cdot S\cdot C_{Cat}^0\cdot\sqrt{D\cdot k_{WNA}}}{1+e^{\left(\frac{F(E^{0,ap}-E)}{RT}\right)}}$	(S27)	$i = \frac{4\cdot S\cdot F\cdot (C_{Cat}^0)^{3/2}\sqrt{\frac{D\cdot k_D}{3}}}{\left(1+e^{\left(\frac{F(E^{0,ap}-E))}{RT}\right)}\right)^{3/2}}$	(S28)	$\frac{i}{4\cdot F\, S} = \Gamma_Q \cdot k_{WNA}$	(S29)
FOWA formula	$\frac{i}{i_p} = \frac{4\cdot 2.24\sqrt{\frac{R\cdot T}{F\cdot v}\cdot k_{WNA}}}{1+e^{\left(\frac{F(E^{0,ap}-E)}{RT}\right)}}$	(S30)	$\frac{i}{ip} = \frac{4\cdot 2.24\cdot\sqrt{\frac{R\cdot T}{3\cdot F\cdot v}\cdot k_D\cdot C_{Cat}^0}}{\left(1+e^{\left(\frac{F(E^{0,ap}-E)}{RT}\right)}\right)^{3/2}}$	(S31)	$\frac{i}{Q_{Ru}} = \frac{k_{WNA}}{1+e^{\left(\frac{F(E^{0,ap}-E)}{RT}\right)}}$	(S32)
TOF-η relationship	$TOF = \frac{k_{WNA}}{1+e^{\left(\frac{F\left(E^{0,ap}-E_{H_2O/O_2}-\eta\right)}{RT}\right)}}$	(S33)	$TOF = \frac{\frac{1}{3}\cdot k_D\cdot C_{Cat}^0}{\left(1+e^{\left(\frac{F\left(E^{0,ap}-E_{H_2O/O_2}-\eta\right)}{RT}\right)}\right)^{3/2}}$	(S34)	$TOF = \frac{k_{WNA}}{1+e^{\left(\frac{F\left(E^{0,ap}-E_{H_2O/O_2}-\eta\right)}{RT}\right)}}$	(S35)
TOF_{MAX} formula	$TOF_{MAX} = k_{WNA}$	(S36)	$TOF_{MAX} = 1/3\cdot k_D\cdot C_{Cat}^0$	(S37)	$TOF_{MAX} = k_{WNA}$	(S38)

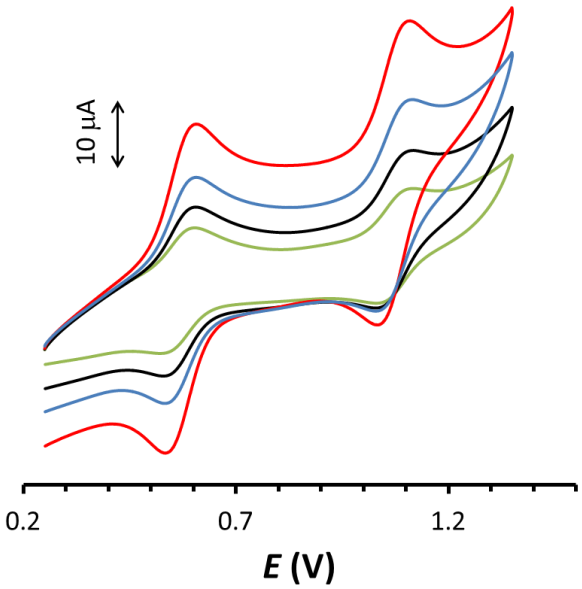

V

Figure S1: CV of complex **3** (1 mM) at pH = 7.0 at different scan rates: 50 mV/s (green), 100 mV/(black), 200 mV/s (blue) and 500 mV/s (red).

Table S2: Comparison of homolytic general Schemes for H+ reduction and water oxidation.

I2M mechanism

$$P \rightarrow Q + e^- \quad \text{(S18)}$$

$$Q + Q \xrightarrow{kD} 2P$$

$$Q + e^- \rightarrow P$$

Homolytic reaction scheme for H^+ reduction reaction[S7,S8]

$$P + A \xleftrightarrow{k1/k-1} B \quad \text{(S39)}$$

$$B + B \xrightarrow{kD} 2Q + C$$

A is a solvent molecule, C is the product and B is the intermediate generated from the reaction "P + A".

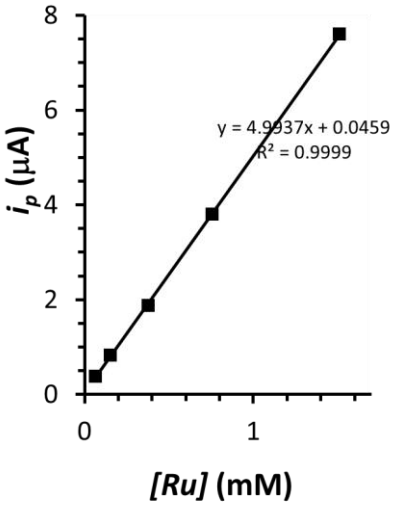

Figure S2: Peak current intensity of the cathodic Ru(III)OH/Ru(II)-OH_2 wave (i_p) of **4** against [**4**] at pH = 7.0.

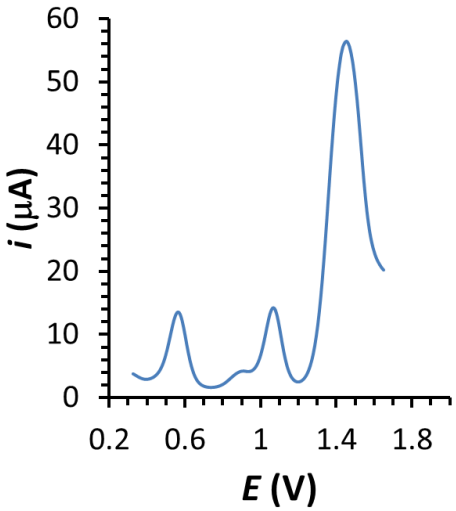

Figure S3: DPV of **3**/**4** solution mixture at pH = 7.0 (3 mM and 1.5 mM respectively).

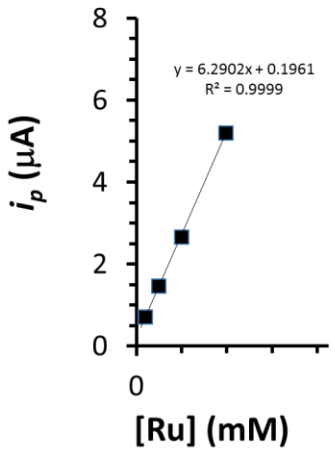

Figure S4: Peak current intensity of the anodic Ru(III)OH/Ru(II)-OH_2 wave (i_p) of **5**$^-$ against [**5**$^-$] at pH = 1.0.

V

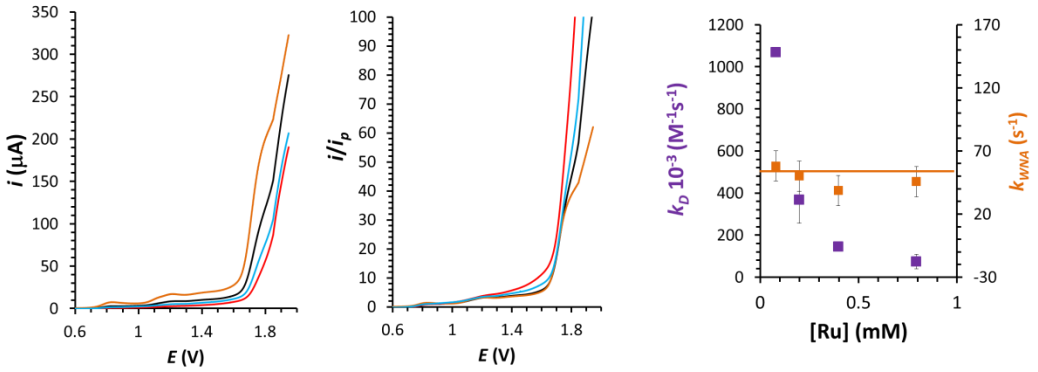

Figure S5 Left: CV of **5**$^-$ solutions at pH = 1.0 at different concentrations (0.79 mM; orange solid line, 0.4 mM; black solid line, 0.2 mM; blue solid line and 0.08 mM; red solid line). Middle: Normalised CV by i_p. Right: calculated k_D and k_{WNA} against [**5**$^-$]. The standard deviation of each point is represented with vertical lines. The orange line indicates the agreement with the WNA mechanism.

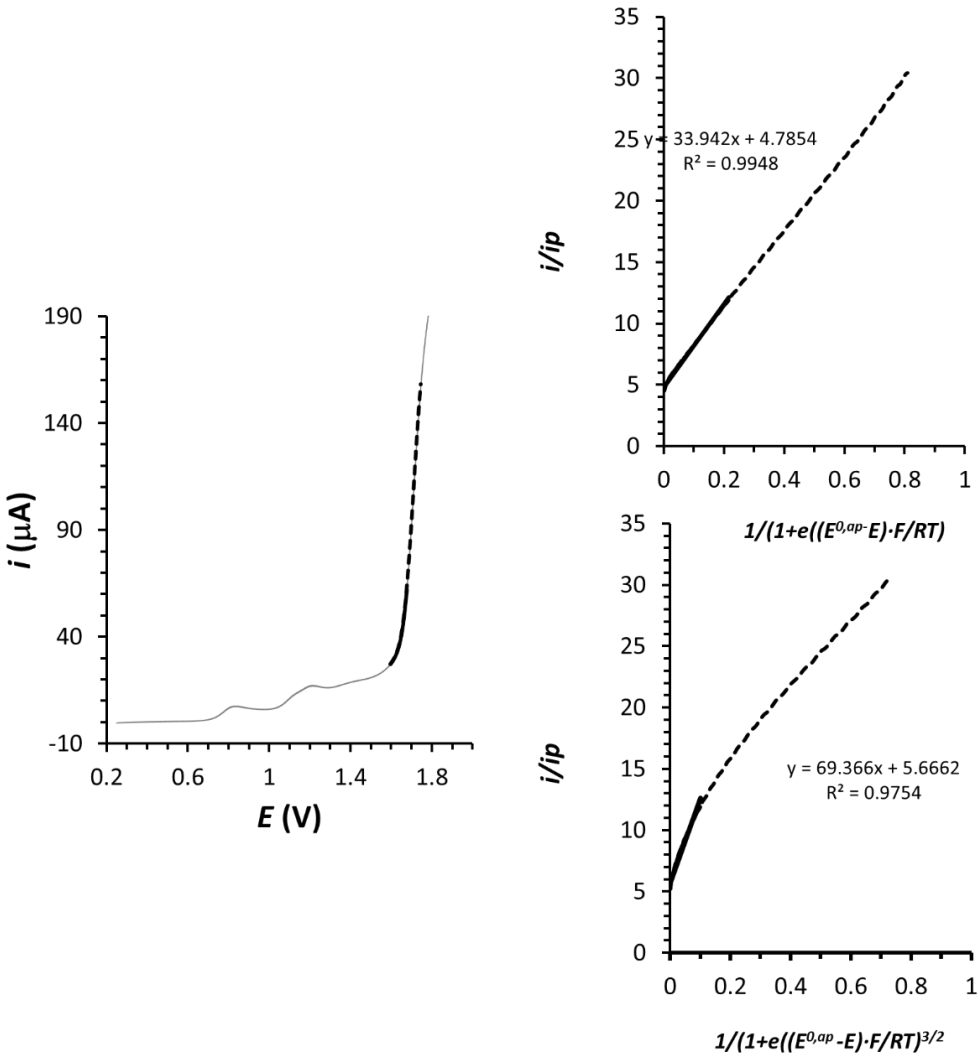

Figure S6: Left, grey solid line shows a CV of **5**$^{-}$ solution at pH = 1.0 (0.4 mM). The black dashed line indicates the data points used for the FOWA. Top right, i/i_p *vs.* $[1/(1+e((E^{0,ap}-E)(F/RT))))]$ plot assuming a WNA mechanism. Bottom right, i/i_p vs $[1/(1+e((E^{0,ap}-E)(F/RT)))^{3/2}]$ plot assuming an I2M mechanism. The fitting points for the extraction of the apparent rate constants at the foot of the wave are represented as a black solid line in the three graphs.

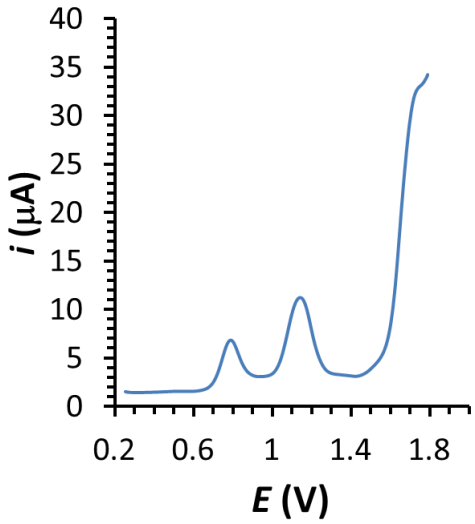

Figure S7: DPV of a $\mathbf{5}^-$ solution at pH = 1.0 (0.79 mM).

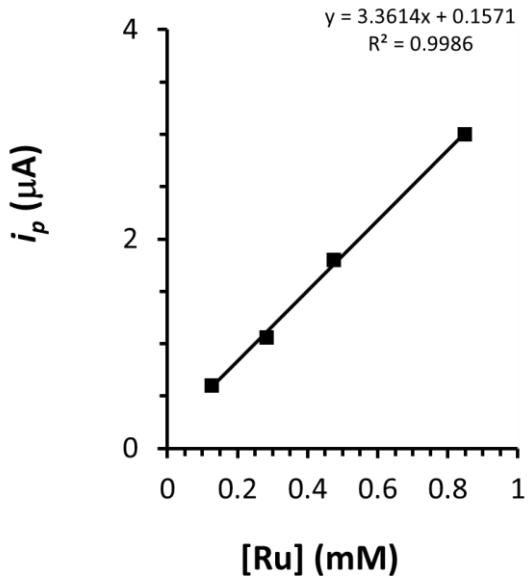

Figure S8: Peak current intensity of the cathodic Ru(III)OH/Ru(II)-OH_2 wave (i_p) of **2** against **[2]** at pH = 7.0.

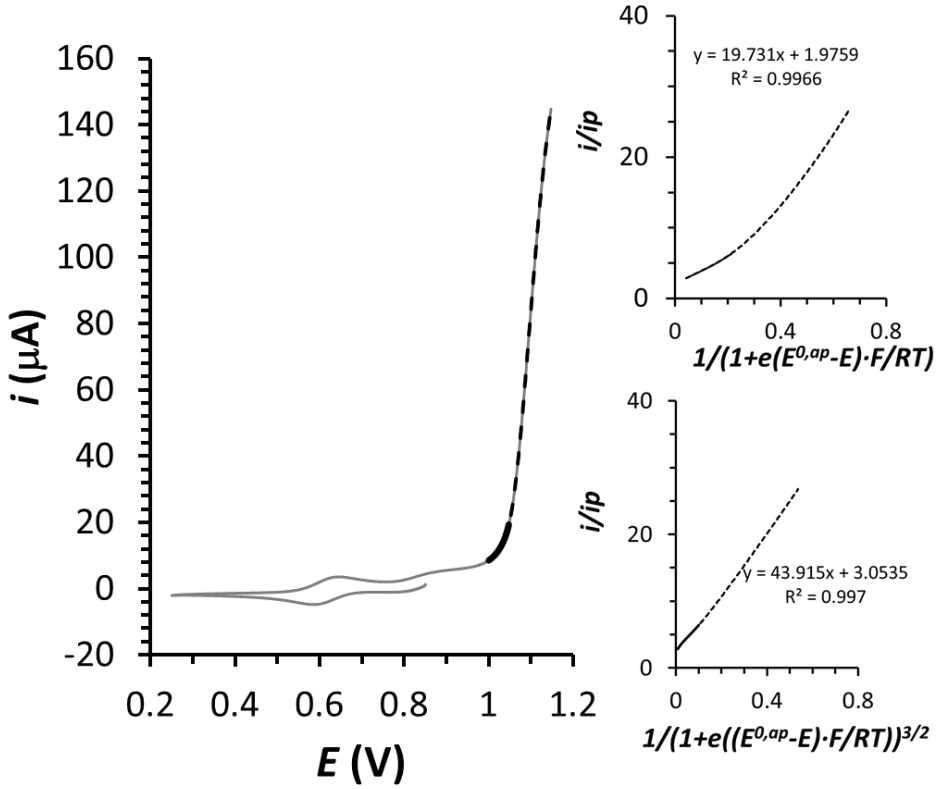

V

Figure S9: Left, grey solid line shows a CV of a **2** solution at pH = 7.0 (0.84 mM). The black dashed line indicates the data points used for the FOWA. Top right, i/i_p *vs.* $[1/(1+e((E^{0,ap}-E)(F/RT)))]$ plot assuming a WNA mechanism. Bottom right, i/i_p vs $[1/(1+e((E^{0,ap}-E)(F/RT)))^{3/2}]$ plot assuming an I2M mechanism. The fitting points for the extraction of the apparent rate constants at the foot of the wave are represented as a black solid line in the three graphs.

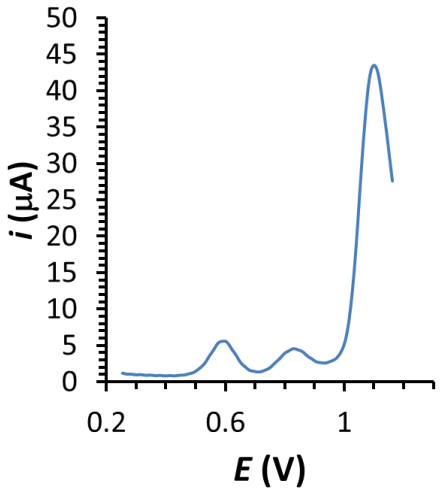

Figure S10: DPV of a **2** solution at pH = 7.0 (0.84 mM)

V

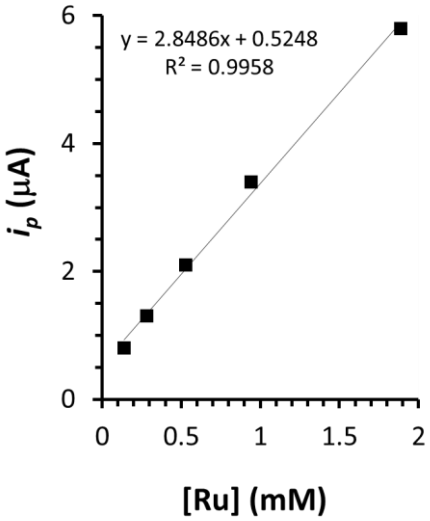

Figure 11: Peak current intensity of the cathodic Ru(III)OH/Ru(II)-OH_2 wave (i_p) of **2** against [**2**] at pH = 12.0.

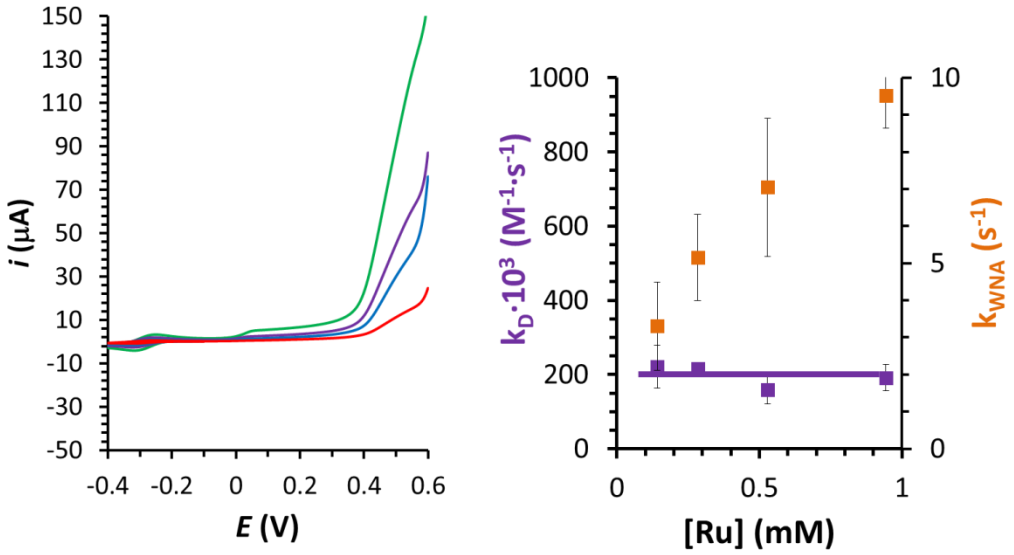

Figure S12: Left: CV of **2** solutions at pH = 12.0 at different concentrations (0.94 mM, green solid line; 0.53 mM purple solid line, 0.28 mM blue solid line and 0.14 mM red solid line). Right: Extracted k_D and k_{WNA} against [**2**] at pH = 12.0. The standard deviation of each point is represented with vertical lines

V

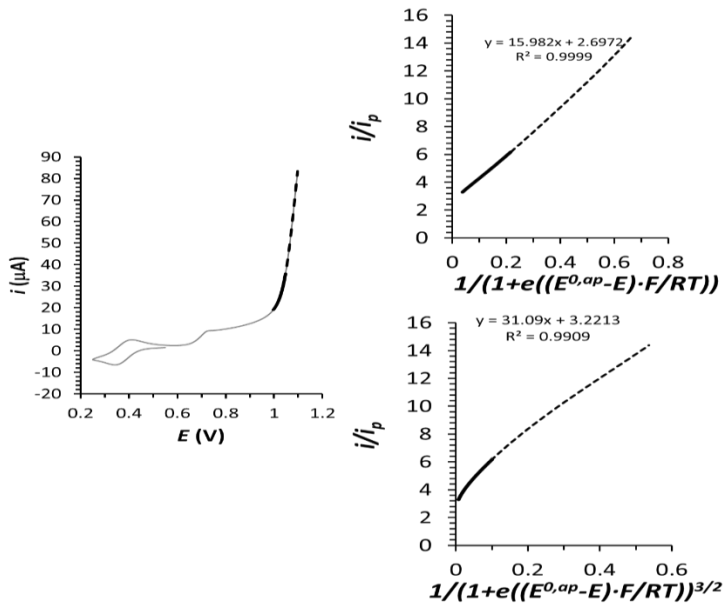

Figure S13: Left, grey solid line shows a CV of **2** solution at pH = 12.0 (1.89 mM). The black dashed line indicates the data points used for the FOWA. Top right, i/i_p *vs.* $[1/(1+e((E^{0,ap}-E)(F/RT))))]$ plot assuming a WNA mechanism. Bottom right, i/i_p vs $[1/(1+e((E^{0,ap}-E)(F/RT)))^{3/2}]$

plot assuming an I2M mechanism. The fitting points for the extraction of the apparent rate constants at the foot of the wave are represented as a black solid line in the three graphs.

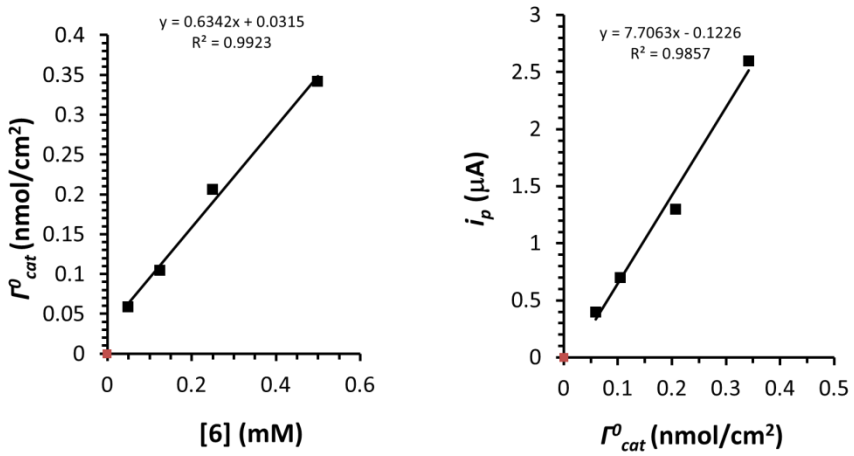

V

Figure S14: Left: Plot of the initial [**6**] used to generate **GC-2** *vs*. the obtained Γ^{0}_{cat}, nmol/cm^2. Right: Plot of peak current intensity of the anodic Ru(III)OH/Ru(II)-OH$_2$ wave of **GC-2**, i_p, in the second cycle against its Γ^{0}_{cat}.

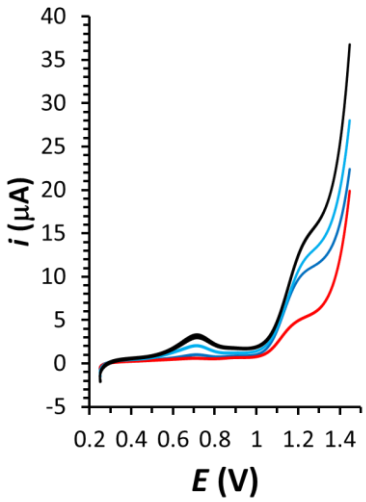

Figure S15: CV of **GC-2** at pH = 7.0 at different Γ^{0}_{cat} (0.34 nmol/cm^2; black solid line; 0.21 nmol/cm^2; light blue solid line, 0.10 nmol/cm^2; dark blue line and 0.06 nmol/cm^2; red solid line).

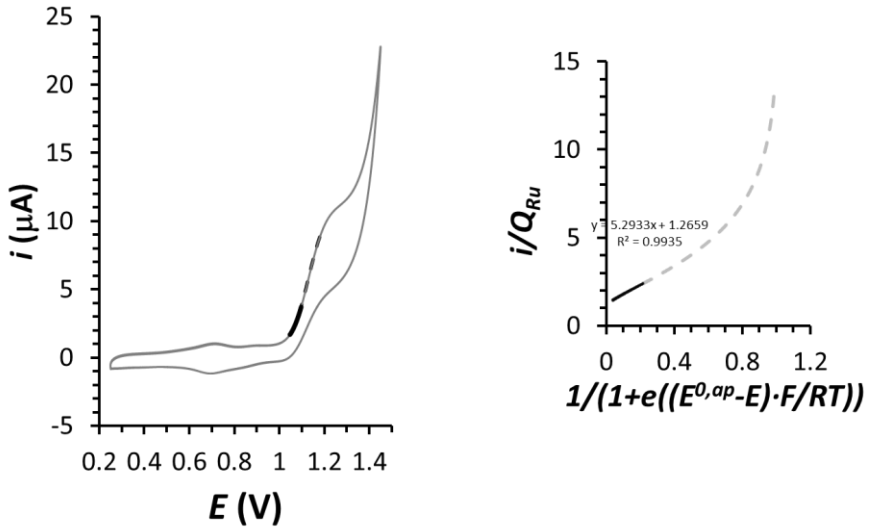

Figure S16: Left, grey solid line shows a CV of **GC-2** solution at pH = 7.0 (Γ^{0}_{cat}=0.21 nmol/cm^2). The black dashed line indicates the data points used to for the FOWA. Right, i/Q_{Ru} *vs*. [1/(1+e(($E^{0,ap}$-*E*)(*F*/*RT*)))] plot assuming a WNA. The fitting points for the extraction of the apparent rate constants at the foot of the wave are represented as a black solid line in the two graphs.

V

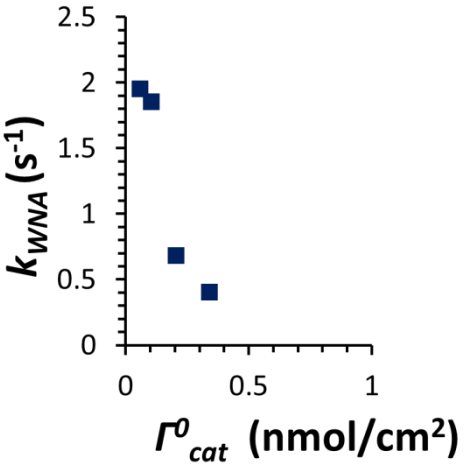

Figure S17: Calculated k_{WNA} against Γ^{0}_{cat} of **GC-2**.

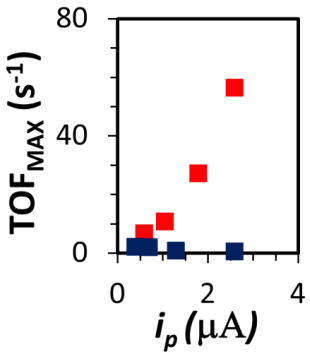

Figure S18: Plot of TOF_{MAX} for **2** (red squares) and **GC-2** (blue squares) *vs*. different i_p values.

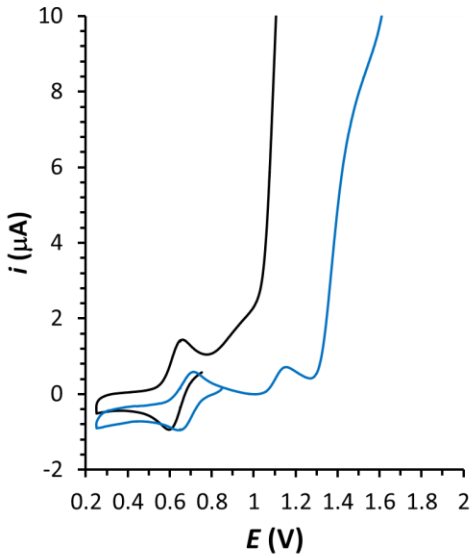

Figure S19: CV of **2** at pH = 1.0 (0.20 mM, blue solid line) and pH = 7.0 (0.20 mM, black solid line). The scan rate was 10 mV/s.

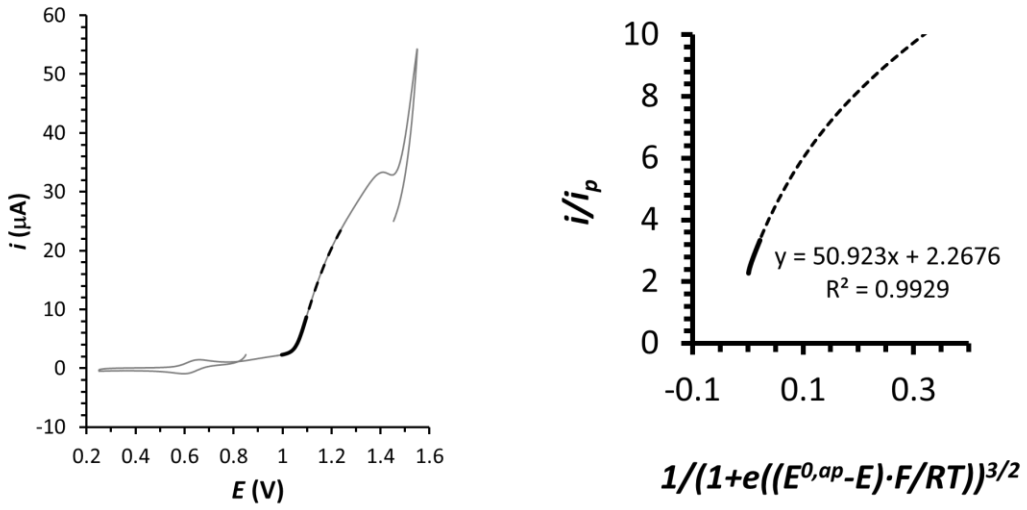

Figure S20: Left, grey solid line shows a CV of **2** solution at pH = 1.0 (**[2]**=0.20 mM). The black dashed line indicates the data points used to for the FOWA. Right, i/i_p *vs*. [1/(1+e(($E^{0,ap}$-*E*)(*F*/*RT*)))$^{3/2}$] plot assuming a I2M mechanism. The fitting points for the extraction of the apparent rate constants at the foot of the wave are represented as a black solid line in the two graphs. The scan rate was 10 mV/s.

V

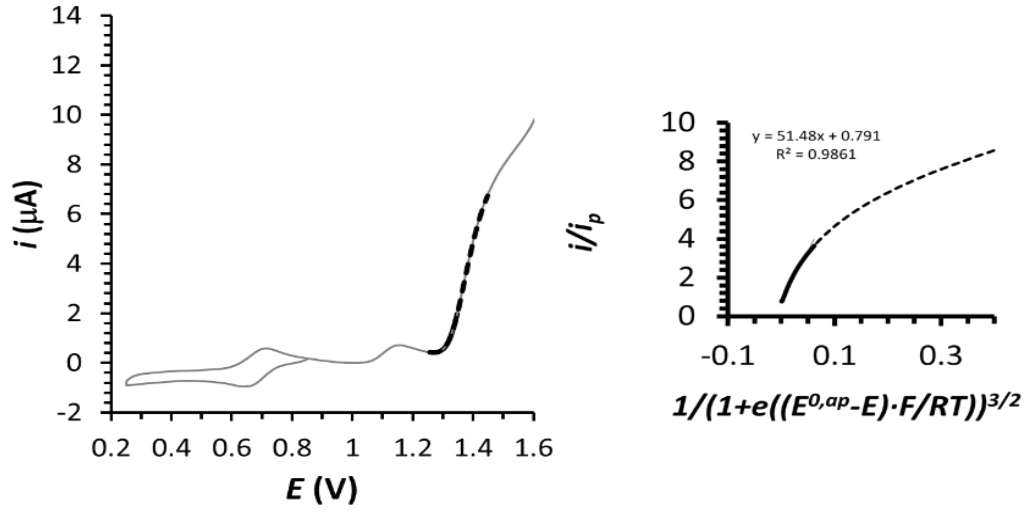

Figure S21: Left, grey solid line shows a CV of **2** solution at pH = 7.0 (**[2]** = 0.20 mM). The black dashed line indicates the data points used to for the FOWA. Right, i/i_p *vs*. [1/(1+e(($E^{0,ap}$-*E*)(*F*/*RT*)))] plot assuming a I2M. The fitting points for the extraction of the apparent rate

constants at the foot of the wave are represented as a black solid line in the two graphs. The scan rate was 10 mV/s

References

S1 L. Duan, F. Bozoglian, S. Mandal, B. Stewart, T. Privalov, A. Llobet and L. Sun, *Nat. Chem.* **2012**, *4*, 418-423.

S2 C. Galaup, J.-M. Couchet, S. Bedel, P. Tisnès, C. Picard, *J. Org. Chem.* **2005**, *70*, 2274-2284.

S3 B. Schneider, S. Demeshko, S. Neudeck, S. Dechert, F. Meyer *Inorg. Chem*. **2013***, 52*, 13230 –13237.

S4 R. Matheu, M. Z. Ertem, J. Benet-Buchholz, E. Coronado, V. S. Batista, X. Sala, A. Llobet, *J. Am. Chem. Soc.* **2015***, 137*, 10786-10795.

S5 S. Neudeck, S. Maji, I. López, S. Meyer, F. Meyer, A. Llobet, *J. Am. Chem. Soc.* **2014***, 136*, 24-27.

S6 R. Matheu, L. Francàs, P. Chernev, M. Z. Ertem, V. Batista, M. Haumann, X. Sala, A. Llobet, *ACS Catal.,* **2015***, 5,* 3422-3429.

S7 C. Costentin, J.-M. Savéant, *ChemElectroChem,* **2014***, 1*, 1226-1236.

S8 See page S24 in the supporting information of Reference S7 for the mathematic equations.

V

Chapter 6

Nature and Behaviour of molecular anodes based on Ru-bda and Ru-tda and carbon surfaces.

Molecular anodes based on the seven-coordinate Ru-bda and Ru-tda complexes on glassy carbon electrodes are prepared. The axial ligands of the Ru-bda complex are modified to introduce diazonium moieties able to generate a C-C bond with the carbon surface through electroreduction while pyrene-modified pyridine ligands are used to immobilize a Ru-tda complex on Multi-Walled Carbon Nanotubes. The performance of the two molecular anodes is assessed while the nature of the molecular catalyst is monitored by X-ray Absorption Spectroscopy and Electrochemistry. Under catalytic conditions, the molecular Ru-bda complex evolves to RuO_2 that turns to be an extremely fast heterogeneous catalyst. The bimolecular nature of the water oxidation mechanism of the Ru-bda catalyst is highlighted as the main cause of unstability under restricted mobility conditions. By contrast, the first order mechanism of the Ru-tda catalysts results in a molecular anode that maintains the molecular nature of the catalyst leading to TON values over one million.

VI

The chapter consist of the following independent papers:

PAPER G Matheu, R.; Francàs, L.; Chernev, P.; Ertem, M. Z.; Batista, V.; Haumann, M.; Sala, X.; Llobet, A. *ACS Catal.* **2015**, *5*, 3422-3429.

PAPER H Creus, J.; Matheu, R.; Peñafiel, I.; Moonshiram, D.; Blondeau, P.; Benet-Buchholz, J.; García-Antón, J.; Sala, X.; Godard, C.; Llobet, A. *Angew. Chem. Int. Ed.* **2016**, *55*, 15382-15386.

PAPER G Behavior of the Ru-bda water oxidation catalyst covalently anchored on glassy carbon electrodes.

Matheu, R.; Francàs, L.; Chernev, P.; Ertem, M. Z.; Batista, V.; Haumann, M.; Sala, X.; Llobet, A. *ACS Catal.* **2015**, *5*, 3422-3429.

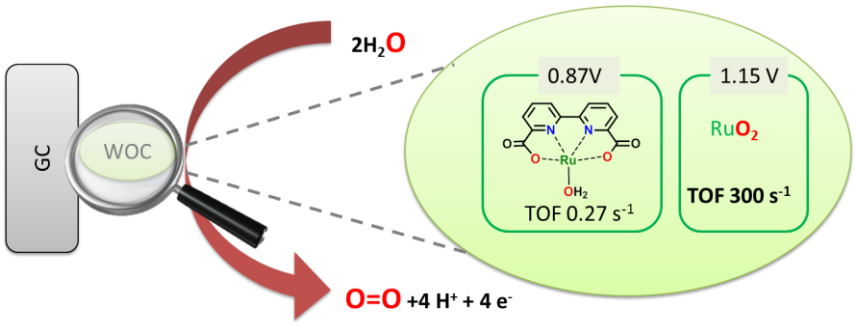

Abstract

Electrochemical reduction of the diazonium complex, $[Ru^{II}(bda)(NO)(N\text{-}N_2)_2]^{3+}$, $\mathbf{2}^{3+}$, ($N\text{-}N_2^{2+}$ is 4-(pyridin-4-yl) benzenediazonium and bda^{2-} is 2,2'-bipyridine-6,6'-dicarboxylate) in acetone produces the covalent grafting of this molecular complex onto glassy carbon (**GC**) electrodes. Multiple cycling voltammetric experiments on the GC electrode generates hybrid materials labeled as **GC-4,** with the corresponding Ru-aqua complex anchored on the graphite surface. **GC-4** has been characterized at pH = 7.0 by electrochemical techniques and XAS, and has been shown to act as an active catalyst for the oxidation of water to dioxygen. This new hybrid material has a lower catalytic performance than its counterpart in homogeneous phase and progressively decomposes to form RuO_2 at the electrode surface**.** Nevertheless the resulting metal oxide attached at the GC electrode surface, **GC-RuO$_2$**, is a very fast and rugged heterogeneous water oxidation catalyst with TOF_is of 300 s^{-1} and TONs > 45000. The observed performance is comparable to the best electrocatalysts reported so far, at neutral pH.

Contributions

Roc Matheu synthetized and characterized the new compounds, performed the electrochemical and spectroscopic analysis and prepared the manuscript.

G 1 Introduction

Catalytic water oxidation to molecular dioxygen is one of the key processes in photocatalytic cells that generate solar fuels by solar water-splitting.[1] In addition, the underlying four-electron/four-proton water oxidation is of biological interest since such reaction takes place at the oxygen-evolving Mn_4Ca complex of photosystem II in green plants and algae.[2]

Significant developments in the field of water oxidation catalysis have emerged over the last few years, including both molecular systems[3,4] and metal-oxide catalysts.[5-7] Water oxidation catalysts (WOCs) benefit from molecular toolkit that exploit electronic and steric effects, and can be efficiently combined to generate extremely fast, oxidatively rugged catalysts.[8-16] For such purpose, the effects of ligand perturbations on catalyst performance need to be fully understood, including for example changes in ligand coordination modes, hydrogen-bonding, coordination numbers, inductive effects and site isolation. Finally, molecular WOCs also benefit from an arsenal of spectroscopic techniques that can be applied to molecules and allow to derive detailed information on molecular and electronic structures. [17] In addition, anchoring WOCs on electrode surfaces is a very attractive strategy for generation of hybrid materials for heterogeneous water oxidation. [18-24]

VI

Hybrid materials are very attractive since they can provide a large degree of flexibility to build photoelectrochemical cells for water splitting. [25-27] On the other hand, recent contributions have shown that metal oxides obtained from transition metal complexes exhibit highly active water oxidation catalysis. The nature of the transition metal complex as well as the oxide formation protocol strongly influence catalytic performance. [6,28-30]

RuO_2 has long been known to be an effective electrocatalytic material for water oxidation to molecular dioxygen.[31-32]Recent work has focused on the relationship of particle size and shape with catalytic water oxidation performance, at different pHs, including catalysts immobilized on different electrode surfaces. [33-36] Here, we complement earlier studies by exploring the catalytic activation of graphite carbon electrodes by using the molecular Ru-aqua complex **GC-4** (See Scheme 1), obtained by reduction of the corresponding diazonium salt. Furthermore, we analyze the catalytic performance of these new hybrid materials with regard to water oxidation to molecular dioxygen reaction, and the fate of the Ru-complex precursor after catalytic performance.

G 2 Results

G 2.1 Preparation and Electrochemical Anchoring of $\mathbf{2}^{3+}$ into Graphitic Surfaces.

The synthetic strategy followed for the preparation of glassy carbon electrodes modified with molecular Ru-bda (bda is [2,2'-bipyridine]-6,6'-dicarboxylate) based water oxidation catalysts is presented in Scheme 1. Reaction of $[Ru(DMSO)_4Cl_2]$, bda^{2-} and 4-(pyridin-4-yl)aniline (N-NH_2) generates the diamino complex $[Ru(bda)(N\text{-}NH_2)_2]$, **1**. Treatment of **1** with nitric oxide produces the oxidation of the amino groups to the corresponding highly reactive diazonium salts together with the formation of a Ru-NO group, generating $[Ru^{II}(bda)(NO)(N\text{-}N_2)_2]^{3+}$, $\mathbf{2}^{3+}$, as can be observed in Scheme 1. Complex $\mathbf{2}^{3+}$ is then used as the starting material for the formation of hybrid materials upon electrochemical reduction of the diazonium derivatives. Complexes **1** and $\mathbf{2}^{3+}$ were characterized by the usual analytic and spectroscopic techniques including NMR spectroscopy (see SI) since both of them are diamagnetic.

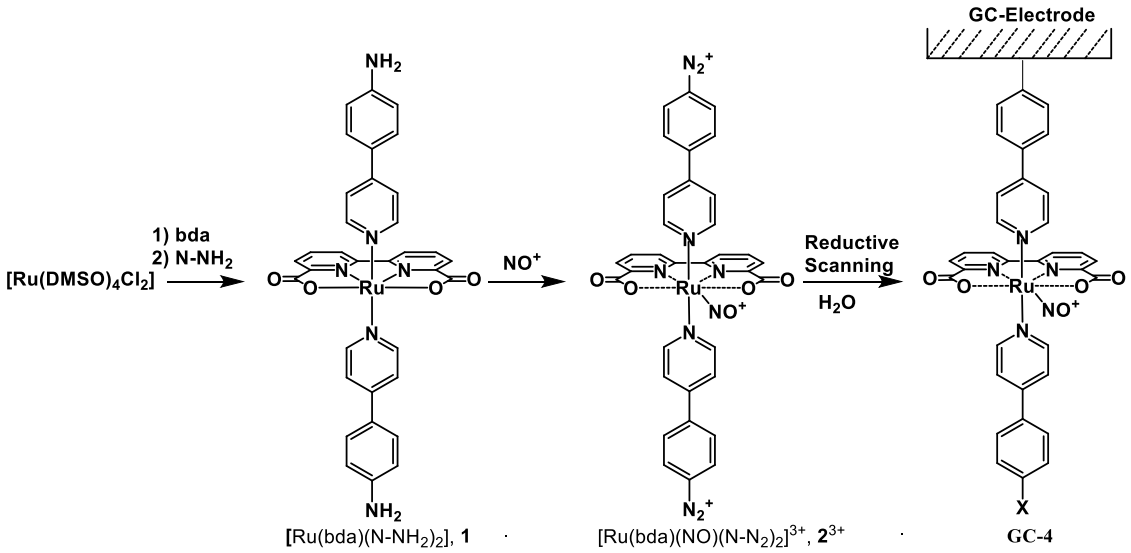

Scheme 1. Synthetic strategy used for the preparation of **GC-4** modified electrodes. Bda^{2-} is [2,2'-bipyridine]-6,6'-dicarboxylate, N-NH_2 is 4-(pyridin-4-yl)aniline and X = H and/or OH. The dashed lines at the first coordination sphere of the Ru metal center indicate bonds that are being simultaneously formed and broken.

The electrochemical properties of the complexes described in this work were investigated by means of cyclic voltammetry (CV). All the potentials are reported *vs*. SSCE unless explicitly stated otherwise. Reduction of the Ru-bda diazonium salt complex $\mathbf{2}^{3+}$ on a glassy carbon electrode in acetone generates the hybrid material **GC-4X** (where X refers to a Ru vacant site where an acetone, or an aqua ligand can coordinate). This material in turn generates the Ru-aqua complex on the surface of the electrode, **GC-4** (see Scheme 1)**,** upon several CV cycling experiments in a

neat pH 7 phosphate buffer solution, as described below. The graphitic surfaces used to anchor the Ru complex $\mathbf{3}^{2+}$ are depicted in Figure 1. Glassy carbon disks, **GC**, were used for the general evaluation of the redox properties of $\mathbf{2}^{3+}$ and its surface anchored derivatives. Glassy carbon rods, **GCr**, were used because its high surface area allows to deposit very low concentrations of the active species. Glassy carbon thin plates, **GCp**, were used for synchrotron measurements and finally reticular vitreous carbon, commonly named "carbon sponge", **GCs**, were used for bulk electrolysis experiments because of its very high surface area.

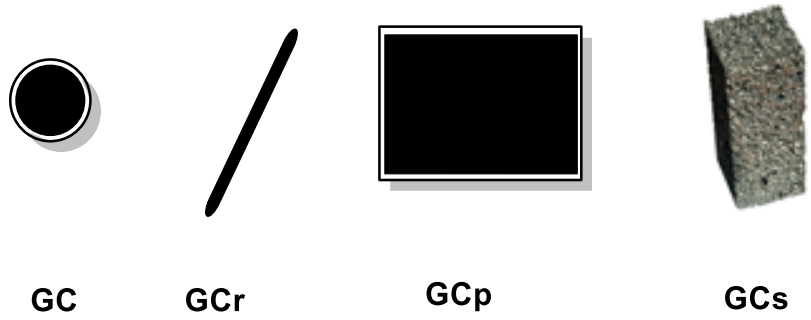

Figure 1. Drawing of working glassy carbon electrodes used in this work. Glassy carbon disk, **GC** (ϕ = 0.3 cm, S = 0.07 cm^2), glassy carbon rods, $\mathbf{GCr_x}$ (ϕ = 5 or 7 mm x 5 cm length and labeled $\mathbf{GCr_5}$ and $\mathbf{GCr_7}$ respectively), glassy carbon plates **GCp** (180 μm x 25 mm x 15 mm) and reticular vitreous carbon commonly named carbon sponge, $\mathbf{GC_s}$,(1 cm^3, S = 10 cm^2, 20 ppi).For the rotating disk electrode, a glassy carbon disk of ϕ = 0.4 cm (S = 0.125 cm^2) was used

Figure 2 shows the electrochemical response obtained for $\mathbf{2}^{3+}$ in acetone using a glassy carbon electrode disk (GC) of 0.07 cm^2 surface area. The scanning starts at 0.40 V towards the anodic region up to 0.80 V and then the potential is reversed at -0.40 V and swept back to 0.80 V. The large reductive irreversible wave at $E_{p,c}$ = 0.25 V (labeled *2* in Figure 2, left) is associated with the reduction of the diazonium group of $\mathbf{2}^{3+}$ leading to a carbon radical generation, followed by C-C bond formation with the graphite electrode.[37,38]Depending on the graphitic material, and given the axial nature of the two diazonium salts, the molecular complex can be anchored through any of the two sides. If only one side is anchored then one of the axial ligands will end up forming a terminal phenyl, or phenol group, or both. [37,38] From an electrochemical point of view, the activity of these complexes might be practically identical and thus will not be discriminated in the following.

VI

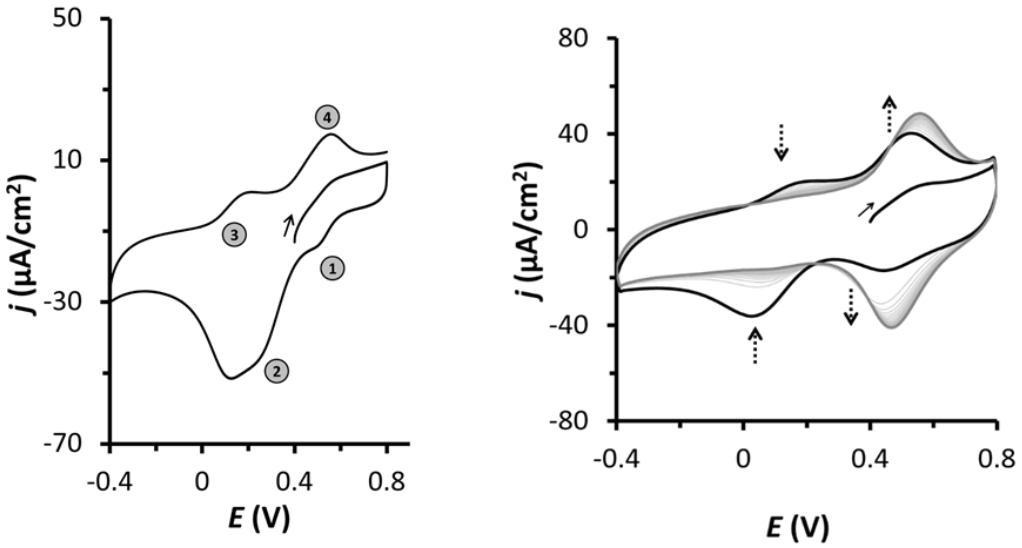

Figure 2. Left, cyclic voltammetry showing the electrochemical response of $\mathbf{2}^{3+}$ dissolved in acetone, on a glassy carbon working electrode disk (see text for details). The solid arrow indicates the scan direction. Right, 20 **r**epetitive cyclic voltammetric scans using **GC-4X** as the starting material in neat acetone, showing the disappearance of the wave due to the Ru-NO group at 0.15 V and the increase of the wave at 0.55 V (dashed arrows indicate increasing or decreasing current intensities upon scanning).

VI

The quasi-reversible wave at 0.15 V ($E_{p,a}$ = 0.20 V ; $E_{p,c}$ = 0.10 V; ΔE = 100 mV; labeled *3* in Figure 2) is associated with the one electron redox process of the nitrosyl group, both for the one just anchored on the glassy carbon electrode and the one that is in solution, associated with $\mathbf{2}^{3+}$. Finally the wave at 0.52 V ($E_{p,a}$ = 0.58 V ; $E_{p,c}$ = 0.46 V; ΔE = 120 mV; labeled *1* and *4* in Figure 2) can be due to the oxidation of the initial complex ($\mathbf{2}^{3+}$) in solution as well as several Ru(III/II) processes of anchored species labeled **GC-4X** (X = acetone, water, NO or a vacant site) *vide infra*.

Because of the low stability of the nitrosyl group at low oxidation states under ambient light and high phosphate buffer concentrations,[39] the reduction wave at 0.15 V leads to the release of the nitrosyl group generating a vacant site. The latter can be potentially occupied by other coordinating molecules such as acetone or water depending on the conditions, as has also been observed for related Ru-NO complexes.[40,41] This can be clearly seen in Figure 2 (right), where a modified electrode generated in the same manner as in Figure 2 is transferred to a clean acetone solution with supporting electrolyte only. Upon 20 cycles from -0.40 to 0.80 the wave associated with the nitrosyl reduction diminishes whereas the wave associated with the **GC-4X**, III/II, process progressively increases. The direct interconversion is further corroborated by the fact that the overall charge at the cathodic III/II wave at the 20th cycle is practically the same as the sum of the initial III/II waves plus the one for the nitrosyl at the first scan. Alternatively, If **GC-4X**

is cycled in a pH=7 aqueous solution up to 1.2 V, the conversion from **GC-4X** to **GC-4** is much faster and with a single scan a complete conversion is obtained as shown in Figure S15 in the SI.

The amount of mass deposited on the electrode can be controlled by changing the applied potential, the time period for which this potential is applied, or the concentration of the initial diazonium salt $\mathbf{2}^{3+}$. Changing only initial concentration of the diazonium salt, while keeping the same protocol just described, provides an exquisite control of the mass deposited on the electrode surface (See SI for further details).

*G 2.2 The Nature and Activity of the **GC-4** Hybrid Materials at Low Potentials.*

The electrochemical properties of **GC-4** have been investigated by multiple scanning CV in water at pH 7.0, as displayed in Figure 3. The upper part of Figure 3 depicts the electrochemical performance of **GC-4** up to 0.90 V *vs.* SSCE (all redox potentials reported in this work are versus the SSCE reference electrode unless explicitly mentioned) where the III/II couple at 0.40 V is clearly seen as well as the electrocatalytic wave associated with the V/IV couple that starts increasing its intensity at approx. 0.75 V. The IV/III couple that is located at 0.60 V is very weak as in the homogeneous phase probably due to slow proton coupled electron transfer process as has been observed for related Ru-aqua complexes.[42] The CV of **GC-4** nicely parallels that of $[Ru(bda)(4\text{-Me-py})_2]$[10] in the homogeneous phase at the same pH=7 and thus corroborates the integrity of the molecular structure even when the complex is anchored on the surface.

VI

Multiple scans, from -0.40 to 0.90, were carried out to evaluate the electrocatalytic performance of **GC-4** and its structural integrity. As can be observed in Figure 3 (top), for increasing number of cycles, the intensity of the catalytic wave decreases as well as the charge under the III/II wave. This observation suggests the presence of a deactivation pathway that slowly reduces the performance of the **GC-4** material. Indeed, after 20 cycles, the charge below the III/II couple is reduced by 15 % while the intensity of the electrocatalytic wave decreases by 20% of its initial value (the second cycle is always taken into consideration for these measurements). These experiments were also performed at 1.00, 1.10 and 1.20 V, as reported in Figure 3 (bottom) and Figures S17 and S18 (SI).

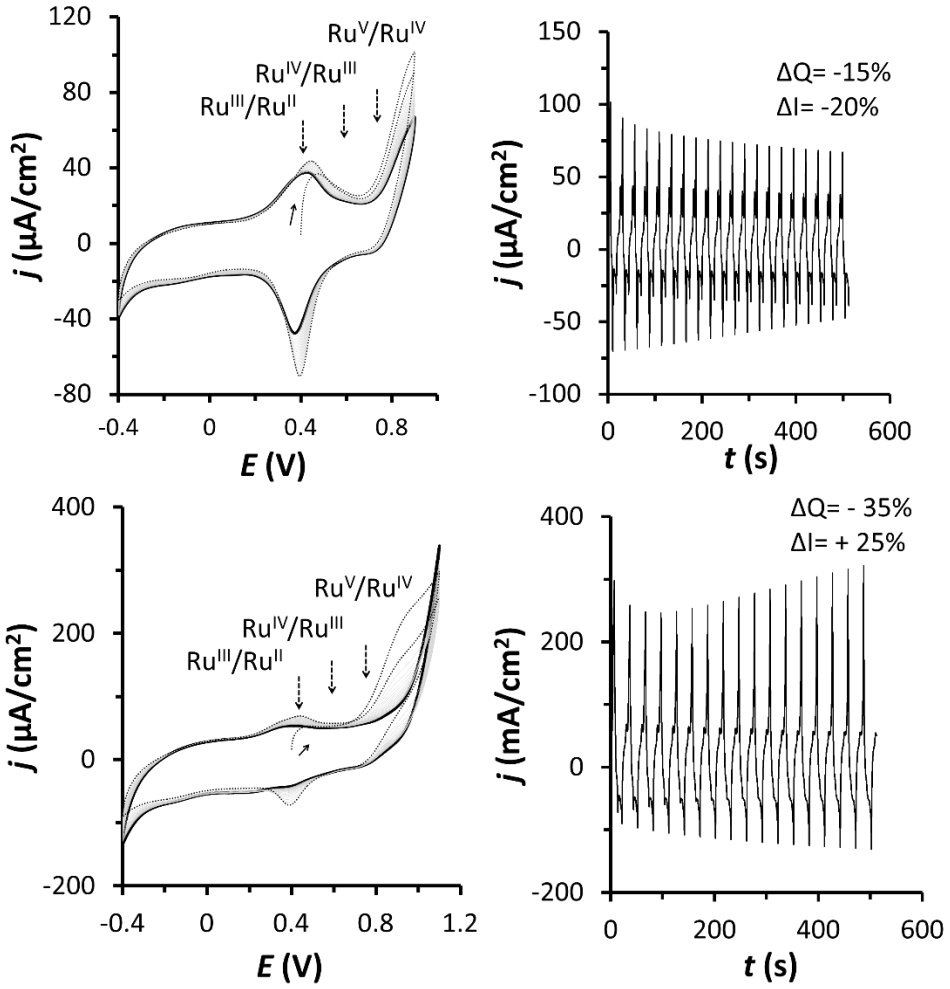

VI

Figure 3. Cyclic voltammetry analysis of the electrocatalytic performance of **GC-4** at pH = 7.0 upon 20 repetitive scans up to 0.90 V (top) and up to 1.10 V (bottom). Solid arrows indicate the starting potential of the first cycle. The dashed line corresponds to the first cycle whereas the black line corresponds to the last one. In gray are depicted the rest of the cycles. ΔQ refers to the change of charge under the anodic wave at 0.50 V from the first to the last cycle. ΔI refers to the change of intensity of the anodic electrocatalytic wave at 0.90 V for the top experiments and at 1.10 V for the bottom. Dashed arrows indicate the redox couples of **GC-4** (Ru^{V}/Ru^{IV}, Ru^{IV}/Ru^{III} and Ru^{III}/Ru^{II}).

Chronoamperometric measurements were carried out at E_{app} = 0.87 V, allowing to calculate an indicative TOF of 0.27 s^{-1} assuming a 100% faradaic efficiency (see Figure S19). The approximate TOF_i compares well with that of a previously reported Ru-bda complex anchored on GC, following a related immobilization strategy.[22]

The multiple cycling performed at 1.10 V shows how the intensity of the III/II wave rapidly decreases after 20 cycles to approximately 35% of its original charge whereas, in sharp contrast now, the intensity at 1.10 V initially decreases but then rapidly increases by 25 %. These phenomena are due to the depletion of the Ru-OH_2 active species from the surface of the

electrode, concomitant with the generation of new species that are much more active than the Ru-OH_2 but shows a foot of the electrocatalytic wave that is anodically shifted to approximately 1.10 V. These new highly active species are due to the formation of RuO_2 on the surface of the **GC** electrode, as will be demonstrated in the next section, and will be labeled **GC-RuO_2** from now on throughout this manuscript. Interestingly, as is the case for most oxides,[5-7] the CV of the **GC-RuO_2** is featureless except for the electrocatalytic wave.

*G 2.3 Nature and Activity of the **GC-4** Hybrid Materials at High Potentials.*

We have anchored the Ru-aqua complex on large surface glassy carbon thin plates **GCp** (180 µm x 15 mm x 25 mm) to characterize the nature of the species on the electrode surface during catalytic turnover, following the evolution of reactive species by both electrochemistry and XAS. A similar protocol, as in the case of the **GC** electrodes, was employed here to generate the corresponding **GCp** hybrid materials.

Figure 4 shows the electrochemical activity of a **GCp-4X** material when exposed to 50 consecutive scans, from 0.00 to 1.20 V. The first scan mainly transforms **GCp-4X** into **GCp-4**. The increase of the anodic limit to 1.20 V increases the speed of the transformation of both **GCp-4X** into **GCp-4** and **GCp-4** into **GCp-RuO_2**. This observation is consistent with the featureless response of **GCp-RuO_2** except for the large electrocatalytic wave. Thus, the materials generated by electrooxidation involve a mixture of **GCp-4** and **GCp-RuO_2** with a relative composition that depends on the number of cycles. Furthermore, the absence of any other wave in the CV reveals the lack of intermediate species in this conversion, indicating a very fast and progressive transformation from **4** to **RuO_2** at the electrode surface. Figure 4 (top left) shows that the intensity under the III/II wave has decreased by about 50 % after 25 cycles, suggesting that about half of the initial amount of **4** has been transformed into **RuO_2**.

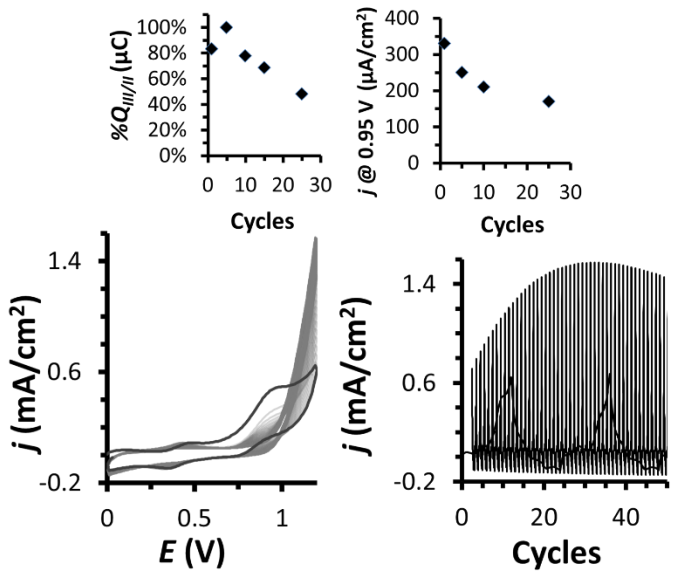

Figure 4. Repetitive cyclic voltammograms (50 cycles) for **GCp-4X** at pH = 7.0 up to 1.20 V. Bottom left, *j* vs. *E* representation. The black solid line corresponds to the first cycle whereas the rest are drawn in grey. Bottom right, *j vs*. *E* representation as a function of cycles. Top left, plot of the charge under the anodic wave at 0.45 V upon cycling. Top right, plot of current density at 0.95 V *vs*. number of cycles (time).

VI

Modified glassy carbon plates obtained at different voltammetric cycles, labeled **GCp-4$_n$** (n = 0, 5, 10, 25) where "n" indicates the number of cycles (Figure 4), were analyzed by XAS. The XAS results obtained for these four samples are summarized in Figure 5 and in the SI. After grafting complex **2**$^{3+}$onto **GCp** electrodes, both the K-edge and EXAFS spectra of **GCp-4$_0$** indicated that the overall structure around the Ru center was preserved, although a slight increase of the Ru-N/O bond lengths was observed in **GCp-4$_0$** (Table S1). For increasing numbers of CV scans, an increase of the K-edge energy was observed (Figure 5B) and for **GCp-4$_{25}$** the increase was about ~0.5 eV larger than for **GCp-4$_0$**. Assuming a K-edge shift of ~1.7 eV per Ru oxidation step, our results suggests that ~30 % of the initial Ru(III) was oxidized to $Ru^{IV}O_2$. Further, EXAFS analysis revealed a slight decrease of the shorter Ru-N/O bond lengths in **GCp-4$_n$** for increasing CV scan numbers and an increase of the Fourier-Transform (FT) peaks around 3 Å. The ~3 Å FT features and the corresponding EXAFS oscillations in the k-range of about 9-12 $Å^{-1}$ were similar to the spectral features of a RuO_2 sample. Accordingly, EXAFS simulations yielded a new Ru-Ru distance of ~3.6 Å which is similar to the Ru-Ru distance in RuO_2.(see Table S1 in the SI). Such distance becomes more prominent for increasing numbers of CV scans (Figure 5D). The value of N_{Ru-Ru} of ~1.3 suggests that ~20 % of the ruthenium in **GCp-4$_{25}$** is present in the form of **RuO_2**. The value obtained here for the transformation of **4** to **RuO_2** on the **GCp-4$_{25}$** electrode is substantially lower than the one obtained by CV probably due to the fact that not all the generated **RuO_2** remains

tightly attached to the electrode surface and is partially washed off during the rinsing protocol used for the XAS sample preparation.

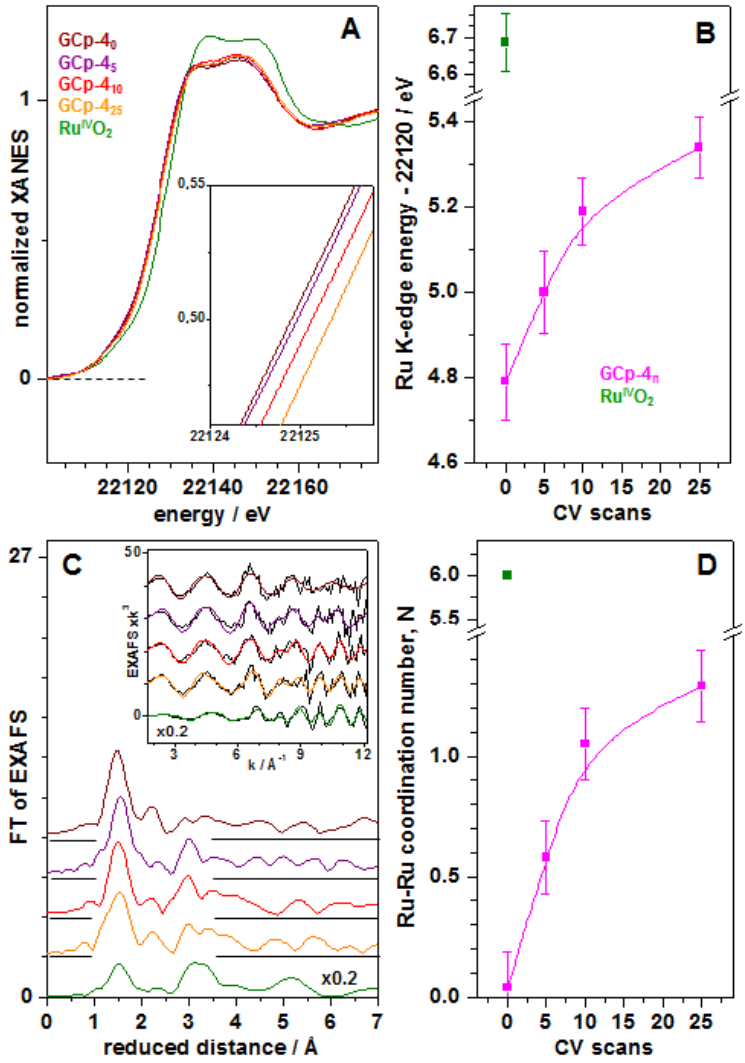

Figure 5: X-ray absorption spectroscopy analysis of **GCp-4$_n$** and **RuO$_2$**. (A) Ru K-edge spectra. Inset, magnification of spectra around edge half-height. (B) Ru K-edge energies (determined at edge half-height). Error bars represent the accuracy of the energy calibration procedure. (C) Fourier-transforms (FTs) of EXAFS spectra. FTs were calculated for k-values of 1.7-12.2 Å^{-1} and using cos^2 windows extending over 10 % at both k-range ends. Colors refer to the samples as indicated in (A), spectra were vertically shifted for comparison. Inset, EXAFS oscillations in k-space. Thin black lines are experimental data whereas thick (colored) lines are simulations using parameters shown in Table S1 in the SI. (D) Coordination number (*N*) of the Ru-Ru distance (~3.57 Å) of **RuO$_2$**, facilitating determination of the relative amounts of the oxide in the samples. Colors refer to samples as indicated in (B), error bars represent the approximate range of *N*-values obtained for using a Ru-Ru distance that was fixed to its value in RuO$_2$ or (slightly) variable in the EXAFS simulations for **GCP-4$_n$**

VI

Further evidence for the formation of RuO_2 comes from the XPS analysis of **GCr$_7$-4** and **GCr$_7$-RuO$_2$**, that contain basically the initial homogeneous catalyst anchored at a glassy carbon rod and RuO_2 respectively (see section below for more details and the SI for the spectra). Indeed the signal associated with the N-1s region is practically at blank level in the **GCr$_7$-RuO$_2$** material, clearly indicating that the original ligands have disappeared.

G 2.4 Quantitative Analysis and Performance of Hybrid Materials for Catalytic Water Oxidation.

The catalytic performance of **RuO$_2$**, electrodeposited on graphite electrodes by over-oxidation of the molecular precursor **4,** was evaluated by CV and chronoamperometric methodologies. For such purpose, electrodeposition was performed on standard **GC** disk electrodes achieving surface concentrations close to a monolayer. **GC** rods of 5 and 7 mm diameter were also used to increase the surface area and to drastically decrease the amount of Ru complex anchored on the surface.

Initially, complex **2**$^{3+}$ was anchored on the **GC** or **GCr$_x$** (x = 5 or 7) electrodes, following the protocols as previously described. An adequate concentration of the complex was chosen to control the amount of deposited material. Then, the electrode surface was sonicated and rinsed with acetone and cleaned with a phosphate buffer solution at pH 7. Subsequently, the new material was scanned 3 times from -0.4 V to 0.6 V in an aqueous solution at pH 7. The amount of the complex on the electrode surface was quantified by integrating the charge below the oxidative waves at 0.52 V and 0.15 V. Finally, a potential of 1.20 V was applied for 6 minutes to ensure complete conversion from **GCr$_7$-4X** to **GCr$_7$-RuO$_2$**.

The catalytic activity of the new materials was analyzed by CV and chronoamperometry at pH 7.0. Figure 6 (left) shows the CV of **GCr$_7$-RuO$_2$** with a surface concentration of 25 pmols/cm^2, exhibiting a huge electrocatalytic wave starting at 1.10 V that reaches impressive current densities above 1.5 mA/cm^2. Chronoamperometric experiments at E_{app} = 1.275 V (η = 0.70 V *vs*. the 4e$^-$ oxidation of water to dioxygen, for 360 seconds) were used to calculate TOF$_i$. A plot of TOF$_i$ *vs*. the RuO_2 superficial concentration at the electrode is offered in Figure 6 (right) and a respective Tafel plot in Figure S20. As it can be observed in Figure 6 (right) it is impressive to see the large increase of TOF$_i$ as the Γ decreases. In the particular case of **GCr$_7$-RuO$_2$** with Γ = 1.0 pmol the TOF$_i$ reaches a value close to 300 cycles per second which is among the highest reported in heterogeneous phase,[19,22-24] reaching values very similar to the best ones obtained so far in homogeneous phase.[10]

In order to be able to compare the performance of our electrode material with previous works reported in the literature for RuO_2 and other oxides deposited at the surface of electrodes, we analyzed the roughness factor (RF) and the water oxidation catalytic activity following the benchmark proposed by Jaramillo et al.[43] A glassy carbon electrode disk (r = 0.20 cm) was used to analyze the double layer capacitance in the absence of faradaic processes to determine the electrochemically active surface area (ECSA) and RF, see Figure S21. Our experiments yielded an RF = 1-2 which indicates a surface coverage of RuO_2 close or slightly above to one monolayer which is reasonable coming from a very small loading of the initial diazonium salt, $\mathbf{2}^{3+}$. The estimation of the RF enabled us to obtain the specific current density, j_s, defined as the geometrical current density divided by RF. This parameter allows thus a fair comparison with other electrocatalytic materials since it takes into account the real surface area of the electrode. With regard to catalyst that consist on evaluating current densities (both j and j_s) as function activity we carried out the test recommended by Jaramillo et al. of potential using a rotating disk electrode (RDE) at 1600 rpm under 1 atmosphere of O_2 under steady state conditions using the same GC electrode, see Figure S22. Here our experiments show that to reach a j_s = 1 mA/cm^2 at pH = 7.0 an overpotential (η) of 0.65 V is needed. Under the same conditions the cobalt oxide water oxidation catalyst named "CoPi", that has been thoroughly studied,[44-45]needs η = 1.2 V at pH = 0 and η = 0.45 V at pH = 14. Under static conditions at pH = 7 CoPi needs η = 0.58 V to reach a j_s = 0.2 mA/cm^2, [46]whereas **GC-RuO$_2$** need only 0.50 V (see the supporting information section for additional details). The latter manifests that the **GC-RuO$_2$** electrode prepared in this work is among the best electrocatalytic materials reported so far.

Finally bulk electrolysis experiments were also carried out using high surface area reticulated carbon sponge electrodes **GCs** (20 ppi; volume = 1 cm^3). Following a similar protocol as for the carbon rod electrodes we generated **GCs-4** and **GCs-RuO$_2$**. The latter was used to carry out a bulk electrolysis experiment in a two compartment cell with an E_{app} = 1.15 V (η = 0.6 V) for two hours containing a Clark electrode to measure the molecular oxygen generated in the gas phase. A plot of current intensity and [O_2] *vs*. time is presented in Figure S23. It is impressive to see again that during the first 30 minutes TONs higher than 25000 are achieved with basically 100 % Faradaic efficiency. After 100 minutes the TON reaches a value of 45000 although now the Faradaic efficiency drops, most likely due the oxidation of the carbon sponge electrode as has been observed before.[47]

VI

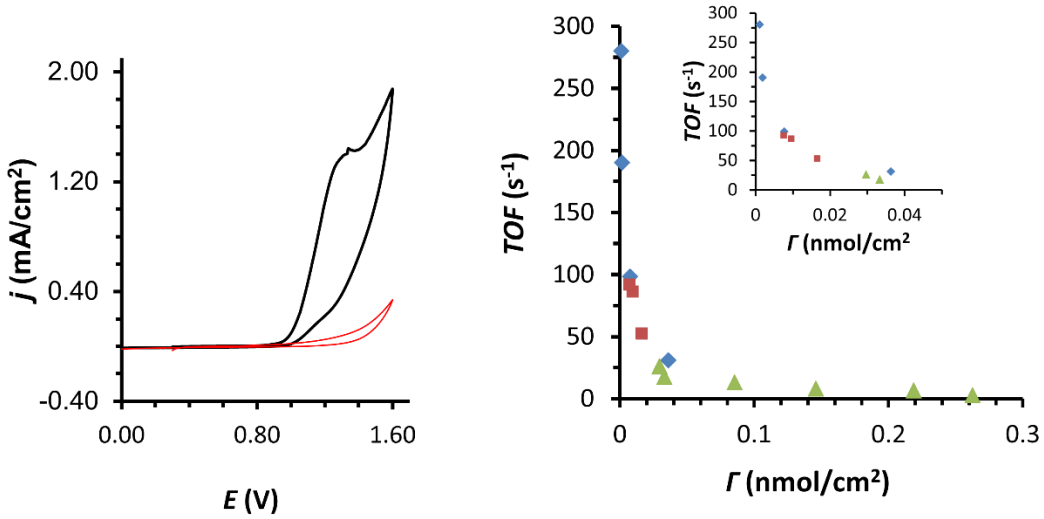

Figure 6. Left, cyclic voltammetry of **GCr$_7$-RuO$_2$** with a superficial concentration of 25 pmols/cm^2 at pH = 7.0, showing a large electrocatalytic wave starting at 1.10 V (black line) and bare **GCr$_7$** at 20 mV/s of scan rate. Right, plot of TOF for a series of **GCr$_7$-RuO$_2$** (blue diamonds), **GCr$_5$-RuO$_2$** (red squares) and **GC-RuO$_2$** (green triangles) and inset in the 0-0.05 nmol/cm^2 region. TOF are calculated from chronoamperometric experiments at 1.273 V (η = 0.70 V) for 360 s, after blank subtraction and assuming 100 % Faradaic efficiency.

VI

G 3 Discussion

G 3.1 Anchored WOCs and the Nature of Ru-bda on Graphitic Surfaces

Anchoring molecular WOCs on solid surfaces is an attractive strategy to generate hybrid solid-state materials that can be used to carry out heterogeneous water oxidation catalysis. Depending on the nature of the materials, water oxidation anodes or photoanodes can be built.[18-23,48-49] Anchored catalysts are very useful for building photoelectrochemical cells for water splitting since they provide a flexible engineering platform. However, one of the most challenging aspects is the proper characterization of the surface-immobilized species before, during, and after catalysis.

A number of WOCs have already been ***covalently*** anchored to metal-oxide surfaces, using carboxylate or phosphonate functionalities.[18-20]In addition, a few of them have been anchored on graphite surfaces.[22-24] The graphitic surfaces provide high conductivity, low-cost materials and are readily available in a myriad of conformations. In addition, invariably, every molecular water oxidation catalyst necessarily needs to cycle through a labile Ru-OH$_2$, or Ru-OH type of intermediate species. The oxide surfaces can potentially compete for this bond and thus generate Ru-O$_{surface}$ bonds that in turn deactivate the molecular catalyst. Such deactivation process does not occur on graphitic surfaces or to a much lesser extend in Glassy Carbon

electrodes since the atomic ratio C/O is usually below 14%.[50] Therefore, from the functional perspective, GC surfaces might have advantages as solid supports when compared to metal-oxides. As a drawback, they are susceptible to oxidation under high applied potentials, so the graphitic surface can be oxidized and the C-C bond between the surface and the molecular catalyst can be broken. However, under 'reasonable' potentials the oxidation of the surface is negligible. In addition, new carbon-based materials such as the Boron Doped Diamond (BDD) [51] or *nano*-ITO-Reticulated Vitreous carbon (*nano*-ITO-RVC) [52] are incredibly stable even at very high potentials.

Our strategy was to use diazonium salts attached to the axial ligands that basically maintain the intrinsic electronic properties of the metal center in the original complex. Upon controlled reduction, they readily attach to the surface of the electrode generating hybrid materials. CV, XPS and especially XAS spectroscopy allows a thorough characterization of the nature of the anchored species, allowing for characterization of the fresh catalyst before turnover and for monitoring the fate of the catalyst under normal operating conditions.

G 3.2 Catalytic Performance of the Anchored Catalysts

At low potentials, up to the electrocatalytic wave, the **GC-4** behaves in a relatively discrete manner achieving TOF_i of 0.27 s^{-1} at 0.87 V. After a few cycles, the catalyst slowly deactivates. This is in sharp contrast with the spectacular performance and stability of the catalyst in the homogeneous phase, where a TOF_i close to 1000 cycles per second with an oxidative efficiency close to 100 % is observed under optimized conditions using Ce(IV) as a primary oxidant. The radically different behavior of the supported catalyst, when compared to the complex in solution, might be due to dimerization of the complex in the homogeneous phase upon reaching the high oxidation state Ru(V) to generate the RuOORu species via an I2M mechanism and subsequently dioxygen evolution.[10] The low translational mobility of the anchored Ru complex, due to the covalent C-C bond with the graphitic surface, precludes the dimer formation and favors the water nucleophilic attack type of mechanism. Such process has higher activation energy and significant deactivation pathways, as judged by the loss of activity after a few catalytic cycles.

At higher potentials, the electrocatalytic wave shifts anodically by approx. 200 mV, indicating that a new material is formed while the original catalyst is depleted. Surprisingly, the newly generated material is extraordinarily active towards water oxidation. Such material is unambiguously characterized as a form of electrodeposited RuO_2. The transformation occurs without forming any detectable reaction intermediates, implying that it is rapidly completed

through ligand degradation possibly all the way to CO_2.[53,54]The decomposition might happen in conjunction with ligand loss to the solution. Thus, the anchored molecular catalyst, for instance **GCr_7-4,** acts as a precursor for the generation of RuO_2 electrodeposited on the electrode surface, forming **GCr_7-RuO_2**, with TOF_i close to 300 s^{-1} and TONs >45000.

At this point, it is of interest to compare the activity of our materials to those that have already been reported in the literature. This is a very difficult task, due the different conditions under which the catalysts are described. To objectively evaluate the performance of the electrocatalytic materials, Jaramillo *et al.* have described benchmark tests that consists in calculating electroactive surface areas (ECSA), roughness factors (RF) and measurements of current densities (**j** and **js**) as a function of overpotential values.[43]Following this benchmark tests, a range of oxides including those of Co, Ni and Ir have been evaluated at pH = 0.0 and 14.0. These extreme conditions are needed to come up with the best performance for these oxides. Both at pH = 0.0 and pH = 14.0, IrOx turns out to be the best catalyst whereas CoPi performs relatively well at pH = 14.0. Our catalyst exhibits high performance even at pH = 7.0, thus we compare our electrocatalytic materials with those of CoPi at pH = 7.0, for which the needed information is available.[46] The fact that our systems are comparable, or slightly better, in terms of specific current densities than those of CoPi manifests the excellent performance for oxygen evolution of our hybrid electrocatalyst materials. In addition, while **GC-RuO_2** works in a neat pH = 7.0 electrolyte solution, the CoPi the systems need a 0.5 mM solution of Co(III) so that a significant amount of CoOx remains at the electrode.

Another interesting aspect of our system is the inverse correlation of the electrocatalytic activity versus surface concentration. This phenomenon has already been described for metal oxide nanoparticles (NP) and in particular for gold oxides NP,[55] and has been ascribed to a combination of factors including electronic and geometrical effects.[55-57] From an electronic perspective, the smaller the particle (or nanoparticle) the higher the number of Ru atoms with low coordination sites. An additional influence to the performance can also be due to a synergistic interaction of the electrode surface and the catalyst NP as well as the superficial charge of the NP. From a geometrical perspective, different crystal facets can have different reactivity and the decrease of particle size can also generate an increase of these active facets with regard to the non-active ones. In addition, NP can also have a certain degree of fluxionality that might influence performance. At present, we do not know which one of these factors and to what extend might be responsible for the inverse correlation. Further analysis of this aspect will be reported in the future.

G 4 Conclusions

We have synthesized Ru-bda complexes with axial pyridyl ligands, functionalized with diazonium salts that serve to attach the complexes to graphitic surfaces under reductive treatment. The resulting surface functionalization generates a solid-state material with modest catalytic activity. However, under performance conditions, it readily decomposes to form a highly dispersed RuO_2 thin-film exhibiting outstanding electrocatalytic performance for electrocatalytic dioxygen evolution by water-splitting.

G 5 Acknowledgments

A.L. thanks MINECO (CTQ-2013-49075-R, SEV-2013-0319) and "La Caixa" foundation for financial support. R.M. thanks "La Caixa" foundation for a PhD grant. M.H. thanks the Deutsche Forschungsgemeinschaft for financial support (grant Ha3265/6-1) and for a Heisenberg Fellowship and the German Bundesministerium für Bildung und Forschung for funding within the Röntgen-Angström Cluster (grant 05K14KE1). We thank S. Reschke and M. Görlin for help in XAS data collection and M. Nachtegaal at SuperXAS of SLS for excellent technical support. M.Z.E. was funded by a Computational Materials and Chemical Sciences project at Brookhaven National Laboratory under contract DE-AC02-98CH10886 with the U.S. DOE.. V.S.B. acknowledges supercomputer time from NERSC and financial support as part of the Argonne-Northwestern Solar Energy Research (ANSER) Center, an Energy Frontier Research Center funded by the U.S. Department of Energy, Office of Science, Office of Basic Energy Sciences under Award Number DE-SC0001059. X.S. thanks MINECO (CTQ2011-26440) for financial support.

VI

G 6 References

1 Molecular Water Oxidation Catalysis: A Key Topic for New Sustainable Energy Conversion Schemes. **2014** Edited by A. Llobet. John Wiley and Sons Ltd.
2 Rappaport, F.; Guergova-Kuras, M.; Nixon, P. J.; Diner, B. A.; Lavergne, J. *Biochemistry* **2002**, *41*, 8518-8527..
3 Singh, A.; Spiccia, L. *Coord. Chem. Rev.* **2013**, *257*, 2607-2622.
4 Sala, X.; Maji, S.; Bofill, R.; Garcia-Anton, J.; Escriche, L.; Llobet, A. *Acc. Chem. Res.* **2014**, *47*, 504-516.
5 Trotochaud, L.; Ranney, J. K.; Williams, K. N.; Boettcher, S. W. *J. Am. Chem. Soc.* **2012**, *134*, 17253-17261.
6 Smith, R. D. L.; Prévot, M. S.; Fagan, R. D.; Zhang, Z.; Sedach, P. A.; Siu, M. K. J.; Trudel, S.; Berlinguette, C. P. *Science* **2013**, *340*, 60-63.
7 Suntivich, J.; Gasteiger, H. A., *Nat. Chem*. **2011**, *3*, 546-550.
8 Concepcion, J. J.; Tsai, M. K.; Muckerman, J. T.; Meyer, T. J. *J. Am. Chem. Soc.* **2010**, *132*, 1545-1557.
9 Yin, Q.; Tan, J. M.; Besson, C.; Geletii, Y. V.; Musaev, D. G.; Kuznetsov, A. E.; Luo, Z.; Hardcastle, K. I.; Hill, C. L. *Science* **2010**, *328*, 342-345.
10 Duan, L.; Bozoglian, F.; Mandal, S.; Stewart, B.; Privalov, T.; Llobet, A.; Sun, L. *Nat. Chem.* **2012**, *4*, 418-423.

11 Karlsson, E. A.; Lee, B.-L.; Åkermark, T.; Johnston, E. V.; Kärkäs, M. D.; Sun, J.; Hansson, O.; Bäckvall, J.-E.; Åkermark, B. *Angew. Chem., Int. Ed.* **2011**, *50*, 11715-11718.
12 Zhang, M.-T.; Chen, Z.; Kang, P.; Meyer, T. J. *J. Am. Chem. Soc.* **2013**, *135*, 2048-2051.
13 Lopez, I.; Ertem, M. Z.; Maji, S.; Benet-Buchholz, J.; Keidel, A.; Kuhlmann, U.; Hildebrandt, P.; Cramer, C. J.; Batista, V. S.; Llobet, A. *Angew. Chem., Int. Ed.* **2014**, *53*, 205-209.
14 Neudeck, S.; Maji, S.; Lopez, I.; Meyer, S.; Meyer, F.; Llobet, A. *J. Am. Chem. Soc.* **2014**, *136*, 24-27.
15 Richmond, C. J.; Matheu, R.; Poater, A.; Falivene, L.; Benet-Buchholz, J.; Sala, X.; Cavallo, L.; Llobet, A. *Chem. Eur. J.* **2014**, *20*, 17282-17286.
16 Wang, L.; Duan, L.; Wang, Y.; Ahlquist, M. S. G.; Sun, L. *Chem. Commun.* **2014**, *50*, 12947-12950.
17 See for instance: a) Moonshiram, D.; Jurss, J. W.; Concepcion, J. J.; Zakharova, T; Alperovich, I.; Meyer, T. J.; Pushkar, Y. *J. Am. Chem. Soc.*, **2012**, *134*,*4625*-4636. b) Alperovich, I.; Moonshiram, D.; Concepcion, J. J.; Pushkar, Y. *J. Phys. Chem. C*. **2013**, *117*, 18994–19001. c) Stull, J. A.; Stich, T. A.; Hurst, J. K.; Britt, R. D. *Inorg. Chem.* **2013**, *52*, 4578–4586.
18 Chen, Z.; Concepcion, J. J.; Jurss, J. W.; Meyer, T. J. *J. Am. Chem. Soc.* **2009**, *131*, 15580-15581.
19 Ashford, D. L.; Lapides, A. M.; Vannucci, A. K.; Hanson, K.; Torelli, D. A.; Harrison, D. P.; Templeton, J. L.; Meyer, T. J. *J. Am. Chem. Soc.* **2014**, *136*, 6578-6581.
20 Toma, F. M.; Sartorel, A.; Iurlo, M.; Carraro, M.; Parisse, P.; Maccato, C.; Rapino, S.; Gonzalez, B. R.; Amenitsch, H.; Da Ros, T.; Casalis, L.; Goldoni, A.; Marcaccio, M.; Scorrano, G.; Scoles, G.; Paolucci, F.; Prato, M.; Bonchio, M. *Nat. Chem.* **2010**, *2*, 826-831.
21 Tong, L.; Gothelid, M.; Sun, L. *Chem. Commun.* **2012**, *48*, 10025-10027.
22 Li, F.; Zhang, B.; Li, X.; Jiang, Y.; Chen, L.; Li, Y.; Sun, L. *Angew. Chem., Int. Ed.* **2011**, *50*, 12276-12279.
23 Mola, J.; Mas-Marza, E.; Sala, X.; Romero, I.; Rodríguez, M.; Viñas, C.; Parella, T.; Llobet, A. *Angew. Chem., Int. Ed.* **2008**, *47*, 5830-5832.
24 deKrafft, K. E.; Wang, C.; Xie, Z.; Su, X.; Hinds, B. J.; Lin, W. *ACS Appl. Mater. Interfaces* **2012**, *4*, 608-613.
25 Hambourger, M.; Gervaldo, M.; Svedruzic, D.; King, P. W.; Gust, D.; Ghirardi, M.; Moore, A. L.; Moore, T. A. *J. Am. Chem. Soc*., **2008**, *130*, 2015-2022.
26 Youngblood, W. J.; Lee, S.-Y. A.; Kobayashi, Y.; Hernandez-Pagan, E. A.; Hoertz, P. G.; Moore, T. A.; Moore, A. L.; Gust, D.; Mallouk, T. E. *J. Am. Chem. Soc.*, **2009**, *131*, 926-927.
27 Li, L.; Duan, L.; Xu, Y.; Gorlov, M.; Hagfeldt, AS.; Sun, L. *Chem. Commun*., **2010**, *46*, 7307-7309.
28 Wang, D.; Ghirlanda, G.; Allen, J. P. *J. Am. Chem. Soc*. **2014**, *136*, 10198–10201
29 Hong, D.; Jung, J.; Park, J.; Yamada, Y.; Suenobu, T.; Lee, Y.-M.; Nam, W.; Fukuzumi, S. *Energy Environ. Sci.*, **2012**, *5*, 7606-7616.
30 Chen, G.; Chen, L.; Ng, S.-M.; Lau, T.-C. *ChemSusChem*, **2014**, *7*, 127-134.
31 Harriman, A.; Pickering, I. J.; Thomas, J. M.; Christensen, P. A. *J. Chem. Soc., Faraday Trans.* **1988**, *84*, 2795-2806.
32 Over, H. *Chem. Rev.* **2012**, *112*, 3356 –3426.
33 Zhang, Y.; Judkins, E. C.; McMillin, D. R.; Mehta, D.; Ren, T. *ACS Catal.* **2013**, *3*, 2474-2478.
34 Zhang; Y.; Ren, T. *Chem. Commun.* **2012**, *48*, 11005 -11007.
35 Okeyoshi, K.; Yoshida, R. *Adv. Funct. Mater.* **2010**, *20*, 708-717.
36 Lee, Y.; Suntivich, J; May, K. J.; Perry, E. E.; Shao-Horn, Y. *J. Phys. Chem.Lett.* **2012**, *3*, 399-404.
37 Belanger, D.; Pinson, J. *Chem. Soc. Rev*. **2011**, *40*, 3995-4048.
38 Pinson, J.; Podvorica, F. *Chem. Soc. Rev.* **2005**, *34*, 429-439.
39 Gomes, A. J.; Espreafico, E. M.; Tfouni, E. *Mol. Pharmaceutics* **2013**, *10*, 3544-3554.
40 Roveda, A. C., Jr.; Bueno-Ruiz-Papa, T.; Castellano, E. E.; Wagner-Franco, D. *Inorg. Chim. Acta* **2014**, *409*, 147-155.
41 Doro, F. G.; Rodrigues-Filho, U. P.; Tfouni, E. *J. Colloid Interface Sci*. **2007**, *307*, 405-417.
42 Llobet, A.; Doppelt, P.; Meyer, T. J. *Inorg. Chem.* **1988**, *27*, 514-520
43 McCrory, C. C. L.; Jung, S.; Peters, J. C.; Jaramillo, T. F. *J. Am. Chem. Soc.* **2013**, *135*, 16977-16987.
44 Other metal oxides behaved similarly *e.g*: CoOx, CoFeOx, NiOx, showing an overpotential between 0.3 V and 0.5 V at pH = 14 and between 0.8 V and 1.2 V at pH = 0.
45 IrO_2 oxide nanoparticled behaved better than other oxides at pH=0 with an overpotential of 0.3 V at pH=0 as described in Ref. 38.
46 Kanan, M. W.; Nocera, D. G. *Science* **2008**, *321*, 1072-1075.
47 Barnett, S. M.; Goldberg, K. I.; Mayer, J. M. *Nat. Chem.* **2012**, *4*, 498-502.

48 Vannucci, A. K.; Alibabaei, L.; Losego, M. D.; Concepcion, J. J.; Kalanyan, B.; Parsons, G. N.; Meyer, T. J. *Proc. Natl. Acad. Sci. U. S. A.* **2013**, *110*, 20918-20922.
49 Gao, Y.; Ding, X.; Liu, J.; Wang, L.; Lu, Z.; Li, L.; Sun, L. *J. Am. Chem. Soc.* **2013**, *135*, 4219-4222.
50 McCreery, L. R. *Chem. Rev.* **2008**, *108*, 2646–2687.
51 Luong, J. H. T.; Male, K. B.; Glennon, J. D. *Analyst* **2009**, *134*, 1965-1979.
52 Méndez, M. A.; Alibabaei, L.; Concepcion, J. J.; Meyer, T. J. *ACS Catal.* **2013**, *3*, 1850-1854.
53 Francas, L.; Sala, X.; Escudero-Adan, E.; Benet-Buchholz, J.; Escriche, L.; Llobet, A. *Inorg. Chem.* **2011**, *50*, 2271-2781.
54 Hong, D.; Mandal, S.; Yamada, Y.; Lee, Y.-M.; Nam, W.; Llobet, A.; Fukuzumi, S. *Inorg. Chem.* **2013**, *52*, 9522-9531.
55 Carchini, G.; Almora-Barrios, N.; Revilla-López, G.; Bellarosa, L.; García-Muelas, R.; García-Melchor, M.; Pogodin, S.; Błoński, P.; López, N. *Top Catal.* **2013**, *56*, 1262-1272.
56 Valden, M.; Lai, X.; Goodman, D. W. *Science* **1998**, *281*, 1647-1650.
57 Xhou, Z.; Flytzani-Stephanopoulos, M.; Saltsburg, H.; *J. Catal.*, **2011**, *280*, 255−263.

G 7 Supporting Information

Paper G: Behavior of the Ru-bda water oxidation catalyst covalently anchored on glassy carbon electrodes

VI

Materials

All the reagents were purchased from Sigma-Aldrich unless indicated differently. RuCl3·3H2O was supplied by Alfa Aesar. 4-pyridine-4-yl-phenylamine (N-NH2) was purchased from ChemCollect. Ligands 6,6'-dicarboxylic acid-2,2'-dipyridyl (H2bda)S1 and [RuCl2(DMSO)4]S2 were prepared according to the literature procedures. High-purity deionized water was obtained by passing distilled water through a nanopure Milli-Q water purification system. Methanol (MeOH) was distilled over Mg/I2. All synthetic manipulations were routinely performed under nitrogen atmosphere using Schlenk tubes and vacuum-line techniques.

Synthesis of [Ru(bda)(N-NH_2)$_2$] (**1**). A sample of [$RuCl_2(DMSO)_4$] (300 mg, 0.62 mmol), 6,6'-dicarboxylic acid-2,2'-dipyridyl (151 mg, 0.62 mmol) and Et_3N were mixed and degassed in dry MeOH (12 mL), refluxed for 3 hours and cooled down to RT. 4-pyridine-4-yl-phenylamine (N-NH_2) (210 mg, 1.24 mmol) was then added to the reaction mixture and the solution was further refluxed for 7 hours. During that time a brown precipitate appeared which was filtered off and dried under vacuum. The brown solid was then dissolved in a mixture of 2,2,2-Trifluoroethanol (TFE) and dichloromethane (4:100) and added to an alumina column (eluted with 4% TFE, 4% MeOH in DCM). The eluent was then reduced to 50 mL and diethyl ether was added to obtain **1** a brown crystalline solid that was filtered on a frit and dried under vacuum (100 mg, 25% yield). ^{1}H-NMR (500 MHz, [d4]-methanol): δ = 6.69 (4H, dd, *J* = 1.9, 6.8 Hz), 7.37 (4H, dd, *J* = 1.4, 5.5 Hz), 7.43 (4H, dd, *J* = 1.9, 6.8 Hz), 7.70 (4H, dd, *J* = 1.4, 5.5 Hz), 7.90 (2H, t, *J* = 7.9 Hz), 8.07 (2 H, dd, *J* = 1.0, 7.9 Hz), 8.60 (2H, dd, *J* = 1.0, 7.9 Hz).^{13}C-NMR (125 MHz, [d4] Methanol) δ = 116.1, 121.7, 124.9, 126.1, 127.1, 129.0, 132.9 , 150.3, 152.0, 152.7, 157.7, 161.7, 175.3. The assignment of resonances can be found in Figures S1 and S2. UV-Vis (CH_3OH) [λ, nm (ε, M^{-1} cm^{-1})]: 366 (52208), 294 (30372). $E_{1/2}$(Acetone, 0.1 M TBAP): 0.35 V *vs.* SSCE. ESI-HRMS *m/z*: Calc for $C_{34}H_{28}N_6O_4Ru^+$: 684.1053, found: 684.1051. *Anal.* Calc. for [Ru(bda)(N-NH_2)$_2$]·$\frac{1}{2}$ CH_2Cl_2 · $\frac{1}{2}$ $CH_3CH_2OCH_2CH_3$ ($C_{36.5}H_{32}ClN_6O_{4.5}Ru$): C, 57.44%; H, 4.23%; N, 11.01. Found: C, 57.61%; H, 4.34%; N, 11.05%.

Synthesis of [Ru(bda)(NO)(N-N_2)][PF_6]$_3$.KPF_6 ((**2**)(PF_6)$_3$) was adapted from the literature.[S3] A sample of $NaNO_2$ (30 mg, 0.43 g) was dissolved in 0.5 M HCl (2 mL) and added drop wise to a suspension of **1** (100mg, 0.14 mmol) in 0.5 M HCl (24 mL). After stirring for 30 minutes, a saturated solution of KPF_6 in 0.5 M HCl was used to precipitate the product as a powder. The solid was filtered in a frit, washed with water, ethanol and diethyl ether and dried under vacuum (80 mg, 42% yield). The red powder could be recrystallized by adding ether to an acetone solution of (**2**)(PF_6)$_3$. The resulting solid could be stored under N_2 in the fridge for several weeks. All solutions and materials were kept under ice during the manipulation to maintain the

VI

temperature between 0 ºC and 5 ºC. ^{1}H-NMR (500 MHz, [d6]-acetone, T=273K): δ= 8.13 (4H, d, *J* = 6.2 Hz), 8.42 (4H, d, *J* = 8.6 Hz), 8.56 (2H, s, *J* = 6.2), 8.9 (2H, t, *J* = 7.9 Hz), 9.0 (4H, d, *J* = 8.6 Hz), 9.25 (2H, d, *J* = 7.9 Hz). ^{13}C-NMR (125 MHz, [d6] Acetone) δ = 154.7, 153.2, 149.9, 147.6, 147.0, 134.5, 131.5, 130.3, 126.6, 117.9. The assignment of resonances can be found in Figures S6 and S7. UV-Vis (CH_3OH) [λ, nm (ε, M^{-1} cm^{-1})]: 386 (5236), 300 (36881). Anal. Calc. for [Ru(bda)(NO)(N-N_2)$_2$][PF_6]$_3$·KPF_6 ($C_{34}H_{22}F_{24}KN_9O_5P_4Ru$): C, 30.90%; H, 1.63%; N, 9.29. Found: C, 30.98%; H, 1.94%; N, 9.43%.

General instrumentation

Electrospray ionization (ESI) and matrix-assisted laser desorption ionization (MALDI) mass spectrometry (MS) experiments were performed on a Waters Micromass LCT Premier equipment and a Bruker Daltonics Autoflex equipped with a nitrogen laser (337 nm), respectively. UV–Vis spectroscopy was performed on a Cary 50 Bio (Varian) UV–Vis spectrophotometer with 1 cm quartz cells. A 400 MHz Bruker Avance II spectrometer and a Bruker Avance 500 MHz were used to carry out NMR spectroscopy. FT-IR measurements were carried out on a Bruker Optics FTIR Alpha spectrometer equipped with a DTGS detector, and a KBr beamsplitter at 4 cm^{-1} resolution.

VI

Electrochemical methods

General considerations

All static electrochemical experiments were performed in a PAR 263A EG&G potentiostat or in an IJ-Cambria HI-660 potentiostat, using a three-electrode cell. Cyclic Voltammograms (CV) were recorded at 100 mV·s^{-1} scan rate, unless explicitly expressed. $E_{1/2}$ values reported in this work were estimated from CV experiments as the average of the oxidative and reductive peak potentials ($E_{p,a}$ + $E_{p,c}$)/2. The Rotating disk Voltammograms were recorded in a IJ-Cambria HI-700D bipotentiostat in a RDDE-3A apparatus (ALS company, Japan).

Working Electrodes

Glassy carbon disk (ϕ = 0.3 cm, S = 0.07 cm^2, **GC-**), carbon rods (ϕ = 5, 7 or 10 mm x 5 cm length and called: **GCr$_5$-** and **GCr$_7$-** respectively) (HTW®), glassy carbon plates (2.5 cm x 1.5 cm x 0.001 cm, **GCp-**) (HTW®) and reticular vitreous carbon (1 cm^3, estimated S = 10 cm^2, **GCs-**) (20 ppi, Doucel®) were used as working electrodes. All Glassy Carbon electrodes (except for **GCs-** and **GCp-**) were polished successively with 1.0, 0.3, and 0.05 µm alumina (Al_2O_3), sonicated with MeCN for 15 minutes and washed with acetone.

Counter Electrodes

The counter electrode was a Pt disk for **GC-**, a Pt wire for **GCp-**, **GCr$_5$-**, **GCr$_7$-** and a Pt grid for **GCs-** unless indicated.

Reference Electrodes

A Sodium Saturated Calomel Electrode (SSCE) was used as a reference electrode in general. In specific cases the Ag/Ag$^+$ (aqueous, 4.0 M) or Hg/Hg_2SO_4 electrodes were also used as reference electrodes and potentials were converted to SSCE.

Supporting Electrolytes

Acetone solutions for electrochemical experiments consisted of a 0.1 M solution of tetrabutylammonium hexafluorophosphate (TBAP) and pH = 7.0 phosphate buffered solution (47 mM, I = 0.1 M) was prepared by dissolving the corresponding amounts of NaH_2PO_4 and Na_2HPO_4. No additional salts were added.

Three-electrode cells volume and geometric surface area estimation

For **GCr$_5$-** and **GCr$_7$-** a 15 mL vial was used as electrochemical cell. The cell was filled with 8 mL of a acetone solution of (**2**)$(PF_6)_3$ or of a pH = 7 phosphate buffer solution and the height of the rod immersed in the solution was estimated to be 3.1 cm, which resulted in geometric surface areas for **GCr$_5$-**, **GCr$_7$-** of 5.0 cm^2 and 7.2 cm^2 respectively. For **GCp-**, a total volume of 10 mL was used in a 20 mL vial and the estimated surface area for **GCp-** was 1 cm^2.

General procedure for catalyst anchoring

The Glassy Carbon electrode (**GC-**,**GCr$_5$-**, **GCr$_7$-**, **GCp-** or **GCs-**) was modified by applying a first segment of potential from 0.4 V to 0.8 V and subsequent complete cycles (from 0.8 V to -0.4 V). As a general procedure and unless indicated, a solely complete cycle (from 0.8 V to -0.4 V) after the first segment (0.4 V/0.8 V) was applied. A representative example of the modification of the electrodes is given in Figure 2. Once modified, **GC-4X** were washed and sonicated in acetone for 2 minutes and dried under N_2.

Estimation of Q_{Ru} and the superficial concentration (Γ) of GC-4

The modified glassy carbon electrode (**GC-4X** ,**GCr$_5$-4X**, **GCr$_7$-4X**, **GCp-4X** or **GCs-4X)** was used as a working electrode in a fresh pH = 7 phosphate buffered solution and cycled between -0.4 V and 0.6 V two times. Q_{Ru} was estimated by adding the charge integrated under the oxidation

VI

waves at 0.11 V and 0.51 V in the second scan. **Γ** was estimated by applying the formula: $\Gamma\left(\frac{mol}{cm^2}\right) = \frac{QRu}{n \cdot A \cdot F}$. Where n is the number of mols, A is the surface of the electrode (cm^2) and F is the Faradaic constant.

Turn Over Frequencies (TOF) TOF were calculated using the formula ($Q_{cat}/4 \cdot Q_{Ru} \cdot t$), were Q_{cat} was determined subtracting the blank charge to the charge obtained from the catalytic current at applied potential for t (s) time

Electrochemically active Surface Area ECSA, Roughness Factor (RF) estimation

The electrochemically active surface area (ECSA) was estimated from the electrochemical double-layer capacitance of the catalytic surface as published in the literature. [S4] CVs at different scan rates were performed in the non-faradaic region of the voltammogram. The range was centered in ±0.05 V of the Open Circuit Potential (0.12 V) of a freshly prepared **GC-RuO$_2$** (Γ= 0.2 nmol/cm^2, [**2**$^{3+}$]= 1 mM, S=0.125 cm^2) under 1 atm of O_2 in a pH=7 solution.

The electrochemical double-layer capacitance, $\mathbf{C_D}$, was calculated by plotting i_c (the non-faradaic current at 0.12 V) vs the scan rate (n) (eq. S1). $\mathbf{C_D}$ of a **GC-RuO$_2$** was extracted from the average of three replicates slope (9±2 mF).

$$i_c = n \cdot \mathbf{C_D} \qquad \text{(S1)}$$

The electrochemically active surface area (ECSA) was estimated by dividing the electrochemical double-layer capacitance $\mathbf{C_D}$ by specific capacitance of an ideal planar RuO_2 nanoparticle electrode ($\mathbf{C_s}$) (eq. S2)

$$\text{ECSA} = \mathbf{C_D/C_s} \qquad \text{(S2)}$$

Values of **Cs** reported in the literature for metal nanoparticles electrodes range from 20 mF/cm^2 to 120 mF/cm^2. In the case of RuO_2 nanoparticles in a planar electrode, **Cs** is usually between 60 mF/cm^2 – 80 mF/cm^2. [S4,S5]

However, a general value of $\mathbf{C_s}$=37.5 mF/cm^2 was used for RF estimation in line with the general $\mathbf{C_s}$ used by Jaramillo et al to compare the loading and performance of different metal oxides in the oxygen evolving reaction.[S4]

The Roughness Factor was calculated by dividing ECSA by the geometrical area (S), eq. S3.

$$RF = ECSA/S \qquad \text{(S3)}$$

$\underline{j_s \text{ comparison}}$

Under these assumptions the estimated RF is between 1-2 for **GC-RuO$_2$** (Γ = 0.2 nmol/cm^2, [**2**$^{3+}$]= 1 mM, S=0.125 cm^2). RF=1.9 was used to calculate the specific current densities (**js**) from **Cs**=37.5 mF/cm^2.

For the comparison of the specific current densitities (**j$_s$**) of **GC-RuO$_2$** with other systems in the literature (*e.g* CoPi at pH = 7), geometrical current densitiy reported was divided by RF reported by Jaramillo *et al* [S4] for each specific system.

Sample preparation for X-ray Absorption Spectroscopy (XAS) and measurements

RuO_2 powder was diluted with Boron Nitride (BN) with a 1:4 ratio (Ru:BN) by weight.

A group of 24 **GCp-4X** were identically prepared from a 0.5 mM **2**$(PF_6)_3$ solution using carbon plates **GCp-** as working electrode. The 24 **GCp-4X** were used to prepare 6 **GCp-4$_0$**, 6 **GCp-4$_5$**, 6 **GCp-4$_{10}$** and 6 **GCp-4$_{25}$** as detailed:

GCp-4$_0$: The 6 **GCp-4X** were individually cycled (5 times, from 0 V to 0.8 V), washed with water, dried under N_2 and frozen. Once the 6 **GCp-4X** were cycled identically, they were stacked and kept under liquid N_2 until measurement.

GCp-4$_5$: The 6 **GCp-4X** were individually cycled (5 times, from 0 V to 1.2 V), washed with water, dried under N_2 and frozen. Once all modified identically, they were stacked and kept under liquid N_2 until measurement.

GCp-4$_{10}$ and **GCp-4$_{25}$** were modified as **GCp-4$_5$** but 10 and 25 cycles (from 0 V to 1.2 V) were performed respectively.

XAS at the ruthenium K-edge was performed at the SuperXAS beamline at Swiss Light Source (SLS at Paul Scherrer Insitute, Villigen, Switzerland) with the storage ring operated in top-up mode (400 mA). Fluorescence-detected XAS spectra were measured with a 12-element energy-resolving Ge-detector (Canberra) shielded by an Mo foil (25 µm) against scattered incident X-rays) on samples held in a liquid-helium cryostat (Oxford) at 20 K using excitation by X-rays from a channel-cut [Si111] monochromator. Harmonics rejection was achieved by a platinum-covered toroidal mirror in grazing incidence. The beam was shaped by slits to a spot size on the sample

VI

of about 4x0.5 mm^2. Energy calibration of each scan was done using the peak at 22117 eV in the first derivative of absorption spectra of a Ru–metal powder measured in parallel to the samples. For XAS on immobilized Ru complexes, 6 glassy carbon sheets with sub-monolayer coverage of the complexes were stacked in the cryostat and placed at an angle of 45° to the incident beam. Up to 15 XAS spectra of each sample (scan duration ~20 min per sample spot) were averaged, normalized, and EXAFS spectra were extracted as described previously. [S6] EXAFS simulations were carried out using the in-house software SimX[S7] and phase functions calculated with FEFF8. [S8]

XPS experimental details

XPS measurements were performed at room temperature with a SPECS PHOIBOS 150 hemispherical analyzer (SPECS GmbH, Berlin, Germany)) in a base pressure of $1x10^{-10}$ mbar using monochromatic Al Kα radiation (1486.74 eV) as excitation source.

Preparation of Samples: **GCr$_7$-4** (Γ = 0.2 nmol/cm^2), **GCr$_7$**-RuO_2 (Γ = 0.2 nmol/cm^2) and bare **GCr$_7$** (grey solid line) were prepared on **GCr7** electrodes that were cut to a length of 0.5 cm to fit the size of the XPS analyzer. **GCr$_7$-4** was obtained by cycling 2 times **GCr$_7$-4X** between 0 V to 0.9 V at pH=7. **GCr$_7$**-RuO_2 was obtained by cycling **GCr$_7$-4X** 50 times between 0 V to 1.2 V.

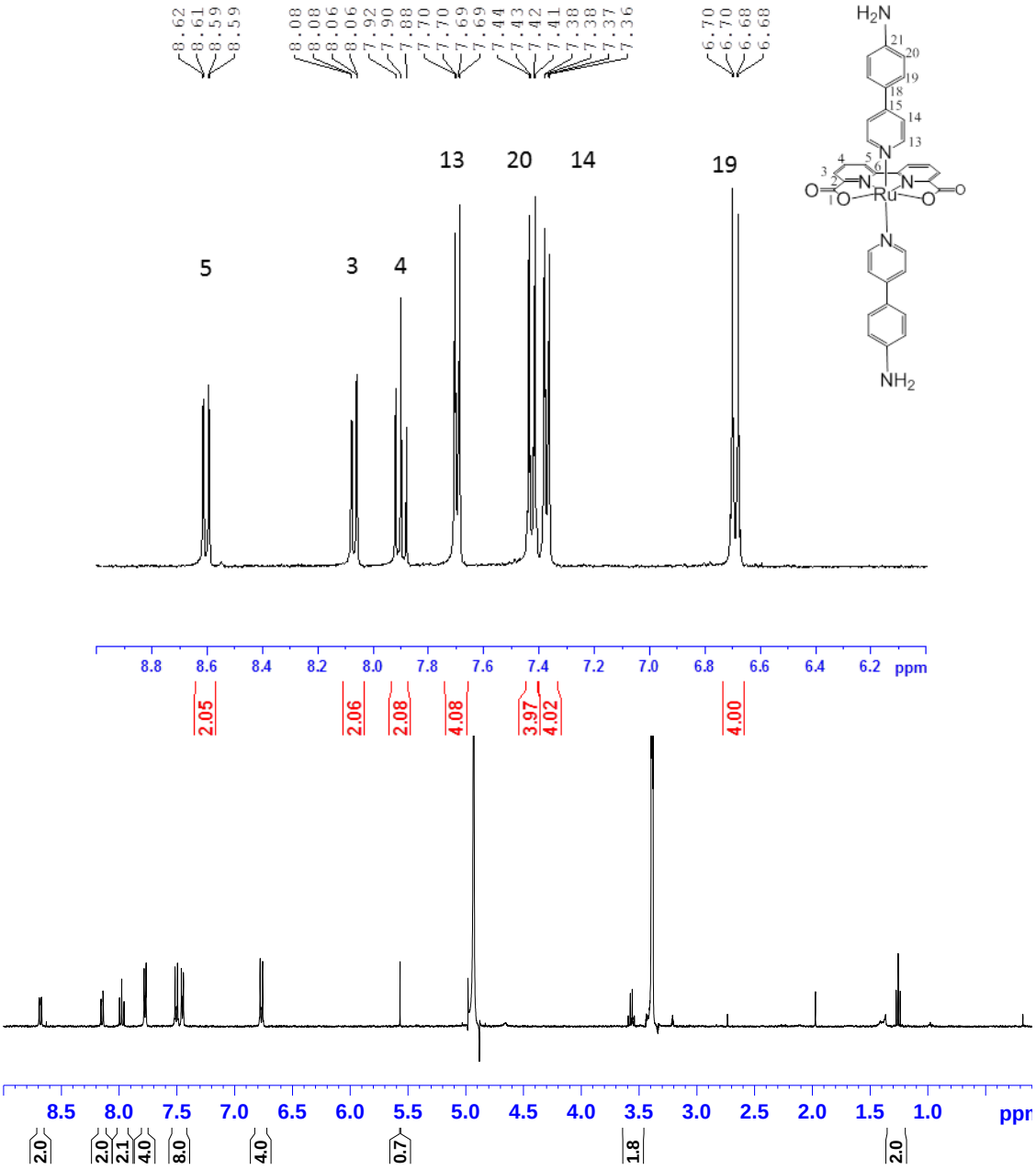

Figure S1. ^{1}H-NMR of **1** in [d4]-methanol, T=298K (bottom) and enlargement between 9.0 and 6.0 ppm.

VI

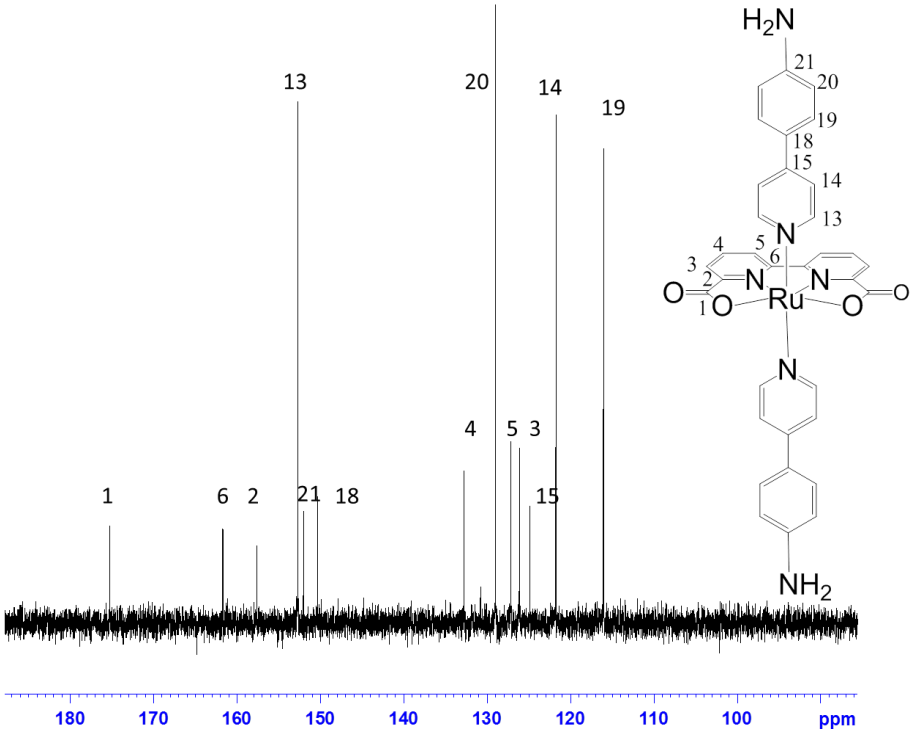

Figure S2. ^{13}C-{H}-NMR of **1** in [d4]-methanol, T=298K.

VI

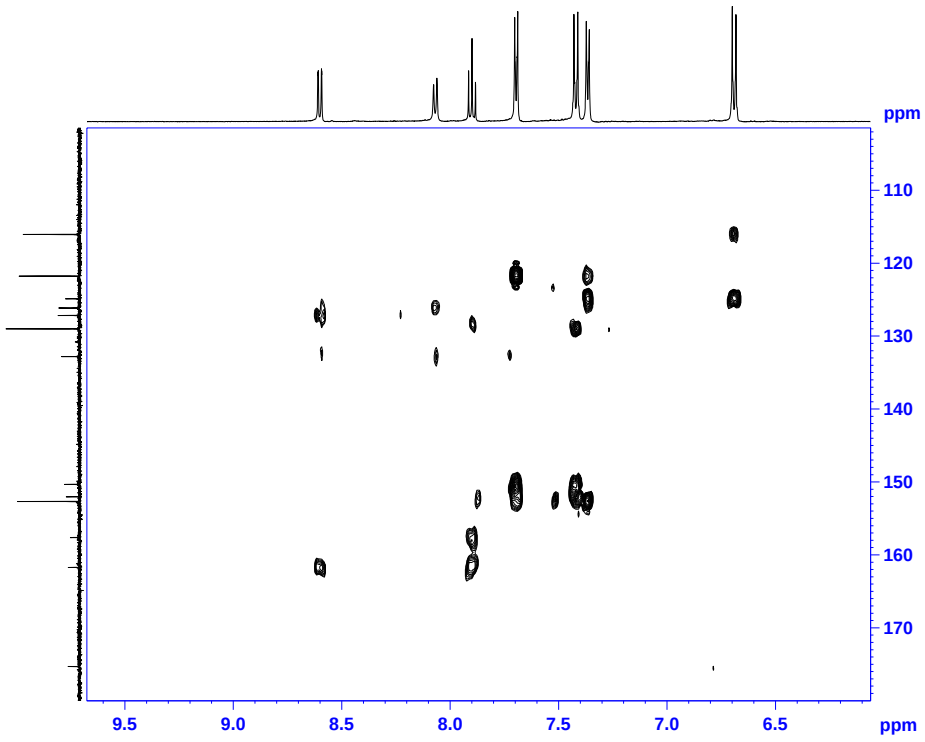

Figure S3. ^{1}H-^{13}C-HMBC NMR of **1** in [d4]-methanol, T=298K.

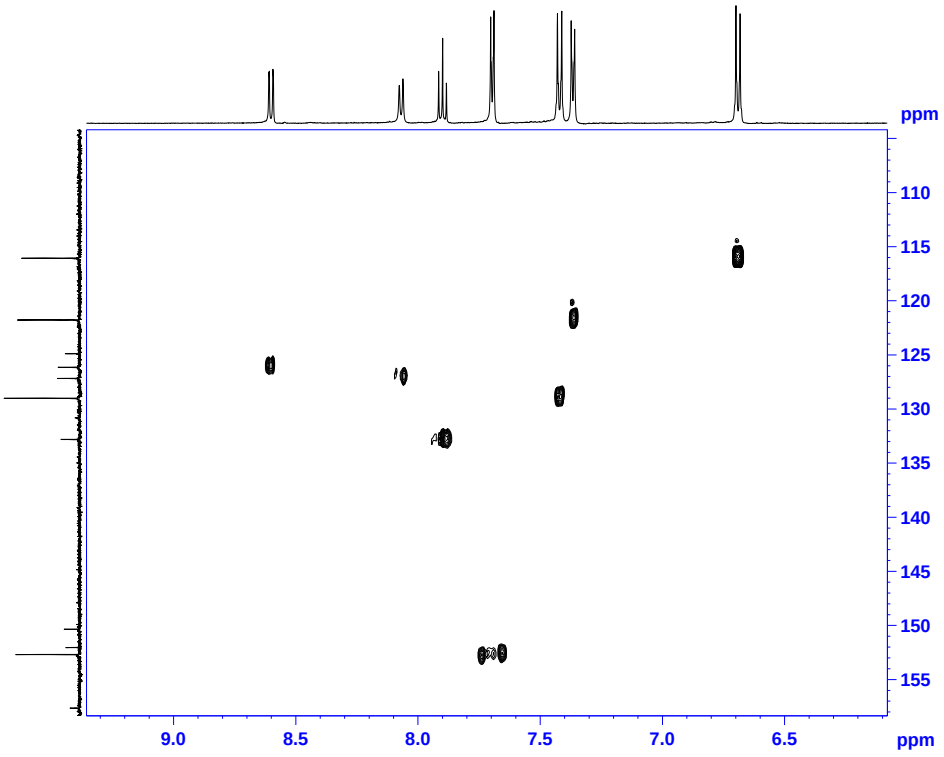

Figure S4. ^{1}H-^{13}C-HSQC NMR of **1** in [d4]-methanol, T=298K

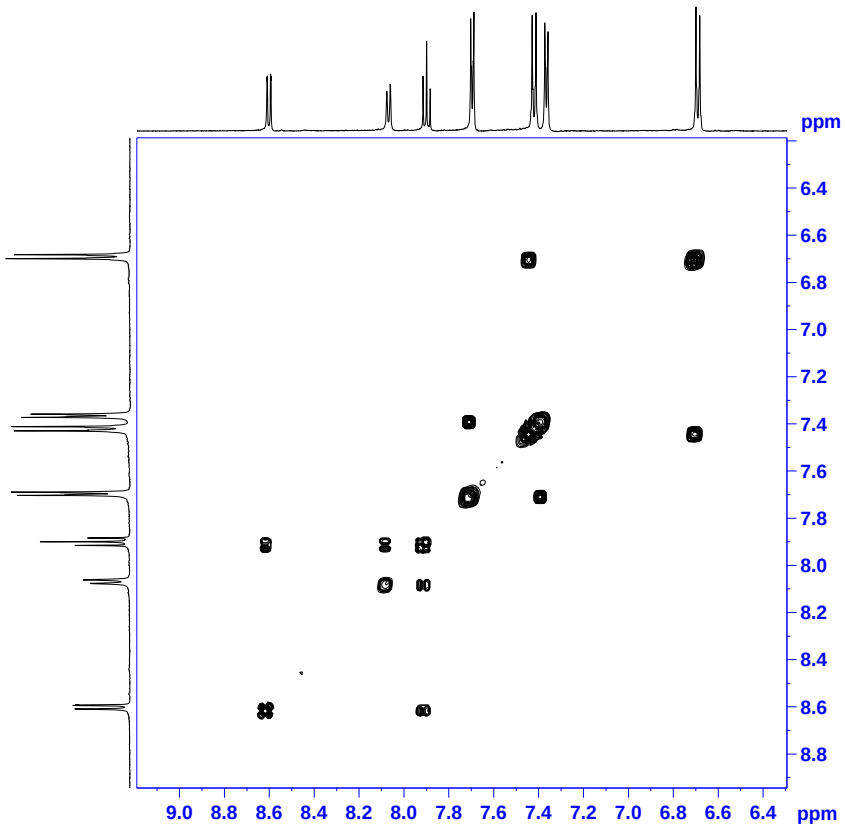

Figure S5. ^{1}H-^{1}H-COSY NMR of **1** in [d4]-methanol, T=298K

VI

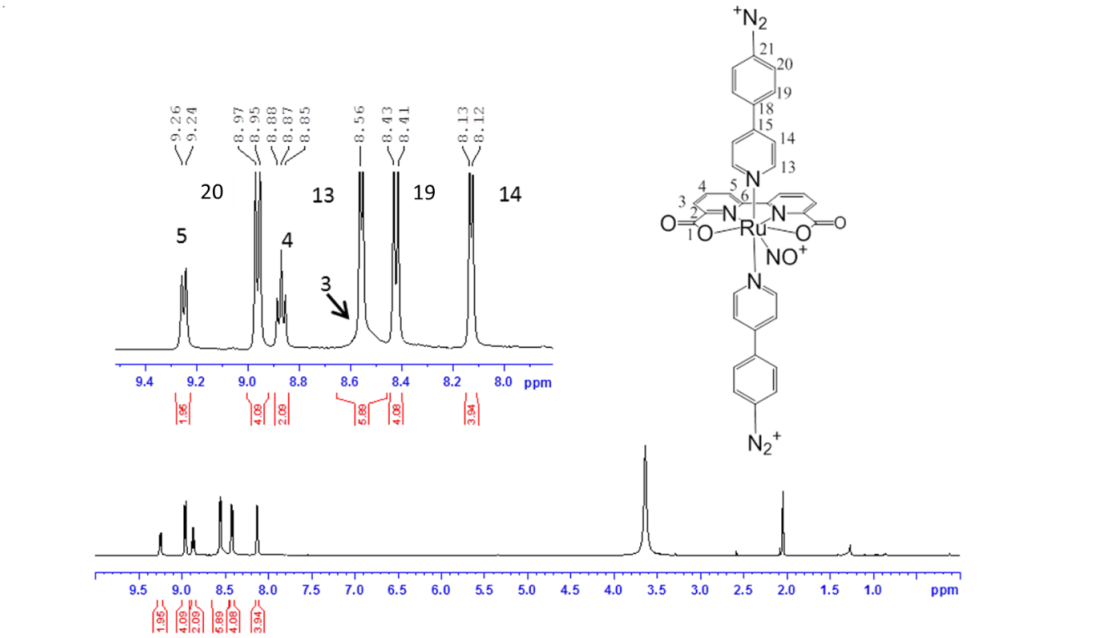

Figure S6. ^{1}H-NMR of (**2**)$(PF_6)_3$ in [d6]-acetone, T=273K. Inset: enlargement in the 9.6-7.8 ppm region.

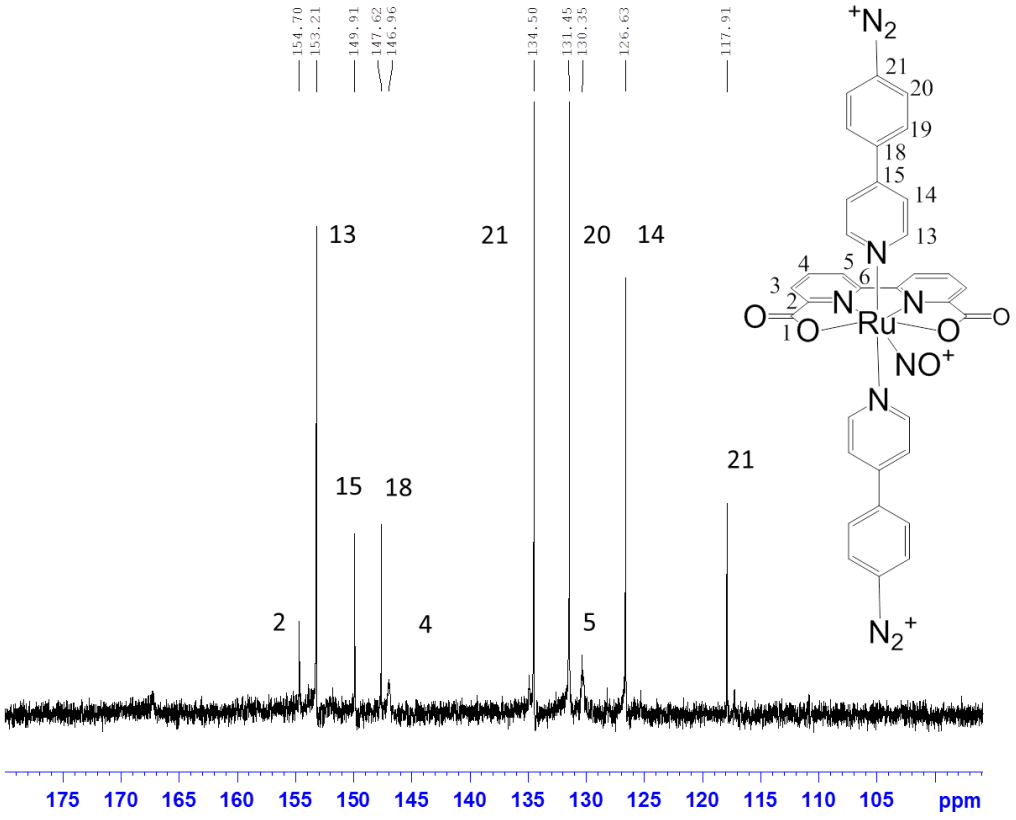

Figure S7. ^{13}C-{H}-NMR of **2**$(PF_6)_3$ in [d6]-acetone, T=273K.

VI

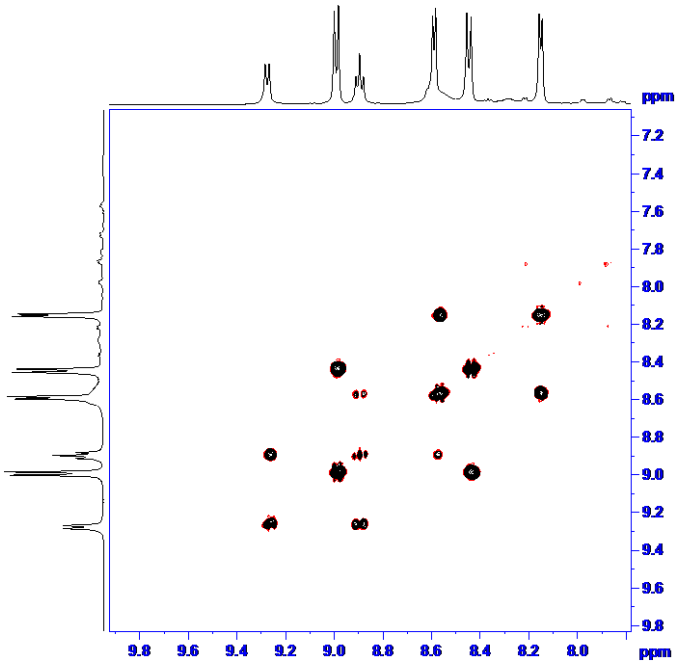

Figure S8. ^{1}H-^{1}H COSY NMR of (**2**)$(PF_6)_3$ in [d6]-acetone, T=273K

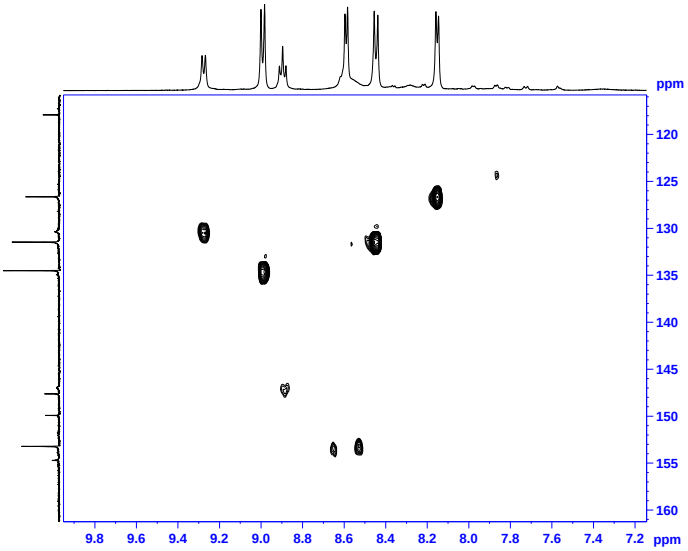

Figure S9. ^{1}H-^{13}C-HSQC NMR of (**2**)$(PF_6)_3$) in [d6]-acetone, T=273K.

VI

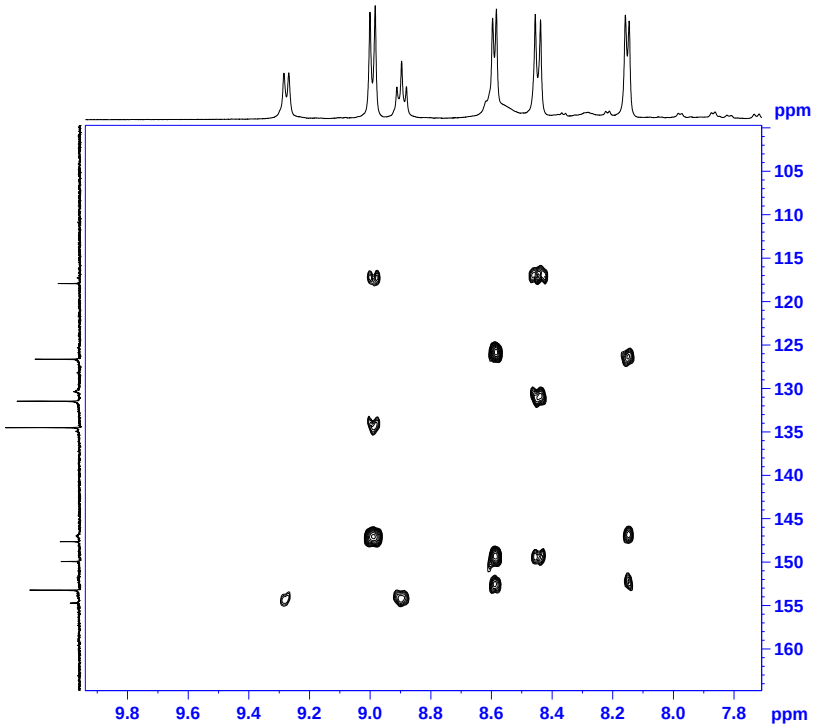

Figure S10. ^{1}H-^{13}C-HMBC NMR of (**2**)$(PF_6)_3$) in [d6]-acetone, T=273K.

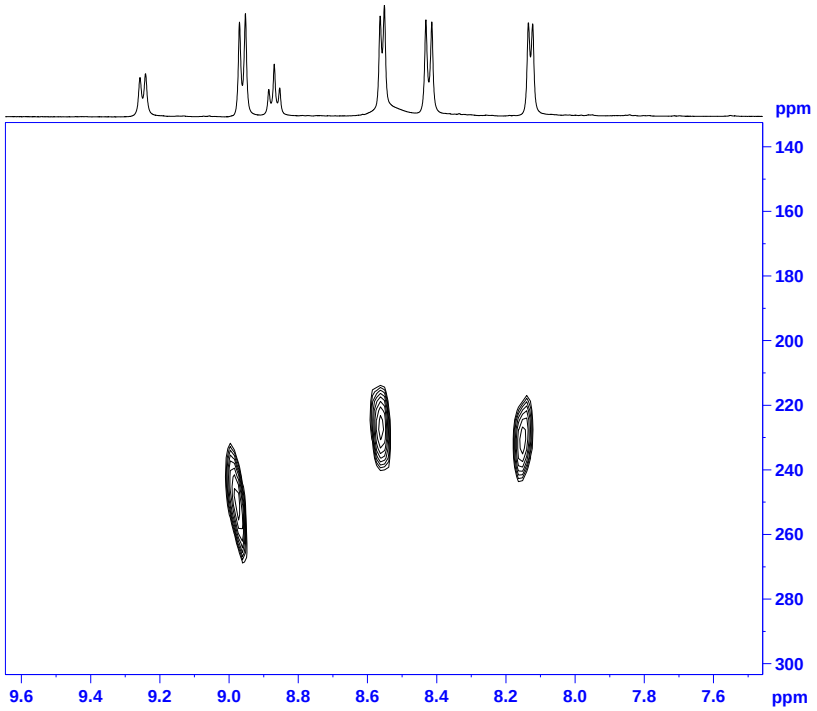

Figure S11. ^{1}H-^{15}N-HMBC NMR of (**2**)$(PF_6)_3$) in [d6]-acetone, T=273K.

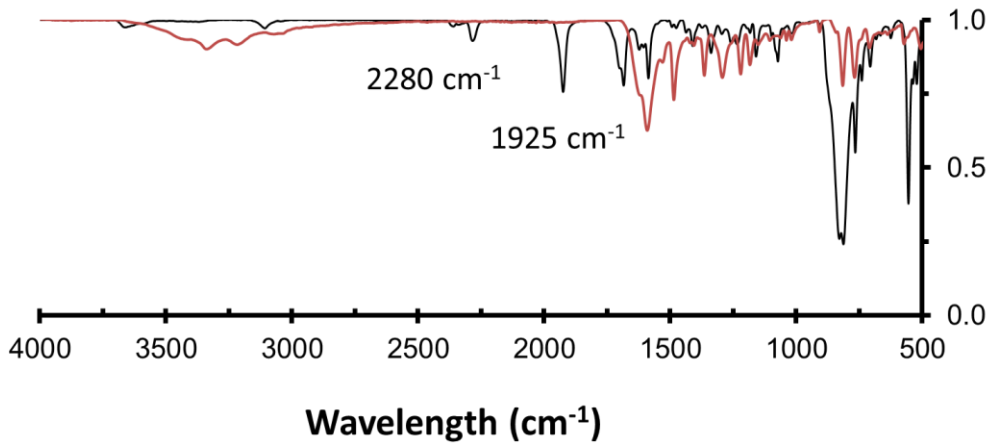

Figure S12. IR spectra for compounds: **1**(red) and (**2**)$(PF_6)_3$ (black).

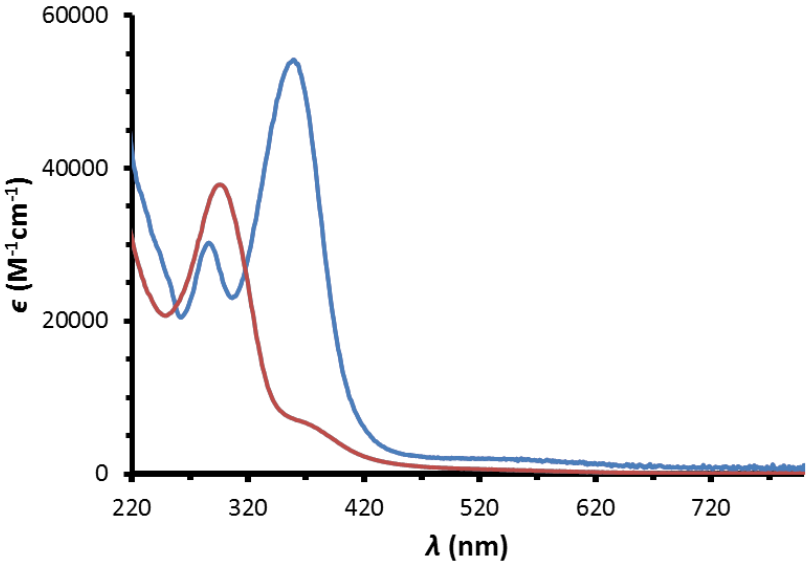

Figure S13. UV-Vis spectra for compound **1** (0.01 mM, blue line) and **2**$(PF_6)_3$ (0.03 mM, red line).

VI

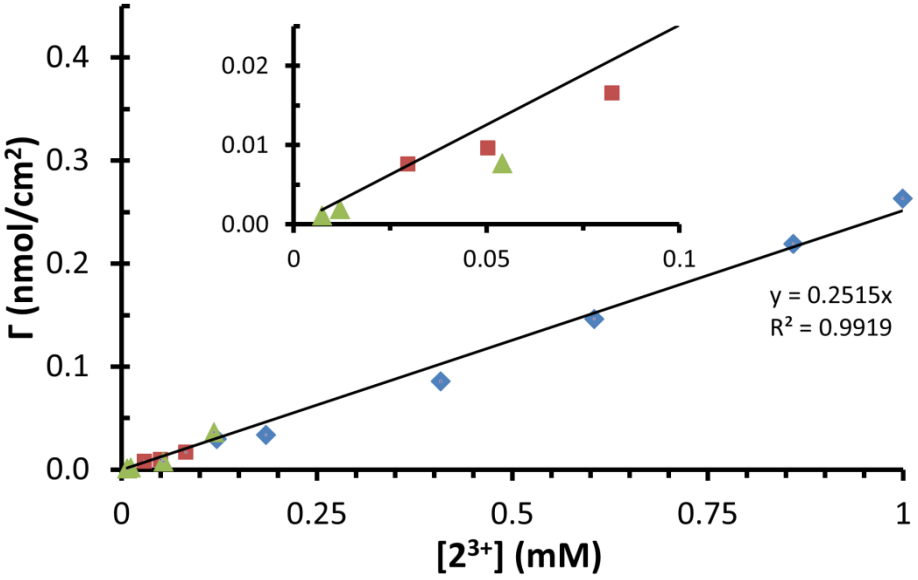

Figure S14. Representation of the superficial concentration *Γ* (nmol/cm^2) of **4X** versus diazonium salt concentration used to modify the electrodes. Three carbon electrodes were modified to cover the whole [**2**$^{3+}$] range (**GC- , GC$_5$- and GC$_7$-**). The superficial concentration of **GC-4X** (blue diamonds), **GCr$_5$-4X** (red squares) and **GCr$_7$-4X** (green triangles) were estimated in a pH = 7.0 buffered solution by integrating the oxidative waves as explained above. Inset shows an enlargement of the graph in the region of [**2**$^{3+}$] between 0 and 0.1 mM.

VI

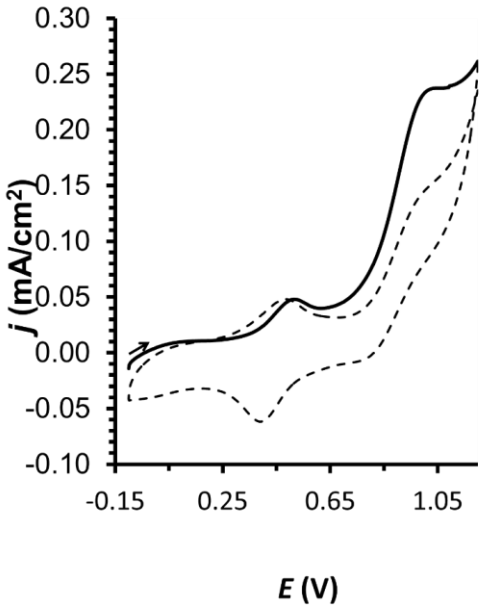

Figure S15: Cyclic voltammetric analysis of **GC-4X** in the two first scans (1st as a solid line and 2nd as a dashed line) from -0.1 V to 1.2 V to convert **GC-4X** to **GC-4** in a pH=7 solution.

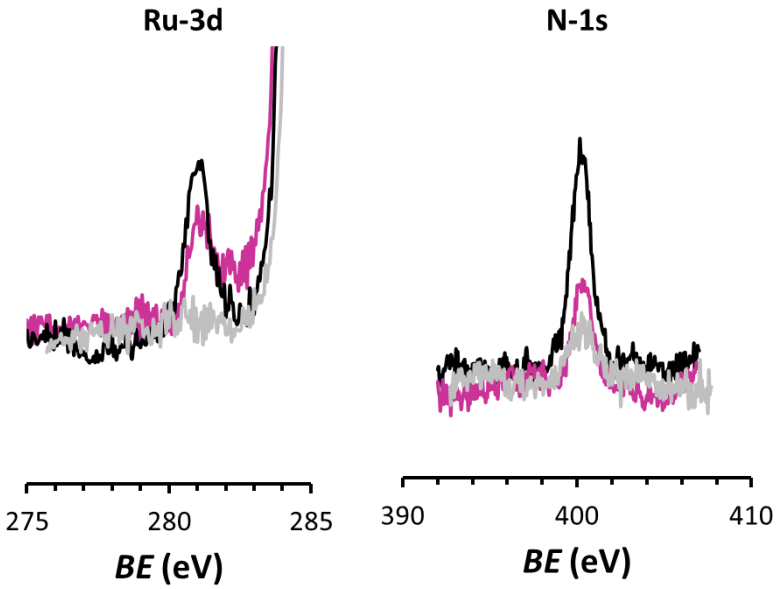

Figure S16: XPS of the Ru(3d) and N-1s regions (left and right respectively) of **GCr$_7$-4** (red solid line, Γ = 0.2 nmol/cm^2), **GCr$_7$**-RuO_2 (magenta solid line, Γ = 0.2 nmol/cm^2) and bare **GCr$_7$** (grey solid line). The y axis represents arbitrary counts and the counts have been normalized against the C-1s signal of each sample.

VI

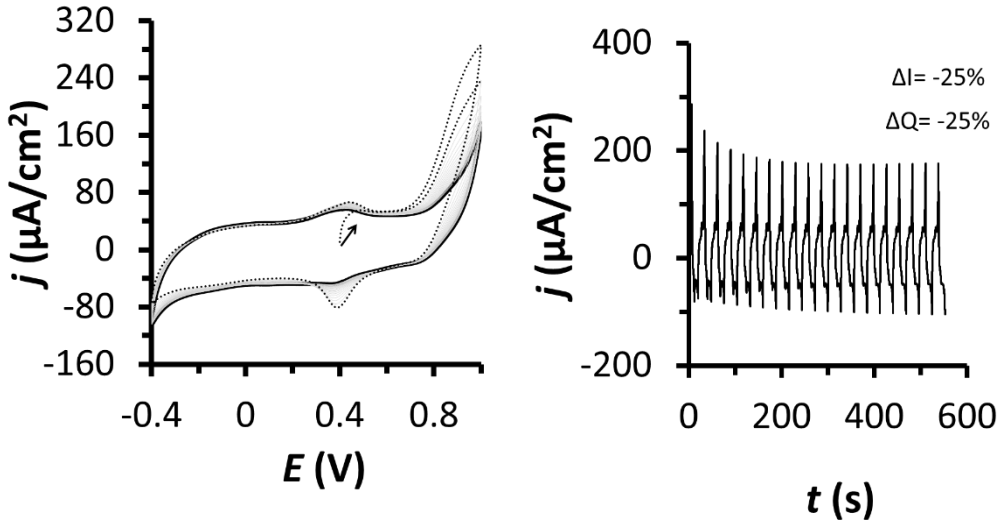

Figure S17: Cyclic voltammetric analysis of the electrocatalytic performance of **GC-4** upon 20 repetitive scans up to 1.0 V. Current density *vs.* potential (left) and current density *vs.* time (right) for a 20-cycle CV between -0.4 V and 1.0 V in a pH = 7 phosphate buffered solution. **GC-4X** (Γ = 0.2 nmol/cm^2, [**2**$^{3+}$]= 1 mM, S=0.07 cm^2) was converted to **GC-4** cycling 20 times between -0.4 V and 0.7 V. The current and charge loss, ΔI and ΔQ respectiviely, indicates the charge of the 0.51 V wave lost and current lost at E=1.0 V between the second and the last cycle. The dashed line corresponds to the first cycle whereas the black line corresponds to the last one. In grey are depicted the rest of the cycles.

VI

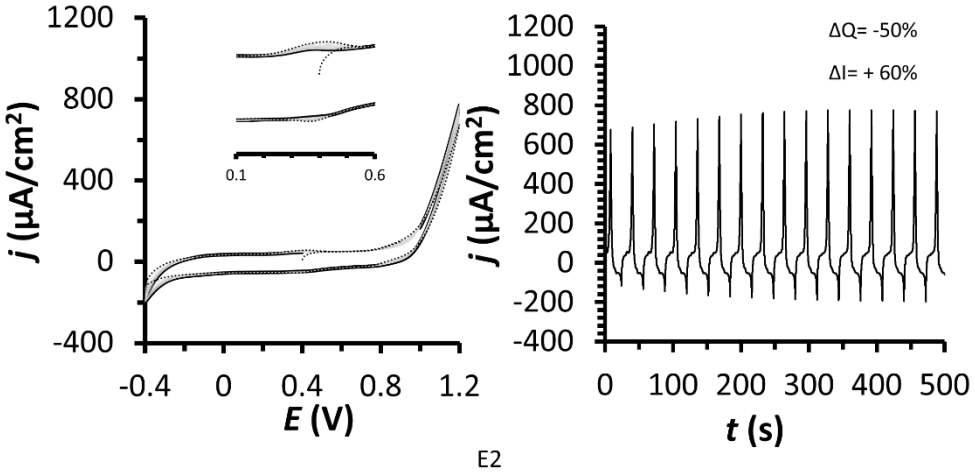

E2

Figure S18: Cyclic voltammetry analysis of the electrocatalytic performance of **GC-4** upon 20 repetitive scans up to 1.2 V. Current density vs potential (left) and current density vs time (right) for a 20-cycle CV between -0.4 V and 1.2 V in a pH=7 phosphate buffered solution. **GC-4X** (Γ= 0.2 nmol/cm^2, [**2**$^{3+}$]= 1 mM, S=0.07 cm^2) was converted to **GC-4** cycling 20 times between -0.4 V and 0.7 V and was previously cycled between -0.4 V and 0.7 V and -0.4 V and 0.9V (see Figure S17). The current and charge loss, ΔI and ΔQ respectiviely, indicates the charge of the 0.52 V oxidative wave lost and current lost at E=1.2 V between the second and the last cycle. The dashed line corresponds to the first cycle whereas the black line corresponds to the last one. In grey are depicted the rest of the cycles.

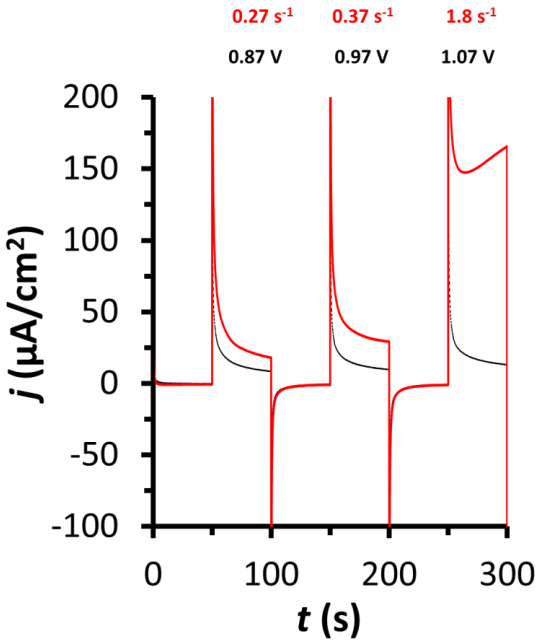

Figure S19. Chronoamperometric measurement performed in a potassium phosphate buffer (pH 7.0, I=0.1 M) of **GC-4** (red trace) and the bare **GC**- (black trace) under application of a sequence of potential steps shown in black above. **GC-4X** was used as working (modified with a [$\mathbf{2}^{3+}$] = 1 mM and Γ = 0.2 nmol/cm^2), Pt mesh as counter and SSCE as reference electrodes.

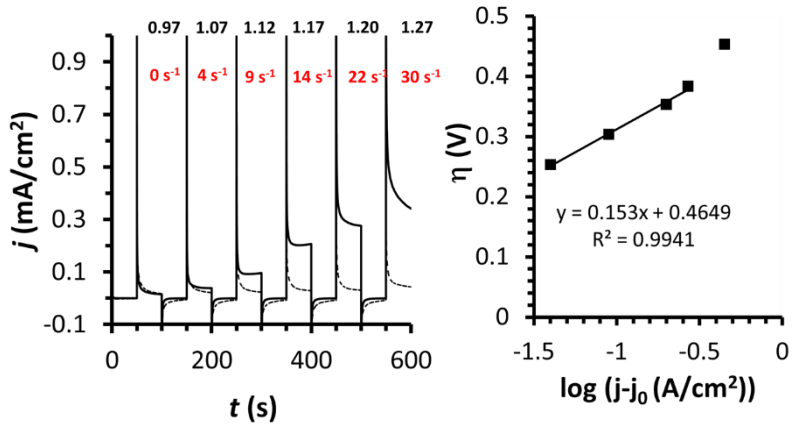

Figure S20. Left: Chronoamperometric measurement performed in a potassium phosphate buffer (pH 7.0, I = 0.1 M) of **GC-RuO$_2$** (solid trace, 0.04 nmol/cm^2) and the bare **GC**- (dashed trace) under application of a sequence of potential steps in volts shown in black above. **GC-RuO$_2$** was used as working, Pt mesh as counter and SSCE as reference electrodes. Right: Tafel plot versus overpotential (η) of **GC-RuO$_2$**.

Table S1: EXAFS simulation parameters.[a]

	N [per Ru atom] / R [Å] / $2\sigma^2$ x10^3 [Å^2]		R_F [%]
	Ru-C,N,O	Ru-Ru	
RuO_2	6* / 1.97 / 2	6* / 3.57 / 2	33.6
GC_p-4_0	3* / 2.02 / 7[&] 3* / 2.13 / 7[&] 10* / 3.02 / 29	0.04[§] / 3.57* / 2*	30.4
GC_p-4_5	3* / 2.00 / 4[&] 3* / 2.11 / 4[&] 10* / 3.04 / 34	0.58[§] / 3.57* / 2*	33.4
GC_p-4_{10}	3* / 1.99 / 5[&] 3* / 2.10 / 5[&] 10* / 3.09 / 27	1.05[§] / 3.57* / 2*	32.2
GC_p-4_{25}	3* / 1.98 / 6[&] 3* / 2.14 / 6[&] 10* / 3.07 / 33	1.29[§] / 3.57* / 2*	35.5

[a] N, coordination number; R, interatomic distance; $2\sigma^2$, Debye-Waller factor; R_F, error sum calculated for reduced distances of 1-3.5 Å. Fit restraints: *fixed parameters, [#]coordination numbers were coupled to yield a sum of 6, [&]Debye-Waller factors were coupled to yield the same value for the respective shells, [§]N was restraint to values ≥0.01. Multiple-scattering contributions were neglected in the EXAFS fits.

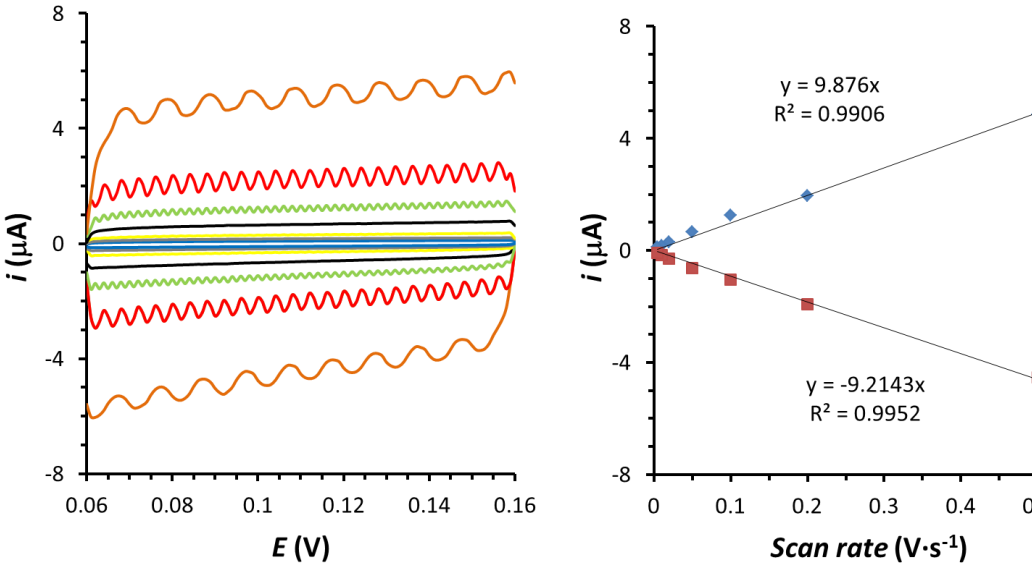

Figure S21: Representative double layer capacitance (C_D) measurements to determine ECSA of **GC-RuO$_2$** (Γ= 0.2 nmol/cm^2, [**2**$^{3+}$]= 1 mM, S = 0.125 cm^2). Left: CV was measured in the non faradaic region (OCP ± 0.05 V) at different scan rates: 0.5 V/s (orange line), 0.2 V/s (red line), 0.1 V/s (green line), 0.05 V/s (black line), 0.02 V/s (yellow line), 0.01 V/s (grey line) and 0.005 V/s (blue line). The working electrode was kept 10 seconds before running every segment. Right: The anodic and cathodic charging currents at 0.1 V are represented against the scan rate. A glassy carbon disk (r= 0.2 cm, S= 0.125 cm^2) was used as working electrode and was modified from a 1mM of **2**$^{3+}$ solution and converted to RuO_2 by applying

a potential E_{app} = 1.2 V during 400 seconds. The measurements were done in a static pH= 7 solution under 1 atm of O_2.

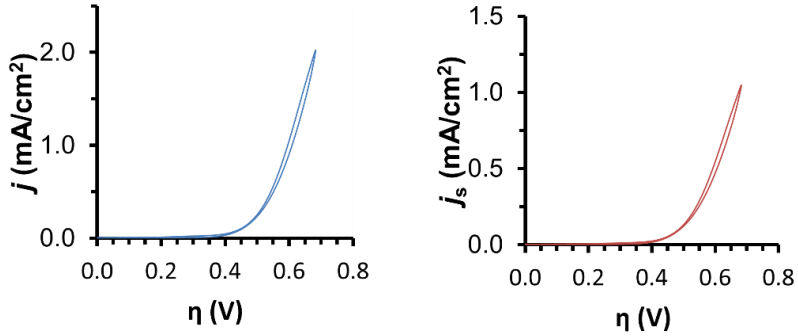

Figure S22: Rotating disk voltammograms of **GC-RuO₂** (Γ= 0.2 nmol/cm², [**2**$^{3+}$]= 1 mM, S=0.125 cm², RF= 1.9) at pH=7 under steady state conditions: 1 atm O_2, rpm=1600 and the scan rate was 10 mV/s. Left: plot of geometric current density, ***j*** (calculated by dividing the current intensity by the geometric area of the electrode) *vs*. overpotential. Right: Plot of specific current density, j_s (calculated by dividing geometric current density by estimated RF) *vs*. overpotential. **GC-RuO₂** (S= 0.125 cm²) was used as working electrode and was modified from 1 mM of **2**$^{3+}$ and converted to RuO_2 by applying a potential of E= 1.2V for 400 seconds.

VI

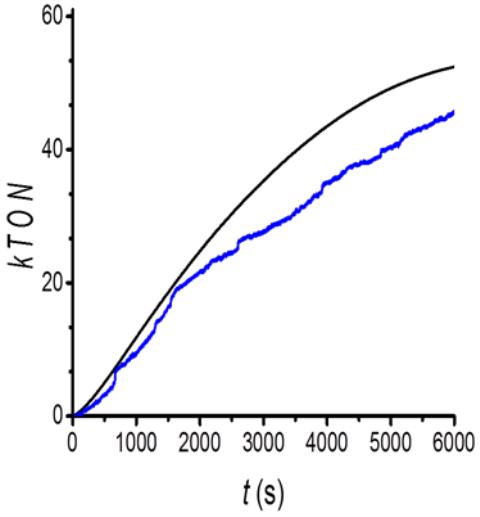

Figure S23. Oxygen-monitored bulk electrolysis (E_{app} = 1.15 V vs SSCE) using **GCs**-RuO_2 as working, Pt grid as counter and Ag/AgCl (sat KCl) as a reference electrodes**.** The number of TON vs time calculated from the current passed (black line) and from the amount of oxygen detected from the Clark electrode. No O_2 increase was detected during the bulk electrolysis (E_{app} = 1.15 V vs SSCE) of a bare **GCs-**. **GCs-4X** was prepared from a solution 0.5 mM (**2**)$(PF_6)_3$ and transformed to **GCs-**RuO_2 by applying a potential of 1.2 V for 6 minutes. The bulk electrolysis was performed in a 15 mL two-compartment cell filled with 12 mL of a phosphate buffered solution at pH = 7 (I = 0.1 M). The cell was refrigerated at 298 K for the whole experiment. A clark electrode was used to measure oxygen evolution. A Clark electrode was used to detect oxygen and was calibrated by accurately adding different volumes of 99% pure oxygen.

References:

S1 Duan, L.; Bozoglian, F.; Mandal, S.; Stewart, B.; Privalov, T.; Llobet, A.; Sun, L. *Nat. Chem.* **2012**, *4*, 418-423.
S2 Evans, I. P.; Spencer A.; Wilkinson, G.; *J. Chem. Soc., Dalton Trans.* **1973**, 204-209.
S3 Belanger, D.; Pinson, J. *Chem. Soc. Rev.* **2011**, *40*, 3995-4048.
S4 McCrory, C. C. L.; Jung, S.; Peters, J. C.; Jaramillo, T. F. *J. Am. Chem. Soc.* **2013**, *135*, 16977-16987.
S5 Over, H. *Chem. Rev.* **2012**, *112*, 3356-3426.
S6 (a) Vigara, L.; Ertem, M. Z.; Planas, N.; Bozoglian, F.; Leidel, N.; Dau, H.; Haumann, M.; Gagliardi, L.; Cramer, C. J.; Llobet, A. *Chem. Sci.* **2012**, *3*, 2576-2586. (b) Planas, N.; Christian, G.; Roeser, S.; Mas-Marza, E.; Kollipara, M.-R.; Benet-Buchholz, J.; Maseras, F.; Llobet, A. *Inorg. Chem.* **2012**, *51*,1889-1901.
S7 Dau, H.; Liebisch P.; Haumann, M; *Anal. Bioanal. Chem.* **2003**, *376*, 562-583.
S8 Zabinsky, S. I.; Rehr, J. J.; Ankudinov, A. L.; Albers, R. C. and Eller, M. J. *Phys. Rev.* **1995**, *52*, 2995-3009.

PAPER H A Million Turnover Molecular Anode for Catalytic Water Oxidation

Creus, J.; Matheu, R.; Peñafiel, I.; Moonshiram, D.; Blondeau, P.; Benet-Buchholz, J.; García-Antón, J.; Sala, X.; Godard, C.; Llobet, A. *Angew. Chem. Int. Ed.* **2016**, *55*, 15382-15386.

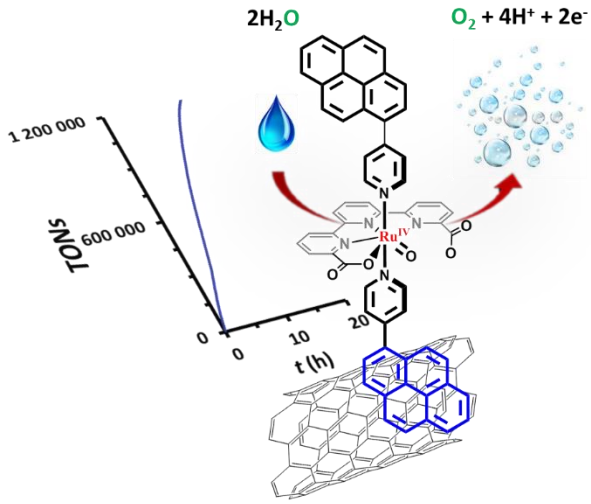

Abstract

Molecular Ru based water oxidation catalysts precursors of general formula [Ru(tda)(L^i)$_2$] (tda^{2-} is [2,2':6',2''-terpyridine]-6,6''-dicarboxylato; L^1 = 4-(pyren-1-yl)-N-(pyridin-4-ylmethyl)butanamide, **1b**; L^2 = 4-(pyren-1-yl)pyridine), **1c**), have been prepared and thoroughly characterized. Both complexes contain a pyrene group allowing ready and efficiently anchoring via π interactions on Multi-Walled Carbon Nanotubes (MWCNT). These hybrid solid state materials are exceptionally stable molecular water oxidation anodes capable of carrying out more than a million Turnover Numbers (TNs) at pH 7 with an E_{app}=1.45 V vs. NHE without any sign of degradation. XAS spectroscopy analysis before, during and after catalysis together with electrochemical techniques allow to monitor and verify their unprecedented oxidative ruggedness.

Contributions

Jordi Creus and Roc Matheu designed together the project, synthetized , performed the electrochemical measurements and prepared the manuscript.

VI

H 1 Introduction

Visible light induced water splitting to produce hydrogen fuel is one of the potential alternatives to fossil fuels.[1] To achieve this goal, powerful and rugged Water Oxidation Catalysts (WOCs) that can be anchored onto solid-state devices to facilitate water splitting cell assembling and engineering are needed.[2-5]In the molecular front, it is imperative to have water oxidation catalysts that can work under restricted translational mobility conditions,[6] and whose O-O bond formation step occurs via a "Water Nucleophilic Attack" mechanism (WNA).[7,8] Molecular WOCs whose low energy O-O bond formation pathways in homogeneous phase occur via an "Interaction of 2 M-O units" (I2M) might still be able to carry out the catalytic water oxidation reaction at the surface of an electrode, but will need to proceed through higher energy pathways that can lead to catalyst degradation.[5] Further, given the intrinsic high energy demands for the water oxidation catalysis, it is essential that the anchoring groups that act as an interface between the catalysts and surface are oxidatively resistant.

Here on, we report new hybrid materials consisting of molecular WOCs anchored onto Multi-Walled Carbon Nanotubes (MWCNTs) via π-stacking interactions.[9] The resulting materials are extremely stable and allow the anchoring of a large amount of catalyst giving Turnover Numbers (TNs) over a million without apparent deactivation.

VI

H 2 Results and Discussion

In a recent publication,[10] we have reported the synthesis of complex $\{Ru^{II}(tda)(py)_2\}$, **1a**, (for a drawing of tda^{2-} see Scheme 1) and have shown that in its high oxidation states (IV) acts as a precursor for the formation of $\{Ru^{V}(O)(tda)(py)_2\}^{+}$. The latter is the most powerful molecular water oxidation catalyst described to date achieving Turnover Frequencies (TOF) in the range of 50.000 s^{-1}. In addition, we showed that the rate determining step for the water oxidation reaction is the O-O bond formation, which in this case occurs via WNA, as evidenced by kinetics and further supported by DFT calculations.

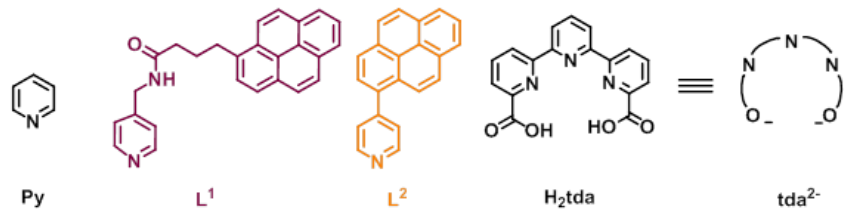

Complex-Material/Axial L	py	L^1	L^2
$[Ru^{II}(tda)L_2]$	**1a**	**1b**	**1c**
$[Ru^{II}(tda)L_2]$@MWCNT@GC	--	**2b**	**2c**
$[Ru^{IV}(tda)L_2]^{2+}$@MWCNT@GC	--	$\mathbf{2b}^{2+}$	$\mathbf{2c}^{2+}$
$[Ru^{IV}(O)(tda)L_2]$@MWCNT@GC	--	**3b**	**3c**

Scheme 1. Drawing of the ligands discussed in the present work (top) and complex labelling strategy (bottom).

Given the remarkable performance of $\{Ru^{V}(O)(tda)(py)_2\}^{+}$, we proceeded to anchor it on conductive solid supports with the aim of generating a powerful hybrid anode for the electrocatalytic oxidation of water to dioxygen, that could be potentially incorporated in water splitting devices. For this purpose, we used MWCNTs as support, given their high stability, conductivity and large electrochemically active surface area.[7,11] Further, MWCNTs were selected because of their inertness as compared to oxides that can potentially block labile Ru-aqua groups and thus reduce or even suppress the activity of the catalyst.[12] Moreover, this anchoring approach avoids the use of phosphonate or carboxylate moieties that have a limited stability in water in the presence of a supporting electrolyte under irradiation.[13] In order to anchor our catalyst on MWCNTs, we prepared pyridyl type of ligands functionalized with the pyrenyl group as shown in Scheme 1, so that they can be anchored on MWCNTs via π-stacking interactions without significantly modifying the intrinsic electronic and geometrical properties of the parent complex.[14] We synthesized ligand L^1 that contains an amide group as previously described,[15] and a new ligand L^2 that contains a direct C-C bond between the pyridyl group and the pyrene moiety, see Supporting Information (SI) for details. The latter strategy avoids the use of easily oxidizing methylene groups, which is fundamental for the long-term performance of any molecular water oxidation catalysts.[16]

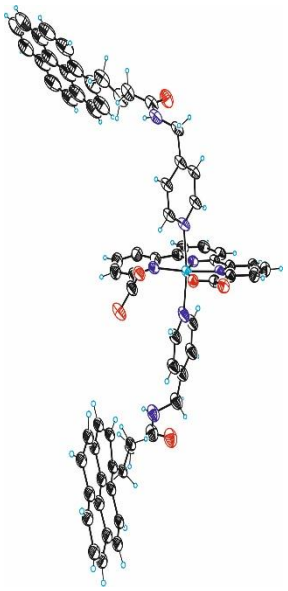

Figure 1. ORTEP plot of the catalyst precursor $\{Ru^{II}(tda)(L^1)_2\}$, **1b**, (ellipsoids drawn at 50% probability). Color code: Ru, cyan; N, navy blue; O, red; C, black; H, small cyan open circles.

The synthesis of complexes $\{Ru(tda)(L^i)_2\}$ (i = 1, **1b**; i = 2, **1c**), is straightforward and similar to related complexes (see details of the synthesis in the SI).[10,15]A single crystal X-ray structure has been solved for **1b** and its ORTEP plot is shown in Figure 1. The latter complex shows a distorted octahedral coordination around the Ru(II) metal ion with the tda^{2-} ligand acting in a κ-N^3O fashion and leaving one of the carboxylate moieties uncoordinated. The axial positions are occupied by two pyridyl moieties from two L^1 ligands. Overall, the structure of **1b** shows a very similar first coordination sphere for the reported Ru as compared to **1a**.[8] In order to further electronically and structurally characterize these complexes, X-ray Absorption Spectroscopy (XAS) was carried out for powders of **1a**, $\{Ru^{III}(tda)(py)_2\}(PF_6)$ (**1a**(PF_6)), $\{Ru^{IV}(tda)(py)_2\}(PF_6)_2$ (**1a**$(PF_6)_2$), **1b** and RuO_2 and the results are shown in Figure 2A and the SI. In all cases the half-edge energies obtained from X-ray Absorption Near Edge Structure (XANES) were consistent with the oxidation state assignment, and the metric parameters obtained by Extended X-ray Absorption Fine Structure (EXAFS) were very similar to those of related X-ray structures (Table S3).[8]

Glassy Carbon Disks (GC_d, S = 0.07 cm^2) were used as working electrodes (WE) for all the electrochemical work described here except when larger surface areas were needed. In the latter case, Glassy Carbon Plates (GC_p, S = 1 cm^2) were used. Further, a Pt disk and a $Hg/HgSO_4$ electrode were used as auxiliary and reference electrode respectively. All the potentials reported here are converted to NHE by adding 0.65 V.

Conductive electrode materials were prepared by depositing a few µL of a suspension of MWCNTs on the surface of glassy carbon electrodes. The solvent was then allowed to evaporate and the new materials were labeled as "MWCNT@GC". They were then soaked in a solution of the catalyst precursor **1b** or **1c** affording the hybrid anode materials "{Ru^{II}(tda)(L^{i})$_2$}@MWCNT@GC" (i = 1, **2b**; i = 2, **2c**), that contained the catalyst precursor attached to the MWCNTs and were characterized by electrochemical techniques and XAS.

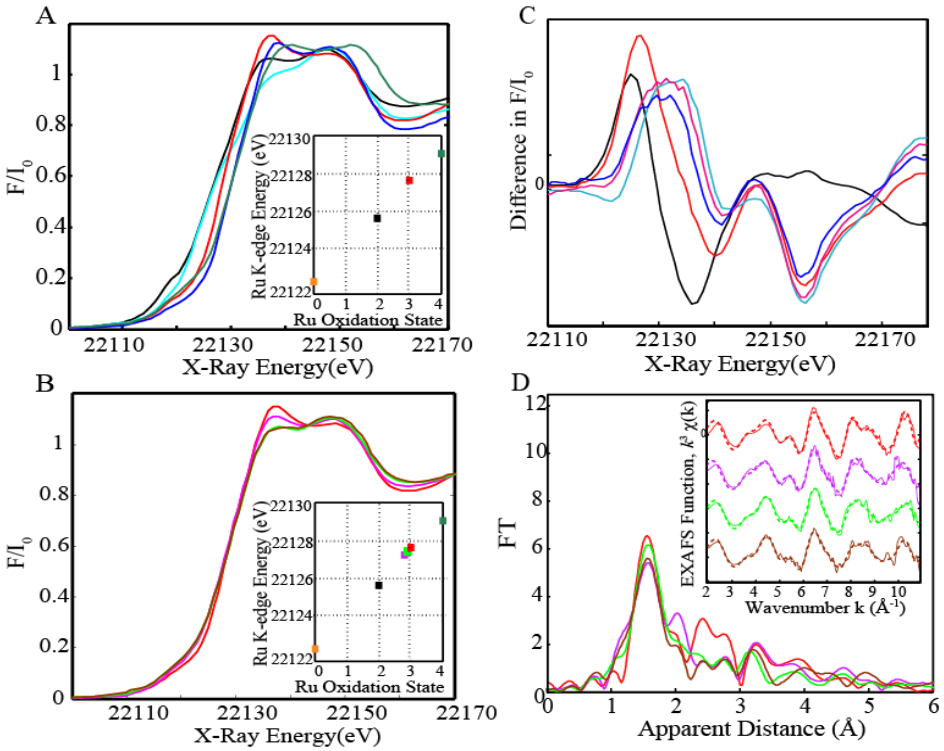

Figure 2. A, Normalized Ru K-edge XANES for **1a** (black), **1b** (cyan), **1a**$^{+}$ (red), **1a**$^{2+}$ (blue) and RuO_2 (dark green). *Inset*: Plot of half k-edge energy *vs*. oxidation state for Ru^0 metal (orange), **1a** and **1b** (black), **1a**$^{+}$ (red) and RuO_2 (dark green). B, Normalized Ru K-edge XANES for **1a**$^{+}$ (red), **2b**^{0} (magenta), **2b'** (light green) and **2b"** (brown). *Inset*: Plot of half k-edge energy vs oxidation state (same color code as in A) **2b^{0}** (magenta), **2b'** and **2b"** (light green). C, Difference spectra for: **1b**-**1a**$^{+}$ (black), **1b**-RuO_2 (red), **1a**$^{+}$-RuO_2, (cyan), **2b**-RuO_2 (magenta) and **2b"**-RuO_2 (blue). D, Fourier transforms of k^3-weighted Ru EXAFS for the Ru(III) complexes, **1a**$^{+}$ (red) and **2b**$^{+}$: (**2b^{0}**-20% **1b**) magenta, (**2b'**-10% **1b**) (light green) and (**2b''**-10% **1b**) brown. D. Back Fourier transformed experimental (solid lines) and fitted (dashed lines) $k^3\chi(k)$. Experimental spectra were calculated for k values of 1.941-10.9 $Å^{-1}$.

The amount of molecular complex deposited on the surface of the electrode turned out to be of Γ_{2b} = 6.35 nmol/cm^2 for **2b** and Γ_{2c} = 0.20 nmol/cm^2 for **2c.** Further, XAS was carried out for **2b** anchored on GC_p in order to additionally characterize the nature of these hybrid materials. Unfortunately, the lower catalyst loading obtained for **2c**, even supported in the GG_p electrode, prevented its XAS analysis. For **2b** it was found that the nature of the molecular species attached

VI

to the surface of the MWCNTs was identical to those of the precursor complexes, except that atmospheric oxygen had oxidized the initial Ru(II) complex to Ru(III) by 80%, as revealed by XANES and EXAFS (Figure 2B, Table S2). Additional evidence for this oxidation phenomenon was obtained by measuring the Open Circuit Potential (OCP) as a function of time for a sample of **2b** in an open atmosphere (see Figure S29). We labelled this partially oxidized material as **2b**^{0}, and showed that its Ru *κ*-edge at half peak neatly correlates with oxidation state 2.8 and thus indicates that the sample **2b**^{0} contains 80% **2b**$^{+}$ and 20% **2b** (Figure 2B, magenta). In addition, the simulated EXAFS experiments for **2b**$^{+}$ (**2b**^{0}-20% **1b**) also gives very good fits and thus further supports this point (see Figure 2D, Figure S32, Table S4 and Table S5 (fit 4)). The EXAFS simulations were carried out assuming a coordination number of 6 (5N, 1O) for Ru(II) and assuming the typical pseudo-octahedral geometry expected for a Ru(II) d^{6} ion. On the other hand, for Ru(III) a coordination number of "6.5" was assumed (5N, 1O, 0.5O), with a distorted octahedral coordination containing an additional oxygen contact (Ru-O distance of 2.4 Å), in a similar manner as found in the X-ray structure of **1a**$^{+}$ (Figure S31, Table S4, fit 12). [8] The data fit obtained for **1a**$^{+}$ is very similar to that obtained for **2b**$^{+}$ reflecting their structural similarities.

To generate the active catalyst at the surface of the electrode material, a potential of 1.25 V was applied for 500 s under stirring at pH 12 to **2b** or **2c**. This process oxidizes the initial Ru(II) complex to its oxidation state IV, where the coordination of a hydroxide anion occurs readily, [8] as indicated in the equations 1 and 2 for **2b**.

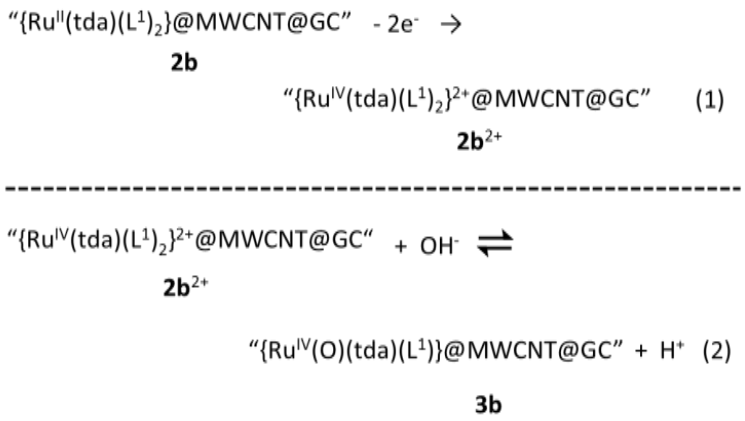

Once generated, the active hybrid materials were removed from the pH 12 solution, rinsed with water and introduced in another solution at pH 7. Under these conditions, a mixture of **2b**$^{2+}$ and **3b** is generated with an approximate ratio of 5:1 that remains in equilibrium, as deduced from cyclic voltammetry (CV) experiments at pH 7 (See Figure 3 left).

Figure 3 shows that for the precursor material, waves for the III/II and IV/III couples are observed at 0.55 V and 1.10 V respectively, together with a large current density that appears at 1.3-1.4 V associated with the oxidation of the MWNCTs. On the other hand, on the CV of the **2b**$^{2+}$:**3b** mixture, additional small waves appear in the 0.6-0.9 V potential range associated with the electroactivity of the anchored {Ru^{IV}(O)(tda)(L^{1})$_2$} catalyst, **3b**, as we have earlier described for its homologue {Ru^{IV}(O)(tda)(py)$_2$} in homogeneous phase. [8]

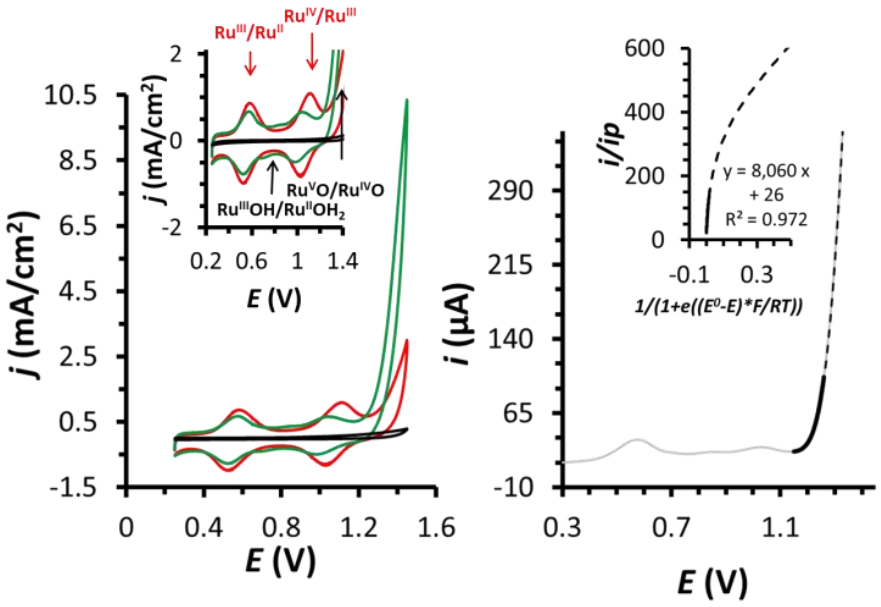

Figure 3. Left, CV for **2b** in a pH 7 solution at a scan rate of 100 mV/s from 0.25 to 1.45 V, with a surface coverage of Γ_{2b} = 6.35 nmol/cm2 (red line) using GC$_d$ as WE. Green line, CV of a mixture of **2b**$^{2+}$:**3b** ($\Gamma_{2b^{2+}}$ = 2.66 nmol/cm2 and Γ_{3b} = 0.55 nmol/cm2) under the same conditions. In black a blank for MWCNT@GC$_d$. Inset, enlargement of the 0.2-1.4 V potential zone. Right, linear sweep voltammetry at pH 7 for the **2b**$^{2+}$:**3b** mixture (grey solid line). Inset, plot of i/i_p *vs*. [1/(1+e((E^0-E)*F/RT))]. The black dashed line in both cases represents the experimental data used for the FOWA analysis, and the black solid line shows the experimental data used for the extraction of TOF$_{max}$ = 8935 s^{-1} for **3b**.

Finally, a very large electrocatalytic current due to the oxidation of water to dioxygen associated with the Ru(V)/Ru(IV) couple occurs at 1.2-1.3 V, manifesting the high activity of this catalytic hybrid material. Interestingly, current densities above 10 mA/cm^2 are achieved here that are assumed to be critical for a potential construction of a water splitting device.[17]

We quantified the performance of this new solid state molecular-anode for water oxidation, comparing its performances with its homogeneous homologue by carrying out a Foot of the Wave Analysis (FOWA)[18] also at pH 7 (see Figure 3). A TOF$_{max}$ = 8935 s^{-1} was obtained from the fitted data similar to that obtained for {Ru^{IV}(O)(tda)(py)$_2$}.[8] This is extremely important because

VI

it clearly shows that the activity of the catalyst anchored on a solid support, under translationally restricted mobility conditions, is maintained. It thus allows transferring the information obtained in homogeneous phase to the desired solid-state anode material, thanks to the WNA nature of the O-O bond formation step that occurs both in homogeneous phase and anchored. This is in sharp contrast with the related complex $\{Ru^{IV}(O)(bda)(4\text{-Me-py})_2\}$ (bda^{2-} is 6,6'-dicarboxylate-2,2'-bypyridine), that mechanistically operates via a bimolecular I2M mechanism.[19] The latter, once anchored needs to change its mechanism to a higher energy pathway that significantly decrease the TOF_{max} values and leads to degradation.

The activity of "$\{Ru^{IV}(O)(tda)(L^2)_2\}$@MWCNT@GC", **3c**, at pH 7 was also evaluated in a similar manner as that of **3b**, giving a TOF_{max} = 8076 s^{-1}. This is very similar to that obtained for **3b** (see Figure S24), further supporting the suitability of the chosen heterogenization strategy. The long-term stability of these new solid-state hybrid molecular anodes were evaluated at pH 7 based on repetitive CV, bulk electrolysis and XAS, shown in Figures 2 and 4. The upper part of Figure 4 displays 1000 repetitive CV scans carried out at 100 mV/s for the anodes containing mixtures of $\mathbf{2b}^{2+}$:**3b** and $\mathbf{2c}^{2+}$:**3c**, between 0.25 and 1.45 V. For the case of $\mathbf{2b}^{2+}$:**3b** (Figure 4, top left), as the repetitive cycles proceed, both the intensity of the electrocatalytic current and the intensity of the waves due to the catalyst precursor progressively decrease, until no electroactivity is observed. Thus as the catalytic reaction proceeds, the catalyst and catalyst precursor progressively disappear from the surface of the electrode, most likely due to the oxidation of the linker. In sharp contrast for the case of $\mathbf{2c}^{2+}$:**3c**, the intensity of the electrocatalytic current decreases by approx. 65% of its initial value but the electroactivity of the precursor catalysts, $\mathbf{2c}^{2+}$, remains intact as shown in Figure 4, top right. The change in the intensity of the electrocatalytic current at 1.45 V is attributed to a shift of the equilibrated species between precursor $\mathbf{2c}^{2+}$, and the active catalytic species **3c** that occurs during long-term catalysis.

A similar trend is observed when bulk electrolysis experiments using GC_d electrodes are carried out at pH 7 with an applied potential of 1.45 V as can be seen in Figure 4, bottom. For the system $\mathbf{2b}^{2+}$:**3b** (red line), the initial current density reaches a value of 2 mA/cm^2, but as time elapses the current density progressively decreases to less than 0.25 mA/cm^2 after 2.5 h. On the other hand, for the $\mathbf{2c}^{2+}$:**3c** system (blue line) the initial current density is 1.5 mA/cm^2, and it decreases to 0.7 mA/cm^2 at about 40 minutes and then remains constant. While the hybrid anode $\mathbf{2c}^{2+}$:**3c** is extremely stable generating roughly 0.18 million TNs without apparent deactivation, $\mathbf{2b}^{2+}$:**3b** slowly deactivates but still giving a remarkable final TNs of 0.67 million. TNs in the range of 1.2 million can be obtained for $\mathbf{2c}^{2+}$:**3c** under similar conditions but by running the experiment for longer periods of time (12h; see figure S26). The strikingly different long-term performances of

these two anode materials are associated with the different oxidative stability of their linking moieties as discussed above for the repetitive CV experiments.

These results manifest again the importance of ligand design for long lasting anodes for water splitting applications that if properly designed can parallel the performance of related oxide based electroanodes.[20] Finally, a bulk electrolysis experiment was performed in a GC_p for **2b**$^{2+}$:**3b** under similar conditions, and the amount of O_2 generated was measured via a Clark electrode on the gas phase giving a Faradaic efficiency close to 100%, showing once more the ruggedness of the present system (Figure S27).

The structure of the hybrid material **2b**$^{2+}$:**3b** was also analyzed by XAS, using glassy carbon plates GC_p and the results are reported in Figure 2, S31, S32 and Tables S3 and S5. Two samples of the hybrid material **2b**$^{2+}$:**3b** ($\Gamma_{\mathbf{2b}^{2+}}$ = 0.57 ± 0.16 nmol/cm^2 and $\Gamma_{\mathbf{3b}}$= 0.64 ± 0.24 nmol/cm^2; $\Gamma_{\mathbf{2b}^{2+}}$:$\Gamma_{\mathbf{3b}}$=0.89 ± 0.20 nmol/cm^2) were exposed to a bulk electrolysis experiment at pH 7, with an applied potential of 1.45 V for 1000 s for the first sample and for 1h for the second one.

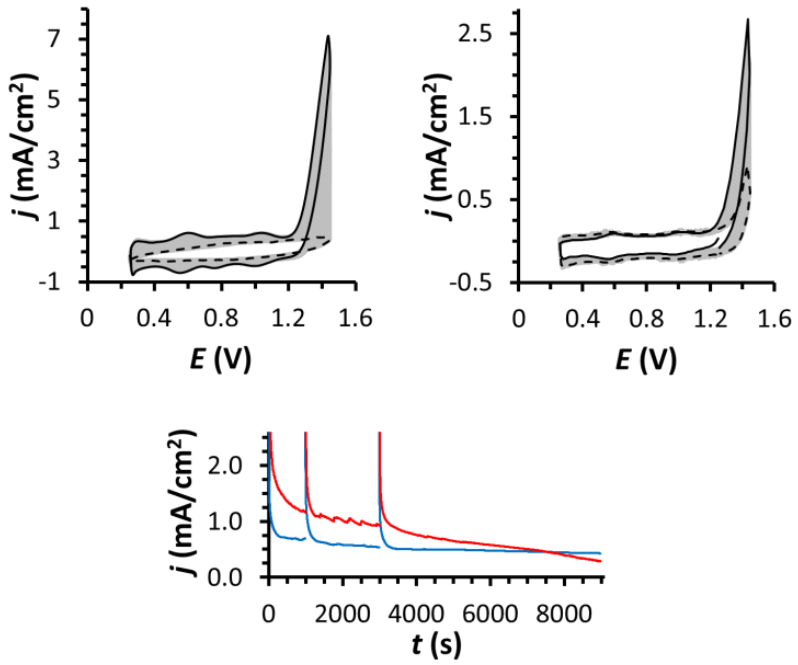

Figure 4. Top, 1000 repetitive CV scans at pH 7 at a scan rate of 100 mV/s from 0.25 to 1.45 V for **2b**$^{2+}$:**3b** (left, $\Gamma_{\mathbf{2b}^{2+}}$ = 2.07 nmol/cm^2 and $\Gamma_{\mathbf{3b}}$ = 0.36 nmol/cm^2) and **2c**$^{2+}$:**3c** (right, $\Gamma_{\mathbf{2c}^{2+}}$ = 0.13 nmol/cm^2 and $\Gamma_{\mathbf{3c}}$ = 0.03 nmol/cm^2) at GC_d. Black solid line is the first cycle, black dashed line is the 1000th cycle. In grey are 2nd-999th cycles. Bottom, bulk electrolysis of **2b**$^{2+}$:**3b** (red, $\Gamma_{\mathbf{2b}^{2+}}$ = 2.10 nmol/cm^2 and $\Gamma_{\mathbf{3b}}$ = 0.40 nmol/cm^2) and **2c**$^{2+}$:**3c** (blue, $\Gamma_{\mathbf{2c}^{2+}}$ = 0.11 nmol/cm^2 and $\Gamma_{\mathbf{3c}}$ = 0.03 nmol/cm^2) in a phosphate buffered solution at pH 7 at E_{app} = 1.45 V under stirring using GC_d as WE. The experiments were stopped at 1000 s and 3000 s and then subsequently reinitialized. See Figure S28 for an analogous experiment on bare MWCNT@GC_d.

Subsequently a CV was carried out with a final potential of 0.2 V that generated the catalyst precursor and the active catalyst at oxidation state II, that are labeled as **2b**' and **2b**'' for the samples exposed to 1000 s and 1h electrolysis, respectively, and left in open air for a week. As was also the case for **2b**^{0}, XANES spectra show half peak κ-edge energies that indicate that initial Ru(II) complex is oxidized to Ru(III) by 90% in both cases (see Table S2 and top inset in Figure 2B). In addition, the EXAFS (see Figures 2D, S31, Table S3 and Table S5 (fits 4, 8 and 12)) point out that the samples before catalysis **2b**^{0} and after 1000 s and 1h catalysis **2b**' and **2b**" respectively, are practically identical to **1a**$^+$, after subtraction of their Ru(II) contribution, and thus confirms the presence of **2b**$^+$. This is a very important result since it shows that the nature of the catalyst remains intact after catalysis. In addition, XAS spectroscopy unambiguously shows the absence of any traces of RuO_2 after 1h catalysis. This can be monitored by the specific peak at 22156 eV, nicely visualized through the difference spectra in Figure 2C, that is highly characteristic of RuO_2 as well as by the absence of RuO_2 in the EXAFS spectral features shown in Figure 2D and S32. This is again very significant since it clearly demonstrates the molecular nature of the catalysis in heterogeneous phase, in sharp contrast with many instances where the original molecular catalyst is transformed to the corresponding metal oxide that ends up being the real active catalyst.[5]

VI

H 3 Conclusions

In conclusion, the present work reports a million turnover molecular electroanode that consists of a molecular Ru catalyst anchored on the surface of MWCNTs via a pyrenyl functionality. The extraordinary unprecedented stability of the molecular catalyst is a result of a bottom up approach that includes a thorough mechanistic understanding of the water oxidation catalyst steps involved in water nucleophilic attack events. XAS spectroscopy has been shown to be a very valuable tool in the solid state to monitor the long-term stability and molecular nature of the anchored water oxidation catalysts.

H 4 Acknowledgements

A.L., X.S. and J.G-A thank MINECO (CTQ-2013-49075-R, SEV-2013-0319; CTQ-2014-52974-REDC and CTQ2015-64261-R). J.C. and R.M respectively thank UAB, "Euroregió Pirineus Mediterrània" and "La Caixa" for PhD grants. D.M. acknowledges support from the US DOE, Contract No. DE-AC02-06-CH11357. J.G-A. thanks Serra Húnter Program.

H 5 References

1 N. S. Lewis, *Science* **2016**, *351,*19201-19209.

2 L. Alibabaei, B. D. Sherman, M. R. Norris, M. K. Brennaman, T. J. Meyer, *Proc. Natl. Acad. Sci. USA* **2015**, *112*, 5899-5902.
3 X. Elias, Q. Liu, C. Gimbert-Suriñach, R. Matheu, P. Mantilla-Perez, A. Martinez-Otero, X. Sala, J. Martorell, A. Llobet, *ACS Catal.* **2016**, 3310-3316.
4 J. H. Kim, Y. Jo, J. H. Kim, J. W. Jang, H. J. Kang, Y. H. Lee, D. S. Kim, Y. Jun, J. S. Lee, *ACS Nano* **2015**, *9*, 11820-11829.
5 G. Pastori, K. Wahab, A. Bucci, G. Bellachioma, C. Zuccaccia, J. Llorca, H. Idriss, A. Macchioni, *Chem. Eur. J.* **2016**, *22*, 13459-63
6 R. Matheu, L. Francàs, P. Chernev, M. Z. Ertem, V. Batista, M. Haumann, X. Sala, A. Llobet, *ACS Catal.* **2015**, 3422-3429.
7 X. Sala, S. Maji, R. Bofill, J. Garcia-Anton, L. Escriche, A. Llobet, *Acc. Chem. Res.* **2014**, *47*, 504-516.
8 J. J. Concepcion, J. W. Jurss, J. L. Templeton, T. J. Meyer, *J. Am. Chem. Soc* **2008**, *130*, 16462-16463
9 .N. Karousis, N.Tagmatarchis. D. Tasis *Chem. Rev.* **2010**, *110*, 5366.
10 R. Matheu, M. Z. Ertem, J. Benet-Buchholz, E. Coronado, V. S. Batista, X. Sala, A. Llobet, *J. Am. Chem. Soc.* **2015**, *137*, 10786-10795.
11 C. C. L. McCrory, S. Jung, I. M. Ferrer, S. M. Chatman, J. C. Peters, T. F. Jaramillo, *J. Am. Chem. Soc.* **2015**, *137*, 4347-4357.
12 L. Francàs, C. Richmond, P. Garrido-Barros, N. Planas, S. Roeser, J. Benet-Buchholz, L. Escriche, X. Sala, A. Llobet, *Chem. Eur. J.* **2016**, *22*, 5261-5268.
13 J. T. Hyde, K. Hanson, A. K. Vannucci, A. M. Lapides, L. Alibabaei, M. R. Norris, T. J. Meyer, D. P. Harrison, *ACS Appl. Mater. Interfaces* **2015**, *7*, 9554-9562.
14 A. Maurin, M. Robert, *J. Am. Chem. Soc.* **2016**, *138*, 2492-2495.
15 F. Li, B. Zhang, X. Li, Y. Jiang, L. Chen, Y. Li, L. Sun, *Angew. Chem. Int. Ed.* **2011**, *50*, 12276-12279.
16 D. Hong, S. Mandal, Y. Yamada, Y.-M. Lee, W. Nam, A. Llobet, S. Fukuzumi, *Inorg. Chem.* **2013**, *52*, 9522-9531.
17 M. G. Walter, E. L. Warren, J. R. McKone, S. W. Boettcher, Q. Mi, E. A. Santori, N. S. Lewis, *Chem. Rev.* **2010**, *110*, 6446-6473.
18 C. Costentin, S. Drouet, M. Robert, J.-M. Savéant, *J. Am. Chem. Soc.* **2012**, *134*, 11235-11242.
19 L. Duan, F. Bozoglian, S. Mandal, B. Stewart, T. Privalov, A. Llobet, L. Sun, *Nat. Chem.* **2012**, *4*, 418-423.

H 6 Supporting Information

Paper H: A Million Turnover Molecular Anode for Catalytic Water Oxidation

Outline

VI

VI

MATERIALS

General Considerations

All the reagents were purchased from Sigma-Aldrich and used without further purification unless explicitly indicated. Multi-Walled Carbon Nanotubes (MWCNTs) were purchased from HeJi, Inc. (Zengcheng city, China) in bulk with >95% purity, >50 nm OD and ~10 µm length. $RuCl_3 \cdot 3H_2O$ was supplied by Alfa Aesar, 6,6'-Dicarboxylic acid-[2,2':6',2"-terpyridyl] (H_2tda), {$RuCl_2(DMSO)_4$} and 4-(pyrene-1-yl)-N-(pyridine-4-ylmethyl)butanamide (**L^1**) were prepared according to literature procedures.[S1,S2,S3] Powder samples of complexes {Ru^{II}(tda)$(py)_2$}, **1a**, {Ru^{III}(tda)$(py)_2$}(PF_6), **1a**(PF_6), and {Ru^{IV}(tda)$(py)_2$}$(PF_6)_2$, **1a**$(PF_6)_2$, were prepared as recently described.[S4] Dicloromethane (CH_2Cl_2), tetrahydrofuran (THF), toluene and diethyl ether (Et_2O) were dried and purified with a solvent purification system Pure SOLV system-4®. High-purity deionized water was obtained by passing distilled water through a nanopure Milli-Q water purification system. All synthetic manipulations were routinely performed under N_2 or Ar atmosphere using Schlenk tubes and vacuum-line techniques.

Synthesis of ligands and complexes

VI

4-(pyrene-1-yl)pyridine, L^2. A mixture of 1-pyreneboronic acid (540 mg, 2.2 mmol), 4-bromopyridine hydrochloride (400 mg, 2 mmol), $Pd(OAc)_2$ (50 mg, 0.22 mmol, 10% mol), K_2CO_3 (830 mg, 6 mmol) and tetrabutylammonium bromide (TBAB, 645 mg, 2 mmol), were refluxed under stirring in a mixture of degassed H_2O:toluene (2:9) at 120 °C overnight under argon. After cooling down to r.t., the mixture was filtered through a pad of Celite®. The solution was extracted 3 times with 5 mL of H_2O, the organic layer was dried with anhydrous Mg_2SO_4 and the solvent was removed under vacuum. The product was purified by silica column chromatography using a 1:5 mixture of hexane:ethyl acetate (EtOAc) to yield L^2 as a yellow solid (350 mg, 63%). ^{1}H NMR (400 MHz, d_4-MeOD) δ = 7.75 (d, J=6.1 Hz, 2H), 8.04 (d, J=7.9 Hz, 1H), 8.13 (m, J=8.1 Hz, 3H), 8.20 (d, J=9.0 Hz, 1H), 8.23 (d, 9.0 Hz, 1H), 8.31 (m, 2H), 8.35 (d, J=7.9 Hz, 1H), 8.79 (d, J=6.1 Hz, 2H). ^{13}C NMR (101 MHz, d_4-MeOD) δ = 151.6, 150.2, 135.2, 133.0, 132.8, 132.1, 129.4, 129.2, 129.2, 128.3, 128.1, 127.5, 127.1, 126.8, 126.4, 125.9, 125.7, 124.9. MS (ESI$^+$) *m/z* found: 280.1, calc.: 280.1. Anal. Calc. for $L^2 \cdot 0.45$ EtAcO ($C_{22.8}H_{16.6}NO_{0.9}$): C, 85.85%; H, 5.25%; N, 4.39 %. Found: C, 85.89%; H, 5.34 %; N, 4.57 %.

{Ru(tda)(L^1)$_2$}, 1b. A mixture of {$RuCl_2(DMSO)_4$} (150 mg, 0.31 mmol), 6,6'-dicarboxylic acid-[2,2':6',2"-terpyridyl] (100 mg, 0.31 mmol) and Et_3N (0.2 mL) in dry MeOH (6 mL), was refluxed for 6 hours under N_2 and cooled down to room temperature. A brown solid appeared in the reaction mixture that was filtered and was washed with MeOH and diethyl ether. The brown solid (100 mg) and L^1 (150 mg, 0.40 mmol) were then dispersed in a MeOH:H_2O 3:2 degassed mixture (50 mL) and refluxed for seven days. The reaction mixture was cooled down to room temperature and a pink solid was separated from the solution. This solid was then dissolved in a mixture of Et_3N, trifluoroethanol (TFE) and dichloromethane (DCM) in a 1:10:100 ratio, and purified by silica column chromatography using a mixture of MeOH:Et_3N:TFE:DCM (5:3:10:100), to yield **1b** as a purple solid (50 mg, 14 %). ^{1}H NMR (d_4-MeOD) δ = 2.06 (q, J=7.5 Hz, 4H), 2.31 (t, J=7.5 Hz, 4H), 3.19 (t, J=7.5 Hz, 4H), 4.18 (s, 4H), 6.99 (d, J=6.7 Hz, 4H), 7.66 (t, J=7.9 Hz, 2H), 7.71 (t, J=8.0 Hz, 1H), 7.80 (d, J=7.8 Hz, 2H), 7.86 (d , 7.9 Hz, 2H), 8.00 (m, 4H), 8.04 (m, 7H), 8.08 (s, 4H), 8.12 (d, J=7.8 Hz, 2H), 8.19 (m, 4H), 8.23 (m, 4H). ^{13}C NMR (d_4-MeOD) δ = 27.5, 32.2, 34.9, 41.0, 122.9, 123.0, 123.1, 123.1, 124.5, 124.5, 124.6, 124.7, 124.8, 125.7, 125.9, 126.3, 126.9, 127.1, 127.2, 128.4, 129.9, 130.9, 131.4, 131.7, 135.8, 135.9, 149.5, 152.1, 157.7, 157.8, 161.8, 171.0, 174.5. MS (ESI$^+$) m/z found: 1177.308, calc.: 1177.310. Anal. Calc. for **1b**·5H_2O ($C_{67}H_{59}N_7O_{11}Ru$): C, 64.93 %; H, 4.80 %; N, 7.91 %. Found: C, 65.06%; H, 5.02 %; N, 7.64 %.

VI

{Ru(tda)(L^2)$_2$}, 1c. A mixture of {$RuCl_2(DMSO)_4$} (75 mg, 0.15 mmol), 6,6'-dicarboxylic acid-[2,2':6',2"-terpyridyl] (50 mg, 0.16 mmol) and Et_3N (0.1 mL) in dry MeOH (3 mL), were refluxed for 6 hours under N_2 and then cooled down to room temperature. A brown solid appeared in the reaction mixture that was filtered, washed with MeOH and diethyl ether. The brown solid (50 mg) and L^2 (56 mg, 0.20 mmol) were dispersed in a MeOH:H_2O (3:2) degassed mixture (25 mL) and refluxed for three days. The reaction mixture was cooled down to room temperature, and a brown solid precipitated in the reaction flask. It was washed with H_2O, MeOH and diethyl ether and dried under vacuum, to yield **1c** as an orange-brown powder (60 mg, 41 %). ^{1}H NMR (500 MHz, $CDCl_3$) δ = 8.40 (d, *J* = 8.1 Hz, 2H), 8.32 (d, *J* = 3.0 Hz, 4H), 8.24 (d, *J* = 7.6 Hz, 2H), 8.19 (d, *J* = 7.5 Hz, 2H), 8.17 (d, *J* = 8.1 Hz, 2H), 8.14 (m, 6H), 8.08 – 8.02 (m, 7H), 8.00 (d, *J* = 9.3 Hz, 2H), 7.89 (d, *J* = 9.2 Hz, 2H), 7.74 (d, *J* = 7.9 Hz, 2H), 7.36 (d, *J* = 6.7 Hz, 4H). ^{13}C NMR (126 MHz, $CDCl_3$) δ = 212.4, 171.4, 163.0, 157.6, 157.2, 151.6, 150.6, 136.9, 132.1, 131.8, 131.4, 130.7, 128.7, 128.1, 127.9, 127.2, 126.9, 126.8, 126.5, 126.1, 125.6, 125.5, 125.0, 124.9, 124.6, 123.7, 123.3, 123.2, 122.8. MS (MALDI) *m/z* found: 979.4, calc.: 979.2. Anal. Calc. for **1c**·5.75H_2O ($C_{59}H_{46.5}N_5O_{9.75}Ru$)*:* C, 65.46 %; H, 4.33 %; N, 6.47%. Found: C, 65.19 %; H, 3.88 %; N, 6.35 %.

Preparation of electrodes on Glassy Carbon disks (GC_d)

A general scheme for the preparation of the electrodes is shown in Figure S21.

"MWCNT@GC_d". A dispersion of MWCNTs (10 mg, HeJi, Inc., China) in THF (10 mL) was sonicated for 60 minutes. Then, a 5 µL sample of this dispersion was added by drop casting to a GC_d (0.07 cm^2) and air-dried.[S5] This drop casting process was repeated three times on each GC_d electrode.

"{Ru^{II}tda)(L^1)$_2$}@MWCNT@GC_d", ***2b*.** The MWCNT@GC_d electrode was dipped in a solution of **1b** (0.1 mM) in MeOH overnight. Then, the electrode was washed with 200 µL of MeOH, 200 µL of water and dried with a N_2 flow.

"{Ru^{II}(tda)(L^2)$_2$}@MWCNT@GC_d", ***2c*.** The MWCNT@GC_d electrode was dipped in a solution of **1c** (0.5 mM) in a $CHCl_3$:TFE (trifluoroethanol) mixture (80:20) overnight. Then, the electrode was washed with 200 µL of a $CHCl_3$:TFE mixture (80:20), 200 µL of water and dried with a N_2 flow.

"[{Ru^{IV}(tda)(L^1)$_2$}$^{2+}$@MWCNT@GC_d]:[Ru^{IV}(O)(tda)(L^1)$_2$}@MWCNT@GC_d]", ***2b*$^{2+}$:*3b*.** The **2b** material was immersed in a pH = 12 solution and used as a working electrode (WE) together with a Pt disk as a counter electrode (CE) and a Hg/Hg_2SO_4 as a Reference Electrode (RE), in a typical three electrode cell configuration. A potential of 1.25 V was then applied to **2b** for 500 seconds generating a mixture of **2b**$^{2+}$:**3b** (see Table S1 for coverages and ratios in GC_d and GC_p). Then the working electrode was removed from the cell and rinsed with water.

"[{Ru^{IV}(tda)(L^2)$_2$}$^{2+}$@MWCNT@GC_d]:[Ru^{IV}(O)(tda)(L^2)$_2$}@MWCNT@GC_d]", ***2c*$^{2+}$:*3c*.** An analogous strategy as in **2b**$^{2+}$:**3b** was followed to obtain the mixture of **2c**$^{2+}$ and **3c**.

Preparation of electrodes on Glassy Carbon Plates (GC_p)

"MWCNT@GC_p". A dispersion of MWCNTs (10 mg, HeJi, Inc., China) in THF (10 mL) was sonicated for 60 minutes. Then, a 50 µL sample of this dispersion was added by drop casting to a GC_p and air-dried. This drop casting process was repeated three times on each GC_p electrode. The coating with MWCNTs was applied only to one side of the plates and a tape was used to limit this coating to only 1 cm^2 of the GC_p.

"{Ru^{II}tda)(L^1)$_2$}@MWCNT@GC_p", ***2b***. The electrode MWCNT@GC_d was dipped in a solution of **1b** (0.1 mM) in methanol overnight. Then, the electrode was washed with 500 µL of MeOH, 500 µL of water and dried with a N_2 flow. A cyclic voltammogram was performed (E_i =

0.25 V, E_c = 1.45 V, E_f = 0.25 V, total scans = 2, where E_i is initial potential, E_c is the change potential and E_f is the final potential), using **2b** as a working electrode (CE = Pt disk, RE = Hg/Hg_2SO_4) to estimate the coverage of the electrode ($\Gamma_{\mathbf{2b}}$ = 3.48 ± 0.86 nmol·cm^{-2}). The CV was analogously performed to three glassy carbon plates that were then rinsed with water and air-dried. For XAS analysis, the three identical electrodes were wrapped in thin 3 µm mylar film and analyzed together. The samples were then kept under ambient conditions until the XAS measurement (circa a week). See the XAS methods section for further details about the XAS analysis.

"[{Ru^{IV}(tda)(L^1)$_2$}$^{2+}$@MWCNT@GC_d]:[Ru^{IV}(O)(tda)(L^1)$_2$}@MWCNT@GC_d]", ***2b^{2+}:3b.*** A potential of 1.25 V was applied to **2b** for 500 seconds at pH = 12, using **2b** as working electrode (CE = Pt disk, RE = Hg/Hg_2SO_4). After the bulk electrolysis, the electrode was removed from the three-electrode cell and was rinsed with water. Then the modified electrode was immersed in a pH = 7.0 solution and a cyclic voltammogram was performed (E_i = 0.25 V, E_c = 1.45 V, E_f = 0.25 V, total scans = 2) using the modified glassy carbon plate as working electrode (CE = Pt disk, RE = Hg/Hg_2SO_4) to estimate the ratio of **2b^{2+}**:**3b** complexes in the electrode ($\Gamma_{\mathbf{2b}^{2+}}$ = 0.57 ± 0.16 nmol·cm^{-2} and $\Gamma_{\mathbf{3b}}$ = 0.64 ± 0.24 nmol·cm^{-2}, $\Gamma_{\mathbf{2b}^{2+}}$:$\Gamma_{\mathbf{3b}}$, 0.90 ± 0.20). The electrode was rinsed with water and air-dried. For XAS analysis, three identical electrodes were wrapped in thin 3 µm mylar film and analyzed together. The samples were then kept under ambient conditions until the XAS measurement (circa a week). See the XAS methods section for further details about the XAS analysis.

VI

"[{Ru^{IV}(tda)(L^1)$_2$}$^{2+}$@MWCNT@GC_d]:[Ru^{IV}(O)(tda)(L^1)$_2$}@MWCNT@GC_d]", ***2b^{2+}:3b*** *after catalysis (1000 s and 3600 s) at pH = 7.* The modified electrodes containing a 1:1 mixture of **2b^{2+}**:**3b** were immersed in a pH = 7 solution and a bulk electrolysis (E_{app} = 1.35 V) was applied for 1000 seconds using a modified glassy carbon plate as working electrode (CE = Pt disk, RE = Hg/Hg_2SO_4). After bulk electrolysis, a cyclic voltammogram was performed (E_i = 0.25 V, E_c = 1.45 V, E_f = 0.25 V, total scans = 2) to estimate the remaining ratio of **2b^{2+}**:**3b** complexes ($\Gamma_{\mathbf{2b}^{2+}}$ = 0.56 nmol·cm^{-2} and $\Gamma_{\mathbf{3b}}$ = 0.41 nmol·cm^{-2}, $\Gamma_{\mathbf{2b}^{2+}}$:$\Gamma_{\mathbf{3b}}$, 1.37:1). For XAS analysis, three identical electrodes were wrapped in thin 3 µm mylar film and analyzed together.

The same procedure was followed to other modified electrodes containing a 1:1 mixture of **2b^{2+}**:**3b**, and a bulk electrolysis (E = 1.35 V) was applied for 3600 seconds in a pH = 7 solution, using a modified glassy carbon plate as working electrode (CE = Pt disk, RE = Hg/Hg_2SO_4). A cyclic voltammogram (E_i = 0.25 V, E_c = 1.45 V, E_f = 0.25 V, total scans = 2) was performed using a glassy

carbon plate as working electrode (CE = Pt disk, RE = Hg/Hg_2SO_4) to estimate the remaining ratio of **2b**$^{2+}$:**3b** complexes ($\Gamma_{2b^{2+}}$ = 0.54 nmol·cm^{-2} and Γ_{3b} = 0.28 nmol·cm^{-2}, $\Gamma_{2b^{2+}}$:Γ_{3b}, 1.93:1).

In all cases for the XAS analysis, three electrodes modified in an identical manner were stacked together and wrapped in thin 3 µm mylar film. The samples were then kept under ambient conditions until the XAS measurement (circa a week). This samples suffered partial metal oxidation from Ru(II) to Ru(III) by ambient oxygen and are labelled **2b**^{0} (**2b**$^{2+}$:**3b** before catalysis), **2b'** (**2b**$^{2+}$:**3b** after 1000s catalysis) and **2b''** (**2b**$^{2+}$:**3b** after 1h catalysis).

METHODS AND INSTRUMENTATION

General Considerations

Electrospray Ionization (ESI) and Matrix-Assisted Laser Desorption Ionization (MALDI) Mass Spectrometry (MS) experiments were performed on a Waters Micromass LCT Premier equipment and a Bruker Daltonics Autoflex equipped with a nitrogen laser (337 nm), respectively. A 400 MHz Bruker Avance II spectrometer or a Bruker Avance 500 MHz was used to carry out NMR spectroscopy at room temperature unless otherwise specified. The TGA experiments were carried out in the furnace of a Mettler Toledo TGA/SDTA851 instrument. The pH of the solutions was determined by a pHmeter (CRISON, Basic 20+) calibrated before measurements through a standard solutions at pH = 4.01, 7.00 and 9.21. Oxygen evolution was analyzed with a gas phase Clark type oxygen electrode (Unisense Ox-N needle microsensor) and calibrate by the addition of small quantities of oxygen (99%).

Thermogravimetric Analysis (TGA)

For a typical TGA experiment, 1-2 mg of solid were placed in the sample holder of the furnace and the material was heated up at a rate of 10 °C·min^{-1} under N_2, while the weight was recorded continuously from 30 °C to 900 °C. The weight loss of the organic part was used to calculate the percentage of ligand stacked onto the MWCNTs. The ligand loss was attributed to the weight loss observed between 250 and 450 °C.

The hybrid L^1@MWCNT was prepared by dispersing 5 mg of MWCNT in a L^1 solution in ethanol (1 mg/mL) in the ultrasound for 1h. The resulting dispersion was filtered, washed with diethyl ether, and dried under vacuum and in an oven at 60 °C for 12h. The weight loss at the 250-450 °C range was of ~3% and it was attributed to the percentage of ligand on the hybrid L^1@MWCNT.

Electrochemical methods

All the electrochemical experiments were performed in a PAR 263A EG&G potentiostat or in an IJ-Cambria HI-660 potentiostat.

Electrodes

Either a glassy carbon disk (GC_d, ϕ = 0.3 cm, S = 0.07 cm^2) or a glassy carbon plate (GC_p, 20 mm x 10 mm x 180 µm) were used as working electrode (WE). In the case of GC_p the surface dipped in the electrochemical solution was 1 cm^2.

A Pt disk (ϕ = 0.3 cm, S = 0.07 cm^2) was used as counter electrode (CE) and a Hg/Hg_2SO_4 (K_2SO_4 saturated) electrode was used as a reference electrode (RE), except for the oxygen monitored bulk electrolysis that a Ag/AgCl (KCl sat.) was used as RE and a Pt grid as a CE, and for the XAS samples preparation that a Pt grid was also used.

Cyclic Voltammetry (CV)

For, CV a 20 mL vial was used as an electrochemical cell. A home-made Teflon cap with holes for the three electrodes was used as a lid to ensure a reproducible distance between the electrodes. The scan rate was 100 $mV \cdot s^{-1}$ unless otherwise stated. IR compensation was applied at 95% when the current density was above 1 $mA \cdot cm^{-2}$.

VI

Differential Pulse Voltammetry (DPV)

For DPV a 20 mL vial was used as an electrochemical cell. A home-made Teflon cap with holes for the three electrodes was used as a lid to ensure a reproducible distance between the electrodes. The DPV parameters were ΔE = 4 mV, Amplitude = 50 mV, Pulse width = 0.05 s, Sampling width = 0.0167 s, Pulse period = 0.2 s. IR compensation was applied at 95%.

Bulk electrolysis

For bulk electrolysis experiments, a 10 mL two-compartment cell with a separation membrane between the two compartments was used. Both compartments were filled with 5 mL of pH = 7 solution and both compartments were equipped with a stirring bar.

In the case of the oxygen-monitored bulk electrolysis, a GC_p was used as WE, a Pt grid as CE and a Ag/AgCl (KCl sat.) as a RE. A Clark electrode was used to measure oxygen evolution and to calculate the Faradaic efficiency. The Clark electrode was calibrated by adding different volumes

of 99% pure oxygen at the end of the experiment. The CE was placed in one compartment and the other was provided with WE, RE and Clark electrode.

Surface coverage (Γ)

The surface coverage (Γ) of the complexes on the electrodes was estimated by applying the formula Γ (mol·cm^{-2}) = Q / (n*S*F). In the case of species **2b**, **2c**, **2b^{2+}** and **2c^{2+}**, Q is the charge under the Ru^{III}/Ru^{II} reduction wave at 0.5 V in CV; in the case of **3b** and **3c** Q is the charge under the $Ru^{III}OH/Ru^{II}OH_2$ reduction wave at 0.7 V in CV (see Figure S22 for an example). n is the number of electrons involved in the electron transfer (1 e^- in all the cases), S is the surface of the electrode (GC_d, S = 0.07 cm^2; GC_p, S = 1 cm^2) and F is the Faradaic constant. The ratio between **2b^{2+}:2b** and **2c^{2+}:3c** was calculated dividing the Γ of the former by the Γ of the latter.

The average coverage was estimated from 3 independent experiments and the standard deviation between samples was used as an error. For individual experiments, the exact coverage of the sample is provided in the captions of the figures.

Electrochemical Solutions

VI

All solutions used in this work possessed an ionic strength equal to 0.1 M. pH = 7 buffered solution was prepared by mixing 2.3156 g of NaH_2PO_4 (0.0193 mol) and 3.7761 g of Na_2HPO_4 (0.0266 mol) in 1000 mL of Mili-Q water and no additional salts were added. pH = 12 buffered solution was prepared by mixing 1.0363 g of Na_2HPO_4 (0.0073 mol) and 2.0656 g of Na_3PO_4 (0.0126 mol) in 1000 mL of Mili-Q water and no additional salts were added.

Foot of the wave analysis (FOWA)

The analysis was performed by following the procedure of Savéant *et al* in the literature.[S4,S6] The expression (equation S1) was deduced for a general scheme where a single chemical step, which is the rate determining step and a fast single electron transfer, is responsible for the rate of the reaction.

$$\frac{i}{Q_R} = \frac{k_{WNA}}{1 + exp(\frac{F(E-E^O)}{RT})} \quad \text{(S1)}$$

R is the gas constant, T is the temperature, k_{WNA} is a pseudoconstant and E is the applied potential. The charge of the cathodic wave of the $Ru^{III}OH/Ru^{II}OH_2$ redox couple was used as Q_R

as an approximation. E^0 is the apparent potential for the Ru^{V}/Ru^{IV} redox couple, which was extracted from DPV of the same electrode.

The value of k_{WNA} is equivalent to TOF_{MAX} (s^{-1}) in the used electrocatalytic scheme. TOF_{MAX} is the maximum Turn Over Frequency (s^{-1}) that a molecule can catalyze the water oxidation reaction when E tends to infinite potential.[S6]

Single-crystal X-Ray Diffraction (XRD) Methods

Data collection: The measured crystals were prepared under inert conditions immersed in perfluoropolyether as protecting oil for manipulation.

Crystal structure determination for compound **1b** was carried out using a Rigaku diffractometer equipped with a Pilatus 200K area detector, a Rigaku MicroMax-007HF microfocus rotating anode with MoK_α radiation, Confocal Max Flux optics and an Oxford Cryosystems low temperature device Cryostream 700 plus (T = -173 °C). Full-sphere data collection was used with ω and φ scans. *Programs used:* Data collection CrystalClear[S7], data reduction with CrysAlisPro[S8] V/.60A and absorption correction with Scale3 Abspack scaling algorithm.[S9]

Structure Solution and Refinement: Crystal structure solution was achieved using the computer program SHELXT.[S10] Visualization was performed with the program SHELXle.[S11] Missing atoms were subsequently located from difference Fourier synthesis and added to the atom list. Least-squares refinement on F^2 using all measured intensities was carried out using the program SHELXL 2015.[S12] All non-hydrogen atoms were refined including anisotropic displacement parameters. The asymmetric unit contains one molecule of the metal complex and 1.25 methanol molecules. The metal complex is disordered in two orientations. The central part with the Ru atom is shifted in two orientations with a ratio of 73:27. One of the pyrene groups is disordered in two different positions with a ratio of 50:50. In one of the disordered positions the pyrene is located on a center of inversion sharing its inverted orientations with a neighboring molecule. In the second disordered part it is also sharing its position with a neighboring molecule. The other pyrene group is also disordered but in this case it is located in the same place with slightly shifted positions. The 1.25 methanol molecules are disordered in six positions with an occupancy of 0.3:0.3:0.2:0.20.15:0.10. Crystallographic data has been deposited at the Cambridge Crystallographic Data Center with a reference number “CCDC 1489305”. In the Checkcif the structure has three B alerts related to short distances between hydrogen atoms. Due to the high disorder of the molecule it was not possible to avoid the relatively short distances between these hydrogen atoms

X-ray Absorption Spectroscopy (XAS) Methods.

X-ray absorption spectra were collected at the Advanced Photon Source(APS) at Argonne National Laboratory on bending magnet beamline 20 at electron energy 23 KeV and average current of 100 mA. The radiation was monochromatized by a Si(110) crystal monochromator. The intensity of the X-rays were monitored by three ion chambers (I_0, I_1 and I_2) filled with 70% nitrogen and 30% argon and placed before the sample (I_0) and after the sample (I_1 and I_2). Ru metal was placed between ion chambers I_1 and I_2 and its absorption was recorded with each scan for energy calibration. The samples were kept at 20 K in a He atmosphere at ambient pressure. Hybrid materials **2b**^{0}, **2b'** and **2b''** were recorded as fluorescence excitation spectra using a 13-element energy-resolving detector. Solid reference samples **1a**, **1b**, **(1a(PF$_6$))** and **(1a(PF$_6$)$_2$)** and **RuO$_2$** were diluted with Boron Nitride in 1:5 ratio, pressed between 3 µm polypropylene film and mylar tape and measured in a continuous helium flow cryostat in transmission mode. Around 5-10 XAS spectra were collected for each sample. No more than 5 scans were taken at each sample position at any condition. Three glassy carbon sheets with sub-monolayer coverage of the hybrid materials were on the other hand stacked on top on each other and wrapped in thin 3 µm mylar film. They were measured in fluorescence mode with a 13-element Germanium detector, in a continuous helium flow cryostat. Around 30 XAS spectra of each sample were collected. For the detailed preparation of the samples, see experimental section above. Care was again taken to measure at several sample positions on each sample and no more than 5 scans were taken at each sample position. In order to reduce the risk of sample damage by x-ray radiation, 80% flux was used in the defocused mode (beam size 5500 µm(Horizontal) x 600 µm(Vertical)) and no damage was observed scan after scan to any samples. All samples were also protected from the x-ray beam during spectrometer movements by a shutter synchronized with the scan program. Ru XAS energy was calibrated by the first maxima in the second derivative of the ruthenium metal X-ray Absorption Near Edge Structure (XANES) spectrum.

VI

Extended X-ray Absorption Fine Structure (EXAFS) Analysis

Athena software[S13] was used for data processing. The energy scale for each scan was normalized using Ruthenium metal standard. Data in energy space were pre-edge corrected, normalized, deglitched (if necessary), and background corrected. The processed data were next converted to the photoelectron wave vector (k) space and weighted by k^3. The electron wave number is defined as $k = [2m(E - E_0)/\hbar^2]^{1/2}$, E_0 is the energy origin or the threshold energy. K-space data were truncated near the zero crossings k = 1.941 to 13.2 Å^{-1} for the solid reference complexes

and k =1.941 to 10.9 $Å^{-1}$ for the hybrid materials, in Ru EXAFS before Fourier transformation. The k-space data were transferred into the Artemis Software for curve fitting. In order to fit the data, the Fourier peaks were isolated separately, grouped together, or the entire (unfiltered) spectrum was used. The individual Fourier peaks were isolated by applying a Hanning window to the first and last 15% of the chosen range, leaving the middle 70% untouched. Curve fitting was performed using *ab initio*-calculated phases and amplitudes from the FEFF8[S14] program from the University of Washington. *Ab initio*-calculated phases and amplitudes were used in the EXAFS equation

$$\chi(k) = S_0^2 \sum_j \frac{N_j}{kR_j^2} f_{eff_j}(\pi, k, R_j) e^{-2\sigma_j^2 k^2} e^{\frac{-2R_j}{\lambda_j(k)}} \sin(2kR_j + \phi_{ij}(k)) \qquad \text{(S2)}$$

where N_j is the number of atoms in the j^{th} shell; R_j the mean distance between the absorbing atom and the atoms in the j^{th} shell; $f_{eff_j}(\pi,k,R_j)$ is the *ab initio* amplitude function for shell *j*, and the Debye-Waller term $e^{-2\sigma_j^2 k^2}$ accounts for damping due to static and thermal disorder in absorber-backscatterer distances. The mean free path term $e^{\frac{-2R_j}{\lambda_j(k)}}$ reflects losses due to inelastic scattering, where $\lambda_j(k)$, is the electron mean free path. The oscillations in the EXAFS spectrum are reflected in the sinusoidal term $\sin(2kR_j + \phi_{ij}(k))$, where $\phi_{ij}(k)$ is the *ab initio* phase function for shell *j*. This sinusoidal term shows the direct relation between the frequency of the EXAFS oscillations in k-space and the absorber-backscatterer distance. S_0^2 is an amplitude reduction factor.

The EXAFS equation [S15] (Eq. S2) was used to fit the experimental Fourier isolated data (q-space) as well as unfiltered data (k-space) and Fourier transformed data (R-space) using *N*, S_0^2, E_0, *R*, and σ^2 as variable parameters (Table S4, S5). *N* refers to the number of coordination atoms surrounding Ru for each shell. The quality of fit was evaluated by R-factor and the reduced Chi^2 value. The deviation in E_0 ought to be less than or equal to 10 eV. R-factor less than 2% denotes that the fit is good enough[S15] whereas R-factor between 2 and 5% denotes that the fit is correct within a consistently broad model. The reduced Chi^2 value is used to compare fits as more absorber-backscatter shells are included to fit the data. A smaller reduced Chi^2 value implies a better fit. Similar results were obtained from fits done in k, q, and R-spaces.

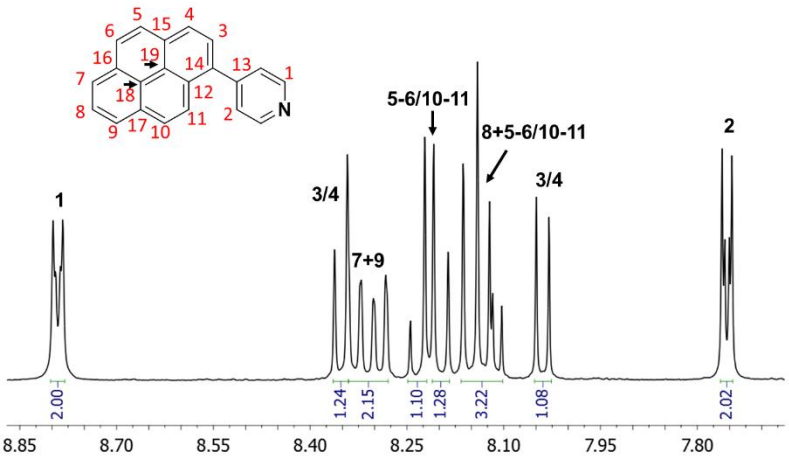

Figure S1. ^{1}H NMR of L^{2} in d_4-MeOD.

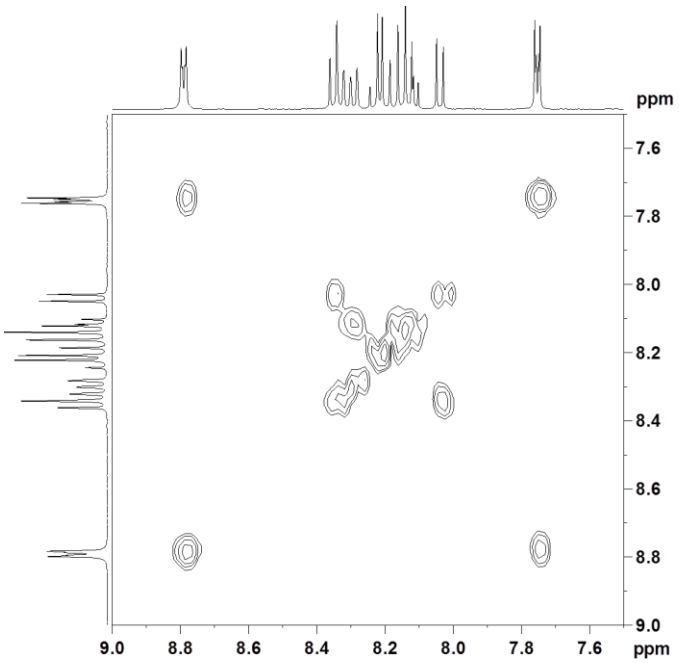

Figure S2. ^{1}H-^{1}H COSY NMR of L^{2} in d_4-MeOD.

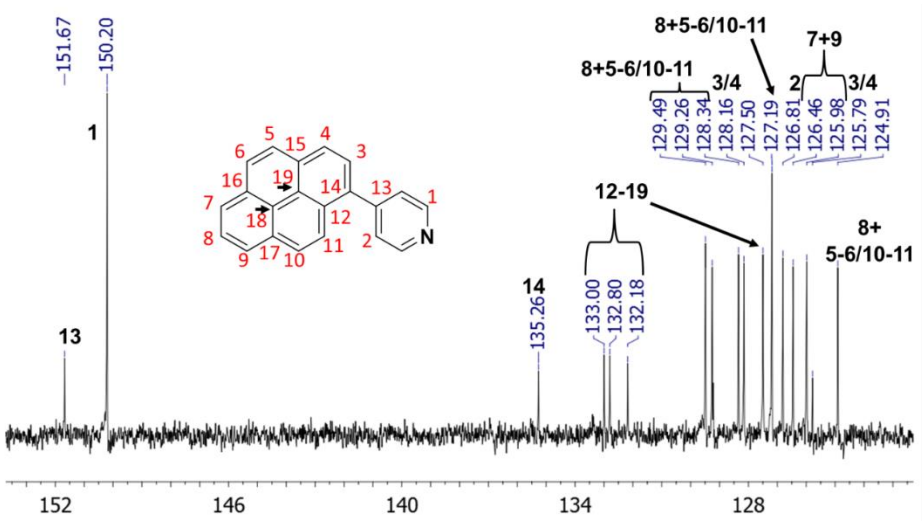

Figure S3. ^{13}C NMR of L^2 in d_4-MeOD.

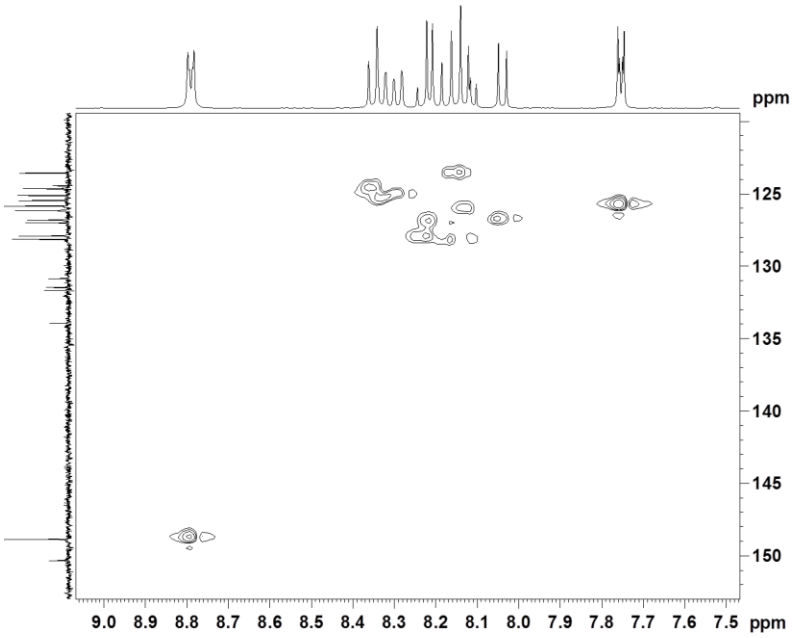

Figure S4. ^{1}H-^{13}C HSQC NMR of L^2 in d_4-MeOD.

VI

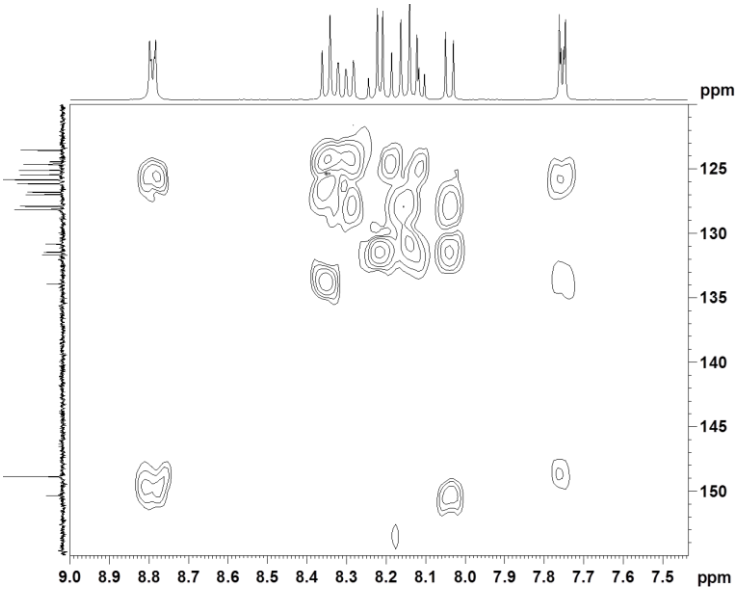

Figure S5. ^{1}H-^{13}C HMBC NMR of L^2 in d_4-MeOD.

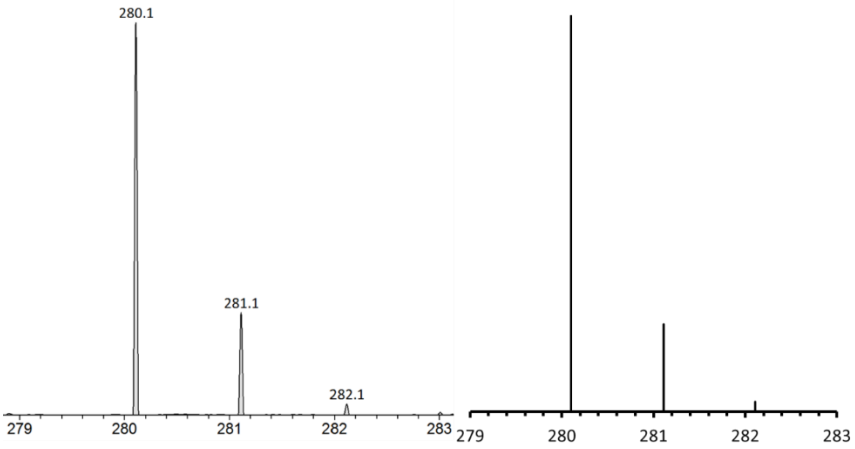

Figure S6. MS (ESI+) L^2 (left, 280.1) and simulated (right, 280.1).

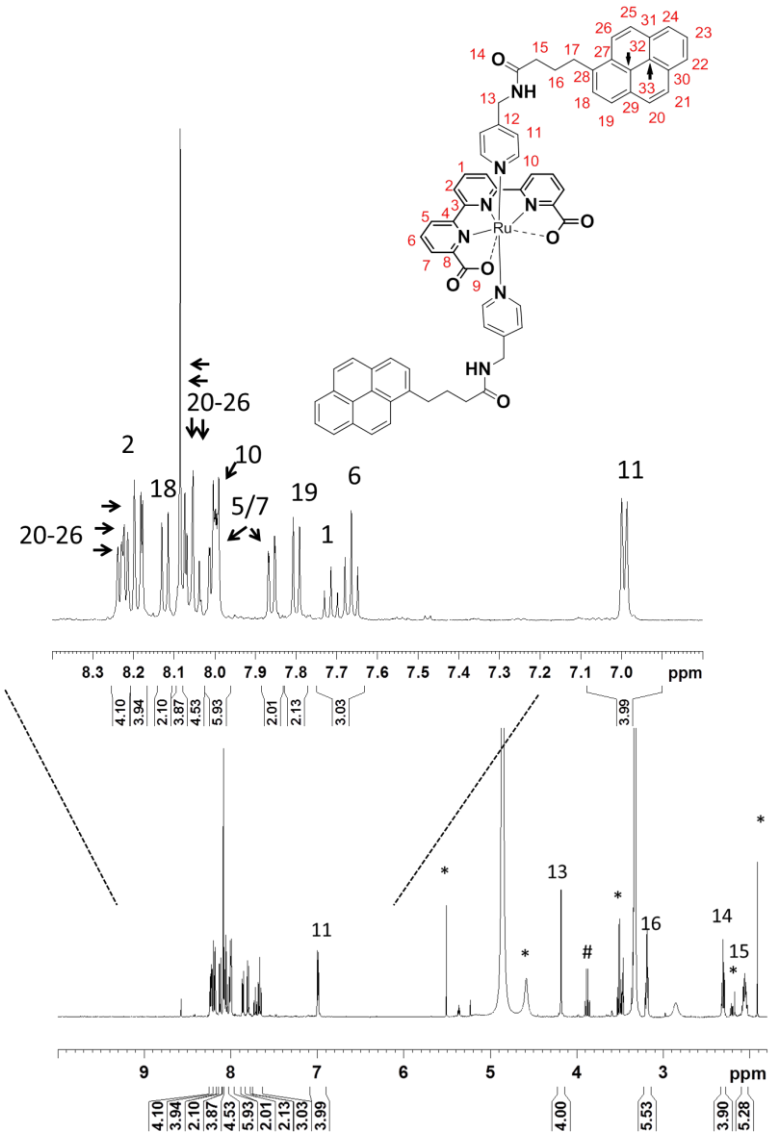

Figure S7. ^{1}H NMR of **1b** in d_4-MeOD and enlargement in the 7-8.5 ppm region (inset). Asterisks indicate the resonances assigned to the impurities of the NMR solvent (see Figure S12) and the hashtag indicates the $–CH_2-$ resonance of free Et_3N.

VI

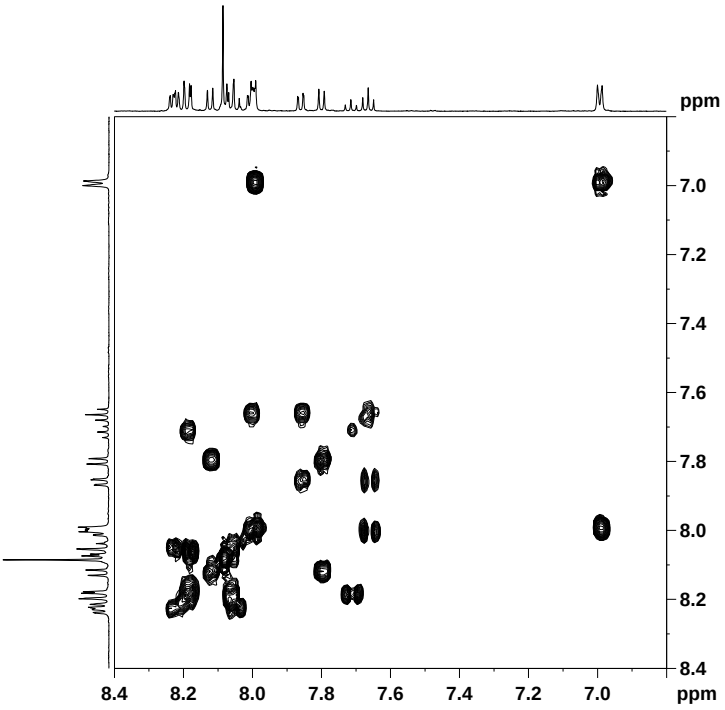

Figure S8. ^{1}H-^{1}H COSY NMR of **1b** in d_4-MeOD.

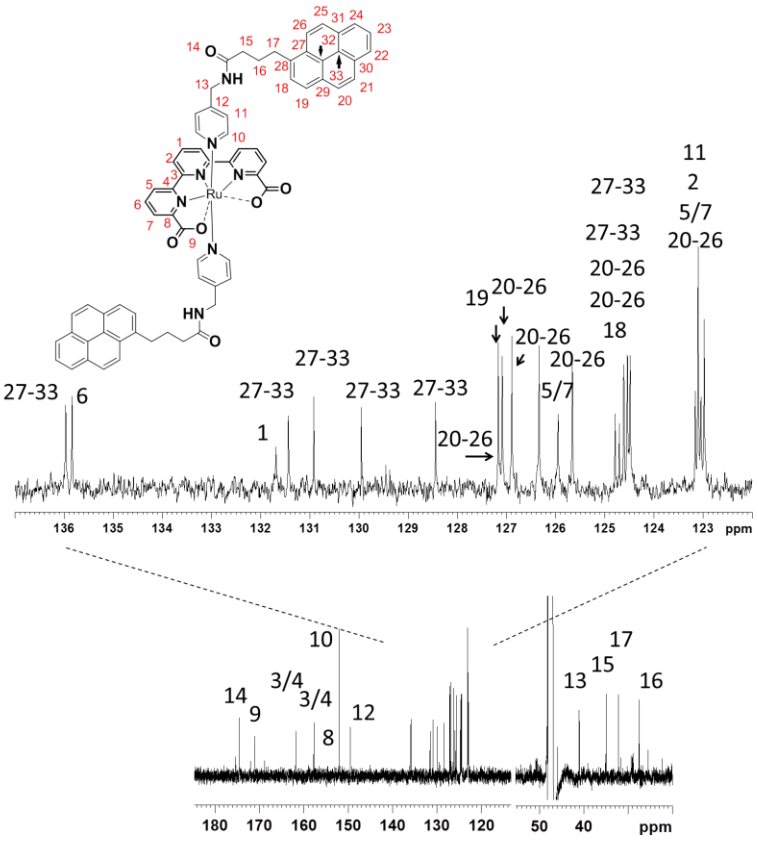

Figure S9. ^{13}C NMR of **1b** in d_4-MeOD.

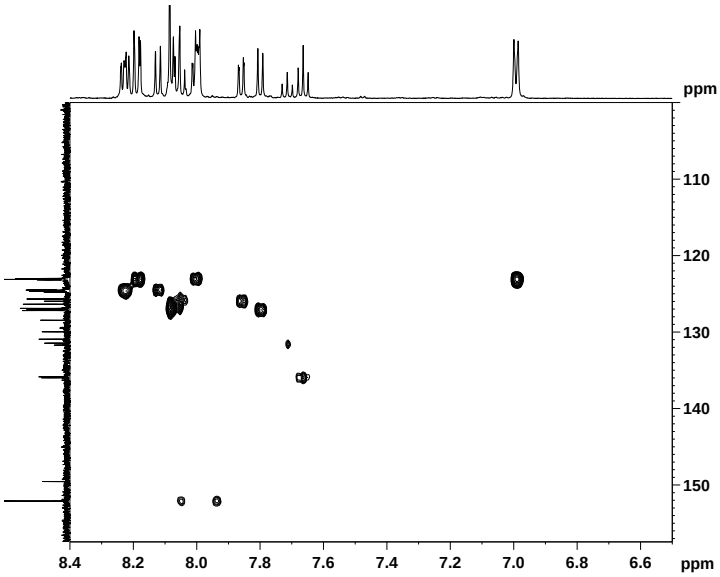

Figure S10. ^{1}H-^{13}C HSQC NMR of **1b** in d_4-MeOD.

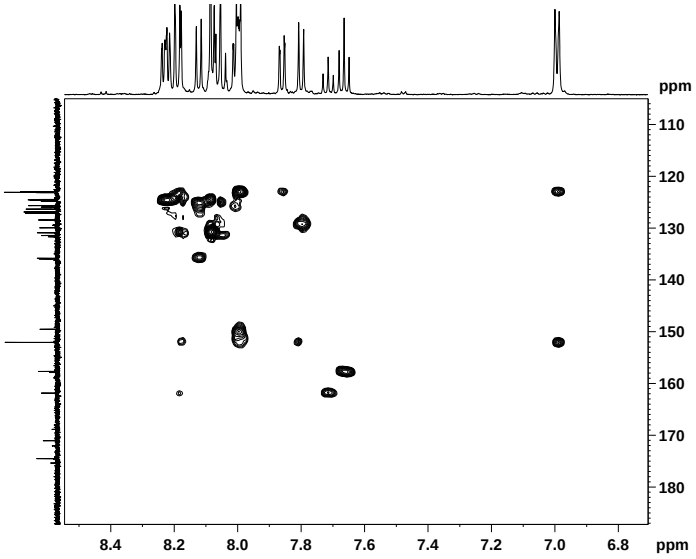

Figure S11. ^{1}H-^{13}C HMBC NMR of **1b** in d_4-MeOD.

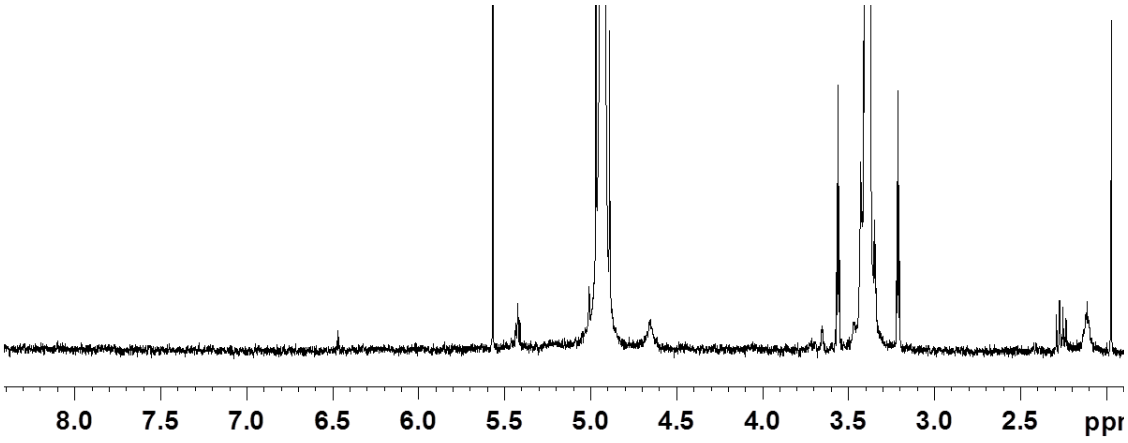

Figure S12. ^{1}H NMR of d_4-MeOD solvent

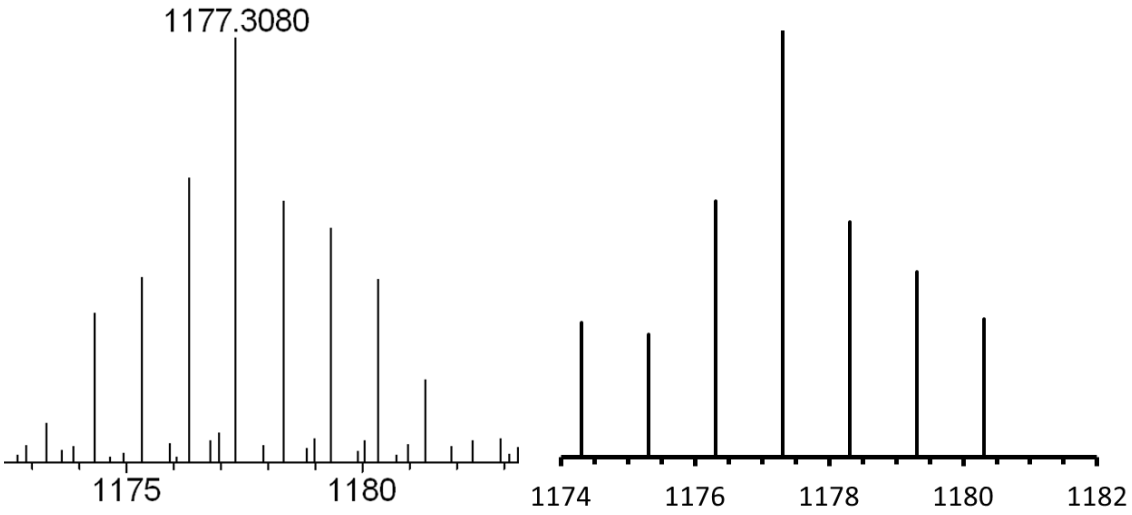

Figure S13. MS (ESI+) of **1b** (left, 1177.3080) and simulated (right).

VI

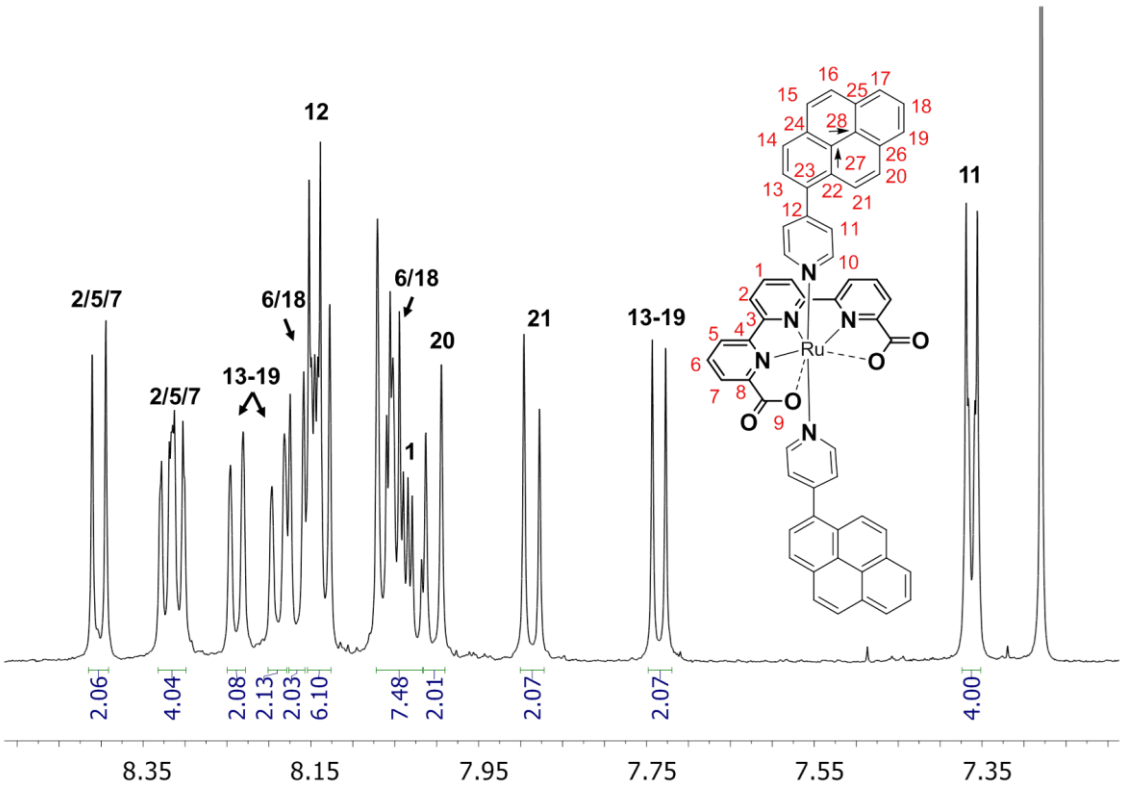

Figure S14. ^{1}H NMR of **1c** in $CDCl_3$:d_3-TFE (4:1).

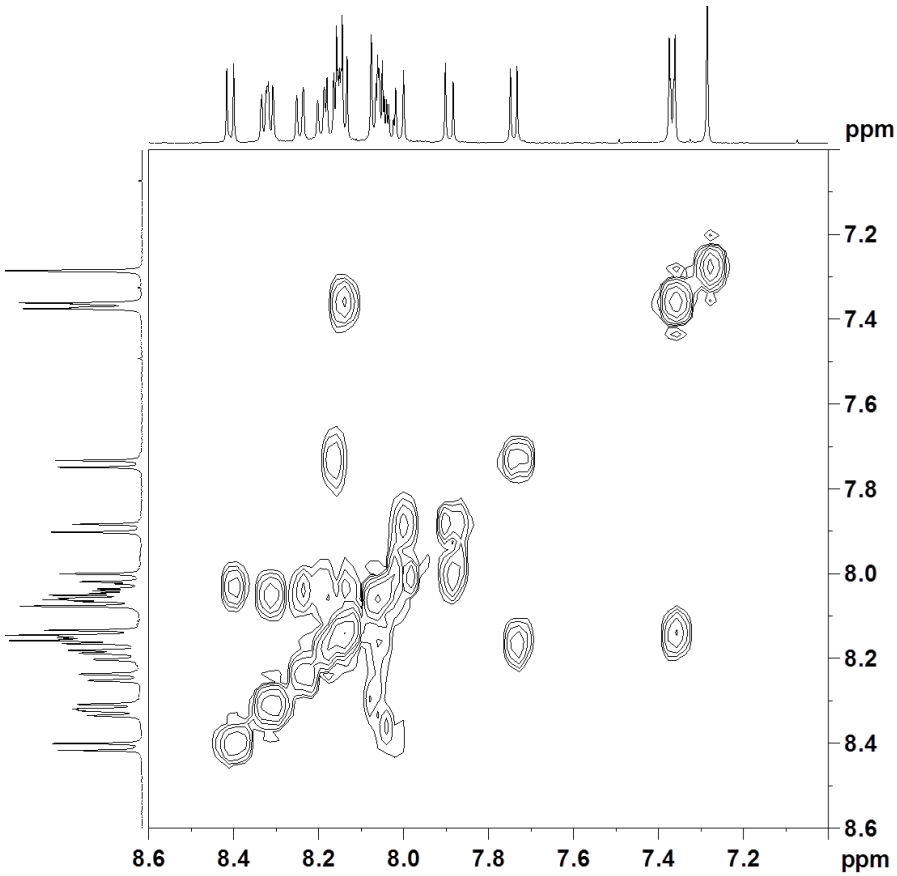

Figure S15. ^{1}H-^{1}H COSY of **1c** in $CDCl_3$:d_3-TFE (4:1).

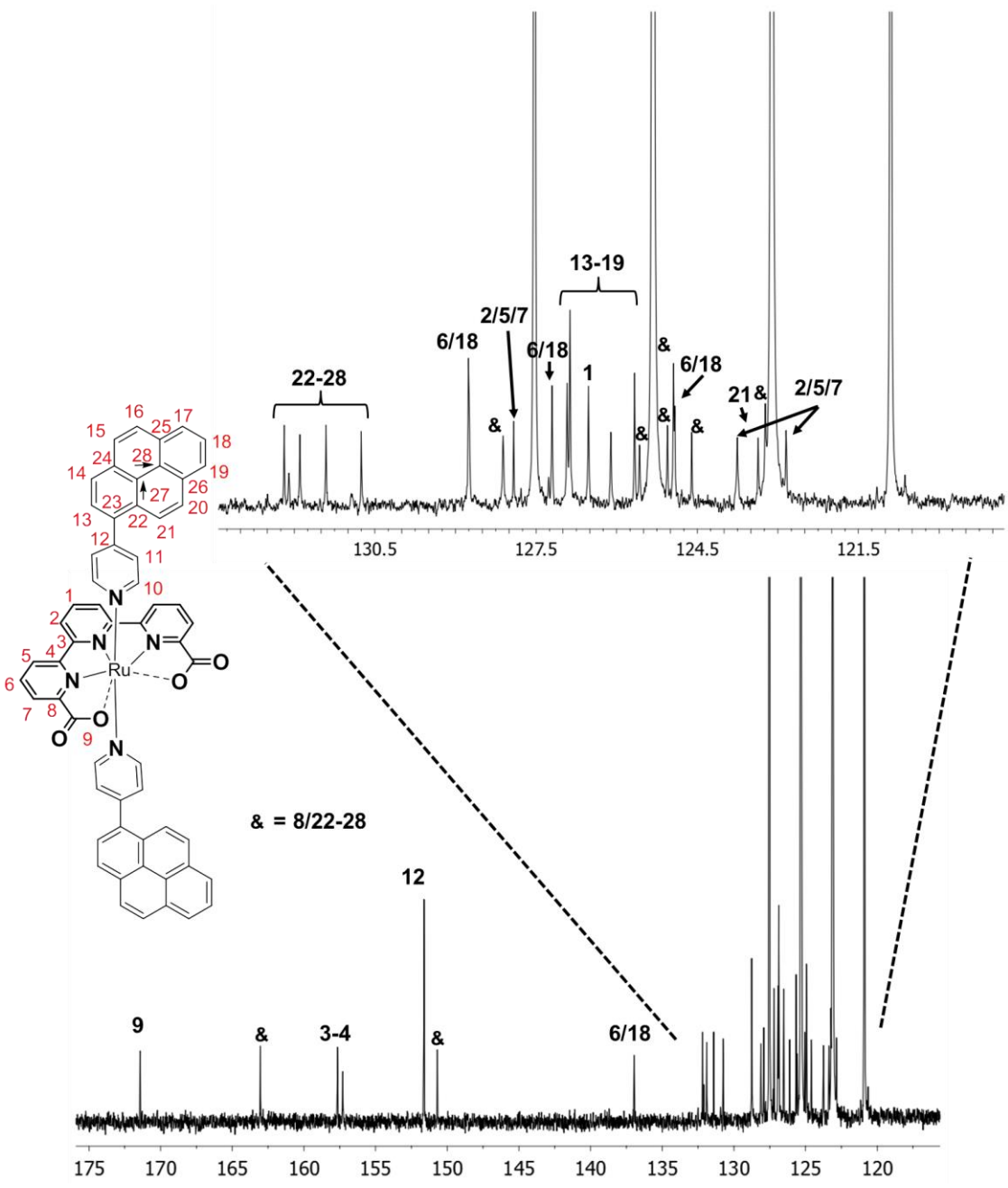

Figure S16. ^{13}C NMR of **1c** in $CDCl_3$:d_3-TFE (4:1).

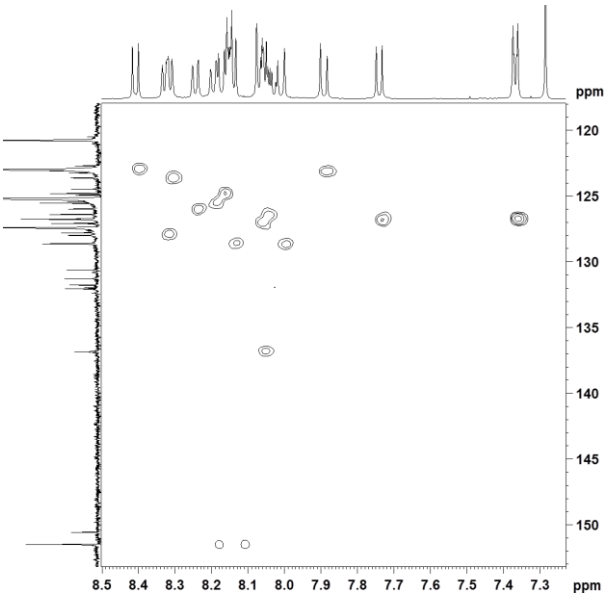

Figure S17. ^{1}H-^{13}C HSQC of **1c** in $CDCl_3$:d_3-TFE (4:1).

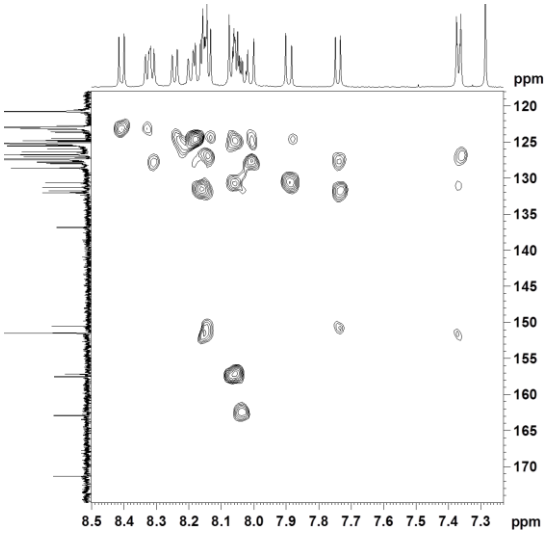

Figure S18. ^{1}H-^{13}C HMBC of **1c** in $CDCl_3$:d_3-TFE (4:1).

VI

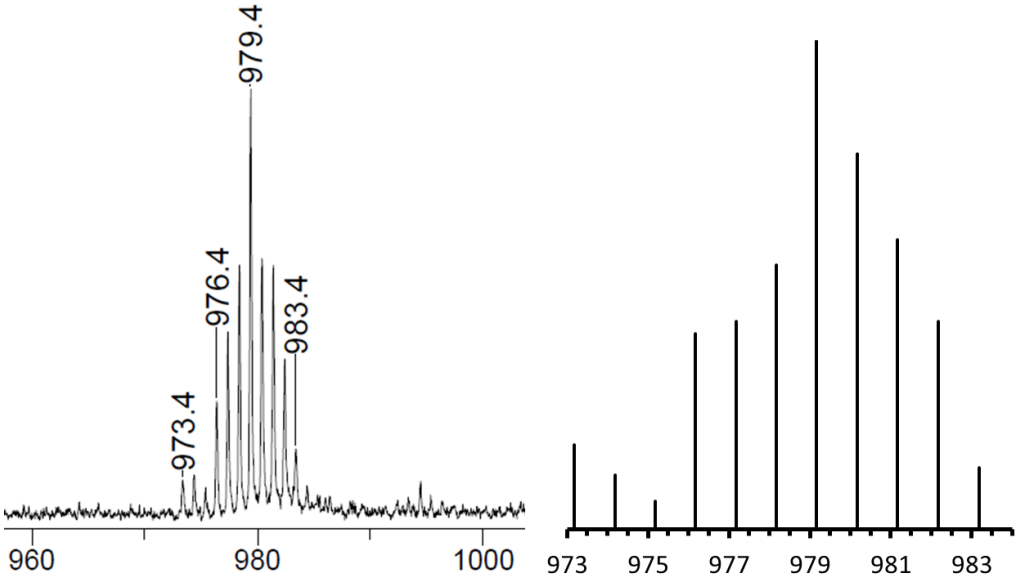

Figure S19. HR-MS (MALDI) of **1c** (left) and simulated (right).

VI

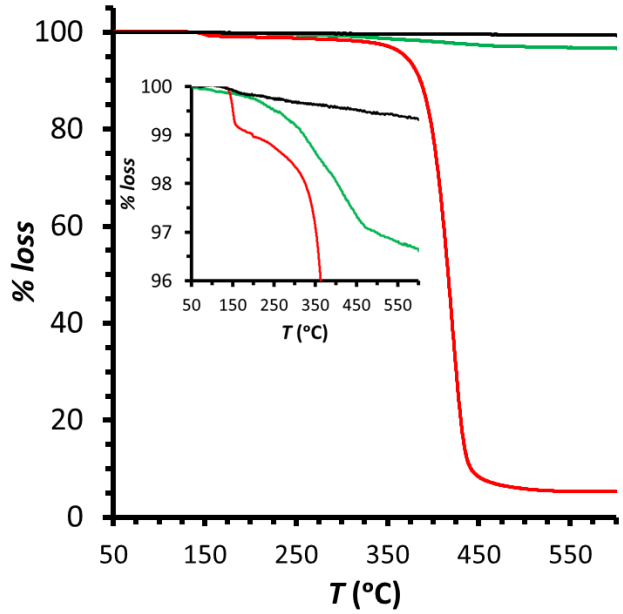

Figure S20. TGA plot of MWCNTs (black), L^1 (red) and L^1@MWCNT (green). The plot shows a loss of ~3 % of mass at 250-450 °C which corresponds to the percentage of ligand anchored by π-stacking onto the MWCNTs. See methods section for further details.

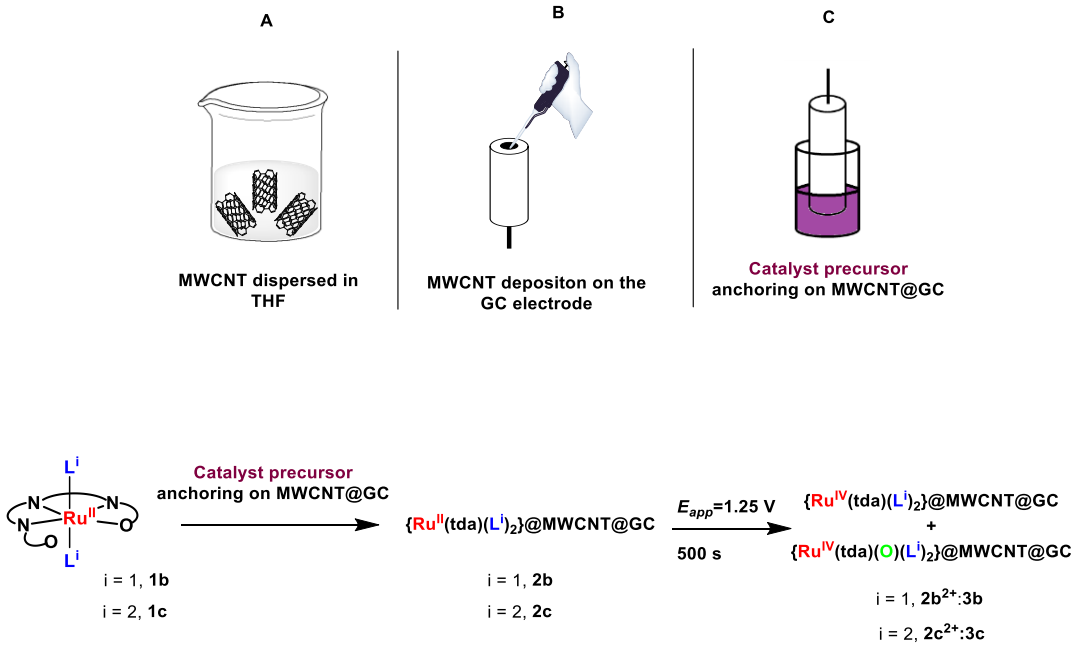

Figure S21. Top, A -> B -> C sequence of operations followed for the preparation of catalyst precursors anchored on MWCNT attached at the surface of GC electrodes. Bottom, reaction scheme followed for the preparation of mixtures of **2b**$^{2+}$:**3b** or **2c**$^{2+}$:**3c.**

Table S1. Averaged Surface Coverages (Γ, nmol·cm^{-2}) of complexes **2b**, **2b**$^{2+}$, **3b**, **2c**, **2c**$^{2+}$ and **3c** in GC_d and GC_p. See experimental methods section for further details regarding electrode preparation and surface coverage estimation.

	Surface Coverages (Γ, nmol·cm^{-2})	**Ratio of 3x:2x**
2b on *GC$_d$*	5.29 ± 1.10	--
2b^{2+}**:3b** on *GC$_d$*	2.22 ± 0.51, 0.43 ± 0.17	5.16 (± 1.89):1
2b on *GC$_p$*	3.48 ± 0.86	--
2b^{2+}**:3b** on *GC$_p$*	0.57 ± 0.16, 0.64 ± 0.24	0.89 (± 0.20):1
2c on *GC$_d$*	0.26 ± 0.05	--
2c^{2+}**:3c** on *GC$_d$*	0.13 ± 0.02, 0.03 ±0.01	4.33 (± 0.36):1

VI

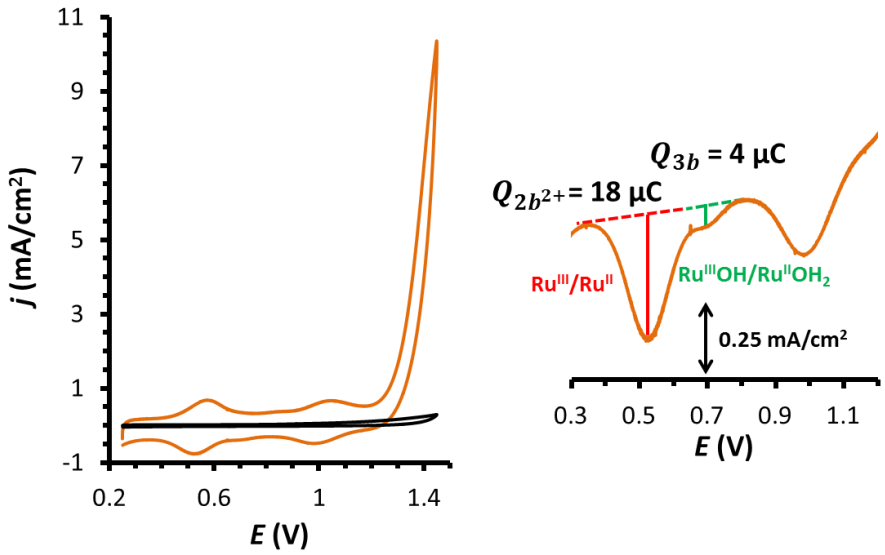

Figure S22. Left, in orange cyclic voltammogram of pH = 7 solution containing a modified electrode with a mixture of **2b**$^{2+}$:**3b** ($\Gamma_{2b^{2+}}$ = 2.66 nmol/cm^2 and Γ_{3b} = 0.55 nmol/cm^2). In black, a blank for MWCNT@GC$_d$ under the same conditions. Right, example of the estimation of the surface coverage Γ (nmol·cm^{-2}) from a cyclic voltammetry of a mixture of **2b**$^{2+}$**:3b** (orange line). We use Γ = Q / (n*S*F), where Q is the charge under the Ru^{III}/Ru^{II} reduction wave at 0.5 V in CV (red lines in the example); in the case of **3b** and **3c** Q is the charge under the Ru^{III}OH/Ru^{II}OH$_2$ reduction wave at 0.7 V in CV (green lines in the example).

VI

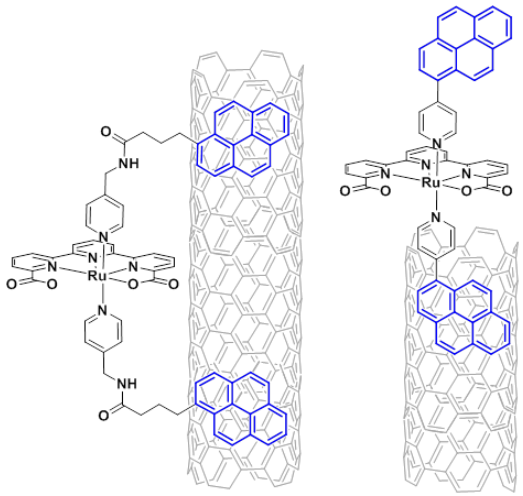

Figure S23. Schematic representation of the anchoring of complexes **1b** (left) and **1c** (right) in MWCNT.

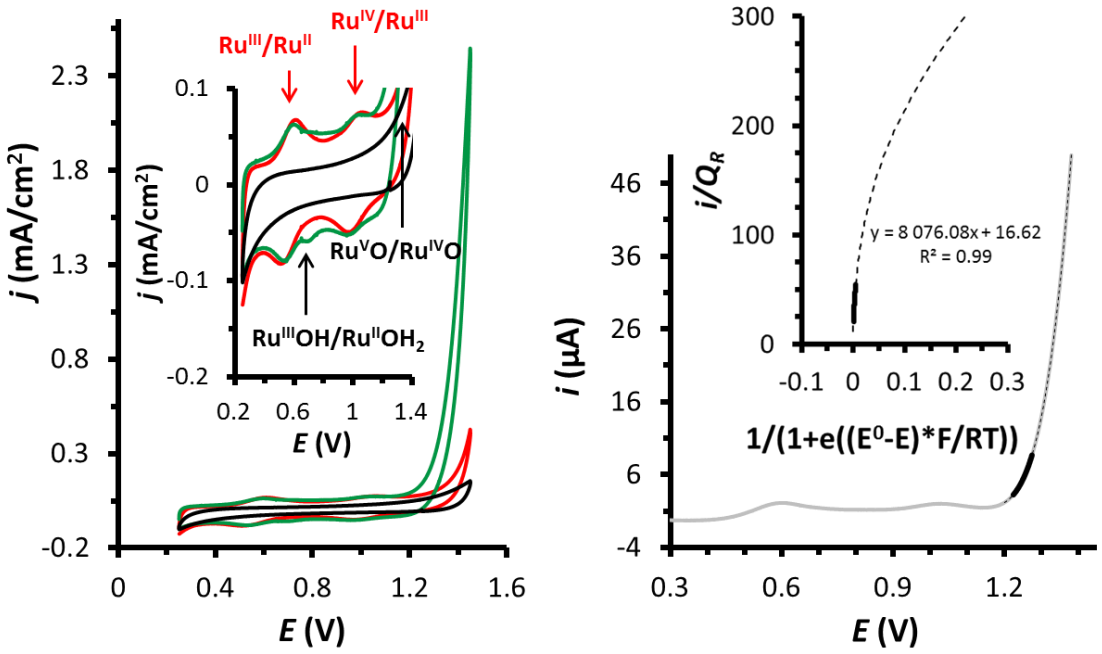

Figure S24. Left, cyclic voltammogram of a pH = 7 solution containing the electrode with the catalyst precursor **2c**, with a surface coverage of Γ_{2c} = 0.21 nmol/cm^2 (red line) using GC$_d$ as working electrodes. Green line, CV of a mixture ($\Gamma_{2c^{2+}}$ = 0.14 nmol/cm^2 and Γ_{3c} = 0.03 nmol/cm^2) under the same conditions. In black a blank for MWCNT@GC$_d$. Inset, enlargement of the 0.2-1.4 V potential zone with the assignment of redox couples. Right, linear sweep voltammetry at pH = 7 for the **2c^{2+}:3c** mixture (grey solid line). Inset, plot of i/Q_R *vs*. [1/(1+e((E^0-E)*F/RT))]. The black dashed line in both cases represents the experimental data used for the FOWA analysis, and the black solid line shows the experimental data used for the extraction of TOF$_{max}$ = 8076 s^{-1} for **3c**.

VI

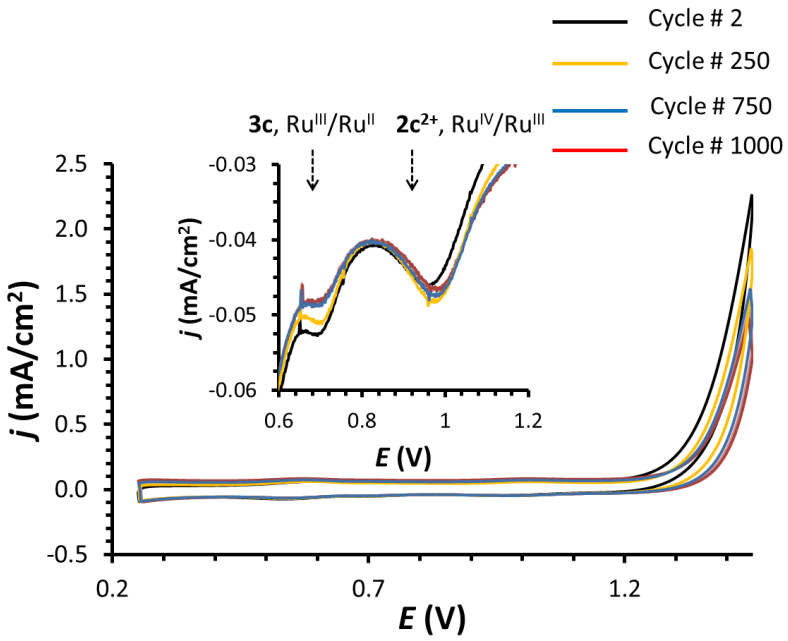

Figure S25. Selected CVs of a 1000 repetitive CV scans experiment (black solid line; 2nd Cycle, orange solid line; the 250th cycle, blue solid line; 750th line and red solid line; 1000th cycle) from an initial ratio of **2c**$^{2+}$:**3c** (right, $\Gamma_{2c^{2+}}$ = 0.13 nmol/cm^2 and Γ_{3c} = 0.03 nmol/cm^2) at GC_d at pH 7 at a scan rate of 100 mV/s.

VI

This repetitive CV experiments allow monitoring of the slow equilibrium between **3c** (the catalyst) and **2c**$^{2+}$ (the catalyst precursor) that occurs at pH = 7 during catalysis indicated in equation S1 below,

$$\underset{\mathbf{2c}^{2+}}{\{Ru^{IV}(tda)(L^2)_2\}@MWCNT@GC\}^{2+}} + OH^- \rightleftharpoons \underset{\mathbf{3c}}{\{Ru^{IV}(tda)(O)(L^2)_2\}@MWCNT@GC\}} + H^+ \quad \text{eq. S1}$$

The black line represents the second scan and thus is taken as a reference. At the 250th scan, orange line, the intensity of the cathodic wave for the IV/III redox potential ($i_{p,c}$ - **2c**$^{2+}$) has increased by 1.8 μA/cm^2 while the intensity of the IV/III cathodic wave for **3c** ($i_{p,c}$ - **3c**) has increased roughly about the same magnitude. This clearly indicates that as the reaction proceeds the equilibrium is shifted to the left (eq. S1), that is toward the precursor.At the 750th scan, blue line, the ($i_{p,c}$ - **2c**$^{2+}$) now decreases by 0.8 μA/cm^2 with regard to the 250th scan (yellow line) and the ($i_{p,c}$ - **3c**) also decreases now by again 2.6 μA/cm^2. This is due to both a further shift to the left of equilibrium shown in equation 1 and to the partial detachment of the MWCNT most likely due to a mechanical friction effect. The 1000th scan, red line, shows a continuation of the effects just described.

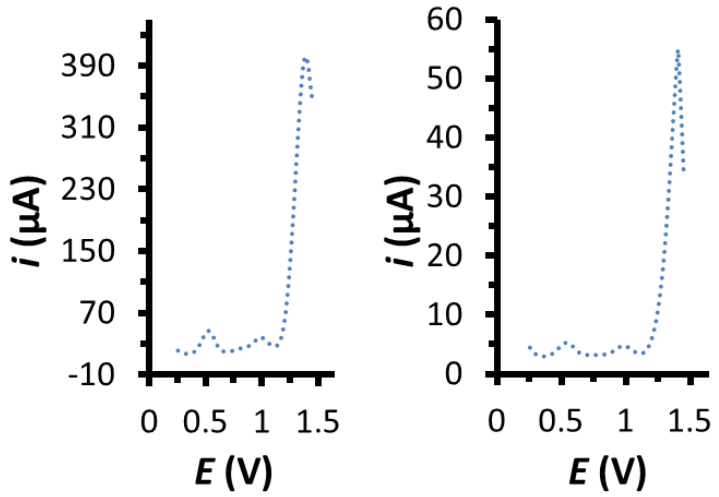

Figure S26. DPV experiments for hybrid materials at a GC_d working electrode at pH = 7: left, **2b^{2+}:3b** ($\Gamma_{2b^{2+}}$= 2.66 nmol·cm^{-2}, Γ_{3b}= 0.55 nmol·cm^{-2}; 5:1 ratio); right, **2c^{2+}:3c** ($\Gamma_{2c^{2+}}$ = 0.14 nmol·cm^{-2}, Γ_{3c} = 0.03 nmol·cm^{-2}, 4.7:1 ratio). See electrochemical methods for DPV experimental details.

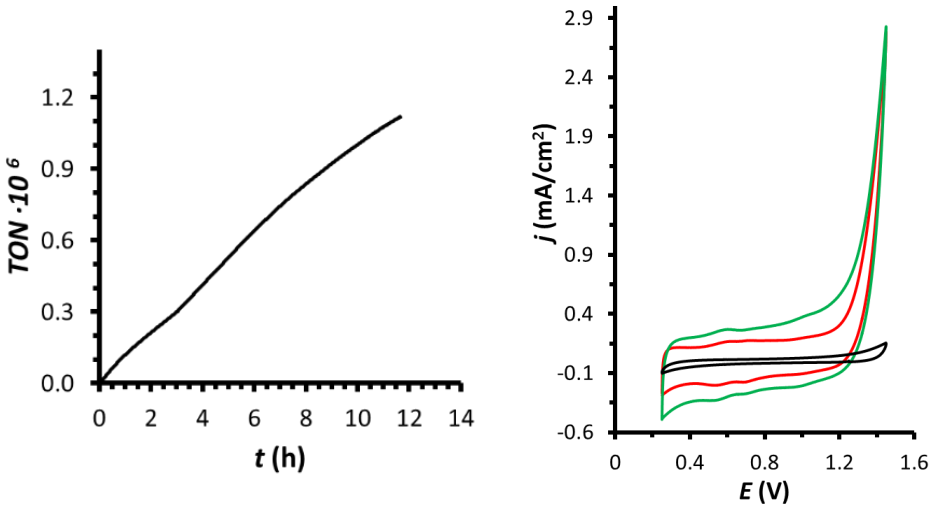

Figure S27. Left, plot of TON *vs*. time obtained from a bulk electrolysis experiment of **2c^{2+}:3c** ($\Gamma_{2c^{2+}}$ = 0.14 nmol·cm^{-2} and Γ_{3c} = 0.03 nmol·cm^{-2}, 9:2 ratio, TOF= 40 s^{-1}) using a GC_d as a working electrode at pH = 7 at an E_{app} = 1.45 V. The measured Resistance of the system was R = 200 Ohms at the end of the bulk electrolysis. Right, cyclic voltammogram of a pH = 7 solution of **2c^{2+}:3c** before (red line) and after (green line) the bulk electrolysis showing that the initial complex remains intact. A CV (black line) of a bare MWCNT@GC_d is also show for comparison.

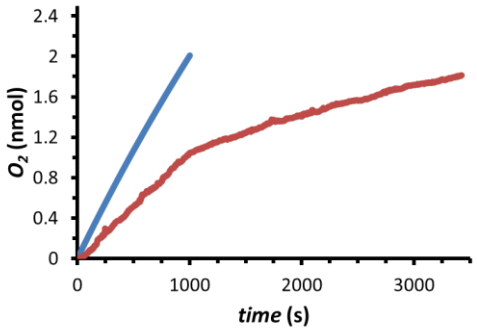

Figure S28. Plot of oxygen generation vs. time based on a bulk electrolysis experiment for the hybrid material **2b^{2+}:3b** ($\Gamma_{2b^{2+}}$ = 0.50 nmol·cm^{-2} and Γ_{3b} = 0.40 nmol·cm^{-2}; 5:4 ratio) using a GC_p working electrode at pH = 7 at an E_{app} = 1.5 V. In blue, the amount of oxygen generated based on the current density assuming 100% Faradaic efficiency and in red is the O_2 generated measured in the gas phase with a Clark electrode. The applied potential was stopped after 1000 s (see blue curve) but the O_2 evolution continued for 2500 s more (see red curve) due to the O_2 bubbles trapped at the working electrode. At 3500 s the Faradaic efficiency reach a value of 91%. The remaining current is due to the oxidation of the graphitic electrode.

VI

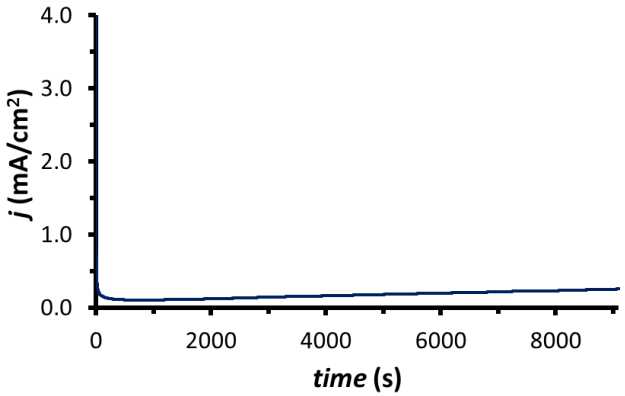

Figure S29: Bulk electrolysis experiment of a bare MWCNT@GC_d at pH = 7 and E_{app} = 1.45 V.

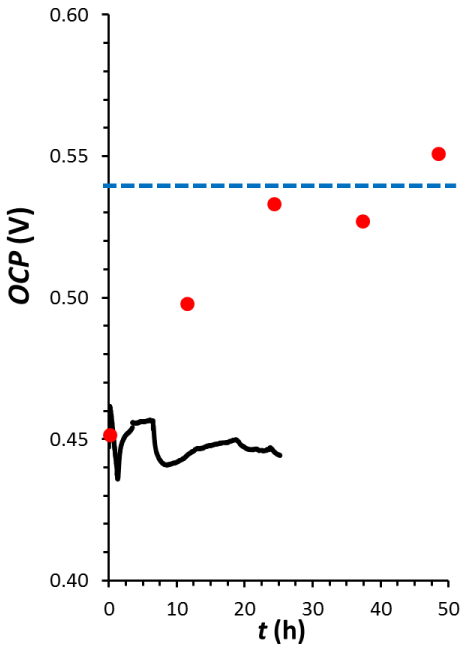

Figure S30. Open Circuit Potential (OCP) monitoring over time of freshly prepared **2b**. Black line, plot of continuous *OCP vs*. *t* for **2b** soaked in a pH = 7 solution. Red dots, plot of *OCP vs*. *t* for **2b** kept in the air and only soaked at pH = 7 for occasional OCP measurement every 12 hours. The blue dashed line indicates the $E^{o}_{III/II}$ for **2b** extracted from DPV after the last experiment at 50 h.

VI

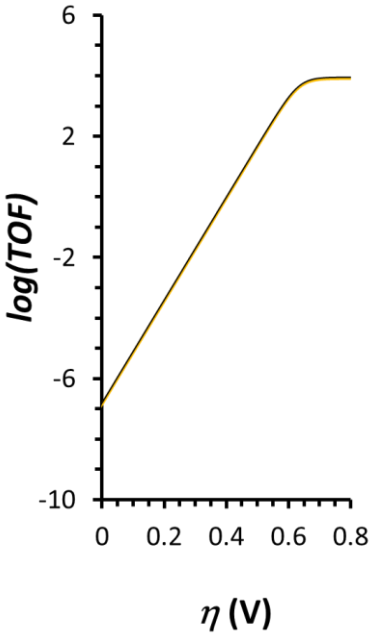

Figure S31: Catalytic Tafel plots of complexes **3b** (black line) and **3c** (orange line)**.**

Table S2. Comparison of XANES energy for reference complexes and those on glassy carbon sheets.

Sample	Energy at Normalized fluorescence 0.5	Percentage presence of Ru(III)
Ru^0	22122.60	-
1a	22125.81	-
1b	22125.81	-
1a(PF_6)	22127.73	-
1a($(PF_6)_2$	22129.08	-
RuO_2	22129.08	-
$2b^0$	22127.34	80 % Ru (III) + 20 % Ru(II)
2b'	22127.54	90 % Ru(III) + 10 % Ru(II)
2b''	22127.54	90 % Ru(III) + 10 % Ru(II)

VI

Given the partial oxidation of **$2b^0$** by 20%, it meant that real samples reaching the synchrotron were composed of (80% **$2b^+$** and 20% **2b**). Since we did not have the XAS data for pure **2b** we used that of **1b**, which by CV we know are basically identical. Therefore, the EXAFS analysis carried out is for **$2b^0$**-20% **1b**. The data obtained in this way coincides very nicely with that of **$1a^+$** (which we assume will be very similar to **$2b^+$** based on electrochemical experiments), and thus clearly indicates the presence of 80% **$2b^+$**, in the **$2b^0$** sample.

We used the same methodology for **2b'** and **2b''** subtracting 10% of **1b**, according to their k-edge energies. Here, an additional approximation is done since **2b'** and **2b''** might contain a certain amount of reduced **3b** species. However we are not expecting them to be significant since it is known that in homogeneous phase the corresponding Ru-OH or Ru-OH_2 species readily

evolve towards the formation of the precursor complexes **1a** or **1a**$^{+}$ depending on the initial oxidation state.

Table S3. Metric parameters obtained for complexes **1a**, **1a**$^{+}$, **1a**$^{2+}$, **2b**^{0}**-1b**, **2b'-1b, 2b''-1b** obtained from EXAFS (XAS) and from X-ray crystallography (XR) when available.

							2b^{+}		
Complex	**1[a]**		**1a^{+}**		**1a^{2+}**		**2b^{0}-1b[a]**	**2b'-1b[a]**	**2b''-1b[a]**
Dist.[b]/Tech.	**XR**	**XAS[c]**	**XR**	**XAS[c]**	**XR**	**XAS[c]**	**XAS[c]**	**XAS[c]**	**XAS[c]**
Ru-N3	1.93	1.93 (2)	2.13	2.11 (6)	2.09	2.11 (5)	2.11 (6)	2.10 (6)	2.10 (6)
Ru-N2	1.93	...	2.04		2.12				
Ru-N1	2.14	2.04 (3)	2.06		2.11				
Ru-N4$_{ax}$	2.10	...	2.07		2.10				
Ru-N5$_{ax}$	2.08		2.09		2.10				
Ru-O1	2.20	2.19 (1)	2.20		2.02	2.02 (2)			
Ru-O2[d]	--	- -	2.33	2.36 (1)	2.02		2.46 (1)	2.47 (1)	2.43 (1)

[a] The label **2b^{0}-1b**, corresponds to the sample **2b^{0}** with a subtraction of 20% **1b**, as discussed in the main text. The label **2b'-1b** and **2b''-1b** corresponds to **2b'** and **2b''** with 10% **1b** subtraction.

[b] Distances between Ru and the atoms in its first coordination sphere. The labeling scheme is the same as the one used for XR data of **1** depicted in figure below. All distances in Å.

[c] In parenthesis, *N*, is the coordination number defined as the number of atoms associated with a particular distance. Additional EXAFS fit parameters (Debye-Waller factors and error sums) are given in the Tables S4-S5. N and O coordination is indistinguishable in EXAFS analysis as are the locations of ligands in equatorial or axial positions; in the Table the distances from EXAFS have no particular ordering.

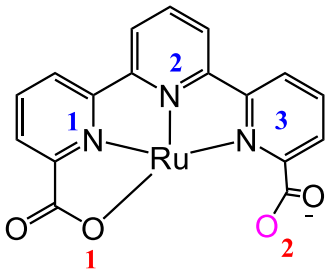

[d] for Ru(III) this corresponds to a contact (named half coordination in the main text) whereas for Ru(IV) it corresponds to a full seven coordination.

VI

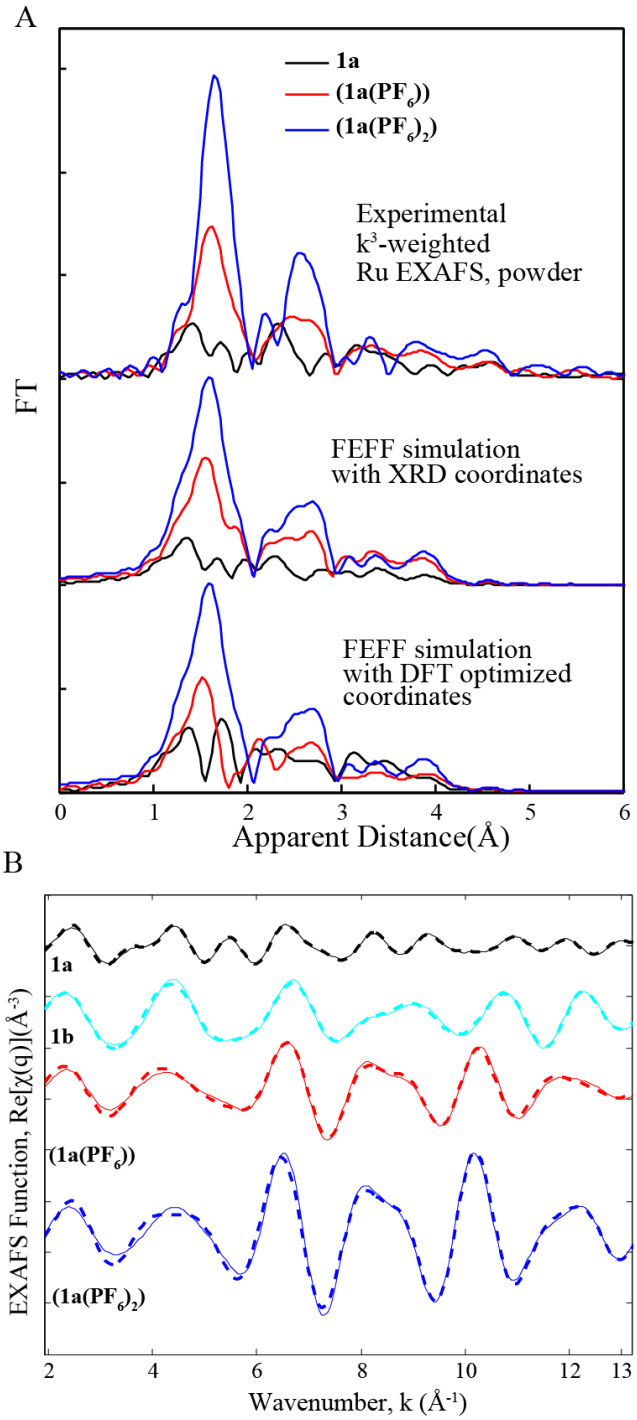

VI

Figure S31 A. Fourier transforms of k^3-weighted Ru EXAFS of 1a, ($1a(PF_6)$), ($1a(PF_6)_2$), obtained from powders . EXAFS spectra simulated with FEFF software is shown for comparison. Coordinates of all atoms[4] from X-ray structures and DFT optimized coordinates were used as input. EXAFS fits for the first coordination sphere and for the entire spectrum are shown in Figure S32 and Table S4.**B.**Back Fourier transformed experimental (solid lines) and

fitted (dashed lines) Re[χ(q)](Å^{-3}) for **1a** (fit 4 in Table S4), **1b** (fit 8 in Table S3), **1a(PF$_6$)** (fit 12 in Table S4) and **1a(PF$_6$)$_2$** (fit 16 in Table S4).

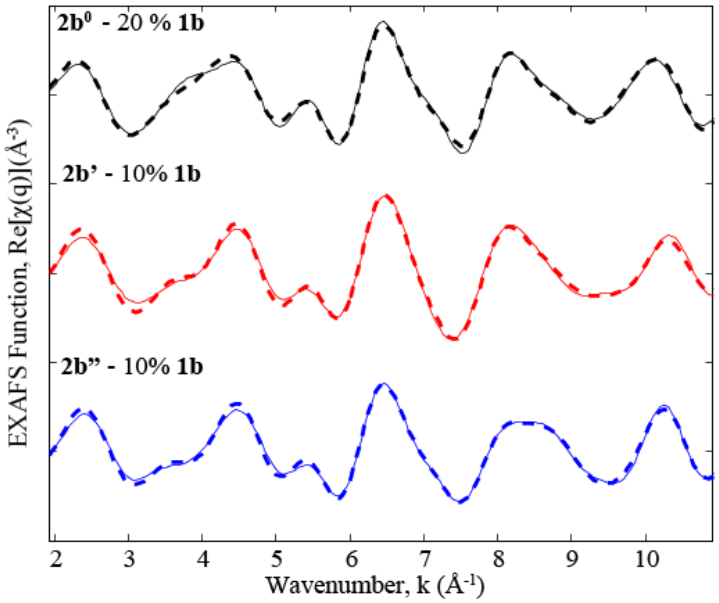

Figure S32. Back Fourier transformed experimental (solid lines) and fitted (dashed lines) Re[χ(q)](Å^{-3}) for **2b$^+$** (**2b^0**-20% **1b**), **2b$^+$** (**2b'**-10% **1b**) and **2b$^+$** (**2b''**-10% **1b**). See fits 4, 8 and 12 respectively in Table S5.

Table S4. EXAFS fits of reference compounds **1a, 1b, 1a(PF$_6$)** and **1a(PF$_6$)$_2$**.

VI

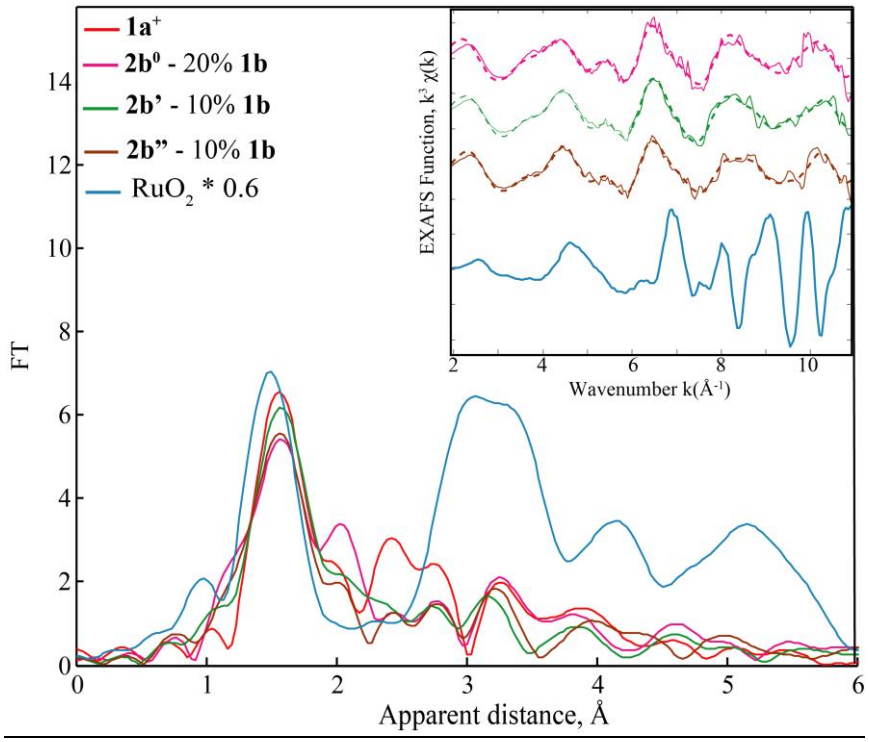

VI

Figure S33. Fourier transforms of k^3-weighted Ru EXAFS of **1a**$^+$, **2b**$^+$ (**2b**^{0}-20% **1b**), **2b**$^+$ (**2b'**-10% **1b**) and **2b**$^+$ (**2b''**-10% **1b**) and RuO_2. Inset: Back Fourier transformed experimental (solid lines) and fitted (dashed lines) $k^3\chi(k)$. Experimental spectra were calculated for k values of 1.941-10.9 Å^{-1}. This figure also shows that RuO_2 EXAFS spectral features were absent on all samples deposited on carbon plates clearly showing absence of any RuO_2 decomposition product.

Sample	Fit	Peak	Shell, N	R, Å	E_0	ss.^{2} (10^{-3})	R-factor	Reduced Chi-square
1a	1	I	Ru-N,2	1.94	-11.6	13.1	0.0253	44.1
			Ru-N,3	2.05				
	2	I	Ru-N,2	1.93	-9.5	10.0	0.0249	74.7
			Ru-N,3	2.05				
			Ru-O,1	2.17				

	3	I,II	Ru-N,2	1.92	0.48	29.8	0.0087	516
			Ru-N,3	2.03		8.2		
			Ru-O,1	2.17		3.3		
			Ru-C,9	2.93		9.7		
			Ru-C,4	3.26		15.3		
	4	I,II,	Ru-N,2	1.93	3.3	29.0	0.0029	207
		III	Ru-N,3	2.04		7.2		
			Ru-O,1	2.19		1.5		
			Ru-C,9	2.94		7.8		
			Ru-C,4	3.17		8.8		
			Ru-C,4	3.50		2.6		
			Ru-C,4	3.67		0.8		
			Ru-O,1	4.06		4.0		
1b	5	I	Ru-N,6	2.02	-6.4	6.9	0.0042	200
	6	I	Ru-N,5	2.01	-9.2	4.6	0.0041	283
			Ru-N,1	1.86				
	7	I	Ru-N,4	2.03	-3.6	2.1	0.0017	221
			Ru-N,1	1.90		2.0		
			Ru-N,1	2.20		2.1		
	8	I,II	Ru-N/O,4	2.08	1.6	1.4	0.0010	51.0
			Ru-N,1	1.91		4.7		
			Ru-N,1	2.26		6.4		
			Ru-C,8	2.98		14.4		

			Ru-C,5	3.34		9.6		
1a(PF_6)	9	I	Ru-N,7	2.08	1.2	5.6	0.0129	1218
	10	I	Ru-N/O,6	2.08	0.01	4.9	0.0020	233
			Ru-O,1	2.37				
	11	I	Ru-N/O,6	2.10	4.1	5.0	0.0030	179
			Ru-O,1	2.36		3.6		
			Ru-C,8	3.00		3.6		
			Ru-C,5	3.30		5.7		
	12	I	Ru-N/O,6	2.11	6.4	5.0	0.0022	87
			Ru-O,1	2.36		3.5		
			Ru-C,8	3.01		3.3		
			Ru-C,5	3.32		5.6		
			Ru-C,8	3.70		12.4		
			Ru-C,5	4.24		2.3		
1a(PF_6)$_2$	13	I	Ru-N,7	2.11	3.0	2.0	0.0013	4754
	14	I	Ru-N,5	2.10	-3.6	3.7	0.0002	4308
			Ru-O,1	1.93		7.3		
	15	I	Ru-N,5	2.09	-7.7	4.3	0.0002	4219
			Ru-O,2	1.93		5.3		
	16	I,II	Ru-N,5	2.11	0.43	0.4	0.0004	320
			Ru-O,2	2.02		2.3		
			Ru-C,12	3.02		2.7		

- The amplitude reduction factor, S_0^2 was fixed to 1.
- Peak I refers to the region between 1/1.2-2/2.2 Å, peak I,II to 1.2-3 Å and peak I,II,III to 1.2-4.1 Å

Table S5. EXAFS Fits of **2b**$^+$ for (**2b**^{0}-20% **1b**), (**2b'**-10% **1b**) and (**2b''**-10% **1b**).

Sample	Fit	Peak	Shell, N	R, Å	E_0	ss.^{2} (10^{-3})	R-factor	Reduced Chi-square
2b^0-20% **1b**	1	I	Ru-N,7	2.09	-0.4	6.6	0.0390	418
	2	I	Ru-N/O,6	2.11	3.0	5.6	0.0056	80
			Ru-O,1	2.46				
	3	I,II	Ru-N/O,6	2.10	2.2	6.8	0.0022	33
			Ru-O,1	2.46		0.1		
			Ru-C,8	3.00		10.3		
			Ru-C,5	3.35		13.0		
	4	all	Ru-N/O,6	2.11	4.4	7.1	0.0020	16
			Ru-O,1	2.46		0.8		
			Ru-C,8	3.02		8.1		
			Ru-C,5	3.34		7.9		
			Ru-C,8	3.68		7.2		
			Ru-C,4	4.20		1.9		
2b'-10% **1b**	5	I	Ru-N,7	2.10	2.5	6.8	0.0119	709
	6	I	Ru-N/O,6	2.10	3.2	6.0	0.0031	300
			Ru-O,1	2.47				
	7	I,II	Ru-N/O,6	2.10	3.3	6.5	0.0008	150

VI

			Ru-O,1	2.47		0.9		
			Ru-C,8	3.01		9.8		
			Ru-C,5	3.35		9.1		
	8	all	Ru-N/O,6	2.10	4.6	6.4	0.0004	22
			Ru-O,1	2.47		1.7		
			Ru-C,8	3.00		8.0		
			Ru-C,5	3.33		13.7		
			Ru-C,8	3.64		9.7		
			Ru-C,4	4.22		1.6		
2b''-10% **1b**	9	I	Ru-N,7	2.10	2.2	8.0	0.0082	195
	10	I	Ru-N/O,6	2.09	4.0	6.9	0.0010	31
			Ru-O,1	2.43				
	11	I,II	Ru-N/O,6	2.10	5.1	7.4	0.0004	18
			Ru-O,1	2.43		4.6		
			Ru-C,8	3.05		11.7		
			Ru-C,5	3.37		6.3		
	12	all	Ru-N/O,6	2.10	6.3	7.4	0.0004	9
			Ru-O,1	2.43		4.4		
			Ru-C,8	3.04		10.2		
			Ru-C,5	3.35		8.9		
			Ru-C,8	3.68		8.4		
			Ru-C,4	4.26		1.6		

- The amplitude reduction factor, S_0^2 was fixed to 1
- Peak I refers to the region between 1.2-2.25 Å, peak I,II to 1.2-3 Å and all to 1.2-4.1 Å

References

S1 C. Galaup, J.-M. Couchet, S. Bedel, P. Tisnès, C. Picard, *Org. Chem.* **2005**, *70*, 2274-2284.
S2 I. P. Evans, A. Spencer, G. Wilkinson, *J. Chem. Soc., Dalton Trans.* **1973**, 204-209
S3 F. Li, B. Zhang, X. Li, Y. Jiang, L. Chen, Y. Li, L. Sun, *Angew. Chem. Int. Ed.* **2011**, *50*, 12276-12279.
S4 R. Matheu, M. Z. Ertem, J. Benet-Buchholz, E. Coronado, V. S. Batista, X. Sala, A. Llobet, *J. Am. Chem. Soc.* **2015**, *137*, 10786-10795.
S5 E. J. Parra, F. X. Rius, P. Blondeau, *Analyst* **2013**, *138*, 2698-2703.
S6 C. Costentin, S. Drouet, M. Robert, J.-M. Savéant, *J. Am. Chem. Soc.* **2012**, *134*, 11235-11242.
S7 Data collection with CrystalClear-SM Expert 2.1 b29. Rigaku 2013.
S8 Data reduction with CrysAlisPro 1.171.38.37f (Rigaku OD, 2015).
S9 Empirical absorption corrrection using sperical harmònics implemented in Scale3 Abspack scaling algorithm, CrysAlisPro 1.171.38.37f (Rigaku OD, 2015).
S10 SHELXT; G.M. Sheldrick, *Acta Cryst*. **2015**, A71, 3-8.
S11 SHELXle; Huebschle, C.B.; Sheldrick, G.M.; Dittrich, B. *J. Appl. Cryst.* **2011**, *44*, 1281-1284.
S12 SHELXL; Sheldrick, G.M. *Acta Cryst*. **2015**, C71, 3-8. SHELXT
S13 B. Ravel, M. Newville, *J.Synch. Rad.* **2005**, *12*, 537-541.
S14 J. J. Rehr, R. C. Albers, *Rev.Mod. Phys.* **2000**, *72*, 621-654.
S15 D. C. Koningsberger, R. Prins, *X Ray Absorption: Principles, Applications, Techniques of EXAFS, SEXAFS and XANES*; John Wiley & Sons,

UNIVERSITAT ROVIRA I VIRGILI
SEVEN-COORDINATE COMPLEXES FOR WATER OXIDATION CATALYSIS: FROM MOLECULAR CHARACTERIZATION TO SOLID STATE PHOTOCATALYSIS
Roc Matheu Montserrat

Chapter 7

Photoelectrochemical Behavior of Ru-Based Water-Oxidation Catalysts Bound to TiO_2-Protected Si Photoanodes

A molecular photoanode based on a Ru-tda catalyst and a Si semiconductor is tested for catalytic photoelectrochemical water oxidation to O_2. The Ru based hybrid photoanode is remarkably stable for over 60 minutes at current densities of 1 mA cm^{-2}, maintaining intact the nature of the Ru-tda catalyst. The novel Si/TiO_2/C configuration permits an exquisite and unprecedented monitoring of the nature and fate of the molecular species in the photoanode before and during catalysis.

VII

The chapter consist of the following independent papers:

PAPER I Matheu, R.; Moreno, I.; Sala, X.; Brunschwig, B. Gray, H. B.; Llobet, A.; Lewis, N. S. *J. Am. Chem. Soc.* **2017**, *139*, 11345-11348.

PAPER I Photoelectrochemical Behavior of Ru-Based Water-Oxidation Catalysts Bound to TiO_2-Protected Si Photoanodes

Matheu, R.; Moreno, I.; Sala, X.; Brunschwig, B. Gray, H. B.; Llobet, A.; Lewis, N. S. *J. Am. Chem. Soc.* **2017**, *139*, 11345-11348.

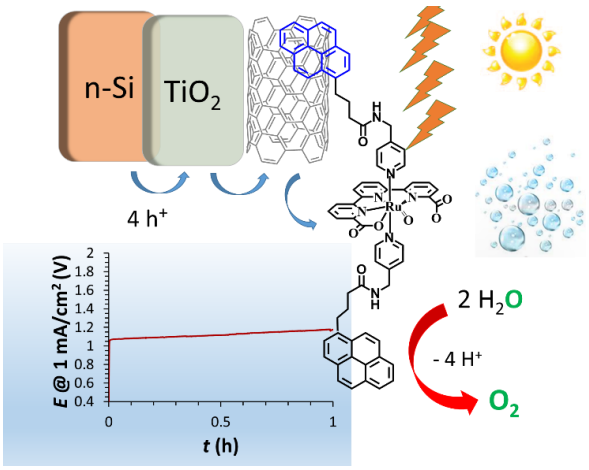

Abstract

A hybrid photoanode based on a molecular water oxidation precatalyst attached to TiO_2-protected n-Si exhibited current densities of 1 mA cm^{-2} for > 1 h at pH = 7 at 1.07 V vs the normal hydrogen electrode (NHE). The photoanode was prepared from TiO_2-protected n- or p^+-Si coated with multiwalled carbon nanotubes (CNT) and the ruthenium-based water oxidation precatalyst [Ru^{IV}(tda)(py-pyr)$_2$(O)], **1(O)** and/or its precursor [Ru(tda)(py-pyr)$_2$], **1**, (tda^{2-} is [2,2′:6′,2″-terpyridine]-6,6″-dicarboxylato and py-pir is 4-(pyren-1-yl)-N-(pyridin-4-ylmethyl)butanamide), n-Si/TiO_2/C/CNT/[**1**+**1(O)**]. The photoelectrode has been characterized and tested for catalytic photoelectrochemical water oxidation to O_2(g). The Ru complexes were immobilized by π–π stacking onto CNTs that had been deposited by drop casting onto Si electrodes coated with 60 nm of amorphous TiO_2 and 20 nm of a layer of sputtered C. The hybrid materials were characterized by scanning-electron microscopy (SEM), energy-dispersive X-ray spectroscopy (EDX) and electrochemical techniques including cyclic voltammetry (CV). At pH = 7 with 3 Sun illumination, the n-Si/TiO_2/C/CNT/[**1**+**1(O)**] electrodes exhibited current densities of 1 mA cm^{-2} at 1.07 V vs NHE. The current density was maintained for >200 min at a constant potential while intermittently collecting CVs. The voltammograms indicated that some of the Ru was still in a molecular form for the duration of the test, which yielded a light-induced turnover number of ≈ 60,000 for O_2(g) generation assuming that the molecular species **1(O)** was fully responsible for the catalysis of O_2(g) evolution.

Contributions

Roc Matheu was involved in all parts of this work

I 1 Introduction

Sustainable production of solar fuels depends on the oxidation of water to O_2(g) to provide an electron source for the concurrent formation of reduced energy-rich molecules.[1] Over the last decade, the specific activity of transition-metal complexes for evolution of O_2(g) from water has increased by four orders of magnitude[2,3]due to judicious design of the ligand environment[4,5] together with the spectroscopic and electrochemical characterization of intermediates[2,6-8]and the suppression of decomposition pathways.[9]

Anchoring molecular catalysts onto anodes and photoanodes can modify their reaction pathway and can degrade or even improve the activity of the catalyst. Rapid hole trapping by the catalyst could also improve the stability of the light absorber by competing with corrosion or passivation reactions arising from photogenerated charge-carriers in the valence band of the semiconductor.[10]

Molecular complexes immobilized on conductive electrode surfaces have been shown to provide current densities between 0.015 mA cm^{-2} and 0.5 mA cm^{-2} for several hours of O_2(g) evolution from water.[11,12] The immobilized complexes have shown turnover numbers (TON) of 10^4–10^6, comparable to their performance in the homogeneous phase. In contrast, photoanodes functionalized with molecular catalysts have been limited to current densities of ~1 mA cm^{-2} for <20 min,[13,14] and exhibit a decrease in specific activity compared to their behavior in homogeneous conditions, as evidenced by TONs < 1000. Most photoanode designs are based on dye-sensitized schemes in which a $[Ru(bpy)_3]^{2+}$ derivative dye and a molecular water-oxidation catalyst are co-anchored onto the surface of a large band-gap semiconductor. The dyes are responsible for light absorption and electron injection into the semiconductor, while the holes are responsible for catalyst activation that eventually leads to water oxidation. This strategy is generally limited by rapid back electron-transfer processes, dye photodegradation, and desorption of the both the dye and the catalysts.[15,16]

An alternative to dye-sensitized oxide-based photoelectrodes is to couple a water-oxidation catalyst to a small band-gap semiconductor, such as Si, GaAs or GaP that has been protected with a coating based on TiO_2, NiO_x or CoO_x.[17,18] This coating strategy has been shown to produce stable photoanodes that can operate for months under strongly anodic conditions in highly alkaline or near-neutral pH electrolytes.[18]

VII

We report herein a hybrid molecular photoanode synthesized by coupling the molecular water oxidation precatalyst [Ru^{IV}(tda)(py-pyr)$_2$(O)], **1(O)**, (tda^{2-} is [2,2':6',2''-terpyridine]-6,6''-dicarboxylato; py-pyr is 4-(pyren-1-yl)-N-(pyridin-4-ylmethyl)butanamide) (Chart I) to a protected Si semiconductor photoelectrode (Scheme I). In molecular form, complex **1(O)** exhibits maximum turnover frequencies of > 7700 s^{-1} at pH = 7 for water oxidation to O_2(g), and is generated from the precursor complex [Ru^{II}(tda)(py-pyr)$_2$], **1**.

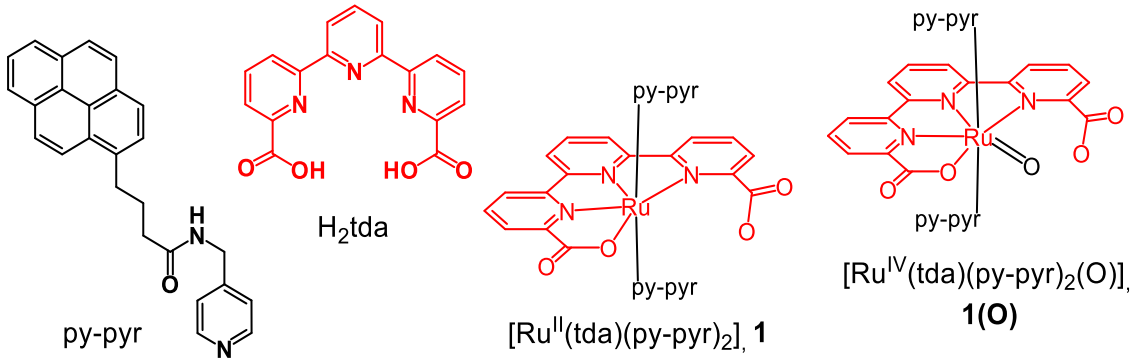

Chart 1: Ligands and complexes employed in this work.

I 2 Results and discussion

Scheme I describes the preparation of the hybrid Si photoanodes. Phosphorous doped n-Si wafers (Addison Engineering, Inc.; resistivity ρ = 0.1-0.3 Ω·cm) were used to assess the performance of the electrodes under illumination, whereas highly boron-doped p^+-Si electrodes (Addison Engineering, Inc.; ρ < 0.005 Ω·cm) were used to assess the electrochemical properties of Si-based electrodes in the dark. The Si substrates were coated with 60 nm of amorphous TiO_2 produced by atomic-layer deposition (ALD).[18] 20 mm of graphitic carbon was sputtered onto the TiO_2 to avoid deleterious effects associated with the resistance of the top-most TiO_2 layer.[18] A thick layer of multiwalled carbon nanotubes (CNT) was then drop cast over the Si/TiO_2/C substrate. A layer of poly(methyl methacrylate) (PMMA) was drop cast on top of the CNT, to enhance the mechanical stability of whole assembly, producing a material that is designated herein as Si/TiO_2/C/CNT. The CNT layer was 14 ± 1 μm thick, as evidenced by scanning-electron microscopy (SEM) (Figure S2). A pattern of holes was then scratched on top of the CNT to improve the light absorptivity by the Si in the presence of the thick overlayer of black CNT. Scanning-electron microscopy (SEM) indicated that the holes constituted ~18% of the projected area of the resulting Si electrodes (Figure S2). The Si/TiO_2/C/CNT substrates were then soaked for 12 h in a solution of complex **1,** to immobilize the complex on the CNT layer and to generate the Si/TiO_2/C/CNT/**1** substrates (see Supporting Information for experimental details).

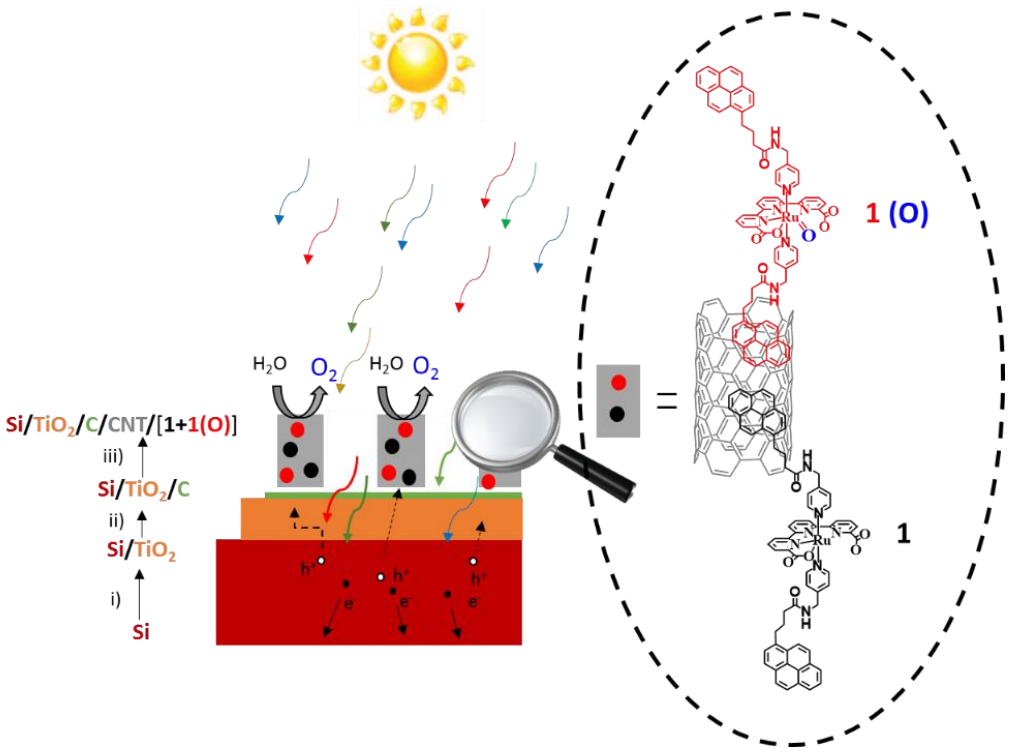

Scheme 1. Schematic representation of a cross-section of a Si photoanode decorated with the molecular water oxidation precatalyst **1(O)** (red circles). The photoanode contains a 20 nm carbon layer (green) that had been sputtered over a 60 nm TiO_2 layer (orange) previously deposited by ALD over Si (red). Afterwards CNTs (grey) were deposited over this material by drop casting and then the precatalyst **1** (black circles) was attached to the electrode via π– π stacking interactions. Further activation of the precatalyst led to the formation of the final photoanode "Si/TiO_2/C/CNT/[**1**+**1(O)**]".

VII

The electrical properties of the p^{+}-Si electrodes without an attached catalyst were analyzed by measuring the current density vs potential *(J- E)* response in a 350 mM $[Fe(CN)_6]^{3-}$ - 50 mM $[Fe(CN)_6)]^{4-}$(aq) solution. The p^{+}-Si/TiO_2/C electrodes exhibited small (~60 mV) resistive losses at anodic current densities of 10 mA cm^{-2}, in accord with previous reports for p^{+}-Si/TiO_2 electrodes.[18] The resistance of the p^{+}-Si/TiO_2/C/CNT electrodes (~30 mV) was less than that of p^{+}-Si/TiO_2/C electrodes, presumably due to the roughness of the CNT layer. Figure S5 shows the CVs for the n-Si electrode with and without the CNT layer. The capacitance charging currents are much larger for the electrodes with the CNT layer ~0.2 mA cm^{-2} at a scan rate of 40 mV s^{-1}, this suggest an increase in electrochemically active surface area of the electrode on the order of 50 (see Supporting Information). The electrochemical response of the electrodes was identical regardless of whether the coating contained PMMA, confirming the electrochemical inertness

of the PMMA under the test conditions and indicating that the PMMA layer did not block solution contact with the electrode.

For n-type electrodes, measurements under illumination allowed estimation of the photovoltage (V_{oc}) and the photogenerated current density (J_l). Under simulated 1 Sun illumination, the n-Si/TiO_2/C electrode showed V_{oc} = -295 ± 20 mV and J_l = 10.7 ± 1.7 mA cm^{-2}, similar to related photoanodes in 350 mM $[Fe(CN)_6]^{3-}$ - 50 mM $[Fe(CN)_6)]^{4-}$ - 1.0 M KCl(aq). [18,19] n-Si/TiO_2/C/CNT electrodes with no holes exhibited virtually no light-induced current density (J =0.08 ± 0.01 mA cm^{-2}), whereas with holes present, the value of J_l = 2.0 ± 0.3 mA cm^{-2} was consistent with the 18% of exposed area arising from the hole patterning step.

Figure 1A shows the CVs for p^+-Si/TiO_2/C/CNT/**1** and n-Si/TiO_2/C/CNT/**1** electrodes at pH = 7.0 in the dark and under 3 Sun illumination, respectively. The voltammetry exhibited two reversible waves that shifted by -240 mV between the p^+-Si and n-Si electrodes, consistent with the measured V_{oc} in contact with $[Fe(CN)_6]^{3-/4-}$(aq). The two redox waves are consistent with the III/II and IV/III redox couples of complex **1** anchored at the photoanode. The midpoints of the redox waves on molecularly functionalized p^+-Si surfaces were at nearly identical potentials to those exhibited by **1** in homogeneous solution using glassy carbon as a working electrode.[3] Integration of the charge under the waves yielded a coverage of 14.6 ± 2.4 nmol cm-^{2} and 13.0 ± 2.2 nmol cm^{-2} for p^+-Si and n-Si electrodes, respectively (Figure S6; Table S1). The amount of **1** on the surface and its size suggests that the surface of the CNTs is about fully covered. The increase in current density at potentials > 1.3 V vs the normal hydrogen electrode, NHE, is consistent with oxidation of the CNT.[12]

VII

$$Si/TiO_2/C/CNT/\mathbf{1} - 2e^- \rightarrow Si/TiO_2/C/CNT/\mathbf{1}^{2+} \quad (1)$$

$$Si/TiO_2/C/CNT/\mathbf{1}^{2+} + OH^- \rightleftharpoons Si/TiO_2/C/CNT/[\mathbf{1(O)}] + H^+ \quad (2)$$

To generate the water oxidation precatalyst **1(O)** at the surface, the surface-bound complex **1** was electrochemically oxidized from the II to the IV oxidation state, and held at an oxidizing potential to allow partial incorporation of an aqua ligand in the coordination sphere (eqs 1, 2). Accordingly, p^+-Si/TiO_2/C/CNT/**1** electrodes were subjected to chronoamperometry (CA) for 150 s at E = 1.30 V in the dark, whereas n-Si/TiO_2/C/CNT/**1** electrodes were maintained for 150 s at E = 1.10 V under 3 Sun illumination. The resulting electrodes were rinsed with water and introduced into a fresh solution at pH = 7.

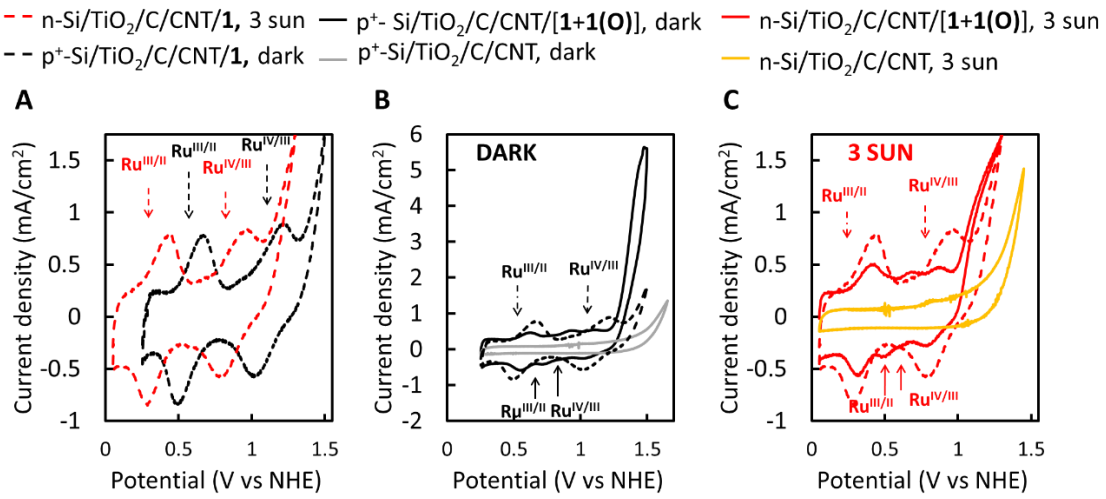

Figure 1. A, CV of p⁺-Si/TiO₂/C/CNT/**1** in the dark (black dashed line) and n-Si/TiO₂/C/CNT/**1** (red dashed line) under 3 sun illumination at pH = 7 together with the assignment of the redox processes shown in dashed black and red arrows, respectively. **B**, CV of p⁺-Si/TiO₂/C/CNT/**1** (black dashed line), p⁺-Si/TiO₂/C/CNT/[**1**+**1(O)**] (black solid line) and a bare p⁺-Si/TiO₂/C/CNT electrode (grey solid line) in the absence of illumination at pH = 7, together with the assignment of the redox processes of complex **1** and complex **1(O)** indicated with dashed and black arrows, respectively. **C**, CV of n-Si/TiO₂/C/CNT/**1** (red dashed line), n-Si/TiO₂/C/CNT/[**1**+**1(O)**] (red solid line) and a bare n-Si/TiO₂/C/CNT electrode (orange solid line) under 3 sun illumination at pH = 7 together with the assignment of the redox processes of complex **1** and complex **1(O)** indicated with dashed and solid red arrows, respectively. A Pt wire was used as a counter electrode and Hg/Hg₂SO₄ as reference electrode. The measured potentials were converted to NHE by addition of 0.65 V to the experimentally measured values.

VII

Figures 1B and 1C show the cyclic voltammetry of the activated precatalyst on n-Si/TiO₂/C/CNT/[**1**+**1(O)**] and p⁺-Si/TiO₂/C/CNT/[**1**+**1(O)**] electrodes with and without illumination, respectively. Figure 1B shows the CV behavior of a p⁺-Si/TiO₂/C/CNT/[**1**+**1(O)**] electrode as well as p⁺-Si/TiO₂/C/CNT/**1** and a bare p⁺-Si/TiO₂/C/CNT electrode. The appearance of waves ascribable to **1(O)** in the 0.65 to 0.96 V region was accompanied by the growth of catalytic current in the 1.20 to 1.45 V potential range. Similar behavior was observed in the voltammetry of n-Si/TiO₂/C/CNT/**1** and n-Si/TiO₂/C/CNT/[**1**+**1(O)**] electrodes under 3 Sun illumination at pH = 7 (Figure 1C), with the expected -240 mV potential shift relative to the analogous p⁺-Si electrodes. The magnitude of the voltammetric peaks in the 0.4 to 0.7 V region correlated with the increase in current density in the 1.0 to 1.30 V region associated with electrocatalytic oxidation of water to dioxygen. The n-Si electrodes under 3 Sun illumination exhibited a plateau of the catalytic current at positive potentials (Figure 1C). Figure 2A shows

the voltammetry of n-Si/TiO_2/C/CNT/[**1**+**1(O)**] electrodes under 1, 2 and 3 sun illumination, respectively, clearly indicating the plateau behavior of the catalytic response under these conditions.

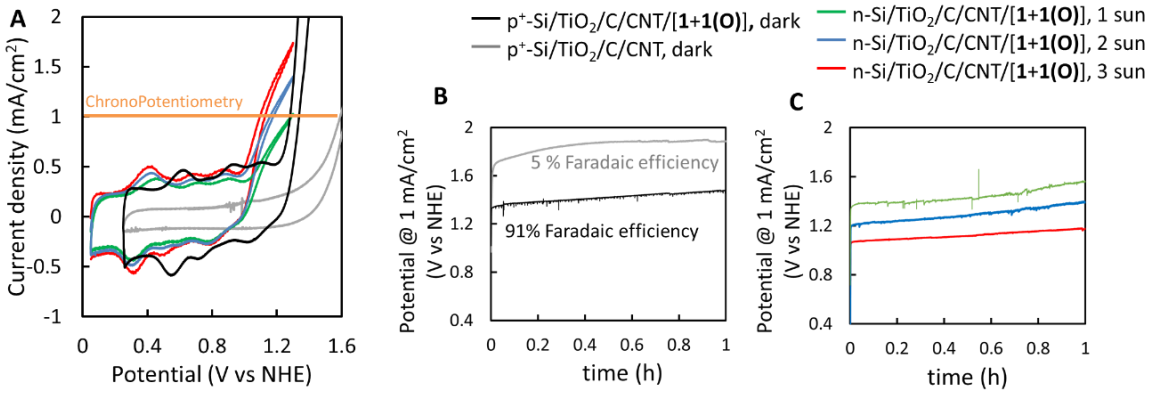

Figure 2. **A**, CV of the n-Si/TiO_2/C/CNT/[**1**+**1(O)**] electrodes at pH = 7 under 1, 2 and 3 sun illumination (green, blue and red lines) (scan rate 40 mV s^{-1}), respectively, together with the cyclic voltammetry of p^+-Si/TiO_2/C/CNT/[**1**+**1(O)**] (black line) and bare p^+-Si/TiO_2/C/CNT (grey line) electrodes at pH = 7 in the dark. **B**, Chronopotentiometry (CP) at 1 mA cm^{-2} for p^+-Si/TiO_2/C/CNT/[**1**+**1(O)**] (black line) and bare p^+-Si/TiO_2/C/CNT (grey line) electrodes at pH = 7 in the dark. **C**, CP at 1 mA cm^{-2} for n-Si/TiO_2/C/CNT/[**1**+**1(O)**] under 1, 2 and 3 Sun (green, blue and red lines), respectively. A Pt wire was used as a counter electrode and a Hg/Hg_2SO_4 electrode was the reference electrode. The measured potentials were converted to NHE by adding 0.65 V to the values observed experimentally.

VII

Figure 2B shows chronopotentiometry at 1 mA cm^{-2} for a p^+-Si/TiO_2/C/CNT/[**1**+**1(O)**] electrode and for a bare p^+-Si/TiO_2/CNT electrode, respectively, while the amount of oxygen generated was measured with a Clark electrode placed at the headspace of the electrochemical cell. Faradaic efficiencies for O_2(g) evolution were >90% for the p^+-Si/TiO_2/C/CNT/[**1**+**1(O)**] electrodes. Similar Faradaic efficiencies were obtained for the related catalyst in solution[3] or for **1(O)** immobilized on CNT. [3,12] The Faradaic efficiency for O_2(g) production was ~5% for the bare p^+-Si/TiO_2/C/CNT electrode (Figure S7).

An analogous chronopotentiomety experiment was performed for n-Si TiO_2/C/CNT/[**1**+**1(O)**] electrodes in the presence of 1, 2 or 3 Sun illumination, respectively (Figure 2C). The difference in the initial potential is in accord with the negative shift in potential provided by the photoelectrode relative to the p^+-Si electrode. At longer times, the three electrodes exhibited an increase in potential regardless of the light intensity.

After O_2 evolution, the voltammetry indicated that the catalytic activity and the precatalyst loading decreased by 30–50% relative to their initial values, but no new electroactive species

were detected in the voltammetry (Figure S8). This behavior is consistent with the partial loss of CNT-Ru material from the electrode. A positive shift in potential was observed during a 3 h chronopotentiometric experiment at J = 1 mA cm^{-2} for n-Si/TiO_2/C/CNT/[**1**+**1(O)**] under 3 Sun illumination at pH = 7, consistent with a decrease of the catalytic activity correlated with the decrease in the amount of precatalyst on the photoanode as monitored by cyclic voltammetry (see Figure S9). Assuming that the O_2(g) evolution arose solely from the **1(O)** molecular species implies a TON of ≈ 6.0 x 10^4 for the n-Si/TiO_2/C/CNT/[**1**+**1(O)**] photoanode (Table S3). Formation of trace amounts of RuO_2 as the actual catalytic species cannot be ruled out from the available data. For comparison, dye-sensitized photoanode systems in which a chromophore, typically a $[Ru(bpy)_3]^{2+}$-type of complex modified with a phosphonic acid functionalization, and a water-oxidation catalyst modified in a similar manner, are assembled at the surface of a large band-gap metal oxide semiconductor, such as TiO_2,[20] yield current densities of 1 mA cm^{-2} for < 20 min of O_2(g) evolution.[13,14]

The hybrid molecular photoanode described herein provides facile anchoring of the precatalyst through the pyrene group. The present Si/TiO_2/C configuration allows evaluation of the electrochemical features of the precatalyst over a large potential window, in contrast to wide band-gap oxide based semiconductors (e.g WO_3, $BiVO_4$) which often mask the electroactivity of the catalyst at very positive potentials. The cyclic voltammetric behavior of Si/TiO_2/C/CNT/[**1**+**1(O)**] allows evaluation of the loading, nature of the bound complexes, and stability of the complex during and after the catalysis.[9] The high stability of the π–π bond between the pyrene functionality of the water oxidation precatalyst and the CNT contrasts with the limited stability of a M-OP bond for binding either chromophores or catalysts in the dye-sensitized solar cell configurations, due to the competing effect of the buffer solutions for the same surface bond.[15] The simplicity of the precatalyst anchoring process may facilitate extension of the approach to applications such as the light-induced transformation of organic substrates.[21]

The low-energy pathway associated with catalysis effected by **1(O)** is believed to involve a water nucleophilic attack mechanism, WNA,[2,3] which is compatible with the restricted mobility conditions produced when the catalyst is anchored on a photoanode.[12] This putative mechanism is consistent with the observed increase in stability of the photoanode described herein as compared to electrodes that use a Ru-bda (bda is 2,2'-bipyridine-6,6'dicraboxylate) moiety, whose low-energy water-oxidation pathway is believed to involve a metal-based bimolecular mechanism, I2M,[7] ultimately leading directly to decomposition to RuO_2.[9] Very rapid water oxidation catalysts can improve the overall stability of the functionalized electrode by rapidly

VII

quenching the highly reactive holes generated after light illumination of the TiO_2-protected Si photoanode.

The light-induced water oxidation potential ranged from 1.2 to 1.4 V, whereas the potential of the top of the Si valence band is ~ 1 V vs NHE.[22] Due to band-edge movement, the Si/TiO_2/C configuration is consequently advantageous over a DSSC approach in which water oxidation will occur only at potentials more negative than those of the Ru(III)/Ru(II) couple in the $[Ru(bpy)_3]^{2+}$-type of dye used as the light absorber.

An important limitation of the n-Si photoanodes investigated herein is the reduced amount of light absorption by the Si due to absorption by the relatively thick CNT layer that covers ~80% of the surface. Small but non-zero oxidation of the CNT support, presumably correlated with the deanchoring process, also occurs in parallel to the water oxidation process. The latter desorption can in principle be overcome by the use of water oxidation catalysts that operate at lower overpotentials, as such species are developed.

I 3 Conclusion

In conclusion, a hybrid photoanode based on a molecular Ru complex attached via π-staking on CNTs previously deposited on a TiO_2 coated Si semiconductor can effect the oxidation of water to O_2(g) with high faradaic efficiency. The Ru based hybrid photoanode is stable for over 60 min of operation at current densities of 1 mA cm^{-2} while maintaining intact the molecular precatalyst. The Si/TiO_2/C configuration permits both facile anchoring of a molecular precatalyst previously functionalized with extended π-systems and facilitates monitoring of the nature of the molecular species on the photoanode before and during catalysis.

VII

I 4 Ackonwledgements

We acknowledge the National Science Foundation under NSF Center CHE-1305124 for support of supplies and equipment for this work. R.M. was supported by a PhD grant from the “La Caixa” foundation. AL and XS acknowledge financial support from MINECO and FEDER (CTQ2016-80058-R, CTQ2015-64261-R, SEV 2013-0319, ENE2016-82025-REDT, CTQ2016-81923-REDC) and Generalitat de Catalunya for project 2014-SGR-915. Instrumentation support was provided by the Molecular Materials Resource Center of the Beckman Institute at the California Institute of Technology. Support at Caltech for I.M.H, N.S.L., B.S.B. and R.M was provided by the National Science Foundation Center for Chemical Innovation: Solar Fuels, grant CHE-1305124. We also acknowledge K. Sun for helpful discussions.

I 5 References

1 McCrory, C. C. L.; Jung, S.; Ferrer, I. M.; Chatman, S. M.; Peters, J. C.; Jaramillo, T. F. *J. Am. Chem. Soc*. **2015**, *137*, 4347-4357.

2 Concepcion, J. J.; Tsai, M. K.; Muckerman, J. T.; Meyer, T. J. *J. Am. Chem. Soc*. **2010**, *132*, 1545-1557.

3 Matheu, R.; Ertem, M. Z.; Benet-Buchholz, J.; Coronado, E.; Batista, V. S.; Sala, X.; Llobet, A. *J. Am. Chem. Soc.* **2015**, *137*, 10786-10795.

4 Wasylenko, D. J.; Ganesamoorthy, C.; Henderson, M. A.; Koivisto, B. D.; Osthoff, H. D.; Berlinguette, C. P. *J. Am. Chem. Soc*. **2010**, *132*, 16094–16106.

5 Richmond, C. J.; Matheu, R.; Poater, A.; Falivene, L.; Benet-Buchholz, J.; Sala, X.; Cavallo, L.; Llobet, A. *Chem. Eur. J.* **2014**, *20*, 17282-17286.

6 Duan, L.; Bozoglian, F.; Mandal, S.; Stewart, B.; Privalov, T.; Llobet, A.; Sun, L. *Nat. Chem.* **2012**, *4*, 418-423.

7 Bozoglian, F.; Romain, S.; Ertem, M. Z.; Todorova, T. K.; Sens, C.; Mola, J.; Rodríguez, M.; Romero, I.; Benet-Buchholz, J.; Fontrodona, X.; Cramer, C. J.; Gagliardi, L.; Llobet, A. *J. Am. Chem. Soc*. **2009**, *131*, 15176-15187.

8 Moonshiram, D.; Pineda-Galvan, Y.; Erdman, D.; Palenik, M.; Zong, R.; Thummel, R.; Pushkar, Y. *J. Am. Chem. Soc*. **2016**, *138*, 15605-15616.

9 Matheu, R.; Francàs, L.; Chernev, P.; Ertem, M. Z.; Batista, V.; Haumann, M.; Sala, X.; Llobet, A. *ACS Catal.* **2015**, *5*, 3422-3429.

10 Brennaman, M. K.; Dillon, R. J.; Alibabaei, L.; Gish, M. K.; Dares, C. J.; Ashford, D. L.; House, R. L.; Meyer, G. J.; Papanikolas, J. M.; Meyer, T. J. *J. Am. Chem. Soc*. **2016**, *138*, 13085-13102.

11 Chen, Z.; Concepcion, J. J.; Jurss, J. W.; Meyer, T. J. *J. Am. Chem. Soc* **2009**, *131*, 15580-15581.

12 Creus, J.; Matheu, R.; Peñafiel, I.; Moonshiram, D.; Blondeau, P.; Benet-Buchholz, J.; García-Antón, J.; Sala, X.; Godard, C.; Llobet, A. *Angew. Chem. Int. Ed.* **2016**, *55*, 15382-15386.

13 Gao, Y.; Ding, X.; Liu, J.; Wang, L.; Lu, Z.; Li, L.; Sun, L. *J. Am. Chem. Soc*. **2013**, *135*, 4219-4222.

14 Sheridan, M. V.; Sherman, B. D.; Coppo, R. L.; Wang, D.; Marquard, S. L.; Wee, K.-R.; Murakami Iha, N. Y.; Meyer, T. J. *ACS Energy Lett.* **2016**, *1*, 231-236.

15 Hyde, J. T.; Hanson, K.; Vannucci, A. K.; Lapides, A. M.; Alibabaei, L.; Norris, M. R.; Meyer, T. J.; Harrison, D. P. *ACS App. Mat. Inter.* **2015**, *7*, 9554-9562.

16 Wee, K.-R.; Brennaman, M. K.; Alibabaei, L.; Farnum, B. H.; Sherman, B.; Lapides, A. M.; Meyer, T. J. *J. Am. Chem. Soc.* **2014**, *136*, 13514-13517.

17 Zhou, X.; Liu, R.; Sun, K.; Papadantonakis, K. M.; Brunschwig, B. S.; Lewis, N. S. *Energy Environ. Sci.* **2016**, *9*, 892-897.

18 Hu, S.; Shaner, M. R.; Beardslee, J. A.; Lichterman, M.; Brunschwig, B. S.; Lewis, N. S. *Science* **2014**, *344*, 1005-1009.

19 Note that the calibration of the light intensity was performed before the addition of the $Fe^{III}(CN)_6$ / $Fe^{II}(CN)_6$ solution.

20 Gratzel, M. *Acc. Chem. Res.* **2009**, *42*, 1788-1798.

21 Farras, P.; Di Giovanni, C.; Clifford, J. N.; Garrido-Barros, P.; Palomares, E.; Llobet, A. *Green Chem.* **2016**, *18*, 255-260.

22 Plymale, N. T.; Ramachandran, A. A.; Lim, A.; Brunschwig, B. S.; Lewis, N. S. *J. Phys. Chem. C* **2016**, *120*, 14157-14169.

I 6 Supporting Information

Paper I Photoelectrochemical Behavior of Ru-Based Water-Oxidation Catalysts Bound to TiO_2-Protected Si Photoanodes

Roc Matheu,[1,2] Ivan A. Moreno-Hernandez,[3] Xavier Sala,[4] Harry B. Gray,[3,5] Bruce S. Brunschwig,[5] Antoni Llobet,*[1,4] Nathan S. Lewis*[3,5,6]

Outline

VII

VII

MATERIALS & METHODS

General Materials

Na_2HPO_4, NaH_2PO_4, $K_3Fe(CN)_6$, $K_4Fe(CN)_6{\cdot}3H_2O$, NH_4OH, HCl, poly(methyl methacrylate) (PMMA), tetrakis-dimethylamidotitanium (99.999%) (Sigma-Aldrich), anhydrous methanol (99.8%, Sigma-Aldrich), tetrahydrofuran (99.9 %, inhibitor free, Sigma Aldrich) and buffered HF (Transene Company, Inc.) were used as received. Silicon wafers (Addison Engineering, Inc.), multiwalled C nanotubes (D.D > 50 nm) (HeJi, Inc), In–Ga eutectic alloy (99.99%) (Alfa-Aesar), and Ag Paint (SPI, INC) were purchased from commercial suppliers. The pyrolytic graphite target, 99.999% pure C, was acquired from ACI Alloys and was used as a C target for sputtering. The $Ru(tda)(py\text{-}pyr)_2$ complex was synthesized as reported previously. [S1]

General methods

A Fuji F200 Ultratech was used for ALD and an AJA Orion was used for sputtering. An environmental Scanning Electron Microscope from FEI (Quanta 600) with an EDX detector (Oxford Instruments) was used for EDX and SEM measurements, and an EPSON Perfection v39 was used as an optical scanner. The pH of the solutions was determined by a pHmeter (CRISON, Basic 20+) that was calibrated before measurements by use of standard solutions at pH= 4.01, 7.00 or 9.21. Oxygen evolution was analyzed with a gas-phase Clark-type oxygen electrode (Unisense Ox-N needle microsensor) that was calibrated by addition of small quantities of O_2(g) (99%). A Dektak XT stylus was used for profilometry.

Preparation of Si/TiO_2/C substrates

The preparation was adapted from the literature.[S2] n-Si(100) wafers (P-doped with a resistivity ρ = 0.1-0.3Ω·cm, 525 ± 25 μm thick) or p^+-Si(100) wafers (B-doped with ρ < 0.005 Ω·cm, 381 ± 25 μm thick) were cleaned using an RCA etch process that consisted of (1) etching the wafer with buffered HF(aq); (2) soaking the wafer in a 5:1:1 (by volume) $H_2O/H_2O_2/NH_4OH$ solution at 75 °C for 10 min; (3) etching the wafers again with buffered HF(aq); and then (4) soaking the wafers in a 5:1:1 H_2O/H_2O_2/HCl solution at 75 °C for 10 min. TiO_2 was deposited on the films by ALD using tetrakis-dimethylamidotitanium (TDMAT) and H_2O as reagents. Each ALD cycle consisted of a 0.060 s pulse of distilled, deionized H_2O (18.2 MΩ·cm resistivity, Millipore) followed by a 0.25 s TDMAT pulse. After each pulse, N_2(g) was purged through the chamber for 15 s at a flow rate of 20 sccm. A total of 1250 cycles were performed. The substrate was maintained at 150 °C during the deposition, and the TDMAT precursor was heated to 75 °C with a heating jacket. The

H_2O was maintained at room temperature. C was sputtered using a pyrolytic graphite target in an Ar plasma. A RF power source of 150 W was maintained for 2 h and the gas flow rate was 20 psi of Ar at a total pressure of 5 mTorr. No heating was provided to the samples during deposition. The thickness of the layer was determined by profilometry.

Preparation of Si/TiO_2/C/CNT substrates

The Si/TiO_2/C substrates were cleaved into pieces ~ 0.25 cm^2 in area, with the actual area measured using an optical scanner and ImageJ software. A suspension of multiwalled carbon nanotubes (CNT) was prepared by sonicating the CNT for 1 h in tetrahydrofuran (THF) (1 mg / 1 mL). 600 μL cm^{-2} of the suspension was then deposited on the Si/TiO_2/C substrates, using several volumes (10 times 60 μL cm^{-2}) with the use of an Eppendorf pipette, to avoid overflow. The solvent was air-dried for 10 min and 60 μL cm^{-2} of a PMMA solution in dichloromethane (0.25 mg mL^{-1}) was added onto the electrodes. This gives a nominal coverage of 0.6 mg CNT/cm^2. The samples were dried and holes were patterned using a 0.64 ± 0.01 mm diameter mask with a pitch of 1.02 ± 0.05 mm (Figure S1). The surface area of the CNT is 40–600 cm^2/mg giving the ratio of the surface area of the CNT to the geometric area of 24–360.[S3] This is in line with the ration estimated below from electrochemical measurements.

*Preparation of Si/TiO_2/C/CNT/**1** substrate*

Si/TiO_2/C/CNT substrates were soaked in a solution of complex **1** in methanol (0.30 mM) for 12 h, rinsed with a fresh solution of methanol, air-dried, and analyzed by energy-dispersive X-ray spectroscopy (EDX) and electrochemical techniques. The EDX of the modified electrodes clearly showed the incorporation of the Ru on the substrates (Figure S3).

*Preparation of Si/TiO_2/C, Si/TiO_2/C/CNT and Si/TiO_2/C/CNT/**1** electrodes*

The preparation of electrodes based on Si/TiO_2/C, Si/TiO_2/C/CNT and Si/TiO_2/C/CNT/**1** substrates was adapted from the literature.[S2] In–Ga eutectic alloy was used to scribe the back side of the samples to make an Ohmic contact. A Sn-coated Cu wire was passed through a glass tube and affixed to the In-Ga by Ag paint. Once the Ag paint had dried, epoxy was used to seal the samples to the glass tube. The resulting exposed active area of each electrode was measured with an optical scanner and ImageJ software. The area of the final samples was between 0.1 cm^2- 0.2 cm^2.

*Preparation of Si/TiO_2/C/CNT/[**1+1(O)**] electrodes*

Electrodes of Si/TiO_2/C/CNT/**1** were used as working electrodes in a pH = 12 phosphate solution in which a Pt wire and Hg/Hg_2SO_4 were used as counter and reference electrodes, respectively. A potential of 1.30 vs NHE was applied to the p^+-Si/TiO_2/C/CNT/**1** electrodes in the absence of illumination whereas a potential of 1.10 V vs NHE was applied to the n-Si/TiO_2/C/CNT/**1** electrodes under 3 Suns illumination. The electrodes were then rinsed with fresh water and dried in air.

Preparation of Phosphate solutions

pH = 7.0 buffered solution (*I* = 0.1 M): powders of NaH_2PO_4 (2.31 g, 0.0193 M) and Na_2HPO_4 (3.77g, 0.0266 M) were dissolved with sufficient deionized H_2O to make up 1 L of solution.

pH = 12.0 buffered solution (*I* = 0.1 M): powders of Na_2HPO_4 (10.293g, 0.0073 M) and Na_3PO_4 (2.06g, 0.0126 M) were dissolved with sufficient deionized H_2O to make up 1 L of solution.

Photoelectrochemical Methods

Instruments

A Bio-Logic model SP-200 potentiostat or a CHI660d potentiostat were used in a 3-electrode configuration.

VII

$Fe(CN)_6^{3-}/Fe^{II}(CN)_6^{4-}$, pH =7 and pH = 12 measurements

Techniques

Cyclic voltammetry (CV) was performed at 40 mV s^{-1} unless otherwise specified. Chronoamperometry was used for the generation of **1(O)** by applying a potential of 1.05 V to n-Si electrodes and 1.30 V to p^+-Si electrodes. Chronopotentiometry was performed at 1 mA cm^{-2}. For all measurements at pH = 7, the electrochemical data were corrected for uncompensated resistance (90 % corrected).

Surface roughness was estimated for Si/TiO_2/C/CNT electrode by estimating the capacitance of the electrode from the CV, Figure S5. The figure shows a difference between the cathodic and anodic scans of ~0.2 mA cm^{-2} at a scan rate of 40 mV s^{-2}. This gives a nominal capacitance of ~2 cm^{-2} geometric area. Nominally a specific capacitance of ~0.04 mF cm^{-2} electrochemically active area

is found.[S4] This gives an approximate ratio for the electrochemically active surface area to the geometric area of 50.

Electrodes

An n-Si/TiO_2/C/CNT/[**1+1(O)**] sample or p^+-Si/TiO_2/C/CNT/[**1+1(O)**] sample was used as a working electrode. For $Fe(CN)_6^{3-}/Fe^{II}(CN)_6^{4-}$(aq) measurements, two distinct Pt disks were used as the counter and reference electrode, respectively. For measurements at pH =7 and at pH = 12, a Pt wire was used as a counter electrode and $Hg/Hg_2S_2O_4$ was used as a reference electrode. The Pt wire was separated from the solution by a membrane.

Cells

A 100 mL home-made cell consisted of 5 openings at the top into which the working, counter and reference electrodes were placed, with the cell also containing a 12 x 3 mm stir bar.

Solutions

A phosphate buffered solution was used for measurements at pH= 7 and at pH = 12. For $Fe(CN)_6^{3-}/Fe^{II}(CN)_6^{4-}$ measurements, a solution containing 350 mM of $Fe(CN)_6^{3-}$, 50 mM $K^-/Fe^{(}CN)_6^{4-}$ and 1.0 M KCl(aq) was used.

VII

Light source and calibration

Illumination during cyclic voltammetry measurements was provided by a Xe lamp (300 W, USHIO) with a quartz filter (cut off at 400 nm). Before addition of solution to the cell, a Si photodiode was used to calibrate the light intensity incident onto the working electrode.

O_2 Evolution

Bulk electrolysis was performed using a 10 mL two-compartment cell with a membrane separator between the two compartments. Both compartments were filled with 5 mL of pH = 7 solution and both compartments were equipped with a stir bar. A Ag/AgCl (KCl sat.) electrode was used as the reference. The counter electrode was placed in one

compartment and the working electrode, reference electrode and a Clark electrode to measure oxygen evolution and to calculate the Faradaic efficiency, were in the other compartment. The Clark electrode was calibrated by addition of known volumes of 99% pure O_2(g) at the end of the bulk electrolysis.

Surface coverage Estimation (Γ)

The surface coverage (Γ) of complexes **1** and **1(O)** on the electrodes was estimated by applying the formula Γ (mol·cm^{-2}) = Q / (n*S*F), where Q is the charge under the Ru^{III}/Ru^{II} cathodic wave of the **1** and **1(O)** species, n is the number of electrons involved in the electron transfer (1 e^- in all the cases), S is the surface area of the electrode, and F is Faraday's constant. The integration of the cathodic wave for the two species requires the use of a baseline for each peak. The drawing of am accurate baseline is difficult, particular for the **1(O)** peak, since the two peaks are close together, Figure S6. The ratio between **1**:**1(O)** was calculated by dividing the Γ of the former by the Γ of the latter. Figure S6 provides an example of the estimation of the coverage, whereas Table S1 contains the resulting coverage values.

The average coverage was estimated from 5 independent experiments and the standard deviation between samples was used to estimate the standard error; however, the actual error maybe significantly large due to systematic error in drawing the baseline. For individual experiments, the value for the coverage of the sample is provided in the captions of the related figures.

Table S1: Loading of the molecular complexes **1** and **1(O)** on n-Si/TiO_2/C/CNT/**1,** n-Si/TiO_2/C/CNT/[**1**+**1(O)**], p^+-Si/TiO_2/C/CNT/**1** and p^+-Si/TiO_2/C/CNT/[**1**+**1(O)**] electrodes.

	Γ_1 (nmol cm^{-2}) on Si/TiO_2/C/CNT/**1**	Γ_1 /$\Gamma_{1(O)}$ (nmol cm^{-2}) on Si/TiO_2/C/CNT/[**1**+**1(O)**]
p^+-Si	14.6 ± 2.4	3.0 ± 0.8 / 1.2 ± 0.6 (ratio $_{1/1(0)}$ = 2.5 ± 1.0)
n-Si	13.0 ± 2.2	2.9 ± 0.8 / 0.7 ± 0.3 (ratio $_{1/1(0)}$ = 4.2 ± 1.3)

Table S2: Current density (*J,* mA cm^{-2}) measured at 1.30 V for n-Si/TiO_2/C/CNT/[**1**+**1(O)**] electrodes at pH = 7 at different light intensities

1 Sun	2 Sun	3 sun
J = 0.9 ± 0.1 mA cm^{-2}	J = 1.4 ± 0.1 mA cm^{-2}	J = 1.8± 0.2 mA cm^{-2}

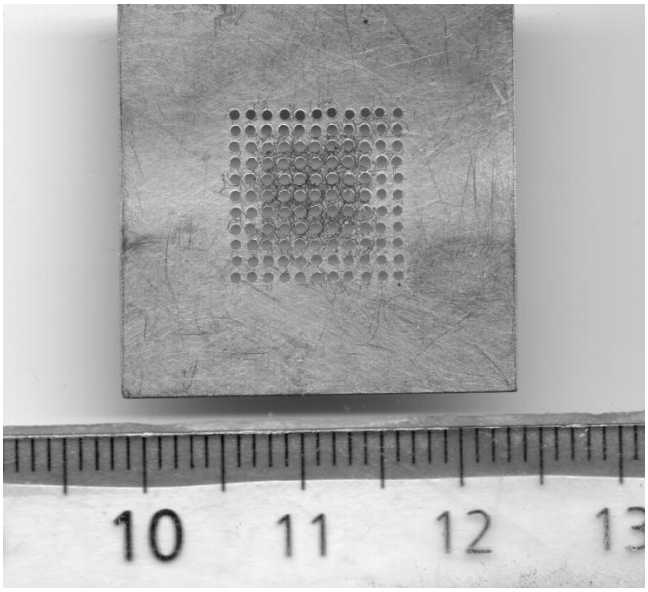

Figure S1: Aluminum foil with patterned 0.32 ± 0.01 mm^2 holes (diameter = 0.64 ± 0.01 mm)) with a pitch of 1.02 ± 0.05 mm that was used to prepare Si/TiO_2/C/CNT electrodes.

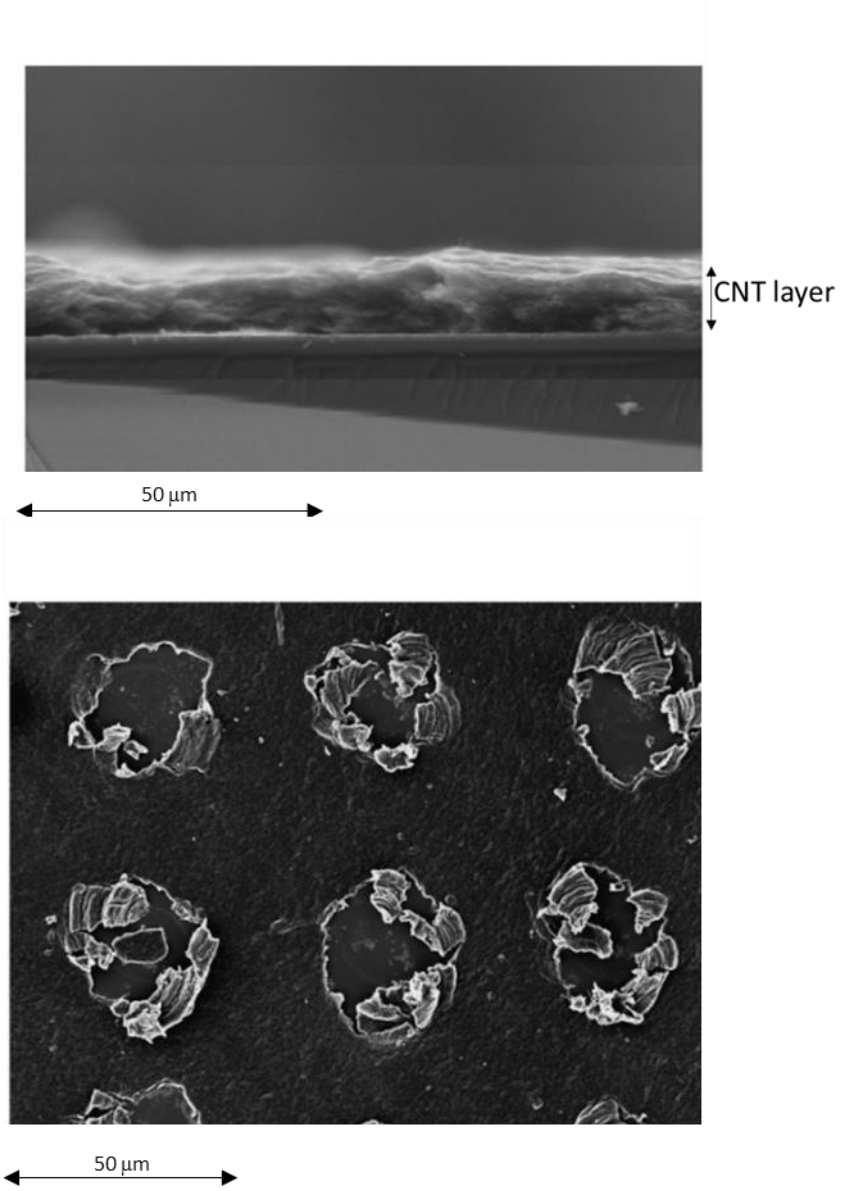

Figure S2: Representative SEMs of Si/TiO_2/C/CNT/**1** electrodes: Top, cross-section showing the 14 ± 1 µm thick layer of of CNT; Bottom, front view of Si/TiO_2/C/CNT/**1** showing the 0.21 ± 0.01 mm^2 holes (diameter = 0.52 ± 0.02 mm) separated by 1.10 ± 0.06 mm. The measured size of the holes lead to an estimated 18% of area of the Si/TiO_2/C/CNT/**1** substrates exposed to the illumination.

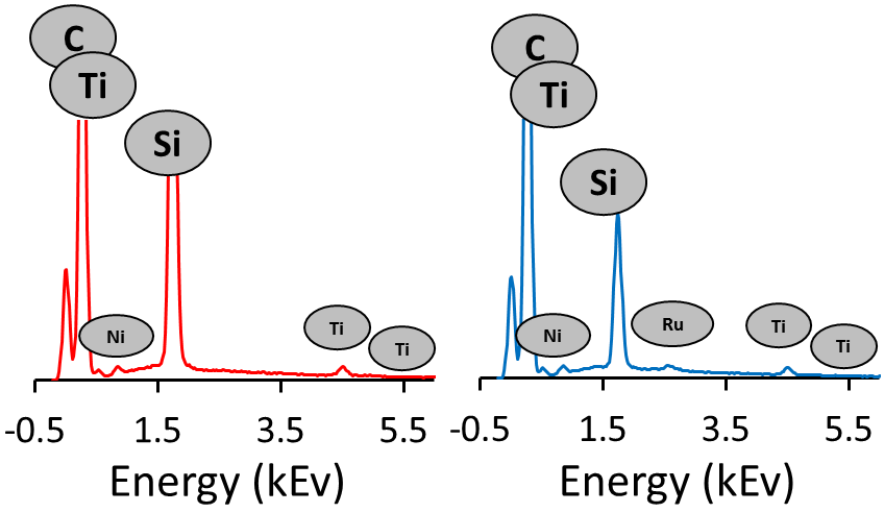

Figure S3: EDX profiles of a Si/TiO_2/C/CNT sample before (left) and after (right) soaking in a solution that contained **1**: left, EDX spectra of substrates after soaking (Si/TiO_2/C/CNT)**;** and right EDX spectra of Si/TiO_2/C/CNT/**1**. The measured amount in the Si/TiO_2/C/CNT/**1** substrate was 0.8 % by weight.

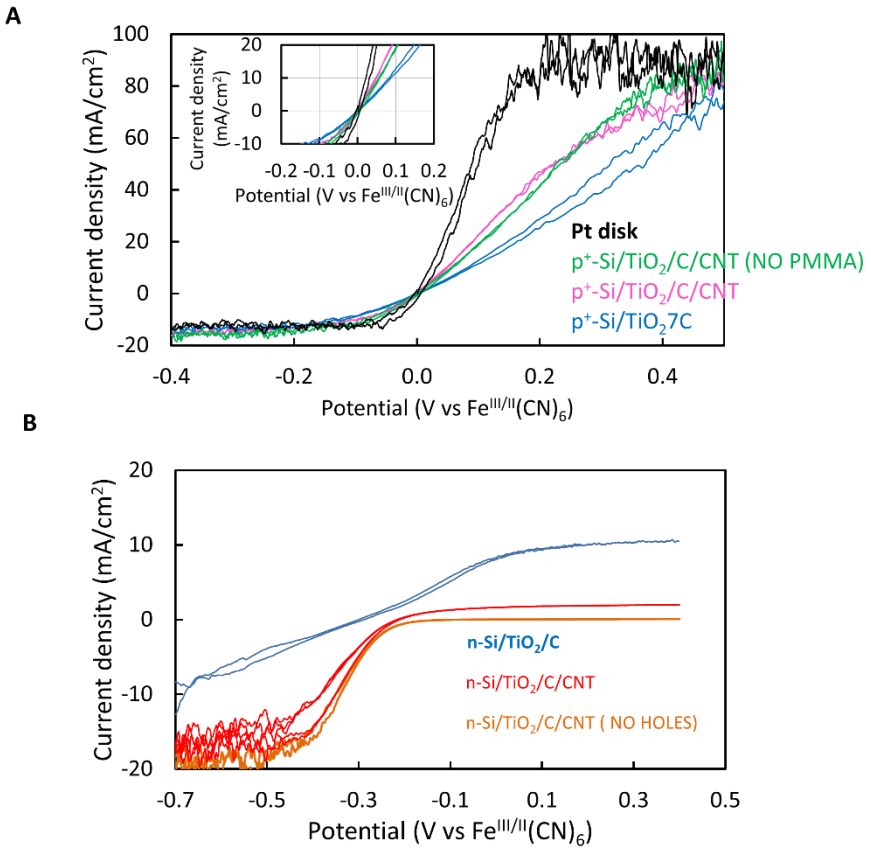

Figure S4. Determination of the photoelectrochemical properties of p^+ and n- $Si/TiO_2/C/CNT$ electrodes by electrochemical measurements in $Fe(CN)_6^{3-/4-}$(aq). **A** Cyclic voltammetry for p^+-$Si/TiO_2/C$ electrodes in $Fe(CN)_6^{3-/4-}$ (350 mM, 50 mM, 1.0 M KCl(aq), scan rate 40 mV s^{-1}) compared to a Pt disk (dark line). Inset: Expansion of the -10 mA cm^{-2} to 10 mA cm^{-2} current density region. Relative to the Pt disk, at 10 mA cm^{-2} on p^+-$Si/TiO_2/C$ (blue solid line) and p^+-$Si/TiO_2/C/CNT$ (pink solid line) electrodes, the potential loss was ~ 60 mV and 30 mV, respectively. The electrochemical response of p^+-$Si/TiO_2/C/CNT$ was essentially identical with and without a PMMA layer (pink and green lines respectively). **B** Representative cyclic voltammetry for n-Si electrodes in a $Fe(CN)_6^{3-/4-}$ solution (350 mM, 50 mM, 1.0 M KCl(aq)) under 1 Sun illumination. The V_{oc} and the light-limited current density (J_l) wre estimated from the average behavior of 3 independent electrodes: $Si/TiO_2/C$,blue solid line, V_{oc} = -295 ± 20 mV, J_l = 10.7 ± 1.7 mA cm^{-2}; $Si/TiO_2/C/CNT$, red solid line, V_{oc} = -220 ± 20 mV mV, J_l = 2.0 ± 0.3 mA cm^{-2}; and $Si/TiO_2/C/CNT$ without holes, orange solid line, V_{oc} = -70 ± 30 mV, J_l = 0.08 ± 0.01 mA cm^{-2}.

VII

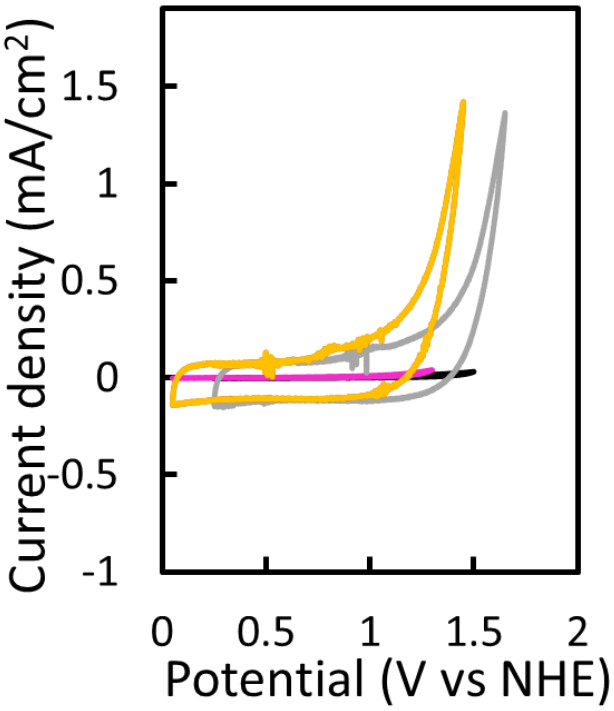

Figure S5. Cyclic voltammetry of bare n-Si/TiO_2/C/CNT (yellow line) and n-Si/TiO_2/C electrodes under 3 Suns illumination (pink line) at pH = 7 together with CVs of p^+-Si/TiO_2/C/CNT (grey line) and p^+-Si/TiO_2/C (black line) electrodes in the dark at pH = 7**.**

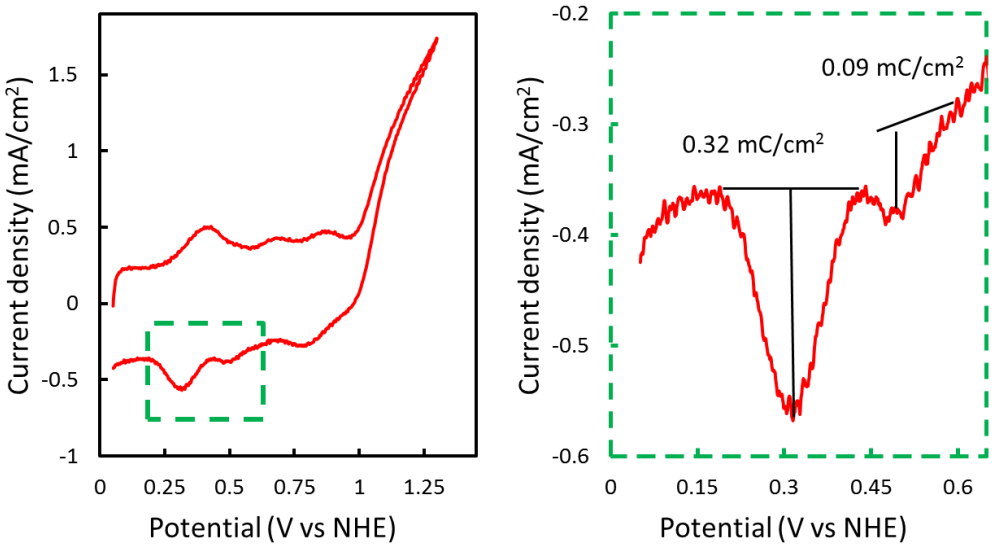

Figure S6: Cyclic voltammetry of n-Si/TiO_2/C/CNT/[**1**+**1(O)**] (Γ_1 = 3.25 nmol cm^{-2}, $\Gamma_{1(0)}$ = 0.9 nmol cm^{-2}, ratio $_{1/1(0)}$ = 3.3) under 3 Suns illumination at pH = 7 (red line, left) together with a representation of the integration of the III/II cathodic waves of **1** and **1(O)** species, to determine the surface coverage (right). The scan rate was 40 mV s^{-1}.

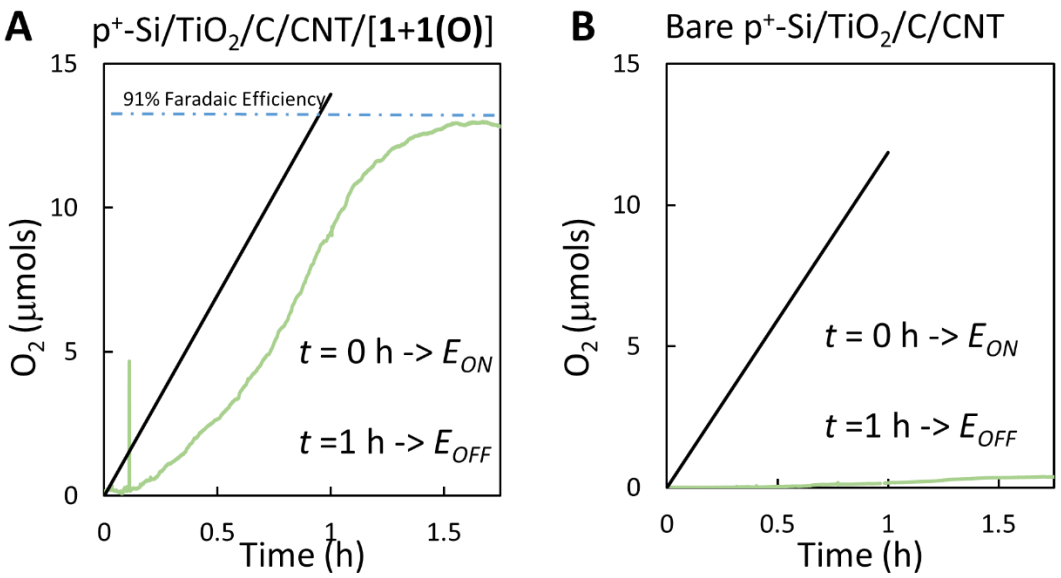

Figure S7. Representative plot for measured O_2 evolution (green solid lines) and theoretical O_2 evolution (black solid line) against time for **A**, a p^+-Si/TiO_2/C/CNT/[**1**+**1(O)**] electrode ((Γ_1 = 2.7 nmol cm^{-2}, $\Gamma_{1(0)}$ = 1.0 nmol cm^{-2}, ratio **1**/**1**(0) = 2.7, S = 1.5 cm^2), and **B**, a bare p^+-Si/TiO_2/C/CNT electrode (S = 1.4 cm^2). The oxygen evolution was a result of a chronopotentiometry at j =1 mA cm^{-2} and the theoretical oxygen evolution (nO_2) was calculated applying the formula $nO_2=Q/(4\cdot F)$, where Q is the charge passed during the experiment and F is Faraday's constant.

VII

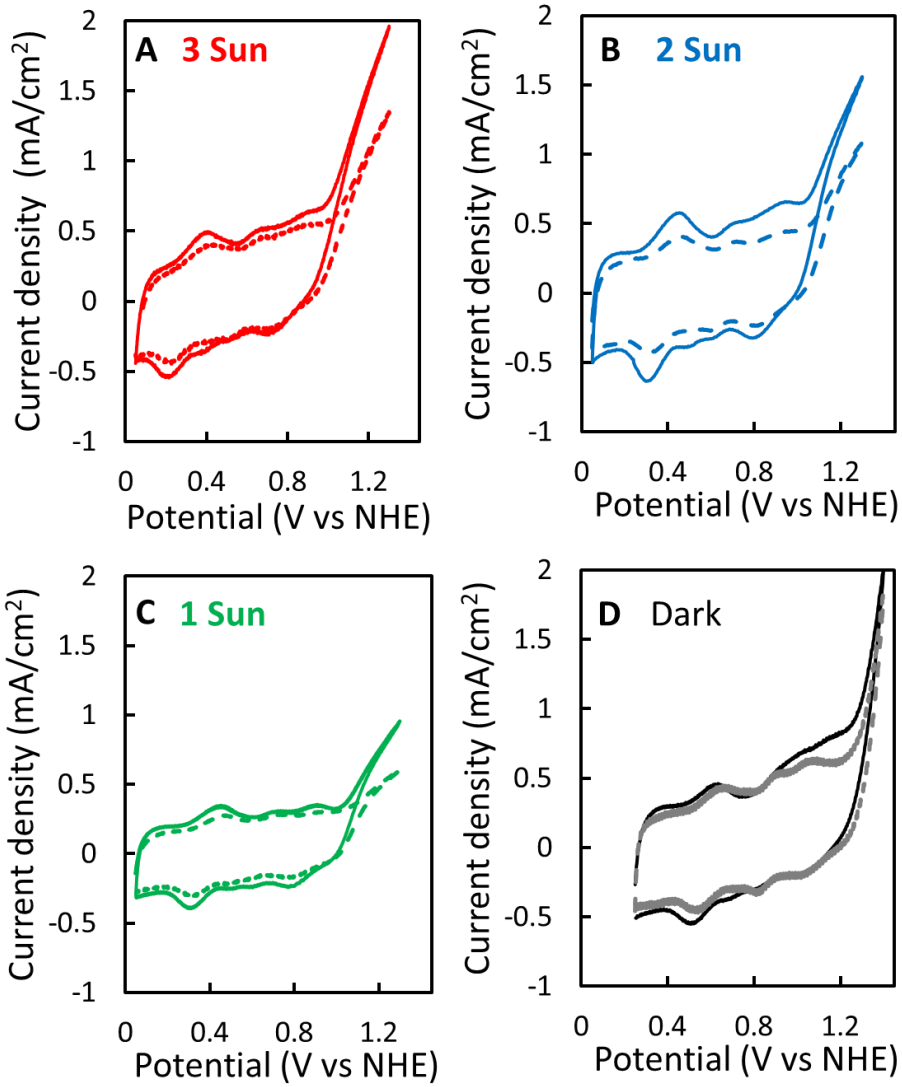

Figure S8: Cyclic voltammetries before (solid lines) and after (dashed line) of a Chronopontentiometric experiment at j = 1 mA cm^{-2} at pH = 7 and the scan rate was 40 mV s^{-1}: **A**, n-Si/TiO_2/CNT/C/[**1**+**1(O)**] under 3 sun illumination (Γ_1 = 3.62 nmol cm^{-2}, $\Gamma_{1(0)}$ = 0.9 nmol cm^{-2}, ratio $_{1/1(0)}$ = 3.9); **B**, n-Si/TiO_2/CNT/C/[**1**+**1(O)**] under 2 suns illumination (Γ_1 = 3.3 nmol cm^{-2}, $\Gamma_{1(0)}$ = 0.9 nmol cm^{-2}, ratio $_{1/1(0)}$ = 3.5); **C**, n-Si/TiO_2/CNT/C/[**1**+**1(O)**] under 1 sun illumination (Γ_1 = 2.7 nmol cm^{-2}, $\Gamma_{1(0)}$ = 0.8 nmol cm^{-2}, ratio $_{1/1(0)}$ = 3.5); and, **D**, p$^+$-Si/TiO_2/CNT/C/[**1**+**1(O)**] in dark conditions (Γ_1 = 2.9 nmol cm^{-2}, $\Gamma_{1(0)}$ = 2.5 nmol cm^{-2}, ratio $_{1/1(0)}$ = 2.5). See Figure 2 in the main section for the chronopotentiometry data.

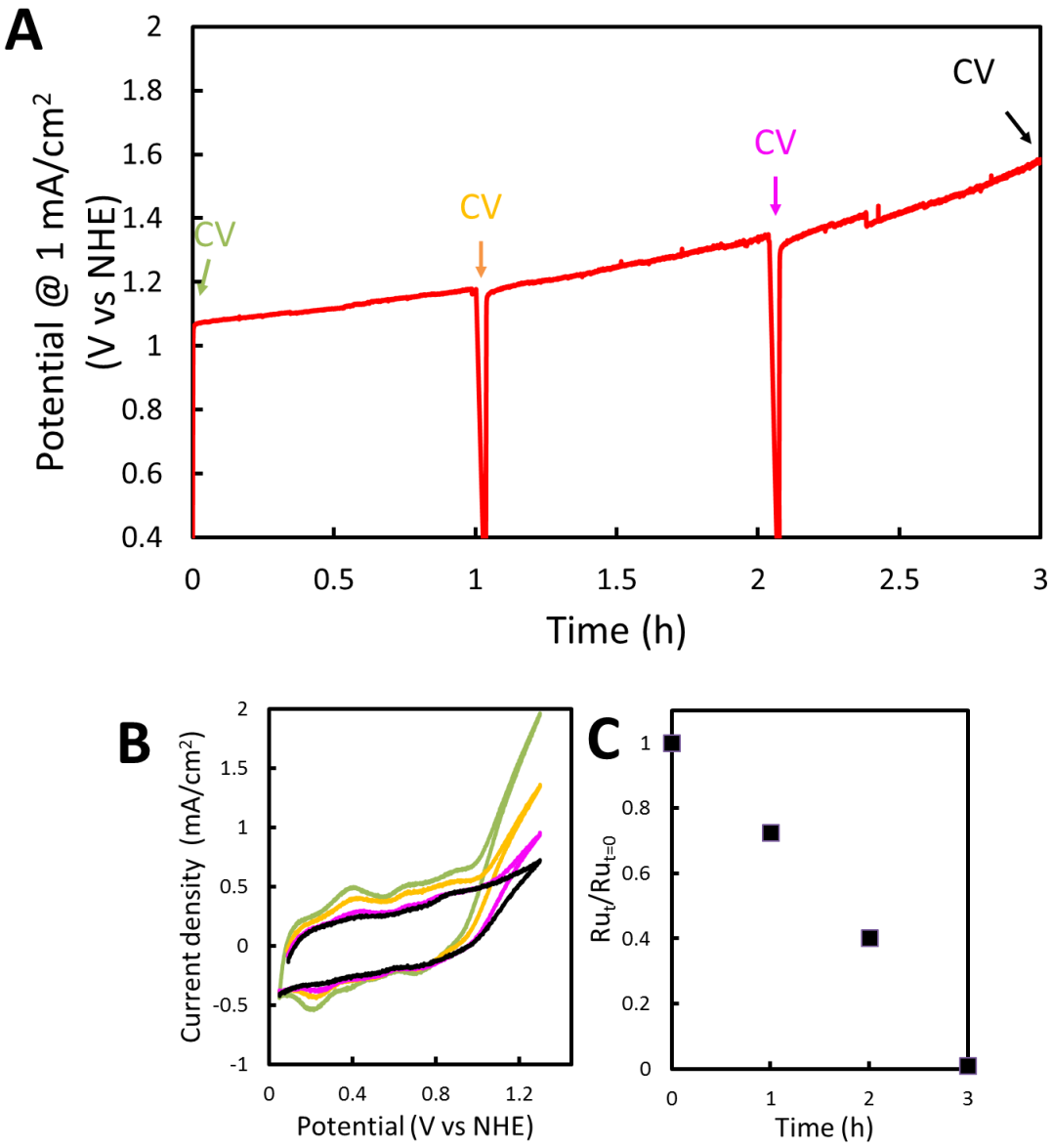

Figure S9: A, Chronopotentiometry (set j = 1 mA cm^{-2}) for n-Si/TiO_2/C/CNT/[**1**+**1(O)**] (Γ_1 = 3.62 nmol cm^{-2}, $\Gamma_{1(0)}$ = 0.9 nmol cm^{-2}, ratio $_{1/1(0)}$ = 3.9) under 3 suns illumination at pH = 7. **B**, CVs of the electrodes were performed at t = 0, 1, 2 and 3 h. **C**, Normalized quantification of the loss of $Ru_t/Ru_{t=0}$ against time (t). $Ru_t/Ru_{t=0}$ was estimated from the charge of cathodic III/II wave of complex **1.** See Table S3 for the estimation of the turnover numbers.

VII

Table S3: Estimation of Turn Over Number assuming that **1(O)** is responsible for the all the catalytic O_2 evolution in the three-hour Chronopotentiometry (Figure S9).

	nmols 1(0)	**nmols O_2**	**TONS**
0 h < t < 1 h	0.142	1436	10 112
1 h < t < 2 h	0.099	1436	14 500
2 h < t < 3 h	0.035	1436	40 000
Total			~ 60 000

References

S1 Creus, J.; Matheu, R.; Peñafiel, I.; Moonshiram, D.; Blondeau, P.; Benet-Buchholz, J.; García-Antón, J.; Sala, X.; Godard, C.; Llobet, A. *Angew. Chem. Inter. Ed.* **2016**, *55*, 15382-15386.

S2 Hu, S.; Shaner, M. R.; Beardslee, J. A.; Lichterman, M.; Brunschwig, B. S.; Lewis, N. S. *Science* **2014**, *344*, 1005-1009.

S3 HeJi supplier, www.nanotubeseu.com/nano/products/M4906/main.html

S4 McCrory, C. C. L.; Jung, S.; Ferrer, I. M.; Chatman, S. M.; Peters, J. C.; and Jaramillo, T. F. *J. Am. Chem. Soc.* **2015**, *137*, 4347-4357.

Chapter 8

General Conclusions

The specific conclusions of each work are disclosed in Chapters 3-7. Four general conclusions are exposed in this Chapter (abridged in this first page and developed later) in order to summarize the present doctoral thesis.

- ✓ Two new families of Ru complexes containing the pentadentate ligands **tda**$^{2-}$ and **t5a**$^{3-}$ generate the fastest molecular water oxidation catalysts described up to date ([2,2':6',2''-terpyridine]-6,6''-dicarboxylate = **tda**$^{2-}$, 2,5-bis(6-carboxylatopyridin-2-yl)pyrrol-1-ide = **t5a**$^{3-}$).

- ✓ Intramolecular H bonding empowers water oxidation catalysis by rocketing the reaction rate and increasing the acidity of the Ru-OH_2 group.

- ✓ The second-order water oxidation mechanism of Ru-**bda** complexes (**bda**$^{2-}$ = [2,2'-bipyridine]-6,6'-dicarboxylate) hinders their performance in conditions of restricted mobility and therefore their value for the generation of hybrid anodes and photoanodes.

- ✓ Ru-**tda** catalysts, with a first-order reaction mechanism, are the perfect molecular candidates for the generation of fast and rugged hybrid anodes and photoanodes for water oxidation.

VIII

*Two new families of Ru complexes containing the pentadentate ligands **tda**$^{2-}$ and **t5a**$^{3-}$ generate the fastest molecular water oxidation catalysts reported up to date ([2,2':6',2''-terpyridine]-6,6''-dicarboxylate = **tda**$^{2-}$, 2,5-bis(6-carboxylatopyridin-2-yl)pyrrol-1-ide = **t5a**$^{3-}$).*

Inspired by Ru-**bda** complexes (**bda**$^{2-}$ is ligand [2,2'-bipyridine]-6,6'-dicarboxylate), the fastest water oxidation catalyst available in 2012, two new families of seven-coordinate complexes bearing a pentadentate **tda**$^{2-}$ or **t5a**$^{3-}$ ligand were prepared and characterized (Figure 1). In the new complexes, the pentadentate ligands coordinate to the equatorial plane of the Ru metal center while pyridine ligands lay in the axial positions. In basic solution both Ru-**tda** and Ru-**t5a** complexes suffer partial displacement of the equatorial ligand by hydroxide species leading to dangling carboxylate/pyridyl-carboxylate moieties, respectively. The generated species, $[Ru^{IV}(OH)(\mathbf{tda}\text{-}\kappa\text{-}N^3O)(py)_2]^+$ and $[Ru^{IV}(OH)(\mathbf{t5a}\text{-}\kappa\text{-}N^2O)(py)_2]$, oxidize water at very high TOF (8 000 – 10 000 s^{-1}) at pH = 7.0 and represent the fastest water oxidation catalysts in the literature. The very fast kinetics of these catalysts is mainly attributed to the role of the dangling carboxylate as proton acceptor in an intramolecular fashion. In addition, a new electrochemical method based on the Foot of the Wave Analysis (FOWA) has shown that these complexes, besides fast, fulfill the requirement of being *first-order* water oxidation catalysts, a key requirement for their inclusion on molecular anodes and photoanodes.

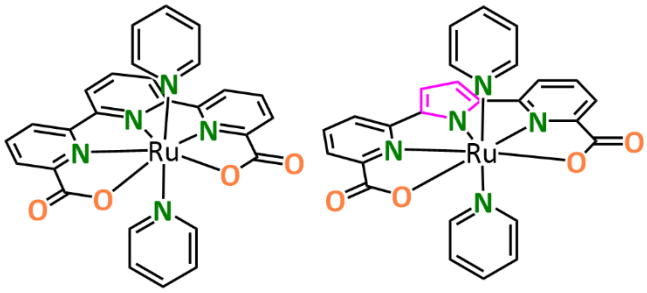

$[Ru^{IV}(\mathbf{tda}\text{-}\kappa\text{-}N^3O^2)py_2]^{2+}$ $[Ru^{IV}(\mathbf{t5a}\text{-}\kappa\text{-}N^3O^2)py_2]^{2+}$

Figure 1. Stucuture for $[Ru^{IV}(\mathbf{tda}\text{-}\kappa\text{-}N^3O^2)py_2]^{2+}$and $[Ru^{IV}(\mathbf{t5a}\text{-}\kappa\text{-}N^3O^2)py_2]^{2+}$ complexes**.** The **tda**$^{2-}$ ligand is 2,2':6',2''-terpyridine]-6,6''-dicarboxylate and the **t5a**$^{3-}$ ligand is 2,5-bis(6-carboxylatopyridin-2-yl)pyrrol-1-ide.

Intramolecular H bonding empowers water oxidation catalysis by rocketing the water oxidation catalysis rate and increasing the acidity of the Ru-OH_2 group.

Intramolecular H bonding was a new feature for water oxidation catalysts and its influence on their catalytic performance was unknown. Two new Ru-**tda** complexes bearing one and two

aqua ligands at the axial positions, $[Ru^{III}(\mathbf{tda}\text{-}\kappa\text{-}N^3O^2)(py)(OH^{ax})]^+$ and $[Ru^{III}(\mathbf{tda}\text{–}\kappa\text{-}N^3O^2)(OH^{ax})_2]^+$ respectively, have been prepared and characterized. These complexes do not show significant H bonding in their structures and they display moderate activity as water oxidation catalysts. This permitted the qualitative rationalization of the role of intramolecular H bonding on multiple parameters such as the acidity of the Ru-OH moieties, the overpotential or the catalytic rate. In addition, the quantification of these effects have revealed that the intramolecular H bonding is able to boom the catalytic activity up to 4 orders of magnitude and to increase the acidity of the Ru-OH group by 8 units (Figure 2).

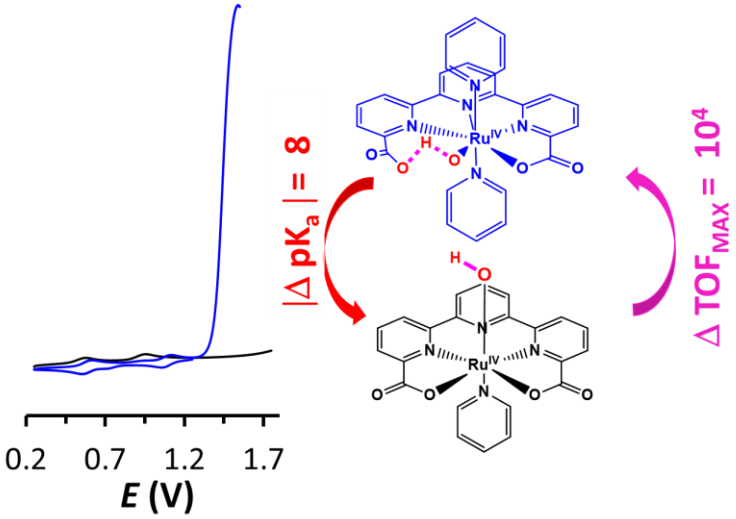

Figure 2. Reactivity of two Ru-**tda** complexes bearing a Ru-OH in an axial position (black line and drawing) or in the equatorial position (blue line and drawing).

VIII

*The second-order water oxidation mechanism of Ru-**bda** complexes (**bda**$^{2-}$ = [2,2'-bipyridine]-6,6'-dicarboxylate) hinders* their performance in conditions of restricted mobility and therefore their value for the generation of hybrid anodes and photoanodes.

The dinuclear nature of the O-O bond formation mechanism of Ru-**bda** complexes has been confirmed by comparing the catalytic behavior of complexes bearing isoquinoline ligands (that favor pi pi stacking) and Me-py-py ligands (that disfavor pi pi stacking), being the catalytic activity of the former three orders of magnitude faster than that of the latter (Figure 3, left). Further modification of the axial pyridyl ligands allows immobilizing Ru-**bda** on a glassy carbon surface through the electroreduction of a diazonium salt. However, the impossibility to perform water oxidation through a second order mechanism in conditions of restricted mobility degrades the molecular complex to RuO_2. Surprisingly, the latter resulted very active in water oxidation catalysis with TOF values of c.a. 300 s^{-1} (Figure 3, right). The degradation of the anchored Ru-**bda** complex indicates the need of developing anodes and photoanodes based on fast *first-order* water oxidation catalysts.

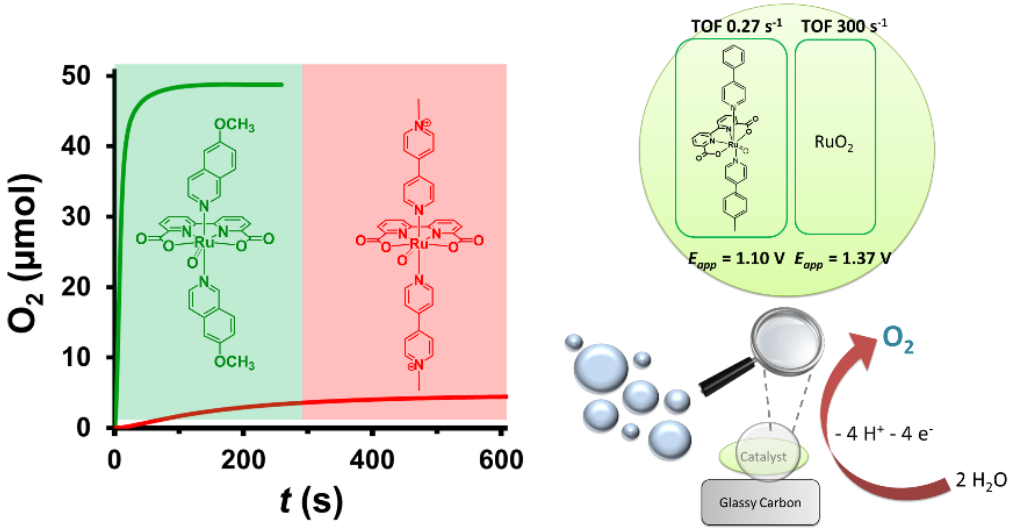

Figure 3. Performance of two Ru-**bda** catalyst in solution (left) and inmobilized on the surface throught the electroreduction of a diazonium salt (right)**.**

VIII

*Ru-**tda** catalysts, with a first order reaction mechanism, are the perfect molecular candidates for the generation of fast and rugged hybrid anodes and photoanodes for water oxidation.*

The fast *first-order* Ru-**tda** water oxidation catalyst has been slightly modified in remote positions to generate hybrid molecular anodes and photoanodes. The immobilization of Ru-**tda** complexes bearing a pyrene-containing pyridine ligand via pi pi staking on Multi-Walled Carbon Nanotubes (MWCNTs) allowed the preparation of powerful anodes and photoanodes. Due to the *first-order* mechanism of the molecular catalyst, when the hybrid Ru-**tda**@MWCNTs is combined with glassy carbon a molecular anode stable for more than 1 000 000 turnovers is obtained (Figure 4, left). A related procedure can be used for the preparation of photoanodes based on a TiO_2 coated n-Si semiconductor, MWCNTs and the Ru-**tda** complex that performs sustained photoinduced water oxidation at 1 mA/cm^2 for over 60 minutes (Figure 4, right). This system also allows the monitoring of the anchored molecular species before and during catalysis and it is the best-performing molecular photoanode up to date.

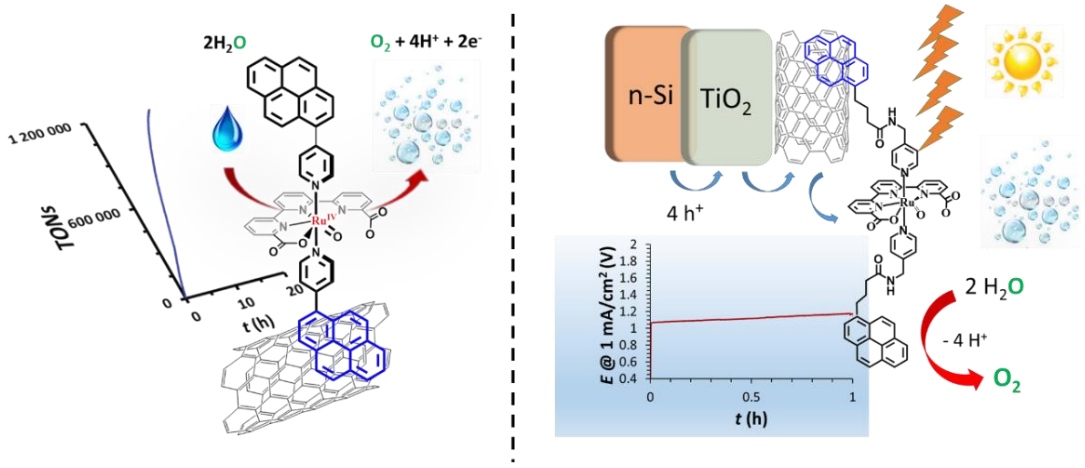

Figure 4. Molecular anode based on the Ru-**tda** complex immobilized on carbon nanotubes (Ru-**tda**@MWCNTs) through pi-pi stacking (left). Molecular photoanode based on the Ru-**tda** complex and TiO_2-proctected n-Si (right).

VIII

UNIVERSITAT ROVIRA I VIRGILI
SEVEN-COORDINATE COMPLEXES FOR WATER OXIDATION CATALYSIS: FROM MOLECULAR CHARACTERIZATION TO SOLID STATE PHOTOCATALYSIS
Roc Matheu Montserrat

Chapter 9

Annexes:

This chapter comprises two works that are closely related to this thesis. In the first work, the seven-coordinate ($[Ru^{IV}(tda)(py)_2(O)]$) catalyst is studied in a photocatalytic system with $[Ru^{III}(bpy)(bpy\text{-}COOEt)_2]^{3+}$ as sensitizer and $Na_2S_2O_8$ as sacrificial electron acceptor by optical techniques, including transient absorption spectroscopy and photoluminescence quenching. In the second work, the RuO_2 anode that results from the degradation of the Ru-bda complex described in Chapter 6 has been assembled with a triple homo-junction polymer cell with enough potential for the energetically demanding water splitting reaction.

The chapter consist of the following independent papers:

PAPER J Francas, L.; Matheu, R.; Pastor, E.; Reynal, A.; Berardi, S.; Sala, X.; Llobet A.; Durrant, J. R. *ACS Catal.* **2017**, *7*, 5142–5150

PAPER K Elias, X.; Liu, Q.; Gimbert-Suriñach, C.; Matheu, R.; Mantilla-Perez, P.; Martinez-Otero, A.; Sala, X.; Martorell, J.; Llobet, A. *ACS Catal.* **2016**, 5, 3310-3316.

IX

PAPER J Kinetic analysis of an efficient, molecular light-driven water oxidation system

Francas, L.; Matheu, R.; Pastor, E.; Reynal, A.; Berardi, S.; Sala, X.; Llobet A.; Durrant, J. R.
ACS Catal. **2017**, *7*, 5142–5150

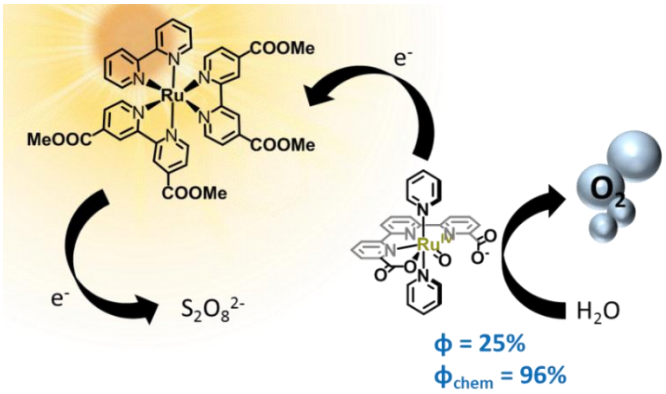

Abstract

We report an efficient molecular light-driven system to oxidize water to oxygen and the kinetic analysis of the factors determining the efficiency of the system. The system comprises a highly active molecular catalyst ($[Ru^{IV}(tda)(py)_2(O)]$), $[Ru^{II}(bpy)(bpy\text{-}COOEt)_2]^{2+}$ (**RuP**) as sensitizer and $Na_2S_2O_8$ as sacrificial electron acceptor. This combination exhibits a high quantum yield (25%) and chemical yield (93%) for photo-driven oxygen evolution from water. The processes underlying this high performance are identified using optical techniques including transient absorption spectroscopy and photoluminescence quenching. A high catalyst concentration is found to be required to optimize the efficiency of electron transfer between the oxidized sensitizer and the catalyst, which also has the effect of improving sensitizer stability. The main limitation of the quantum yield is the relatively low efficiency of $S_2O_8^{2-}$ as an electron scavenger to oxidize the photoexcited ruthenium sensitizer **RuP*** to 2 **RuP**$^+$, mainly due to competing back electron transfers to the **RuP** ground state. The overall rate of light-driven oxygen generation is determined primarily by the rate of photon absorption by the molecular sensitizer under the incident photon flux. As such the performance of this efficient light-driven system is limited not by the properties of the molecular water oxidation catalyst, which exhibits both good kinetics and stability, but rather by the light absorption and quantum efficiency properties of the sensitizer and electron scavenger. We conclude by discussing the implications of these results for further optimization of molecular light-driven systems for water oxidation.

Contributions

Roc Matheu synthetized and characterized the Ru catalysts, performed the electrochemical and photocatalytic analysis and prepared the manuscript.

J 1 Introduction

Harnessing solar energy to drive the synthesis of hydrogen from water, and the reduction of CO_2 to other fuels such as methanol, offers a renewable, carbon zero (for H_2) or neutral (CO_2 reduced fuels) pathway to reduce our dependency on fossil fuels. This process is called artificial photosynthesis, because it mimics plant's use of solar energy, water and CO_2 to store energy in chemical bonds. As in natural photosynthesis, one of the key processes that need to take place is water oxidation, in which four electrons and four protons are extracted from two water molecules, producing molecular oxygen. This process is both kinetically and energetically demanding. A key challenge in this field is thus the development of suitable water oxidation catalysts (WOCs) that drive water oxidation induced by light. In recent years, substantial progress has been reported on molecular water oxidation catalysts [1,2] although light-driven water oxidation activity has been demonstrated in only a small number of cases.[3-11] Furthermore analyses of the kinetic processes determining the efficiency of these photoactivated systems, have been very limited to date and in several cases the molecular catalyst has been reported to degrade to the corresponding metal oxide.[3,6-9]

Homogeneous photoactivated water oxidation systems typically consist of ternary systems including a light harvesting molecule, such as $[Ru(bpy)_3]^{2+}$ (bpy is 2,2'-bipyridine; see Chart 1 for a chemical structures), a sacrificial electron acceptor, such as persulfate and a water oxidation catalyst. Amongst all the reported molecular water oxidation catalysts, ruthenium complexes exhibit the highest performances when driven both chemically and electrochemically. However, such catalysts often exhibit rather poor efficiencies when used in light-driven systems, with quantum yields for oxygen generation per incident photon typically being ≤ 10 %.[3,4a] These modest efficiencies for light-driven systems have typically been assigned to limitations associated with the low turnover frequencies (TOF) of the molecular water oxidation catalyst, as well as the severe overpotentials required to drive the catalytic reaction. As such, efforts in this field have been recently focused on improving both the overpotential requirements and TOF's for molecular water oxidation catalysts. It is worth mentioning here that increasing the catalyst-dye interactions via a supramolecular approach can also significantly enhance quantum yields.[5]

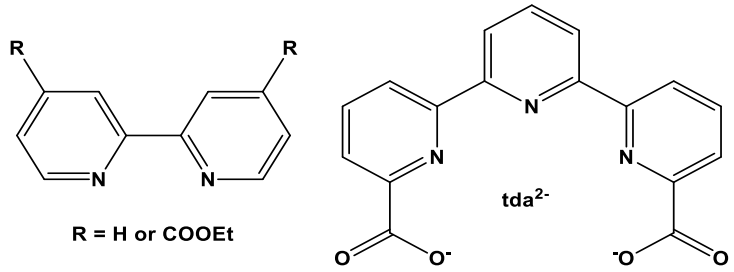

Chart 1. Key ligands used in this work

Recently, we have reported[2] a highly efficient Ru based water oxidation catalyst $[Ru^{IV}(tda)(py)_2(O)]$, (abbreviated from now on as **Ru^{IV}=O**; py is pyridine and tda^{2-} [2,2':6',2''-terpyridine]-6,6''-dicarboxylato; see Chart 1), that is generated in neutral or basic pH from its precursor $[Ru^{IV}(tda\text{-}\kappa\text{-}N^3O^2)(py)_2]$, **$Ru^{IV}$-tda**. The **$Ru^{IV}$=O** complex oxidizes water to dioxygen elecrocatalytically at pH = 7 with a maximum turnover frequency of 8,000 s^{-1} and is therefore an ideal candidate for use in light-driven catalysis. Herein, we have employed this catalyst in a ternary photoactivated system, using a Ru-bpy derivative as a sensitizer and persulfate as a sacrificial electron acceptor. This yields a remarkably efficient homogeneous light-driven water oxidation system. We have used electrochemical, steady state and transient spectroscopic techniques to study the key steps occurring in this three-component system and to obtain a detailed kinetic analysis of the different reactions involved, and the efficiencies of the key individual steps. Our study provides insight to loss pathways in light-driven molecular water oxidation systems and highlights potential routes of improvement.

J 2 Results

*J 2.1 Dark redox processes for the **Ru-tda** molecular catalyst.*

We first consider the dark redox chemistry of the molecular water oxidation catalyst employed in this study. Recently we have reported a family of Ru complexes containing the pentadentate ligand tda^{2-} that coordinates the metal center in the equatorial plane so that the remaining two axial coordination positons can be occupied by monodentate ligands such as pyridine.[2] At ruthenium oxidation state II the tda^{2-} ligand binds in a tetradentate manner, $[Ru^{II}(tda\text{-}\kappa\text{-}N^3O)(py)_2]$, labelled as **$Ru^{II}$-tda** (Scheme 1) but upon two successive one-electron oxidation the latter yields the seven coordinate complex $[Ru^{IV}(tda\text{-}\kappa\text{-}N^3O^2)(py)_2]$, **$Ru^{IV}$-tda**, where now the tda^{2-} ligand acts in a pentadentate fashion as shown in the upper part of Scheme 1. As has been previously reported, pure samples of these complexes can be obtained either chemically or electrochemically by bulk electrolysis and have been individually characterized. The redox potentials of these complexes are outlined in Scheme 1. [2] Chemically the oxidation can be

achieved using Ce(IV) ($E^{o}_{IV/III}$ = 1.7 V at pH = 1.0)[12] or with $[Ru(bpy)_3]^{3+}$ ($E^{o}_{III/II}$ = 1.2 V). All potentials discussed in this work are reported *vs*. NHE.

In the present context, it is important to note that persulfate acts as an oxidative reagent. Indeed, a 1 mM solution of **Ru^{II}-tda** is slowly oxidized to its Ru(III) species with a 100 mM solution of $S_2O_8^{2-}$ both at pH = 7 and at pH = 1 as shown in Figure 1 and the ESI. On the other hand, under similar conditions **Ru^{IV}-tda** is slowly reduced to Ru(III) at pH = 7, but is stable at pH =1.0 (see SI text and Figure S1 for details).

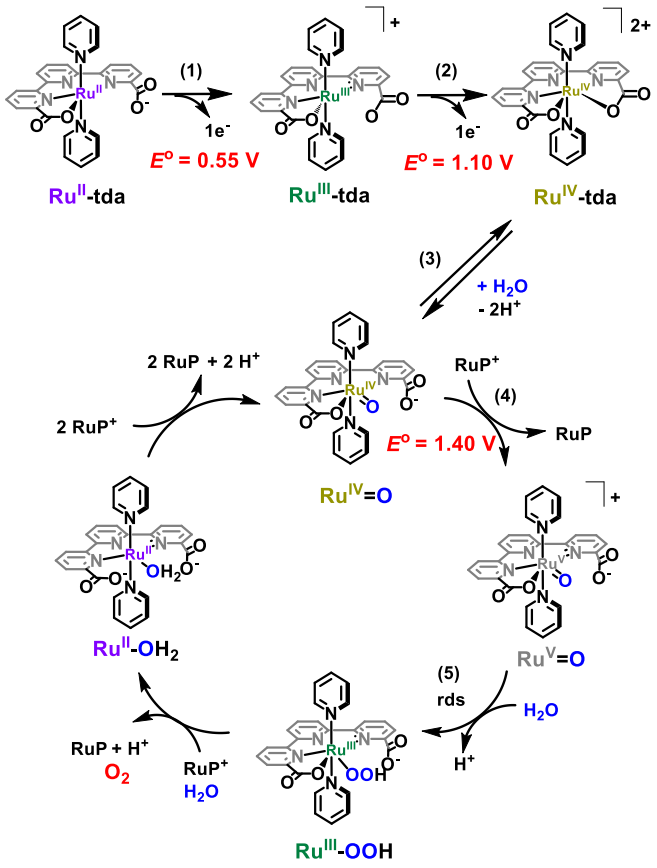

Scheme 1. Ru-tda catalyst precursor at different oxidation sates and simplified catalytic water oxidation cycle proposed for $[Ru^{IV}(tda)(py)_2(O)]$, Ru^{IV}=O, at pH = 7.[2]

At pH = 7 the **Ru^{IV}-tda** complex undergoes aquation to generate $[Ru^{IV}(tda)(py)_2(O)]$, **Ru^{IV}=O** (see equation 3 in Scheme 1), which is an efficient electrochemical water oxidation catalyst (WOC). This aquation process only takes place at oxidation state IV as has been detailed in our previous publications. [2] The catalytic cycle followed by this complex has been described recently and a simplified reaction sequence is illustrated in Scheme 1.[2] A key step in this cycle is the **Ru^{IV}=O** to **Ru^{V}=O** oxidation, which occurs electrochemically at 1.40 V, followed by O-O bond formation via a water nucleophilic attack (WNA) pathway that generates the corresponding **Ru^{III}OOH**. The

latter step has been reported as the rate determining step (rds) of the whole catalytic cycle. [2] A specific feature of this catalytic system is the equilibrium between the catalyst precursor (**Ru-tda**) species and those of the catalyst (**Ru-H_2O**) (equation 3, Scheme 1). For the light-driven system reported herein, we found this equilibrium to be a function of the irradiation time (See figure S6 in the SI). After 2 min irradiation, as employed in our transient absorption measurements described below, cyclic voltammetry data indicates that the ratio of **[Ru-H_2O]:[Ru-tda]** is 1:50; over long irradiation periods (1 hour) the ratio increases up to 2.6:1 . These results indicates that at pH = 7 under the light-driven catalytic conditions the water molecule is able to coordinate to the metal center and that we can accumulate more aqua species at longer time scales.

In addition, it is important to bear in mind that at pH = 1 the aquation reaction (equation 3, Scheme 1) does not occur and thus at this pH the complex does not show any catalytic activity. [2]

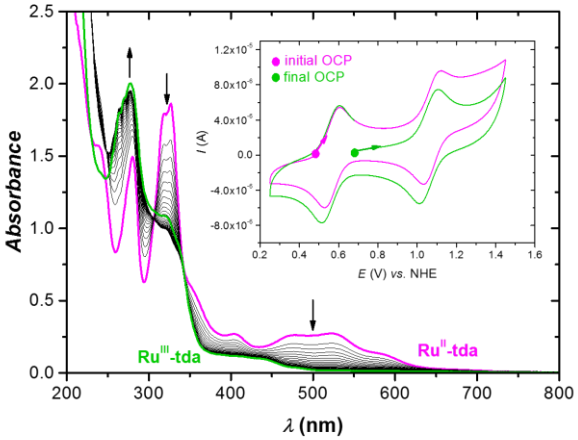

Figure 1. UV-Vis kinetic monitoring for the oxidation of a 4 μM Ru^{II}-tda by 10 mM $S_2O_8^{2-}$ in the dark in a 25 mM phosphate buffer aqueous solution, the ionic strength was adjusted at 0.1 M by the addition of Na_2SO_4 . Pink trace, initial spectrum. Green trace final spectrum after 20 consecutive scans measured every 5 s' during 1h. Inset, Cyclic Voltammetry and Open Circuit Potential measured before the addition of persulfate (pink trace) and after 1 hour reaction time (green trace). Scan rate = 100 mV/s. The arrow indicates the scan direction.

Chemically the key oxidation of **Ru^{IV}=O** to **Ru^{V}=O** cannot be accomplished with $[Ru^{III}(bpy)_3]^{3+}$ because its III/II redox potential is too low. However the ethyl ester derivative $[Ru^{III}(bpy)(bpy\text{-}COOEt)_2]^{3+}$ (bpy-COOEt, is 4,4'-ethyl ester dicarboxyalte-2,2'-bipyridine; see Chart 1), **RuP^{+}**, has a E^o = 1.62 V[4a] and thus has sufficient thermodynamic driving force to carry out the redox

reaction. Therefore, **RuP^{+}** can potentially be used do drive all the oxidation reactions involved in the catalytic cycle displayed in Scheme 1, and is employed in the study herein.

J 2.2 Light-Induced water oxidation catalysis

In order to carry out the light-induced water oxidation catalysis we use the **Ru^{IV}=O** species described above as the catalyst (generated in situ from its **Ru^{III}-tda** precursor), driven by **RuP^{+}** generated from **RuP** with light irradiation in the presence of an excess of a sacrificial electron acceptor, such as $S_2O_8^{2-}$. For this purpose the reaction conditions were initially optimized in the absence of catalyst.

J 2.2.1 Photochemical system optimization in the absence of water oxidation catalyst

Under irradiation conditions in the presence of $S_2O_8^{2-}$, the generation of **RuP^{+}** is described by the equations 1-4 shown in Table 1, where the efficiency definitions are also indicated. A schematic representation of these reactions is also illustrated in Scheme 2.We optimized this process ($S_2O_8^{2-}$ concentration and ionic strength) based on steady state photoluminescence (PL) experiments following the quenching of the excited stated, **RuP***, by persulfate (see equation 2, Table 1, also Figures S2 and S3 in the SI). This quenching process has been widely studied in the literature for $[Ru(bpy)_3]^{2+}$ [3,6,13] and is known to be a complex system due to the ionic pairing between the **RuP^{+}** and the $S_2O_8^{2-}$, which causes a linearity loss in the Stern Volmer plots (see Figure S2b in the SI) associated with a change in ionic strength in the medium.[14] We found optimal reaction conditions at pH = 7, using a 25 mM phosphate buffer (from now on labelled as 7-phbf). These are thus the conditions that will be used throughout the present work unless explicitly mentioned. Under these conditions, a persulfate concentration range of 10-100 mM gives quenching efficiencies ϕ_q of 0.75-0.90 respectively (See Table 1 for efficiency definitions and Fig S2).

Transient absorption spectroscopy was used to investigate the electron transfer kinetics involved in the binary solution of **RuP** dye and $S_2O_8^{2-}$. These processes have been widely studied for the commonly employed $[Ru(bpy)_3]^{2+}$ dye. [3,6,13,15] The change in absorbance of **RuP** in the presence of $S_2O_8^{2-}$ after photoexcitation is characterized by a negative photobleach feature at wavelengths shorter than 600 nm and a positive photoinduced absorbance at the 650-800 nm region (See Figure S3), assigned to the photoinduced generation of **RuP^{+}**, by analogy with $[Ru(bpy)_3]^{2+}$. These transient absorption signals decay with a half-life time ($t_{50\%}$) of 0.7 s, as illustrated at 460 nm in Figure 2 (orange trace) and assigned to decay of photogenerated **RuP^{+}**

species back to its ground state, **RuP**. The raise of these **RuP**$^{+}$ signals was observed to be biphasic, with an initial instrument response limited (< 150 ns) rise, followed by a slower ($t_{1/2}$ = 3.8 µs) rise, as shown in Figure S4. Following an analogous study by Scandola and coworkers,[7] the initial rise is assigned to the direct oxidation of photogenerated **RuP*** by $S_2O_8^{2-}$ termed "direct oxidation" (eq. 2, Table 1), and the subsequent microsecond phase to diffusion limited oxidation of **RuP** by the radical $SO_4^{\cdot-}$ to generate again **RuP**$^{+}$, named "dark oxidation" (eq. 3, Table 1 and Scheme 2). The efficiency of the dark oxidation relative to the preceding direct oxidation can be estimated from the relative amplitudes of these two phases, giving a value of ϕ_d = 0.6,[3,7] (see Table 1 for details). The combination of these Transient Absorption Spectroscopy (TAS) and PL experiments allow to calculate an overall quantum efficiency for the **RuP**$^{+}$ generation, ϕ_{RuP+} = 0.56, that considers both the direct and dark processes (see Table 1 for definition), corresponding to the generation of 1.12 **RuP**$^{+}$ species per absorbed photon.

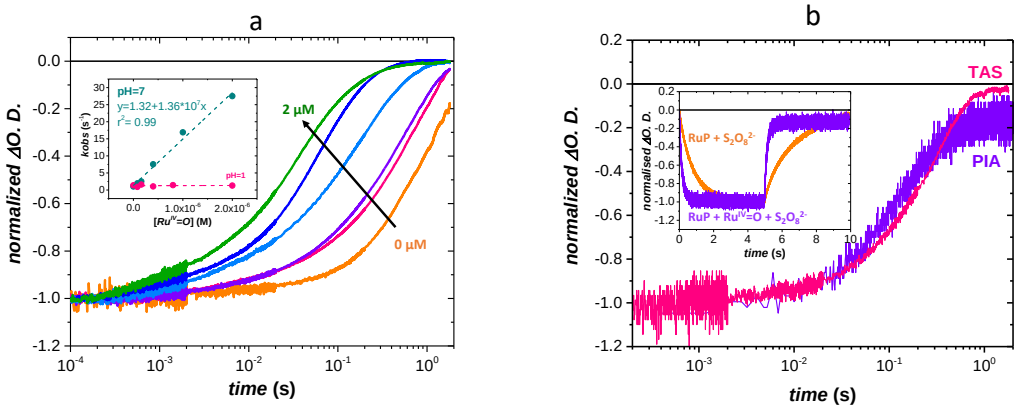

Figure 2. a, Normalized TA decays probed at 460 nm (λ_{ex} = 500 nm; laser intensity = 177.48 µJ cm^{-2}) for a 7-phbf solution RuP (20 µM), $S_2O_8^{2-}$ (10 mM) in the absence of catalyst (orange trace) and with different [Ru^{IV}=O] (pink, 80 nM; violet, 160 nM; light blue, 0.4 µM; dark blue, 1 µM, green 2 µM) that were generated from the corresponding [Ru-tda] precursors (see text). Data collected under N_2 at 10 µs-2 s timescales. Inset, plot of k_{obs} *vs*. [Ru^{IV}=O] at pH = 7 and pH -= 1. b, TAS decays measured at 460 nm under pulsed laser (pink) and 5 s LED irradiation (15.4 mW cm^{-2}) (violet). Data shown for a 20 µM RuP, 10 mM $Na_2S_2O_8$ and 40 µM Ru^{II}-tda solution that generates a [Ru^{IV}=O] = 0.8 µM. Inset, full linear timescale traces of the transient signal under LED excitation showing the change of both at light on and light off, in the absence (orange) and presence of 0.8 µM Ru^{IV}=O (violet).

J 2.2.2 System optimization in the presence of the water oxidation catalyst

Once the combination of **RuP** dye and sacrificial electron acceptor had been optimized and the main kinetic and spectroscopic parameters unveiled for this binary system, the next step involved the addition of the water oxidation catalyst into the system.

Figure 3 shows that, in the absence of persulphate, the emission spectrum of a 4 µM **RuP** is not quenched by the addition of 4 µM of the catalyst precursor **Ru^{II}-tda** in a 7-phbf solution (orange). However, when a solution of 10 mM persulfate is added to the **RuP / Ru^{II}-tda** solution, the emission is quenched by 60%, approximately independent of the catalyst concentration (ϕ_q as a function of [$S_2O_8^{2-}$] in the presence of catalyst is presented in Figure S5). We find that under identical conditions (Compare Figure S2a and S5 in the SI) in the absence of **Ru^{II}-tda**, the quenching yield is ϕ_q = 0.75, indicating that in the former case the presence of the Ru catalyst reduces the efficiency of the electron scavenging, possibly due to additional deactivation pathways. With ϕ_q = 0.60 in the presence of the catalyst and the sacrificial agent, then the overall quenching efficiency for the generation of **RuP$^+$** is, ϕ_{RuP+} = 0.50 (i.e.: one **RuP$^+$** per photon absorbed

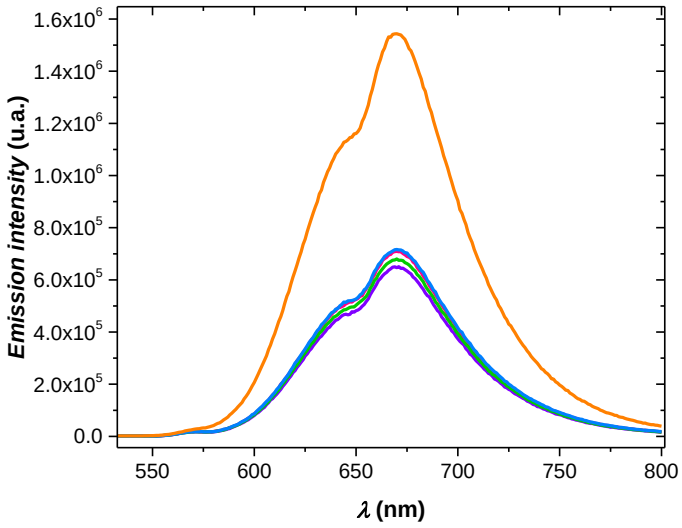

Figure 3. Emission spectra of a 4 µM RuP and 4 µM Ru^{II}-tda solution (orange) in the absence of a sacrificial electron acceptor. Emission spectra of RuP (4 µM), $Na_2S_2O_8$ (10 mM) and different

IX

Table 1. Efficiencies of Light and Dark Reactions Studied.

Process	Chemical Reaction	Effiency Definition.
Light absorption:	RuP + hν -> RuP* (1)	
Direct generation of **RuP**$^{+}$:	RuP* + $S_2O_8^{2-}$ -> RuP^{+} + SO_4^{2-} + $SO_4^{\cdot-}$ (2)	$\phi_q = 1–I/I_0$ [a]
Dark generation of **RuP**$^{+}$:	RuP + $SO_4^{\cdot-}$ -> RuP^{+} + SO_4^{2-} (3)	$\Phi_d = \frac{\Delta O.D._{\cdot d}}{\Delta O.D._{\cdot I}}$ [b]
Overall rxs (1)-(3)	2 RuP + hν + $S_2O_8^{2-}$ -> 2RuP^{+} + 2 SO_4^{2-} (4)	$\Phi_{RuP+} = \frac{1}{2}\{\phi_q(1+\phi_d)\}$
Bimolecular electron transfer	RuP^{+} + Ru^{IV}=O -> RuP + Ru^{V}=O (5)	$\Phi_{ET} = 1 - \frac{k_0}{k_{obs}}$ [c]
Measured oxygen quantum yield	hν 2 H_2O --------> O_2 + 4H^{+} + 4e^{-} (6)	$\Phi_{O2} = \frac{2 \times (O_2\ molecules)_t}{Absorbed\ photons \times \Delta t \times Area}\ x\ 100\%$ [d]
Calculated oxygen Quantum yield		$\phi_{Total} = \phi_{RuP+} * \phi_{ET} * \phi_{Cat}$ [e]

[a] I and I_0 are the photoluminescence intensities in the presence and absence of $S_2O_8^{2-}$ respectively.[b] From TAS decays probed at 460 nm in the absence of catalyst: ΔO.D.$_{\cdot I}$, is the amplitude of the initial phase of the decay probed at 460 nm. ΔO.D.$_{\cdot d}$, is the amplitude of the second phase (see Figure S4).[12] [c] From TAS decays probed at 460 nm with different catalyst concentrations: k_0 = 1/$t_{50\%}$ without Catalyst and k_{obs}= 1/$t_{50\%}$ in the presence of catalyst. [d] This calculation assumes an ideal quantum efficiency of 2 photons per molecule of oxygen, accounting for the ideal generation of two **RuP**$^{+}$ per photon and four **RuP**$^{+}$ per oxygen molecule. [e] ϕ_{Cat} is the chemical efficiency of water oxidation by the catalyst, assumed herein to correspond to the Faradaic efficiency measured under electrochemical oxidation.

J 2.2.3 Kinetic characterization of the light-induced reaction between the catalyst and the dye with the complete system.

Transient absorption spectroscopic measurements with the complete system involving the dye, the sacrificial electron acceptor and the water oxidation catalyst were carried out in order to investigate the kinetic processes involved. All TAS measurements were performed after a 2 minute sample irradiation in order to equilibrate all the species in solution and thus measured

under steady state catalytic conditions. Under these conditions, the catalyst precursor equilibrates with the active catalytic species (see equation 3 in Scheme 1). The relative concentrations were estimated to be 50:1 **Ru^{IV}-tda:Ru^{IV}=O** , after 2 minute irradiation, as discussed above (see Figure S6 in the SI). The kinetic analysis shown in Figure 2a inset supports the extrapolation of this ratio at different precursor concentrations. However with low intensity irradiation the catalyst concentration might be even lower.

Figure 2a shows the **RuP^+** bleach signal decay kinetics at 460 nm in the presence of $Na_2S_2O_8$ as a function of catalyst precursor **Ru^{II}-tda** concentration in a 7-phbf solution. The decay kinetics observed in the TAS experiments correspond to the slowest ET transfer step (equation 4, Scheme 1), that is a bimolecular interaction between **Ru^{IV}=O** and **RuP^+**. As shown in Figure 2, the decay kinetics accelerate with increasing the catalyst's concentration. The half-times of these decays fitted well with a simple bimolecular expression with a reaction time linearly dependent on the catalyst concentration. This is in agreement with a pseudo-first order behavior where the **[Ru^{IV}=O]** >> **[**RuP^+**]**, and thus k_{ET} can be extracted from the plot of k_{obs} *vs*. [**Ru^{IV}=O**] as shown in the inset of Figure 2 and described in equations 5a-5c).

$$v = k_{ET}\,[Ru^{IV}{=}O][RuP^+] \quad (5a)$$

$$[Ru^{IV}{=}O] >> [RuP^+];\ k_{obs} = k_{ET}[Ru^{IV}{=}O] \quad (5b)$$

$$v = k_{obs}[RuP^+] \quad (5c)$$

The calculated electron transfer constant is $k_{ET} = 1.4\cdot10^7\ M^{-1}\ s^{-1}$. Further evidence that confirms the pseudo-first order nature of the reaction comes from the transient absorption decays using laser intensities of 180 and 20 μJ/cm^2 (Figure 4). These experiments generate different concentrations of **RuP^+** depending on the energy used but the normalized bleach kinetics is independent of [**RuP^+**], consistent with the pseudo-first order behavior indicated in the suite of equations 5a-5c.

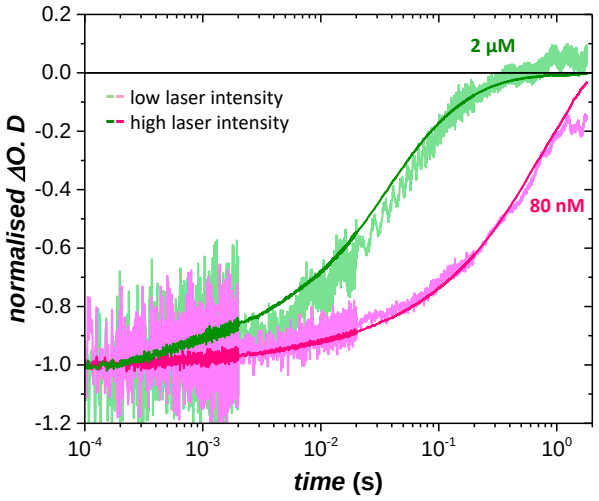

Figure 4. Normalized transient absorption decays at 460 nm of a 20 µM RuP, 10 mM $Na_2S_2O_8$ solution (7-phbf), containing two Ru^{IV}=O concentrations (violet, 80 nM; green, 2 µM) in a 7-phbf solution. Data collected under N_2 at a 10 µs-2 s timescale after dye excitation (λ_{ex} = 500 nm), using two different laser intensities of 180 (dark line) and 20 (light line) µJ cm^{-2}.

We next estimate the quantum efficiency of the oxidation of **Ru^{IV}=O** by **RuP^+**. This, ϕ_{ET}, can be estimated from the acceleration of the **RuP^+** bleach decays (Figure 2a) at different catalyst concentrations (see Table 1). Such analysis gives ϕ_{ET} values that range from of 0.45 at initial 4 µM **Ru^{II}-tda** to an impressive 0.96 at 100 µM as is discussed further below.

Photoinduced Absorbance (PIA) experiments were undertaken on the same ternary system at pH = 7 employed in Figure 2a, using quasi-steady state irradiation achieved by 5 s 365 nm LED (light emitting diode) excitation pulses; the results are shown in Figure 2b. The inset shows full time traces measuring the **RuP^+** bleach signal in the presence and absence of **Ru^{IV}=O**. In the absence of catalyst, a **RuP^+** bleach signal is observed, with a rise and fall times of ~ 1 s ($t_{50\%}$), assigned to the accumulation of oxidized **RuP^+** under these quasi steady state conditions. The rise and fall times ($t_{50\%}$) of ~ 1s are consistent with the **RuP^+** lifetime observed under laser excitation in the absence of catalyst with TAS measurements (Figure 2a). In the presence of the **Ru^{IV}=O** catalyst, the LED irradiation resulted in a faster **RuP^+** bleach rise and decay due to electron transfer between the dye and catalyst. The decay kinetics of the **RuP^+** bleach signal, monitored when the LED is turned off, and assigned to the oxidation of **Ru^{IV}=O** under these quasi-steady state conditions, are shown in the main part of Figure 2b (violet trace) and are strikingly similar to those one obtained under short pulse laser excitation (pink trace). These

experiments support our previous assumption that the TAS experiments are indeed already under steady state conditions. In addition, a similar PIA experiment was carried out using a Clark electrode to simultaneous measure the formation of O_2, further confirming the mentioned steady state equilibrium (see Figure S7).

Similar experiments were carried out at pH = 1, where the aquation reaction (reaction 3, Scheme 1) does not occur. At this pH and under steady state conditions the catalyst precursor is oxidized to its higher oxidation states **Ru^{IV}-tda** but no further reactions occur because no catalytic species can be generated.[2] In agreement with this, the TAS kinetics of the bleach (k_{obs}) were observed to be independent of the catalyst precursor concentration, as can be observed in the inset of Figure 2a (see also Figure S9). This is a key result that further supports our discussion above that at pH = 1, light irradiation (such as the 2 minute light equilibration time employed prior to our TAS measurements) results in the initial catalyst precursor at oxidation state II being completely driven to its oxidation state IV species **Ru^{IV}-tda**, with this species being unable to undergo further oxidation by **RuP^{+}**.

2.3 Light-driven O_2 generation

With the above-described quasi-steady state irradiation conditions, we were in a position to design steady state experiments for light-induced water oxidation using **RuP** as photosensitizer, **Ru^{II}-tda** as a water oxidation catalyst precursor and persulfate as sacrificial electron acceptor in a 7-phbf solution. Figure 5a shows the oxygen evolution profiles as a function of time during one hour of irradiation, measured with a gas phase Clark electrode, for different **Ru-tda** concentrations ranging from 1-90 μM in the presence of 10 mM persulfate and 200 μM **RuP** at 7-phbf.

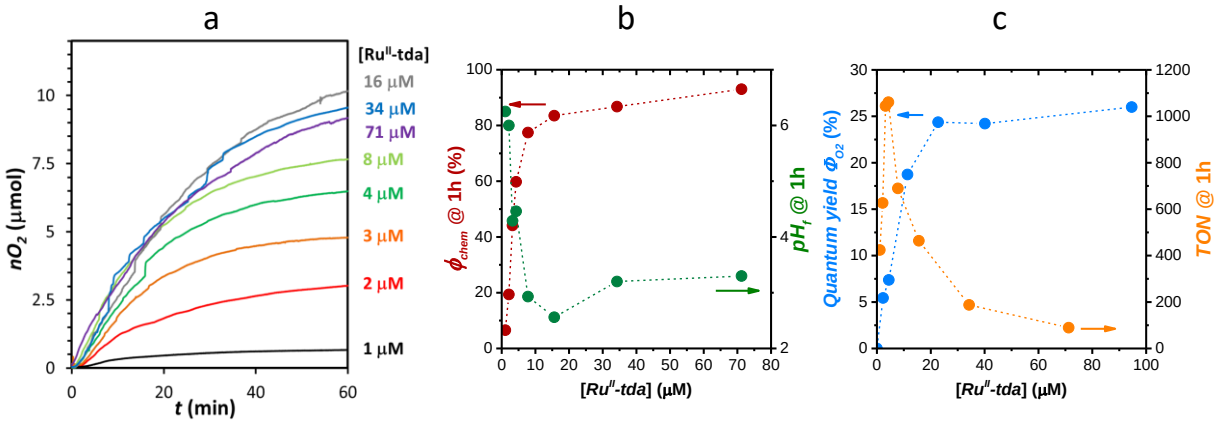

Figure 5. Bulk oxygen evolution experiments measured in the gas phase during 1 h irradiation (1 sun) at different [Ru^{II}-tda] (black, 1 μM; red, 2 μM; orange, 3 μM; dark green, 4 μM; light green, 8 μM; grey, 16 μM; blue, 34 μM, violet, 71 μM) containing the following $Na_2S_2O_8$ concentration: black, 9.9 mM; red 9.9 mM; orange, 10.9 mM; dark green, 10.9 mM; light green, 9.9 mM, grey, 12.4 mM; blue, 10.7 mM and violet, 10 mM and 0.2 mM RuP in a 2 mL 7-phbf solution. (a) Oxygen evolution *vs*. time. (b) Chemical efficiency (red) and final pH_f (green) *vs*. [Ru^{II}-tda] that after one hour irradiation is partially converted to the catalyst giving a final ratio [Ru^{IV}=O]/[Ru^{II}-tda] = 2.5, see SI. (c) Initial Quantum yield (ϕ_{O2}) (turquoise) and TONs (orange) based on the final [Ru^{IV}-=O].

Figure 5b shows a plot of the chemical efficiency, ϕ_{Chem}, defined as (2 x moles of oxygen generated/ moles of persulfate added) x 100. It is interesting to see how increasing the concentration of **Ru^{II}-tda** from 1 to 16 μM ϕ_{Chem} also increases from 7 to 80%. Upon further increase of **Ru^{II}-tda** concentration, the chemical efficiency levels off reaching about 93% at 90 μM. This result shows that for this system at high catalyst concentrations, the overall amount of oxygen generated is limited only by the amount of sacrificial electron donor added to the solution, confirming the high efficiency and stability of the catalyst under the present conditions. Indeed it is also impressive to see that the system achieves a value of 1050 turnovers per hour with a 4 μM **Ru^{II}-tda** (3 μM **Ru^{IV}=O**) concentration, ranking amongst the most efficient light-induced molecular water oxidation catalysts reported (Figure 5c).[3-4,6-11]

The low chemical efficiency at low catalyst concentrations is consistent with the lower quantum efficiency for the oxidation of the catalyst by **RuP$^+$** (ϕ_{ET}) determined from our transient absorption data above, and indicates that competing deactivation pathways become important. The main deactivation processes for **RuP$^+$** are likely to be associated with the oxidation of the bpy ligand of the **RuP** dye by the **RuP$^+$** species as well as by the radical $SO_4^{\cdot-}$ species, as has been previously proposed for related systems.[15] These deactivation pathways also result in significant dye degradation, apparent from progressive photobleaching of the dye optical absorption, which was most pronounced at low catalyst concentrations. (see Figure S11 in the SI).[4a,15]

During the light-driven catalytic experiments, as oxygen is released four protons are generated per molecule of oxygen and even under a buffered solution the pH significantly decreases, as shown in Figure 5b. The pH decrease can alter the rates of electron transfer, which will probably be slower at lower pH due to the decrease in energetic driving force,[2] as well as changing the equilibrium of equation 3 (Scheme 1) that is responsible for the generation of the active species. Therefore, it can significantly influence the delicate balance among the different chemical reactions involved in this complex process. The addition of alkali to reverse this pH change would result in a significant increase in ionic strength of the system, which will also decrease the **RuP^{+}** generation efficiency, thus preventing efficientrecycling of the system.

Quantum efficiencies for oxygen generation (ϕ_{O2}) were calculated based on the initial rates of oxygen formation and the density of photons absorbed per second as indicated in Table 1 and the SI, and displayed in Figure 5c as a function of catalyst precursor concentration. As can be observed in Figure 5c, ϕ_{O2} increases with increasing [**Ru^{II}-tda**] and closely parallels that of ϕ_{Chem}. However while for the latter we reach values close to 100%, for the former it levels off at approximately 25% for 20 μM **Ru^{II}-tda**; this photon to oxygen quantum efficiency still constitutes the highest efficiency reported to date for this type of molecular light-driven water oxidation systems. We note that our calculation of ϕ_{O2} assumes, conservatively, that each absorbed photon can optimally generate two **RuP^{+}** and therefore that ϕ_{O2} = 100 % would correspond to one molecule of O_2 per two photons. The factors still limiting this impressive quantum efficiency will be discussed below.

J 3 Discussion

We have demonstrated that the proper combination of a dye, **RuP^{+}**, a water oxidation catalyst, **Ru^{IV}=O,** and persulfate as sacrificial electron acceptor can constitute a light-driven system with unprecedentedly high chemical (ϕ_{Chem} = 96%) and quantum (ϕ_{O2} = 25%) efficiencies, for the light-induced oxidation of water to molecular oxygen. This is achieved thanks primarily to the high stability and extremely fast water oxidation kinetics associated with the **Ru^{IV}=O** catalyst. The latter is generated in situ from the **Ru^{II}-tda** catalyst precursor under irradiation. Both catalyst and catalyst precursor remain in equilibrium during the steady state oxygen formation under which the transient absorption spectroscopic measurements are carried out in the present work. Under these conditions we measure the rate constant for electron transfer from **RuP^{+}** to **Ru^{IV}=O** to be k_{ET} = 1.4·10^{7} M^{-1} s^{-1}. This rate constant is obtained based on a simple kinetic model assuming a pseudo-first order regime where [**RuP^{+}**] << [**Ru^{IV}=O**]. This is further corroborated by identical kinetic decay of samples irradiated with lasers of different intensity (See Figure 4). Similar kinetics were also obtained from quasi-steady state irradiation conditions (Figure 2b). Finally an indirect additional support is obtained based on the

unchanged kinetics at pH = 1 with different catalyst concentrations, pH conditions under which the catalyst is trapped in its inactive **Ru^{IV}-tda** state. The value of k_{ET} obtained for our system is one to two orders of magnitude slower than for related systems with polyoxometalate complexes reported in the literature,[3,7a,8]However in these cases there was no proof of oxygen formation during the time scale of the measurements and therefore they may be related to the oxidation of an intermediate at low oxidation states, that are known to be much faster.[16]

Scheme 2 summarizes the main reactions occurring in the present system including the kinetics of each individual step. Once the **RuP*** is generated, all the main productive process involved in the generation of O_2 occur within the time scale of ns to ms, including oxidation of the water oxidation catalyst. This molecular water oxidation catalyst exhibits both exceptional stability and the potential to drive water oxidation with a TOF of up to 8,000 s^{-1}. These very favorable light-driven kinetics and catalyst characteristics are presumably responsible for the record high quantum yields obtained.

The quantum efficiency for oxygen evolution ϕ_{O2} corresponds to the efficiency with which our light-driven systems utilizes absorbed photons to drive water oxidation, and is therefore a key measure of the efficiencies of the molecular processes determining system function. The three main processes involved in this light-driven catalytic function, as depicted in Scheme 2, correspond to: (1) **RuP^{+}** generation with a quantum efficiency of ϕ_{RuP+} (determined per 0.5 absorbed photons, as discussed above), (2) electron transfer between **RuP^{+}** and **Ru^{IV}=O** under constant illumination, with a quantum efficiency of ϕ_{ET} and (3) water oxidation by the oxidized catalyst to yield molecular oxygen generation, with an efficiency of ϕ_{CAT}. The efficiencies ϕ_{RuP+} and ϕ_{ET} , determined from our kinetic analyses above, are plotted in Figure 6 as a function of **Ru^{II}-tda** concentration. For ϕ_{CAT}, we assume a value of 92%, determined from the faradaic efficiency of this catalyst under electrocatalytic system (see further discussion below).[2] This figure also includes a plot of the overall system quantum efficiency calculated from these three separate efficiencies: $\phi_{TOTAL} = \phi_{RuP+} * \phi_{ET} * \phi_{CAT}$ as well as the directly measured quantum efficiency for oxygen evolution ϕ_{O2}. The near unity value of this Faradaic efficiency is further supported by our high chemical efficiency (93%) measured under light-driven catalytic operation. It is apparent from Figure 6 that the quantum yields of oxygen evolution measured directly from oxygen concentration measurements (ϕ_{O2}) show similar behaviour to those calculated from our kinetic analyses (ϕ_{TOTAL}). Our calculated maximal quantum yield is in reasonable agreement with our measured one, differing by 18 % (we discuss the origin of this difference below). As such we can conclude that the kinetic data and analysis we report herein are indeed able to determine the main factors limiting the quantum efficiency of our light-driven system.

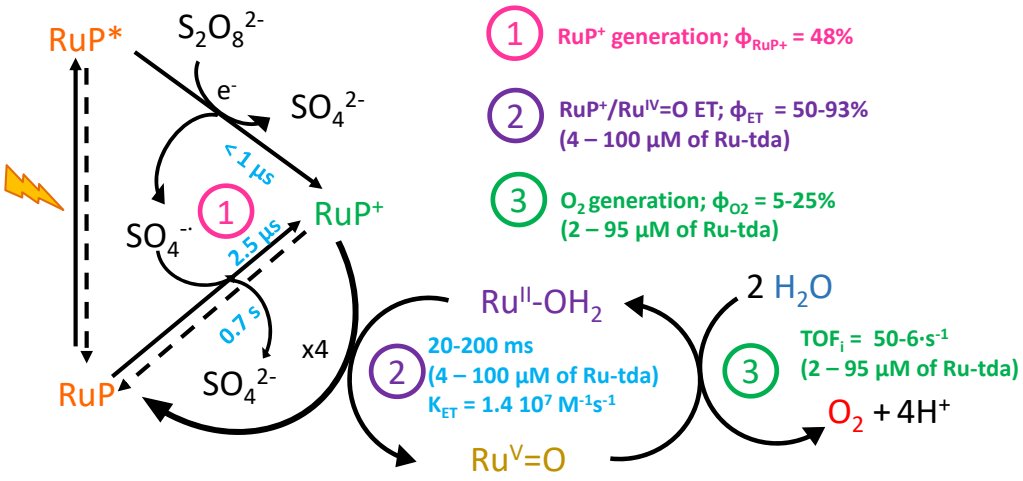

Scheme 2. Main processes and their time scales involved in the oxygen evolution reaction involving the RuP dye, the Ru^{IV}=O water oxidation catalyst and persulfate as sacrificial electron acceptor in a 7-phbf solution. (1) RuP^+ photogeneration. (2) Electron transfer between RuP^+ and the Ru^{IV}=O catalyst. (3) Initial dioxygen generation from water in the photoactivated system.

As has been discussed above, the measured quantum yield of O_2 (ϕ_{O2}) depends on the catalyst concentration (light blue trace Figure 6). We can assign this dependency to the increased efficiency of electron transfer between **RuP⁺** and **Ru^{IV}=O** with increasing catalyst concentration. (Compare violet trace with light and dark blue lines, Figure 6). This is related to the bimolecular nature of the process, with increasing the catalyst concentration enhancing the probability that **RuP⁺** species will oxidize a catalyst molecule rather than alternative oxidation substrates. This phenomena has been previously reported, but, the instability of the catalyst at high concentrations prevented the achievement of high efficiencies.[3,6b,8b,9] In the literature there are other examples showing that enhancement of the interaction between the dye and the catalyst increases the quantum yields by favouring the dye-catalyst electron transfer.[5,6a,8a,10] In our system the stability of the **RuP** sensitizer is also improved by increased catalyst concentration (Figure S11). The susceptibility of **RuP** to irreversible decomposition in its oxidized state has been reported previously, and is most likely associated with secondary oxidations of the bpy ligands.[15] It is striking that for the light-driven system reported herein, the system stability is not limited by catalyst degradation but rather by the degradation of the sensitizer, as well as the increase in ionic strength and proton concentration during operation.

It is also apparent from Figure 6 that the largest quantum efficiency loss (~ 50 %) results from inefficient generation of **RuP⁺** by the sacrificial electron donor $S_2O_8^{2-}$ (ϕ_{RuP+}). Whereas in principle this sensitizer/donor system should yield two **RuP⁺** per photon, in practice inefficiencies in both oxidation reactions result in only 0.98 **RuP⁺** per photon. We expected to enhance this efficiency by increasing the concentration of $S_2O_8^{2-}$, but lower oxygen yields were measured, assigned to the resulting higher

ionic strength and/or lower pH, reducing the efficiency of catalyst oxidation by **RuP^{+}**. Furthermore, at low catalyst concentrations, additional quantum efficiency losses result from the inefficient catalyst oxidation by **RuP^{+}** (ϕ_{ET}). Remarkably, the efficiency of this photoactivated system for oxygen generation is not limited by the activity of the catalyst, whereas by the photon flux and the generation of the **RuP^{+}**. This analysis therefore clearly identifies that further advances in system performance will require focus on the development of the sensitizer and sacrificial electron donor systems, rather than on the improvement of the catalyst turn over frequency.

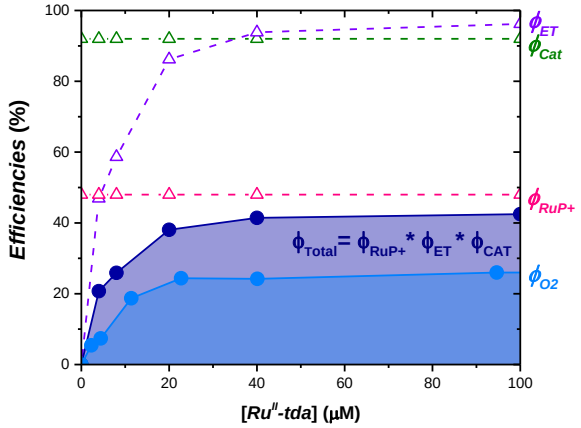

Figure 6. Summary of the efficiencies of the light-driven system as a function of [Ru^{II}-tda]. Dashed lines represent the estimated efficiencies for the individual processes: RuP^{+} generation (ϕ_{RuP+}) (pink); Electron transfer between RuP^{+} and Ru^{IV}=O accumulated in the steady state of the catalytic cycle (ϕ_{ET}) (violet); Faradaic efficiency of Ru^{IV}=O under electrocatalytic conditions (ϕ_{CAT}) (green). Solid lines indicate the quantum yield efficiency estimated from: bulk oxygen generation (ϕ_{O2}) (light blue) and from spectroscopic experiments (Φ_{TOTAL}) (dark blue).

The above discussion has focused on the chemical and quantum efficiencies of our light-driven system. We now turn to consider the rate of oxygen evolution. Whilst the **Ru^{IV}=O** WOC is capable of a TOF of 8,000 s^{-1} when driven electrochemically, in the light-driven system reported herein, the light-driven TOF is in the range of 6 - 50 s^{-1} (determined as moles of oxygen per second / moles of **Ru^{IV}=O**. The light-driven catalytic TOF increases upon lowering the concentration of the catalyst, indicating that it is not limited by the **Ru^{IV}=O** WOC performance. Rather it will be determined by the flux of photons absorbed by the system, and by the quantum yield associated with the use of the absorbed photons to drive water oxidation. Under one sun irradiation, the absorbed photon flux is 0.17 μmoles s^{-1}. Using the value for ϕ_{TOTAL} determined above under conditions of maximal oxygen evolution rate (40 μM of **Ru^{II}-tda** added, corresponding to 1.6 nmoles **Ru^{IV}=O**), this absorbed photon flux should results in a TOF of 22 s^{-1}, compared to a measured TOF under these conditions of 13 s^{-1}. These calculations confirm

that the final performance is mainly determined by the absorbed photon flux, with the difference between our measured and calculated TOF's indicating an additional loss pathway.

There is an additional efficiency loss not accounted for by our kinetic analysis; this most probably results from the different conditions, **RuP^{+}** concentration and **Ru^{IV}=O / RuP^{+}** / $S_2O_8^{2-}$ ratio, employed for our spectroscopic and bulk oxygen measurements. These differences could mainly effect the efficiencies related with the oxidized dye generation (ϕ_{RUP+})and the electron transfer between the **RuP^{+}** and the **Ru^{IV}=O** (ϕ_{ET}). The dependency of light-driven catalytic quantum yield upon **Ru^{II}-tda** concentration estimated from O_2 bulk and from spectroscopic measurements, suggests that the most inefficient process is the oxidized dye generation (ϕ_{RUP+}).

The absorbed photon flux limitation we observe herein reflects the limited light harvesting capability of our light-driven system. We note that increasing the concentration of the sensitizer will not substantially improve this, as over the spectral range of absorption of the sensitizer, almost all photons are absorbed. The ratio of sensitizer per catalyst can be improved by lowering the catalyst concentration, but at the expense of lowering ϕ_{ET}, the efficiency of electron transfer from the oxidized sensitizer to the catalyst. This light harvesting limitation is addressed in photosynthetic organisms by the assembly of large antenna complexes (100's of molecular light absorbers) funneling excitation energy into each catalytic site. Our observation that the effective TOF of our light-driven system is limited primarily by light harvesting efficiency is further evidence of the high performance of the molecular water oxidation catalyst employed herein.

J 4 Conclusions

Herein we have reported a remarkably efficient molecular light-driven system for oxidation of water to oxygen and have undertaken a kinetic analysis of the factors determining the efficiency of this system. At high concentrations of catalyst, the system operates with a quantum yield of 25% and a chemical efficiency of 93 %, the highest reported to date for this type of light-driven system, attributed primarily to favorable electron transfer and oxygen evolution kinetics. A high catalyst concentration is found to be required to optimize the efficiency of electron transfer between the oxidized sensitizer and the catalyst, which also has the effect of improving sensitizer stability. The main limitation to the light-driven system quantum efficiency is found to be the relatively low efficiency of $S_2O_8^{2-}$ as an electron scavenger to oxidize **RuP*** to **RuP^{+}** , mainly due to the competing relaxation back to the **RuP** ground state. The overall rate of light-driven oxygen generation is found to be determined primarily by the incident photon flux. The **Ru^{IV}=O** catalyst is found to be so robust and fast that neither the system efficiency nor lifetime are limited by its performance. As such we conclude that the performance of this remarkably efficient light-driven oxygen production system is limited not by the

properties of the catalyst, but rather by the sensitizer and electron scavenger properties and by the incident photon flux.

J 5 Acknowledgment

We acknowledge financial support from the European Research Council (project Intersolar 291482), L.F. thanks the EU for a Marie Curie fellowship (658270) and Cost Action CM1202. E.P. thanks the EPRSC for a DTP scholarship. A.R. thanks the Royal Society of Chemistry for a Research Fund Grant (RF17-3475). R.M thanks "La Caixa" foundation for a PhD scholarship. Financial support from MINECO and FEDER (CTQ-2016-80058-R, CTQ2015-64261-R, CTQ-2014-52974-REDC, SEV-2013-0319) is also gratefully acknowledged.

J 6 References

1 (a) Tong, L.; Thummel, R. P. *Chem. Sci.* **2016,** *7*, 6591-6603. (b) Yamamoto, M.; Tanaka, K. *ChemPlusChem* **2016,** 81, 1028-1044. (c) Sander, A. C.; Maji, S.; Francàs, L.; Böhnisch, T.; Dechert, S.; Llobet, A.; Meyer, F. *ChemSusChem* **2015,** 8, 1697-1702. (d) Garrido-Barros, P.; Funes-Ardoiz, I.; Drouet, S.; Benet-Buchholz, J.; Maseras, F.; Llobet, A. *J. Am. Chem. Soc.* **2015**, 137, 6758-6761. (e) J. D. Blakemore, R. H. Crabtree and G. W. Brudvig, *Chem. Rev.* **2015**, 115, 12974-13005 (f) Neudeck, S.; Maji, S.; López, I.; Meyer, S.; Meyer, F.; Llobet, A. *J. Am. Chem. Soc.* **2014,** 136, 24-27. (g) Llobet, A. *Molecular Water Oxidation Catalysis: A Key Topic for New Sustainable Energy Conversion Scheme*, 1st Edition, John Wiley & Sons, Chichester, 2014. (h) Kärkäs, M. D.; Verho, O.; Johnston, E. V.; Åkermark, B. *Chem. Rev.* **2014**, 114, 11863-12001.

2 Matheu, R.; Ertem, M. Z.; Benet-Buchholz, J.; Coronado, E.; Batista, V. S.; Sala, X.; Llobet, A., *J. Am. Chem. Soc.* **2015,** 137, 10786-10795.

3 Lewandowska-Andralojc, A.; Polyansky, D. E.; Zong, R.; Thummel, R. P.; Fujita, E. *Phys. Chem. Chem. Phys.* **2013,** 15, 14058-14068.

4 (a) Berardi, S.; Francàs, L.; Neudeck, S.; Maji, S.; Benet-Buchholz, J.; Meyer, F.; Llobet, A. *ChemSusChem* **2015,** 8, 3688-3696. (b) Xu, Y.; Fischer, A.; Duan, L.; Tong, L.; Gabrielsson, E.; Åkermark, B.; Sun, L., *Angew. Chem. Int. Ed.* **2010,** 49, 8934-8937. (c) Roeser, S.; Farràs, P.; Bozoglian, F.; Martínez-Belmonte, M.; Benet-Buchholz, J.; Llobet, A. *ChemSusChem* **2011,** 4, 197-207.(d) Laine, T. M.; Karkas, M. D.; Liao, R.-Z.; Akermark, T.; Lee, B.-L.; Karlsson, E. A.; Siegbahn, P. E. M.; Akermark, B. *Chem. Commun.* **2015,** 51, 1862-1865. (e) Wang, L.; Duan, L.; Tong, L.; Sun, L. *J. Catal.* **2013,** 306, 129-132.(f) Tong, L.; Wang, Y.; Duan, L.; Xu, Y.; Cheng, X.; Fischer, A.; Ahlquist, M. S. G.; Sun, L. *Inorg. Chem.* **2012,** 51, 3388-3398. (g) Kärkäs, M. D.; Åkermark, T.; Johnston, E. V.; Karim, S. R.; Laine, T. M.; Lee, B.-L.; Åkermark, T.; Privalov, T.; Åkermark, B. *Angew. Chem. Int. Ed*. **2012**, 51, 11589-11593.(h) Karlsson, E. A.; Lee, B.-L.; Åkermark, T.; Johnston, E. V.; Kärkäs, M. D.; Sun, J.; Hansson, Ö.; Bäckvall, J.-E.; Åkermark, B. *Angew. Chem. Int. Ed.* **2011,** 50, 11715-11718. (i) Xu, Y.; Fischer, A.; Duan, L.; Tong, L.; Gabrielsson, E.; Åkermark, B.; Sun, L. *Angew. Chem. Int. Ed.* **2010,** 49, 8934-8937. (j) Xu, Y.; Duan, L.; Tong, L.; Akermark, B.; Sun, L., *Chem. Commun.* **2010,** 46, 6506-6508. (k) Duan, L.; Xu, Y.; Gorlov, M.; Tong, L.; Andersson, S.; Sun, L. *Chem. Eur. J.* **2010,** 16, 4659-4668. (l) Besson, C.; Huang, Z.; Geletii, Y. V.; Lense, S.; Hardcastle, K. I.; Musaev, D. G.; Lian, T.; Proust, A.; Hill, C. L. *Chem. Commun.* **2010,** 46, 2784-2786. (m) Duan, L.; Xu, Y.; Zhang, P.; Wang, M.; Sun, L. *Inorg. Chem.* **2010,** 49, 209-215.

5 Li, H.; Li, F.; Zhang, B.; Zhou, X.; Yu, F.; Sun, L. *J. Am. Chem. Soc.* **2015,** 137, 4332-4335.

6 (a) Geletii, Y. V.; Huang, Z.; Hou, Y.; Musaev, D. G.; Lian, T.; Hill, C. L. *J. Am. Chem. Soc.* **2009,** 131, 7522-7523. (b) Huang, Z.; Geletii, Y. V.; Musaev, D. G.; Hill, C. L.; Lian, T. *Ind. Eng. Chem.*

Res. **2012,** 51, 11850-11859. (c) Kaledin, A. L.; Huang, Z.; Geletii, Y. V.; Lian, T.; Hill, C. L.; Musaev, D. G. *J. Phys. Chem. A* **2010,** 114, 73-80.

7 (a) Natali, M.; Orlandi, M.; Berardi, S.; Campagna, S.; Bonchio, M.; Sartorel, A.; Scandola, F. *Inorg. Chem.* **2012,** 51, 7324-7331. (b) La Ganga, G.; Puntoriero, F.; Campagna, S.; Bazzan, I.; Berardi, S.; Bonchio, M.; Sartorel, A.; Natali, M.; Scandola, F. *Farad. Discuss.* **2012,** 155, 177-190.

8 (a) Orlandi, M.; Argazzi, R.; Sartorel, A.; Carraro, M.; Scorrano, G.; Bonchio, M.; Scandola, F. *Chem. Commun.* **2010,** 46, 3152-3154. (b) Pizzolato, E.; Natali, M.; Posocco, B.; Montellano Lopez, A.; Bazzan, I.; Di Valentin, M.; Galloni, P.; Conte, V.; Bonchio, M.; Scandola, F.; Sartorel, A. *Chem. Commun.* **2013,** 49, 9941-9943.

9 (a) Song, F.; Ding, Y.; Ma, B.; Wang, C.; Wang, Q.; Du, X.; Fu, S.; Song, J. *Energy Environ. Sci.* **2013,** 6, 1170-1184. (b) Han, X.-B.; Zhang, Z.-M.; Zhang, T.; Li, Y.-G.; Lin, W.; You, W.; Su, Z.-M.; Wang, E.-B. *J. Am. Chem. Soc.* **2014,** 136, 5359-5366.

10 (a) Car, P.-E.; Guttentag, M.; Baldridge, K. K.; Alberto, R.; Patzke, G. R. *Green Chem.* **2012,** 14, 1680-1688. (b) Kaveevivitchai, N.; Chitta, R.; Zong, R.; El Ojaimi, M.; Thummel, R. P. *J. Am. Chem. Soc.* **2012,** 134, 10721-10724.

11 Lv, H.; Song, J.; Geletii, Y. V.; Vickers, J. W.; Sumliner, J. M.; Musaev, D. G.; Kögerler, P.; Zhuk, P. F.; Bacsa, J.; Zhu, G.; Hill, C. L. *J. Am. Chem. Soc.* **2014,** 136, 9268-9271.

12 Parent, A. R.; Crabtree, R. H.; Brudvig, G. W. *Chem. Soc. Rev.* **2013,** 42, 2247-2252.

13 (a) Henbest, K.; Douglas, P.; Garley, M. S.; Mills, A. *J. Photochem. Photobiol.* **1994,** 80, 299-305. (b) White, H. S.; Becker, W. G.; Bard, A. J. *J. Phys. Chem.* **1984,** 88, 1840-1846.

14 Rybak, W.; Haim, A.; Netzel, T. L.; Sutin, N. *J. Phys. Chem.* **1981,** 85, 2856-2860.

15 (a) Ghosh, P. K.; Brunschwig, B. S.; Chou, M.; Creutz, C.; Sutin, N. . *J. Am. Chem. Soc.* **1984,** *106*, 4772-4783. (b) Limburg, B.; Bouwman, E.; Bonnet, S. *ACS Catal.* **2016,** 6, 5273-5284.

16 (a) Romain, S.; Bozoglian, F.; Sala, X.; Llobet, A. *J. Am. Chem. Soc.* **2009,** 131, 2768-2769. (b) Bozoglian, F.; Romain, S.; Ertem, M. Z.; Todorova, T. K.; Sens, C.; Mola, J.; Rodríguez, M.; Romero, I.; Benet-Buchholz, J.; Fontrodona, X.; Cramer, C. J.; Gagliardi, L.; Llobet, A. *J. Am. Chem. Soc.* **2009,** 131, 15176-15187.

J Supporting Information

Paper J : Kinetic analysis of an efficient, molecular light-driven water oxidation system

Outline

S1. Experimental Section

Transition metal complexes.

The complexes **RuP** ($[Ru^{II}(bpyCO_2Et)_2(bpy)](PF_6)_2$) [S1] and **$Ru^{II}$-tda** ($[Ru(tda)(py)_2]$) [S2] were synthesized as reported in the literature.

Oxygen measurements.

A. For total amount of generated oxygen.

Two mL of a mixture containing $Na_2S_2O_8$ (10 mM), **RuP** (200 μM) and **Ru^{II}-tda** (0-71 μM) in a pH = 7 solution were added in a water-jacketed 4 mL flask. The pH = 7 solution consisted of phosphate buffer solution (25 mM) that Na_2SO_4 was added to have an ionic strength of I = 0.1 M . The flask was sealed with a septum and the mixture degassed for 1 hour by bubbling nitrogen. A Clark oxygen sensor (Unisense OX-NP)was inserted in the cell and the mixture irradiated using a 150 W Xenon Arc Lamp (LS-150, ABET technology) with a cut off filter (λ > 400 nm, 25 mm). The light intensity was calibrated to 1 sun (100 mW cm^{-2}) previous to the experiment and the temperature was maintained constant at 25 ^{o}C. At the end of the experiment, the cell was degassed with nitrogen and calibrated adding known amounts of oxygen.

B. Initial oxygen generation

The photoinduced water oxidation experiments were performed in a specific dark chamber (Hansatech Instruments, Inc) with an integrated Clark-type (Hansatech Instruments, Inc) electrode that could measure the produced oxygen in the liquid phase (no headspace is left in this kind of experiment). Before each experiment, the oxygen sensor was calibrated with the fully air- and nitrogen-saturated solution. In a typical experiment, 2 mL of a mixture containing $Na_2S_2O_8$ (10 mM), **RuP** (200 μM) and **Ru^{II}-tda** (2-95 μM) in pH = 7 solution was introduced into the dark chamber, thermostated at 25.0 ^{0}C. The solution was stirred and degassed during 1 h, and the chamber was finally closed with a screw cap equipped with a septum. After the calibration and baseline collection, the solution was irradiated by opening the windows of the chamber. The illumination was provided by a 150 W Xenon Arc Lamp (LS-150, ABET technology), equipped with a 400 nm cut off filter and calibrated to 1 sun (100 mW cm^{-2}) by using a calibrated silicon photodiode.

Electrochemistry.

Cyclic voltammetry (CV) experiments were performed on an IJ-Cambria CHI-660 potentiostat using a three-electrode cell: a glassy carbon electrode (3 mm diameter) was used as working electrode, a

platinum wire as the auxiliary electrode, and a Hg/Hg_2SO_4 (K_2SO_4 sat.) as reference electrode. Typical CV experiments were carried out at a scan rate of 100 mVs^{-1}. All the potentials are reported *vs* NHE by adding 0.65 V to the measured potential.

UV-Vis Spectroscopy.

A Cary 50 (Varian) or a Lambda 25 (Perkin Elmer) UV/Vis spectrophotometers were used to carry out the steady state UV-Vis spectroscopy.

Transient Absorption Spectroscopy (TAS).

The microsecond-second transient absorption decays were recorded using laser excitation pulses (6 ns) generated from a tunable optical parametric oscillator (Opolette 355, when the excitation λ was 500 nm). A liquid light guide with a diameter of 0.5 cm was used to transmit the laser pulse to the sample.The excitation density was typically adjusted to 170 μJ cm^{-2}, unless otherwise stated. A quartz halogen lamp (100 W, Bentham, IL 1) with a stabilized power supply (Bentham, 605) was used as the probe light source. To reduce stray light, scattered light, and sample emission, two monochromators (OBB-2001, Photon Technology International) and appropriate optical cut-off filters were placed before and after the sample. The probe light passing through the sample was detected using a Si photodiode (Hamamatsu Photonics, S1722-01). The signal was passed through an amplifier (Costronics Electronics) and then measured using a digital oscilloscope (Tektronix 3012).

When the excitation λ was 355 nm, a Nd:YAG laser (Big Sky Laser Technologies Ultra CFR Nd:YAG laser system, 6 ns pulse width, and 0.5 Hz). A liquid light guide with a diameter of 0.5 cm was used to transmit the laser pulse to the sample. The probe light source was a tungsten lamp (Bentham IL1 tungsten lamp), and the probing wavelength was selected by using a monochromator (OBB-2001 dual grating, Photon Technology International) placed prior to the sample. Transient absorption data was collected with a Si photodiode (Hamamatsu S3071). The information was passed through an amplifier box (Costronics) and recorded using a Tektronics TDS 2012c oscilloscope (microsecond to millisecond timescale) and a National Instruments (NI USB-6211) DAQ card (millisecond to second timescale). The data was processed using home-built software based on Labview. The decays observed are the average between 16 and 32 averages laser pulses.

The measurements were carried out in 25 mM phosphate buffer, and the mixtures (specified in each experiment) where stirred and degassed during one hour under dark conditions. Then the sample was equilibrated during 2 min under the set-up conditions.

Photoluminescence (PL).

Steady-state photoluminescence measurements were carried out in air using a Fluorolog FM-32 spectrofluorometer (Horiba Jobin Yvon) with a visible detector.

Photo Induced Absorption (PIA).

Photo-induced absorption (PIA) spectroscopy allows long-lived photogenerated species to be monitored under pseudo steady-state conditions. During these experiments, the sample was illuminated with light pulses (approximately 5 s on/5 s off), provided by a 365 nm LED (pump light). The change in absorbance was recorded using a probe light, which consisted in a tungsten lamp (Bentham IL1 tungsten lamp), and the probe wavelength was selected using a monochromator (OBB-2001, Photon Technology International) placed prior to the sample. Several long pass and band pass filters (Comar Instruments) were used to attenuate the pump light arriving at the detector. Transmitted photons were collected with a Si photodiode (Hamamatsu S3071). The bare detector signal recorded with a National Instruments (NI USB-6211) DAQ card (without amplification).

As for the TAS experiments, the samples were prepared in 25 mM phosphate buffer (the concentration of the different species are indicated in each experiment) and stirred and degassed during one hour under dark conditions prior to the measurement. The sample was then equilibrated during 2 minutes in the experiment set-up. The decays presented herein correspond to the average of 20 to 50 LED pump pulses.

S2. Quantum Yield, Efficiencies and TOF Calculations

A. Quantum yield for oxygen generation, ϕ_{O2}.

The following equation was used to estimate the quantum yield (ϕ_{O2}):

$$\Phi_{O2} = \frac{2 \times (O_2\ molecules)_t}{Absorbed\ photons \times \Delta t \times Area} \times 100$$

Where,

$(O_2\ molecules)_t$ refers to the number of generated oxygen molecules at the selected time.

Absorbed photons: This number was extracted from the normalized solar spectrum for the absorption of a **RuP** solution (200 µM) with the same optical path length and concentration than that of the catalytic experiments. This gives a value of: 5.855 x 10^{20} photons·s^{-1}·m^{-2}.

Δt: time, measured in seconds, at which the maximum amount of oxygen is achieved in the linear part of the kinetic curve (typically between 10-20 s, depending on the concentration of the catalyst used).

Area: Irradiated area of the reaction mixture: 1.77x 10^{-4} m^2.

B. RuP^+ generation efficiency calculation, ϕ_{RuP+}

The RuP^+ generation takes place via two different pathways, one taking place in the dark and the other one in the light. So the final efficiency has to take into account both pathways.

RuP + hν -> RuP*

Light RuP* + $S_2O_8^{2-}$ -> RuP^+ + SO_4^{2-} + $SO_4^{-\cdot}$ (ϕ_q)

Dark RuP + $SO_4^{-\cdot}$ -> RuP^+ + SO_4^{2-} (ϕ_d)

Quenching efficiency (ϕ_q) is 0.6. This value is estimated from lumiscence quenching measurements $\Phi_q = (1 - I/I_0)$ where I is the intensity of the emission spectra containing $Na_2S_2O_8$ and I_0 is the intensity of the emission spectra when $Na_2S_2O_8$ is not present

ϕ_d: can be estimated from TAS experiments of **RuP** in the presence of the sacrificial electron acceptor (Figure S4). The initial signal amplitude ($\Delta O.D._I$) is proportional to the photogeneration of RuP^+, while the second raise in the ΔO.D. ($\Delta O.D._d$) corresponds to the RuP that has reacted during the dark process.

$$\Phi_d = \frac{\Delta O.D._d}{\Delta O.D._l} = 0.6$$

The final efficiency (ϕ_{RuP+}) can be estimated, assuming that 2 photons are needed to generate 4 molecules of RuP^+, as:[S3]

$$\Phi_{RuP+} = \frac{1}{2}\{\Phi_q(1+\Phi_d)\} = 0.48$$

C. Electron transfer (ET) efficiency calculation, ϕ_{ET}

The efficiency of an electron transfer is defined as:

$$\Phi_{ET} = \frac{k_{ET}}{k_0 + k_{ET}}$$

And we know that, $k_{obs} = k_0 + k_{ET}$

Combining the two equations above, we obtain:

$$\Phi_{ET} = 1 - \frac{k_0}{k_{obs}}$$

Where the following values are estimate from from TAS measurements probed at 460 nm (Figure 2a, main section) of a RuP (20 µM) 25 mM phosphate buffer solution catalyst

In the absence of catalytst $k_0 = 1/t_{50\%}$

At different catalyst concentrations $k_{obs} = 1/t_{50\%}$ (at the desired catalyst concentration)

D. TOF calculations

In this work, we have estimate the TOF (s^{-1}) using two different approaches, and their values are shown in Table S2:

1. Initial TOF_i was calculated using the following equation:

$$TOF_i(s^{-1}) = \frac{moles\ of\ O_2}{(moles\ of\ \boldsymbol{Ru^{IV}=O}) \times\ time\ (s)}$$

Moles of O_2 corresponds to the initial O_2 generation slopes shown in Figure S10

Moles of ***Ru^{IV}=O*** were estimated using **Ru-tda/Ru^{IV}=O** ratio of 1/50, and taking into account the total used volume (2 mL).

2. TOF was determined by the photon flux:

$$TOF(s^{-1}) = \frac{\frac{dhv}{dt}(moles\ of\ photon\ per\ s)}{2\ \times\ moles\ of\ \boldsymbol{Ru^{IV}=O}} \times \varphi_{TOTAL}$$

Where,

dhv/dt is the photon flux determined from the photons absorbed by the reaction mixture calculated from the normalized solar spectrum (Figure S11) which turn to be 5.855 x 10^{20} photons·s^{-1}·m^{-2}. Taking into account that the illuminated area is: 1.77x 10^{-4} m^2, the photon flux is 1.7 x 10^{-7} moles hv s^{-1}.

Moles of ***Ru^{IV}=O*** were estimated using **Ru-tda/Ru^{IV}=O** ratio of 1/50, and taking into account the total used volume (2 mL).

The factor of ½ is added to take into account that we need 2 photons to generate one molecule of O_2.

φ_{TOTAL} is the calculated efficiency from our optical experiments as: $\phi_{Total} = \phi_{RuP+} \cdot \phi_{ET} \cdot \phi_{Cat}$

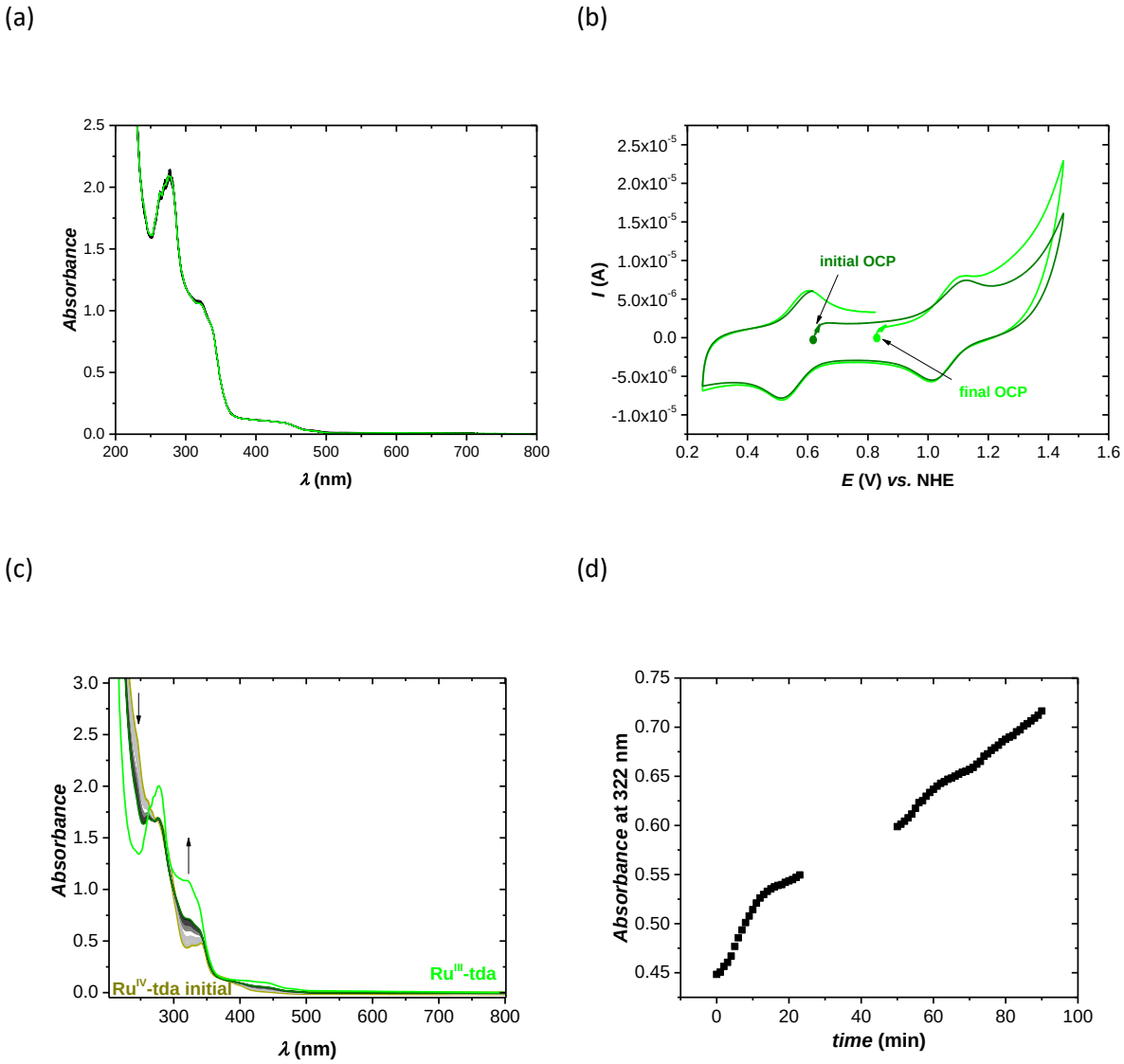

Figure S1A. (a) UV-Vis spectra recorded during 1 h of the evolution of a 4 μM **Ru^{III}-tda** in a 10 mM $Na_2S_2O_8$ solution adjusted at pH 7. (b) Cyclic voltammetry of a solution containing 0.1 mM **Ru^{III}-tda** and 10 mM $Na_2S_2O_8$, adjusted at pH 7. OCP = open circuit potential. (c) UV-Vis spectra recorded during 90 min of the evolution of a 4 μM **Ru^{IV}-tda** in a 10 mM $Na_2S_2O_8$ solution adjusted at pH 7. (d) Kinetic profile of the convertion of **Ru^{IV}-tda** to **Ru^{III}-tda** monitored at 322 nm in a 10 mM $Na_2S_2O_8$ solution adjusted at pH = 7.

(a)

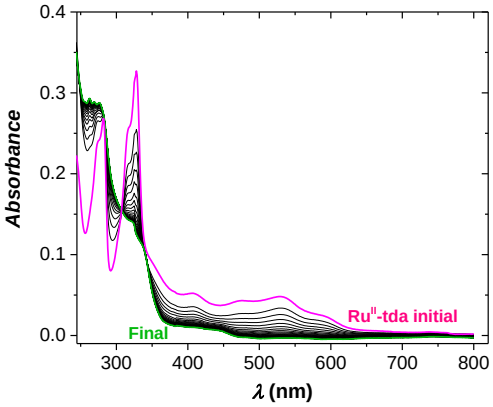

(b)

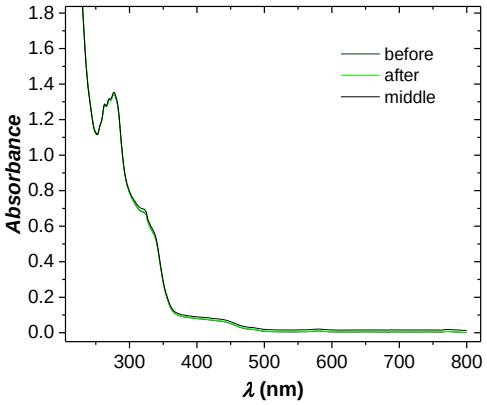

(c)

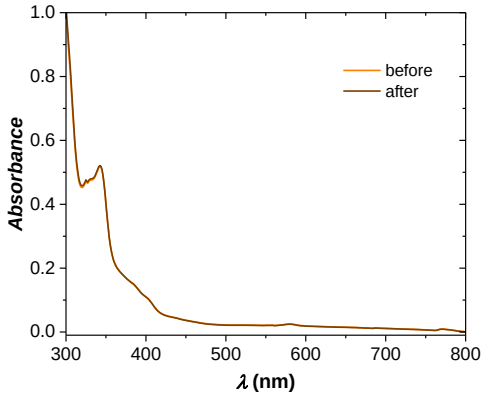

Figure S1B. UV-Vis spectra recorded during 1 h of the evolution at pH = 0.9 (0.1 M H_2SO_4 aqueous solution) under dark conditions of a: (a) 0.7 µM **Ru^{II}-tda** in a 10 mM $Na_2S_2O_8$; (b) 4 µM **Ru^{III}-tda** in a 10 mM $Na_2S_2O_8$ solution; (c) 4 µM **Ru^{IV}-tda** in a 10 mM $Na_2S_2O_8$ solution.

(a)

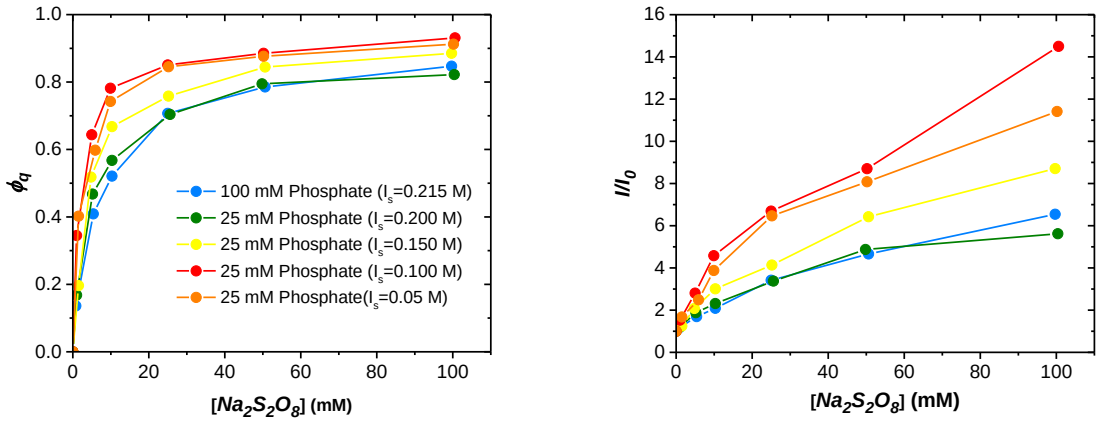

Figure S2. (a) Luminescence quenching efficiency of the photoreaction of **RuP** with $Na_2S_2O_8$ calculated as: $\Phi_q = (1 - I/I_0)$ where I is the intensity of the emission spectra containing $Na_2S_2O_8$ and I_0 is the intensity of the emission spectra when $Na_2S_2O_8$ is not present. (b) Stern-Volmer plots for the same measurements. Experimental conditions: 4 µM **RuP** in a pH = 7 phosphate buffer solution with different ionic strength (I_s) adjusted with Na_2SO_4: (red) 25 mM phosphate, I_s = 0.05; (orange) 25 mM phosphate, I_s = 0.1 M; (yellow) 25 mM phosphate, I_s = 0.15 M; (green) 25 mM phosphate buffer, I_s = 0.2 M; (light blue) 100 mM phosphate, I_s = 0.25 M.

(a) (b)

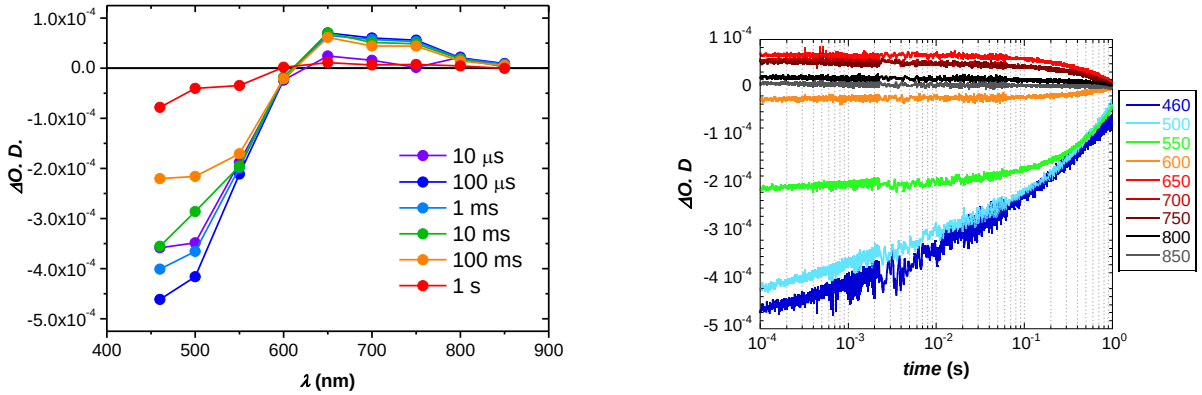

Figure S3. Transient absorption spectra (a) and Transient absorption decays (b) of a **RuP** (40 µM) and $Na_2S_2O_8$ (10 mM) solution in water, containing a phosphate buffer (25 mM). The measurements were perfomed under N_2, collected at a timescale between 10 µs and 1 s after dye excitation at λ_{ex} = 355 nm (laser intensity 350 µJ cm^{-2}).

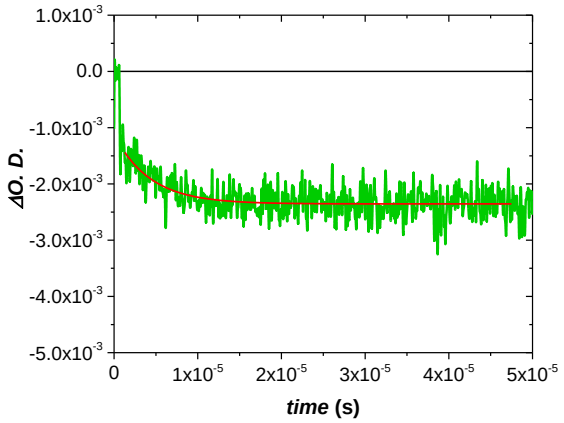

Figure S4. Transient absorption decays probed at λ = 460 nm of **RuP (**40 µM) and $Na_2S_2O_8$ (10 mM) an aqueous solution containing a phosphate buffer (25 mM). The measurements were done under N_2 and collected at a timescale between 1 µs and 5 µs after dye excitation at λ_{ex} = 500 nm (laser intensity 173 µJ cm^{-2}).

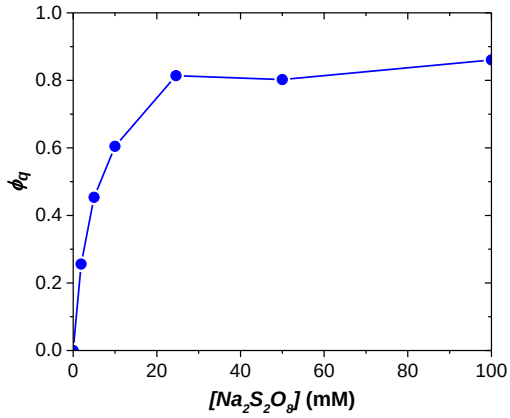

Figure S5. Luminescence quenching efficiency of **RuP** (4 µM) in the presence of **Ru^{II}-tda** (4 µM) in a 25 mM (I = 0.05 M) phosphate buffer aqueous solution containing different amounts of $Na_2S_2O_8$ (0-1-5-10-25-50-100 mM). The luminescence quenching efficiency was calculated as $\Phi_q = (1–I/I_0)$.

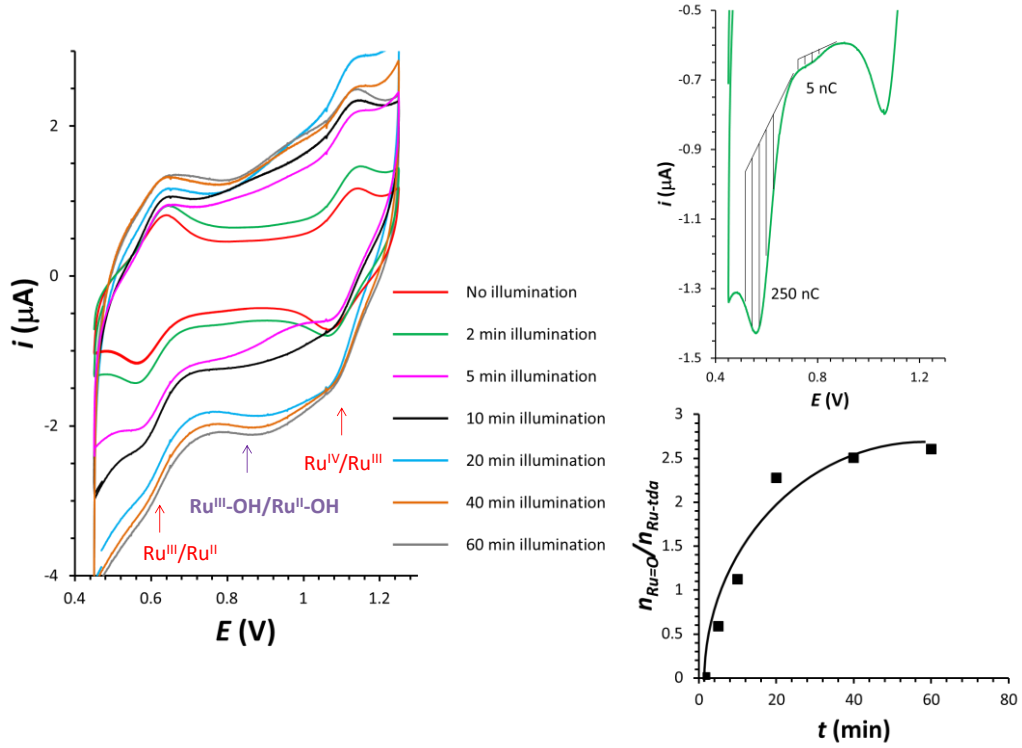

Figure S6. Estimation of the ratio of **Ru^{IV}=O/Ru-tda** under illumination by cyclic voltammetry (CV)**.** Left, CVs for a 7-phbf solution containing 0.2 mM **RuP**, 10 mM $Na_2S_2O_8$ and 43 µM **Ru^{II}-tda** in the absence of light (red line) and under illumination at different times: 2 minutes (green line); 5 minute (pink line); 10 minutes (black line); 20 minutes (cyan line); 40 minutes (orange line); and 60 minutes (grey line). The redox processes of complexes **Ru^{IV}=O** and **Ru^{IV}-tda** are indicated in the CV by purple and red arrows, respectively. The wave of the III/II process of **Ru^{IV}=O** shifts towards anodic potentials at longer times due to the pH increase as measured in the main section. Top Right, CV of

IX

the solution containing 0.2 mM **RuP**, 10 mM $Na_2S_2O_8$ and 43 µM **Ru^{II}-tda** illuminated 2 minutes and representative estimation of the $\mathbf{n_{Ru=O}/n_{Ru\text{-}tda}}$ ratio. The ratio was estimated by integrating the charge of the cathodic wave of the III/II process of the **Ru^{IV}=O** and **Ru-tda** at 0.76 V and 0.55 V respectively**.** The integration was performed using the CHI software. Bottom Right, Plot showing the evolution of the $\mathbf{n_{Ru=O}/n_{Ru\text{-}tda}}$ ratio against time. $\mathbf{n_{Ru=O}/n_{Ru\text{-}tda}}$**:** 2 minutes, 0.02; 5 minute, 0.6; 10 minutes, 1.1; 20 minutes, 2.3 ; 40 minutes, 2.5; and 40 minutes, 2.6

Table S1. Calculated k_{obs} of the electron transfer between the dye **RuP^{+}** and the catalyst at pH = 7 (Figure 2a, main section) and pH = 1 (Figure S8). See main text for details.

[**Ru^{II}-tda**] (µM)	$t_{50\%}$, pH = 7 (s^{-1})	k_{obs}, pH = 7 (s^{-1})	$t_{50\%}$, pH = 1 (s^{-1})	k_{obs}, pH = 1 (s^{-1})
0	0.665	1.5	0.5	1.3
4	0.353	1.96	0.75	0.9
8	0.275	2.52	0.43	1.6
20	0.0918	7.55	0.65	1.0
40	--	--	0.48	1.4
50	0.041	16.9	--	--
100	0.0252	27.5	0.53	1.3

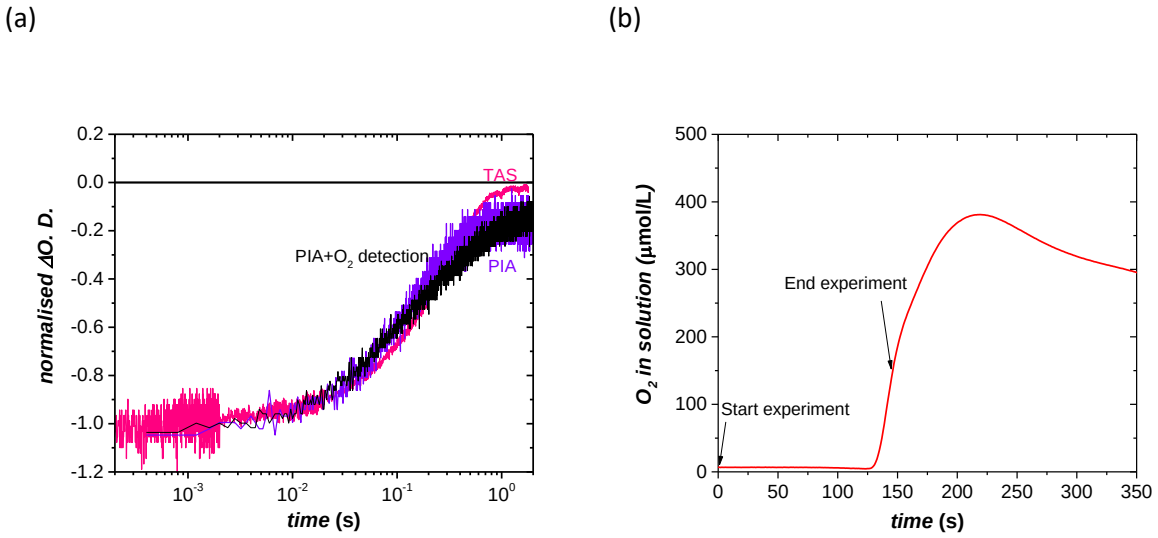

Figure S7. (a) Comparison between the TAS decays probed at 460 nm under pulsed 500 nm laser (pink) and 5 s (15.4 mW cm^{-2} at 365 nm) LED irradiation without in-situ O_2 measurement (violet) and with O_2 measurement (black). Data shown for a 20 μM **RuP**, 10 mM $Na_2S_2O_8$ and 40 μM **Ru^{II}-tda** solution. (b) In-situ O_2 measurement using a clark electrode in liquid phase without stirring, when recording the black trace of Figure S7a,for 15 averages (150 s). The time delay between the O_2 evolution and caesura and the time of the experiment is due to the diffusion of the O_2 to the tip of the clark electrode during the experiment.

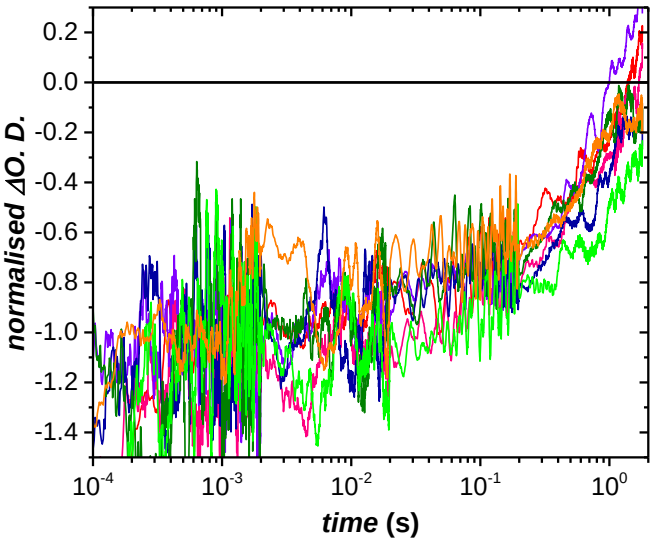

Figure S8. Transient absorption decays probed at 460 nm of a solution, containing 20 μM **RuP**, 10 mM $Na_2S_2O_8$ and 0-4-8-20-50-100 μM (orange, pink, violet, light blue, dark blue and green, respectively) of **Ru^{II}-tda** in water pH = 1 ([H_2SO_4] = 0.1 M); under N_2, collected at a timescale between

IX

10 µs and 2 s after dye excitation at λ_{ex} = 500 nm (laser intensity 183.2 µJ cm^{-2})). All the samples were freshly prepared and measured after 1 h of preparation, underN_2.

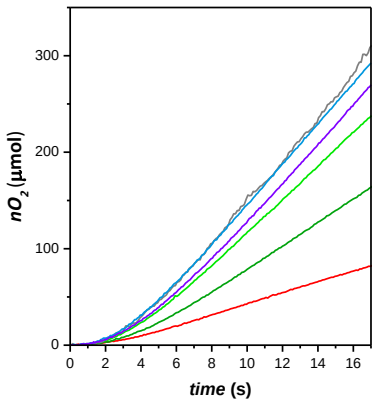

Figure S9. Initial oxygen evolution against time at different **Ru^{II}-tda** concentrations: 2 (red), 4 (dark green), 11 (light green), 22 (blue), 40 (violet) and 95 (grey) µM). Measurement carried out by a liquid phase clark electrode (Hansatech).

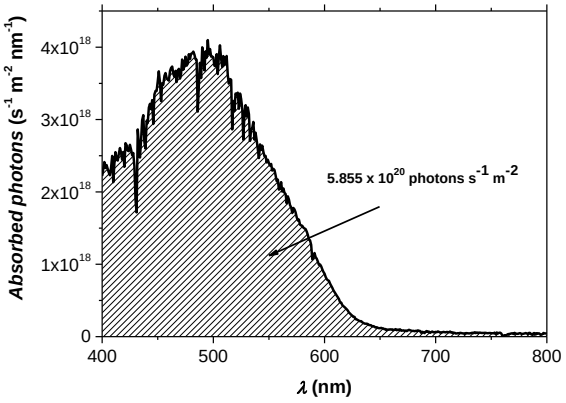

Figure S10. Photons absorbed by the reaction mixture calculated from the normalized solar spectrum. The integration of the resulting normalized spectrum gives 5.855 x 10^{20} photons·s^{-1}·m^{-2}.

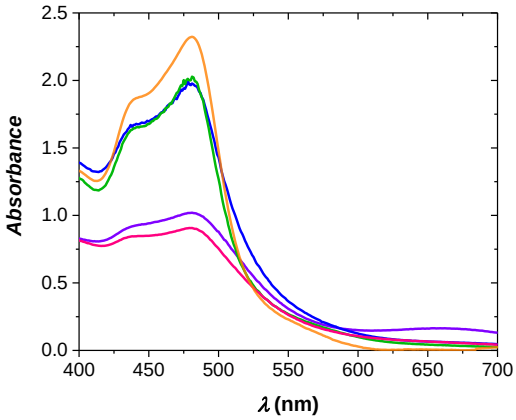

Figure S11. UV-Vis spectra of **RuP**.(0.2 mM), $Na_2S_2O_8$ (10 mM) in 25 mM phosphate buffer (pH = 7, phbf-7): Orange, before illumination and in the absence of catalyst. And after 10 min of 1 sun Xe- lamp irradiation (150 W Xe Arc Lamp with a cut off filter (λ > 400 nm, 25 mm)) containing different amounts of catalyst: dark blue, 23 µM [**Ru^{II}-tda**]; Green, 11 µM [**Ru^{II}-tda**]; Violet, 4 µM [**Ru^{II}-tda**]; Pink, 2 µM [**Ru^{II}-tda**].

Table S2. Estimated TOFs from the experimental initial O_2 slopes (TOF_i) and from the photon flux (TOF). See experimental section for further details.

[**Ru^{II}-tda**] (µM)	TOF_i (s^{-1})	TOF (s^{-1})
2.2	51.3	94
4.4	35.8	94
11.4	35.3	53.6
22.7	23	37
40.1	12.9	22
94.6	5.9	9.4

References

S1 Farnum, B. H.; Jou, J. J.; Meyer, G. J. *Proc. Natl. Acad. Sci.* **2012,** 109, 15628-15633.

S2 Matheu, R.; Ertem, M. Z.; Benet-Buchholz, J.; Coronado, E.; Batista, V. S.; Sala, X.; Llobet, A. *J. Am. Chem. Soc.* **2015,** 137, 10786-10795.

S3 Lewandowska-Andralojc, A.; Polyansky, D. E.; Zong, R.; Thummel, R. P.; Fujita, E. *Phys. Chem. Chem. Phys.* **2013,** 15, 14058-14068.

PAPER K Neutral water splitting catalysis with a high FF triple junction polymer cell

Elias, X.; Liu, Q.; Gimbert-Suriñach, C.; Matheu, R.; Mantilla-Perez, P.; Martinez-Otero, A.; Sala, X.; Martorell, J.; Llobet, A. *ACS Catal.* **2016**, 5, 3310-3316.

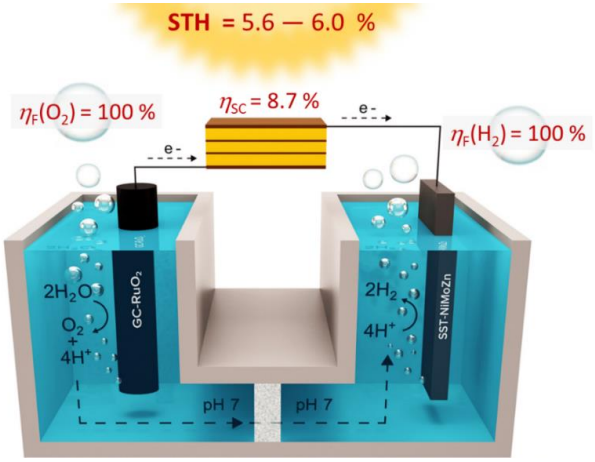

Abstract

We report a photovoltaics-electrochemical (PV-EC) assembly based on a compact and easily processable triple homo-junction polymer cell with high fill factor (76%), optimized conversion efficiencies up to 8.7 % and enough potential for the energetically demanding water splitting reaction (Voc = 2.1 V). A platinum-free cathode made of abundant materials is coupled to a ruthenium oxide on glassy carbon anode (GC-RuO_2) to perform the reaction at optimum potential (ΔE = 1.70-1.78 V, overpotential = 470-550 mV). The GC-RuO_2 anode contains a single monolayer of catalyst corresponding to a superficial concentration (Γ) of 0.15 nmol cm^{-2} and is highly active at pH 7. The PV-EC cell achieves solar to hydrogen conversion efficiencies (STH) ranging from 5.6 to 6.0 %. As a result of the solar cell's high fill factor, the optimal photovoltaic response is found at 1.70 V, the minimum potential at which the electrodes used perform the water splitting reaction. This allows generating hydrogen at efficiencies that would be very similar (96%) to those obtained as if the system were to be operating at 1.23 V, the thermodynamic potential threshold for the water splitting reaction.

Contributions

Roc Matheu synthetized the RuO_2 anode and performed the electrochemical experiments regarding total water splitting and water oxidation.

K 1 Introduction

Among all renewable energies, photovoltaics (PVs) is the most easily integrable[1-3] in an urban environment where most of the electricity consumption occurs and where the energy distribution system is the largest. However, electricity production from sunlight is intermittent and does not always match the consumption pattern. It has been proposed that an optimal solution to perfectly combine photovoltaic integrability with a variable energy demand is to use the excess electricity produced during peak irradiation to drive the water splitting reaction to generate hydrogen fuel, so that the energy is stored in the form of chemical bonds.[4] Such energy production would have a close to negligible environmental impact while its distribution could be carried out effectively with the already existing natural gas pipelines. Unfortunately, at present there are no PV hydrogen production systems that may offer integrability, low cost, durability and a high efficiency in one.

Different PV approaches using either multi-junction or series connected cells have been proposed to overcome the high thermodynamic potential of ΔE^o = 1.23 V of the water oxidation reaction.[5-19] Over-potentials associated with the reaction kinetics raise the required voltage by several hundreds of mV to 1.5 V or higher. Early examples used multiple junction silicon solar cells coupled to noble metal electrodes like platinum.[5-7] Although high solar to hydrogen (STH) conversion efficiencies were achieved, the prohibitive costs of both the solar cells and the metal catalysts hampered the implementation of a large scale hydrogen generation. Recent approaches have replaced the expensive silicon triple junctions by metallic chalcogenide materials,[10] perovskites,[14-16] dye-sensitized,[17,18] or polymer[18] solar cells. However, either harsh alkaline, pH=14 in the majority of them, or acidic conditions were used to minimize the overpotentials and increase the STH efficiency of the system. The corrosion associated to such harsh conditions prevents a practical large scale hydrogen production using ocean or river water which is found close to a neutral pH.

In here, for an optimal water splitting reaction minimizing the overpotential limitation, we implemented a photovoltaic-electrochemical (PV-EC) system using a one-blend polymer triple junction cell which exhibits a high fill factor (FF) overcoming the FF of the single junction counter parts. This implies that at the lowest measured water splitting voltage of 1.70 V, the STH conversion efficiency under 1 sun AM1.5G illumination is as high as 96 % of the maximum efficiency possible corresponding to an ideal operation at the thermodynamic potential threshold. This is combined with the use of platinum free anode and cathode electrodes immersed in a water solution buffered at pH 7. A glassy carbon rod with an extremely small amount of RuO_2 catalyst anchored on the graphite surface was used as anode (GC-RuO_2). In such GC-RuO_2 electrode configuration a strong catalytic activity for water oxidation is achieved at pH 7 with an amount of Ru that is at least 100 times smaller than the Ru found

in commonly used RuO_x electrodes.[8,18b,20-23]Such a strong catalytic activity results from an optimum electrode surface morphology that consists of a monolayer of fully active material where all the available catalytic sites are accessible for the water oxidation reaction. The preparation of the electrode is based on using a ruthenium molecular precursor [24,25]that interconverts into the final RuO_2 active species upon electrochemical treatment, details on the synthesis and characterization of this anode can be found in Ref. [25]. We demonstrate that a high STH conversion efficiency at pH 7 is possible when the triple junction cell and GC-RuO_2 anode are combined with a cathode made of earth abundant materials deposited on a stainless steel plate (SST-NiMoZn).[11,26,27]When the described system is compared to a Pt-anode and Pt-cathode electrode configuration, we obtain a 250 mV reduction in the overpotentials for operation at pH 7. The overall PV-EC system we implement uses compact devices, earth abundant materials or very small amounts of rare metals, operates at the pH water is found in nature and the stability of the PV device under 1 sun illumination is ensured when a proper encapsulation is applied.[28]

K 2 Results and Discussion

K 2.1 Optimal triple junction polymer solar cell

The open circuit voltage of a single junction polymer cell is not sufficient to overcome the potential barrier for the water splitting chemical reaction. To achieve a V_{oc} of 2.1 V we piled up three single junction cells of the same PTB7:PC_{71}BM blend (Fig. 1a). This blend has been shown to exhibit one of the top single junctio[29]or homo-tandem[30,31] polymer cell performances. By using the same blend in the three sub-cells we simplify the fabrication procedure while at the same time we ensure a homogenous electrical performance throughout the device. This resulted in FFs as high as 76%, significantly higher than the 71% averaged by the single junction counterparts. Such high FFs, essential to minimize the impact of the overpotentials in the water splitting reaction, are in correspondence to the use of very thin active blend layers combined with a light absorption shared by the three sub-cells. In the single junction counterpart recombination is larger given that full light absorption is carried out by just one single junction.

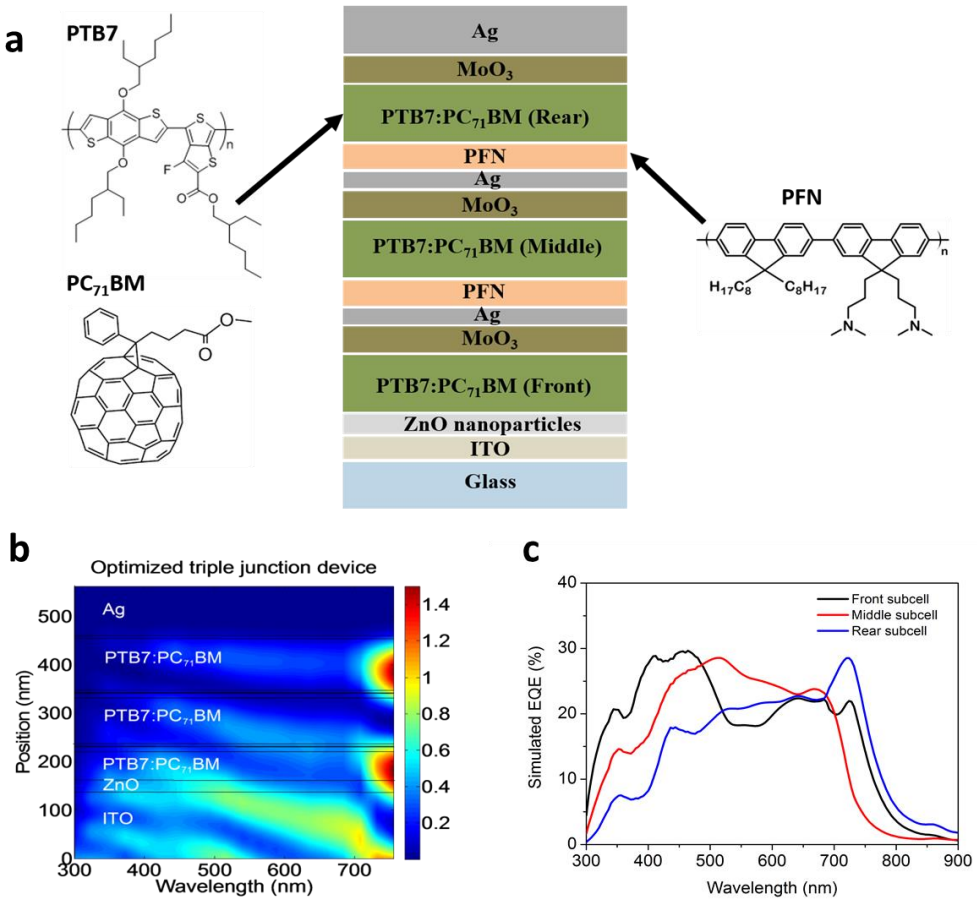

Figure 1 Optically optimal triple junction cell **a)** Schematic representation of the triple junction solar cells and molecular structure of its organic polymers. PTB7, Poly({4,8-bis[(2-ethylhexyl)oxy]benzo[1,2-b:4,5-b']dithiophene-2,6-diyl}{3-fluoro-2-[(2-ethylhexyl)carbonyl]thieno[3,4-b]thiophenediyl}. $PC_{71}BM$, [6, 6]-phenyl-C_{71} butyric acid methyl ester. PFN, poly [(9,9-bis(3'-(N,N-dimethylamino)propyl)-2,7-fluorene)-alt-2,7-(9,9–dioctylfluorene. **b)** Calculated electrical field intensity normalized with respect to the incident field intensity as a function of wavelength for an optimized triple junction organic solar cell architecture. **c)** Calculated EQE for each one of the three sub-cells in an optimized architecture.

Reaching the optimal light harvesting in triple junction PV architectures with high number of layers can only be achieved by setting a target solution and implementing an inverse solving problem approach to reach that solution.[1] In particular, the cell fabricated in this work has a total of thirteen layers with the configuration indicated in Fig. 1a. In addition, a series connected triple junction device requires matching of the short-circuit currents of the three sub-cells. This current matching combined with the largest possible short circuit current is the solution targeted by our numerical approach based on the transfer matrix[32,33] to numerically compute the electrical field distribution and light absorption within each one of the cell layers. The optimal electrical field intensity profile and simulated EQEs for each one of the sub-cells in the triple junction device is shown in Fig. 1b and 1c, respectively. The electric field intensity shows maxima in the rear sub-cell for the near infrared wavelengths, in the

middle sub-cell for the wavelength range between 500 and 600 nm, and in the front sub-cell for the near UV range (Fig. 1b). Such field distribution implies that absorption at shorter wavelengths is dominated by the front sub-cell, in the middle range of the visible spectrum is dominated by the middle sub-cell, and at the near infrared by the rear sub-cell. Such perfectly balanced light absorption distribution among the three cells is clearly seen in the simulated EQEs shown in Fig. 1c. Such large differences in the EQE can be explained in part by the different thicknesses of the layers, but also because of the interference. As can be seen in Fig. 1b constructive interference of the incident and reflected waves tends to favor IR shifted absorption for the rear cell and UV shifted absorption for the front cell. In one of the architectures leading to such optimal light absorption, the PTB7:PC71BM layer thicknesses were determined to be 60 nm, 105 nm, and 110 nm for the front, middle, and rear sub-cells, respectively. These values were used to fabricate triple-junction devices with measured conversion efficiencies up to 8.7% under AM 1.5G illumination at 100 mW/cm^2 and V_{oc} equivalent to 2.1 V. A typical current density−voltage (J−V) curve of the triple junction cell is shown in Fig. 2, with its relevant parameters marked in red. The potential extracted at the maximum power point of the cell was close to 1.76 V, 530 mV higher than the thermodynamic potential for the water splitting reaction. The high fill factor of the solar cell used (76%) ensures that the water splitting efficiency loss due to the catalyst overpotential will be minimum as opposed to a single junction series connection of three cells of the same polymer type that would exhibit a smaller FF around 71% (Fig. S2), or alternative options where the V_{oc} of the configuration would be too large.[34]

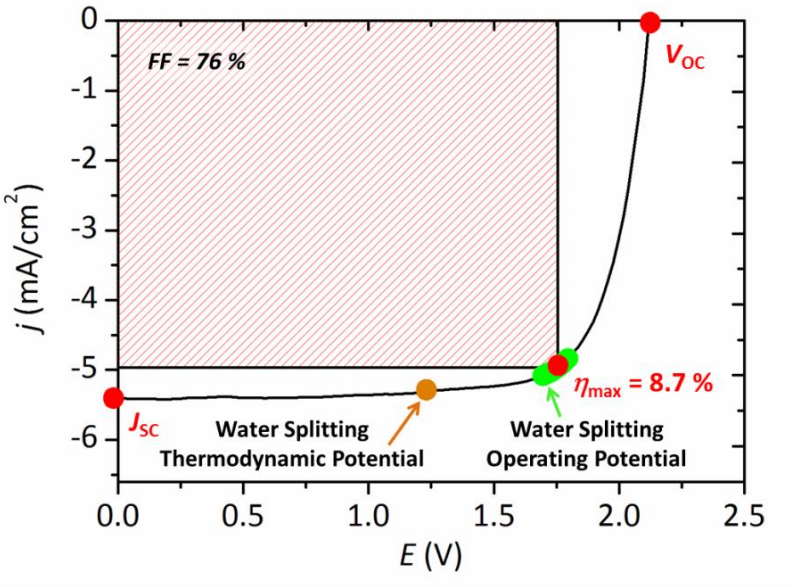

Figure 2. *j*/*E* curve of triple junction cell. V_{OC} = 2.13 V, J_{SC} = 5.4 mA/cm^2, FF = 76% and η_{max} = 8.7% where the water splitting thermodynamic potential (orange) and water splitting operating potential range (green) are indicated. V_{OC}: open circuit potential, J_{SC}: short circuit current density, FF: fill factor and η_{max} = cell efficiency at maximum power point.

K 2.2 Coupled GC-RuO_2 anode and SST-NiMoZn cathode for water splitting catalysis

With the aim of minimizing the cost of the final PV-EC device for ultimate applications, we used a cathode of NiMoZn[26,27]on stainless steel electrode (SST-NiMoZn) made of earth abundant materials and an anode made of RuO_2 on glassy carbon electrode (GC-RuO_2).[25] The selected GC-RuO_2 anode is particularly interesting because it has an extremely low catalyst loading with a superficial concentration (Γ) of 0.15 nmol cm^{-2} and a roughness factor (RF) of 1-2, consistent with one monolayer of active material (see supporting information). These values are much lower than those of commonly used RuO_x or IrO_x based electrodes, that are usually prepared using electrochemical deposition from $RuCl_3$,[20,21] dropcasting of suspensions with post-annealing processes[23] or sputtering techniques.[21,23]These deposition methods give layers of RuO_2 with thickness from tens of nanometers (*e.g.* 70 nm in ref 21) up to a few micrometers (*e.g.* 2.3 µm in ref 22). By using the molecular catalyst precursor methodology[25] we have a full control of the starting monolayer of ruthenium deposited on the electrode, that upon oxidative scans, converts into small RuO_2 particles with a very high surface area available for the water oxidation reaction. Environmental scanning electron microscopy analysis did not show the RuO_2 nanoparticles due to their small size, below the detection limit of the instrument. However, the nature of the catalyst have been thoroughly investigated using electrochemical and XAS techniques.[25] Despite the low catalyst loading, the activity of this GC-RuO_2

anode is very high at pH 7 as demonstrated by cyclic voltammetry experiments. The catalytic wave due to water oxidation shows a significant negative shift of the onset of the catalysis of *ca.* 250 mV compared to a platinum mesh electrode (Fig. 3a).

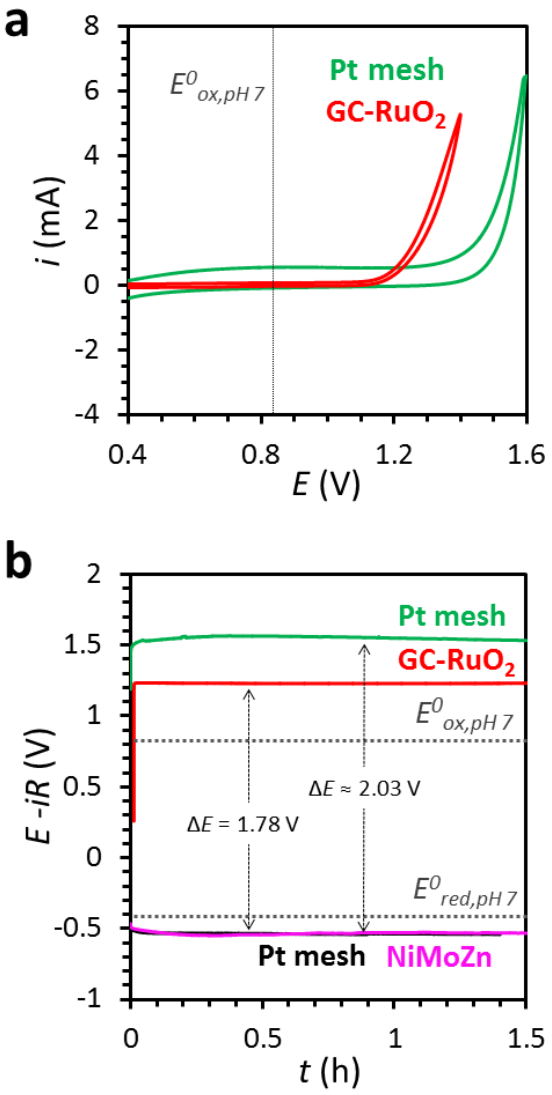

Figure 3. a) Cyclic voltammetry experiments of a GC-RuO_2 (red) and platinum mesh (green) working electrodes. **b)** Chronopotentiometry experiments at a fixed current of +405 µA for GC-RuO_2 (red) and Pt mesh (green) or –405 µA for NiMoZn (pink) and Pt mesh (black). All experiments in a) and b) were done in a two compartment cell, in degased 0.1 M phosphate buffer, at pH 7.0, using a platinum mesh as counter electrode and Ag/AgCl as reference electrode. The potentials are given against the NHE reference electrode using the conversion $E_{NHE} = E_{Ag/AgCl} + 0.2$. The thermodynamic potentials for the water oxidation (E^0_{ox}, pH 7 = 0.817 V) and water reduction (E^0_{red}, pH 7 = –0.413 V) reactions at pH 7 are indicated in grey dotted lines.

The performance of the GC-RuO_2 and SST-NiMoZn electrodes was tested independently by means of chronopotentiometry experiments in a three electrode configuration cell at pH 7. These experiments

allowed us to simulate a real water splitting reaction that we would later do using the triple junction organic photovoltaic cell. We fixed the current at +405 μA and –405 μA for the GC-RuO_2 anode and SST-NiMoZn cathode respectively (red and pink traces, Fig. 3b). Analogous experiments were done for a platinum mesh anode and a platinum mesh cathode for comparison (green and black traces, Fig. 3b). All electrodes are stable under operating conditions, showing no loss of activity over the course of the experiment. It is interesting to see that the potential required for the water reduction reaction is exactly the same for both cathodes, the NiMoZn and Pt, accounting for less than 100 mV of overpotential, as had been previously reported in the literature.[26,27] On the other hand and consistent with the cyclic voltammetry experiments in Fig. 3a, the performance of the GC-RuO_2 is considerably superior to that of platinum, which requires 250 mV more of potential than the former. Chronopotentiometry analysis of an ITO-CoPi[35-38] type electrode shows that our PV-EC system can also operate with such cobalt based anode, but with a Δ*E ca.* 100 mV higher than that of GC-RuO_2 and *ca.* 2000 times higher catalyst loading ($\Gamma \approx$ 0.30 μmol cm^{-2}, Fig. S1). Thus, according to the chronopotentiometry experiments the voltage required to perform the water splitting reaction for the GC-RuO_2/SST-NiMoZn couple is Δ*E* = 1.78 V, which accounts for an overpotential of 550 mV. This value is *ca.* 250 mV lower than that observed for the Pt/Pt or Pt/SST-NiMoZn couples with Δ*E* = 2.03 (790 mV overpotential). The GC-RuO_2 anode not only minimizes the voltage at which the PV-EC device will operate, but also performs 9000 turnovers for a typical 1.5h experiment, accounting for an impressive TOF of 1.7 s^{-1}.

K 2.3 Bias-free water splitting catalysis with PV-EC cell at pH = 7

Water splitting experiments were performed illuminating a triple junction solar cell (η_{TJSC} = 8.2-8.7%) connected to a GC-RuO_2 anode and SST-NiMoZn cathode in a two electrode configuration setup in a pH 7 phosphate buffer solution (Fig. 4a). One of the advantages of this electrode combination is that both are highly selective, and back reactions are almost non-existent. However, a setup configuration in a two-compartment electrochemical cell separated by a glass frit was preferred, allowing for independent gas collection and avoiding potentially explosive gas mixtures. The current density versus time profile of a typical reaction is given in Fig. 4b. After an approximate 10 minutes stabilization time the current reaches a steady state at 4.5 mA/cm^2, and the operating potential remains at Δ*E* = 1.70-1.75 V for the whole duration of the experiment. This operating current density (J_{OP}) in mA/cm^2 can be used in

$$STH = \frac{J_{OP} \cdot 1.23 \cdot \eta_F}{P_{Solar}} \qquad (1)$$

where η_F is the Faradaic efficiency and P_{Solar} the power density, to determine the STH to be 5.6% under 1 sun AM 1.5G illumination. As shown in Fig 5 and using the full PV-EC system, continuous gas production was detected over a period of five hours with faradaic efficiencies close to 100% for both gases and no apparent loss of activity.

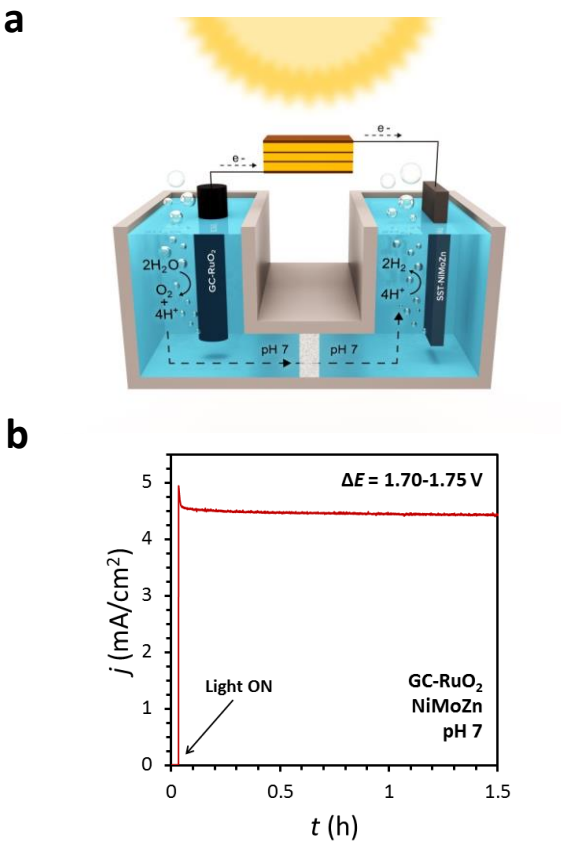

Figure 4. Water splitting EC-PV system **a)** Schematic representation of the setup for the water splitting experiments using a triple junction organic solar cell, GC-RuO_2 anode and SST-NiMoZn cathode. **b)** Current *vs* time profile of a water splitting experiment using a triple junction solar cell (η_{TJSC} = 8.5 %), GC-RuO_2 anode and SST-NiMoZn cathode in a two electrode configuration and a two compartment cell containing 0.1 M phosphate buffer, pH = 7.0, under AM 1.5 G illumination with a GG400 filter. The operating potential of the reaction was measured manually and is also indicated. After 1.5 h, the amount of evolved gas accounted for TON_{Ru} = 9 000 and TOF = 1.7 s^{-1}, where TON_{Ru} = mols O_2/mols of Ru and TOF = mols O_2/(mols of Ru×second).

When performing the water splitting reactions we measured working voltages in the range of Δ*E* = 1.70-1.80 V, which closely matched the Δ*E* = 1.78 V and 1.76 V calculated from the chronopotentiometry experiments and the maximum power point of our triple junction solar cell, respectively (Fig. 2 and Fig. 3b). The minimum potential of 1.7 V measured at some instances with the triple junction cell relative to the chronopotentiometry measurement shown in Fig. 3b may

correspond to slight differences in the RuO_2 layer coating the GC rod. The system is sensitive to high energy light as illustrated in Fig. S3. While an initial value of STH = 6.0% is obtained under full spectrum illumination, it decreases down to STH = 4.1% after 1.5 h. The cell degradation induced by the UV radiation can be eliminated by placing in front of the solar cell a 400 nm cut-off wavelength low band pass light filter. In that case we obtained stable profiles as can be seen in Fig. 4b and Supplementary Fig. S3. These STH values are amongst the highest reported in the literature for PV-EC hybrid devices that do not use silicon or group III-V semiconductors as light absorber, including two recently reported perovskite-$BiVO_4$ or perovskite-Fe_2O_3 tandem assemblies (STH = 2.5 % and 2.4 % respectively),[15-16] polymer solar cell (STH = 3.1-5.4 %)[18] or dye sensitized solar cell (STH = 3.1 %).[17] The parameters that allowed us to improve the latter reported benchmarking are: *i*) the high fill factor (76%) of the employed triple junction cell, as opposed to the 55-60% obtained for similar configurations[18b] and *ii*) the high performance of the GC-RuO_2 electorode at pH 7, that operates at sufficiently low overpotential. Both parameters are keys to minimize the efficiency loss during operating conditions. Other successful PV-EC examples include series connected PV cells based on either perovskite[14] or CIGS[10] semiconducting materials that provide the desired voltage and reach STH higher than 10%. In these last two cases the conditions of the water splitting reaction are either strongly alkaline (1M NaOH) for the former or highly acidic (3M H_2SO_4) for the latter.

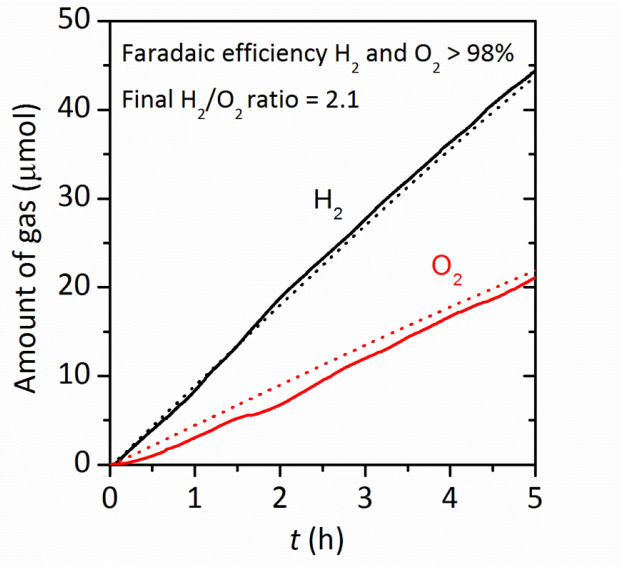

Figure 5. Gas evolution of a water splitting experiment using a triple junction solar cell (η_{TJSC} = 8.2%), GC-RuO_2 anode and SST-NiMoZn cathode in a two electrode configuration and a two-compartment cell, containing 0.1M phosphate buffer, pH = 7, under 1 sun irradiation (λ > 400 nm). The dotted lines represent the 100% faradaic efficiency based on the charge passed during electrolysis while the solid lines represent the gas measured with Clark electrode sensors.

In the same conditions and configuration described in Fig. 4 we performed experiments simulating a more realistic scenario where long term stability is crucial for practical implementation. Water splitting was performed using a larger electrochemical cell to fit higher quantities of gases produced. After a 16 h illumination period the cells were kept in the dark for 8 h, after which time the experiment was resumed. The triple junction cell showed remarkable stability retaining 87 % of its initial efficiency after the first experiment and 82 % after the second one. A third cycle was performed accounting for a total illumination time of 50h and maintaining a 79 % of the efficiency (Fig. S3 in the supporting information). The changes in the shape of the j/E curve and its fill factor bring the optimal power point of the solar cell to lower potentials and decrease the overall efficiency of the system; since the water splitting reaction works at a constant potential in the range of 1.70-1.80 V, the current that passes through the system becomes lower. However, it is remarkable to see that at the end of the 50h illumination time all parameters still show 75% of their initial value or higher. To the best of our knowledge, this is one of the few examples that a PV-EC device, not containing silicon or a III-V semiconductor, shows such remarkable stability when tested for this time periods. Recent results demonstrate that under the proper fabrication procedure, encapsulation and adequate UV filtering solar cells based on PTB7 polymers are very stable and could improve the performance at long time

experiments. Indeed, the backbone of the polymer does not show any degradation after more than 500 h under 1 sun continuous illumination.[28]

K 3 Conclusions

We have implemented a system where a 6% STH efficiency in the production of hydrogen is achieved at neutral pH. The system relies on a simple triple junction cell with an optimal light absorption and electrical performance. A cell FF as high as 76% allows for a water splitting reaction at a rate (current density) which is up to 96% the rate one would achieve if water splitting were to be carried out just above the thermodynamic potential threshold of 1.23V. In the triple junction studied the water splitting and the maximum power point are very close implying minimal electrical power losses. The catalysts used either for the oxidation or reduction part of the reaction use earth abundant materials or extremely small quantities of rare elements as Ru. To achieve a similar performance with the standard Pt electrodes one would have to raise the pH of the water solution to 14, otherwise at pH 7 the efficiency with such electrodes would remain close to just 3.5%. By anchoring Ru complexes on the surface of a glassy carbon rod, we have been able to reduce by several orders of magnitude the amount of RuO_2 needed with regard to previous anode configurations using that metal oxide. In such rod all the existing catalyst centers form a monolayer fully accessible to water molecules for oxidation, and the catalyst is highly active at pH 7. On the other hand, the electrical power is obtained from a PV cell based on a simple triple junction configuration where the three active layers are based on the same PTB7 polymer blend. PTB7 has been demonstrated to be one of the most efficient organic donor materials in photovoltaic cells. Additionally, PTB7 based cells are optimal for the development of a PV technology with a high potential for integration. Finally, recent work demonstrates that, contrary to results reported in prior studies, PTB7 based cells can be made very sable when the adequate cell fabrication procedure, encapsulation, and light filtering are applied.[28]

The system we report may ensure for the first time an eco-friendly large scale production of hydrogen from water at a neutral pH. The overall system is compact and has the potential to be fabricated at a low cost to effectively compete against other alternatives as hydrogen production from methane where the cost is low but the environmental impact is large. Last but not least, PTB7 based cells can be made semi-transparent which makes them an optimal technology for the integration in the glass façades of city buildings where the electricity consumption is largest and where an infrastructure for natural gas distribution, which can be effectively utilized for the distribution of hydrogen, is already existing.

K 4 Experimental section

Materials. The PTB7 and PFN polymers from 1-Material, $PC_{71}BM$ (purity > 99%) from American Dye Source and ZnO nanoparticles (N-10, 6083, 2.5 wt% in isopropyl alcohol) from Nanograde were used as received. Photoactive material PTB7: $PC_{71}BM$ (1:1.5 wt %) were dissolved in chlorobenzene/1, 8-diiodoctane (97:3 vol %) mixture solvent, at a total concentration of 25 mg/mL. PFN was dissolved in methanol (1.0 mg mL^{-1}) in the presence of small amount of acetic acid (10 µL mL^{-1}), which was filtered with 0.45µm PTFE filter prior to use. ZnO solution was diluted with isopropyl alcohol (1:1, vol %) prior to use. The ZnO formulation is very stable and the performance would not drop even when left in air for more than one year. Ruthenium molecular precursor $[Ru(bda)(NO)(N\text{-}N_2)_2][PF_6]_3$ and the derivative GC-RuO_2 electrodes were prepared according to the literature, details about area and catalyst loading can be found in the supporting information.[24] The SST-NiMoZn cathodes were prepared following a modified procedure found in the literature, details found in the supporting information.[11]

Device fabrication and characterization. Triple junction devices were fabricated by spin-casting ZnO solution on the pre-cleaned ITO patterned glass substrates (Lumtec, 15 Ω/sq) and annealing at 120 °C in glovebox for 10 min to form a 20 nm condensed electron transporting layer. The active layer of the front sub-cell (~ 60 nm) was then spin-coated on the ZnO surface and the films were dried under high vacuum (< 5×10^{-6} mbar) for one hour. Afterwards, interconnecting layer (ICL) of MoO_3 (10 nm, 0.5 Å /s)/ultrathin Ag (0.5 nm, 0.2 Å/s)/ PFN (10 nm) was deposited sequentially. Then, the active layer of the middle sub-cell (~ 105 nm) was spin-coated on the PFN surface, dried by vacuum for one hour. The second ICL was deposited using exactly the same procedure as the first one. The active layer of the rear sub-cell (~ 110 nm) was deposited on top of the second ICL and again left to dry in vacuum for 1 hour. Finally, MoO_3 (5 nm, 0.5 Å /s) and Ag (150 nm, 1 Å /s) electrodes were sequentially deposited through a shadow mask by thermal evaporation (< 5×10^{-6} mbar), which defines the device area of 9.0 mm^2. The triple-junction solar cells were encapsulated with glass slides using a UV-curable epoxy (ELC-4908, Electro-Lite Corp) in a N_2 glovebox before testing in ambient air. Current–voltage characteristics were measured under 1 sun AM 1.5G simulated sunlight (ABET Sol3A, 1000 W/m^2) with a Keithley 2420. The illumination intensity of the light source (Xenon lamp, 300W, USHIO) was determined using a Hamamatsu monocrystalline silicon reference cell calibrated by ISE Fraunhofer.

K 5 Acknowledgements

We acknowledge financial support from MINECO and the “Fondo Europeo de Desarrollo Regional” (FEDER) through grants MAT2014-52985-R, CTQ-2013–49075-R, SEV-2013-0319, and CTQ2014-52974-

REDC. We also acknowledge financial support from the EU COST actions CM1202 and CM1205, and the EC FP7 Program (ICT-2011.35) under grant agreement n° NMP3-SL-2013-604506. C.G.S. is grateful to AGAUR and GenCat for a "Beatriu de Pinós" postdoctoral grant. R.M thanks "La Caixa" Foundation for a PhD grant and Q.L acknowledges Erasmus Mundus doctorate program Europhotonics (Grant No. 159224-1-2009-1-FR-ERA MUNDUS-EMJD).

K 6 References

1 Betancur, R.; Romero-Gomez, P.; Martinez-Otero, A.; Elias, X.; Martorell J. *Nature Photonics* **2013**, 7, 995-1000.

2 Zhao, Y.; Meek, G. A.; Levine, B. G.; Lunt, R. R. *Adv. Opt. Mater.* **2014**, 2, 606-611.

3 Chen, Ch-Ch.; Dou, L.; Gao, J.; Chang, W-H.; Li, G.; Yang, Y. *Energy Environ. Sci.* **2013**, 6, 2714-2720.

4 Walter, M. G.; Warren, E. L.; McKone, J. R.; Boettcher, S. W.; Mi, Q.; Santori, E. A.; Lewis N. S. *Chem. Rev.* **2010**, 110, 6446-6473.

5 Ager, J. W.; Shaner, M. R.; Walczak, K. A.; Sharp, I. D.; Ardo, S. *Energy Environ. Sci.*, **2015**, *8*, 2811-2824.

6 Khaselev, O.; Turner, J. A. *Science*, **1998**, 280, 425-427.

7 Khaselev, O.; Bansal, A.; Turner, J. A. *Int. J. Hydrogen Energy*, **2001**, 26, 127-132.

8 Licht, S.; Wang, B.; Mukerji, S.; Soga, T.; Umeno, M.; Tributsch *H. Int. J. Hydrogen Energy* **2001**, 26, 653-794.

9 Cox, C. R.; Lee, J. Z.; Nocera, D. G.; Buonassisi, T. *Proc. Natl. Acad. Sci. U.S.A.* **2014**, 111, 14057-14061.

10 Jacobsson, T. J.; Fjällström, V.; Sahlberg, M.; Edoff, M.; Edvinsson, T. *Energy Environ. Sci.* **2013**, 6, 3676-3683.

11 Reece, S. Y.; Hamel, J. A.; Sung, K.; Jarvi, T. D.; Esswein, A. J.; Pijpers, J. J. H.; Nocera, D. G. *Science* **2011,** *334,* 645.

12 Vito, C.; Berardi, S.; Caramori, S.; Argazzi, R.; Carli, S.; Meda, L.; Tacca, A.; Bignozzi, C. *Phys. Chem. Chem. Phys* **2013,** *15,* 13083-13092.

13 Han, L.; Abdi, F. F.; van de Krol, R.; Liu, R.; Huang, Z.; Lewerenz, J.; Dam, B.; Zeman, M.; Smets, A. H. M. *Chem. Sus. Chem*. **2014**, 7, 2832-2838.

14 Luo, J.; Im, J-H.; Mayer, M. T.; Schreier, M.; Nazeeruddin, M. K.; Park, N-G.; Tilley, S. D.; Fan, H. J.; Grätzel, M. *Science* **2014,** *345,* 1593.

15 Chen, Y-S.; Manser, J. S.; Kamat, P. V. *J. Am. Chem. Soc.* **2015**, 137, 974-981.

16 Gurudayal, S. D.; Kumar, M. H.; Wong, L. H.; Barber, J.; Grätzel, M.; Mathews, N. *Nano Lett.* **2015**, 15, 3833-3839.

17 Brillet, J.; Yum, J-H.; Cornuz, M.; Hisatomi, T.; Solarska, R.; Augustynsky, J.; Grätzel, M. *Nature Photonics* **2012,** *6,* 824–830.

18 a) Shi, X.; Zhang, K.: Shin, K.; Ma, M.; Kwon, J.; Choi, I. T.; Kim, J. K.; Kim, H. K.; Wang, D. H.; Park, J. H. *Nano Energy*, **2015**, 13, 182-191. b) Esiner, S.; Willems, R. E. M.; Furlan, A.; Li, W.; Wienk, M. M.; Janssen, R. A. *J. Mat. Chem A* **2015**, 3, 23936-23945.

19 Esiner, S.; Van Eersel, H.; Wienk, M. M.; Janssen, R. A. J. *Adv. Mater.*, **2013**, 25, 2932-2936.

20 McCrory, C. C. L.; Jung, S.; Ferrer, I. M.; Chatman, S. M.; Peters, J.; Jaramillo, T. F. *J. Am. Chem. Soc.* **2015**, 137, 4347-4357.

21 Tsuji, E.; Imanishi, A.; Fukui, K.-I.; Nakato, Y. *Electrochimica Acta.* **2011**, 56, 2009-2016.

22 Licht, S.; Wang, B.; Mukerji, S. *J. Phys. Chem. B* **2000**, 104, 8920-8924.

23 Spurgeon, J.; Velazquez, J. M.; McDowell, M. T. *Phys. Chem. Chem. Phys*. **2014**, *16*, 3623-3631.

24 Duan, L.; Bozoglian, F.; Mandal, S.; Stewart, B.; Privalov, T.; Llobet, A.; Sun, L. *Nature Chem.* **2012**, 4, 418-423.

25 Matheu, R.; Francàs, L.; Chernev, P.; Ertem, M. Z.; Batista, V.; Haumann, M.; Sala, X.; Llobet, A. *ACS Catalysis*. **2015**, 5, 3422–3429.

26 Stachurski, J. Z. O.; Williamsville, D. P.; Ripa, J. A.; Pokrzyk, G. F. *U. S. Patent* **1982**, 4,354,915.

27 Nocera, D. G. *Acc. Chem. Res.* **2012**, *45*, 767-776.

28 Liu, Q.; Mantilla-Perez, P.; Montes Bajo, M.; Romero-Gomez, P.: Martorell, J. *to be published*.

29 Li, G.; Zhu, R.; Yang, Y. *Nature Photon.* **2012**, 6, 153-161.

30 Bahro, D.; Koppitz, M.; Mertens, A.; Glaser, K.; Mescher, J.; Colsmann, A. *Adv. Energy Mater.* **2015**, *5*, 1501019-1501019.

31 Martínez-Otero, A.; Liu, Q.; Mantilla-Perez, P.; Montes Bajo, M.; Martorell, J. *J. Mater. Chem. A* **2015**, 3, 10681-10686.

32 Mantilla-Perez, P.; Martínez-Otero, A.; Romero-Gomez, P.; Martorell, J. *ACS Appl. Mater. Interfaces* **2015**, 7, 18435-18400.

33 Martínez-Otero, A.; Elias, X.; Betancur, R.; Martorell, J. *Adv. Optical Mater*. **2013**, 1, 37-42.

34 Urbain, F.; Smirnov, V.; Becker, J-P.; Lambertz, A.; Rau, U.; Finger, F. *Sol. Energ. Mater. Sol. Cells* **2016**, 145, 142–147.

35 Kanan, M. W.; Nocera, D. G. *Science* **2008**, 321, 1072-1075.

36 Lutterman, D. A.; Surendranath, Y.; Nocera, D. G. *J. Am. Chem. Soc.* **2009**, 131, 3838-3839.

37 Esswein, A. J.; Surendranath, Y.; Reece, S. Y.; Nocera, D. G. *Energy Environ. Sci.* **2011**, 4, 499-504.

38 Zhong, D. K.; Choi, S.; Gamelin, D. R. *J. Am. Chem. Soc.* **2011**, 133, 18370-18377.

K 7 Supporting information

Paper K: Neutral water splitting with a high FF triple junction polymer cell

Outline

GC-RuO_2 anodes

Carbon substrates and geometric surface:

Glassy carbon rods (HTW®) of two different diameters (5 and 10 mm) were used as graphite support for the anodes. The geometrical surface of the anodes was estimated to be 4.1 cm^2 and 10 cm^2 respectively under our working conditions unless indicated differently. The former was used for 1.5h experiments in a 20 mL total volume electrochemical cell, and the latter was used for longer experiments (>1.5 h) in a 50 mL total volume electrochemical cell.

Procedure for pre-catalyst immobilization:

GC-RuO_2 were prepared according to the literature.[S1] A glassy carbon rod was immersed in a 0.5 mM solution of the ruthenium molecular precursor Ru-MP in acetone containing tetrabutylammoniumhexafluorophosphate (0.1 M) as supporting electrolyte. The glassy carbon rod was used as working electrode, a Pt wire as a counter electrode and SSCE as reference electrode in a three electrode configuration cell with a single compartment.

The GC-Ru-PC modified electrode was used as a working electrode in a three electrode configuration in a two compartment cell at pH 7. A current of 280 µA was applied to convert the grafted ruthenium pre-catalyst (GC-Ru-PC) to RuO_2based electrode (GC-RuO_2) (30 minutes for the rod d=5 mm and 45 minutes for the rod d=10 mm). The GC-RuO_2electrode was then washed with water and air-dried.

Catalyst loading, superficial concentration ($\boldsymbol{\Gamma}$) and TON

The amount of ruthenium catalyst was estimated by integrating the charge under the Ru(III)/Ru(II) redox wave of GC-Ru-PC in a cyclic voltammogram at pH=7 (Q_{Ru}).[S1] Q_{Ru} was used to calculate the superficial concentration and TON by applying the formulas $\Gamma\left(\frac{\mathrm{mol}}{\mathrm{cm}^2}\right) = \frac{\mathrm{QRu}}{\mathrm{A}\cdot\mathrm{F}}$ and $\mathrm{TON} = \frac{\mathrm{Q_{O_2}}}{4\cdot \mathrm{Q_{Ru}}}$. Where A is the geometrical area, F is the Faradaic constant and $\mathrm{Q_{O_2}}$is the charge of the produced oxygen assuming a 100% Faradaic

efficiency. The catalyst (ruthenium) superficial concentration of our GC-RuO_2 electrodes was 0.15 nmol Ru/cm^2.

SST-NiMoZn cathodes

NiMoZn was electrodeposited adapting the same method reported by Nocera.[S2] Stainless steel substrates were covered with tape to expose 1cm^2 and then pre-treated at -2V vs Ag/AgCl in 0.5M H_2SO_4 for 3 min. The NiMoZn was then deposited from a solution containing $NiCl_2 \cdot 6H_2O$ (0.04M), Na_2MoO_4 (0.17M), $Na_4P_2O_7 \cdot 10\ H_2O$ (0.077M), $NaHCO_3$ (0.89M) and $ZnCl_2$ ($3x10^{-4}$M), with hydrazine (0.018M) being added immediately before plating. The current density was 50 mA cm^{-2} for 1 h. Afterwards the deposit was immersed in 10% KOH for 1 night, washed thoroughly with water and dried under air.

ITO-CoPi anodes

CoPi was deposited on ITO, covering the substrate with Teflon tape to expose 1cm^2. A two compartment electrochemical cell with a glass frit junction was used. The working compartment contained a 0.5 mM solution of $Co(NO_3)_2 \cdot 6H_2O$ and 0.1M potassium phosphate (KPi) at pH 7, whereas the auxiliary side contained only KPi. The reference electrode was Ag/AgCl and Pt mesh was used as auxiliary electrode.The catalyst (cobalt) loading of the resulting electrodes was 0.30 µmol/cm^2.

Electrochemical methods

Instrumentation

All electrochemical experiments were performed using a PAR 263A EG&G potentiostat, IJ-Cambria HI-660D or IJ-Cambria HI-600D potentiostat.

IX

Supporting Electrolytes

Phosphate buffered solution (47 mM) was used as electrolyte for all electrochemical experiments at pH 7. Only phosphate anions (H_2PO4^-/HPO_4^{2-}) and K^+ contributed to the ionic strength (I = 0.1 M).

Electrochemical cell

A two-compartments cell of 10 mL per compartment with a separation frit was used for both two–electrode and three–electrodeconfiguration electrochemical experiments unless otherwise indicated. The electrodes were placed inside and connected to the potentiostat. The solution was purged with N_2 for 15-30 minutes prior to the performance of any experiment. A bigger cell (25 mL per compartment) with the same set up was used for experiments that were longer than 1.5h to collect larger amounts of hydrogen and oxygen gas.

Three electrode configuration experiments

All experiments were done in a two compartment cell, the reference and the working electrode were placed in the same and first compartment and the counter electrode was placed in the second compartment. The scan rate in Cyclic Voltammetries (CV) was 100 mV/s and *i*R compensation was applied. Chronopotentiometry was used to simulate a water splitting experiment with a solar cell, using analogous currents (+0.28 mA for the anode and --0.28 mA for the cathode).The counter electrode (CE) was a Pt mesh and the Reference Electrode (RE) was Ag/AgCl (KCl sat.). All the potentials are given against the Ag/AgCl (KCl sat.) unless indicated differently.

Two electrode configuration experiments (water splitting experiments using a triple junction OPV cell)

All experiments were done in a stirred two compartment electrochemical cell using 6mL of 0.1M potassium phosphate buffer (KPi) at pH7 in each compartment.The solution was purged with $N_2$for 15-30 minutes prior to the performance of any experiment.The amount of charge (Q) passing through the cell during the course of the experiments was measured by performing bulk electrolysis with a potentiostat at 0V bias, connecting the working lead to the ITO side of the solar cell and the reference and auxiliary leads

directly to the electrode working as a cathode. In this configuration, the potentiostat works as an ammeter. Although the resistance between the two electrodes was measured before and after the gas production (R ≈ 340-370 Ω), no *i*R compensation was applied.

The amount of hydrogen and oxygen generated by the reactions was measured in the headspaces of each compartment of the electrochemical cell with Clark electrodes (Unisense), waiting at the end of the illuminating period until the signal was no longer increasing. In several cases hydrogen gas was also measured by Gas Chromatography coupled to thermal conductivity detectors, with results being consistent with those obtained with the Clark electrode.

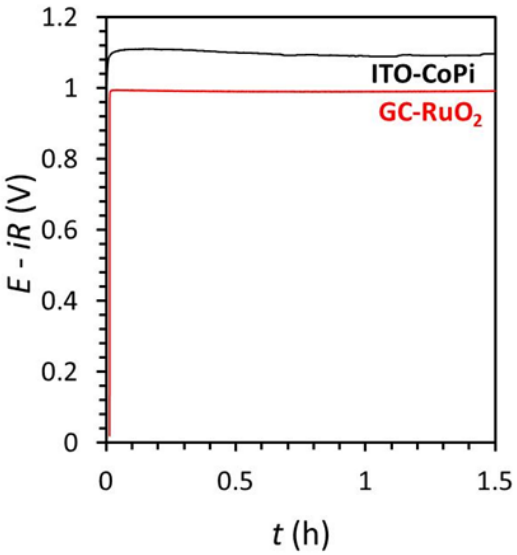

Figure S1. Chronopotentiometry experiments using a two-compartment electrochemical cell, 0.1M phosphate buffer, pH = 7, Ag/AgCl reference electrode, Pt mesh as counter electrode and GC-RuO_2 (d=5mm, red) or ITO-CoPi (black) as working electrode. The anodic current was set at 0.28 mA in both experiments. The potential is given versus the Ag/AgCl electrode.

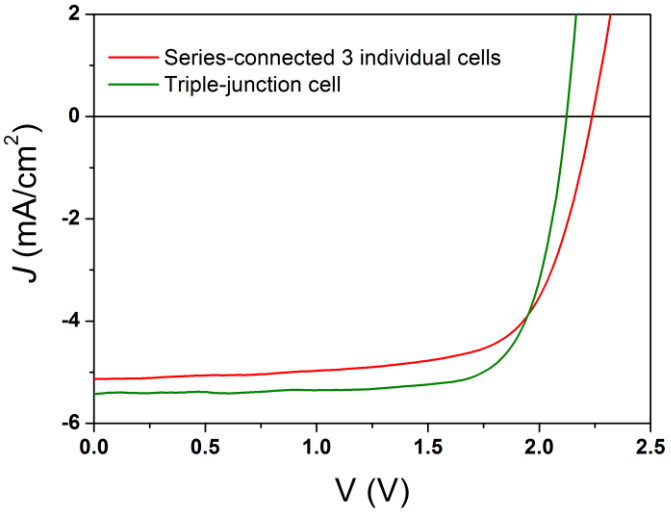

Figure S2. *J*-V curves of triple-junction solar cell and three series-connected solar cell.

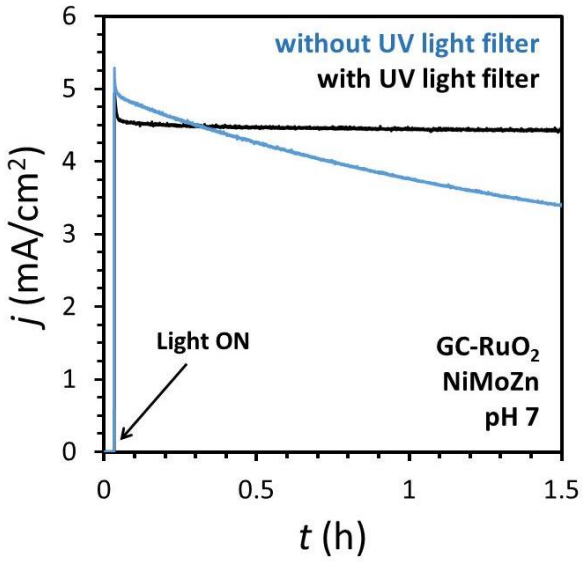

Figure S3. Current *vs* time profile of water splitting experiments using triple junction solar cell, GC-RuO_2 anode and NiMoZn cathode in a two compartment cell containing 0.1M phosphate buffer, pH = 7, under AM 1.5G illumination with a GG400 filter (black trace, η_{TJSC}= 8.2%), and without CG400 filter (blue trace, η_{TJSC} = 8.7%).

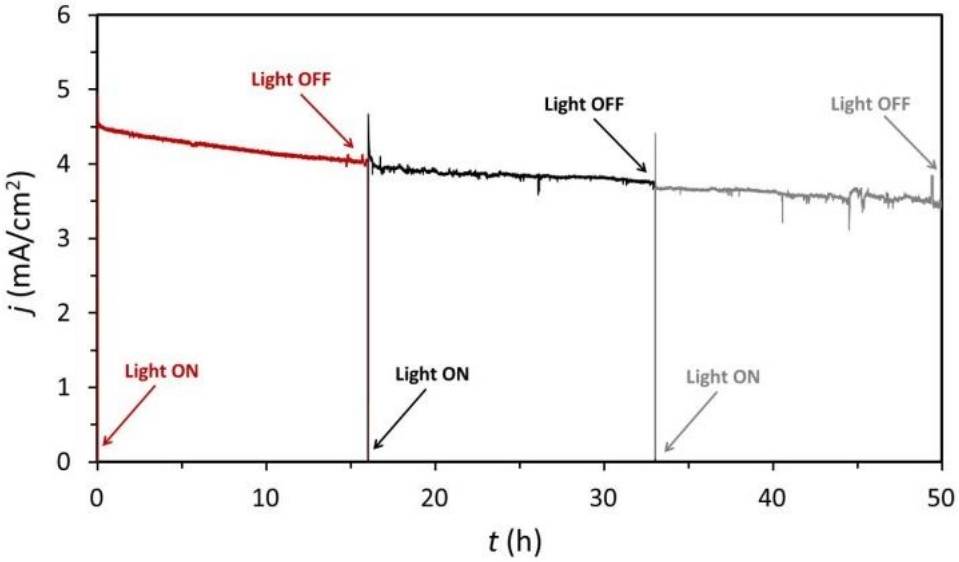

Figure S4. Stability tests of a water splitting experiment using a triple junction solar cell (η_{TJSC} = 8.5 %), GC-RuO_2 anode and SST-NiMoZn cathode in a two compartment cell containing 0.1M phosphate buffer, pH = 7, under AM 1.5G illumination with a

IX

GG400 filter. The current fluctuations are most likely due to the connection of the circuit with the top thin silver contact layer that slowly damages over time.

References

S1 Matheu, R.; Francàs, L.; Chernev, P.; Ertem, M. Z.; Batista, V.; Haumann, M.; Sala, X.; Llobet, A. *ACS Catal*. **2015**, 5, 3422.

S2 Reece, S. Y.; Hamel, J. A.; Sung, K.; Jarvi, T. D.; Esswein, A. J.; Pijpers, J. J. H.; Nocera, D. G. *Science* **2011**, *334,* 645.